

University of Naples Federico II
Department of Pharmacy



Pharmaceutical Sciences
XXX cycle

Design and development of new
nanosystems based on self-assembly
peptides for nanomedicine applications

Tutor Prof. Giancarlo Morelli

Tutor Dott.ssa Antonella Accardo

PhD student Carlo Diaferia



Non abbiamo bisogno di grandi spazi

Ma solo di piccolissime galassie

Per risuonare alla musica dei nostri corpi

1. Introduction

1.1 Bio-medical Imaging: basic principles and techniques	3-4
1.2 Magnetic Resonance Imaging and contrast agents	4-6
1.2.1 Gadolinium based T1 CAs: efficiency and analysis	6-9
1.2.2 Classical CAs based on Gd(III) ions	9-11
1.2.3 Improved supramolecula multi-Gd contrast agents	11-12
1.3 Photoluminescent phenomena	12-13
1.3.1 Fluorescence bio-imaging	13
1.3.2 Principle of fluorescence bio-imaging	14-15
1.3.3 Fluorochromes properties	15-17
1.4 Supremolecular chemistry as new tool for bio-imaging	18
1.4.1 Nanofabrication: bottom-up and top-down approach	18-21
1.4.2 Biomimicry approach: peptide for bottom-up	22
1.5 Amyloids: from pathogenicity to biomimicry starting point	23-24
1.5.1 Amyloid structure	24-25
1.5.2 Aromatic residues: denominator of amyloid fibril formation ..	25-27
1.6 Diphenylalanine: molecular and structural organization	27-29
1.6.1 Diphenylalanine ADNTs: preparation in water	29-30
1.6.2 Preparation by physical methods	30-31
1.6.3 Influence of solvent media	31
1.6.4 Chemical modification: homologues of FF sequence	31-33
1.6.5 Polymer decoration: amphiphilic derivatives	33-34
1.6.6 Application of supramolecula FF-based NPs	34-35

2. Purpose

2.1 Scope and thesis structure	39-41
--------------------------------------	-------

3. Results and discussion

3.1 Section I: Peptide-based materials as supramolecular CAs for MRI

3.1 Peptide-based materials for Magnetic Resonance Imaging	47-49
3.2 Elongation of aromatic framework (Strategy I)	50-51
3.2.1 Elongation of aromatic framework- N deritatization (Strategy Ia)	50-51
3.2.2 Determination of Critical Aggregation Concentration (CAC) ..	51-53
3.2.3 Secondary sctructure assignment	53-58
3.2.4 Solid state characterization: TEM and X-ray Diffraction	58-60
3.2.5 Relaxometry	60-62
3.2.6 Citotoxicity and MRI evaluation of the cellular uptake	62-64
3.3 Elongation of the aromatic framework- Gd containing telechelic PEG end-capped by FF motives (Strategy Ib)	64-65
3.3.1 Peptide synthesis	65-66
3.3.2 Stuctrural characterization	67-69
3.3.3 Secondary structure analysis	69-71
3.3.4 Relaxivity performaces	72-73
3.4 Extension of the aromatic side chian (Strategy II)	74
3.4.1 Synthesis and fluorescence studies	74

3.4.2	Structural characterization	74-78
3.4.3	NMR studies	78-79
3.4.4	Secondary structure assignment.....	79-82
3.4.5	Material characterization and molecular dynamics.....	82-86
3.4.6	Relaxivity performances.....	87-89
3.4.7	Doxorubicin loading assay	89-92
3.II	Section II: Photoluminescent peptide-based materials as supramolecular fluorescent probes	
3.5	Photoluminescent peptide-based nanostructure	95-96
3.6	Design, synthesis and fluorescence spectroscopy	96-98
3.6.1	Secondary structure.....	98-99
3.6.2	Congo Red assays	100-101
3.6.3	Dynamic Light Scattering analysis	101-102
3.6.4	Scanning Electron Microscopy.....	102-104
3.6.5	Wide-Angle and Small-Angle X-ray scattering.....	104-107
3.6.6	Photoluminescence in PEG ₈ -F6 nanostructures	108
3.6.7	Molecular modeling and dynamics.....	108-114
3.7	Photoluminescent peptide-based nanostructures as FRET donor for fluorophore dye	114
3.7.1	Synthesis and preparation of NBD-filled NSs.....	114-116
3.7.2	Structural characterization of NBD-filled NSs: secondary structure	116-118
3.7.3	Photoluminescence properties.....	118-122
3.7.4	Wide and Small-Angle X-ray scattering.....	122-125
3.7.5	Scanning Electron Microscopy	125
3.8	Effect of PEG derivatization on PL phenomena.....	126
3.8.1	Design, synthesis and fluorescence studies.....	126-129
3.8.2	Dynamic Light Scattering	130
3.8.3	Secondary structure characterization.....	130-132
3.8.4	Wide-Angle X-ray scattering	132-135
3.8.5	Scanning Electron Microscopy (SEM)	135-137
3.8.6	Photoluminescence in peptide nanofibers	137-140
3.III	Section III: Peptide-based materials obtained by punctual chemical modification of homophenylalanine sequences	
3.9	Hexapeptide containing Tyrosine residues	143
3.9.1	Synthesis and fluorescence on tyrosinate peptides.....	144-145
3.9.2	Structural characterization in solution	146-147
3.9.3	Structural characterization at solid state	147-149
3.9.4	Molecular modeling and dynamics.....	149-150
3.9.4.1	MD simulation of Y6 system.....	150-154
3.9.4.1	MD simulation of (FY)3 system	154-158
3.9.5	PEG ₈ -(YF)3 gels: rheological characterization	159-160
3.9.6	In vitro biocompatibility profiles of PEG ₈ -(YF)3 gels	160-161
3.10	Self-assembled tetra-tryptophan-based NPs	161-162
3.10.1	Synthesis of PEG6-W4	162-163
3.10.2	Secondary structure assignment.....	163-164
3.10.3	Structural characterization at solid state.....	164-166
3.10.4	Dynamic simulation	166-169

4. Experimental section

4.1 Materials and methods	173
4.2 Peptide and peptide conjugates synthesis.....	173-174
4.3 Preparation of peptide solutions and aggregates.....	174-175
4.4 UV-Vis peptide quantifications.....	175
4.5 Preparation of PEG ₈ -F6- NBD filled nanostructures.....	175
4.6 Preparation of gadolinium(III) and lanthanum(III) complexes	176
4.7 Fluorescence studies and determination of CAC	176
4.8 Circular Dichroism characterization	176-177
4.9 Fourier Transform Infrared spectroscopy (FT-IR)	177
4.10 Dynamic Light Scattering (DLS)	177
4.11 Congo Red (CR) spectroscopy assay.....	177
4.12 CR staining and polarize optical birifringence assay.....	177-178
4.13 Thioflavin T (ThT) spectroscopic assay	178
4.14 ¹ HNMR spectra and experiments	178-179
4.15 Transmission Electron Microscopy (TEM)	179
4.16 Scanning Electron Microscopy (SEM).....	179
4.17 Wide (WAXS) and Small-Angle-X-ray Scattering (SAXS)	179-180
4.18 Fluorescence and confocal microscopy	180
4.19 Water proton relaxation measurements.....	180
4.20 Rheological characterization of PEG8-(FY)3 gels.....	181
4.21 <i>In vitro</i> cytotoxicity studies.....	181-182
4.22 Cellular uptake studies	182-183
4.23 Doxorubicin loading and leakage.....	183
4.24 Molecular modeling and molecular dynamics simulations: systems and notations.....	183-184

5. Conclusion

5.1 General resume, outcomes and conclusions	187-191
----------------------------------------------------	---------

6. Appendixes

6.1 Appendix I	195-200
6.1.1 ¹ HNMR spectra	201
6.1.2 HPLC chromatograms and mass spectrometries	202
6.2 Appendix II	203-211

7. Publications

7.1 Full papers and published articles	215-226
----------------------------------------------	---------

Abbreviations	227-228
---------------------	---------

Bibliografic References	229-242
-------------------------------	---------

Riassunto

I materiali peptidici basati sull'aggregazione di monomeri anfifilici rappresentano, allo stato dell'arte, piattaforme versatili per la moderna scienza dei materiali. Attraverso un appropriato design ed utilizzando metodologie di "bottom-up", strutture supramolecolari ordinate possono essere generate spontaneamente grazie alla formazione di network di interazioni intra- ed inter-molecolari. La presenza di residui aromatici nella struttura primaria rappresenta un sostanziale e comune denominatore strutturale di questa variegata categoria di molecole.

Il capostipite di questa classe di monomeri aromatici è l'omodimero di fenilalanina (Phe-Phe) che, grazie ad una combinazione di interazioni di stacking e di legami ad idrogeno, è in grado di auto-organizzarsi in morfologie estremamente varie, sia nella nano che nella microscala. Gli omodimeri di difenilalanina e i suoi stretti omologhi hanno inoltre dimostrato peculiari caratteristiche fisiche (dal magnetismo alla piezoelettricità) che hanno consentito l'applicazione di tali sistemi nei campi dell'ottica e dell'elettronica. Tuttavia, la spiccata natura aromatica di tali molecole si traduce prevedibilmente in bassi valori di solubilità intrinseca in acqua, fattore quest'ultimo che ha limitato fortemente le prospettive di applicazione nel campo biomedico.

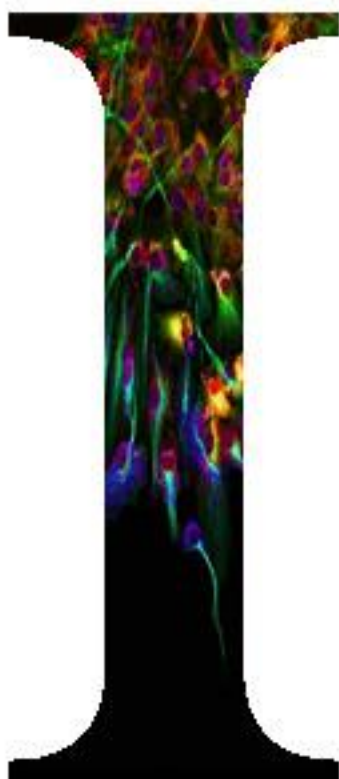
Il presente progetto di dottorato in Scienza del Farmaco (XXX ciclo) ha avuto come scopo la progettazione e lo sviluppo di nuove nanoplateforme basate su peptidi aromatici come sonde per l'imaging diagnostico, con particolare riferimento alle tecnologie MRI (Magnetic Resonance Imaging) e all'imaging in fluorescenza. Questo obiettivo è stato perseguito attraverso un approccio di design chimico razionale sui monomeri costituenti, inserendo opportune modifiche chimiche di sequenza (sostituzioni di residuo, utilizzo di aminoacidi non codificati, alternanza di residui, allungamento del framework amminoacidico) e funzionalizzazioni puntuali (inserzioni di catene PEG, decorazione con chelanti polidentati, complessazione di metalli di interesse diagnostico). La caratterizzazione e lo studio dei nuovi sistemi proposti è stata perseguita attraverso l'utilizzo di tecniche complementari.

Nello specifico, la derivatizzazione di sequenze omopeptidiche (basate su fenilalanina e naftilalanina) con chelanti polidentati per la complessazione di ioni paramagnetici come lo ione Gd(III) ha portato allo sviluppo di una nuova classe di mezzi di contrasto T₁ supramolecolari per MRI. Come ampiamente dimostrato dalla caratterizzazione sia in soluzione che allo stato solido, i nuovi monomeri proposti si auto-organizzano in nanoarchitetture fibrillari con buoni valori di solubilità in acqua e struttura secondaria di tipo β -sheet antiparallelo. L'evidenza di un effettivo incremento del contrasto positivo

delle immagini e l'incapsulamento di molecole farmacologicamente attive apre prospettive di sviluppo di tali sistemi nel campo della medicina teranostica.

L'aggregazione di sequenze di omo-fenilalanine (esaPhe PEGylate) in stabili materiali ricchi in β -sheet è risultata, inoltre, essere correlata a fenomeni di fotoluminescenza. Grazie all'incapsulamento o al confinamento di opportuni fluorofori come l'NBD (4-nitro-7-clorobenzofurazano) ed attraverso fenomeni FRET, la fotoluminescenza intrinseca è stata spostata a più alte lunghezze d'onda (vicino infrarosso). L'incremento del numero di legami ammidici nella porzione PEG in una serie omologhi strutturali ha inoltre evidenziato un red-shift del picco di emissione intrinseco in funzione del numero di legami ammidici.

Le possibili relazioni tra la sequenza chimica dei monomeri peptidici, l'organizzazione finale delle nanostrutture e le caratteristiche fisiche del materiale sono state esplorate attraverso la sintesi di analoghi di sequenza. Nel dettaglio, la parziale o totale sostituzione nella porzione peptidica dei residui di Phe con tirosina (Tyr) ha messo in luce la possibilità di ottenere idrogel peptidici con alti profili di biocompatibilità. L'analisi dell'organizzazione di omologhi di tetra-triptofano (W_4) ha evidenziato l'importanza dei parametri sterici nell'impacchettamento supramolecolare della struttura.



Introduction

Magnetic Resonance Imaging, fluorescence imaging, self-assembly and diphenylalanine-based supramolecular systems

Carlo Diaferia | University of Naples Federico II | XXX cycle

1.1 Bio-medical imaging: basic principles and techniques

Bio-imaging or optical biological imaging is computer vision technology that takes advantage from artificial vision to acquire, capture, extract, process and present structural or functional images of bio-objects or bio-systems. Using a variety of equipment to extract information from biological samples, optical biological imaging is based on the optical contrast (in terms of light reflection, difference of transmission and fluorescence intensity) between the selected samples and the surrounding background region. During the last decades, medical imaging and microscope/fluorescence processing have been taken on a central role referring to the methodologies used to produce images of the human body.¹ These visualisation methods offer the useful advantage to allow a multidimensional analysis scale, from macroscopic anatomical areas, tissues, down to the microscopic cellular, intra-plasmatic and molecular levels (**Figure 1**).

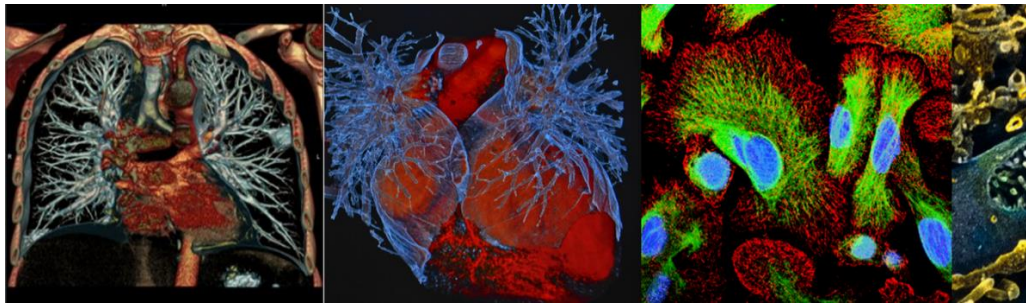


Figure 1: Multidimensional scale of a bio-imaging analysis, from anatomical sectors to organs, cells and organelles.

Consequently, bio-medical imaging techniques have become ones of the most beneficial tools in healthcare science for the diagnosis and treatment of human pathological states. The evolution of bio-medical visualizing techniques from radioisotope imaging to more complex and sensible methodologies, such as Computer-Assisted Tomography (CAT scans), Magnetoencephalogram (MEG), Positron Emission Tomography (PET) and ultrasound imaging, has led to revolutionary improvements in the quality of healthcare available today.²

However, the urgency of more accurate information about the early cellular and molecular pathological contexts explains clearly the need for extending deeply bio-imaging to these organization levels. This knowledge may support rapid detection, screening, diagnosis, and image-guided treatment of life-threatening diseases such as cancer, metabolic inborn errors and neurodegenerative diseases.

Nanotechnology can help in this sense. Innovative nanomaterials (NMs) and nanostructured platforms (NPs) had and have a revolutionary and radical impact to the modern science and technology.^{3,4,5}

One of the important potential applications of nanoparticles is their use as tracer⁶, marker⁷ or contrast agents⁸ for *in vitro* and *in vivo* optical biological imaging. Indeed, nano-particles can offer a number of advantages, including tunable physical properties (e.g. luminescence and ferromagnetism), high stability (e.g. against photobleaching), possibility of targeted delivery, and specific binding *via* chemical functionalization, multimodality (ability to combine several functions in one particle), high sensitivity and selectivity.^{3,4,5}

A number of different limitations affects the currently used medical bio-imaging techniques. Some of them regard the noxious effect of ionizing radiations (X-ray and CAT scan)⁹, the harmful effect of radioactivity (in radioscopic techniques)¹⁰, the low sensibility (e.g. MRI, Magnetic Resonance Imaging)¹¹, the inability to provide resolution smaller than millimetres (as reported for ultrasound imaging)¹² and the general impossibility to distinguish between different pathological compartments (e.g. benign and malignant tumours).¹³

Combining the traditional techniques with the new field of nanotechnology, NMs and NPs can help to overcome some of the previous reported limitations. For this, nanostructured materials became promising tools for a range of bio-imaging techniques.¹⁴

Referring to the object of this PhD final thesis, applications of self-assembly peptide-based materials (PBMs) will be delve into the Magnetic Resonance Imaging (MRI) for obtain T₁ contrast agents and fluorescence imaging.

With the aim of design and perfect innovative and potential bio-imaging nanoprobe and tracers, an initial comprehension of the physical basis of MRI, fluorescence and self-assembly is required.

1.2 Magnetic Resonance Imaging and contrast agent

Magnetic resonance imaging is a non-invasive medical diagnostic bio-imaging procedure. This technique provides images by detecting tiny changes in the structures within the body. In many cases, MRI gives different information about structures in the body that cannot be seen with an X-ray, ultrasound, or CAT scan.

MRI technology is based on the same principles of hydrogen nuclear magnetic resonance (¹HNMR). Detectable signals are generated measuring parameters related to the relaxation of hydrogen nuclei of water excited by magnetic fields.^{15,16} An additional magnetic field in gradient allows retrieving the spatial information in order to obtain 3D images for MRI experiment. (**Figure 2**).

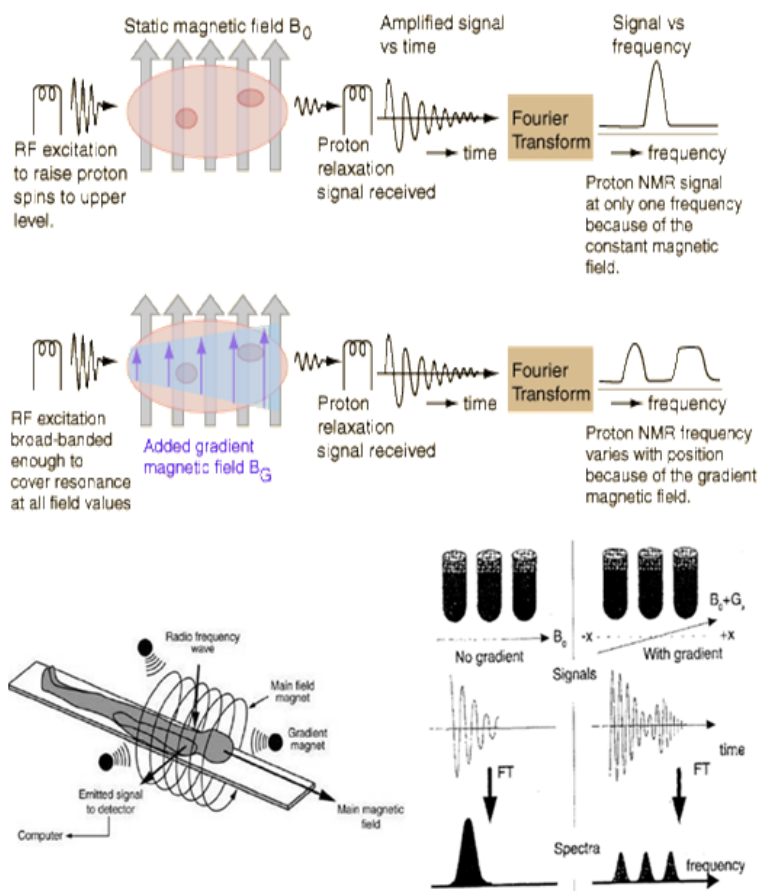


Figure 2: Schematic representation of MRI based physical phenomenon and its application in bio-imaging.

Three parameters affect MRI acquisitions: proton density, longitudinal relaxation time (T_1) and transverse relaxation time (T_2). The variation in the proton density between tissues is not very relevant, so the pulse sequence that measures T_1 and T_2 provides the necessary contrast for diagnosis. Contrast agent (CAs) can enhance the quality of the images in terms of contrast, improving the sensitivity and specificity of MRI technique.¹⁷

The CAs can be classified in two categories, T_1 or T_2 , depending on the ratio between two specific parameters, longitudinal relaxivity (r_1) and the transverse relaxivity (r_2). T_1 agent have an r_2/r_1 slightly higher than 1, give a positive contrast and are usually based on paramagnetic ions (primarily complexes of paramagnetic ions such as Gd, gadolinium)¹⁸, whereas T_2 agent have much higher (>10) ratios, give a negative contrast and are

Introduction: MRI, fluorescence and FF self-assembly systems

based on superparamagnetic compound (especially superparamagnetic iron oxide, *SPIOs*).¹⁹

The performance of a CA agent is evaluated by relaxivity parameter, *R*. Relaxivity described the efficacy of the contrast agent at 1mM concentration in changing the rate of water proton relaxation.²⁰ The physical relaxation process is due to dipole-dipole interactions between the proton nuclear spins and the fluctuating local magnetic field that results from the paramagnetic or superparamagnetic metal center.

1.2.1 Gadolinium based T1 CAs: efficiency analysis

Gadolinium complexes are the most common paramagnetic compounds for obtain T₁ CAs.

Gadolinium (electron configuration: [Xe] 4f⁷5d¹6s², atomic number 64) is a silvery-white, malleable, and ductile rare earth metal. It is found in nature only in oxidized form, and even when separated, it usually has impurities of the other rare earths. Like most of the rare earths, Gd forms trivalent ions with fluorescent properties, and salts of Gd(III) are used as phosphors in various applications.

Due to the high magnetic moment of the paramagnetic Gd³⁺ ion (with its seven unpaired electrons), the relaxation time of water molecules in the proximity of Gd³⁺ ions is greatly reduced and signal intensity is thereby enhanced (**Figure 3**).

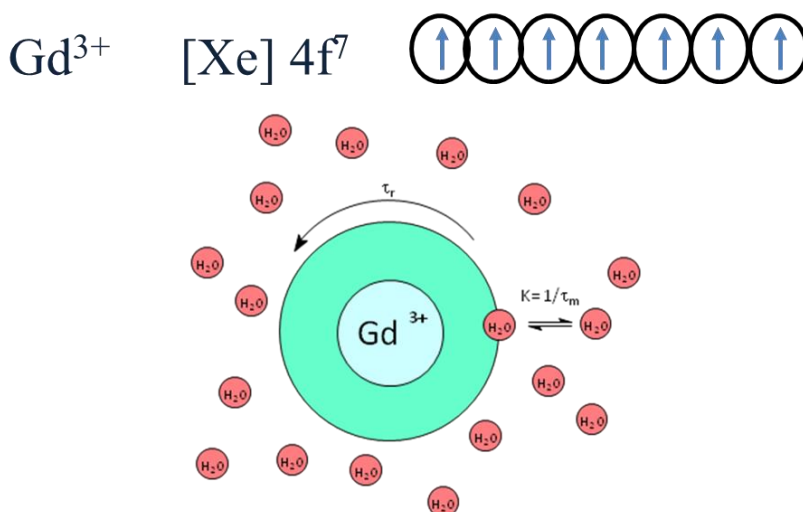


Figure 3: External electronic configuration of paramagnetic Gd³⁺ ions and their influence of water exchange rate (*K*).

The kinds of Gd(III) ions occurring in water-soluble salts are toxic to mammals.²¹ However, chelated Gd³⁺ adducts are far less toxic because they carry the metal through the kidneys for excretion before the free ion can be released into the tissues. For this reason, Gd(III) based CAs are manufactured by a chelating process. The chelating agent, acting as Lewis's base, forms a stable complex around the metal center, saturating seven or eight coordination position and leaving one or two free positions for water molecules.

The coordinated water molecules give a direct contribution to the relaxivity, while the bulk solvent molecules experience the paramagnetic effect when they diffuse around the metal centre.²² These two interactions give the most important contributes to the observed relaxivity and are known as the inner-sphere relaxation rate and outer-sphere relaxation rate, respectively. In addition, water molecules may be retained in the periphery of the coordinated centre by hydrogen bonds for a relatively long time. This phenomenon is referred as the second-sphere relaxation effect.⁸

The overall measured relaxivity (R_1^{obs}) is, thus, a result of different contributions as indicated by **Equation 1**:

$$R_1^{obs} = R_{1\rho}^{IS} + R_{1\rho}^{SS} + R_{1\rho}^{OS} + R_1^W \quad (1)$$

Where $R_{1\rho}^{IS}$, $R_{1\rho}^{SS}$ $R_{1\rho}^{OS}$ are the inner-sphere, the second-sphere and outer-sphere relaxation enhancement in the presence of the paramagnetic complex at 1mM concentration, respectively, and R_1^W is the relaxation rate of the water solvent in the absence of the paramagnetic complex.^{23,24,25}

The inner sphere contribution depends on four factors that, according to **Equation 2**, are: i) the molar concentration of the paramagnetic complex [C], ii) the number of water molecules coordinated to the paramagnetic center, q , iii) the mean residence lifetime of the coordinated water protons τ_m , and iv) their relaxation time, T_{1M} .^{23,24}

$$R_{1\rho}^{IS} = \frac{q[C]}{55.5(T_{1M} + \tau_m)} \quad (2)$$

From **Equation 2**, it is clear that increasing the hydration number, q , will increase the inner-sphere relaxivity. However, an increase in q is often accompanied by a decrease in thermodynamic stability and/or kinetic inertness. T_{1M} , is directly proportional to the sixth power of the distance, r_{GdH} , between the metal centre and the coordinated water protons.

Introduction: MRI, fluorescence and FF self-assembly systems

Moreover, T_{1M} depends from the molecular reorientation time, τ_r , of the chelate, from the applied magnetic field strength, from the electronic relaxation times, T_{iE} ($i = 1, 2$), of the unpaired electrons of the metal (which also depends on the applied magnetic field strength) according to the modified Solomon-Bloembergen equations (**Equation 3** and **Equation 4**):

$$\frac{1}{T_{1M}} = \frac{2}{15} \left(\frac{\mu_0}{4\pi} \right) \left[\frac{\gamma_I^2 g^2 \mu_B^2 S(S+1)}{r_{GdH}^6} \right] \chi \left(\frac{7\tau_{c2}}{1 + \omega_s^2 \tau_{c2}^2} + \frac{3\tau_{c1}}{1 + \omega_I^2 \tau_{c1}^2} \right) \quad (3)$$

$$\frac{1}{\tau_{ci}} = \frac{1}{\tau_R} + \frac{1}{\tau_M} + \frac{1}{T_{iE}} \quad (4)$$

in which γ_I^2 is the square of nuclear giromagnetic ratio, S is the electron spin quantum number (7/2 for Gd(III) ions), g is the electron g -factor, μ_B is the Bohr magneton, r_{GdH} is the electron spin – proton distance, ω_I and ω_S are the nuclear and electron Larmor frequencies respectively, τ_r is the rotational correlation time, related to the reorientation of the metal ion-solvent nucleus vector, and τ_{c1} and τ_{c2} are longitudinal and transverse electron spin relaxation times.

Relaxivity of the contrast agents can be increased, by introducing structural modifications on ligands with the aim to influence the three parameters τ_r , τ_m and T_{iE} .^{26,27} The exchange lifetime τ_m can represent a limiting factor to the attainable relaxation enhancement promoted by the gadolinium complexes. The τ_m is inversely proportional to the water exchange rate ($K_{ex} = 1/\tau_m$). Thus, an increase in the relaxivity can be achieved by increasing the water exchange rate up to an optimal value of exchange rate.

The tuning of the steric environment in the proximity of the Gd(III) centre can increase the dissociative water exchange rate as well as the increase relaxivity.²⁸

At the frequencies most commonly used in commercial tomographs (20 – 60 MHz), the molecular reorientational time τ_r of the Gd(III) chelates is the most important determinant of the observed relaxivity. Therefore, the achievement of higher water proton relaxation rates may be pursued through an increase of this parameter, since the increase of the number of the metal bound water molecules (q), which would lead to the same result, is likely accompanied by a decrease of the stability of the complex. Several strategies are developed in order to lengthen τ_r from a typical range of 50–90 ps to hundreds of picoseconds.

It has been shown that the effectiveness of Gd(III) complexes as CA may be significantly improved by using protein-chelate conjugates in which the metal complex is covalently attached to amino acid residues of the protein²⁹ or by non-covalently binding of the complex to macromolecules.³⁰ This kind of approach permits to couple the strong chelation of the metal ion with the slow molecular tumbling of the macromolecules.

The outer sphere contribution (R_I^{obs}) depends on T_{iE} , on the distance of maximum approach between the solvent and the paramagnetic solute, on the relative diffusion coefficients and again on the magnetic field strength.²⁶

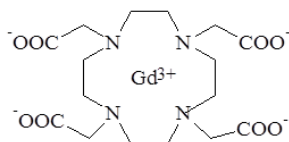
The contribution of the magnetic field strength to the $R_{1\rho}^{IS}$, $R_{1\rho}^{SS}$ and R_I^{obs} values is very important, in fact the analysis of the magnetic field dependence allows the determination of the principal parameters characterizing the relaxivity of a Gd(III) complex. This information can be obtained through a Field-Cycling Relaxometer, an NMR instrument in which the magnetic field is changed to obtain the measure of r_1 on a wide range of frequencies, typically 0.01 – 50 MHz.¹⁰

1.2.2 Classical CAs based on Gd(III) ions

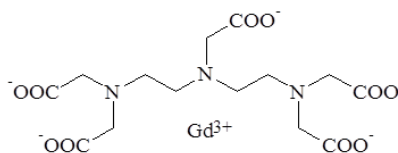
The first gadolinium-based MRI contrast agent, the Gd(III) complex Gd-DTPA (Magnevist®), was prepared by Schering AG in 1981 and approved for clinical use in 1987. It has been administered to more than 20 million patients in more than 15 years of clinical experimentation. Other Gd(III) complexes which became soon available are Gd-DOTA (Dotarem®, Guerbert SA, France), Gd-DTPA-BMA (Omniscan®, GE Health, USA), Gd-HPDO3A (Prohance®, Bracco Imaging, Italy), Gd-MS-325 (Ablavar®, BayerSchering Pharma, USA) and Gd-DTPA-BMEA (OptiMARK®, Mallinckrodt, USA) (**Figure 4**).

These compounds, as all clinical CAs, are regarded as non-specific agents or extracellular fluid space (EFS) agents. They present very similar pharmacokinetic properties because they distribute in the extracellular fluid and are eliminated via glomerular filtration. They are particularly useful to delineate lesions as a result of the disruption of the blood–brain barrier. Successively, two other derivatives of Gd-DTPA have been introduced in the market, Gd-EOBDTPA³¹ (Eovist®, Schering AG, Germany) and Gd-BOPTA (Multihance®, Bracco Imaging, Italy).³² They are characterized by an increased lipophilicity due to the introduction of an aromatic substituent on the carbon backbone of the DTPA ligand. This modification significantly alters the pharmacokinetics and the biodistribution of these CA as compared to the parent Gd-DTPA.

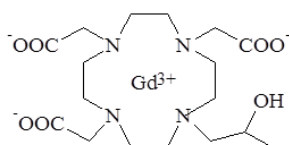
Introduction: MRI, fluorescence and FF self-assembly systems



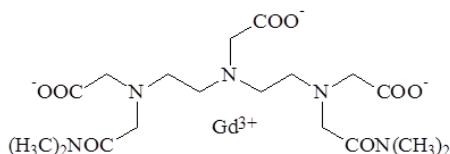
Gd-DOTA
DOTAREM®, Guerbert SA, France



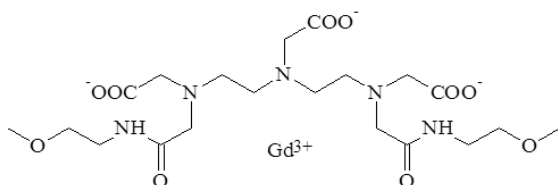
Gd-DTPA
MAGNEVIST®, Schering AG, Germany



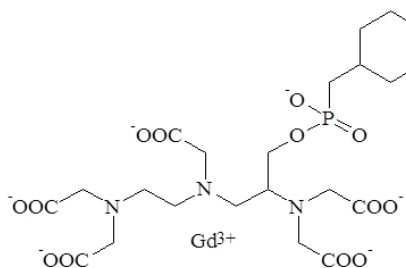
Gd-HPDO3A
PROHANCE®, Bracco Imaging, Italy



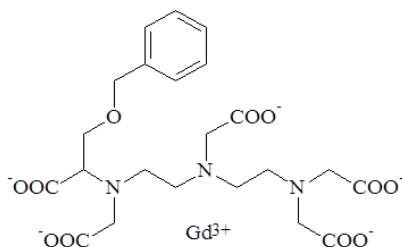
Gd-DTPA-BMA
OMNISCAN®, GE Health, USA



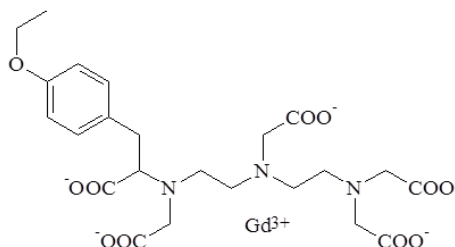
Gd-DTPA-BMEA
OPTIMARK®, Mallinckrodt, USA



Gd-MS-325
ABLAVAR®, BayerSchering Pharma, USA



Gd-BOPTA
MULTIHANCE®, Bracco Imaging, Italy



Gd-EOB-DTPA
EOVIST®, Schering AG, Germany

Figure 4: Structures of the six Gd(III) based MRI contrast agents (DOTAREM®, MAGNEVIST®, PROHANCE®, OMNISCAN®, MS-325 Ablavar®, OptiMARK®) currently used in the clinical practice, and of the two hepatobiliary agents (MULTIHANCE® and EOVISt®) which present pendent hydrophobic phenyl ring as aromatic substituent on the carbon backbone of the DTPA ligand.

These hepatobiliary agents have affinity towards HAS and are specifically uptaken by the hepatocytes. They are partially excreted through the biliary system and the kidneys. By comparing the structure of hepatic agents with that of EFS agents, the liver specificity can be ascribed to the pendent hydrophobic phenyl rings. Both MultiHance® and Eovist® have a faster water exchange rate ($k_{ex} = 7.0 \times 10^6 \text{ s}^{-1}$) and a shorter r_{GdH} than those of Magnevist® because of a more steric environment for water exchange.³³

1.2.3 Improved and supramolecular multi-Gd CAs

The previously reported gadolinium complexes clinically have promising relaxivity behaviour, diffusion, and penetration that can be modified according to different physiological states. The classical Gd complexes are characterized by low molecular weight and rapid *in vivo* elimination and extravasation out of the vasculature that reduces contrast from the neighbours tissue.³⁴

Macromolecular gadolinium complexes have been designed with a molecular weight greater than 30 kDa limiting the extravasation, but favoring the enhanced permeability and retention (EPR).

A relevant aspect of these compounds is the increase of the relaxivity *per* unit dose of the paramagnetic ion. Because of their size, the τ_m is longer than the low molecular weight agents as Magnevist or Dotarem. Additional advantage is the opportunity to append to a macromolecular platform multiple chelates reducing the dose of agent needed for obtaining well-resolved images.

For all these reasons, research was voted to increase relaxivity properties and targeting ability.³⁵ In order to reach this goal, several contrast agents, with improved properties, have been proposed:

- “*multimeric or macromolecular contrast agents*” in which a large number of gadolinium complexes are combined together and the total relaxivity results from the single contribution of each gadolinium ion.^{36,37}
- “*smart contrast agents*” in which a change in the relaxivity value is observed upon activation in the *in vivo* environment where they act.³⁸ Smart contrast agents, also referred to as responsive or activated CAs, are agents that react to variables in their environment, such as temperature³⁹, pH⁴⁰, partial pressure of oxygen⁴¹, metal ion concentration⁴² or enzyme activity⁴³, giving a strong increase or decrease of the observed relaxivity.

Introduction: MRI, fluorescence and FF self-assembly systems

- “target selective contrast agents” in which the gadolinium complex is delivered in a selective way on cells or on tissues of interest by bioactive molecules such as peptides or antibodies.^{44,45}

A plethora of improved and supramolecular multi-Gd CAs have reported over the last 30 years such as dendrimers,⁴⁶ linear polymers,⁴⁷ gadofullerenes,⁴⁸ gadonanotubes,⁴⁹ or large protein derivatives obtained by using the strong interaction present in the avidin-biotin or in the β -cyclodextrin-dextran complexes (**Figure 5**).⁵⁰

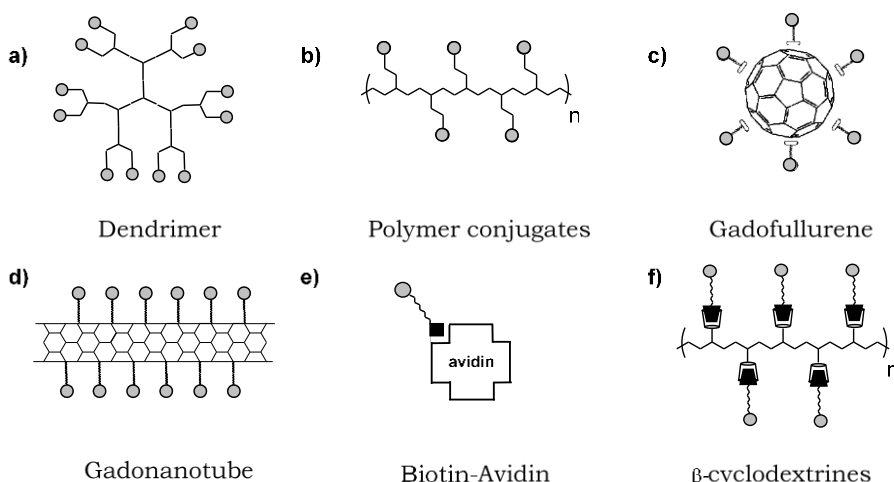


Figure 5: Schematic representation of macromolecular adducts: a) dendrimers; b) linear polymers; c) and d) carbon nanotubes such as gadofullerenes and nanotubes externally derivatized by stable gadolinium complexes, respectively; e) macromolecular adducts obtained by non-covalent interactions between high molecular weight molecules such as avidin or β -cyclodextrin polymers with monomeric gadolinium complexes of biotin or dextran.

1.3 Photoluminescent phenomena: fluorescence and phosphorescence

The totality of phenomena that involves energy absorption and subsequent emission of light are referred generically under the term of photoluminescence (PL). Excitation as consequence of photons absorbance leads to a major class of technically important luminescent molecular entities, correlated to fluorescence and phosphorescence. In a simplistic vision and in the time scale, fluorescence is “fast” phenomenon (requiring ns) while phosphorescence is a “slow” one (longer in time scale, up to hours or even days).

For convenience, the topic of photoluminescence (PL) will be broadly divided into that based on relatively large-scale inorganic materials, mainly exhibiting phosphorescence, and that of smaller dye molecules and new nanomaterials, which can either fluoresce or phosphoresce.⁵¹ Phosphors and fluorophores are luminescent materials that release light when excited by specific wavelength radiation. They are usually microcrystalline powders chemically designed and modified to provide emission in the visible portion of the spectrum (350-700 nm). After decades of research and development, thousands of PL molecules have been synthesized and optimized. In the prospective of this thesis, central role will be give to fluorescence supramolecular probes for potential application in bio-imaging.

1.3.1 Fluorescence bio-imaging

Fluorescent labelling and staining, when combined with an appropriate imaging instrument, is a sensitive and quantitative method that is widely used in molecular biology and biochemistry fields for a variety of experimental, analytical, and quality control applications.^{52,53} The concentrations, chemical modifications, and interactions of biomolecules in complex organisms are generally precisely controlled, both spatially and temporally.

As previously mentioned, deciphering this complex system of interacting molecules inside and among the cells can help the diagnosis and treatment of disease, as well as for research into the basic processes of life.

Fluorescence bio-imaging is an optical imaging technique that uses fluorescence and phosphorescence instead of, or in addition to, reflection and absorption optic phenomena to study the properties of organic or inorganic substances. Compared to other technologies, such as radioisotope labeling, CT, ESR, and electrochemical detection, fluorescent detection and imaging offer a number of important advantages for this purpose, as it enables highly sensitive, multiple label possibility, low hazard, non-invasive, and safe detection using readily available instruments. Another advantage of fluorescence bio-imaging is that the fluorescence signal of a molecule can be drastically modulated and give information about surrounding space.

For bio-imaging application, fluorescent probes are administered to the subject and emit a signal within the body. Fluorescent probes are found be molecules that can interact specifically with biological molecules to induce a concomitant change of their photochemical properties (in terms of fluorescence intensity, excitation/emission wavelength).⁵⁴

1.3.2 Principle of fluorescence imaging

Fluorescence results from a process that occurs when certain molecules (generally polyaromatic hydrocarbons or heterocycles) called fluorophores, fluorochromes, or fluorescent dyes absorb light. Fluorescence phenomenon is simply recapitulated by Jablonski diagram (reported in **Figure 6**), illustrating the processes involved in creating an excited electronic singlet state by optical absorption and subsequent emission of fluorescence.⁵¹ The absorption of light by a population of molecules raises their energy level to a brief excited state (S_1'). As they decay from this excited state, they emit fluorescent light.

The excited state of a fluorophore is characterized by a very short half-life, usually in the order of a few nanoseconds.⁵⁵ During this brief period, the excited molecules generally relax toward the lowest vibrational energy level (S_1) within the electronic excited state (**Figure 6**). The energy lost in this relaxation is generally dissipated as heat. It is from the resulting relaxed singlet excited state (S_1) that fluorescence emission originates.⁵¹

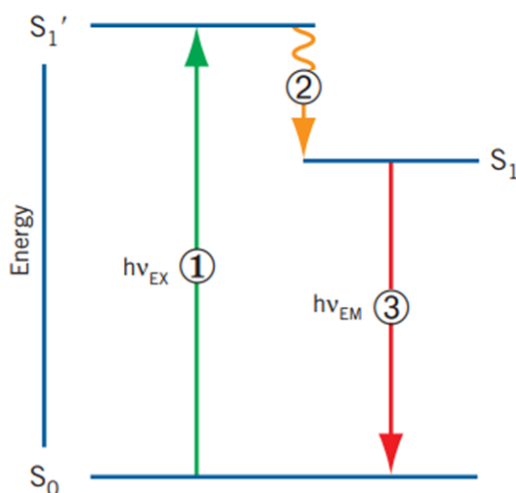


Figure 6: Fluorescence phenomenon is simply illustrated by Jablonski diagram. Process involved in the phenomenon are 1) Excitation; 2) Vibrational relaxation; 3) Emission.

When a fluorochrome molecule falls from the excited state to the ground state, light is often emitted at a characteristic and specific wavelength. The energy of the emitted photon ($h\nu_{EM}$) is related to the difference between the energy levels of the two states.

The energy difference determines the wavelength of the emitted light (λ_{EM}) according to the sequent relation:

$$\lambda_{EM} = hc/E_{EM}$$

in which E_{EM} is the energy difference between the energy levels of the two states during emission (EM) of light, h is the Planck's constant and c represents the speed of light.

A laser-scanning instrument or a CCD-camera can be used to measure the intensity of the fluorescent light and subsequently create a digital image of the sample. Image analysis makes it possible to view, measure, render, and quantify the resulting image.

3.3 Fluorochromes properties

A fluorescent molecule has two characteristic spectra- the excitation and the emission spectra.

The relative probability that a fluorochrome will be excited by a given wavelength of incident light is shown in its excitation spectrum. This spectrum is a plot of total emitted fluorescence versus excitation wavelength, and it is identical or very similar to the absorption spectrum (**Figure 7**).

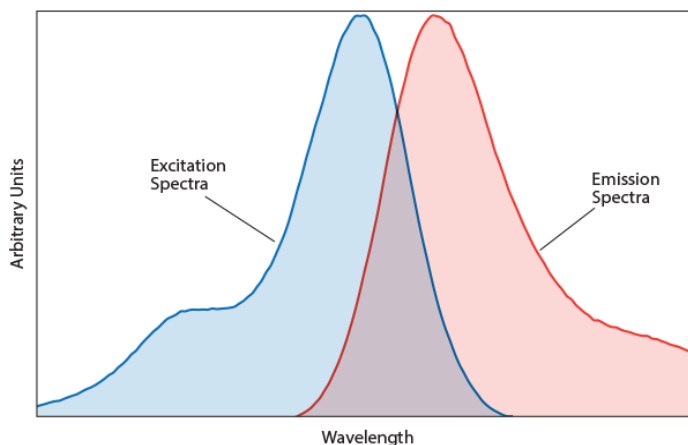


Figure 7: Exemplificative graph for excitation (blue) and emission (red) spectra for a generic fluorescent dye.

The photon energy at the apex of the excitation peak equals the energy difference between the ground state of the fluorochrome (S_0) and a favoured vibrational level of the first excited state (S_1) of the molecule (**Figure 8**).

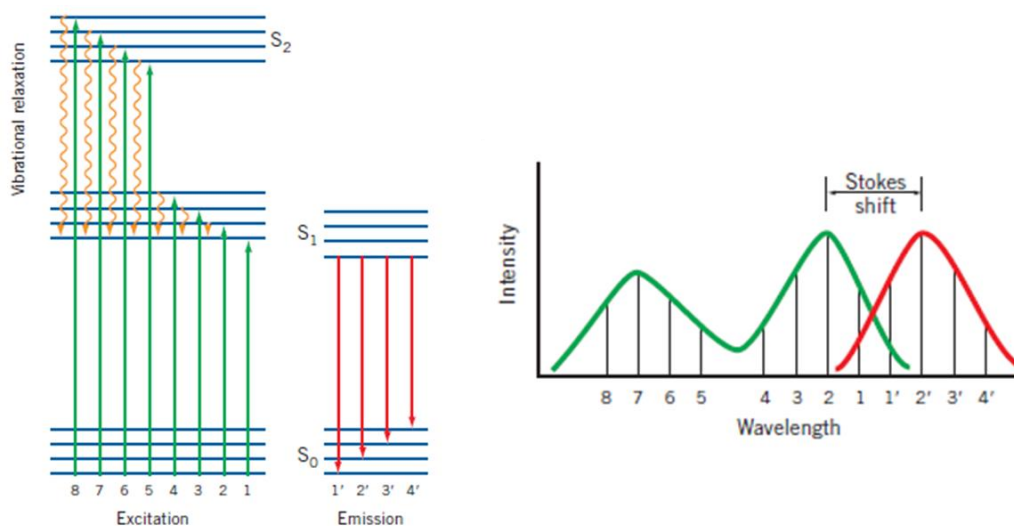


Figure 8: Diagram of energy levels for a generic fluorochrome dye. In green and red are reported the phenomenon and relative spectrum for excitation and emission, respectively. The difference in emission and excitation maximum is identified as Stokes shift.

In some cases, the excitation spectrum shows a second peak at a shorter wavelength (higher energy) that indicates transition of the molecule from the ground state to the second excited state (S_2). The width of the excitation spectrum reflects the fact that the fluorochrome molecule can be in any of several vibrational and rotational energy levels within the ground state and can end up in any of several vibrational and rotational energy levels within the excited state. In practice, a fluorochrome is most effectively excited by wavelengths near the apex of its excitation peak. The shape of the emission band is approximately a mirror image of the longest-wavelength absorption band (**Figure 8**), providing that the vibronic structures of the excited and ground states are similar. In theory, the transition in excitation and transition in emission should occur at the same wavelength. However, this is usually not the case in solution, mainly due to solvent relaxation.⁵⁶

In solution, Stokes shift is predominantly accounted for by solvent effects (increasing with the polarity of the solvent and the polarity of the excited state). Heat exchange is essentially caused by internal vibrational relaxation. The emission spectrum is always shifted toward a longer wavelength (lower energy) relative to the excitation spectrum.

The difference in wavelength between the apex of the emission peak and the apex of the excitation peak is known as the Stokes shift.

This shift in wavelength (energy) represents the energy dissipated as heat during the lifetime of the excited state before the fluorescent light is emitted. The Stokes shift is fundamental to the sensitivity of fluorescent

Introduction: MRI, fluorescence and FF self-assembly systems

techniques because it allows emission photons to be detected against a low background spectrally removed from excitation photons.

The intensity of the emitted fluorescent light is a linear function of the amount of fluorochrome present when the wavelength and intensity of the illuminating light are constant (e.g. when using a controlled laser light source). Although the signal becomes non-linear at very high fluorochrome concentrations, linearity is maintained over a very wide range of concentrations.⁵⁷

Fluorochromes differ in the level of intensity (brightness) they are capable of producing. This is important because a dull fluorochrome is a less sensitive probe than a bright fluorochrome. Brightness depends on two properties of the fluorochrome:

- its ability to absorb light (extinction coefficient)
- the efficiency with which it converts absorbed light into emitted fluorescent light (quantum efficiency)

The brightness of a fluorochrome is proportional to the product of its extinction coefficient (ϵ) and its quantum efficiency (ϕ), as indicated in the following relationship:⁵¹

$$\text{Brightness} \sim \epsilon\phi$$

The extinction coefficient of a fluorochrome is the amount of light that a fluorochrome absorbs at a particular wavelength.

The molar extinction coefficient is defined as the optical density of a 1 M solution of the fluorochrome measured through a 1 cm light path.

For fluorochromes that are useful molecular labels, the molar extinction coefficient at peak absorption is in the tens of thousands.⁵¹

The probability that an excited fluorochrome will emit light is its quantum efficiency and is given by the following ratio:

$$\phi = \text{number of photons emitted} / \text{number of photons absorbed}$$

Values for ϕ range from 0 (for non-fluorescent compounds) to 1 (for 100% efficiency).

Fluorescence intensity is also affected by the intensity of incident radiation. Although in theory, the more intense source will yield the greater fluorescence, in actual practice, photodestruction of the sample can occur when high intensity light is delivered over a prolonged period of time.⁵⁸

1.4 Supramolecular chemistry as new tool for bio-imaging

Since the beginning of the last century, supramolecular chemistry has imposed itself as revolutionary scientific area to the interface of different disciplines, such as chemistry, medicine, material science and biology. Specializing themselves in the manipulation of matter, researchers have tried to obtain various nano-dimensional structures, in terms of morphology, shape, compatibility and functionality, all associated with desirable physical and chemical attributes.^{1,2,3}

The emerging importance of nanotechnology supports the idea of nano-organized systems as versatile starting point for explore new possibility in bio-imaging.

Indeed, bio-imaging probes based on nanoparticles^{14,59} and nanoconjugated polymers⁶⁰ have been introduced, and some of them have already been applied to *in vivo* and *in vitro* imaging.^{61,62}

Regarding the MRI technology, micelles and liposomes were proposed as nanoplatform for bio-imaging applications.^{63,64} They can be obtained by spontaneous self-assembling in aqueous solution of amphiphilic molecules consisting of a hydrophobic and a hydrophilic moiety. The driving forces of the aggregation into well-defined structures derive from the hydrophobic Van der Waals associative interactions and the repulsive interactions between the charged hydrophilic moieties.

Nanotechnology changed also the assortment of fluorescence reporters. NMs came up beside the traditional fluorescent dye. Among them are nano-fibers⁶⁵ and nanotubes⁶⁶, nanocrystals⁶⁷, nanodiamonds⁶⁸ and carbon dots.⁶⁹ They demonstrated diverse photophysical behavior and allow one to obtain diverse information when used in analytical tools or when they form images in biological systems.

Even if small organic fluorescent probes have become indispensable tools, nan-structured particles has attracted great interest for the peculiar and innovative fluorescence features, related to quantum mechanical phenomena like quantum confinement.⁷⁰ According to this evidence, a deep knowledge about nano-fabrication and self-assembling methodologies is required.

1.4.1 Nano-fabrication: bottom-up and top-down approach

The broad use of nanoplatforms for practical applications referenced in literature revealed the need to obtain nanoparticles with well-defined characteristics of uniformity, purity, size, and chemical compositions. Generally, the approaches that may be used for manufacturing different NPs are referred with the generic names of “bottom-up” and “top-down” methodologies (**Figure 9**).

Introduction: MRI, fluorescence and FF self-assembly systems

More specifically, the top-down procedures search for design devices at nano- and micro-scale by using the externally controlled micro-fabrication methods to direct crumbling and dismantling of bulk materials into its meso-components. Examples of this approach are photolithography⁷¹, 3D printing⁷², vapour deposition⁷³ and micropatterning.⁷⁴

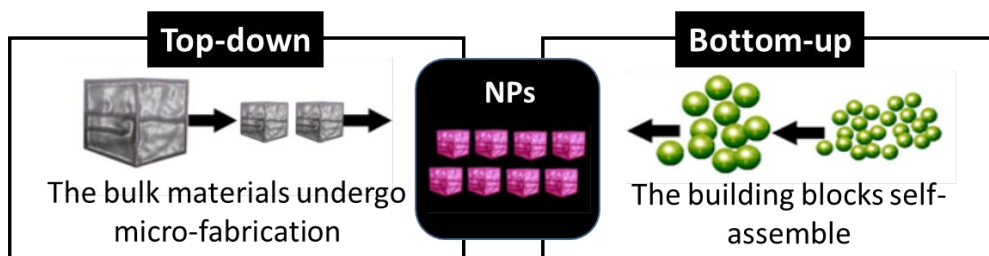


Figure 9: Top-down and bottom-up approaches to generate new nanoplateforms (NPs) associated with desirable physical and chemical attributes.

On the other side, bottom-up methodology takes advantage of chemical properties and combinations of molecular recognition between small molecular monomers. They serve as building blocks to self-organize in complex supramolecular assemblies.

Since the birth of supramolecular chemistry, following Lehn, Cram and Pedersen's study, the comprehension of the forces that rule the intramolecular recognition and the study about non-covalent interactions allowed to use self-assembly phenomena as bottom-up tools.

In the classic way, self-assembly is the spontaneous and reversible organization of molecular entities in orderly structures by weak interactions. In other words, with this term are pinpointed processes in which a cluttered system of pre-existent components create an organized structure or a repetitive modulus as a consequence of specific and local non-covalent interaction (like hydrogen bond, Van der Waals interaction, aromatic staking, London's dispersion forces and metal coordination).

According to Whitesides and Grzybowski' definition, self-assembly phenomena can be identified as either static (S) or dynamic (D).⁷⁵ Self-assembly processes in S class might require energetic activations (mechanical, thermal or chemical ones). These systems, once formed, are in global or local equilibrium at meso- and micro-scales, no needing to dissipate energy. Biological examples of these processes are the formation of phospholipid membrane bilayers, virus capsids, crystal formations and DNA double helix. Otherwise, systems originated by dynamic self-assembly, in order to maintain their organization, require dissipation of their energy. This is the case of more complex entities like cells cytoskeleton and superior organisms.

Introduction: MRI, fluorescence and FF self-assembly systems

Molecular self-assembly is a static and spontaneous process associated with a negative variation of the free energy ($\Delta G < 0$). The interaction network created by the system is a consequence of its tendency to increase the entropy (S), simply referred as the grade of randomness. According to the second law of thermodynamics, entropy can not decrease (it can only remain unchanged as in the adiabatic processes or increase), so each system evolves in the way to increase the randomness ensuring an increase of S . However, assembled systems are recall as more “ordered” than “disordered”. The self-assembly driven by the entropy might appear counterintuitive. This apparent paradox could be explained considering that the thermodynamic behaviour between polar and non-polar entities represents the driving force of this process. The apparent paradox is clarified studying the hydrophobicity of materials, the polar modulus and the electronegativity of constituent of the atoms.

Focusing on aqueous media, the molecules of H_2O form and demolish continuously and spontaneously hydrogen bonds, safeguarding a high grade of randomness and charging neutrality. This tendency affects also the water solubility of the compound.

More specifically, a non-polar molecule (like aromatic/aliphatic compound or fatty acid) induces a more “rigid” behaviour of water molecules that, in order to guarantee electro-neutrality, produce a local increase of order (**Figure 10a**). In the case of amphiphilic molecules, or rather molecules that have simultaneously polar and non-polar regions (surfactants or phospholipids) in molecular structure, the polar part can take part to the dynamic hydrogen bonding process of water whereas non-polar one decrease the entropy as mentioned previously. Increasing the amphiphilic concentration, the molecules start to self-assemble in clusters with the aim to minimize the contact between nonpolar and the aqueous interface, fostering intramolecular non-polar interaction (**Figure 10b**). In addition, the entropic solvent organization was proposed be the a basic phenomenon related to the entropic hydrophobic effect. The hydrophobic effect is the observed tendency of nonpolar substances to aggregate in aqueous media, excluding water molecules According to this prospective, some authors argued that the hydrophobic interaction is mostly an entropic effect originating from the disruption of highly dynamic hydrogen bonds between molecules of liquid water by the nonpolar solute. Consequently, no physical interaction or fundamental forces could be ascribed to hydrophobic forces. However in this manuscript it will be preferred report the aggregation driving force as stacking one.

Depending on different structural parameters identified as “paking parameters” (like ratio between non polar and polar parts or relative size and charges), monomers could aggregate into a range of various and heterogeneous geometries. The local and weak interactions are

Introduction: MRI, fluorescence and FF self-assembly systems

additional and fundamental factors that stabilize and could direct the aggregation process. In fact, although each non-covalent force does not prove energetically relevant (hydrogen bonds: 2–30 kcal/mol, electrostatic forces: 2–21 kcal/mol, hydrophobic forces: 10 kcal/mol and π - π aromatic stacking: 1–11 kcal/mol), the total network of them generates a final condition of high stability and hierarchical order.

The advantage derived by this particular organization is located in the reversibility of the process if it is compared with all-covalent systems (C–C bond: 85 kcal/mol, C–H bond: 103 kcal/mol, C–O bond: 81 kcal/mol). For this reason, the self-assembly process can be reversed or transformed by external stimuli, including pH⁷⁶, temperature⁷⁷ and solvents.⁷⁸

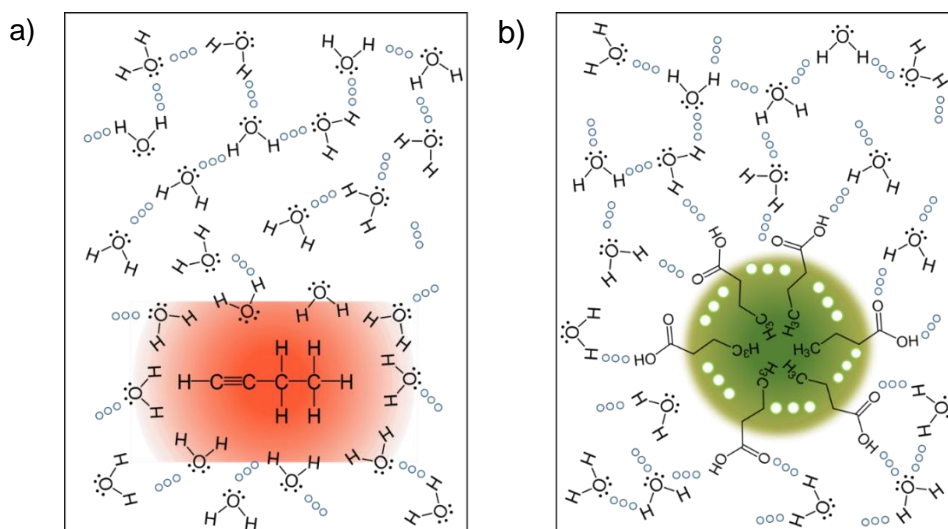


Figure 10: An aliphatic molecule increases the order of aqueous media (red region) inducing a decrease of entropy (a). Amphiphilic molecules submerged in water the aqueous media interact with water by polar region whereas non-polar parts, at a typical concentration, start to interact by non-covalent interaction (white circles) to self-assemble and minimize the non-compatible interfaces areas.

On the evidence that supramolecular self-assembly is the basis of a lot of essential biochemical processes, scientists have begun researching building blocks for bottom-up inspired by biology. In this field and as mentioned before, amphiphilic molecules are particularly attractive building blocks. This new design imitation approach, known as “biomimetic” or “biomimicry”, allows new applications to the nano- and micro-scales inspired by supramolecular molecular biology.

1.4.2 Biomimicry approach: peptide for bottom-up

Among all the natural building blocks proposed for the bottom-up approach, amino acids and peptides open very large prospective for the design and the generation of complex supramolecular architectures. Numerous structures are consequence of natural self-assembly of proteinaceous building blocks and the organization in supramolecular protein structures is a common process in living systems; illustrative examples are viral capsid⁷⁹, fibrils⁸⁰, microtubules⁸¹, and S-layers.⁸² Because of the natural level of organization ranges from nano-to macro-scale, rather than proteins short peptides are proposed as simpler and more controllable constitutive elements to direct the self-assembly on different length-scales.⁸³

Peptides have well-known advantages ranging from high versatility, intrinsic biocompatibility, possibility of functionalization pre- and post-aggregation to high synthetic accessibility and convergence, low immunogenicity and relative low cost.

More than two decade ago, in 1993 Ghadiri and co-workers produced the first demonstration of manufactured supramolecular nanostructures using peptides.⁸⁴ The monomer, a cyclic peptide, was designed and bio-inspired by non-ribosomal bacterial peptides that contain residues in alternate configurations (D and L). This latter structural characteristic allows the stacking of the building blocks, conferring them a flat β -sheet conformation. The interaction network of hydrogen bonding bears the supramolecular structure of hollow cylindrical nanotubes.

At the state of art, a large number of peptide-based building blocks, comprising cyclic peptides⁸⁵, amphiphilic peptides⁸⁶, surfactant-like peptides⁸⁷, dendritic peptides⁸⁸ and aromatic dipeptides⁸⁹, have been considered for generating self-assembled nanostructures.

Both final morphology and properties of the self-assembled system are related to the monomer structure in terms of chemical nature of residues, functional group in side chains and monomer length.

Owing to such unique chemical properties, *de novo* designed peptides can be decorated with chemical functionality, like polymers⁹⁰, alkyl chain and lipids⁹¹, and the sequences can be easily designed as amphiphilic chemical structure, with both hydrophobic and hydrophilic domains in the same building block. Additionally, peptides for bottom-up approach opened many opportunities to the exploration of the relationship between physicochemical properties and the molecular architectures.⁹²

However, all these scientific topics are complementary to the knowledge of the amino acid and peptide chemistry, taking advantage from current synthetic methods and the relative simple chemistry of the amino acids.

1.5 Amyloids: from pathogenicity to biomimicry starting point

At molecular level and in its complex, protein folding is the physical-chemical process by which a protein stabilizes and acquires its three dimensional and functional shape (known as native state).

In biological systems, proteins are synthesized by ribosomes, transforming a sequence of mRNA codons into the correspondent linear chain of amino acids. Amino acids in the unfolded primary sequence start to interact each other to generate the native state. For this, the specific amino acid residues and their position in the polypeptide chain are the driving forces of the folding process (a concept known as Anfinsen's dogma).

The correct folding state is essential to guarantee the protein physiological function and, in normal physiological conditions, all the proteins prove to be degradable and recyclable biochemical entities.⁹³

Alterations or evasion from one of the pathways that control normal proteins turnover and folding (like proteasome⁹⁴ or molecular chaperons⁹⁵) could provoke pathological situations.^{96,97,98}

Between these, amyloidosis represents an inclusive category of disturbs correlated with protein misfolding. This process can be the consequence of different causes such as mistranscription⁹⁹, gene alteration and mutation¹⁰⁰ or mistranslation.¹⁰¹ Modifications of surrounding conditions (pH, temperature, concentrations of salts) could also provoke proteins destabilization, resulting in misfolding or unfolding.^{102,103}

Amyloidosis are transversely characterized by a similar aetiology of extracellular deposition of insoluble and intractable clusters and aggregates of protein-based materials with low molecular weight.¹⁰⁴ This material is usually pinpointed as 'amyloid' because of its propriety to react with iodine, similarly to starch (*amylum* in Latin). Currently, more of 25 proteins are identified as involved in amyloidogenic processes.¹⁰⁵ As mentioned, amyloid fibrillary materials do not represent the native conformation but are an alternative quaternary one, formed because its organization process seems thermodynamically favorable.

Supramolecular aggregated and misfolding protein materials are the hallmark of major human illnesses, including bovine spongiform encephalopathy (mad cow disease),¹⁰⁶ Marfan's syndrome,¹⁰⁷ Creutzfeldt–Jakob disease,¹⁰⁸ Alzheimer's disease,¹⁰⁹ Huntington's¹¹⁰ and Parkinson's disease¹¹¹ and polyneuropathy.¹¹²

Although first identified as pathological entities, a new research line has recently shown that amyloid proteinaceous materials contribute to generate complex and physiological functional materials as constitutive elements.¹¹³ It is demonstrated that amyloid materials have evolved from prokaryotes to eukaryotes as structural matter for a lot of biological

functionality, recognized involved in microbial biofilms formation,¹¹⁴ cell adhesion,¹¹⁵ signal transduction for hormone release,¹¹⁶ templates the synthesis of melanin,¹¹⁷ RNA traffic¹¹⁸ and memory persistence.¹¹⁹

For these reason, the amyloid materials, once exclusively affiliated as pathological structures, are now raising interest as biomimicred self-assembling class of biological building blocks for artificial materials. Their potential engineering is a consequence of the study and comprehension of the supramolecular structuration.

1.5.1 Amyloids structure

An initial theory supposed an amorphous organization of amyloid materials plaques. Isolation of heterogeneous amyloids and their structural characterization confuted this hypothesis (**Figure 11**).¹²⁰ Despite having different physiological functions and chemical structure, all the misfolded amyloid proteins are composed of a quaternary ordered arrangement of many (usually thousands) peptide monomers sharing the same morphologic ultrastructure and resistance to protease degradation.¹²¹

At superior grade of organizations, amyloids plaques appear formed by unbranched, linear and rigid peptide fibrils with non-constant length and medium diameter of 7-10 nm. These assemblies contain usually 2-8 protofilaments (the fibrillar subunits) twisted around each other.^{122,123} In turn, each protofilament is composed by a repeating substructure of beta strand that run perpendicular to the fiber axis, arranging in a polymeric organization of indefinite length known as a cross-beta structure.^{124,125}

In cross-section, amyloid fibrils appear as hollow ribbons or cylinders. All the structure is stabilized by beta sheet packing by specific region of amino acid of interaction, generally aromatic and hydrophobic, called steric zipper-like regions, and by long network of hydrogen bond between beta strands.^{126,127}

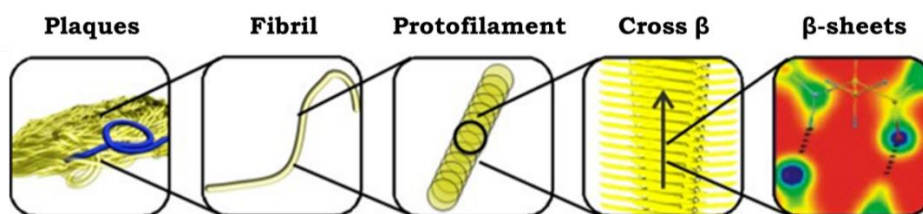


Figure 11: Hierarchical assembly of amyloid materials, from plaques to secondary structure.

This kind of organization is also confirmed by different and complementary techniques. Fluorescent dyes, such as Congo Red

(CR)¹²⁸ and Thioflavin T (Th T)¹²⁹, stain the amyloid fibres and protofilaments while Circular Dichroism¹³⁰, optical birefringence¹³¹ and Infrared spectroscopy¹³² can identify the β -secondary structure. In addition to all of this indirect measurements, organized and partially aligned amyloids materials give a characteristic X-ray diffraction known as "cross- β pattern" (**Figure 12**).¹³³ This evidence is considered the diagnostic and direct hallmark of amyloid structuration. Cross beta pattern consists of two sets of diffraction lines, located on two axes mutually perpendicular (meridional and equatorial directions). Along meridional direction, parallel to fibre axis, an intense and sharp reflection generates an arch at 4.7 Å corresponding to stacking distances between two consecutive β sheets. On the equatorial direction, a signal around 10 Å is generally detectable as index of the distance between stacked β -sheets.¹³³

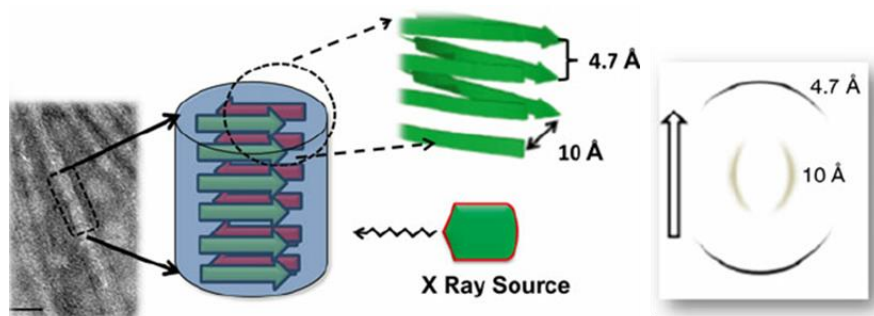


Figure 12: Schematic representation of amyloid organized quaternary structure and its characteristic X-ray cross- β pattern diffractogram collected by fibril exposure at X-ray source. Cross- β pattern is correlated to the stacking distance between β -sheets.

This kind of organization explains the central role of the dense hydrogen bonding network and the strong intermolecular backbone-backbone interactions, both associated to the high Young's and elastic moduli connected to amyloid fibrils. These are only two of the motivation for why amyloid fibrils structures attracted attention. These materials are at the crossing between nanotechnological, medical and biological areas.

5.2 Aromatic residues as molecular denominators of amyloid fibril formation

Concerning the attempts to clarify molecular aspects of fibrils formation, great dedication was devoted toward understanding the rational mechanism underlying amyloid self-assembly.

Introduction: MRI, fluorescence and FF self-assembly systems

As first approach, the design of peptide and peptidoids agents as inhibitors of amyloid formation are pursued.^{134,135} Mediating the process of molecular self-assembly, these compounds paved the way to a reductionist research aimed to determine the minimal intrinsic peptide sequences that would guide the fibres formation. This approach was successfully applied to figure out the basis of amyloid fibril self-assembly of human islet amyloid polypeptides (hIAPP).¹³⁶ IAPP is 37-amino acid hormone responsible to form fibrils in pancreas in case of type II diabetes. The two pentapeptides, hIAPP₁₄₋₁₈ (NFLVH) and hIAPP₁₅₋₁₉ (FLVHS), identified as part of the central molecular recognition module, are able to form fibrillar aggregates.¹³⁷ Analogously, studies about amyloid materials in medullary carcinoma of the thyroid formed by human calcitonin polypeptide hormone (hCT), has demonstrated the formation of amyloid-like fibrils for two peptides (DFNKF and DFNK).¹³⁸ Additionally, a peptide fragment of medin, Med₄₂₋₄₇ (NFGSVQ), the constituent of protinaceous deposits in all the individuals above the age of 60, can mime the fibrillary self-assembly of the full-length polypeptide.¹³⁸

This approach, reducing gradually the high systems complexity, allowed to compare short peptide fragments, identifying the presence of aromatic residues as the common molecular and structural denominators that guide the formation of analogues supramolecular morphologies in different protinaceous building-blocks.

On the basis of this evidence, amyloid fibril formation was attributed to a process in which π -stacking interactions play a key role, providing a high enthalpic contribution (staging hypothesis). These interactions, associated also with the high hydrophobicity, the backbone hydrogen bounding network and β -sheet propensity, should contribute to generate order and directionality in this self-assembly process.

The stacking hypothesis associated with hydrophobicity is particularly suitable regarding the case of $A\beta_{1-40}$ and $A\beta_{1-42}$ polypeptides involved in the formation of Alzheimer's disease plaques.¹⁰⁹ The previously mentioned systematic and reductionist approach was also applied to these peptides, identifying the region $A\beta_{16-22}$ (KLVFFAE) as one of the shorter aggregation-prone sequence.¹⁴⁰ Inside the primary structure, the region 17-21 is the crucial, essential hydrophobic cluster for polymerization of the full-length peptide.^{141,142}

According to the evidence that π - π staging provide a restriction of conformational space, geometry and directionality¹⁴³ in the hydrophobic clusters and that all short peptide able to interact with $A\beta$ contain an analogue recurring part, in 2003 Gazit and Reches pinpointed the diphenylalanine homopeptide (FF or Phe-Phe), in the middle of $A\beta$ (FF, $A\beta_{19-20}$), as core recognition motif of Alzheimer's polypeptide.¹⁴⁴ Initially, the parental origin from amylogenic matrix supported the hypothesis that FF structuration were amyloid too. Meanwhile $A\beta_{1-40/42}$ and $A\beta_{16-22}$ self-

organize in fibril water filled morphology,^{140,145} FF is able to self-assembles into ordered and discrete aromatic dipeptide nanotubes (ADNTs) with micro-scale persistence length in a process identified as “one dimensional crystallization”.¹⁴⁶

The FF motif became of special interest rapidly because it is the first pioneering reported case of minimal amyloid related fibrils formed by an ultra-short and all-aromatic dipeptide. By the unexpected evidence of a novel type of nanomaterial, FF became the paradigm for exploring supramolecular aggregative peptide behaviours representing a new class of simple building blocks containing all the molecular information for the self-assembling.

1.6 Diphenylalanine molecular and structural organization

The organization and the interactions of the individual FF monomers explain the overall properties of the assembled ADNTs. Consequently, the internal arrangement of FF nanotubes was extensively analysed.

Two types of interactions are pinpointed as the driving forces at the basis of supramolecular phenomena. By X ray crystallography studies, π - π interaction (between phenyl rings) and hydrogen bonding (that engage backbone terminals).¹⁴⁷ This hypothesis is consistent with previous evidences that highlight the centrality of π - π staking in the self-organization phenomena more than hydrogen bounding of backbone terminals. A study conducted about eight FF analogues chemically differentiated both at N- and C- terminus (cyclization hand-to-tail, N^α protection via Boc, Fmoc) and at side chain (saturation, *nor*- modification of the phenyl ring) reported that saturated analogues does not show high aggregation propensity, tendencies that are preserved in terminal modified analogues.¹⁴⁸

Molecular Dynamics algorithms, supported and confirmed by X-Ray diffraction, proposed a hierarchical and multiscale aggregative model for diphenylalanine homopeptide based on a particular arrangement of FF monomers in aqueous media.^{149,150} In vacuum, the simulated monomer configuration suggests the two phenyls rings located on either side of the peptide backbone (**Figure 13a**). On the contrary, in polar environment, thanks to the rotational freedom around the peptide bond (θ angle), the two side residues are constricted in the same face of peptide backbone with an unusual torsion dihedral angle between the two side chains centred around 0°(**Figure 13b**). This anomalous configuration is favourable in aqueous media because the hydrophobic groups can be shielded from the non-compatible polar interface, limiting the contacts between aromatic residues and water molecules and increasing the total entropy of the system.¹⁵⁰

Introduction: MRI, fluorescence and FF self-assembly systems

In this conformation, six homopeptides organized in a cyclic hexamer (Van der Waals diameter 9.2 Å) stabilized by head-to-tail hydrogen bonding (**Figure 13c**).¹⁵¹ Subsequently, according to packing parameters, hexamers generate a hexagonal peptide matrix in which hydrophobic groups are packed inside the wall of single ADNT by staking interaction.

Growing in one-dimension propagation, inside the matrix hollow hydrophilic channels and hydrophobic zipper zone (reported in in red and blue in **Figure 13c**, respectively) are recognizable.^{147,149} The water settle in the central columns is an integral participating of the structure both in structural and energetic way. Because hardly removed from it, either by heating or vacuum, it is generally referred as "crystallographic water".

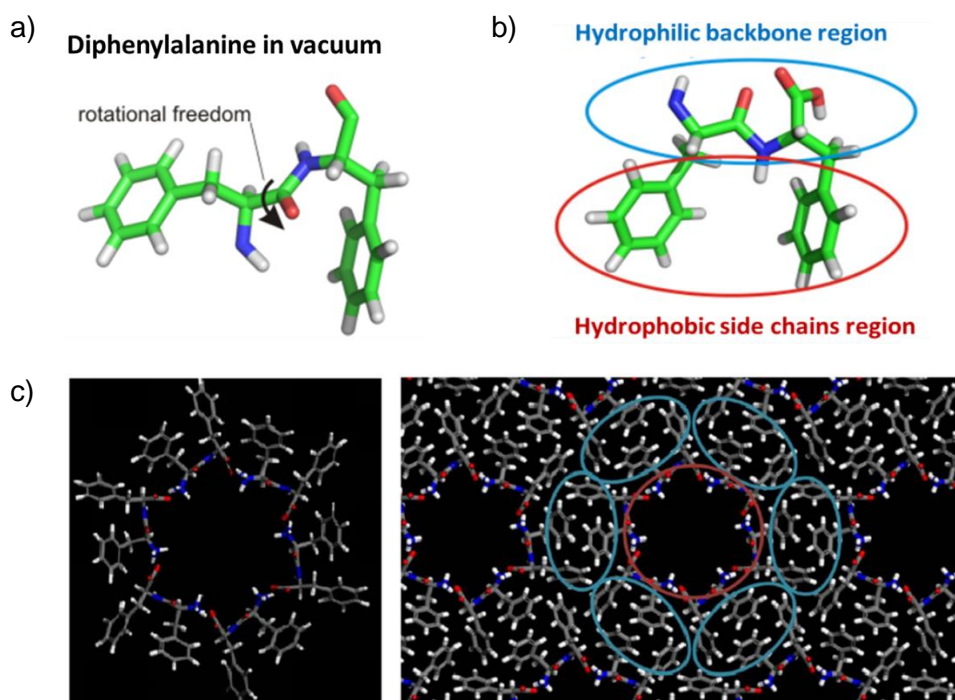


Figure 13: a) Simulated FF conformation in vacuum. b) Side chain constriction in polar environment. Hydrophilic and hydrophobic molecular region are indicated. c) The cyclic hexamer, formed by six homopeptides, generate a peptide matrix in which an hydrophilic (red circle) and staking region (blue circles) can be recognized .

The one-dimension propagation step of the individual ADNT into larger meso-structures is a slower process than the organization of the individual nanotubes. The self-aggregation of them in the matrix further reduces the total entropy so that the packaging of the hydrophobic side

chains alone is not sufficient to lean on the process. Therefore, energy is gained by the creation of larger supra assemblies formed by individual nanotubes fused together. Eventually, the expensive matrix produces sheets and the closure of the two-dimensional layer forms nanotubes with external hydrophobic walls. At larger scale, nanotubes forms bundles in a final arrangement of microscale hollow tubular structures. (**Figure 14**)¹⁵²

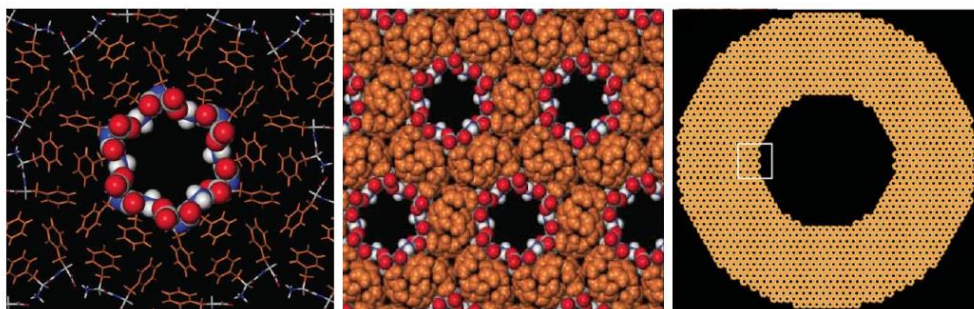


Figure 14: Schematic representation of FF cyclic hexamers (left) in their progressive organization. By clustering together (middle), singles nanotubes form a microscale nanotube (left).

Unexpected mechanical, thermal and chemical properties, not typically associated with biological matter, are related with this aggregation behaviour and inherited from the individual molecules, individual nanotubes or from their mutual intersection. TEM and SEM images for FF nanostructure suggest that ADNTs are rigid and strong assemblies.¹⁵³ Different experiments conducted by AFM highlighted the mechanical proprieties of FF nanotubes like the high stiffness (160 N/m)¹⁵⁴ and a Young's modulus in the range of 19-27 GPa.^{154,155} In addition, ADNTs display remarkable thermal stability up to 90 °C and the surrounding humidity did not seem to affect in any predictable manner these physical properties.¹⁵⁶

Simultaneously, the chemical stability of ADNTs was proved analysing the morphology of preformed aggregate against organic solvents (acetone, ethanol, methanol, acetonitrile),¹⁵⁶ meanwhile the electrical characteristics of ADNTs regard direct conductivity and photoluminescence¹⁵⁷, piezoelectricity¹⁵⁸ and polarization.¹⁵⁹

1.6.1 Diphenylalanine ADNTs: preparation in water

Since the emergence of FF as the simplest self-assembling building blocks and thanks to the ease synthetic accessibility and bulk preparation

possibility, deep exploration FF aromatic homo-dipeptides self-assembly was scrutinized.

The simplest and most common approach for the formation of FF supramolecular structure is the aqueous solution based assembly. This is in routine manufactured by two different methods (or pathways), established by Gazit's and Song's group, respectively. Gazit's protocol (pathway A) involves dissolving FF powder at high concentration (100mg/mL) in the organic fluorinate solvent HFIP (1,1,1,3,3,3-hexafluoropropan-2-ol) followed by a consequent water dilution.¹⁴⁴

In reverse, Song developed a preparation (pathway A*) by which the FF powder in water is heated for thirty minutes at 65°C. Then the sample (as solution) is cooled at room temperature. Once the concentration of the peptide monomers reaches a critical concentration during cooling process, the peptide nanotubes will form in solution.¹⁶⁰ The latter preparation omits the recourse to the toxic HFIP, a well-known mucous and tissues destroyer,¹⁶¹ making this protocol more fitting for pharmaceutical and *in vivo* application.

For completeness, a systematic study about the solubility of diphenylalanine peptide in other solvent system was reported in 2004 by Mason *et al.*, highlighting the accessibility to different morphologies simply changing the self-assembly liquid media characteristics.¹⁶²

1.6.2 Preparation by physical methods

Alternative approaches for the formation of peptide nanostructure involves physical and mechanical methods of manufacturing and can produce different patterns.

Microfluidic technology was successfully applied for the formation of ADNTs mixing in a merging laminar chip channel the FF stock solution in HFIP and water media.¹⁶³ Taking advantage from the low-molecular-weight of monomers and the inherent volatility of aromatic systems, FF dipeptides are also excellent candidates for physical methods that work with thermal induced vapor deposition (physical vapor deposition or PVD methods). Avoiding the use of solvents media, these technologies allowed a vertical deposition of monomers. After the evaporation phase of the powder from a plate at 220°C, peptide monomers undergo a chemical cyclization and finally assembles in a dense and uniform ADNTs nanoforests on a large variety of substrates (maintained at lower temperature, ~80°C).¹⁶⁴ A thin film of FF in HFIP can be converted in peptide nanowires heating it in the presence of aniline vapors. The wires vertical alignment is ensured by the gradient of the aniline vapor away from the support choose for the growth.¹⁶⁵

ADNTs can be manufactured by electrospinning procedures¹⁶⁶ and, in addition, patterned ADNTs organization can be obtained using inkjet technology¹⁶⁷, magnetic fields¹⁶⁸ or Langmuir-Blodgett method.¹⁶⁹

1.6.3 Influence of solvent media

It is increasingly evident the concept that the peptide monomers are able to self-organized in different nanomorphologies (ranging from nanotubes, organogels, nano-rods to spherical vesicles and nanofibers) according to the preparation method. In addition, the selection of the final supramolecular polymorph can be controlled by varying environment conditions parameters such as solvent, temperature or concentration.^{162,170} Regarding this latter parameter, the FF self-assembly was found be a monomer-concentration-induced shape phenomenon, confirming the dependence from concentration and the nucleation-dependent nature of the process.¹⁷¹

Three energy factors were identified by Li *at al.* as determinant parameters for the final morphology: the internal cohesion energy, the shape-dependent curvature elastic energy and the monomer-oligomers interface energy.¹⁷²

Interestingly, Demirel *et al.* described a straightforward and versatile solvent-mediated method for directing the FF self-assembly into tubular or vesicular structures by using ethanol or acetone respectively, while a reversible shape transition from nanotubes to nanovesicles was also observed by concentration modulation of monomers.¹⁷³

1.6.4 Chemical modification: neighbour homologues of FF sequence

A broad chemical exploration of the FF motif enlarged the molecular library of the ancestor peptide through a typical approach used for peptidomimetic compound (modification of the backbone, N-alkylations, protection of terminals, cyclization, inversion of configuration, sequence analogues with non-coded amino acids). This approach was allowed by very simple and easy synthetic access to the chemistry of peptides. Molecular structures of simple representative diphenylalanine-based building blocks are reported in **Figure 15**.

Cationic FF differs from FF (or zwitterionic FF) for the amidation of the C-terminus. In the amide form, the C-terminus is not more able to generate head-to-tail hydrogen bound interaction.

Interestingly, this simple chemical modification, altering the interaction pathway, strongly affect the self-assembling propriety. Cationic FF can self-assemble into nanowires rather than into nanotubes easily.¹⁷⁴

Introduction: MRI, fluorescence and FF self-assembly systems

With the rationale of generate a covalent attachment to fabricated gold electrodes for application in nano-devices, Gazit and Reches discovered that the tripeptide Cys-FF does not self-aggregate in nanotube but rather in regular nanospheres.¹⁴⁶ This evidence is explains by the concept that the introduction of a thiol group contributes energetically to a cross-linking phenomenon that makes possible to warp and to close the stacking layer without interference with π - π -staking interaction along two axes.

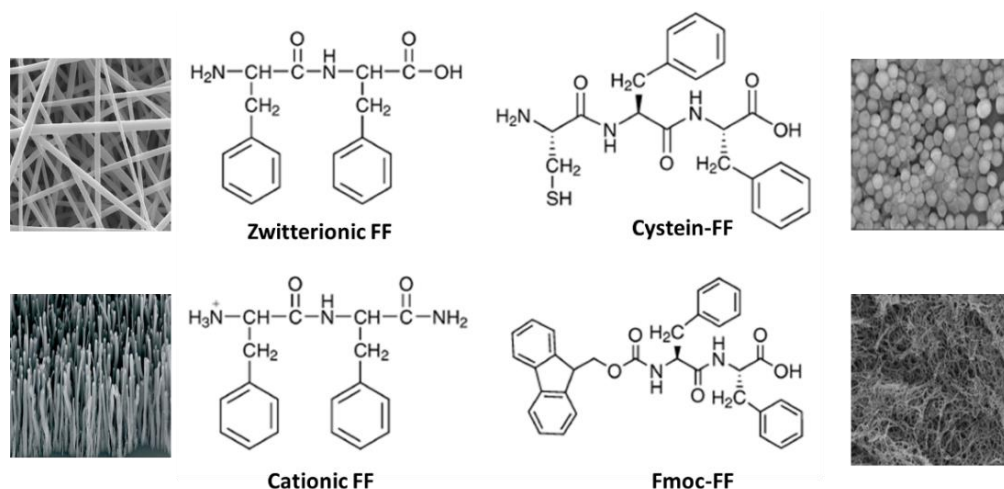


Figure 15: Chemical structure of zwitterionic and cationic FF, Cys-FF and Fmoc-FF. Relative self-assembled morphology is reported in the square image.

Strictly correlated with FF are also the molecules N^α protected and capped. Remarkably, it has been observed that a 9-fluorenylmethoxycarbonyl (Fmoc) protected diphenylalanine (Fmoc-FF), self-assembles into nanofibrils in water and thus results in a hydrogel held together in a network by hydrogen bonding and π - π interaction. The water dilution of a stock solution of Fmoc-FF (in dimethyl sulfoxide or HFIP) forms strong nanostructured hydrogels with remarkable non-Newtonians rheological properties.^{174,175} Compared with other peptide or protein hydrogels, Fmoc-FF hydrogel is considerably stronger and stiffer, and can be stable at a wide range of temperatures and pH values including extreme acidic conditions. Thus Fmoc-FF hydrogels can be more advantageous for certain applications such as controlled drug release and 3D cell culture

The tert-Butyloxycarbonyl (Boc)-FF monomer analogue allows to obtain peptide spheres or small peptide particles when an its HFIP stock solution is diluted in ethanol.¹⁶⁷ Instead, the feasible co-assembly of Boc-FF with FF monomers guides the formation of nanonecklace that show a comparable steel stiffness and applicable as molecular ink.¹⁷⁷

Introduction: MRI, fluorescence and FF self-assembly systems

N-capped FF with heterocyclic, N-indole-FF and N-carbazole-FF, are reported as indicative example of the crucial role of terminal charges in the self-assembly mechanism. Using small angle neutron scattering (SANS) and cryo-TEM techniques revealed indole-FF as able to generate highly bundled fibres network in acidic condition, whereas the more hydrophobic carbazole derivatives self-organize in fibers or wormlike micelles in the same range of pH.¹⁷⁸

Other unique micro-structures, like flat plates, flattened micro-planks and micro-rods, are referred as self-assembly consequences of side-chain elongated diphenylalanine analogues¹⁷⁹ (dihomophenylalanine, DiHpa; di-2-amino-5-phenylpentanoic acid, DiApp; di-2-amino-6-phenylhexanoic acid, DiAph) in which the R lateral group is progressively lengthened by the addition of a methylene. (**Figure 16**)

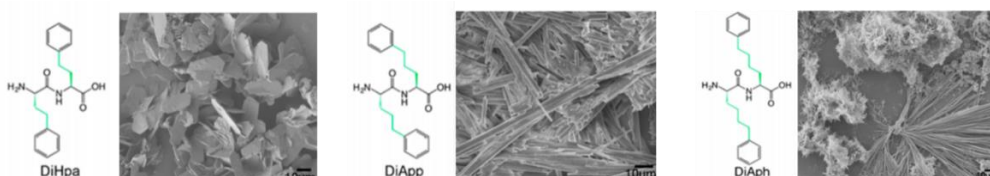


Figure 16: Chemical structure and SEM images of diphenylalanine peptide analogues DiHpa, DiApp.

1.6.5 Polymer decoration: amphiphilic derivatives

Tri-^{180,181}, tetra-^{182,183} and penta-¹⁸³ phenylalanine are further molecular building blocks derived by elongation of FF motif.

As foreseeable, these oligo-Phe sequences show a very low water solubility. For this, oligo-Phe and high aromatic peptide sequences are often decorated with hydrophilic polymers fragment in an effort to improve their hydrophilicity.¹⁸⁴ This aim is particularly relevant for bio-application of self-organized NPs.

The combination of peptides with synthetic polymers permits to synergistically congregate (generally in amphiphilic blocks) peptide functionality and recognition capability with polymer cheapness and responsiveness in order to obtain new molecular building block with enhanced solubility and features.¹⁸⁵

A poly(ethylene oxide)-tetraphenylalanine (PEO-F4) polymer-peptide conjugate has been prepared by Tzokova *et al.*^{184,186} Using a click-reaction between an alkyne-modified peptide and an azide-terminated PEO oligomer the building-block self-assembled in nanotubes, involving the formation of antiparallel β -sheet. The PEO length was also found to affect deeply the aggregation morphology. As the length of the PEO block

is increased, F4 conjugates giving rise to nanotubes, fibers, and wormlike micelles, respectively.^{184,186}

Crystallization effect of a PEG 5000 fragment was identified by Castelletto *et al.* in a tetra-Phe oligo-sequence using different techniques (Polarized Optical Microscopy, X-ray and IR Spectroscopy).¹⁸⁷

The versatility of polymer conjugation was demonstrated also by Liberato. A hybrid material was formulated through the conjugation of electrospun polycaprolactone (PCL) fibers and micro/nanotubes diphenylalanine (FF-MNTs). This material represented a new peptide-based scaffold able to control the drug delivery with a completely biodegradable matrix profile.⁹⁰

The rational design of peptide building blocks and the handy synthetic procedures of polymer decorations make possible to combine peptides self-assembling with a range of other functional moieties. This approach seems to be a good strategy to overcome the low solubility of aromatic self-assembling peptide, opening application in biological, pharmaceutical and medicinal fields.

6.6 Applications of supramolecular FF based NPs

The discovery of supramolecular organization of FF puts into effect the concept of using aromatic building blocks for designing nanometric platforms.

The demonstrated possibility to alter the final morphology of the aggregate (by simply chemical modification, functionalization or ligation) can advantageously have a role in the development of new application in both non-biological and biological fields. In particular, the previously mentioned physical¹⁵³, chemical¹⁵⁶ and thermal^{157,158} stability of FF derivatives opens innovative prospective in material nanoengineering. In this field, the better-known application of carbon nanotubes and semicondu

cting nanowires have inspired the FF purpose in same direction. Two of the principal support that ADNTs can give in nanofabrication concerns the possibility to increase exponentially and functionalize the surface area of interest. This approach was successfully applied to electrodes fabrication for chemical detection of dopamine¹⁸⁸, neurotoxins or glucose.¹⁸⁹

In fabrication and manufacturing areas, peptide nanotubes can work as filler for composite polymers,¹⁹⁰ achieving better materials with enhanced properties of mechanical strength and ions transport.¹⁹¹ In metal organization, the preformed nanotubular structure was utilized as template for silver nanowires.¹⁴⁴

Other remarkable examples regard the use of FF nano-tubes in the optimization process of piezoelectrical systems,¹⁵⁹ the development of

new masks for complex nanowires growth, for nanocables microfluidic chips fabrication.¹⁶⁴

Remarkable improvement concerned the inorganic functionalization of FF-based materials with the possibility to generate hybrid nanocomposites (with Co, Au or Ni) or xerogels.¹⁹² The chemical/optical behaviour of lanthanides ions (like Eu, Gd or Tb) have inspired their incorporation in supramolecular architectures with the aim to improve diagnostic methods, produce photoluminescent layers and increase the bio-imaging performances.¹⁹³

In regards to biological fields, FF based materials have found application prospective for new regenerative medicine therapies. The N-Fmoc protected analogue of diphenylalanine is largely studied for its possibility to generate hard hydrogel as extracellular matrix mimetic and as tri-dimensional support for cell growth.^{174,175} Other hydrogels based on aromatic building blocks have also proven the ability to encapsulate nanocrystal or active pharmaceutical ingredients (API)¹⁹⁴ and be responsive to external stimuli like enzymes, temperature, and light.¹⁹⁵ FF-based nanostructures possess potential for in vitro drug delivery systems and vehiculation of genic therapy.¹⁷⁴



Purposes

Scope and thesis structure

Purposes

2.1 Scope and thesis structure

Peptide-based materials (PBMs) generate by the aggregation of amphiphilic monomers represent a rapidly growing tool within materials science. They have been considered for several applications in different fields from electronic to nanomedicine.

According to an appropriate design, amphiphilic peptides can spontaneously assemble in well-structured supramolecular materials as result of an intricate network of inter- and/or intra-molecular interactions between hydrophobic and hydrophilic portions. The interaction manner can strongly influence both morphology and properties of the final supramolecular materials.

Aromaticity is the terms used to describe the particular molecular stability associated to a cyclic shaped and planar chemical entity with a ring of resonance bonds. The peculiar electronic structure of aromatics molecules arouses their interesting physicochemical properties. All the classes of intermolecular forces known as the aromatic interaction give raise from it. The knowledge and the study of aromatic interaction contaminated peptide based material field too.

To this day, using self-assembly as instrument of bottom-up nano-planning, it is a clear evidence that aromatic peptide sequences, containing phenylalanine (Phe), tyrosine (Tyr) or tryptophan (Trp), can be opportunely modulated to the aim of generate the required supramolecular architecture.

The forefather of this new class of peptide monomers is the well-known diphenylalanine (FF) homopeptide. Through a combination of π - π staking and hydrogen-bonding, different method of preparation, specific pH values or solvent, FF is able to self-organize in different kinds of nano- and macro- morphologies (hollow nanotubes, fibers, vesicles, metastable hydrogels or organogels). By this evidence, many structural analogues of diphenylalanine were studied and peptide nanostructures containing the FF motif or more extended aromatic sequences have been investigated for their mechanical, electrochemical and optical properties, and more recently for some nanomedicine applications. Nevertheless, the majority of studies reported in literature are principally focused on clarifying the physicochemical aspects responsible for array stability in FF based nanostructures, whereas only few studies have been devoted in the investigation of FF aggregates for biomedical applications. This essentially because of the intrinsic low water solubility of these peptide sequences.

According to these considerations, during the three years of the PhD project, novel poly-phenylalanine self-assembling conjugates were carefully designed, synthesized and fully characterized.

The final peptide materials were evaluated for potential applications in bio-imaging field (with particular bearing to Magnetic Resonance Imaging

and fluorescence imaging). It was also appreciated as the chemical modification of the aromatic framework with chelating agents, gadolinium (Gd) complexes, and polyethylene glycol (PEG) fragments with different length can affect the structural organization and the supramolecular behavior of the nanomaterial.

The result produced on the hierarchical organization by the chemical replacement of the Phe with other aromatic amino acids (such as tryptophan, tyrosine and 2-naphthylalanine) was also investigated.

The entirety of collected data during this PhD project permits to highlight the possible relationship existing between the chemical structure of the proposed building blocks, the final supramolecular nanostructure, and their functional features.

In order to simplify the comprehension and the discussion of the results (Chapter III), they will be argued in three separate sections:

- *Section I*: PBMs as supramolecular contrast agents for MRI.
- *Section II*: PBMs as photoluminescent supramolecular probes.
- *Section III*: PBMs obtained by punctual chemical modifications of homophenylalanine sequences.

In *Section I*, an innovative class of supramolecular CAs for MRI, based on peptide self-assembly monomers, is described and analyzed. Different design strategies were applied to obtain and improve the aggregation phenomenon. The structural and relaxometric properties of each self-assembling system are discussed and mutually compared. The improved values of relaxivity and the examined capability to encapsulate the doxorubicin anticancer drug suggest a potential use of the proposed nanostructures as new theranostic platform.

Photoluminescent (PL) phenomena in peptide-based materials are the subject of *Section II*. A class of novel PEGylated homo-phenylalanine was synthesized and, due to the high content of β -sheet, the final self-assembled systems show blue PL emission. A red-shift of the fluorescence was actualized by FRET phenomena between the nanostructure and an internalized NBD dye. Committing to the hydrogen bonding hypothesis, a relationship between observed PL and the number of interaction sites in nanostructures was developed.

In *Section III* the effect of a punctual chemical modification on peptide primary sequence will be elucidated. Hetero- and homo-sequences were derived simply by the replacement of Phe residues with tyrosine and tryptophan ones. Characteristic gelification behavior was found for peptides containing Tyr. WAXS/SAXS studies and molecular dynamic

simulations supported the structural analysis of the new peptide-based materials.

The experimental protocols are totally collected in the dedicated Experimental section.

The full characterization of synthesized peptides, conjugates and derivatives is reported in **Appendix I**, meanwhile additional information, Tables and Figures are gathered together in **Appendix II**.

The first pages of published papers during the PhD period consist of Publication section

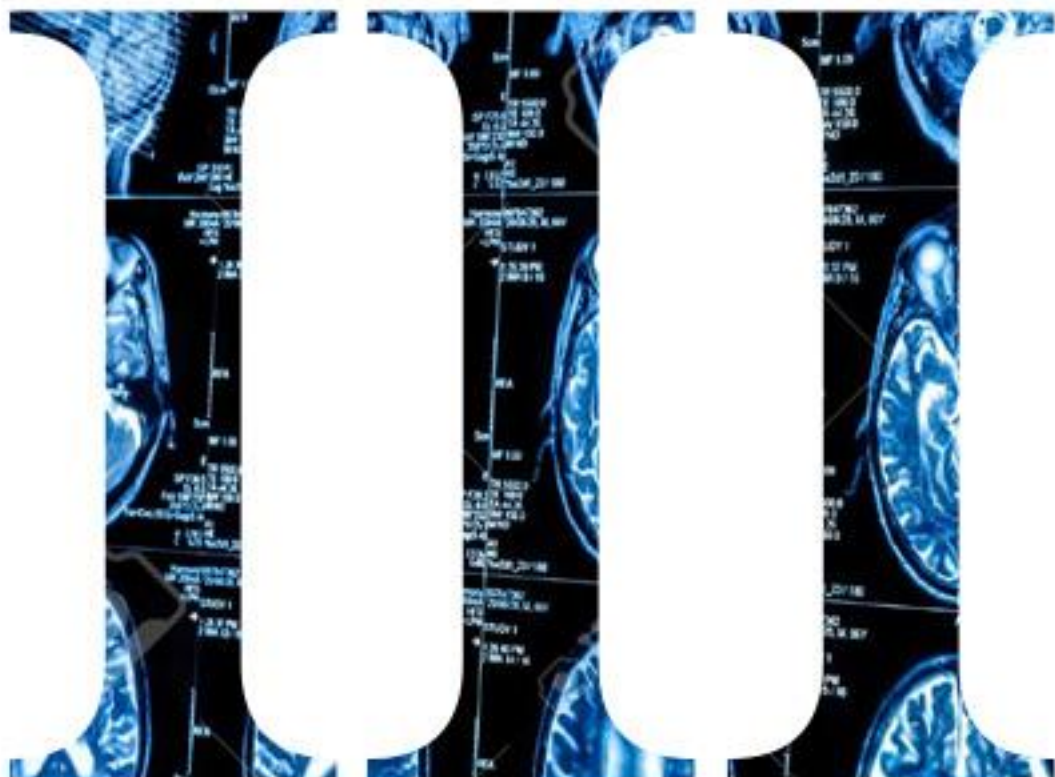
Purposes



Results and discussion

**Design, synthesis, structural characterization
and applications of proposed peptide-based materials**

Carlo Diaferia | University of Naples Federico II | XXX cycle



Section I

**Peptide-based materials as supramolecular
contrast agents for Magnetic Resonance Imaging**

Carlo Diaferia | University of Naples Federico II | XXX cycle

Section I: PBMs as supramolecular contrast agents for MRI

3.1 Peptide-based materials for MRI

Supramolecular contrast agents (CAs)⁶⁴ can be prepared for self-assembling of a monomeric units containing two different portions: i) a chelating agents able to allow kinetically and thermodynamically stable coordination of paramagnetic metal ions (like Gd^{3+} for T_1 positive CAs) for diagnostic applications in MRI, ii) a hydrophobic portion (one or more alkyl chains or a peptide sequence) able to prompt the self-assembling in water.

Due to the well-known capability of the diphenylalanine¹⁴⁴ and of its strictly related derivatives (FFF^{180,181}, FFFF^{182,183}, Fmoc-FF¹⁷⁵, Boc-FF¹⁷⁷) to self-assemble in a large variety of supramolecular nanostructured materials,¹⁹² FF sequence was selected as hydrophobic portion in order to obtain self-assembling monomeric units. Moreover, to enhance the foreseeable low water solubility, different polyethylene glycol (PEG) spacers were inserted at N-terminus between the Gd-complex and the aromatic framework. According to this design approach, the effect of the chemical modification of the FF homodimer has been carefully evaluated in terms of structural organization of the final material.

The relative simple self-organization of di-phenylalanine depends on a combination of two kinds of not covalent interactions: i) head-to-tail backbone hydrogen bonds and ii) π - π stacking between the aromatic ring of side chains.¹⁴⁷

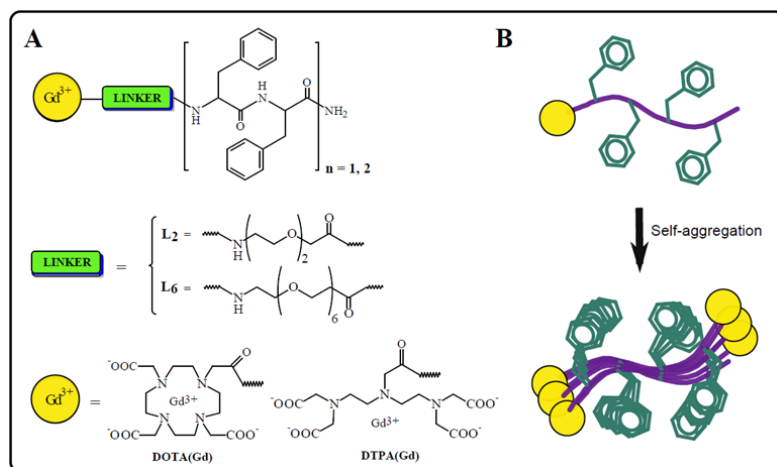


Figure 1: a) Schematic representation of diphenylalanine or tetraphenylalanine designed conjugates obtained using L₂ or L₆ polyethoxylic linkers and the DTPA(Gd) or DOTA(Gd) as gadolinium complexes. b) Putative aggregation pattern for poly-phenylalanine conjugates.

Hydrogen bonds and π - π stacking are weak not covalent interactions that occur only if mutual guidance and directionality of the counterparts

Section I: PBMs as supramolecular contrast agents for MRI

are kept. For a successful design, it is required remember that chemical modifications of Phe-Phe homodimer both at C or N-terminus may destroy the head-to-tail intermolecular hydrogen bonds, whereas π - π intermolecular interaction of the aromatic framework should be kept.

The first and simplest approach used was the derivatization at the N-terminus of the FF sequence with a two different bifunctional chelating agent, 1,4,7,10-tetraazacyclododecane- N,N,N,N- tetraacetic acid (DOTA) or diethylenetriaminepentaacetic acid (DTPA), for achieving Gd(III) coordination. DOTA and DTPA are a cyclic and a linear chelating agent, respectively. The compounds DOTA-F2 and DTPA-F2 (**Figure 1**) were easily synthesized according to solid phase peptide synthesis (SPPS).¹⁹⁶ After purification, products were characterized and identified by LC-ESI mass spectroscopy and ¹HNMR. Extended characterization data are reported in Appendix I

Gadolinium complexation was achieved coincubating peptide conjugates with GdCl₃ in equimolar ratios (1/1).

Independently from the chelating agent used, di-phenylalanine conjugates DOTA(Gd)-F2 and DTPA(Gd)-F2 did not show propensity to aggregate in water solution (data not shown). The verified incapability to self-assemble of these conjugated was related to the steric hindrance of the bulk gadolinium complex and to the loss of head-tail hydrogel bond interaction.¹⁹⁶

In order to restore the self-association between the Phe residues in the monomeric units, we designed and synthesized novel peptide conjugates, DOTA-L₂-F2 and DTPA-L₂-F2 (**Figure 1**), in which an ethoxylic linker, consisting of two (L₂) or six (L₆).

As previously observed for DOTA(Gd)-F2 and DTPA(Gd)-F2, also DOTA(Gd)-L₂-F2 and DTPA(Gd)-L₂-F2 did not show any self-assembling features.

Indeed, fluorescence spectra of these samples showed an emission peak at 282 nm, typically observed for the phenylalanine residue in its monomeric form.

Differently from these peptide conjugates, UV-Vis and fluorescence measurements suggest a weak aggregation tendency for DOTA-L₆-F2 and DTPA-L₆-F2 conjugates, in which L₂ spacer is replaced with L₆ spacer at six ethoxylic units (**Figure 2**).

UV-Vis spectra show the typical maximum of Phe residue at 257 nm ($\rightarrow\pi$ transition of the aromatic residue), and another maximum at 282 nm, distinctive of the Phe excimer formation (data not shown).¹⁸⁷

Accordingly, fluorescence spectrum of DOTA-L₆-F2 at 2.0 mg/mL reported in **Figure 2** clearly shows the monomer emission at 282 nm and the conspicuous excimer emission around 310 nm.^{184,186}

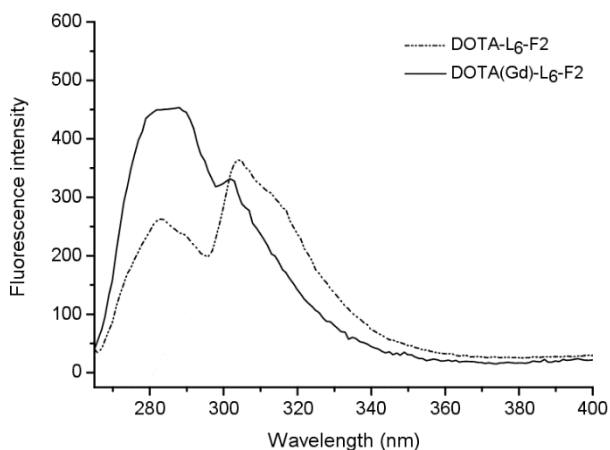


Figure 2: Fluorescence spectra of DOTA-L₆-F2 and its gadolinium complex DOTA(Gd)-L₆-F2 in water solution at 2.0 mg/mL

However, the emission peak of phenylalanine excimer almost disappears after the gadolinium complexation (**Figure 2**). The same behaviour is also displayed by DTPA-L₆-F2. This outcome could be attributed to the higher steric effect of gadolinium complex with respect to the chelating agent as free base.

In order to restore the interactions between the phenylalanine side chains, two different strategy were proposed:

- **Strategy I:** elongation of the aromatic framework by increasing the number of the phenylalanine residues from two to four, keeping unaltered the length of the spacer.^{196,197}
- **Strategy II:** The replacement of the phenylalanine residues with others non-coded amino acids having a more extended aromatic side chain. In particular, was used the 2-naphtylalanine amino acid.¹⁹⁸

3.2. Elongation of the aromatic framework (Strategy I)

According to the first strategy, the aromatic framework was elongated increasing the Phe residue from two to four. In addition, the position of the chelating agent was studied. The chelating agent was alternatively positioned at the N-terminus (**Strategy Ia**)¹⁹⁶ or at the center (**Strategy Ib**)¹⁹⁷ of the molecular organization.

The different position of the chelating agent permits to evaluate how the steric hindrance of the bulk Gd-complex affect the structural and the relaxivity properties of the supramolecular aggregate.

All the peptide conjugates as free bases and as gadolinium complexes were full characterized from the structural point of view both in solution and at the solid state. A variety of techniques such as fluorescence, Circular Dichroism (CD), Fourier Transform Infrared (FTIR), Dynamic Light Scattering (DLS), NMR, Wide-Angle (WAXS) and Small-Angle X-ray Scattering (SAXS) were employed to achieve the definition of the structural organization of the peptide monomeric units in the self-assembled nanostructure. Moreover, the relaxometric behavior, cytotoxicity and cellular uptake in J774A.1 and 3T3 cells of self-organized nanostructures were also investigated.

3.2.1 Elongation of the aromatic framework- N-derivatization (Strategy Ia)

According to the rational of Strategy Ia, two tetra-phenylalanines derivatized on their N-termini with a Gd-complex (DOTA(Gd)-L₆-F4 and DTPA(Gd)-L₆-F4) were synthesized. A PEG linker having six oxyethelenic units was interposed between the chelating agent and the aromatic framework (**Figure 1**).

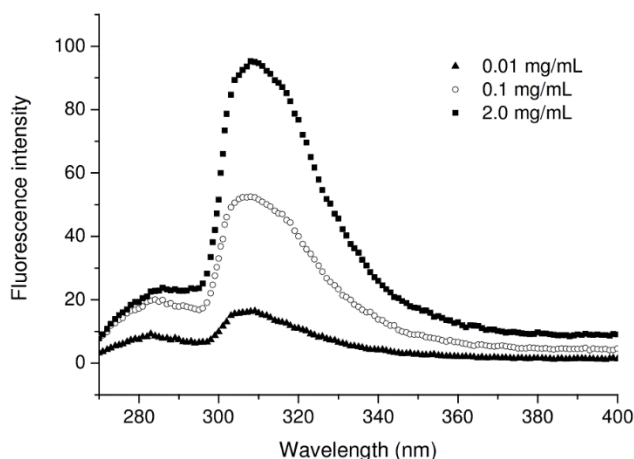


Figure 4. Fluorescence spectra of DOTA(Gd)-L₆-F4 tetra-phenylalanine at 0.01 mg/mL, 0.1 mg/mL and 2.0 mg/mL concentration. All emission spectra were recorded at 25°C between 265 and 400 nm with excitation at 258 nm.

Both the peptide Gd-complexes showed high water solubility: their solutions appear perfectly clear up to 35 mg/mL; whereas higher concentration (~50 mg/mL) leads to a weak hydrogel formation. The same behavior was also observed for L₆-F4 derivative lacking of chelating agent at the N-terminus.¹⁹⁹

Preliminarily, propensity to self-assemble of both peptides was initially evaluated by fluorescence spectroscopy.

As previously described, fluorescence spectrum of Phe based peptides is characterized by an emission peak at 282 nm upon excitation at 257 nm.^{184,186} However, an additional peak at 310 nm appears when the formation of Phe excimers occurs. This phenomenon is often related to the peptide concentration. In **Figure 4**, spectra of DOTA(Gd)-L₆-F4 at three different concentrations (0.01 mg/mL, 0.1 mg/mL and 2.0 mg/mL) are reported. From the inspection of the spectra is clearly visible the excimer emission peak at 301 nm also at low concentration. Furthermore, by increasing the concentration of DOTA(Gd)-L₆-F4 from 0.01 to 2.0 mg/mL, a progressive increase (from 1.7 to 4.0) of the ratio between the fluorescence intensities at λ_{310} and λ_{282} is observed.

3.2.2 Determination of the Critical Aggregation Concentration (CAC)

Critical aggregate concentration (CAC) values of tetra-phenylalanine derivatives as free basis or as gadolinium complexes were quantitatively estimated by using two fluorescence-based methods: i) the 8-anilino-naphthalene-1-sulfonate ammonium salt (ANS) and ii) the pyrene (Pyr). Results obtained with these two complementary methods are listed in **Table 1**.

ANS fluorophore gives fluorescence emission at 460-480 nm only in a hydrophobic environment, such as in the micelle core.⁶³ The fluorescence intensity of an ANS solutions (20 mM in water) at 475 nm as function of tetra-phenylalanine derivatives concentration are reported in **Figure 5**.

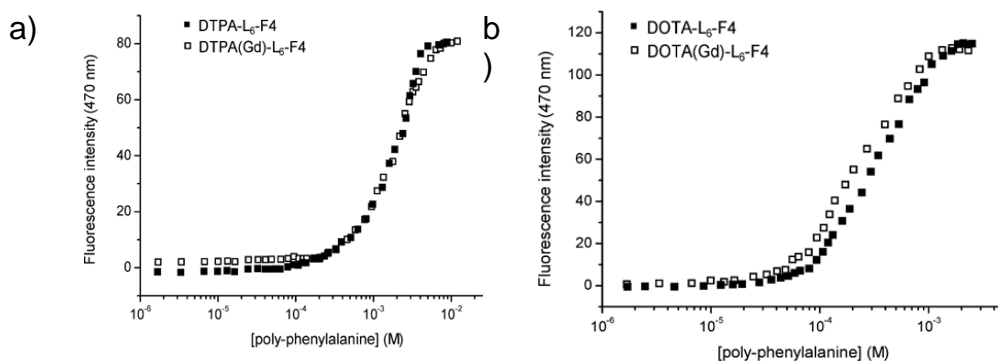


Figure 5: Fluorescence intensity emission of ANS fluorophore at 475 nm vs. concentration of DTPA-L₆-F4 (a) and DOTA-L₆-F4 (b) as free bases or as gadolinium complexes. CAC values are established from the break points.

Section I: PBMs as supramolecular contrast agents for MRI

During the titration experiment, the fluorescence emission of DOTA-L₆-F4 remains unchanged until 75 mM (~ 0.099 mg/mL), whereas an increase in the signal at 475 nm was detected above this concentration value, indicating the self-organization of the tetra-phenylalanine derivative (**Figure 5a**). Usually, in the molecules containing chelating agents, aggregation properties can be influenced by two different phenomena: electrostatic repulsions and/or steric hindrance.²⁰⁰ However, only a slight decrease in the CAC value is observed after the gadolinium complexation that reduces the negative charge from -3 to 0 (CAC = 0.076 mg/mL for DOTA(Gd)-L₆-F4).

On the contrary, a significant change has been observed when DOTA is replaced by the branched chelator DTPA (CAC = 0.59 mg/mL) or by its Gd(III) complex DTPA(Gd) (CAC = 0.51 mg/mL) (**Figure 5b** and **Table 1**).

Table 1. Critical aggregate concentration (CAC) values of tetra-phenylalanine derivatives measured by titration of ANS fluorophore.

Sample	CAC (M)	CAC (mg/mL)
DOTA-L ₆ -F4	$7.5 \cdot 10^{-5}$	$9.9 \cdot 10^{-2}$
DOTA(Gd)-L ₆ -F4	$5.1 \cdot 10^{-5}$	$7.6 \cdot 10^{-2}$
DTPA-L ₆ -F4	$4.5 \cdot 10^{-4}$	$59 \cdot 10^{-2}$
DTPA(Gd)-L ₆ -F4	$3.5 \cdot 10^{-4}$	$51 \cdot 10^{-2}$

These results suggest that the influence of electrostatic repulsions is almost negligible, whereas the replacement of the macrocycle DOTA with the branched and bulky DTPA produces an increase of the CAC values. Aggregation of tetra-phenylalanine derivatives was also investigated by monitoring fluorescence behaviour of pyrene (Pyr). 1 mM Pyr solution was titrated by adding increasing amounts of tetra-phenylalanine derivatives. Fluorescence spectra of Pyr/ DOTA(Gd)-L₆-F4 solutions are reported in **Figure 6a,b**.

Pyr is a poorly soluble water molecule that shows an emission spectrum in water with five vibrational bands when excited at $\lambda = 335$ nm: the first (I_1 at 373 nm) and the third (I_3 at 383 nm) of them are strongly affected by the polarity of the surrounding environment.²⁰¹

Moreover, at high concentration Pyr gives stacking phenomena resulting in excimer's formation that can be diagnosed by the

appearance of a maximum at around 480 nm.²⁰² The addition of small amounts of DOTA(Gd)-L₆-F4 to Pyr solution causes a progressive decrease of fluorescence signal (**Figure 6a**).

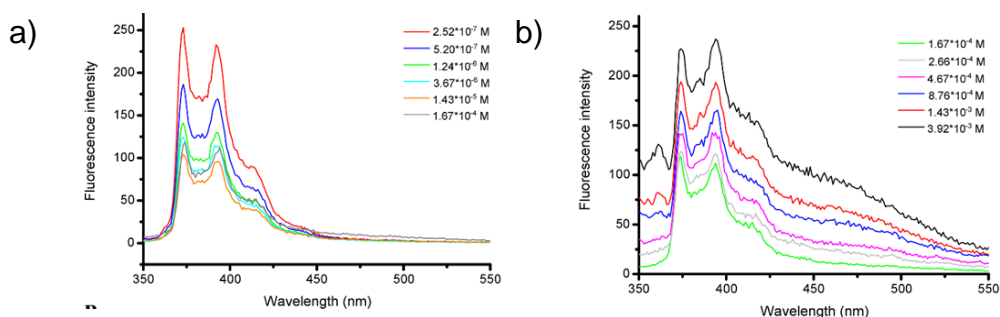


Figure 6: Fluorescence spectra of 1mM pyrene solution titrated with DOTA(Gd)-L₆-F4. Pyr emission spectra were recorded at 25°C between 350 and 550 nm with excitation at 335 nm.

This effect was observed until concentration 14.3 mM of tetra-phenylalanine derivative, in which Pyr/DOTA(Gd)-L₆-F4 molar ratio is 1/10. On the contrary, at concentration of 167 mM and higher, an increase of the fluorescence intensities occurs.

These data indicate that the aggregation phenomenon occurs at concentration within the 14.3 - 167 mM range, in agreement with the CAC value (51 mM) found by ANS titration, suggesting that when DOTA(Gd)-L₆-F4 concentration is lower than 14.3 mM, the predominant effect is a quenching due to the aromatic stacking between phenylalanine residues and pyrene, whereas above this concentration, a Fluorescence Resonance Energy Transfer (FRET) effect occurs in which tetra-phenylalanines, in their aggregated form, act as donor for pyrene.

3.2.3 Secondary structure assignment

The secondary structure of DOTA-L₆-F4 and DTPA-L₆-F4 peptide derivatives, as free bases or as gadolinium complexes, was assessed using circular dichroism (CD in **Figures 7** and **8**) and Fourier transform infrared spectroscopies (FTIR in **Figure 9a**). These spectroscopic methods are typically employed for monitoring the conformational behavior of peptide-based nanostructures and mainly for revealing secondary structural features, such as β -sheet structures, accompanying the formation of amyloid fibers.

CD spectra of solutions at several concentrations were recorded between 280 and 195 nm. CD spectra at concentrations below or close to CAC values clearly show two maxima around 205 and 220 nm, due

Section I: PBMs as supramolecular contrast agents for MRI

to aromatic side-chains stacking, and pronounced minimum at 232 nm, which can be associated with a β -structure^{184,186,203}

From the inspection of **Figure 7**, the CD spectra of peptide derivatives show similar trend irrespective of chelating agent.

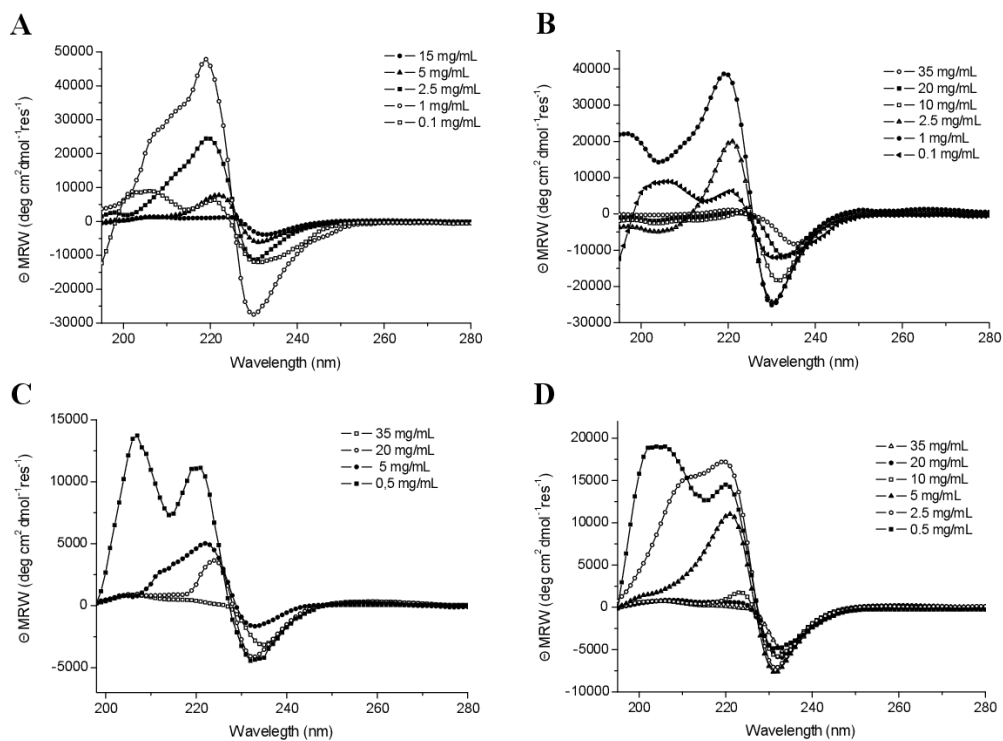


Figure 7: Selected Far-UV CD spectra of (a) DOTA-L₆-F₄, (b) DOTA(Gd)-L₆-F₄, (c) DTPA-L₆-F₄ and (d) DTPA(Gd)-L₆-F₄ in 0.1-35 mg/mL concentration range.

However, the conformational transition described above was detected at higher concentration for DTPA-L₆-F₄ than DOTA-L₆-F₄, in agreement with the difference in CAC values between these conjugates. Dichroic tendency of DOTA(Gd)-L₆-F₄ at 20 mg/mL (well above the CAC value determined by fluorescence) was also evaluated as function of the temperature between 10 and 80°C. At low temperature, it was observed a distinct minimum around 235 nm, typical of the poly-phenylalanine in β -aggregate form (**Figure 8a**).

By increasing the temperature, the shape of the spectra remains unchanged, but a progressive decrease of the signal intensities with a red-shift effect occurs probably due to a progressive unfolding of the peptide conjugate with higher molecular mobility.

However, the conformational features are kept almost until 80°C, thus indicating a good thermal stability of the aggregate.²⁰⁴ The integrity of

Section I: PBM as supramolecular contrast agents for MRI

the gadolinium complex in DOTA(Gd)-L₆-F4 at the final temperature (80 °C) was confirmed by the mass peak reported in **Figure 8b**.

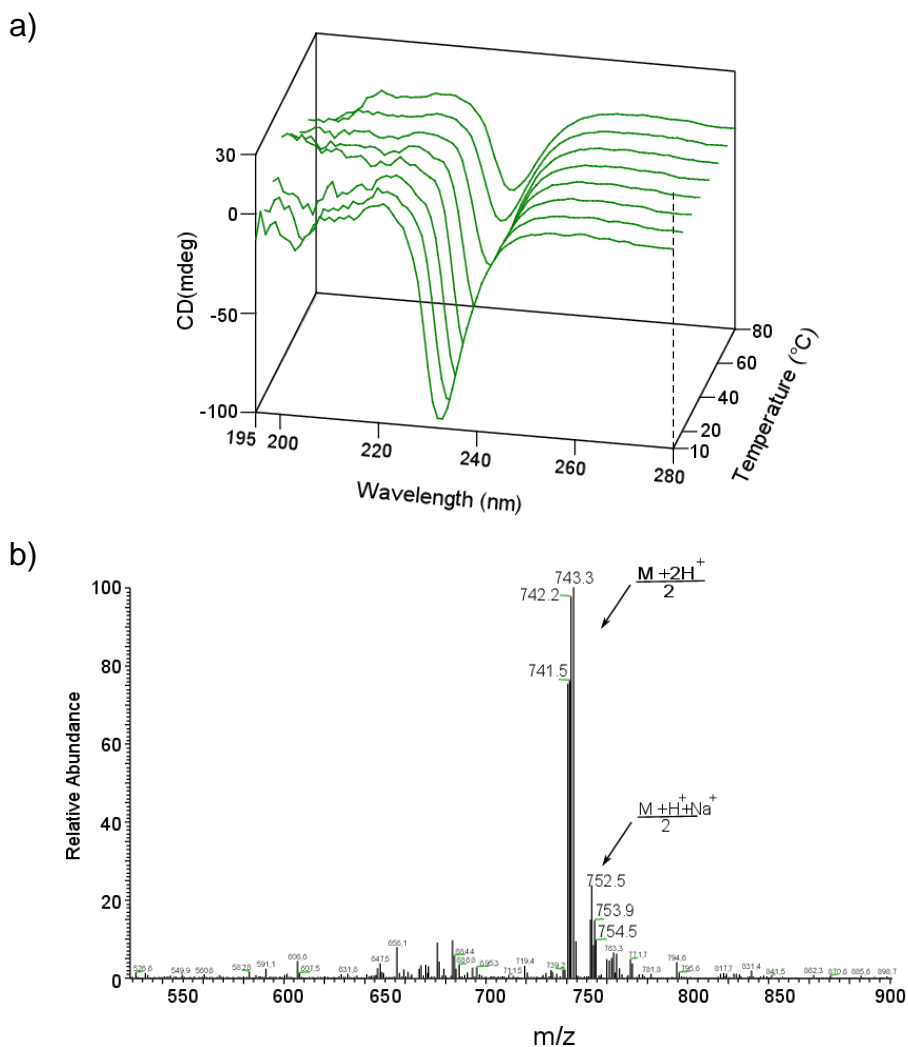


Figure 8: a) CD spectra of DOTA(Gd)-L₆-F4 aggregate solution at 20 mg/mL: aggregate solution was heated from 10 °C to 80 °C; b) ESI mass spectrum of DOTA(Gd)-L₆-F4 after heating at 80 °C.

FTIR spectroscopy is often employed to probe the secondary structure assumed by di- or tetra-phenylalanine derivatives.^{205,206}

Usually, the attention is focused on the amide I bands able to provide information on the secondary structure adopted. FTIR spectra in the amide I region are shown in **Figure 9a** for DTPA(Gd)-L₆-F4 and DOTA(Gd)-L₆-F4 solutions at 2.0 mg/mL.

Section I: PBMs as supramolecular contrast agents for MRI

Both the spectra show a principal peak at 1637 cm^{-1} and a minor peak at 1680 cm^{-1} .

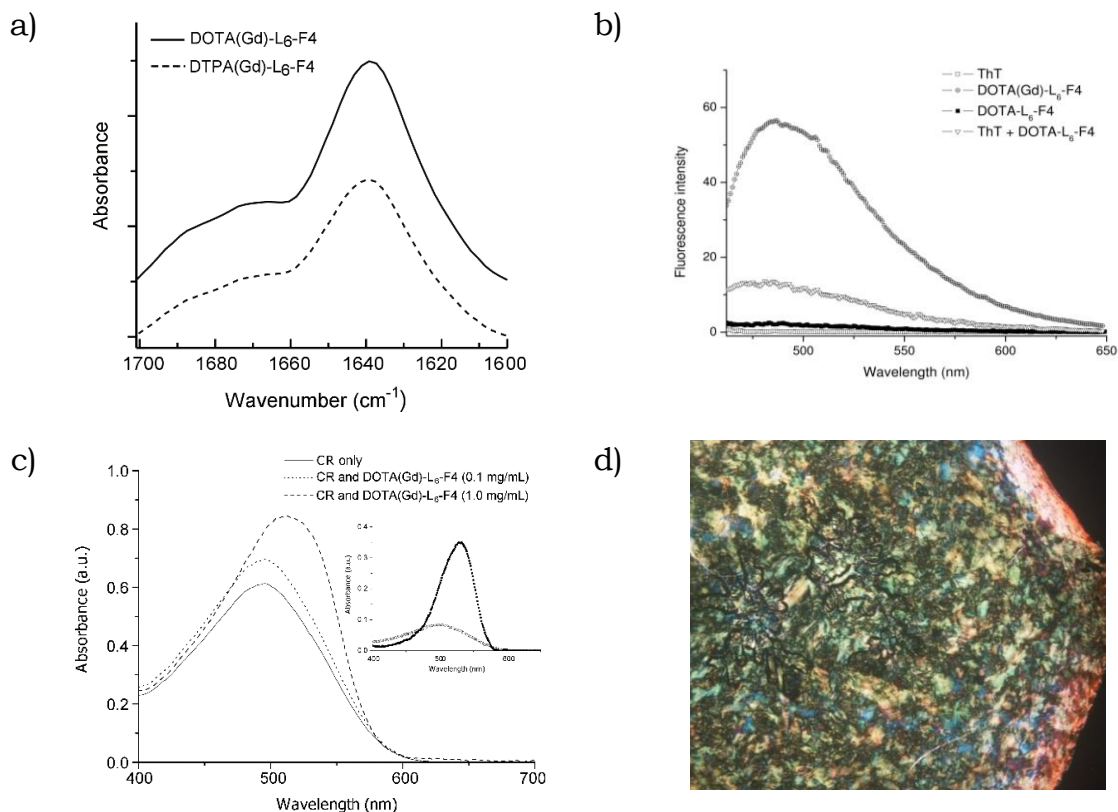


Figure 9: a) FTIR spectra of DOTA(Gd)-L₆-F4 and DTPA(Gd)-L₆-F4 in the amide I region at 2.0 mg/mL concentration. b) Fluorescence spectrum of ThT before and immediately after the addition of DOTA-L₆-F4 in aqueous solution. Spectra of DOTA-L₆-F4 and its gadolinium complex DOTA(Gd)-L₆-F4 are also reported for comparison. Final concentration of poly-phenylalanine derivative in cuvette is 2.0 mg/mL. c) The UV-Vis spectra of DOTA(Gd)-L₆-F4, stained with Congo Red, at 0.1 and 1.0 mg/mL. The spectrum of Congo Red is also reported for comparison. In the insert are reported the spectra of DOTA(Gd)-L₆-F4 0.1 mg (○) and 1.0 mg/mL (●) after the subtraction of CR spectrum. d) Polarized optical microscopy image of dried DOTA(Gd)-L₆-F4 onto a glass microscopy slide stained with Congo Red solution.

The peak at 1637 cm^{-1} is strongly indicative of β -sheet formation, whereas the fewer intensity of the second peak at 1680 cm^{-1} is indicative of an antiparallel orientation of the β -sheets.²⁰⁷ FTIR spectra were also recorded on a dried film of DTPA(Gd)-L₆-F4 and DOTA(Gd)-L₆-F4 (data not shown).

These spectra reported show a similar profile with respect to samples in solution.

Section I: PBMs as supramolecular contrast agents for MRI

Amyloid type fibril formation was also confirmed by using the typical Thioflavin T²⁰⁸ (ThT) and Congo Red spectroscopic assays.²⁰⁹

Fluorescence spectra of ThT, before and after the addition of DOTA-L₆-F₄, are reported in **Figure 9b**. Spectra of DOTA-L₆-F₄ and its Gd(III) complex in absence of ThT are also reported for comparison.

As shown in **Figure 9b**, DOTA(Gd)-L₆-F₄ gadolinium complex alone gives an emission peak in the same region in which the emission of ThT- β aggregate is expected. Therefore, in this sample we cannot attribute the peak at 482 nm to the interaction between ThT and the tetra-phenylalanine aggregate. On the contrary, in its uncomplexed form, DOTA chelating agent did not provide fluorescence signals. The sudden appearance of an emission peak at 482 nm after the addition of DOTA-L₆-F₄ (2.0 mg/mL as final concentration) indicates unambiguously the binding of the ThT to the peptide derivatives.¹²⁵ The fluorescence signal remains unchanged until 2h from the incubation, thus confirming the immediate interaction of ThT with peptides.

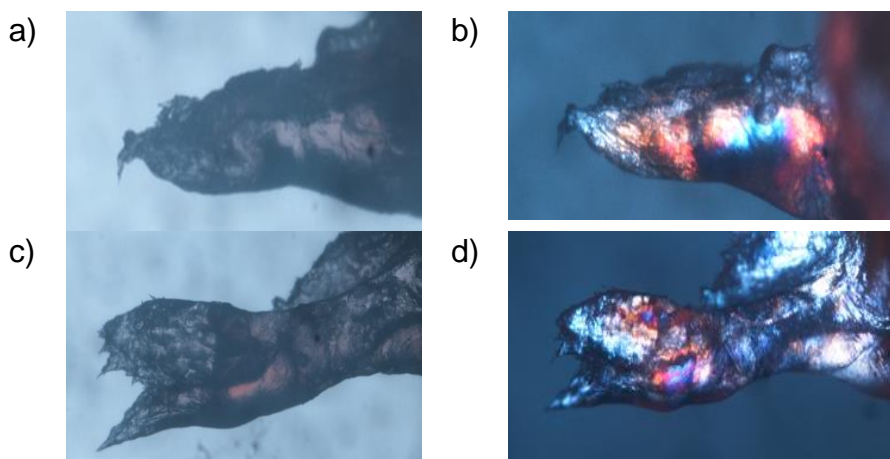


Figure 10: Images of a,b) DTPA(Gd)-L₆-F₄ and c,d) DOTA(Gd)-L₆-F₄ fibers stained with Congo Red and observed with a Nikon microscope under bright field illumination (on the left) and between crossed polars (on the right). Fibers containing Congo Red were obtained by the stretch frame method. 10 μ L of peptide aqueous solution (3 wt%), containing was suspended between the ends of a wax-coated capillary and dried.

The same behavior was also observed for tetra-phenylalanine analogues containing DTPA chelating agent and its gadolinium complex (data not shown). According to the ThT assay, Congo Red (CR) staining (both UV-Vis spectroscopy and polarized optical microscopy) confirms the amyloid type fibril formation.²⁰⁹ CR is an azoic dye, frequently used as indicator of the occurrence of amyloid like fibrils. UV-Vis spectra, reported in **Figure 9c**, show the spectral shift of the

Section I: PBMs as supramolecular contrast agents for MRI

conventional CR band from 488 to 540 nm after the addition of DOTA(Gd)-L₆-F4 in the cuvette for two different concentrations (0.1 and 1.0 mg/mL). At the same time, both air-dried films of Gd(III) poly-phenylalanine derivatives stained with CR and F4 peptide dried fibers containing CR exhibit intense green birefringence when imaged with polarized optical microscopy (**Figure 9d** and **Figure 10**).

3.2.4 Solid state characterization: TEM and X-ray Diffraction

The morphology of the self-assembled nanostructures was also assessed by transmission electron microscopy (TEM) and X-ray diffraction.

Selected images of DTPA(Gd)-L₆-F4 and DOTA(Gd)-L₆-F4 gadolinium complexes in water solution at 5.0 mg/mL show the presence of long nanofibers with a minimum thickness around 10 nm (**Figure 11**).

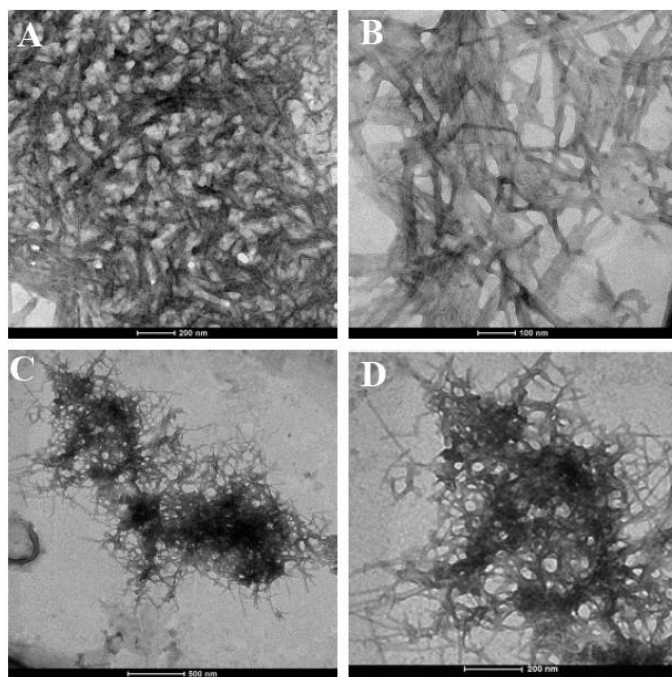


Figure 11: Selected TEM images for (a-b) DOTA(Gd)-L₆-F4 at 5.0 mg/mL and (c-d) DTPA(Gd)-L₆-F4 at 5.0 mg/mL. Scale bars are 200 nm for A and D images; 100 nm for B and 500 nm for C.

The recorded X-ray diffraction (XRD) patterns from DOTA(Gd)-L₆-F4 and L₆-F4 peptide dried stalks are shown in **Figure 12a,b**. Miller indices and *d*-spacings for both fiber types were determined using the software

Section I: PBM as supramolecular contrast agents for MRI CLEARER²¹⁰ and are reported in (**Table A1** and **Table A2** reported in **Appendix II**).

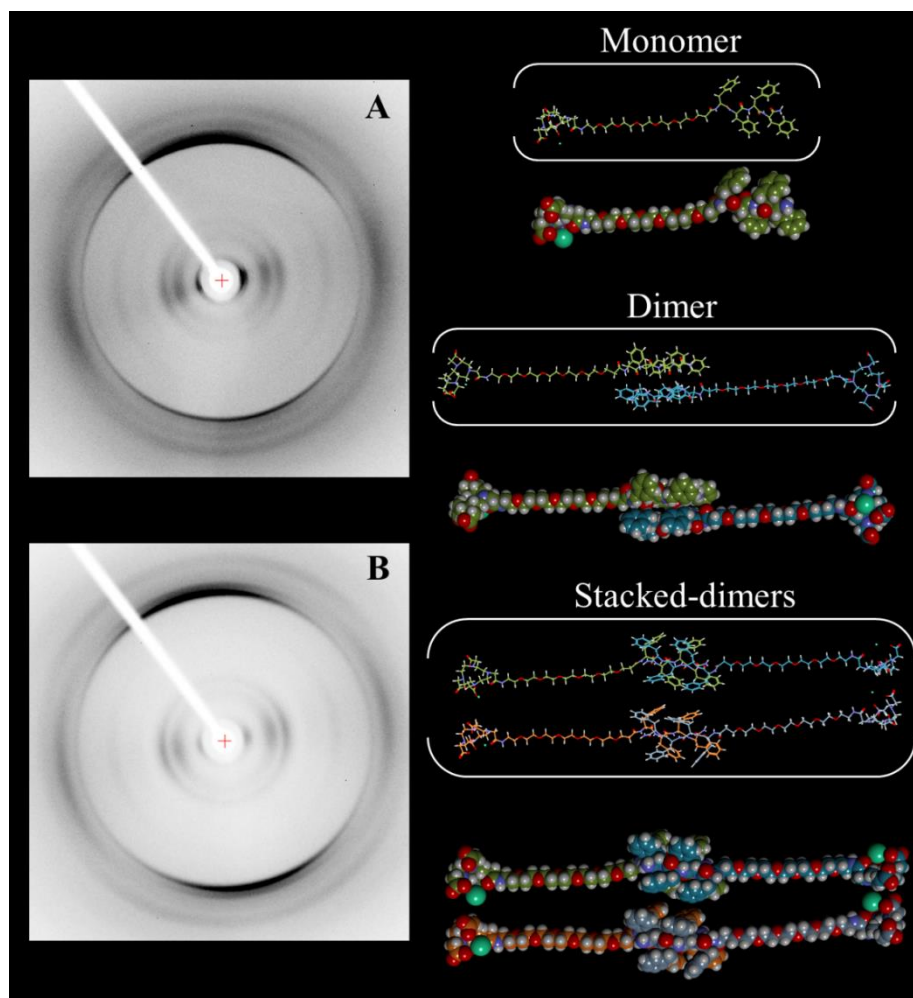


Figure 12: Selected X-ray fiber diffraction for DOTA-L₆-F4 (A) and L₆-F4 (B). These patterns show the diffraction features associated with the b structure. Based on our experimental results, on the right side it is reported a model of DOTA(Gd)-L₆-F4 as monomer, dimer and stacked-dimers.

As clearly indicated from the diffraction pattern, the structural arrangement of the PEGylated cationic tetra-phenylalanine was not significantly affected from the functionalization of the N-terminus with the DOTA (or DTPA, data not shown) chelating agents.¹⁹⁹ Both the X ray diffractions show the typical “cross-β” diffraction pattern of amyloid fibers, with a Bragg spacing of 4.8-4.9 Å along the meridian, generally attributed to the inter-chain distance between the hydrogen-bonded-strands oriented perpendicularly to the fiber axis, and a more diffuse

periodicity of ~ 10 Å in the equatorial direction, usually ascribed to the staking of these β -sheets perpendicularly to the fiber axis.¹²⁴

These XRD and TEM results are in agreement with the above reported CD (**Figure 7**) and IR data (**Figure 9a**) indicating a β -sheet conformation of DOTA(Gd)-L₆-F4 in a dried film. In **Figure 12** it is also reported a simplified theoretical model in extended conformation of DOTA(Gd)-L₆-F4 based on experimental results.

To better appreciate the monomer dimension (estimated in ~ 50 Å), it is imagined that the antiparallel two-stranded in β -disposition pointed up the plane of the paper, and the stacked-dimers with the fiber axis pointed toward the observer.

3.2.5 Relaxometry

As widely described in the Introduction section, Gd-complexes are used as positive MRI contrast agents (CAs) as they are able to strongly enhance the water protons relaxation rate in aqueous solutions thanks to the magnetic dipolar interaction between unpaired electrons on the Gd³⁺ ions and the water protons. Their efficacy as MRI CAs is thus measured on the basis of this ability, which is usually defined as longitudinal “relaxivity” (r_{1p}) and is referred to the water proton relaxation rate of a solution containing one millimolar concentration of the Gd-complex.

The relaxivity of a Gd-containing system depends on the complex interplay among structural, dynamic and electronic parameters.^{15,16} At the frequencies most commonly used in commercial tomographs (20-60 MHz), r_{1p} is generally determined by the reorientational correlation time (τ_R) of the chelate so that high molecular weight systems display higher relaxivity.²¹¹

Based on this property, it is possible to follow the occurrence of an aggregation process involving a Gd-complex through the measure of the water proton longitudinal relaxation rate of its aqueous solution.

The relaxivities of DOTA(Gd)-L₆-F4 and DTPA(Gd)-L₆-F4, measured at 21.5 MHz (0.5 T) and 298K as a function of the complex concentration, are reported in **Figure 13a**. The observed progressive enhancement in relaxivity is indicative of the self-aggregation of the two Gd-complexes. The insert in **Figure 13a** shows an amplification of the graph at low concentration values from which it is possible to observe that DTPA(Gd)-L₆-F4 starts to aggregate at higher concentrations than DOTA(Gd)-L₆-F4, reflecting the CAC values determined by fluorescence spectroscopy.

The analysis of the magnetic field dependence of the relaxivity, obtained through the registration of the so called NMRD (Nuclear Magnetic Resonance Dispersion) profiles, allows the determination of

Section I: PBM as supramolecular contrast agents for MRI

the principal parameters characterising the relaxivity of a Gd(III) chelate.

The NMRD profiles of DOTA(Gd)-L₆-F4 and DTPA(Gd)-L₆-F4, measured at 40 mg/mL concentration, are reported in **Figure 13b**. The shape of both the profiles, with the characteristic peak of relaxivity in the region of Proton Larmor Frequencies 10-70 MHz, is a clear indication that, at this concentration, the Gd-complexes are in an aggregated form.

Data were fitted to the conventional Solomon-Bloembergen-Morgan theory^{212,213} and the relative fitting parameters are reported in **Table 2**.

The high field relaxivity of the two complexes are quite similar, being, at 20 MHz, 14.8 and 14.0 mM⁻¹s⁻¹ for DOTA(Gd)-L₆-F4 and DTPA(Gd)-L₆-F4, respectively. The t_R values found for the two complexes are in fact very close. On the other hand, the big difference in relaxivity observed in the low field region has to be ascribed to the difference in the electronic relaxation time (t_{s0}) of the two Gd-complexes (**Table 2**).

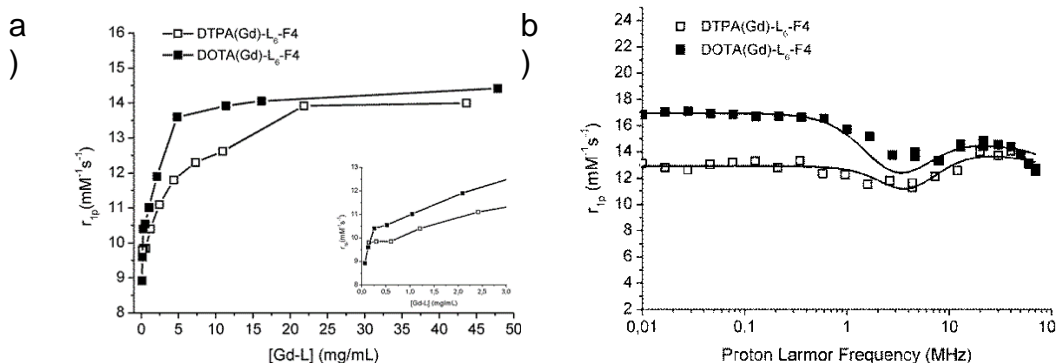


Figure 13: (A) Longitudinal proton relaxivity of DOTA(Gd)-L₆-F4 and DTPA(Gd)-L₆-F4 measured at 21.5 MHz (0.5 T) and 298 K as a function of the concentration of the poly-phenylalanine Gd-complexes. (B) NMRD profiles of the 40 mg/mL aqueous solutions of the two poly-phenylalanine Gd-complexes at 298K. The data refer to 1 mM concentration of the paramagnetic complexes.

It is in fact known, that highly symmetric and rigid DOTA-type chelates generally have longer t_{s0} values than DTPA-like, and this physically translates to a higher low-field relaxivity.²¹⁴

It is worth to note that the t_R values extracted from the fitting procedure for DOTA(Gd)-L₆-F4 and DTPA(Gd)-L₆-F4 in the aggregated form are quite short if compared to those usually found for nano-sized aggregates (1-30 ns).

Likely, this finding can be explained with the occurrence of a quite fast internal motility of the Gd-complexes along the linker spacer with

Section I: PBMs as supramolecular contrast agents for MRI

respect to the overall fibril-like structures, as evidenced in the model arrangement proposed in **Figure 12**.

Table 2. Main relaxometric parameters derived from fitting of NMRD profiles at 21.5 MHz reported in Figure 10B.^[a]

System	r_{1p} ($\text{mM}^{-1}\text{s}^{-1}$)	Δ^2 (s^{-2}) ^[b]	τ_V (ps) ^[c]	τ_{s0} (ps) ^[d]	τ_R (ps) ^[e]
DOTA(Gd)-L ₆ -F4	14.8	8.0×10^{18}	49	212	490
DTPA(Gd)-L ₆ -F4	14.0	1.25×10^{19}	52	127	457

^[a]On carrying out the fitting procedure, some parameters were fixed to reasonable values: $r_{\text{Gd-H}}$ (distance between Gd and protons of the inner sphere water molecule) = 3.1 Å; a (distance of minimum approach of solvent water molecules to Gd^{3+} ion) = 3.8 Å; D (solvent diffusion coefficient) = $2.2 \cdot 10^{-5} \text{ cm}^2 \text{ s}^{-1}$. ^[b]Squared mean transient zero-field splitting (ZFS) energy. ^[c] Correlation time for the collision-related modulation of the ZFS Hamiltonian. ^[d]Electronic relaxation time at zero field (calculated as $1/\tau_{s0} = 12\Delta^2 \times \tau_V$). ^[e]Reorientational correlation time.

3.2.6 Cytotoxicity and MRI evaluation of the cellular uptake

The cytotoxicity of the fibril nanoaggregates of DOTA(Gd)-L₆-F4 and DTPA(Gd)-L₆-F4 has been initially tested in the mouse embryonic fibroblast cell line 3T3 in the concentration range 0.5-5.0 mg/mL (**Figure 14a**). With a view to the subsequent experiments on the evaluation of the MRI cellular response, given that the particles, in this preliminary stage, are not functionalized for a target-specific cellular internalization, it was necessary to push the uptake experiment with an overnight incubation.

The cytotoxicity assay revealed a significant reduction in fibroblast viability along with the increase of the Gd-complexes concentration, with a higher effect in the case of DOTA(Gd)-L₆-F4 particles.

The cytotoxicity appears to be higher than that reported in the case of analogous di-phenylalanine microtubes in the same cell line¹⁵² because of the longer incubation time (overnight in our experiments vs. 2 hours in the literature data¹⁵²).

A recent work on the assessment of the cellular response to dissolution and degradation products from self-assembled Fmoc-FF gels revealed that the critical factor affecting cell viability is the time a gel is allowed to degrade and leach into the media.²¹³

Section I: PBM as supramolecular contrast agents for MRI

It is hypothesized that a way to elude a long incubation time while maintaining a sufficient amount of internalized probes to test their ability to enhance the MRI cellular response would be to use a macrophagic cell line which attitude is to phagocytize a huge amounts of particles in short times. Thus, the cytotoxicity of the fibril nanoaggregates of DOTA(Gd)-L₆-F4 and DTPA(Gd)-L₆-F4 was investigated in J774A.1 mouse macrophages (**Figure 14b**) in the same concentration range (0.5-5.0 mg/mL) but with an incubation time of 3h. In this case, the treated cells showed the same viability of the control cells even at the higher concentrations.

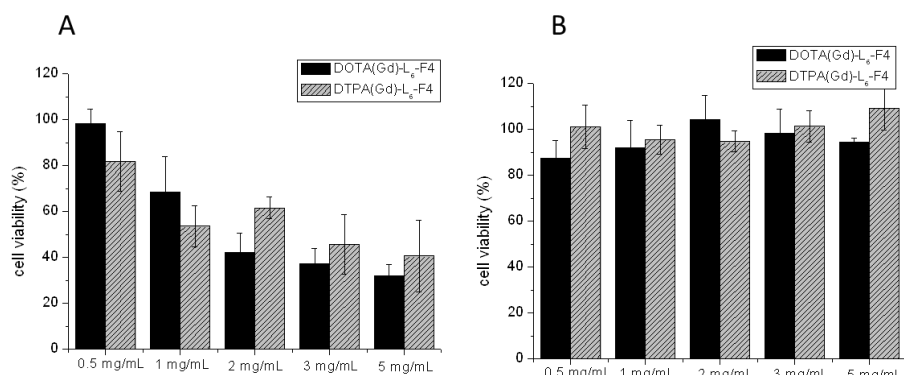


Figure 14: Cell viability percentage, evaluated by CellTiter-Blue[®] reagent test, after overnight treatment of the 3T3 fibroblasts (a) and 3h treatment of J774A.1 macrophages (b) with various concentrations of DOTA(Gd)-L₆-F4 and DTPA(Gd)-L₆-F4. Data are expressed as the mean \pm SD (n = 3).

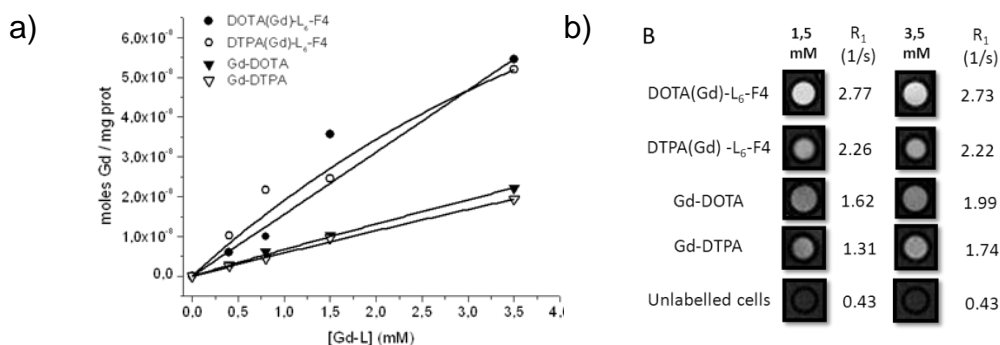


Figure 15: a) Amount of internalized gadolinium ions, evaluated by ICP-MS, in J774A.1 cells incubated with increasing concentrations of DOTA(Gd)-L₆-F4, DTPA(Gd)-L₆-F4, Gd-DOTA and Gd-DTPA for 3 hours. b) T₁-weighted MR-images, and relative observed relaxation rates, of pellets of J774A.1 cells labelled with 1.5 and 3.5 mM DOTA(Gd)-L₆-F4, DTPA(Gd)-L₆-F4, Gd-DOTA and Gd-DTPA.

Section I: PBMs as supramolecular contrast agents for MRI

Next, the uptake efficiency of DOTA(Gd)-L₆-F4 and DTPA(Gd)-L₆-F4 nanoaggregates and their efficacy in enhancing the MR-signal upon internalization, were investigated in J774A.1 cells and compared to those of the parents Gd-DOTA (Dotarem[®], Guerbert SA, France) and Gd-DTPA (Magnevist[®], Schering AG, Germany) complexes. The cells were incubated with increasing concentrations of DOTA(Gd)-L₆-F4 and DTPA(Gd)-L₆-F4 for 3h at 37 °C and the amount of internalized gadolinium determined through ICP-MS analysis (**Figure 15a**).

3.3 Elongation of the aromatic framework- Gd containing telechelic PEG end-capped by FF motives (Strategy Ib).

As an alternative the Gd-complex can be positioned at the center of the aromatic framework. According to this approach, it was designed and the synthesized asymmetric analogue monomer for obtain supramolecular CA. FF-AdOO-Lys(DOTA-Gd)-AdOO-FF [indicated as FF-DOTA(Gd)-FF] is designed as a telechelic PEG-polymer end-capped by FF motives (for a total of four Phe residue for molecule). The Gd-complex is placed at the center of F4-PEG-motive, bounded to a N^E of a lysine (Lys) residue (**Figure 16**).

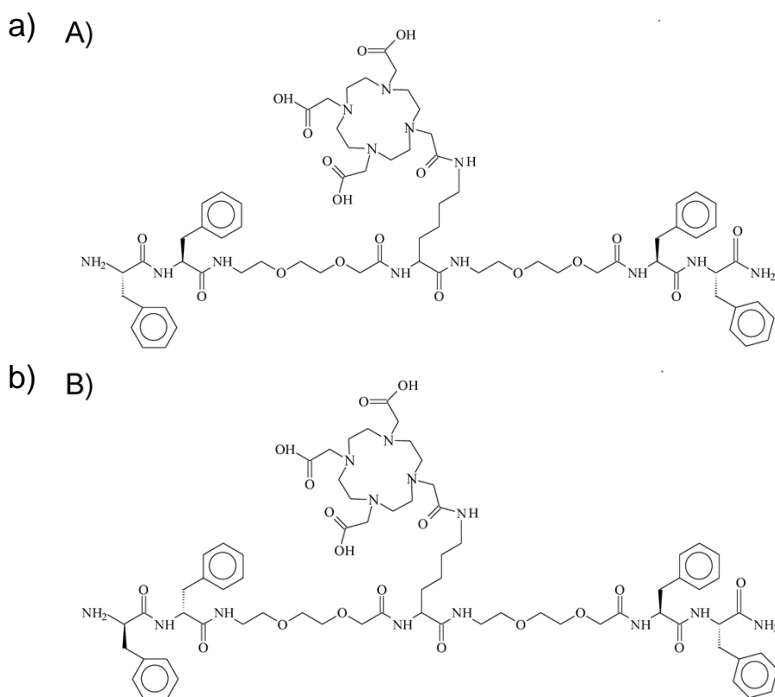


Figure 16: Schematic representation of a) FF-DOTA-FF and b) ff-DOTA-FF.

This peptide conjugate has been designed with the idea to confer higher rigidity to the DOTA(Gd) complex with respect to the already studied tetraphenylalanine derivatives, in which the chelating agent is anchored to a long and flexible oxoethylene linkers.¹⁹⁶ Thanks to their high tendency to associate via non covalent interactions, the two hydrophobic phenylalanine residues on the N and C termini should guarantee aggregating properties for the final adducts.

The objective of this study is aimed to evaluate how the relaxivity properties of the self-assembled CA can be affected by the different position having the Gd(III) complex in the aromatic framework.

Due the high symmetry of the molecule and in order to investigate the effect of the phenylalanine chirality on the self-aggregation and relaxivity properties, an analogue, *ff*-DOTA(Gd)-FF, in which the two L-Phe residues at the N-terminus are replaced with two D-Phe (*f*), was also synthesized and studied.

Schematic representation of FF-DOTA(Gd)-FF peptide conjugate and its analogue *ff*-DOTA(Gd)-FF is reported in **Figure 16a** and **Figure 16b**. On the basis of the literature,¹⁵³ the building block based on the D-amino acid analogue of the FF dipeptide should self-assemble into highly persistent discrete nanotubes having the same structural features as the corresponding L-amino acid peptide.

The observed variations in terms of relaxometric performances are analyzed and correlated to the structural morphology of the aggregate using several techniques: fluorescence, Circular Dichroism (CD) and Fourier Transform Infrared (FTIR) spectroscopies for aggregation tendency and secondary structure determination; Dynamic Light Scattering (DLS) and Transmission Electron Microscopy (TEM) for morphological definition.

3.3.1 Peptide conjugates synthesis

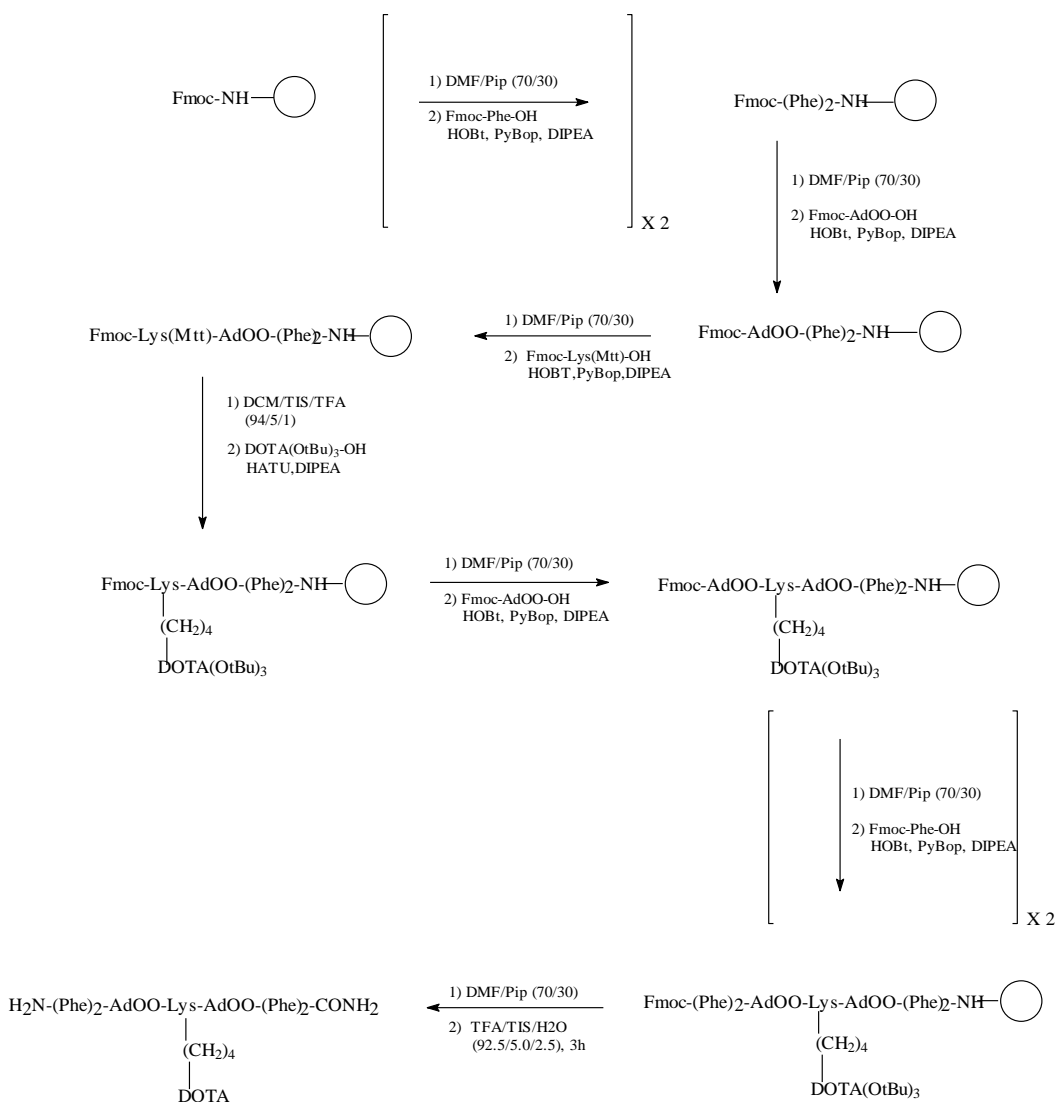
Peptide synthesis of the two gadolinium compounds was performed by using solid phase methods (SPPS) using the Fmoc chemistry²¹⁵, as reported in **Scheme 1**.

In agreement with previous reported synthesis of F4-conjugate,¹⁹⁶ Rink amide MBHA resin, which releases peptide adducts as amide on the C-terminus, was used. After the coupling of two phenylalanine residues and of Fmoc-AdOO-OH ethoxylic spacer on the solid support, a Lys residue orthogonally protected with Mtt on the epsilon amino function was added. The removal of the Mtt protecting group allowed introduction of DOTA(OtBu)₃-OH on the Lys side chain. The synthesis was completed by introducing the second ethoxylic spacer and the other two phenylalanine residues. Therefore the peptide-DOTA(OtBu)₃

Section I: PBMs as supramolecular contrast agents for MRI

derivatives were fully deprotected, cleaved from the resin and purified by RP-HPLC. Purity (> 95%) and identity of the products were confirmed by HPLC and mass spectra. ¹HNMR studies were also performed in CD₃OD solution at 600 MHz and the mono-dimensional spectrum is reported in **Appendix I**.

The complexation of Gd(III) ions to the DOTA containing peptide conjugates to obtain FF-DOTA(Gd)-FF and *ff*-DOTA(Gd)-FF has been carried out by adding equimolar amounts of GdCl₃ to the aqueous solutions of the DOTA derivatives at neutral pH and room temperature, as already reported.¹⁹⁶



Scheme 1: Schematization of the synthetic route for the solid-state obtainment of FF-DOTA-FF.

3.3.2 Structural characterization

Critical aggregation concentration (CAC) values of peptide conjugate FF-DOTA-FF and of its corresponding Gd-complex were determined using the fluorescence spectroscopy. Upon titration of ANS (20 μ M in cuvette) with increasing amounts of our peptide conjugates a distinctive emission peak at 460 nm appears.

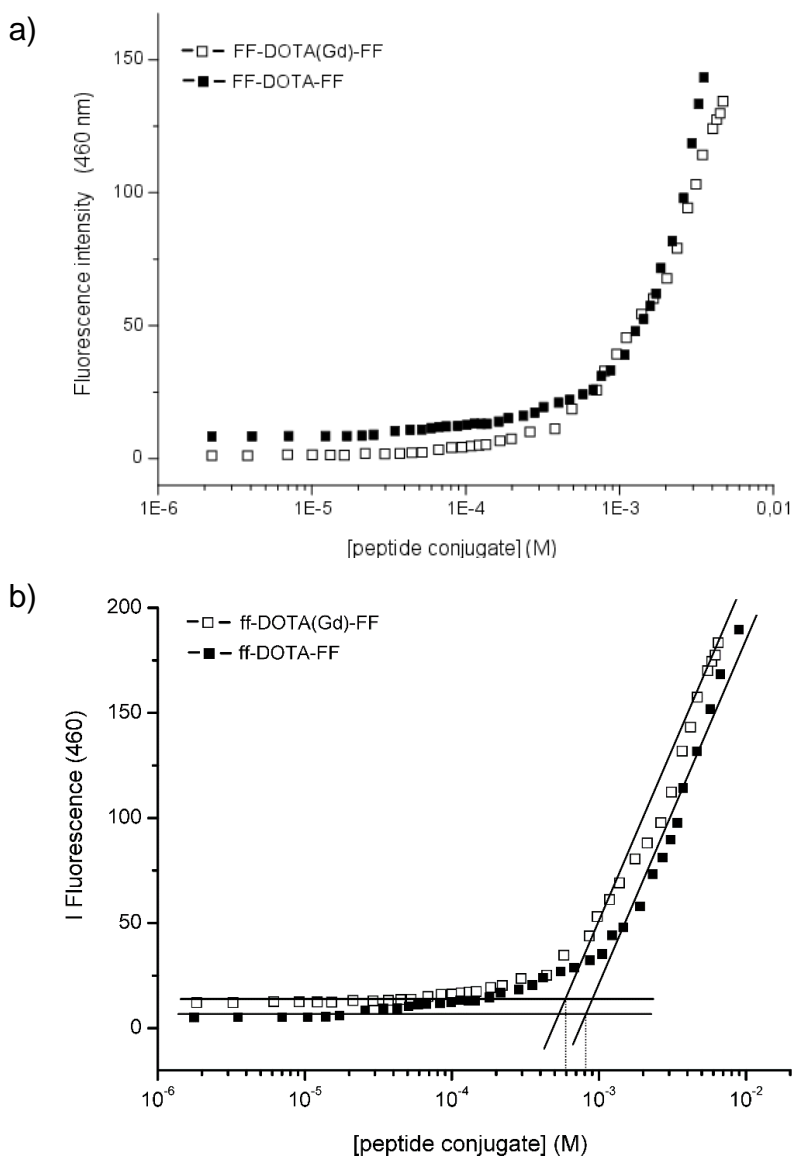


Figure 17: Fluorescence intensity emission of ANS fluorophore at 460 nm versus concentration of FF-DOTA-FF (a) and *ff*-DOTA-FF (b) as free basis and as gadolinium complex. CAC values, established from the break points, are $8.1 \cdot 10^{-4}$ M and $6.0 \cdot 10^{-4}$ M, respectively.

Section I: PBMs as supramolecular contrast agents for MRI

The CAC values have been determined from the graphical break points of the plot in **Figure 17**, in which is reported the variation of the ANS fluorescence intensity as function of peptide concentration.

The CAC values of FF-DOTA-FF peptide conjugate and its Gd-complex are $7.7 \cdot 10^{-4}$ M (1.1 mg/mL) and $5.8 \cdot 10^{-4}$ M (0.9 mg/mL), respectively. By these results, an initial aggregation phenomenon can be assumed starting at concentration of 1.0 mg/mL for the Gd free peptide derivatives. Not significant differences are observed for peptide sequences in which the two Phe in configuration L were replaced with Phe in D ones. (CAC values determined are $8.1 \cdot 10^{-4}$ M and $6.0 \cdot 10^{-4}$ M for *ff*-DOTA-FF and *ff*-DOTA(Gd)-FF, respectively).

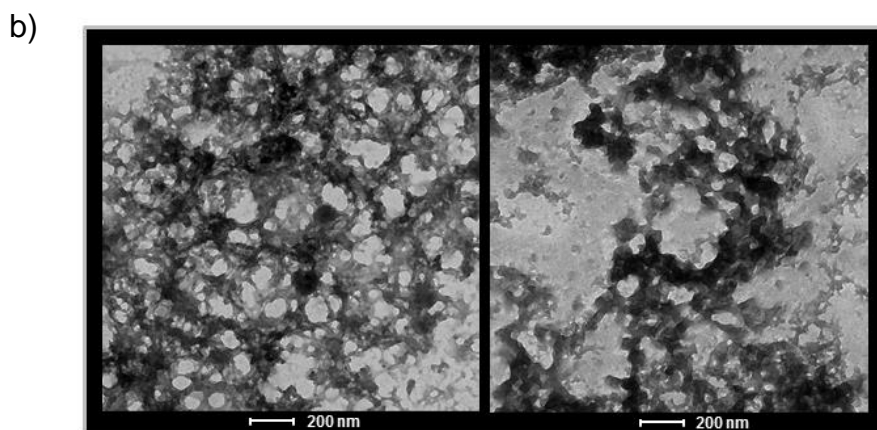
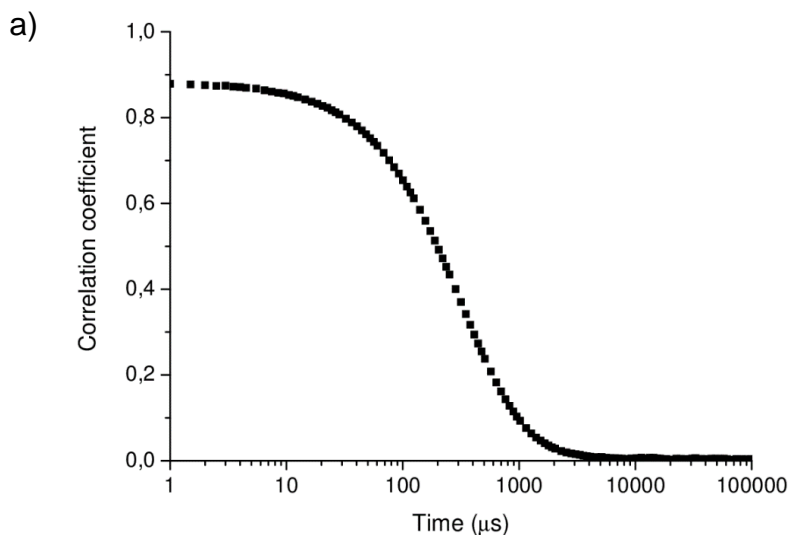


Figure 18: a) Intensity correlation function of FF-DOTA(Gd)-FF. b) Selected TEM images for FF-DOTA(Gd)-FF (left) and *ff*-DOTA(Gd)-FF (right) at 10.0 mg/mL.

As expected, after the gadolinium coordination, the neutralization of the three negative charges on the DOTA macrocyclic chelating agent causes a slight decrease of the CAC value, thus favoring peptide self-aggregation. However, the CAC values, here determined, are one order of magnitude higher than values previously found for DOTA-L₆-F4 and its Gd-complex (0.1 and 0.08 mg/mL).

Self-assembled aggregates were further characterized from the structural and morphological point of view.

Mean diameters and diffusion coefficients of the gadolinium self-assembled contrast agents in water solution were measured by Dynamic Light Scattering (DLS) at 10 mg/mL. The intensity profile of FF-DOTA(Gd)-FF, reported in shows a mono-modal distribution due to translational diffusion process (**Figure 18a**) of aggregate with an apparent translational diffusion coefficient $D = 2.2 \cdot 10^{-12} \text{ m}^2\text{s}^{-1}$. Through the Stokes-Einstein equation, it was calculate the mean diameter of ~ 230 nm, which is compatible with supramolecular aggregates.

The morphology of the self-assembled nanostructures assessed by TEM is reported in **Figure 18b**. Images of the Gd-complex in water solution at 10 mg/mL⁻¹ clearly indicate the presence of fibrillary networks, typically observed for others aromatic-based peptides.

3.3.3 Secondary structure analysis

The secondary structure of the peptide conjugates in water solution was achieved by Circular Dichroism (CD) and Fourier Transform Infrared (FTIR) spectroscopies (**Figure 19**).

CD measurements of the peptides were recorded between 280 and 195 nm at several concentrations in 2.5 - 20 mg/mL range and spectra are reported in **Figure 19a**. CD spectrum of FF-DOTA(Gd)-FF, recorded at 2.5 mg/mL, show two maxima at 202 and 221 nm. These maxima can be attributed to the stacking of the aromatic side chains. The main maximum at 221 nm undergoes to a red-shift as function of the concentration, indicating an increase of the β -sheet content.^{203,216} In **Figure 19b**, CD spectrum of *ff*-DOTA(Gd)-FF at 2.5 mg/mL reveals a minimum at 218 nm, consistent with a substantial β -sheet content. As for FF-DOTA(Gd)-FF analogue, a progressive red-shift of the minimum, due to the increase of concentration, was observed.

Further information on the secondary structure adopted by peptide conjugates and their Gd-complexes was obtained investigating the amide I region of FTIR spectra in aqueous solution (10 mg/mL). FTIR spectra of LLLL isomer and DLLL one showed a similar profile, with very slight differences between the free bases and the Gd-complexes.

Section I: PBMs as supramolecular contrast agents for MRI

From the inspection of the spectra of FF-DOTA-FF and FF-DOTA(Gd)-FF, reported in **Figure 19C**, it is possible to detect with three peaks at 1637, 1674 and 1680 cm^{-1} .

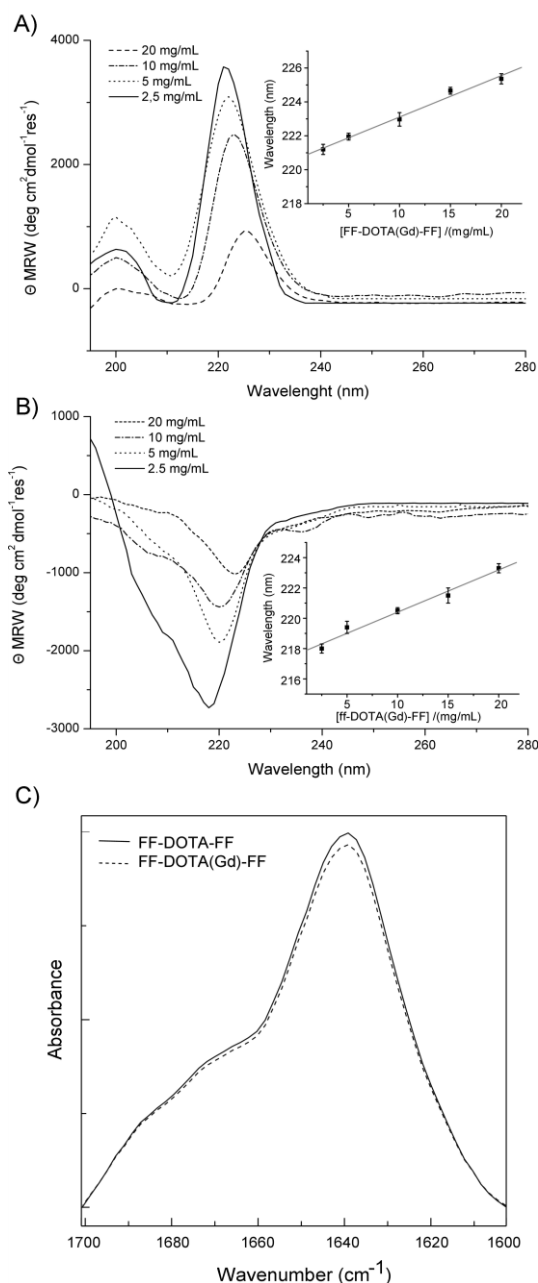


Figure 19: Selected Far-UV CD spectra of (a) FF-DOTA-FF and of (b) FF-DOTA-FF in a concentration range of 2.5-20 mg mL^{-1} . Spectra are recorded between 280 and 195 nm. In the insert it is reported the variation of the wavelength as function of the peptide concentration. c) FTIR amide I region for FF-DOTA-FF and FF-DOTA(Gd)-FF

Section I: PBM as supramolecular contrast agents for MRI

The peak at 1674 cm^{-1} is associated with residual trifluoroacetate counterions,²¹⁷ deriving from the peptide chromatographic purification. Instead, both 1637 and 1680 cm^{-1} are indicative of β -sheet formation with an antiparallel orientation.^{203,216,217}

CD and FTIR results, together with TEM images, indicate the ability of the peptide Gd-complex to self-aggregate in fibrillary and intricate network dominated by an antiparallel β -sheet arrangement.

Based on these results and of the models previously proposed in literature for oligo-phenylalanines, we speculated and proposed one of the possible aggregation pathway (**Figure 20**).

In FF-DOTA(Gd)-FF, or its analogue containing D-Phe, the aromatic framework composed of four Phe residues is interrupted by the -AdOO-Lys[DOTA(Gd)]-AdOO- structural portion. At high concentration, it is feasible that a folding of the peptide backbone occurs as reported in **Figure 20**. This folding should favor the intramolecular approach of phenyl rings of the C and N termini and permits intermolecular T-shape staking. As suggested by CD and FTIR data, the peptide conjugates interact with an antiparallel β -arrangement. From this evidence widely supported by experimental results, it is imagined that the Gd-DOTA complexes point far from the spine of the aggregate.

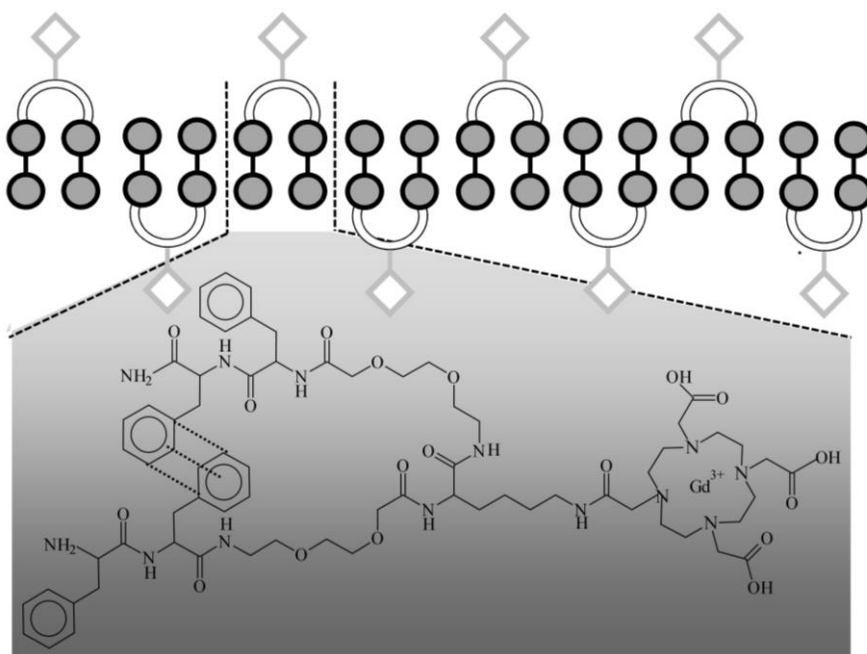


Figure 20: Schematic representation of the proposed aggregation pathway for FF-DOTA-FF peptide conjugate.

3.3.4 Relaxivity performances

The NMRD profiles of FF-DOTA(Gd)-FF and ff-DOTA(Gd)-FF, measured at 50 and 5 mg/mL concentrations, are reported in **Figure 21**. From a qualitative point of view, the shape of the profiles gives information on the aggregation state of the system: low molecular weight Gd-complexes, in fact, show NMRD profiles with a dispersion in the region 1-10 MHz, while a characteristic peak of relaxivity appears, in the region of proton Larmor frequencies 10-70 MHz, in the case of high molecular weight Gd-containing systems. Inspection into **Figure 21** reveals that both FF-DOTA(Gd)-FF and ff-DOTA(Gd)-FF are mostly in monomeric form at a concentration of 5 mg/mL, while, at a concentration ten times higher, the aggregation process is definitively completed, particularly in the case of ff-DOTA(Gd)-FF where the high field relaxivity peak is better evidenced. Data were fitted to the conventional Solomon-Bloembergen-Morgan theory^{212,213} and the relative fitting parameters are reported in **Table 3**.

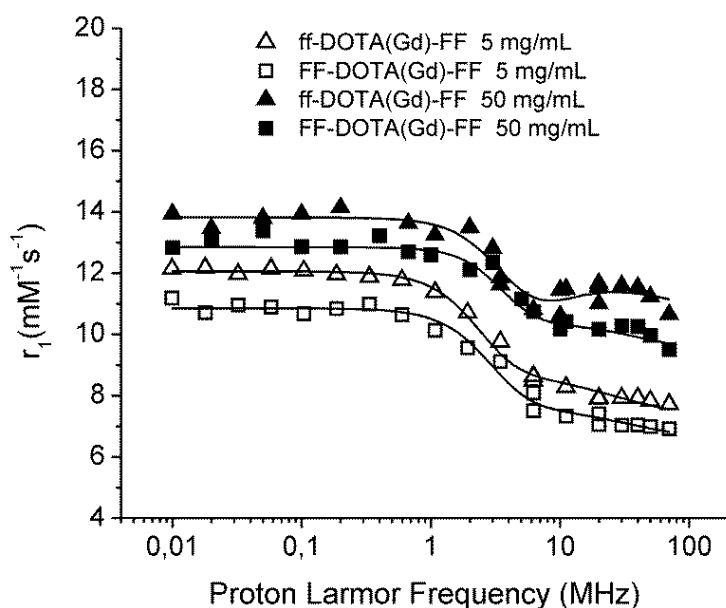


Figure 21: The magnetic-field dependence of the relaxivity (r_1) measured over an extended range of magnetic field strengths (from 0.01 to 70 MHz). The nuclear magnetic relaxation dispersion (NMRD) profiles were obtained for the aqueous suspensions of FF-DOTA(Gd)-FF at 5 mg/mL (\square) and 50 mg/mL (\blacksquare) and ff-DOTA(Gd)-FF at 5 mg/mL (\triangle) and 50 mg/mL (\blacktriangle). The temperature was set to 298K and data were normalized to 1mM concentration of Gd^{3+}

These aggregates showed enhanced properties with respect to low-molecular weight Gd-DOTA complexes. FF-DOTA(Gd)-FF and ff-

DOTA(Gd)-FF complexes showed two different shape of the NMRD profiles at 5 and 50 mg/mL: at high concentration the characteristic peak of high molecular weight Gd-containing system appears in the region of proton Larmor frequencies 10-70 MHz. These result suggests that only well above 5 mg/mL, both the peptide conjugates are definitively self-assembled in a supramolecular structure. As expected, the relaxivity values of the two Gd-complexes ($r_{1p} = 10.1$ and $11.5 \text{ mM}^{-1} \text{ s}^{-1}$) in the aggregated form were found higher those in the monomeric form (7.1 and $7.9 \text{ mM}^{-1} \text{ s}^{-1}$).

Table 3. Main relaxometric parameters derived from fitting of NMRD profiles reported in Figure 21.^[a]

System		$r_{1p}(\text{mM}^{-1} \text{ s}^{-1})$	$\Delta^2(\text{s}^{-2})^{[b]}$	τ_V (ps) ^[c]	τ_{s0} (ps) ^[d]	τ_R (ps) ^[e]
LLLL isomer	monomer	7.1	1.66×10^{19}	32.8	153	190
	aggregate	10.1	1.86×10^{19}	41.0	109	270
LLDD isomer	monomer	7.9	1.06×10^{19}	41.7	188	227
	aggregate	11.5	2.21×10^{19}	35.0	108	341

[a] On carrying out the fitting procedure, some parameters were fixed to reasonable values: $r_{\text{Gd-H}}$ (distance between Gd and protons of the inner sphere water molecule) = 3.1 \AA ; a (distance of minimum approach of solvent water molecules to Gd^{3+} ion) = 3.8 \AA ; D (solvent diffusion coefficient) = $2.2 \cdot 10^{-5} \text{ cm}^2 \text{ s}^{-1}$. [b] Squared mean transient zero-field splitting (ZFS) energy. [c] Correlation time for the collision-related modulation of the ZFS Hamiltonian. [d] Electronic relaxation time at zero field (calculated as $1/\tau_{s0} = 12 \Delta^2 \times \tau_V$) [e] Reorientational correlation time.

The τ_R values found for the two complexes (270 and 341 ps for all L and D/L isomers, respectively) reflect the slight increase in relaxivity passing from LLLL isomer to the DDLL one. However, the τ_R values extracted from the fitting procedure, and consequently the high field relaxivities of the aggregated forms of the two isomers, are shorter than what expected for slowly moving nano-sized aggregates as well as than those ($\tau_R = 490 \text{ ps}$) previously published for DOTA(Gd)-L₆-F4 systems.¹⁹⁶ This finding can be ascribed to their lower tendency to form stably aggregated supramolecular systems if compared to the systems based on the aggregation of tetraphenylalanine peptides derivatives.

3.4 Extension of the aromatic side chain (Strategy II)

The very short peptide conjugate Gd-DOTA-L₆-F2 has been previously synthesized and characterized.¹⁹⁶ Physicochemical characterization pointed out that this peptide was able to weakly self-aggregate and only before Gd coordination. Due to steric repulsion of the Gd-complex, after metal coordination, the dipeptide seems unable to keep π - π interactions.

The replacement of the phenyl group with a more extended aromatic one could in principle restore the stacking.

According to the second strategy principles, the replacement of Phe residues with 2-naphthylalanine (Nal₂), a non coded amino acid having a more extended aromatic group in its side chain, was analysed. In principle, the increase of the aromatic group area could increase the self-assembling propensity of the dipeptide. The novel proposed monomer DOTA-L₆-(2Nal)₂ is schematically reported **Figure 22a**. Both the aromatic conjugate DOTA-L₆-(2Nal)₂ (mentioned as 2Nal₂) and its gadolinium complex Gd-DOTA-L₆-(2Nal)₂ (reported as Gd-2Nal₂) were able to self-assemble spontaneously in water solution.

3.4.1 Structural characterization

The morphology of the supramolecular assemblies as free basis and as Gd-complex was evaluated by transmission electron microscopy (TEM). A deep characterization of nanostructures at the nano- and atomic scale was achieved both in solution and at the solid state with SAXS/WAXS, fluorescence, ¹HNMR, Fourier Transform Infrared (FTIR), circular dichroism (CD), and molecular modelling. The relaxivity properties of these nanostructures were studied. In order to prepare a potential theranostic agent, it was assayed the incorporation of the cytotoxic doxorubicin (DOX) as model drug in the Gd-2Nal₂ paramagnetic nanostructures. DOX is an established anticancer agent clinically effective for the treatment of many cancer types (breast and ovarian cancers).²¹⁸ Fluorescence spectroscopy and ¹HNMR studies and optical microscopy images provide the evidence for their capability to encapsulate doxorubicin.

3.4.2 Synthesis and fluorescence studies

The peptide synthesis of 2Nal₂ was achieved according to the standard protocols of the solid phase synthesis with Fmoc/tBu strategy,²¹⁵ the peptide was then characterized with LC-MS and ¹HNMR (data collected in **Appendix I**). After purification, the DOTA chelating agent was complexed with lanthanide metal ions, i.e. gadolinium (Gd) or

Section I: PBM as supramolecular contrast agents for MRI

lanthanum (La) for MRI or NMR studies, respectively. Nevertheless, in spite of the higher hydrophobicity of the naphthyl group with respect to the phenyl one, the Gd-2NaI₂ derivative keeps high water solubility, and the solutions remain perfectly clear up to 50 mg/mL; whereas a further increase of the concentration causes its hydrogelation. Lowering the temperature below 5°C, fast hydrogel formation occurs yet at 20 mg/mL.

The peptide conjugate Gd-2NaI₂ shows high stability also in physiological conditions (10 mM phosphate buffer 0.9 wt.% NaCl at pH 7.4) (**Appendix II, Figure A1**). In **Figure 23a** and **Figure 23b** are reported fluorescence spectra of 2NaI₂ and Gd-2NaI₂ at several concentrations (from 0.025 to 20.0 mg/mL) obtained by exciting the samples at 280 nm, which corresponds to the wavelength of absorption for the 2-naphthylalanine (**Figure 22b**).

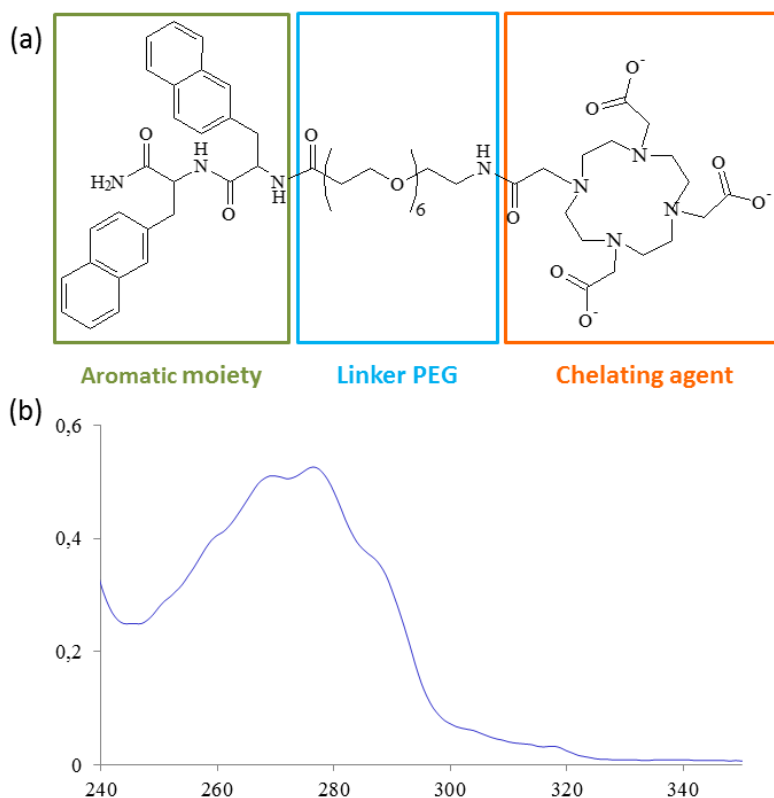


Figure 22: a) Schematic representation of di-aromatic compounds obtained by SPPS with Fmoc chemistry. Conjugates contain an aromatic framework consisting of two 2-naphthylalanine (2-NaI) residues, an ethoxylic linker (L₆) formed by six PEG units and bifunctional and macrocyclic chelating agent (DOTA) for gadolinium (III) coordination. b) UV-Vis spectrum of 2-NaI₂

Section I: PBMs as supramolecular contrast agents for MRI

From inspection of **Figure 22c**, the typical emission spectrum of the 2-naphthyl group with three maxima at 325, 340 and 355 nm, respectively, can be detected.

The fluorescence intensity of 2NaI₂ increases gradually in the range of concentration between 0.025 and 0.2 mg/mL. After this concentration a progressive intensity decrease, attributable to the stacking of the aromatic rings, occurs. Since 2.0 mg/mL, the fluorescence intensity is very low.

From inspection of the inset in **Figure 22b** a weak peak that is centered between 380-430 nm and indicative of excimer formation is visible.

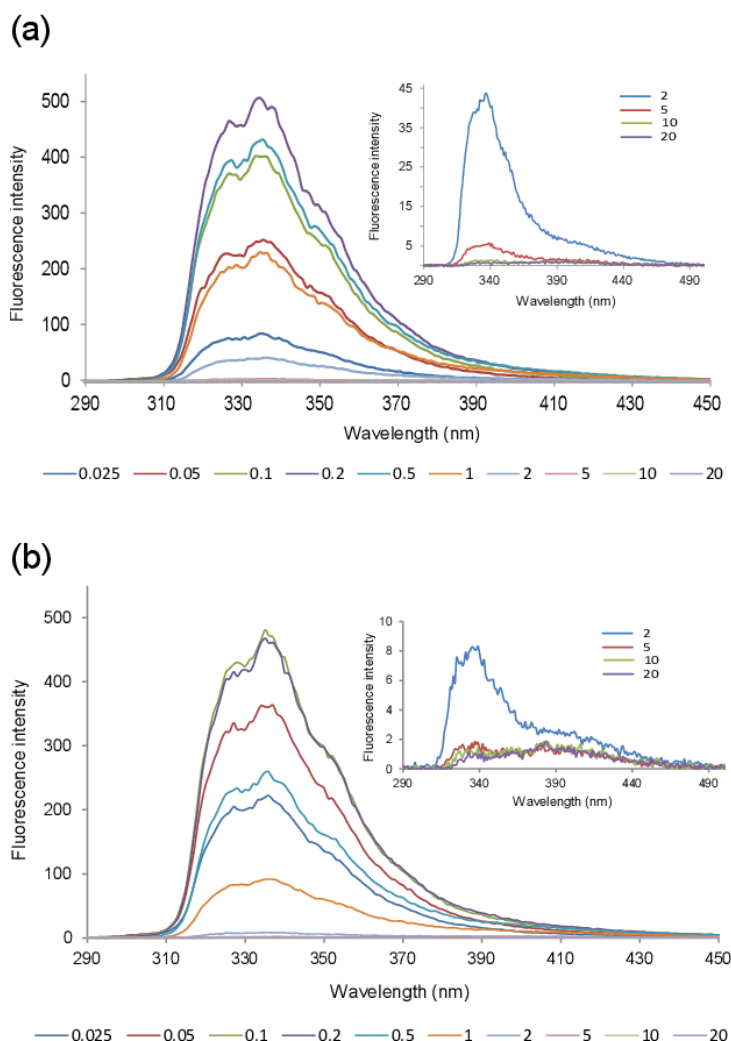


Figure 23: Fluorescence spectra of 2NaI₂ (a) and Gd-2NaI₂ (b) in 0.025-20.0 mg/mL concentration range. Samples were excited at $\lambda = 280$ nm and recorded between 290 and 500 nm.

These results suggest that the peptide derivative begins to undergo self-aggregation phenomena at 0.2-0.5 mg/mL (150-375 μ M). However, the appearance of the excimer peak above 2.0 mg/mL leaves suppose that very stable aggregates can be formed above 2.0 mg/mL. A similar behavior was observed after the gadolinium coordination (see **Figure 22c**). However in Gd-2NaI₂, both the decrease of the fluorescence intensity (0.1 mg/mL) and the appearance of the excimeric peak (1.0 mg/mL) were observed at lower concentration with respect to 2NaI₂, thus confirming that the neutralization of the negative charges on the chelating agent, after the Gd-coordination, induces a better self-assembling in these peptide conjugates.¹⁹⁶

Determination of the critical aggregation concentration (CAC) value of Gd-2NaI₂ was carried out using the previously described ANS fluorescence-based method.⁶³ A solution of ANS in cuvette (20 μ M) was titrated with Gd-2NaI₂ and the fluorescence intensities maximum measured at 470 nm have been plotted in **Figure 24**. CAC value, determined from the graphical break-point, is $\sim 6.70 \cdot 10^{-4}$ M (0.86 mg/mL). This value is 10-fold higher than the CAC value ($5.1 \cdot 10^{-5}$ M, 0.076 mg/mL) previously found for tetraphenylalanine Gd-complex Gd-DOTA-L₆-F4.¹⁹⁶

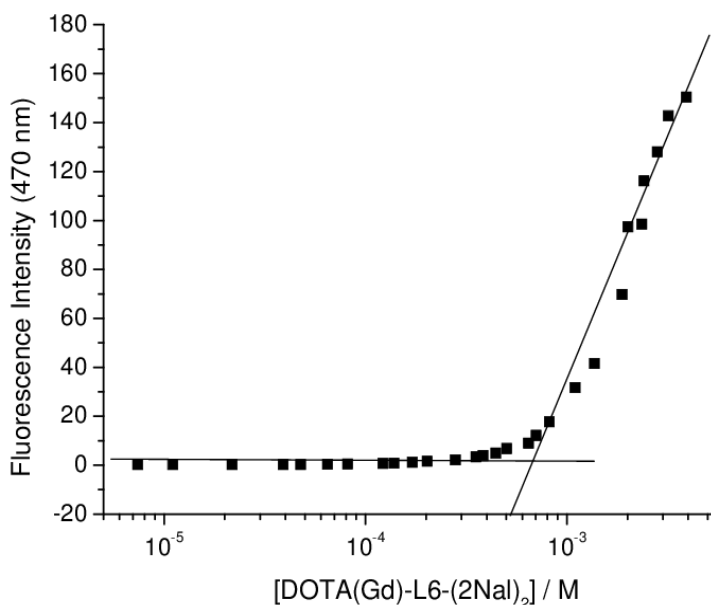


Figure 24: Fluorescence intensity emission of ANS fluorophore at 470 nm vs. concentration of 2NaI₂ Gd(III) complex. CAC value is established from the break point.

This consideration suggests that the replacement of the phenyl ring with the naphthyl one allows to increase the aggregation propensity with

respect to diphenylalanine conjugates (Gd-DOTA-L₆-F2). However from the comparison of CAC values (Gd-DOTA-L₆-F2 > Gd-DOTA-L₆-NaI₂ > Gd-DOTA-L₆-F4) it emerges that the increase of the number of aromatic residues causes a better aggregation with respect to the replacement of Phe with more extended aromatic group.

3.4.3 NMR studies

The fluorescence studies were supported by ¹H NMR measurements (**Figure 25**). 1D [¹H] and 2D [¹H, ¹H] NMR spectroscopy were used to study two different compounds: DOTA-L₆-F2 and 2NaI₂ analogue in absence and in presence of the DOTA coordinated metal ion lanthanum(III), La.

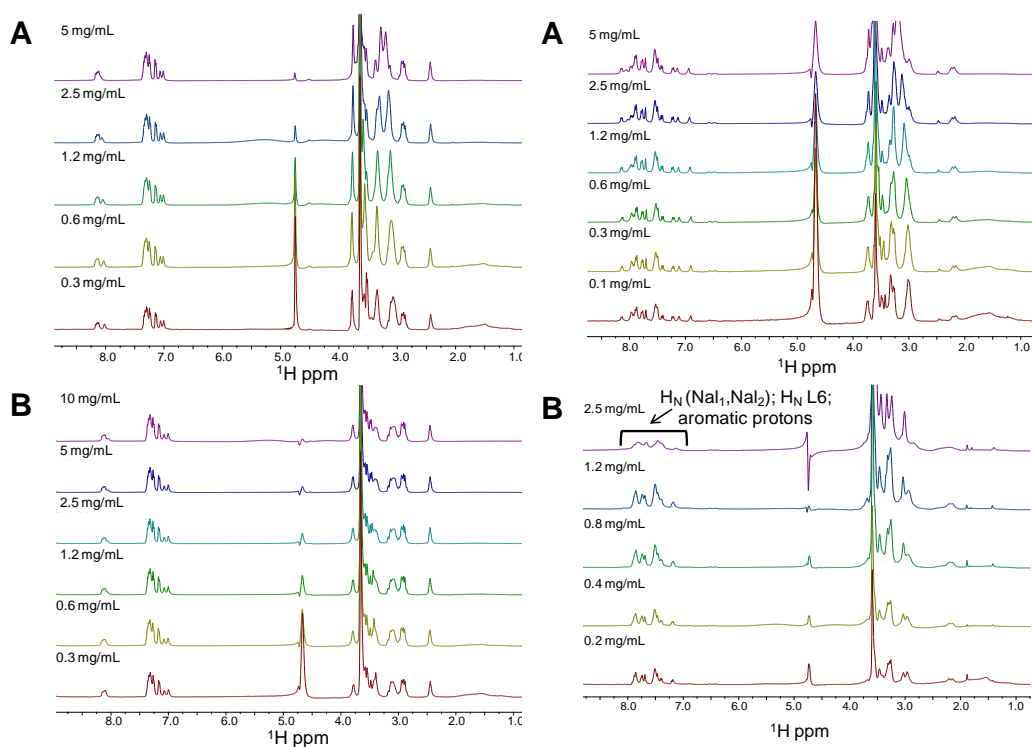


Figure 25: Left panel a) 1D ¹H NMR spectra recorded for DOTA-L₆-F2 at 5 mg/mL (4.8 mM), 2.5 mg/mL (2.4 mM), 1.2 mg/mL (1.2 mM), 0.6 mg/mL (0.6 mM), 0.3 mg/mL (0.29 mM). b) 1D ¹H NMR spectra recorded with La-DOTA-L₆-F2 at 10 mg/mL (8.5 mM), 5 mg/mL (4.3 mM), 2.5 mg/mL (2.1 mM), 1.2 mg/mL (1 mM), 0.6 mg/mL (0.5 mM), 0.3 mg/mL (0.26 mM). Right panel a) 1D ¹H NMR spectra recorded for 2NaI₂ at 5 mg/mL (4.4 mM), 2.5 mg/mL (2.2 mM), 1.2 mg/mL (1.1 mM), 0.6 mg/mL (0.5 mM), 0.3 mg/mL (0.3 mM), 0.1 mg/mL (0.1 mM). b) 1D ¹H NMR spectra recorded with La-2NaI₂ at 2.5 mg/mL (2 mM), 1.2 mg/mL (0.9 mM), 0.8 mg/mL (0.6 mM), 0.4 mg/mL (0.3 mM), 0.2 mg/mL (0.2 mM).

Both DOTA-L₆-F2 and 2NaI₂ present low aggregation propensities. The process of resonance assignments of the two molecules could be easily achieved at a concentration equal to 1 mM (see **Appendix II Tables A3, A4** and **Figure A2**). For the DOTA-L₆-F2 relevant changes in the spectra, indicating occurrence of potential aggregation processes, take place at a concentration higher than 1.2 mg/mL (**Figure 25a**, left panel). In detail by comparing spectra recorded at 0.3 mg/mL and 5.0 mg/mL chemical shift changes appear relevant in the spectral regions between 8.0 and 8.2 ppm, where signals from HN amide protons are present and between 3.0 and 3.5 ppm where several peaks overlap (**Appendix I, Table A4**). However, even at the highest investigated concentrations, peaks in the NMR spectra remain rather sharp thus pointing towards formation of small size aggregates

Once complexed with La(III) the DOTA-L₆-F2 presents similar weak aggregation propensity (**Figure 25b**, left panel). For 2NaI₂ in the absence of coordinated metal ions, from 0.1 mg/mL till 5.0 mg/mL, we cannot reveal significant aggregation as the signals in the NMR spectra do not become broad or change their chemical shifts (**Figure 25a**, right panel). Once La(III) is inserted in 2NaI₂ the aggregation tendency increases and line broadening starts to affect the spectra thus indicating formation of aggregated species already at 0.8 mg/mL concentration; at 2.5 mg/mL concentration extensive line broadening causes partial signal loss thus indicating the presence of larger aggregates (**Figure 25b**, right panel)

Aggregation as witnessed by line broadening is affecting all signals in the NMR spectrum of 2NaI₂ (See for instance the HN amide and aromatic protons region in **Figure 25b**, right panel). This different aggregation property in presence and absence of the metal ion likely indicates that La(III) by neutralizing DOTA negative charges is favoring intermolecular interaction by lowering electrostatic repulsions. Moreover, NMR data show that La-2NaI₂ has a higher tendency to aggregate with respect to La-DOTA-L₆-F2; this outcome can be easily explained by the larger aromatic patches present in the former molecule which are likely favoring larger intermolecular π -stacking interactions. These data indicate consequently that the Gd-2NaI₂ may work better as a potential MRI contrast agent than Gd-DOTA-L₆-F2.

3.4.4 Secondary structure assignment

As for the others peptide conjugates, the secondary structure of 2NaI₂, as free bases or as gadolinium complex, was investigated by CD and by FTIR spectroscopies.

Section I: PBMs as supramolecular contrast agents for MRI

CD spectra, reported in **Figure 26**, were recorded both below and above the self-aggregation concentration. Independently from the coordination of the metal, 2Nal₂ peptide shows a similar dichroic signature: at 0.5 mg/mL, there are two minima around 205 and 218 nm and a maximum at 232 nm.

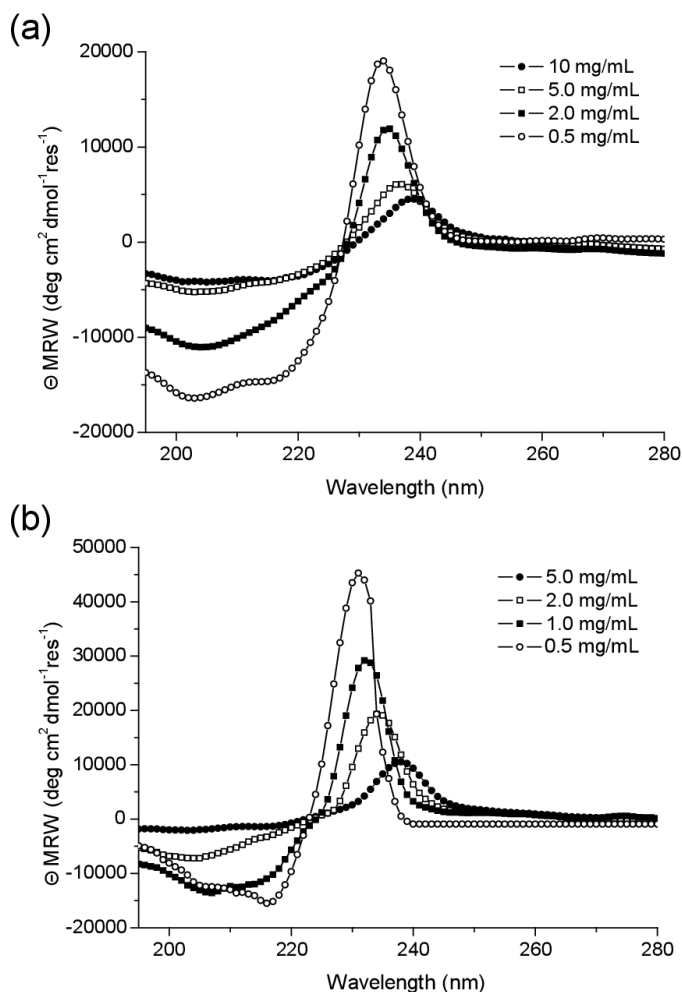


Figure 26: Selected Far-UV CD spectra of 2Nal₂ (a) and Gd-2Nal₂ (b) in a concentration range of 0.5–20.0 mg mL⁻¹. Spectra are recorded between 280 and 195 nm.

This dichroic signature is perfectly identical and symmetric to that previously observed for tetra-phenylalanine conjugates.¹⁹⁶ The two minima are attributable to the stacking between the 2-naphthyl aromatic rings, whereas the maximum is typically observed in presence of β -structure.²⁰³ Above this concentration value a progressive red-shift of the maximum (up to 340 nm), as function of the peptide concentration,

occurs. This spectral shift is accompanied by the decrease of the maximum and by the presence of an isobestic point. Both the shift and the decrease of the maximum indicate the formation in solution of nanostructures with a dominant β -sheet arrangement.²¹⁶

FTIR spectra of 2NaI₂ and Gd-2NaI₂ at 5.0 mg/mL in the amide I region are reported in **Figure 27a**. Spectrum of Gd-2NaI₂ as dried film is also reported. Gd-2NaI₂ FTIR spectra, both at the solid state and in solution, show a dominant peak around 1638 cm⁻¹, expected for β -sheet formation. In addition, both spectra have a secondary peak around 1680 cm⁻¹, that is normally observed for antiparallel orientation of the β -sheet.

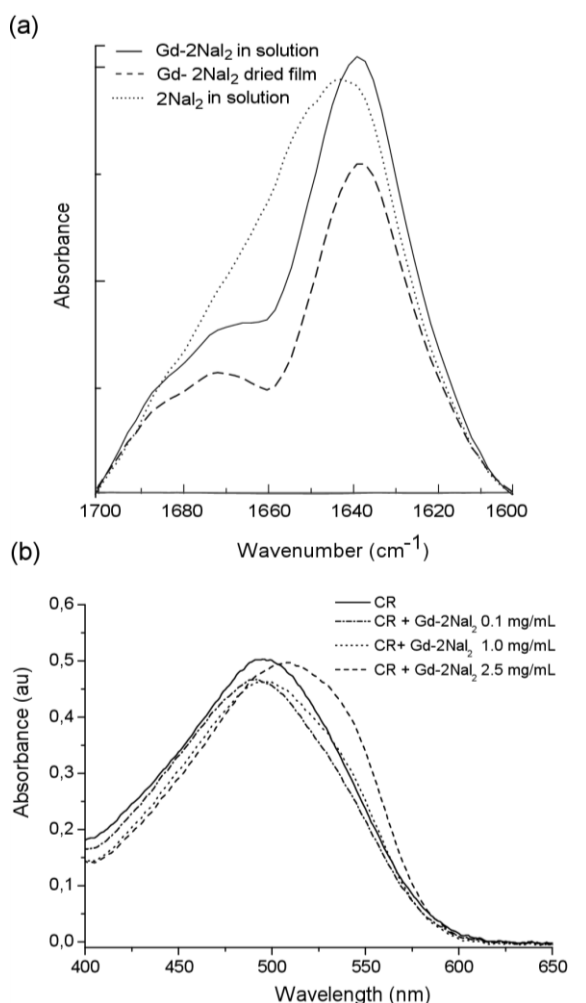


Figure 27: a) FTIR spectra of 2NaI₂ and Gd-2NaI₂ in the amide I region at 5.0 mg/mL. b) UV-Vis spectra of 2NaI₂ and Gd-2NaI₂, stained with Congo Red at 0.1 and 1.0 mg/mL. The spectrum of Congo Red is also reported for comparison.

Section I: PBMs as supramolecular contrast agents for MRI

By comparing these spectra with spectrum of 2NaI_2 , it appears a very broad peak at 1642 cm^{-1} .

The high tendency of $\text{Gd-}2\text{NaI}_2$ to self-aggregate in amyloid-like fibrillary nanostructures in solution was confirmed by Congo Red (CR) staining assay (**Figure 27b**).²⁰⁹ When incubated with fibrillary aggregates, CR spectral profile changes and a shift of the CR band from 490 to 540 nm is expected. CR UV-Vis maximum undergoes a clear shift after incubation with $\text{Gd-}2\text{NaI}_2$ at 2.5 mg/mL. Instead, any variation or a slight shift can be evidenced for CR incubated with 0.1 and 1.0 mg/mL, respectively.

3.6 Materials characterization and molecular modelling

Self-assembled peptide conjugate at 5.0 mg/mL, as free base or as metal complex, was initially characterized using TEM.

TEM images reported in **Figure 28** demonstrate the assembling of both 2NaI_2 and $\text{Gd-}2\text{NaI}_2$ in long fibrillary nanostructures. On the other hand, TEM images of $\text{Gd-DOTA-L}_6\text{-F}_2$ do not show any supramolecular aggregate (data not shown).

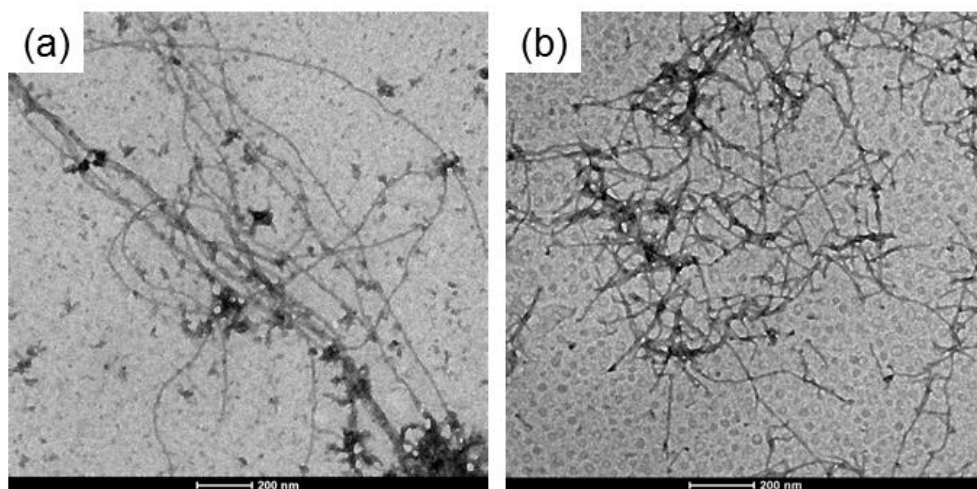


Figure 28: Selected TEM images for 2NaI_2 (a) and $\text{Gd-}2\text{NaI}_2$ (b) at 5.0 mg/mL.

To further analyze the supramolecular morphology of 2NaI_2 and $\text{Gd-}2\text{NaI}_2$ at the micro and nano scale, WAXS and SAXS measurements were performed on dried fibers.

Figure **29a,b** and **30a,b** present the two-dimensional (2D) WAXS and SAXS patterns collected on the 2NaI_2 and $\text{Gd-}2\text{NaI}_2$ samples, respectively. The 2D patterns, once centered, calibrated and radially folded into 1D profiles, are shown in **Figure 29c,d** and **30c,d**, respectively. The low- q region of each WAXS pattern is displayed

separately in **Figure 29e** and **30e** to better visualize the diffraction peaks. The red and black WAXS/SAXS profiles correspond to the meridional and equatorial directions marked by the red arrows in panels (b). The position of most intense meridional and equatorial diffraction peaks are reported in **Table 4**. Both fibers show the typical cross- β fiber 2D WAXS diffraction pattern with the β -strands distance at $d_{\beta 1} = 4.7 \pm 0.3$ Å along the meridional direction (fiber axis)

The 2D SAXS patterns display a clear diffraction structure. The most intense peaks lay along the equatorial direction, for both samples. The presence of a diffraction pattern both in SAXS and in WAXS is fingerprint of a hierarchical organization of the molecules in fibers from the atomic to the nanoscale. The most intense SAXS peak in the Gd-2NaI₂ sample, labelled as e1 in **Figure 30d**, corresponding to $d = 57$ Å, almost disappears in the 2NaI₂, where the most intense SAXS peak occurs at $d = 48$ Å (e2 equatorial peak in **Figure 29d**).

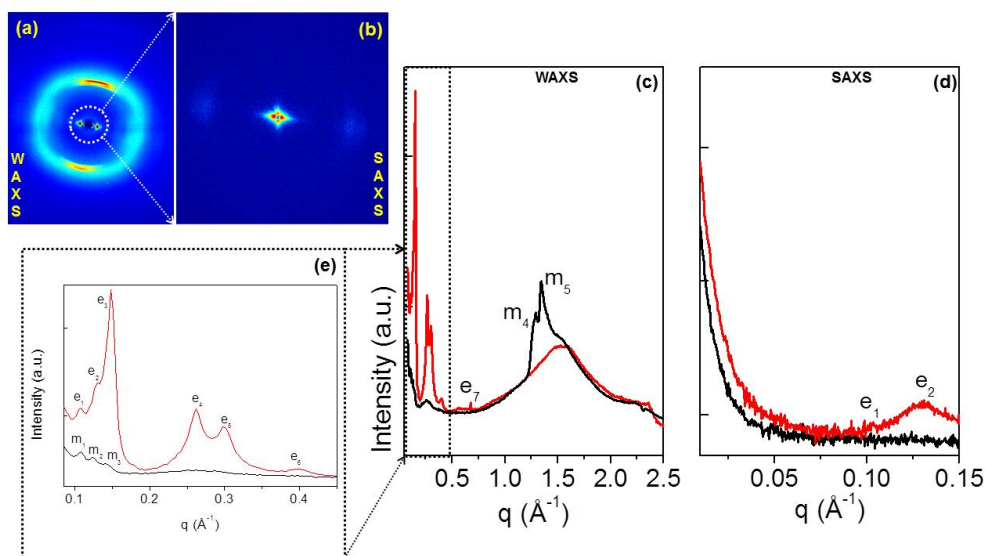


Figure 29: 2NaI₂ fiber at solid state: (a,b) 2D WAXS and SAXS data; (c,d) 1D WAXS and SAXS profiles (red and black corresponding to the meridional and equatorial directions) as obtained once the corresponding 2D WAXS (a) and SAXS (b) data are centered, calibrated and radially folded; the inset in panel (d) refers to the equatorial e2 reflection, with an estimated FWHM(e2-2NaI₂)=19°; (e) expanded WAXS region marked by a dotted rectangle in (c).

It was suggested that the full-width-at-half-maximum along the azimuth angle for the e1 and e2 peaks in the insets of **Figure 30d** and **Figure 29d**, which are FWHM(e1-Gd-2NaI₂)=27° and FWHM(e2-2NaI₂)=19°, respectively. Furthermore, for both aggregates intense equatorial peaks

Section I: PBMs as supramolecular contrast agents for MRI

were observed in WAXS experiments (d range 21-25 Å). Although peaks in this region occur in both 2NaI₂ and Gd-2NaI₂ samples their location and intensity are not identical. This observation suggests that the metal complexation of 2NaI₂ induces some structural rearrangements. Altogether, SAXS and WAXS experiments provide some interesting clues on the organization of the peptide spine of these assemblies at different structural level. In particular, (a) the meridional peak at 4.7 Å atomic distance clearly indicates a cross-β structure in which the β-strands run perpendicular to the fiber axis, (b) the equatorial reflections at 21-25 Å likely represent regularities within the inter-sheet distances, and (c) the peaks at d=48 and 57 Å provide some preliminary information on the nanofiber organization.

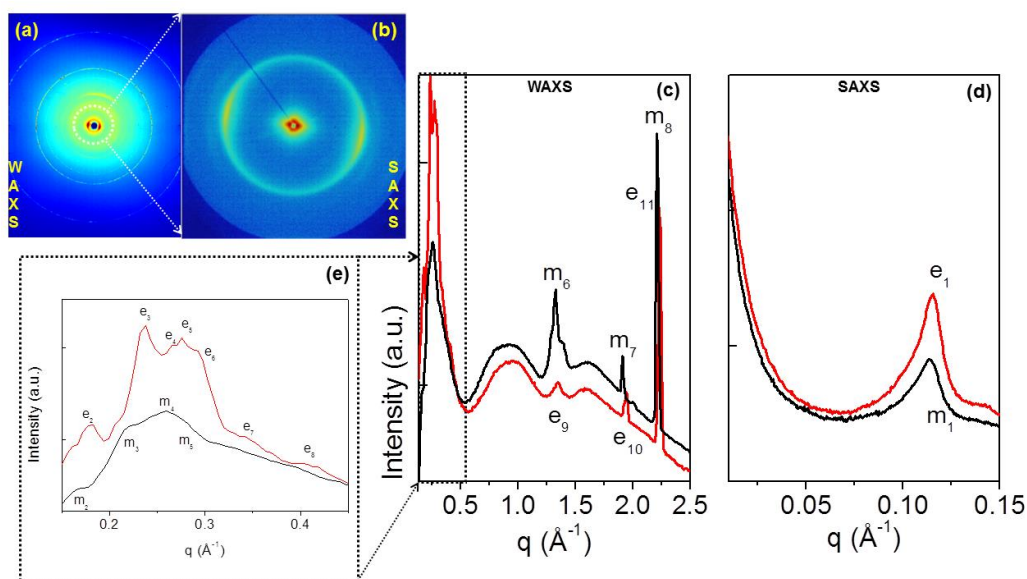


Figure 30: Gd-2NaI₂ fiber at solid state: (a,b) 2D WAXS and SAXS data; (c,d) 1D WAXS and SAXS profiles (red and black corresponding to the meridional and equatorial directions) as obtained once the corresponding 2D WAXS (a) and SAXS (b) data are centered, calibrated and radially folded; the inset in panel (d) refers to the equatorial e_1 reflection, with an estimated FWHM (e_1 -Gd-2NaI₂) = 27°; (e) expanded WAXS region marked by a dotted rectangle in (c).

In this framework, molecular modeling was performed to gain insights into the atomic structure of the peptide moiety of these assemblies using the programs Coot and Pymol. Accordingly, a antiparallel cross-β models was generated, stabilized by four inter-strand hydrogen bonds, to check whether NaI side chains could contribute to the stabilization of

Section I: PBMs as supramolecular contrast agents for MRI

this motif. In particular, it was evaluated the interactions between Nal side chains of consecutive β -strands within the cross β -sheet by considering all its possible rotameric states. It was detected a combinations of rotameric states that maximized hydrophobic interactions between side chains of consecutive strands (**Figure 31a**).

Table 4. q positions, and corresponding $d=2\pi/q$ values, of meridional and equatorial reflections for the 2-Nal and Gd-2Nal₂ fibers. The error on the d values amounts to $\pm 0.3\text{\AA}$.

Label	2-Nal		Gd-2Nal ₂	
	q (\AA^{-1})	d (\AA)	q (\AA^{-1})	d (\AA)
e1	0.11	57	0.11	57
e2	0.13	48	0.18	35
e3	0.15	42	0.24	26
e4	0.26	24	0.26	24
e5	0.3	21	0.28	22.5
e6	0.4	16	0.29	22
e7	--		0.34	18.5
e8	--		0.40	16
e9	--		1.35	4.5
e10			1.94	3
			2.23	2.8
m1	0.11	57	0.11	57
m2	0.125	50	0.17	37
m3	0.14	45	0.22	28.5
m4	1.28	5	0.26	24
m5	1.34	4.7	0.28	22.5
m6	--		1.32	4.75
m7	--		1.9	3.3

Then, it was scrutinized how different β -sheets could laterally interact. It was found that optimal interactions between the Nal side chains of facing β -sheets could be established when the inter-sheet distance was about 16-17 \AA (**Figure 31b**). Notably, although as minor peaks, equatorial reflections with this spacing were observed for both samples (**Figures 29e** and **30e**). However, as mentioned above, the largest equatorial peaks that likely correspond to inter-sheet distances present spacings with $d = 21-25 \text{\AA}$. This observation suggests that there are multiple ways in which β -sheets interact in these assemblies and that other species may mediate these inter-sheet interactions. In this scenario, it cannot be excluded that the hydrophobic rings of individual

Section I: PBMs as supramolecular contrast agents for MRI

Nal molecules intercalate within the hydrophobic surfaces of facing β -sheets (**Figure 31c**)

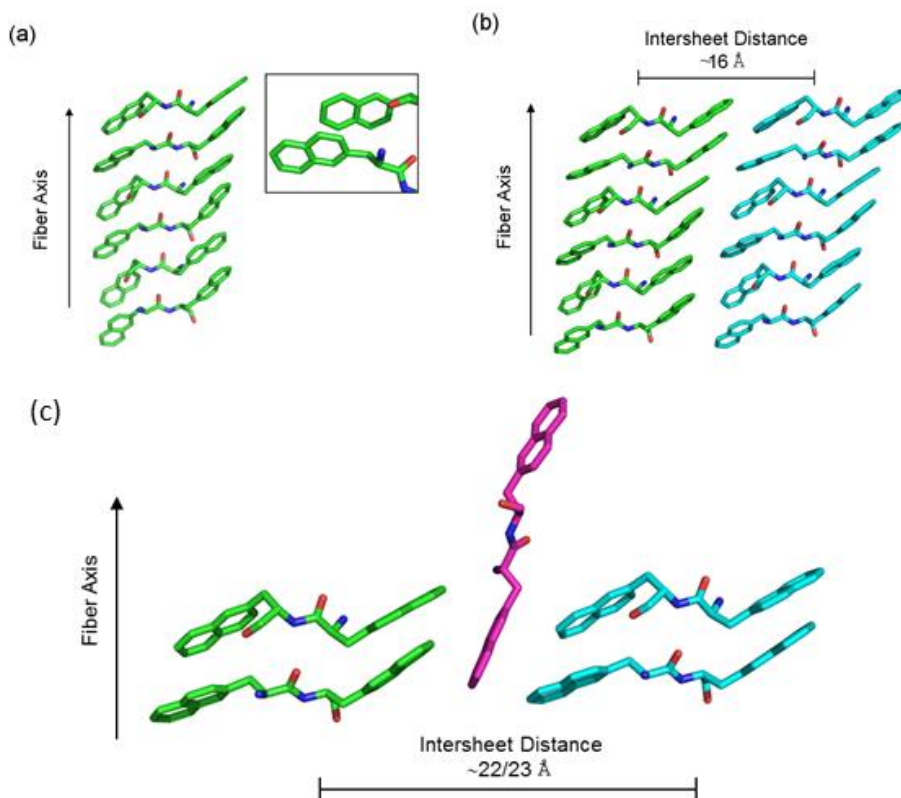


Figure 31: Three-dimensional model of the assembly formed by the peptide moiety of $2\text{NaI}_2/\text{Gd-}2\text{NaI}_2$. In panel (a) the cross β -structure of a single β -sheet is reported. In the inset the extensive hydrophobic interactions established by Nal side chains are highlighted. In panel (b), the possible direct interactions between two facing β -sheets is reported. In panel (c) a three-dimensional model of the possible insertion way of a Nal side chain within the dry interface of two facing β -sheets.

In conclusion, MD simulations suggest that the basic structural elements of these assemblies is a cross β -sheet that is stabilized by both the hydrogen bonding and hydrophobic interactions established by Nal aromatic side chains. The larger size of the Nal hydrophobic side chain compared to Phe makes dipeptide cross β -sheets formed by the former residues stable enough to generate well-defined aggregates at microscale level. Finally, individual β -sheets can then mutually interact in different ways to generate the structural variability of the lateral packing observed in these aggregates.

3.4.6 Relaxivity performances

The relaxivity of Gd-2NaI_2 was measured, at 21.5 MHz (0.5 T) and 298K, as a function of the complex concentration (**Figure 32a**). The observed progressive enhancement in relaxivity is indicative of the fact that a self-aggregation process starts occurring already at very low concentration (ca. 1.0 mg/mL), confirming the values determined by fluorescence spectroscopy and $^1\text{H-NMR}$. At concentrations higher than 10-15 mg/mL the relaxivity R assumes an almost stable value which corresponds to the system in the completely aggregated form. By analyzing the profile of the relaxivity data as a function of the applied field strength (NMRD - Nuclear Magnetic Relaxation Dispersion) it is possible to obtain an accurate determination of the reorientational correlation time (τ_R), that is strictly related to the molecular size of the investigated system. NMRD profiles were acquired below (black circles) and above (white ones) the CAC values determined by ANS titration and $^1\text{H-NMR}$. In **Figure 32b** the NMRD profiles of Gd-2NaI_2 at 1.0 and 25.0 mg/mL concentrations are reported and compared to those of the corresponding di-phenylalanine conjugate $\text{Gd-DOTA-L}_6\text{-F}_2$ at the same concentrations. Data were analyzed using the Solomon-Bloembergen-Morgan model, considering one water molecule in the inner coordination sphere ($q=1$) and fixing the exchange lifetime (τ_M) to a reliable value (700 ps) on the basis of those previously reported for mono-amido DOTA derivatives..

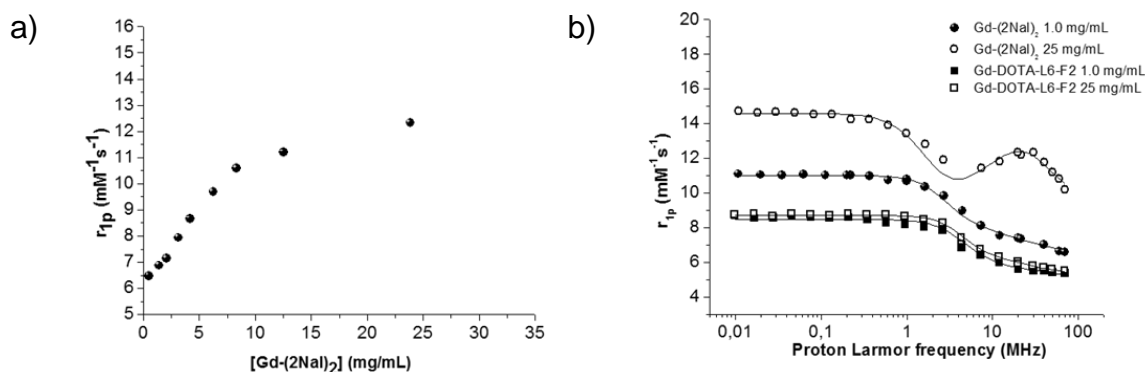


Figure 32: a) Longitudinal proton relaxivity of $\text{Gd-DOTA-L}_6\text{-(2NaI)}_2$ measured at 21.5 MHz (0.5 T) and 298 K as a function of the concentration of the Gd-complex. b) NMRD profiles of $\text{Gd-DOTA-L}_6\text{-(2NaI)}_2$ (1.0 mg/mL (●) and 25.0 mg/mL (○)) compared to those of $\text{Gd-DOTA-L}_6\text{-F}_2$ (1.0 mg/mL (■) and 25.0 mg/mL (□)). Experimental data points were measured on aqueous solutions of the Gd-complexes at 298K. The data refer to 1 mM concentration of the paramagnetic complexes.

Table 5. Main relaxometric parameters derived from fitting of NMRD profiles reported in Figure 32.^[a]

System (mg/mL)		r_{1p} ($\text{mM}^{-1}\text{s}^{-1}$)	τ^2 (s^{-2}) ^[b]	τ_v (ps) ^[c]	τ_R (ps) ^[e]		
Gd-DOTA-(2NaI) ₂	1	7.3	1.02×10^{19}	50	184		
	25	12.3	8.10×10^{18}	43	τ_R^I	τ_R^g	S^2
					423	4800	0.23
Gd-DOTA-F2	1	5.7	2.97×10^{19}	28	120		
	25	6.0	2.28×10^{19}	35	127		

^[a]On carrying out the fitting procedure, some parameters were fixed to reasonable values: $r_{\text{Gd-H}}$ (distance between Gd and protons of the inner sphere water molecule) = 3.1 Å; a (distance of minimum approach of solvent water molecules to Gd^{3+} ion) = 3.8 Å; D (solvent diffusion coefficient) = $2.2 \cdot 10^{-5} \text{ cm}^2 \text{ s}^{-1}$. ^[b]Squared mean transient zero-field splitting (ZFS) energy. ^[c]Correlation time for the collision-related modulation of the ZFS Hamiltonian. ^[d] Electronic relaxation time at zero field (calculated as $1/\tau_{s0} = 12\Delta^2 \times \tau_v$) ^[e] Reorientational correlation time.

The quantitative analysis of the NMRD profile of the aggregated form was not satisfactory when the simple inner- outer-sphere model was used, so the Lipari-Szabo approach was used for the description of the rotational dynamics. This model allows one to take into account the presence of a certain degree of internal rotation superimposed on the overall tumbling motion. These two types of motion, a relatively fast local rotation of the coordination cage about the linker to the peptide scaffold superimposed on the global reorientation of the system, are characterized by different correlation times: τ_R^I and τ_R^g , respectively. The degree of correlation between global and local rotations is given by the parameter S^2 , which takes values between 0 (completely independent motions) and 1 (entirely correlated motions).

Both the shape of the profiles and the τ_R values determined from the fitting of the experimental results (**Table 5**) validate the hypothesis of the formation of aggregates for Gd-2NaI₂ at 25.0 mg/mL.

On the contrary, the system is in the monomeric state when it is dissolved in solution at 1 mg/mL concentration.

In the case of Gd-DOTA-L₆-F2, both qualitative and quantitative analysis confirm the inability of the system to self-aggregate even at high concentration.

The quantitative analysis of the NMRD profiles indicates that both the local and the global rotational correlation times (**Table 5**) are significantly increased as compared to the τ_R value of the Gd-complex

in the monomeric form, whereas the S^2 value is relatively low ($S^2 = 0.23$), suggesting great flexibility of Gd-coordination cage around the oxoethylene linker.

3.4.7 Doxorubicin loading and release

The incorporation and release of Doxorubicin (DOX) into nanostructures was estimated by fluorescence spectroscopy (**Figure 33**, **Figure 34**).

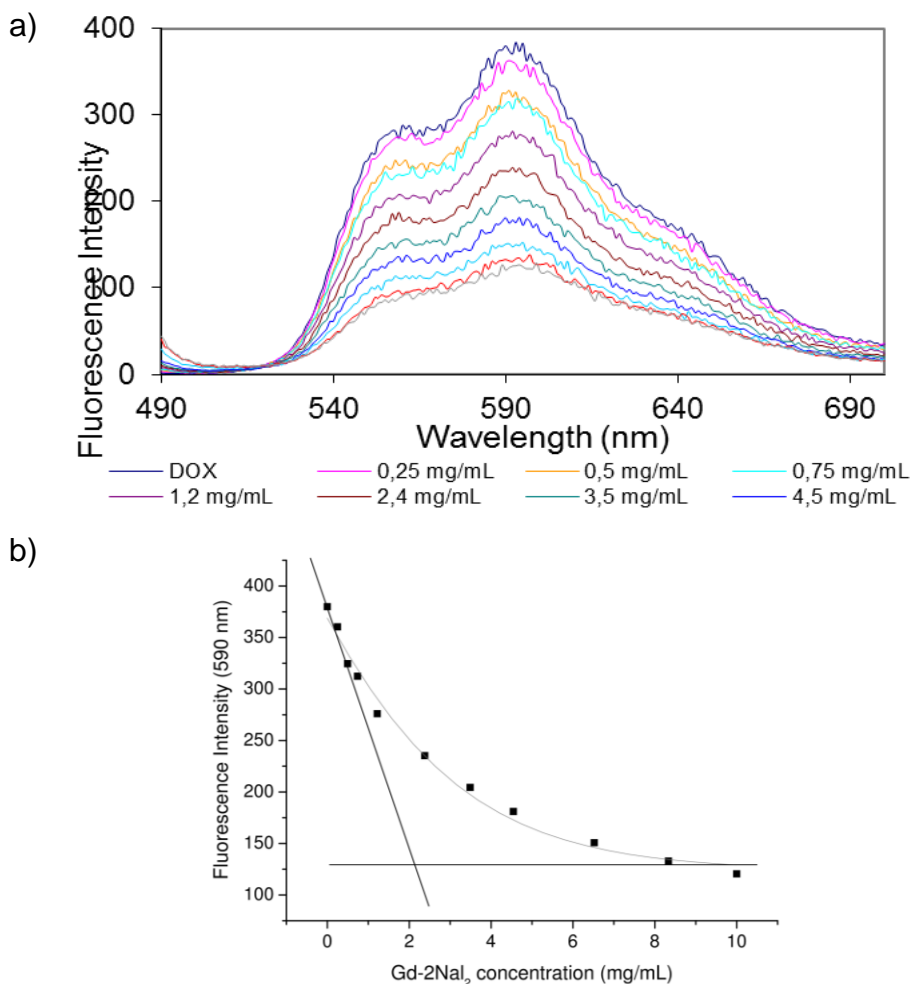


Figure 33: a) Fluorescence spectra of $1 \cdot 10^{-4}$ M DOX ($58 \mu\text{g/mL}$) solution alone and after the addition of growing amounts of Gd-2NaI₂ peptide conjugate (from 0.25 to 10.0 mg/mL). The progressive decrease of the DOX fluorescence intensity is due to the stacking of the anthracycline with the naphthylalanine ring. The excitation wavelength of DOX was settled at 480 nm and spectra recorded between 490 and 700 nm. b) Fluorescence intensity in the maximum at 590 nm as function of the Gd-2NaI₂ concentration reported in mg/mL.

Section I: PBMs as supramolecular contrast agents for MRI

The addition of increasing amounts of the peptide conjugate to the DOX solution causes a progressive decrease of the fluorescence intensity of DOX (**Figure 33a**). This quenching effect is attributable to the electrostatic interaction between the aromatic rings of the anthracycline with the naphthylalanine one.

By plotting the fluorescence intensity in the maximum at 590 nm as function of the Gd-2NaI₂ concentration (**Figure 33b**) we estimated that $g_{\text{Drug}}/g_{\text{Peptide}}$ is 0.028 (~60 μg of DOX for ~ 2.0 mg of peptide). The leakage assay, reported in **Figure 34** indicates a very low efflux of DOX across the peptide aggregate (~ 6% of drug released after 72h).

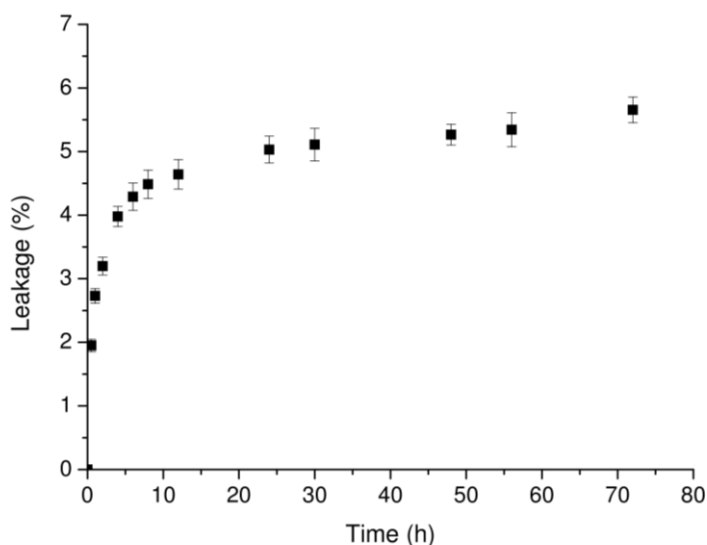


Figure 34: Leakage (%) of DOX from Gd-2NaI₂ aggregates over the time.

The ability of 2NaI₂ aggregates to encapsulate DOX was also checked by running 1D [¹H] spectra of La-2NaI₂ (at 2.5 mg/mL) at increasing DOX concentrations (**Figure 35**).

At a concentration equal to 2.5 mg/mL, as indicated above, La-2NaI₂ has formed relatively large aggregates (**Figure 35a**). In absence of La-2NaI₂, doxorubicin NMR spectrum in water (0.5 mg/mL concentration) contains sharp peaks (**Figure 35b**). In presence of La-2NaI₂ aggregates, doxorubicin signals are large and can be barely recognized in the spectrum, thus indicating the encapsulation of the drug inside the aggregates (**Figure 35c-i**).

The extensive line broadening and loss of signal is caused by the improved relaxation rate reflecting an increase of molecular weight with respect to the free doxorubicin.

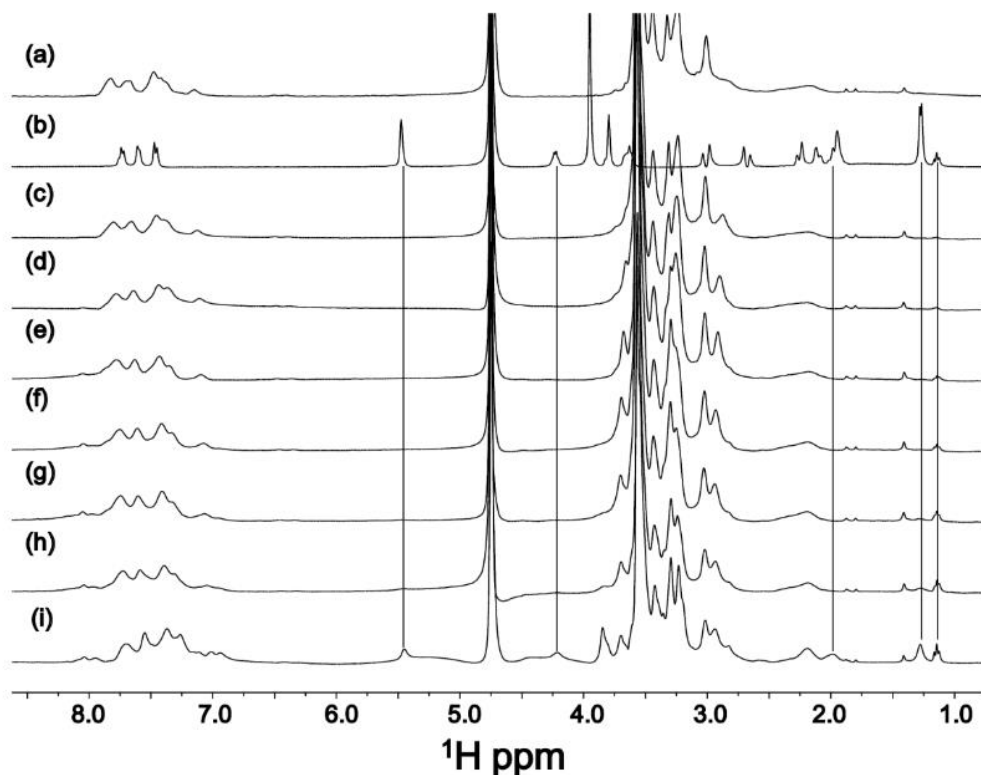


Figure 35. 1D ^1H NMR spectra acquired at 298 K of (a) $\text{La}-(2\text{-Nal})_2$ at 2.5 mg/mL, (b) DOX 0.5 mg/mL, (c) $\text{La}-(2\text{-Nal})_2$ at 2.5 mg/mL+DOX 0.05 mg/mL, (d) $\text{La}-(2\text{-Nal})_2$ at 2.5 mg/mL+DOX 0.1 mg/mL, (e) $\text{La}-(2\text{-Nal})_2$ at 2.5 mg/mL+DOX 0.2 mg/mL, (f) $\text{La}-(2\text{-Nal})_2$ at 2.5 mg/mL+ DOX 0.3 mg/mL, (g) $\text{La}-(2\text{-Nal})_2$ at 2.5 mg/mL+DOX 0.4 mg/mL, (h) $\text{La}-(2\text{-Nal})_2$ at 2.5 mg/mL+DOX 0.5 mg/mL, (i) $\text{La}-(2\text{-Nal})_2$ at 2.5 mg/mL+DOX 1 mg/mL. In the lowest spectrum a few peaks arising from doxorubicin appear, as indicated by the black lines.

Once all the pores inside the supramolecular aggregates of $\text{La}-(2\text{-Nal})_2$ are saturated, the drug starts to be released and this occurs at a concentration of doxorubicin close to 1.0 mg/mL (**Figure 35i**). At this drug concentration signals are still affected by line broadening thus indicating that most of the molecules are still entrapped inside the aggregates. Incorporation of DOX in $\text{Gd}-(2\text{-Nal})_2$ nanostructures was further examined by optical microscopy.

Incorporation of DOX in $\text{Gd}-(2\text{-Nal})_2$ nanostructures was further examined by optical microscopy. **Figure 36** shows polarizing optical micrographs (POM) of empty $\text{Gd}-(2\text{-Nal})_2$ nanostructures compared to DOX filled $\text{Gd}-(2\text{-Nal})_2$ ones. Polarized light interacts strongly with both the birefringent samples, generating contrast with the background.

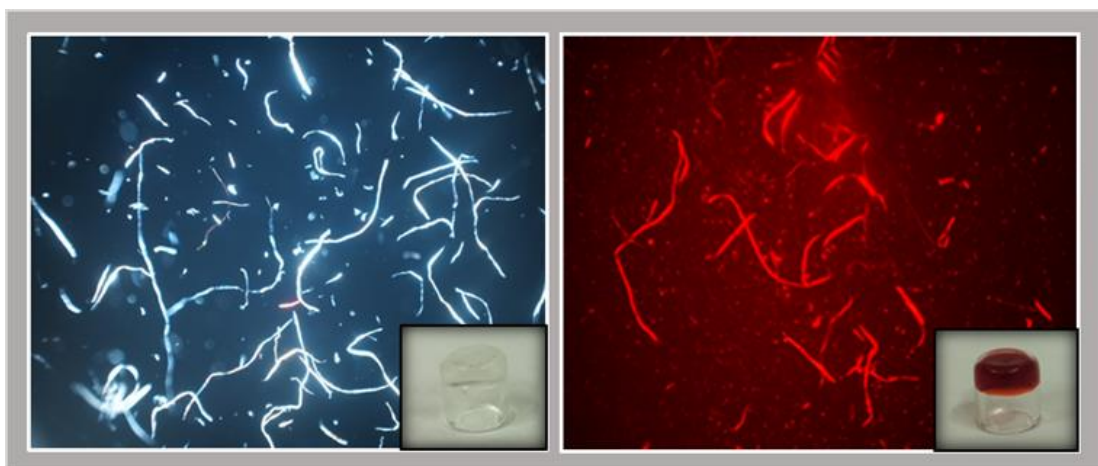
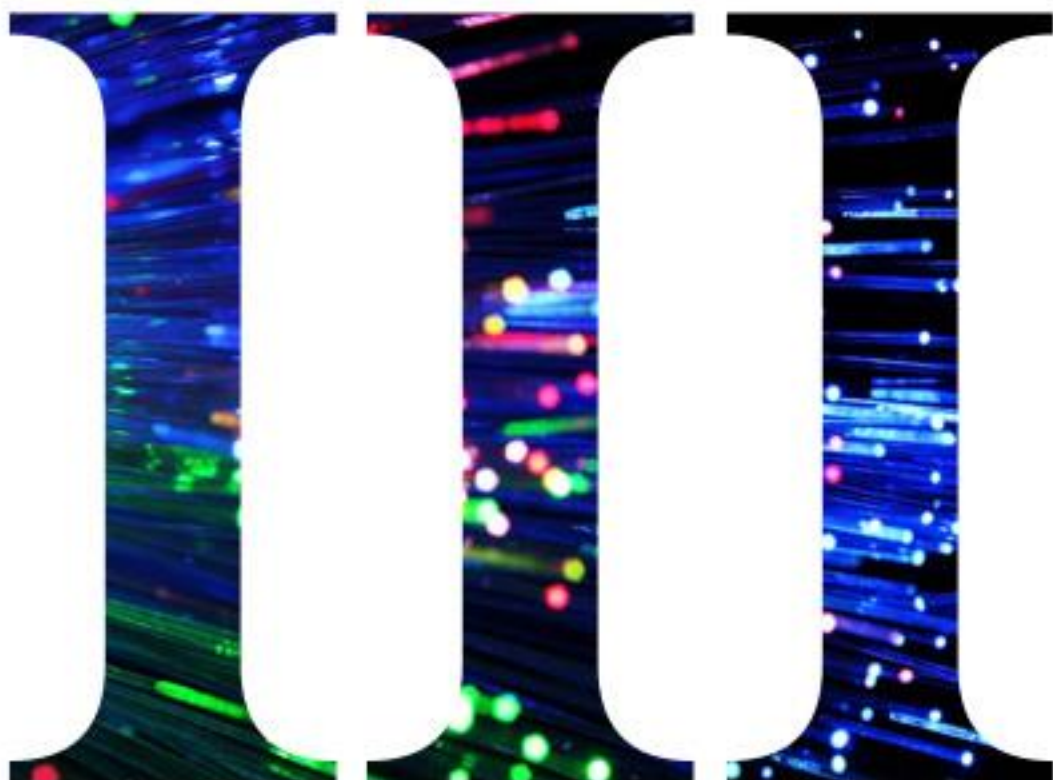


Figure 36: Polarized optical microscopy image of 1-cm vials containing (a) Gd-2NaI₂ and (b) DOX encapsulating Gd-2NaI₂ hydrogels. Images are observed with a Nikon microscope.



Section II

**Photoluminescent peptide-based
material as supramolecular fluorescent probes**

Carlo Diaferia | University of Naples Federico II | XXX cycle

Section II: PBMs as photoluminescent supramolecular probes

3.5 Photoluminescent peptide-based nanostructures

Nowadays, the major obstacle in many applications of light in biomedicine is represented by the limited penetration of light into biological tissue. Optical fibers represent the current gold-standard solution in clinical uses. However, most light-guiding systems are based on solid materials, not compatible with *in vivo* application.²¹⁹ On the other hand, optical waveguides based on biocompatible materials such as silk,²²⁰ polyethylene glycol (PEG),²²¹ and gels²²² present a scarce efficiency for delivering light over an organ-scale distance. The employment of water soluble biocompatible optical fibers based on peptide building blocks with enhanced PL properties could help to overcome these limitations.

In more recent years, a great interest has been generated around peptide-based nanostructures (NSs) with interesting blue-green photoluminescent (PL) properties.²²³ This PL phenomenon has also been observed in FF^{224,225} and FFF²²⁶ nanostructures. This PL phenomenon has been observed exciting self-assembled oligopeptides at 370 or 410 nm, only after heating the sample at 140-180°C, as a consequence of an irreversible reconstructive phase transition in the nanostructure.^{224,225}

A similar PL effect has been also observed for amyloid-like fibrils considering the nanofiber morphology with antiparallel β -sheet structures.²²⁷

The definition of the structural determinants of these intriguing PL properties exhibited by β -cross rich systems is still a debated topic, subject of intense current investigations. However, a proved explanation on the origins of this unexpected PL has not been provided until now and this theme remains currently under debate.

The most accredited hypothesis concerning the origins of the PL is the electron delocalization via hydrogen bonds in the β -sheet rich structure^{223,228,229} or the proton transfer.²³⁰

In order to develop novel bio-imaging tools based on peptide NSs, a novel peptide building block composed of six phenylalanine residues and eight PEG units (PEG₈-F6, **Figure 37a**) was designed and synthesized.²³¹

The high number of Phe residues should prompt the aggregation of the peptide derivative in nanostructures rich of β -sheet structures.

The photoluminescence properties of the self-assembled material have been investigated and correlated with the structural organization of the peptide building block at the micro- and nano-scale. A variety of techniques, including fluorescence, FTIR, CD, DLS, SEM, SAXS and WAXS allowed to:

Section II: PBMs as photoluminescent supramolecular probes

- investigate the aggregation behavior
- assign and study the secondary structure
- visualize the morphology of the final aggregates.

The total characterization of PEG₈-F6 nanostructures in solution highlighted the strong propensity of hexaphenylalanine monomer to self-organize in stable and well-defined NSs with a hydrodynamic diameter of ~ 60 nm and an antiparallel β -sheet arrangement. The proposed NSs showed also a blue PL phenomenon.

Wide-Angle X-ray Scattering characterization on dried fibers also revealed a typical “cross- β ” diffraction pattern observed for amyloid-like fibers with meridional and equatorial peaks at 4.8 Å and 12.5 Å, respectively.¹²⁴ Finally, a model of F6 framework spine in aqueous solution by molecular dynamics (MD) simulations is presented to identify and understand the molecular, chemical and energetic factors controlling the formation of nanostructures.

After the assessment of PEG₈-F6 structural properties we explored:

- the possibility to transfer the intrinsic fluorescence of a cross- β material (donor), like PEG₈-F6 based nanostructures, into an encapsulated fluorescent dye by FRET (Foster Resonance Electron Transfer);
- the effect of the PEG derivatization (length and chemical composition) on the supramolecular organization and on optoelectronic properties of the oligo-Phe building blocks.

3.6 Design, synthesis and fluorescence spectroscopy of PEG₈-F6

PEGylated hexaphenylalanine PEG₈-F6 was obtained by Fmoc/tBu solid phase synthesis in good yield and high purity. LC-MS and ¹HNMR are reported in **Appendix I**.

PEG₈-F6 is formed by two blocks: an aromatic one, formed by the repetition of six phenylalanine residues (F6), and a hydrophilic one composed of eight ethoxylic repetitions, here indicated as PEG₈ (MW ~ 600 Da). This PEG chain was coupled at the N-terminus of the peptide sequence (**Figure 37a**).

The PEG chain was inserted with the aim of producing a water soluble material for a large field of applications and not preclude its potential usage in nanomedicine for the delivery of drugs or contrast agents. Nonetheless, PEG₈-F6 shows very limited solubility in water, whereas it shows an excellent solubility in 1,1,1,3,3,3-hexafluoro-2-propanol

Section II: PBMs as photoluminescent supramolecular probes

(HFIP). After dissolution the peptide solution appear clear up to a concentration of 100 mg/mL. According to the procedure described for cationic diphenylalanine,¹⁴⁴ this stock solution in HFIP was diluted five-fold in water. After dilution and removal of HFIP, peptide solution remains perfectly limpid until 20 mg/mL.

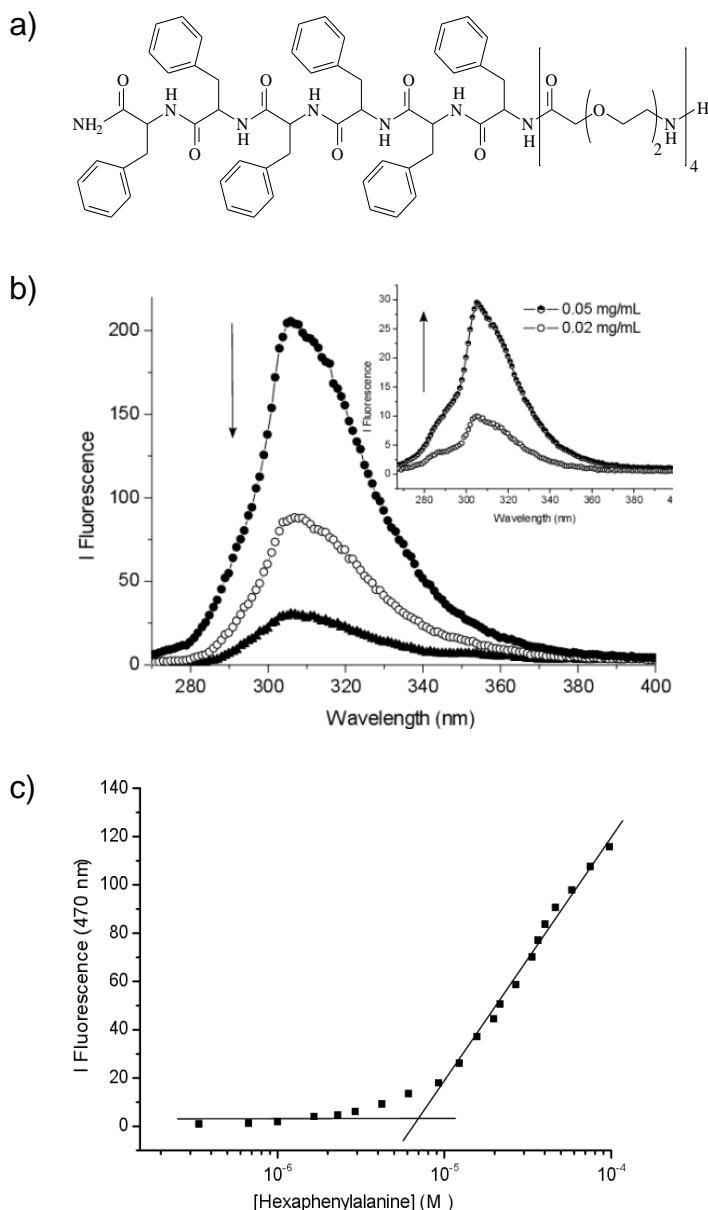


Figure 37: a) Schematic representation of hexaphenylalanine PEG₈-F6. b) Fluorescence spectra of PEG₈-F6 in water solution at 0.1 (●), 1.0 (○) and 2.5 mg/mL (▲). In the insert, fluorescence spectra of PEG₈-F6 at 0.02 and 0.05 mg/mL. All emission spectra were recorded at 25°C between 265 and 400 nm

Section II: PBMs as photoluminescent supramolecular probes

with excitation at 258 nm. c) Figure 1c reports fluorescence intensity emission of ANS fluorophore at 470 nm vs. concentration of PEG₈-F6. CAC values are established from the break point.

The tendency of PEG₈-F6 to self-aggregate was previously evaluated with fluorescence spectroscopy, by exciting the sample at 257 nm (**Figure 37b**).

At all the concentrations studied, the expected emission peak at 282 nm, ascribed to the phenylalanine residue, appears weakly outlined, whereas it is well observable the peak at 310 nm, typical of π -stacking phenomena observed during the excimer Phe formation. This result suggests the high tendency of PEGylated peptide PEG₈-F6 to self-aggregate and indicates that the critical aggregate concentration (CAC) value of this compound is lower than 0.02 mg/mL. However, two different trends can be identified for the maximum as function of the concentration.

At very low concentrations (0.02 and 0.05 mg/mL), the fluorescence intensity at 310 nm increases gradually, whereas at high concentration (0.1, 1.0, and 2.5 mg/mL) an opposite behavior was observed. The decrease of the signal intensity for concentrations above 0.1 mg/mL, can be attributed to quenching that arises from the stacking of the aromatic rings.

A more accurate determination of the critical aggregation concentration (CAC) was carried out using ANS fluorescence-based method. **Figure 37c** reports the fluorescence intensity of an ANS solution (20 μ M in cuvette) at 470 nm, as function of hexaphenylalanine concentration. From the graphical break point it can be established the CAC value (7.5 μ M, 0.01 mg/mL). This value is significantly lower (around one order of magnitude) than the value found for the polymeric tetraphenylalanine analogues previously studied.^{196,197} In details, all the polymeric F4-peptides showed CAC values ranging between 43 and 167 μ M. As expected, the elongation of the aromatic framework from four to six F residues permits to reduce the CAC value and in turn to increase the stability of the aggregate upon dilution.

3.6.1 Secondary structure

Secondary structure of PEGylated hexapeptide in water solution was assessed by CD and FTIR spectroscopies. CD spectra of PEG₈-F6 at 0.1, 1.0 and 10.0 mg/mL, well-above the CAC value, were recorded between 280 and 195 nm and the dichroic behavior was reported in **Figure 38a**.

Due to the very low CAC value of this aromatic derivative, is not able to record CD spectra of acceptable quality for solution concentration below CAC (< 0.01 mg/mL). All the spectra show two peaks: a maximum

Section II: PBMs as photoluminescent supramolecular probes

around 205 nm, attributable to aromatic side-chains stacking, and a minimum around 230 nm, associated with a β -structure.^{184,203,216}

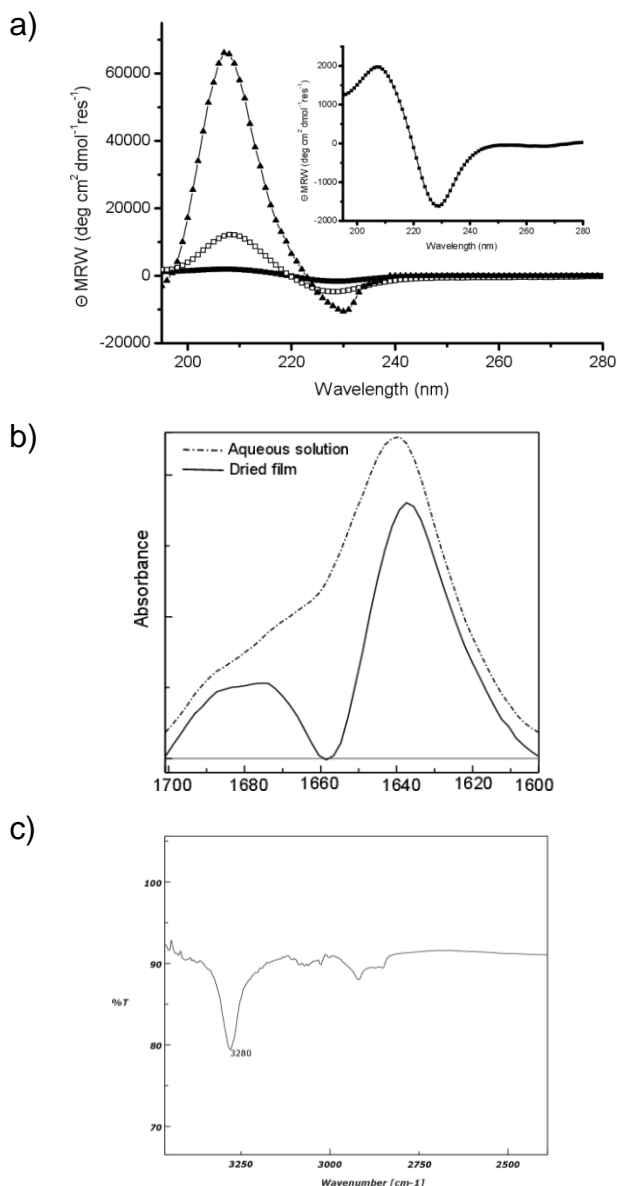


Figure 38: Spectroscopic characterization of PEG₈-F6 by CD and FTIR. a) Far-UV CD spectra of hexaphenylalanine in aqueous solution at 0.1 mg/mL (▲), 1.0 mg/mL (□) and 10.0 mg/mL (■). Spectra are recorded between 280 and 195 nm. In the insert is reported a zoom of PEG₈-F6 spectrum at 10 mg/mL. b) FTIR spectra of PEG₈-F6 in solution and at the solid state, in the amide I region. c) FTIR spectrum of PEG₈-F6 in the region of the NH stretching.

Section II: PBMs as photoluminescent supramolecular probes

However, the relative ratio between the intensity of the two peaks decreases progressively as function of the concentration (from 5.8 to 1.2). This decrease indicates the progressive formation of supramolecular aggregates in solution. According to CD data, the presence of β -sheet structures is supported by FTIR analysis in the region of the amide I vibrational band (1600-1700 cm^{-1}). FTIR spectra for PEG₈-F6, as dried film or in solution (2.0 mg/mL), are reported in **Figure 38b**. Both spectra show a dominant peak at 1637 and 1640 cm^{-1} for dried film and sample in solution, respectively. Peaks at these wavenumbers are strongly indicative of β -sheet formation. In addition, both spectra show a secondary broad peak around 1680 cm^{-1} , that appears better defined for the solid state sample (1672 cm^{-1}). The occurring of this peak indicates an antiparallel orientation of the β -sheet.^{205,206}

FTIR spectrum of PEG₈-F6 shows also a peak at 3280 cm^{-1} , corresponding to NH stretching in fibrillary assembly (**Figure 38c**). As expected, in HFIP FTIR spectrum does not present peaks in the amide I region, thus confirming the disaggregation of PEG₈-F6 in this solvent (data not shown).

3.6.2 Congo Red assays

Further confirmation of PEG₈-F6 ability to aggregate in amyloid-like fibers was obtained with Congo Red staining assay.²⁰⁹ UV-Vis spectra of CR alone and after incubation with 0.1 or 1.0 mg/mL of peptide are reported in **Figure 39a**.

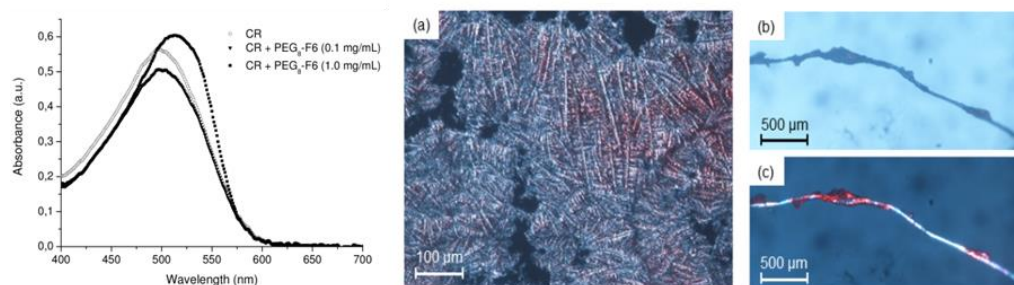


Figure 39: On the left, UV-Vis spectra of PEG₈-F6, stained with Congo Red at 0.1 and 1.0 mg/mL. The spectrum of Congo Red is also reported for comparison. Polarized optical microscopy: a) images of PEG₈-F6 dried onto a glass slide and stained with Congo Red solution; b) and c) PEG₈-F6 fibers stained with CR and observed with a Nikon microscope under bright field illumination and between crossed polars, respectively.

As expected, CR absorbs at 490 nm, whereas a spectral shift of the CR band from 490 to 540 nm was observed for solutions containing 1.0 mg/mL. Instead, only a negligible shift can be invoked for the sample containing 0.1 mg/mL of PEG₈-F6. At the same time, air-dried film and solid state PEG₈-F6 were stained with Congo Red and visualized by optical microscopy under cross-polarized light. From the inspection of Figure 3, both air-dried film (**Figure 39b**) and solid state sample (**Figure 39c**) exhibit the characteristic blue-green birefringence.

3.6.3 Dynamic Light Scattering analysis

DLS measurements were performed in order to reveal the presence of peptide aggregation in solution and to monitor the system evolution as a function of the concentration and time. The intensity profiles of PEG₈-F6 in water solution, in the 0.05 - 5.0 mg/mL range, are reported in **Figure 40** and structural data (mean diameter and diffusion coefficients, *D*) are collected in **Table 6**.

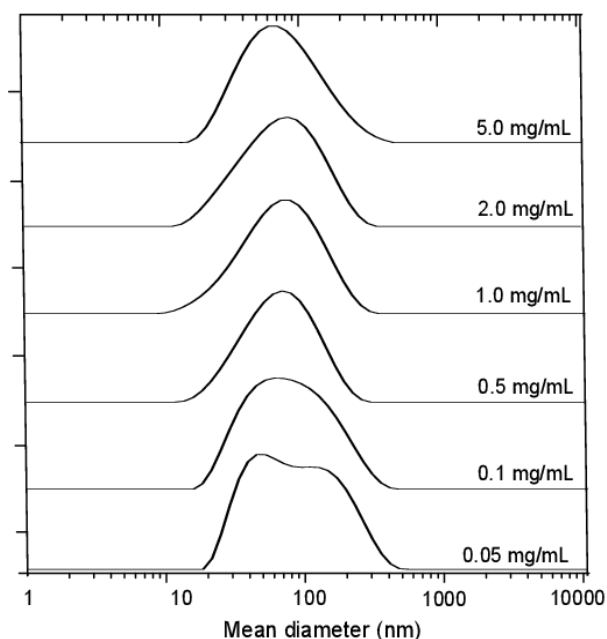


Figure 40: Mean diameter distribution as function of the concentration.

From the inspection of **Figure 40**, monomodal and bimodal distributions were observed for peptide solutions at high concentration (until 0.5 mg/mL) and low concentration (0.1 and 0.05 mg/mL), respectively. These results indicate that PEG₈-F6 nanostructures remain stable upon dilution until 0.5 mg/mL. Below this concentration a second population arises. At the same time, the size of the nanostructures in solution

Section II: PBMs as photoluminescent supramolecular probes

remains unaltered up to one month (data not shown). It is well-known that β -sheet rich peptides tend to aggregate, according to their kinetics, in oligomers, protofibrils and finally in fibers.²³² However, PEGylation of amyloid fragments such as A β (10-35) peptide induces the inhibition of the fibrillation process, as compared to the peptide alone.^{233,234}

Table 6: Mean diameter and diffusion coefficient for PEG₈-F6 in water at different concentration. Each measure is in triplicate.

PEG ₈ -F6 concentration	Mean diameter (nm)	D x 10 ⁻¹² m ² s ⁻¹
5.0 mg/mL	56.9± 0.5	8.66±0.1
2.0 mg/mL	56.7±0.1	8.68 ±0.1
1.0 mg/mL	56.9±0.6	8.65±0.1
0.5 mg/mL	58.8±0.6	8.37±0.1
0.1 mg/mL	67.8±2.1	7.28±0.2
0.05 mg/mL	74.5±0.8	6.60±0.1

3.6.4 Scanning Electron Microscopy

Scanning electron microscopy (SEM) images confirmed the capability of the aromatic peptide to assemble with an high morphological variability (**Figure 41**).

PEG₈-F6 self-assemblies yet at very low concentration (0.05 mg/mL) giving several amorphous conglomerates (**Figure 41a** and **41b**). These data are in good agreement with the critical aggregation concentration experimentally determined (~ 0.01 mg/mL). The increase of the concentration causes changes of the morphology up to obtain long and well-ordered nanostructures at 2mg/mL (**Figure 41**). At 0.2 mg/mL crystallization effects are observed (**Figure 41c** and **41d**).

In FF dipeptide, the crystal structure is due to hydrogen-bonded head-to-tail chains, which form hydrophilic channels embedded in a hydrophobic matrix created by the peptide side chains. However, in this case in which head-to-tail interactions are absent, the crystallization can be attributed to the PEG chain on the N-terminus.²¹⁷ At 0.5 mg/mL formation of highly ordered tree-like multi-branch nanostructures is shown. Several nucleation centers are visible on these multi-branch nanostructures (**Figure 41e** and **41f**). Finally, at 1.0 and 2.0 mg/mL, small conglomerated fibers and very long nanostructures can be observed together on the plate (**Figure 41g** and **41h**).

Many sheaf of fibers with variable length (between 1.5 and 12.5 μ m) and thickness (between 250 and 5000 nm) appear. Each sheaf is

Section II: PBMs as photoluminescent supramolecular probes

formed by small fibers of 65-350 nm width, placed side by side. Beside them, also the long nanostructures (from 150 to 4000 μm) present a high morphological variability: some nanostructures with a flat ribbon shape (**Figure 42a** and **42c**) and others with a twisted ribbon shape (Figure 42b and 42d).

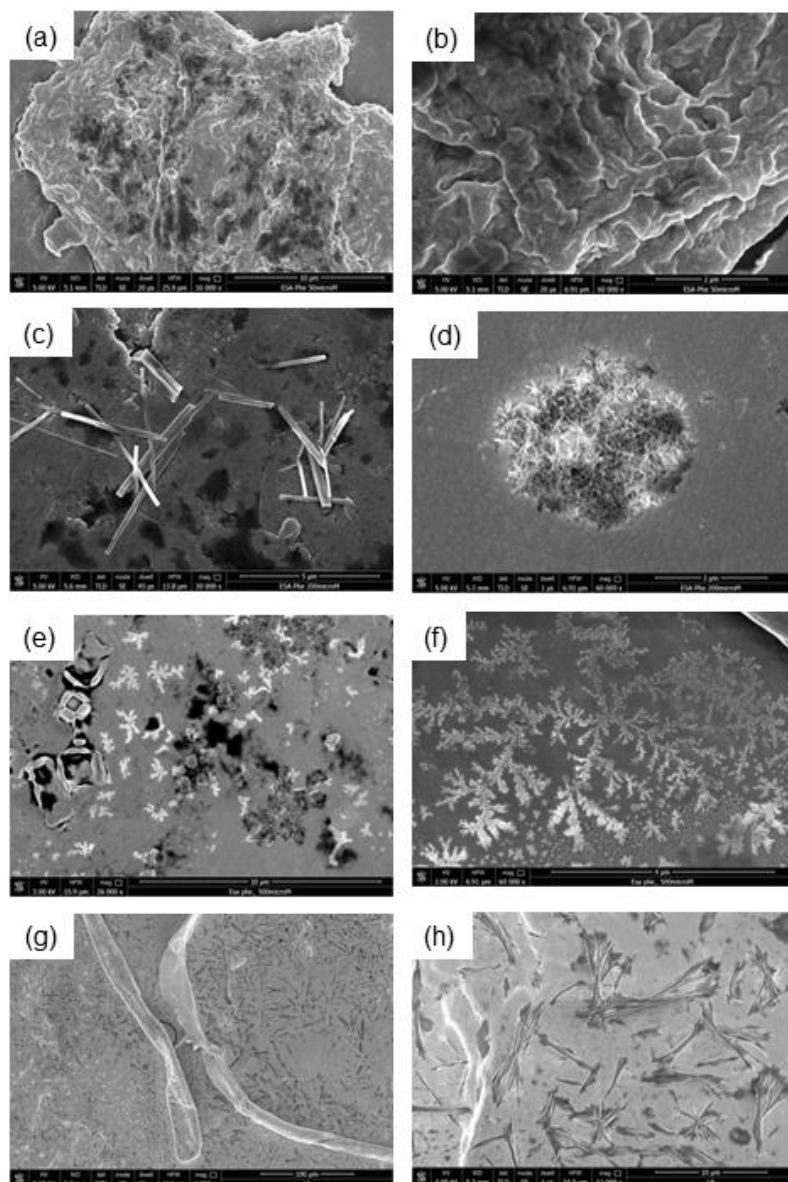


Figure 41: Selected SEM microphoto for PEG₈-F6: (a), (b) 50 $\mu\text{g/mL}$ (16000x, 10 μm and 60000x, 2 μm scale bar, respectively), (c), (d) 0.2 mg/mL (30000x, 5 μm and 60000x, 2 μm scale bar, respectively), (e), (f) 0.5 mg/mL (26000x, 10 μm and 60000x, 4 μm scale bar, respectively), (g), (h) 2 mg/mL (1000x, 100 μm and 12000x, 10 μm scale bar, respectively).

Section II: PBMs as photoluminescent supramolecular probes

Twisted ribbons are expected for amyloid peptides functionalized with short PEG chains.²³⁵ In tubular nanoaggregates (**Figure 42a** and **42c**), the width maintains an homogeneous size (~10-15 μm) along its full length, whereas in the twisted nanostructures thickness changes of 20 μm are measured along the different parts of the aggregate.

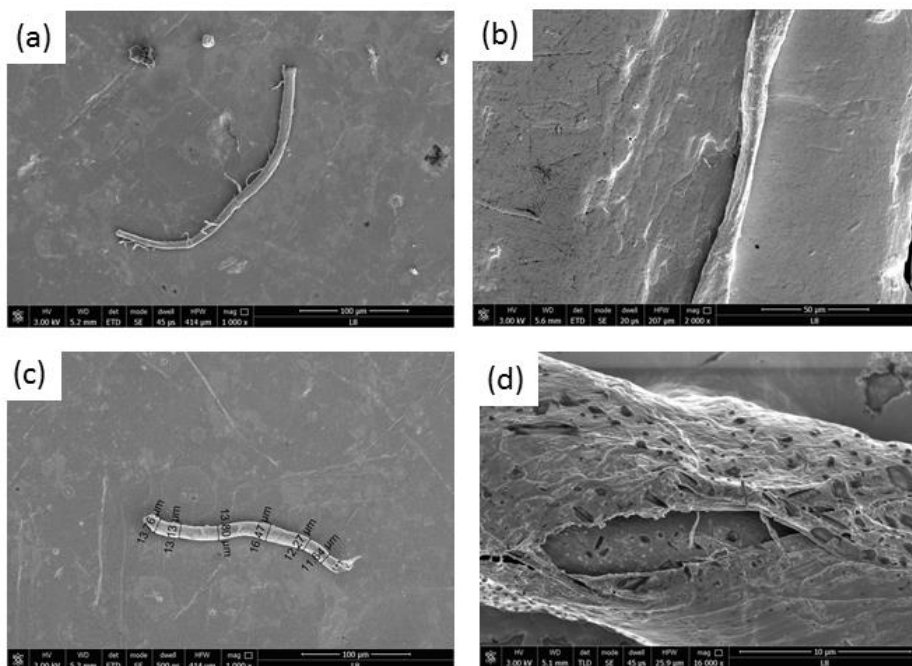


Figure 42: SEM microphotos for PEG₈-F6 nanostructures at 2 mg/mL, with flat (**a** and **c** 1000x, 100 μm scale bar) and twisted shape in evidence (**b**, 2000x, 50 μm scale bar; **d**, 16000x, 10 μm scale bar).

From these images it can realistically speculate that above 1.0 or 2.0 mg/mL the small fibers begin to collapse to give stacks. These stacks aggregate beyond in long nanostructures. DLS and SEM measures indicate different size for self-assembled PEG₈-F6 at the same concentration (for instance at 2.0 mg/mL). However, this mismatch depends on different physical state of the sample, which is in solution and at the solid state for DLS and SEM, respectively.

3.6.5 Wide-Angle and Small-Angle X-ray Scattering

To gain better insight into the assembly process and molecular organizations, ordered fibers in Wide-Angle and Small-Angle X-ray Scattering (WAXS/SAXS) were acquired. **Figure 43a** shows PEG₈-F6

Section II: PBMs as photoluminescent supramolecular probes

dried fibers as placed under the micro-focused X-ray beam. Four different regions were explored, at a relative distance of 0.2 mm, marked as 1 (red), 2 (green), 3 (blue), and 4 (orange) in **Figure 43a**, to control the lateral homogeneity of the fiber.

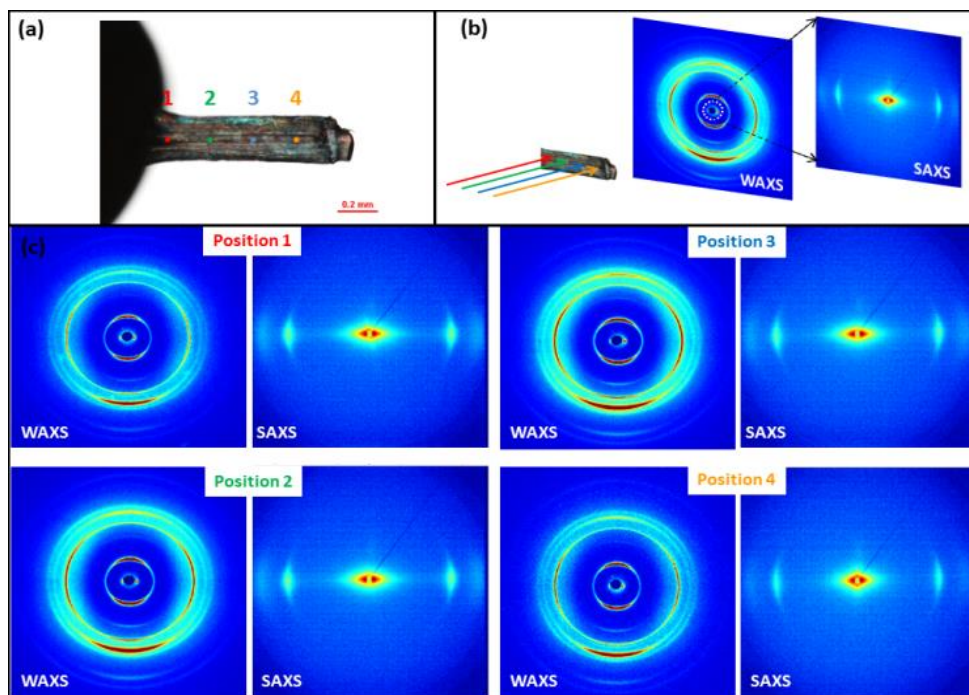


Figure 43: a) PEG₈-F6 sample, as placed under the micro-focused X-ray beam, with marked in red (1), green (2), blue, (3) and orange (4) the regions explored, placed at a relative distance of 0.2 mm; b) WAXS and SAXS data with different slightly overlapped Δq ranges: $\Delta q(\text{WAXS}) = 0.006\text{-}2.5\text{\AA}^{-1}$ and $\Delta q(\text{SAXS}) = 0.007\text{-}0.189\text{\AA}^{-1}$; c) two-dimensional (2D) WAXS and SAXS diffraction patterns collected for each sample position in (a).

The WAXS and SAXS detectors, placed at 10 mm and 2.2 m from the sample allowed to collect the diffraction in two different slightly overlapped Δq ranges: $\Delta q(\text{WAXS}) = 0.006\text{-}2.5\text{\AA}^{-1}$ and $\Delta q(\text{SAXS}) = 0.007\text{-}0.189\text{\AA}^{-1}$. The two-dimensional (2D) WAXS and SAXS diffraction patterns are displayed for each sample position in **Figure 43a**. Several diffraction peaks were measured either along the meridional (along the fiber) and equatorial direction (perpendicular to the fiber) and no difference was found moving across the different positions, proving a high lateral homogeneity of the fiber, either at the atomic (WAXS) and at the nanoscale (SAXS). The 2D WAXS and SAXS patterns were centered, calibrated and folded into one-dimensional (1D) profiles, by

Section II: PBMs as photoluminescent supramolecular probes

integrating along the equatorial and meridional directions (white arrows) of **Figure 44a** and **Figure 44b**, respectively.

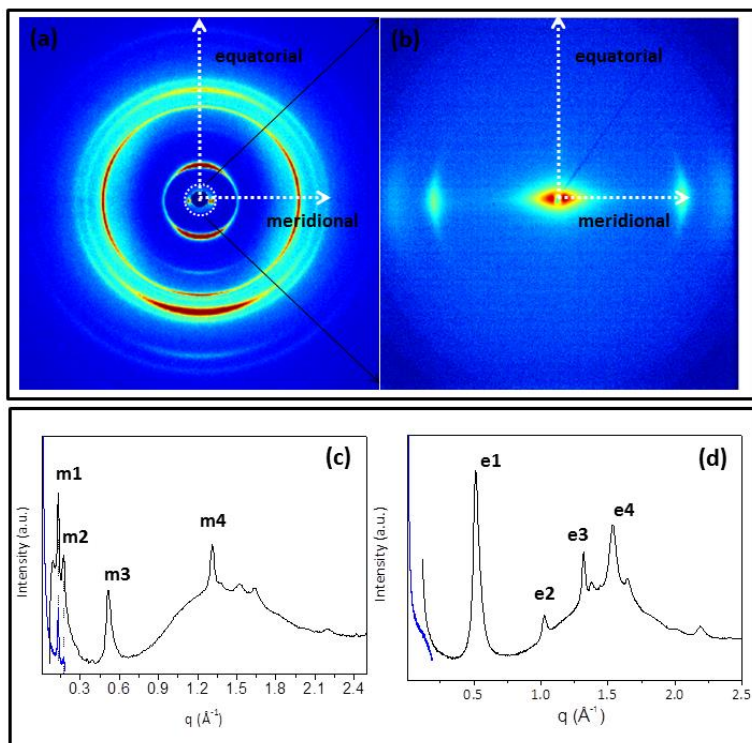


Figure 44: a) 2D WAXS and b) SAXS patterns, recorded for sample position 3; c) meridional and d) equatorial 1D SAXS (blue) and WAXS (black) as obtained once the 2D WAXS (a) and SAXS patterns (b) are centered, calibrated and folded into uni-dimensional (1D) profiles by integrating along the equatorial and meridional directions (white arrows).

The corresponding 1D patterns were reported, as blue (SAXS) and black (WAXS) profiles, in **Figure 44c,d** for the meridional and equatorial direction, respectively. **Table 7** summarizes the peak positions (in q) of the most intense SAXS and WAXS peaks, measured along the equatorial and meridional directions. The same meridional reflections were measured either in SAXS and WAXS, marked as m1 and m2 in **Figure 44c**. No equatorial SAXS peak was detected in the explored range. Therefore, the equatorial profile contains only morphological information. The experimental data were fitted with the GNOM program,²³⁶ as reported in **Figure 45a** (dotted curve corresponds to the experimental data, red line to the fitted profile). The pair distribution function extracted by this analysis, reported in **Figure 45b**, is a typical distribution of an elongated scattering objects. The gyration radius, determined by this analysis, is $R_g = 69 \pm 1 \text{ nm}$. The

Section II: PBMs as photoluminescent supramolecular probes

diffraction peak positions in **Table 2** were converted in lattice spacings (d). Three relevant distances can be distinguished: the typical β -strands distance at $d_{m4}=4.8\pm 0.3$ Å, more represented along the meridional direction; the sharp peak at $d_{e1}=12.2\pm 0.3$ Å, with its replica at half lattice spacing ($d_{e2}=6.1\pm 0.3$ Å), which correspond to the β -sheet distance; the meridional peak at $d_{m1}=48\pm 0.3$ Å, which corresponds to 10 times the β -strands distance. This meridional reflection with the spacing of 48 Å may be indicative of additional regularities along this direction. The presence of a clear fiber diffraction pattern either in SAXS and in WAXS is fingerprint of a hierarchical organization of the molecules in fibers from the atomic to the nanoscale, the latter footprint of the quaternary level of the fiber.

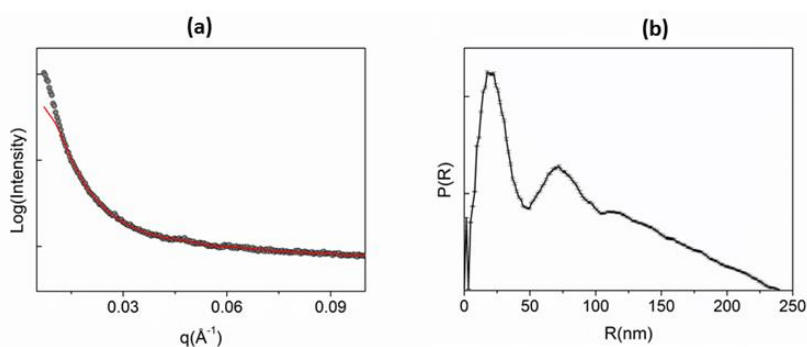


Figure 45: a) Equatorial SAXS (dotted curve) and best fit (full line). b) pair distribution function extracted from (a). The gyration radius, determined by this analysis, is $R_g = 69\pm 1$ nm.

Table 7: Equatorial and meridional reflections for PEG₈-F6 fibers.

Meridional reflections		
Label	q (Å ⁻¹)	d (Å)
m1	0.132	48.0
m2	0.171	37.0
m3	0.514	12.2
m4 (β strand)	1.32	4.8
Equatorial reflections		
e1	0.514	12.2
e2	1.026	6.1
e3 (β strand)	1.319	4.8
e4	1.536	4.1

3.6.6 Photoluminescence in PEG₈-F6 Nanostructures

PEG₈-F6 at a concentration of 10 mg/mL shows a blue PL between 420-460 nm, when the sample is excited at a wavelength of 370 or 410 nm (**Figure 46**). The narrow peak at $\lambda = 420$ nm, that appears upon excitation at 370 nm, can be associated to the Raman scattering in water. PEG₈-F6 keep PL effect also at the solid state. **Figure 46** reports the immunofluorescence and confocal images of the sample deposited on a clean coverslip glass and slowly dried at room temperature.

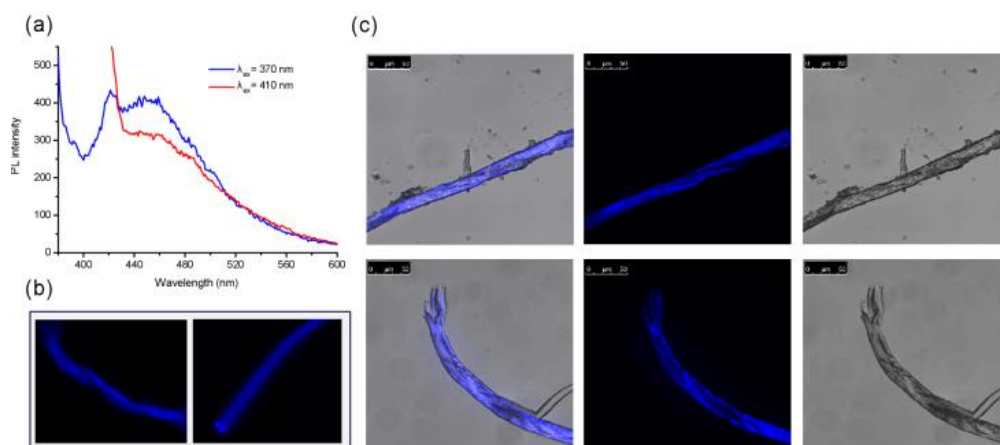


Figure 46: PL of PEG₈-F6 nanostructures at 10 mg/mL. a) Blue PL emission spectra for sample in solution upon excitation at ~ 370 nm (blue line) and at ~ 410 nm (red line). b) Fluorescence microscopy images of dried film of PEG₈-F6 obtained by exciting in the UV spectral region (DAPI filter). c) Confocal microscopy images of dried film of PEG₈-F6: Fluorescence images (on the left), bright field images (on the right) and the merge of fluorescence and bright field images (at the center). Scale bar = 50 μm .

3.6.7 Molecular modelling and dynamics

To gain insights into the atomic structure of these supramolecular aggregates molecular dynamics simulations were performed. Although, in principle, PEG moieties could influence the PEG₈-F6 structure, it was assumed that the self-assembling is essentially dictated by the aromatic peptide region, as PEG is completely disordered, even in the crystal state, in the only 3D-structure available of a highly PEGylated protein.²³⁷ Accordingly, MD simulations were performed on distinct F6 models generated using the steric zipper structure of the KLVFFA hexapeptide as template (**Table A5, Figure A2** in **Appendix II**). These assemblies were characterized by a different number of β -strands per β -sheet.

Section II: PBMs as photoluminescent supramolecular probes

Models here investigated were denoted as SH_x_ST_y_F₆, where x and y indicate the number of β -sheets and β -strands per sheet, respectively; F₆ indicates the number of Phe residues per chain. Preliminary, simulations carried out on the smaller systems (SH₂_ST₁₀_F₆ and SH₂_ST₂₆_F₆) suggested that these steric zipper models were rather stable in the simulation timescale (data not shown).

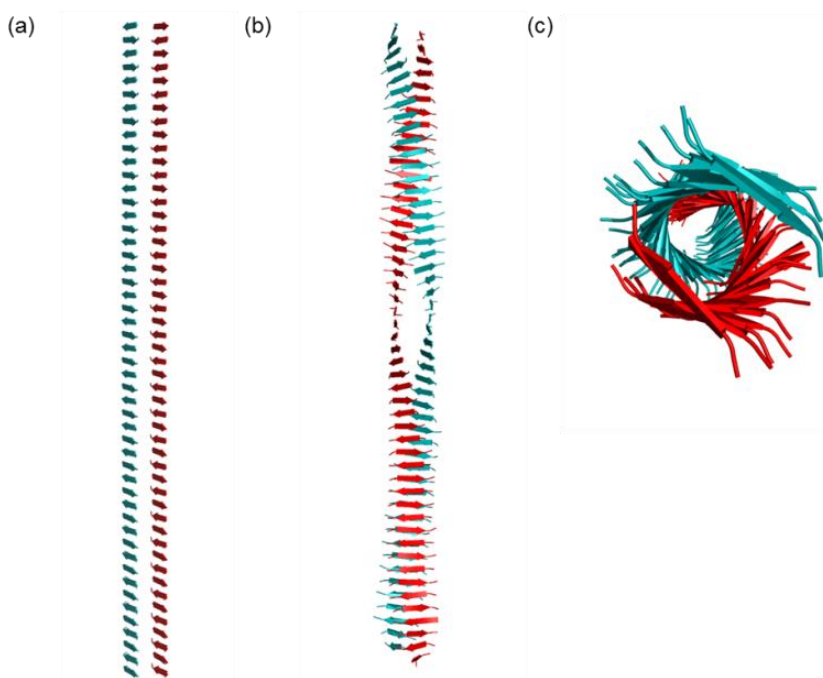


Figure 47: Evolution of the SH₂_ST₅₀_F₆ model during the simulation. Panel (a) shows the starting flat model whereas panels (b) and (c) show two different views of the average structure calculated in the equilibrated region of the trajectory.

However, to reduce the impact of the assembly termination effects, most extensive analyses were conducted on the larger SH₂_ST₅₀_F₆ system (**Figure 47a**). The inspection of the root mean square values (RMSD) of SH₂_ST₅₀_F₆ trajectory structures versus the initial structure clearly shows that the starting model undergoes major transition during the simulation (**Figure 48a,b**).

The analysis of the evolution of the trajectory also indicates that the structural transition is followed by states characterized by rather constant RMSD values (**Figure 48a**). This behavior suggests that the system adopts a novel structural state in the equilibrated region of the trajectory (20-100 ns).

This transition is also coupled with a significant variation of the assembly gyration radius (**Figure 48b**). Notably, the secondary

Section II: PBMs as photoluminescent supramolecular probes

structure of SH2_ST50_F6 is well preserved in the simulation (**Figure 48c**). The visual analysis of trajectory structures clearly indicates that the initially flat SH2_ST50_F6 β -sheet motif undergoes a significant twist.

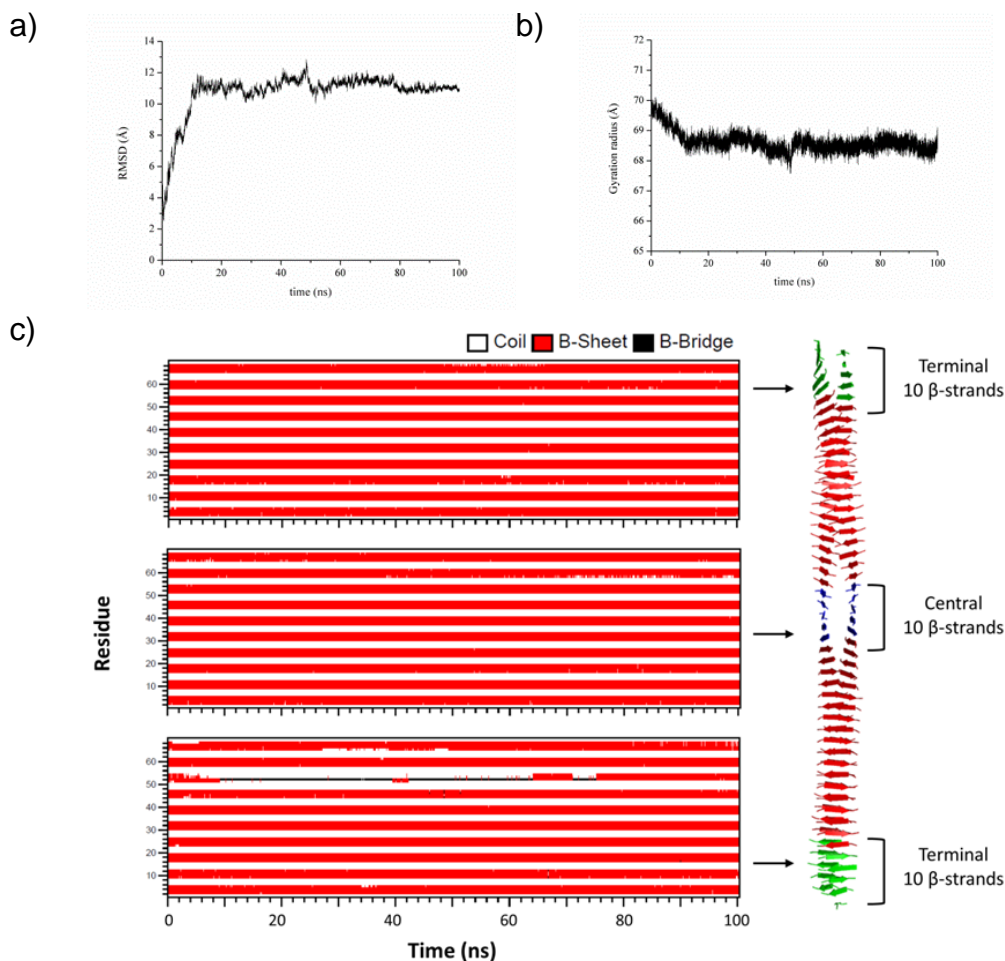


Figure 48: Structural parameters evaluated in the trajectory structures for SH2_ST50_F6: RMSD values of MD structures against the starting flat model computed on the C^α atoms (a), gyration radius (b), and secondary structure time evolution (c). For clarity, the secondary structure is reported only for the residues belonging to the terminal ends and to the central region.

This is also evident when the average structure calculated in the equilibrated region of the trajectory is visualized (**Figure 47b,c**). This behavior has been observed for several other peptides forming cross-beta structures. It has been suggested that the β -sheet twisting is better suited for fiber formation, whereas the growth of single crystals forces the β -sheets to adopt flat states. The analysis of the evolution of the inter-sheet distance shows that the two facing sheets are more

Section II: PBMs as photoluminescent supramolecular probes

separated in the equilibrated region compared to their relative position in the KLVFFA structure (**Figure 49**).

Indeed, in the starting crystallographic KLVFFA structure the distances between facing C^α atoms belonging to the two distinct β -sheet are on average 10.5 Å (range 9.4 – 11.6 Å). The modelling in this scaffold of the F6 homopeptide produces some steric hindrance. Consequently, it was observed an increase of the β -sheet separation during the simulation (**Figure 49**).

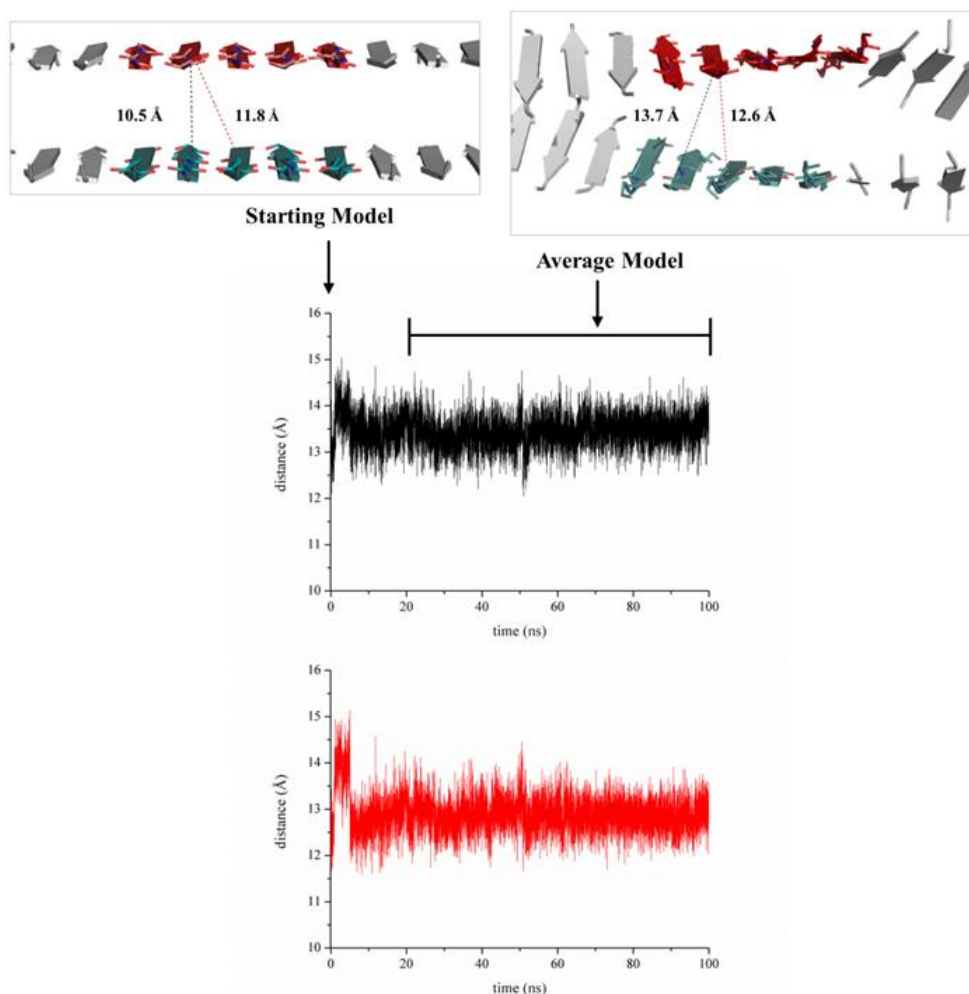


Figure 49: The evolution of the distance between two representative C^α atoms of the facing sheets along the trajectory. The values of the monitored distances for both the flat starting model and the twisted average structure are shown in the insets.

The shortest distances between C^α atoms of the two β -sheets are approximately 12.5 Å. This indicates a close agreement between the inter-sheet distance of the equilibrated model and the WAXS data. The

Section II: PBMs as photoluminescent supramolecular probes

good agreement between the resulting model and the experimental WAXS data corroborate our assumption that PEG moiety has a limited impact on PEG₈-F6 structure, which is essentially dictated by the peptide region. The structural transition occurring in the simulation leads to the staggering of the facing strands of the two β -sheets along the fiber axis.

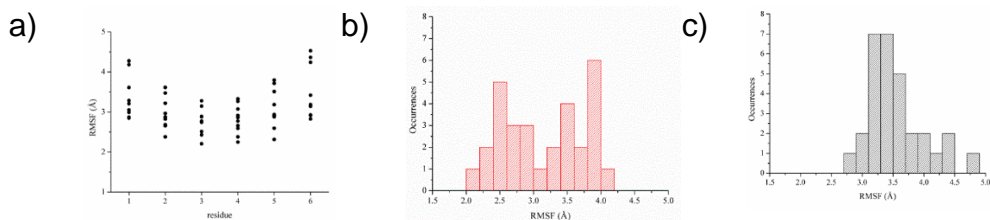


Figure 50: RMSF values of the model computed in the equilibrated region of the trajectory (20-100 ns). In panel (a) the values of RMSF computed on the C α atoms of each strand are shown whereas panels (b) and (c) report the distribution of RMSF values exhibited by the Phe sidechains located in the dry interface and exposed surface, respectively. For clarity only the values of the central ten β -strands are reported.

However, no twisting has been observed for the Gln homopeptides. In this latter case the strong interdigitation of the Gln side chains has likely prevented the β -sheet twisting. The examination of the flexibility of this novel state, carried out by computing root mean square fluctuation (RMSF) values, demonstrates that, with the exception of terminal residues within each strand, the backbone atoms are rather rigid (**Figure 50a**). A limited level of flexibility is also shown by Phe side chains. Indeed, the flexibility of Phe side chain located in the inter-sheet dry interface is comparable to the mobility of the backbone atoms (**Figure 50b**). Phe side chains of the solvent-exposed interface, although displaying larger RMSF values, still retain a restricted mobility. The limited flexibility of Phe side chains is also highlighted by the analysis of their rotameric states. Each strand presents rather recurrent values of the χ_1 dihedral angle (**Figure 51**). All residues within the same strand adopt predominantly the same χ_1 value. Furthermore, strands with all gauche+ (g+) Phe side chains alternate with strands showing all trans (t) rotameric states. This trend does not depend on the location of the Phe residue in terms of dry interface or exposed surface. The inspection of the Phe side chain interactions clearly indicates that this recurrent rotameric motif plays an important role in the stabilizations of the SH2_ST50_F6 assembly. Indeed, the juxtaposition of alternating antiparallel F6 strands with side chains presenting either g+ or t states

Section II: PBMs as photoluminescent supramolecular probes

leads to the formation of staggered π -stacking interactions within the same β -sheet (**Figure 52a**).

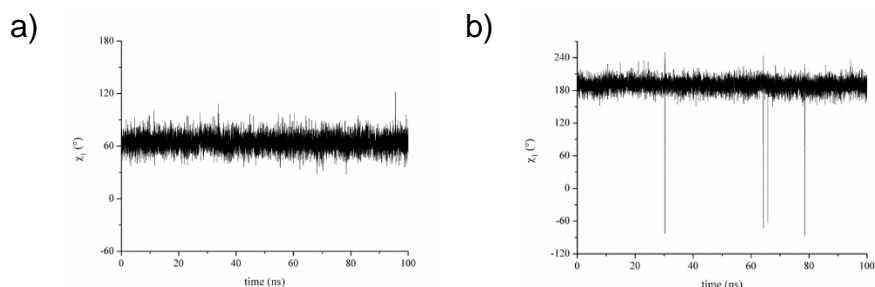


Figure 51: Persistence of Phe side-chain rotameric states along the simulation timescale. Representative examples of Phe side chains adopting either g^+ (a) or t (b) conformations are shown.

In line with literature classification of these interactions, the distance between the centers of mass of the stacking aromatic rings is on average close to 5.0 Å.

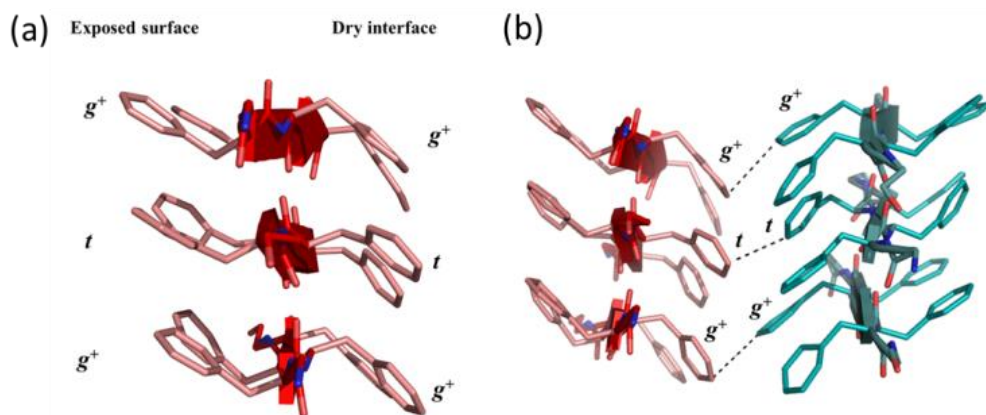


Figure 52: Conformations of the Phe side chains and their interactions at the exposed interface and at the dry interface. The inter-strand interaction within the same sheet are reported in panel (a) whereas the inter-sheet interactions are reported in panel (b). The rotameric states of Phe residues are shown in both panels. The T-shaped interactions established at the dry interface are also indicated in panel (b).

This particular configuration of the Phe side chains within the individual sheets is suitable for the formation of stabilizing interaction at the inter-sheet level. As shown in **Figure 52b**, the dry interface is characterized by the presence of recurrent T-shaped aromatic interactions.

These findings provide a clear structural pattern for the stabilization of antiparallel β -sheets by Phe side chains. They also indicate that individual Phe-rich β -sheets are pre-organized to form steric zipper assemblies. However, Phe side chains, although closely packed through the formation of hydrophobic and steric interactions, do not lead to the inter-digitation that frequently characterizes amyloid-like peptides.

3.7 Photoluminescent PBMS as FRET donor for fluorophore dye

PEG₈-F6 NSs (**Figure 53a**) showed a blue photoluminescence (PL) between 420-460 nm, when excited at wavelengths of 370 or 410 nm. It was explored the possibility to transfer by Förster Resonance Energy Transfer (FRET) phenomenon the fluorescence of a cross- β material (donor), like PEG₈-F6 based nanostructures, into an encapsulated fluorescent dye such as 4-Chloro-7-nitrobenzofurazan (NBD-**Figure 53b**).

Due to its spectral window ($\lambda_{\text{ex}} = 465 \text{ nm}$; $\lambda_{\text{em}} = 530 \text{ nm}$), the poorly water soluble NBD, was chosen as a suitable model fluorophore to check the capability of these peptide-based NSs to transfer by FRET their intrinsic fluorescence to a fluorophore, strictly associated with the peptide NS. The FRET should cause a red-shift of the photoluminescence of the NSs, thus opening concrete opportunity to their application in the bioimaging field.

3.7.1 Synthesis and preparation of NBD filled NSs

PEG₈-F6, composed of six phenylalanine residues and eight ethoxylic groups, is poorly soluble in water, whereas is soluble in 1,1,1,3,3,3-hexafluoro-2-propanol (HFIP) up to 100 mg/mL. Stable and well-organized NSs are obtained by five-fold diluting this stock solution in water and removing the organic solvent by a slow nitrogen flow. NBD dye also has very limited water solubility and good solubility in HFIP. According to these evidences, NBD-filled NSs were synthesized dissolving both PEG₈-F6 and NBD powders (**Figure 53a,b**) in HFIP in 10/1 (w/w) ratio. In this solution, the starting peptide and fluorophore concentrations are 100 and 10 mg/mL, which correspond to $6.8 \cdot 10^{-5}$ and $5.0 \cdot 10^{-5}$ mol, respectively. Subsequently, this solution was diluted in water, HFIP removed and the resulting solution centrifuged to clear the excess of non-encapsulated NBD (**Figure 53c**).

The light yellow supernatant was further purified from potential traces of free NBD by gel-filtration on Sephadex G-50 column.

Section II: PBM as photoluminescent supramolecular probes

According to the dilution achieved during the purification, the final concentration of hexaphenylalanine estimated by UV-Vis was 10 mg/mL.

Due to its low water solubility, the detection and the quantification of encapsulated NBD were unfeasible in water.

Consequently, the amount of NBD encapsulated in NSs (200 $\mu\text{g/mL}$) was determined by UV-Vis on the sample lyophilized and re-dissolved in methanol (**Figure 54a**). From the experimental quantification of the species, the molar ratio between NBD molecule and PEG₈-F6 peptide was determined to be 1:7 mol/mol.

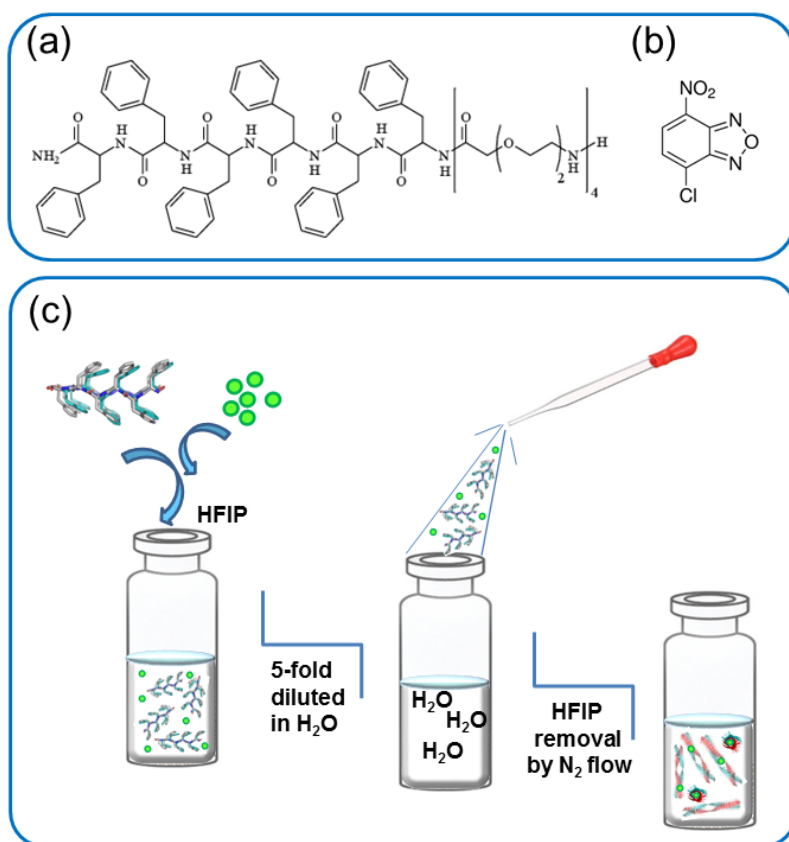


Figure 53: Schematic representation of PEG₈-F6 (a) and NBD chloride (b), respectively. (c) Preparation of NBD/PEG₈-F6 nanostructures: both PEG₈-F6 and NBD were dissolved in 1,1,1,3,3,3-hexafluoro-2-propanol in 10/1 (w/w) ratio. Then, this solution was ten-fold diluted in water and HFIP removed with a slow nitrogen flux.

The fluorescent dye remains associated with the NS also after repeated washing, thus suggesting the existence of a tight interaction between the dye and the NS. In order to exclude the occurrence of a covalent

Section II: PBMs as photoluminescent supramolecular probes

bond between the NBD fluorophore and the N-terminus of the oligopeptide, we analyzed NBD-PEG₈-F6 NSs by LC-MS.

The mass spectrum, reported in **Figure 54b**, shown only the mass corresponding to the peptide.

Altogether, these experiments suggest that, in this preparation protocol, the NBD encapsulation is favored by the self-aggregation of the peptide based NS directly around the NBD dye, as a consequence of the HFIP evaporation.

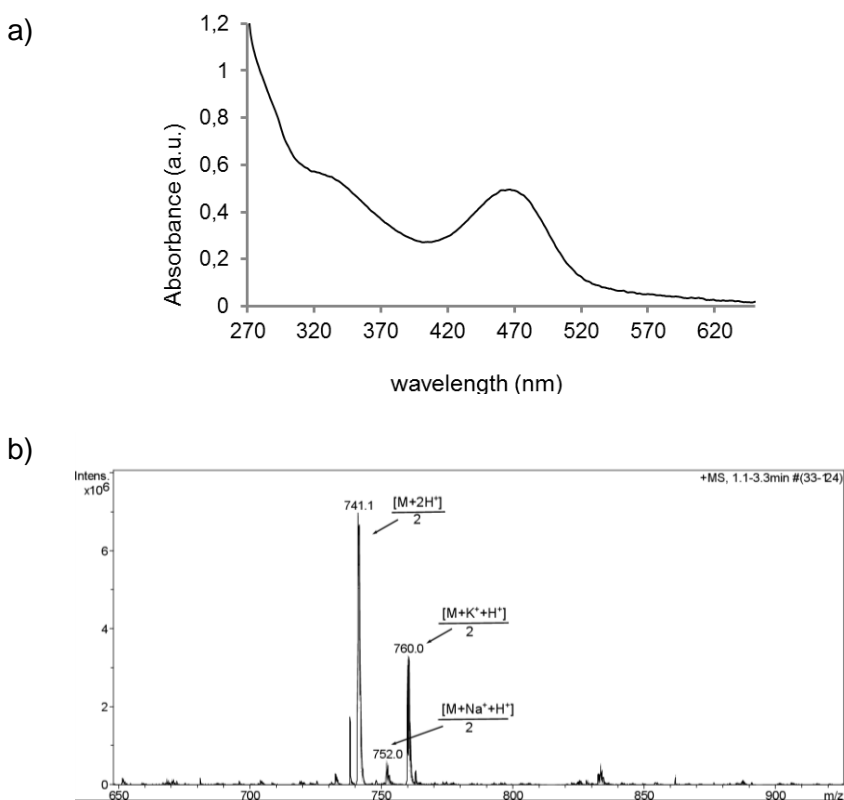


Figure 54: a) UV-Vis Spectrum of NBD/PEG₈-F6 solution, lyophilized and dissolved in methanol. b) ESI spectrum of NBD/PEG₈-F6 solution diluted 10-fold in water.

3.7.2 Structural characterization of NBD-filled NSs: secondary structure

In order to evaluate the potential structural modifications induced by the NBD encapsulation in PEGylated peptide nanostructures, NBD/PEG₈-

Section II: PBMs as photoluminescent supramolecular probes

F6 was deeply characterized at the atomic level by CD and FTIR. CD and FTIR spectra of filled peptide nanostructures are reported in **Figure 55** and **Figure 56**, respectively.

Spectra of the empty NSs are also reported for comparison. CD spectrum of NBD/PEG₈-F6 at 10 mg/mL (**Figure 55a**) shows the same dichroic tendency previously observed for the empty peptide NSs, with a maximum around 205 nm, attributable to aromatic side-chains stacking, and a minimum around 230 nm, associated with a β -structure.

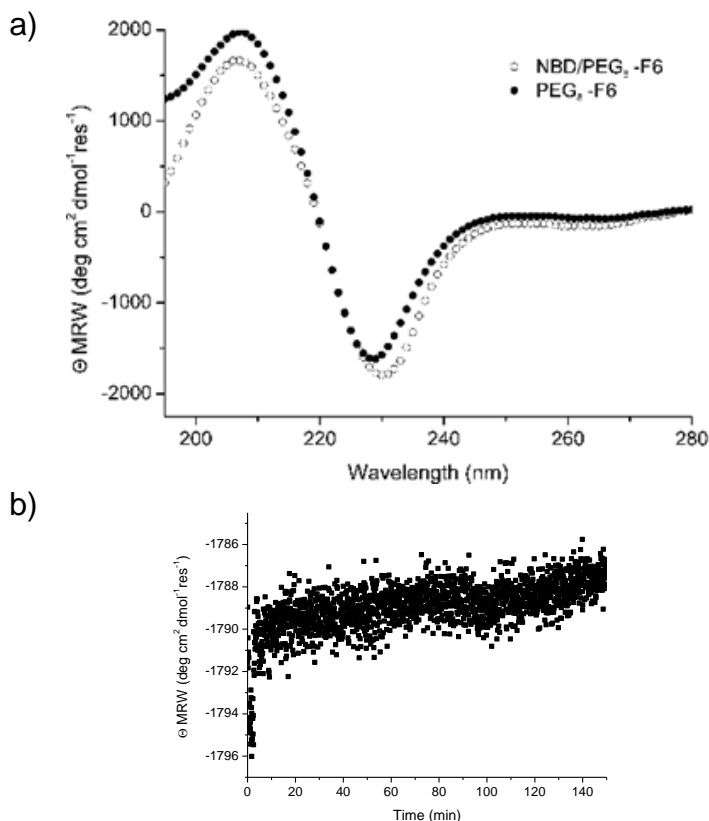


Figure 55: a) Comparison between the CD spectra of PEG₈-F6 and NBD/PEG₈-F6 in water at 10 mg/mL. Spectra were recorded in the range between 280-195 nm and reported in mean residue ellipticity (Θ). b) Molar ellipticity of NBD/PEG₈-F6 in the minimum at 230 nm as function as the time.

A slight red-shift of the minimum, from 227 to 230 nm, occurs for NSs encapsulating NBD. Moreover, the molar ellipticity (θ) of NBD/PEG₈-F6 at 230 nm does not change significantly as function of time (**Figure 55b**). A slight variation of θ value is detectable over time with a more significant variation during the first ten minutes. This trend suggests a time dependent structural rearrangement of the dye containing NS. Analogously to CD data, also FTIR spectra of NBD filled PEG₈-F6 in the

Section II: PBMs as photoluminescent supramolecular probes

region of the amide I vibrational band ($1600\text{--}1700\text{ cm}^{-1}$) are very similar to spectra of empty PEG₈-F6 both in solution and at the solid state (**Figure 56**).

FTIR spectra show a peak at $\sim 1637\text{--}1640\text{ cm}^{-1}$ typically attributable to β -sheet formation. In addition to this peak, all the spectra show a secondary broad peak at $\sim 1680\text{ cm}^{-1}$ that indicates an antiparallel orientation of the β -sheet.^{205,206} These results clearly indicate that although the tight binding between the dye and the peptide NSs, the encapsulation of NBD does not alter significantly the secondary structure of the supramolecular aggregate.

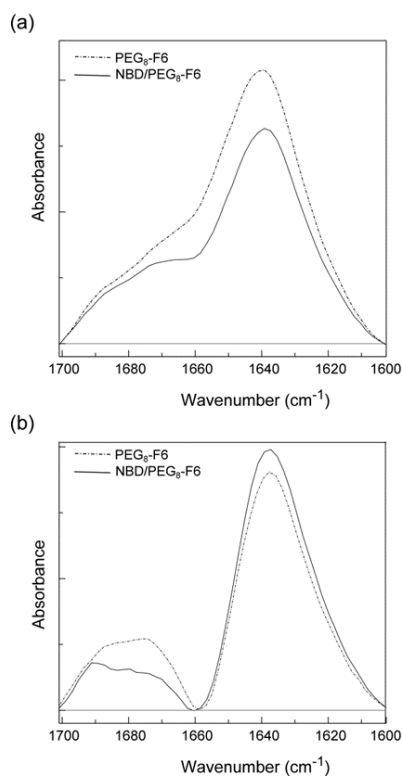


Figure 56: Characterization of the secondary structure: FTIR spectra of PEG₈-F6 and NBD/PEG₈-F6 in solution (a) and at the solid state (b) in the amide I region.

3.7.3 Photoluminescence properties

After association and purification of NBD filled NSs, optoelectronic features were studied both in solution and at the solid state. Differently from the spectra of empty PEG₈-F6 NSs (**Figure 46a**), having an emission peak at 460 nm, NBD/PEG₈-F6 spectra (see **Figure 57a,b**) show a peak at 535 nm, corresponding to the typical emission

Section II: PBMs as photoluminescent supramolecular probes

wavelength of the NBD. The occurrence of this red-shift and the simultaneous disappearance of the expected maximum at 460 nm suggest that NBD dye is close enough to the NSs to accept the energy emitted by the NS according to a FRET phenomenon.

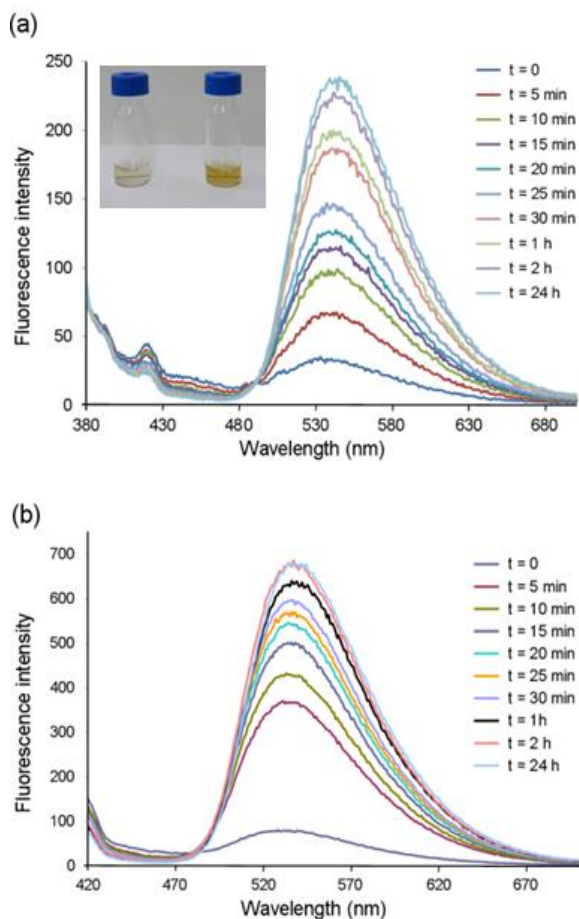


Figure 57: PL of NBD/PEG₈-F6 nanostructures at 10 mg/mL as function of the time. PL emission spectra for sample in solution upon excitation at 370 nm (a) and at 410 nm (b).

The FRET is a distance-dependent physical process by which energy of an excited fluorophore (donor) is transferred non-radiatively to another fluorophore (acceptor). FRET strongly depends from the proximity between the donor and the acceptor species and the maximum of the efficiency occurs if the donor and acceptor are positioned within the Förster radius (the distance at which half the excitation energy of the donor is transferred to the acceptor; typically 3-6 nm).⁵¹ From the qualitative point of view, a macroscopic variation in the color of the solution, from light to dark yellow, was also detected during the time (**Figure 57**, insert).

Section II: PBMs as photoluminescent supramolecular probes

This change of color suggested to follow the fluorescence of the sample upon the time. Surprisingly, we observed a progressive increase of the fluorescence up to 2 h; whereas further increases were not observed after this time.

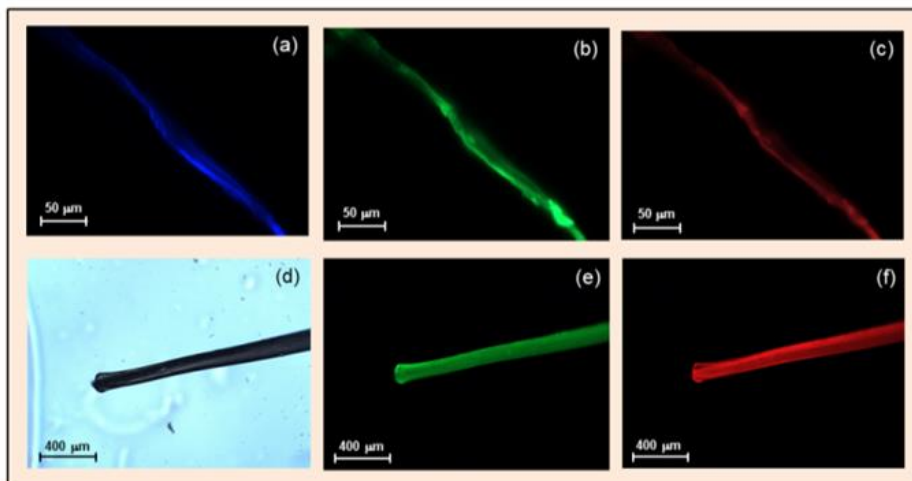


Figure 58: Fluorescence microscopy images of a dried film of NBD/PEG₈-F6 obtained by exciting in the UV spectral region of DAPI (a), GFP (b) and rhodamine (c) filters; and images of NBD/PEG₈-F6 fibers recorded by exciting in the bright light (d), GFP (e) and rhodamine (f) filters.

It is plausible to speculate that this increase of the fluorescence intensity is due to an increase of the fibrillary species in solution during the time. In order to verify this hypothesis, also the kinetic of aggregation of empty PEG₈-F6 nanostructures was studied up to 24 h at the same concentration (data not shown). However, no significant variation could be detected in the fluorescence spectra of empty NSs. This result brought to the conclusion that the kinetic of aggregation for empty NSs is very fast and for this reason not observable.

On the contrary, the increase of the fluorescence of NBD/PEG₈-F6 (**Figure 57**) can depend by a molecular rearrangement of the dye in the peptide aggregate or by a slowing of the kinetic of aggregation of the NS due to the NBD encapsulation. NBD/PEG₈-F6 emits photoluminescence also at the solid state. **Figure 58** reports respectively the immunofluorescence images of the dried sample deposited on a clean coverslip glass (**Figure 58a,b,c**) and of the oriented fibers (**Figure 58d,e,f**) obtained with the stretch frame method. Both the microscopy images of the dried film (**Figure 58a,b,c**) and of the oriented fiber (**Figure 58d,e,f**) demonstrate the capability of NBD/PEG₈-F6 to emit in blue, green and red fields. This result is in

Section II: PBM as photoluminescent supramolecular probes

agreement with the width of the emission peak observed for the sample in solution (**Figure 57**).

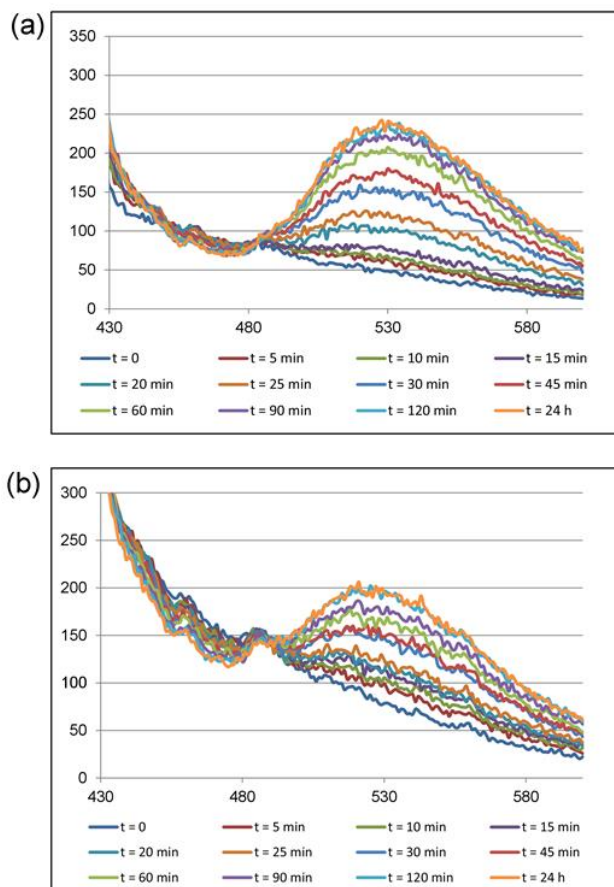


Figure 59: PL emission spectra for NBD/PEG₈-F6 nanostructures in solution upon excitation at 410 nm. In both the samples the concentration of PEG₈-F6 is 10 mg/ml, whereas the concentration of the NBD is 100 µg/mL in (a) and 10 µg/mL in (b)

The same behavior, as function of the time, was also observed in others two preparations, in which the peptide concentration was kept fix at 10 mg/mL, whereas the NBD amount was reduced at 100 or 10 µg/mL (**Figure 59**).

In addition, it was ascertained if it is possible to obtain self-assembled nanostructures (**Figure 60a**) starting from the peptide conjugate NBD-PEG₈-F6, in which NBD is covalently bound to the amine function of the PEGylated hexaphenylalanine.

These nanostructures, which have a univocally defined NBD/PEG₈-F6 ratio (1/1), keep the optoelectronic properties of the NBD-filled NSs (see

Figure 60b) even if they present a lower water solubility due to the N-terminus functionalization. FRET here observed for NBD-PEG₈-F6 is in good agreement with that detected for the covalently conjugates between the α -Synuclein and Yellow Fluorescent Protein (AS-YFP).²³⁸

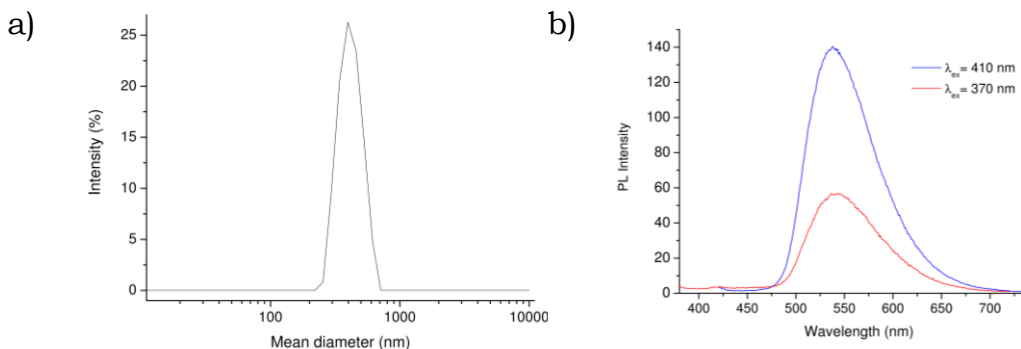


Figure 60: Characterization of NBD-PEG₈-F6 NSs in which NBD dye is covalently bound to the oligo-peptide PEG₈-F6: a) Dynamic Light Scattering spectrum of NBD-PEG₈-F6 in water at 1.0 mg/mL. b) PL emission spectra of NBD-PEG₈-F6 at 1.0 mg/mL upon excitation at ~370 nm (blue line) and at ~410 nm (red line).

3.7.4 Wide- and Small-angle X-ray scattering

To gain deeper insight into the assembly process and molecular organizations, we acquired WAXS/SAXS data on ordered fibers. **Figure 61a** and **61b** show the as-prepared fibers which were placed under the X-ray beam in transmission geometry.

The two-dimensional (2D) WAXS and SAXS fiber diffraction patterns, collected on the PEG₈-F6 and PEG₈-F6/NDB samples, are displayed in Fig. 61 c,d and 61 e,f, respectively. Two main directions are indicated by the white arrows: the meridional direction which coincides to the fiber axis and the equatorial direction, perpendicular to it. They show a cross- β diffraction pattern both in WAXS (atomic distances) and in SAXS (nanoscale distances), fingerprint of hierarchically organized fibers.

The 2D patterns were centered, calibrated and radially folded into uni-dimensional (1D) profiles. WAXS data were integrated across the meridional and equatorial axes and the resulting 1D WAXS profiles displayed in **Figure 61g** (blue for PEG₈-F6 and red for NBD/PEG₈-F6), reporting separately the meridional (upper) and equatorial (lower) profiles. SAXS data were integrated across the whole azimuth and the 1D SAXS profiles were reported in **Figure 46**.

The peak positions (in q) of the most intense WAXS and SAXS peaks, measured along the equatorial and meridional directions are summarized in **Table 8**. Collectively, these experiments indicate that

Section II: PBMs as photoluminescent supramolecular probes

the encapsulation of the dye has a minimal impact on the atomic structure of the peptide spine of these assemblies. Indeed, PEG₈-F6 and NBD/PEG₈-F6 share several meridional and equatorial reflections. The only significant difference is related to the m1 reflection ($d=48\text{\AA}$) of PEG₈-F6 which disappears in NDB/PEG₈-F6 (marked by the arrows in **Figure 61 e,f,h**).

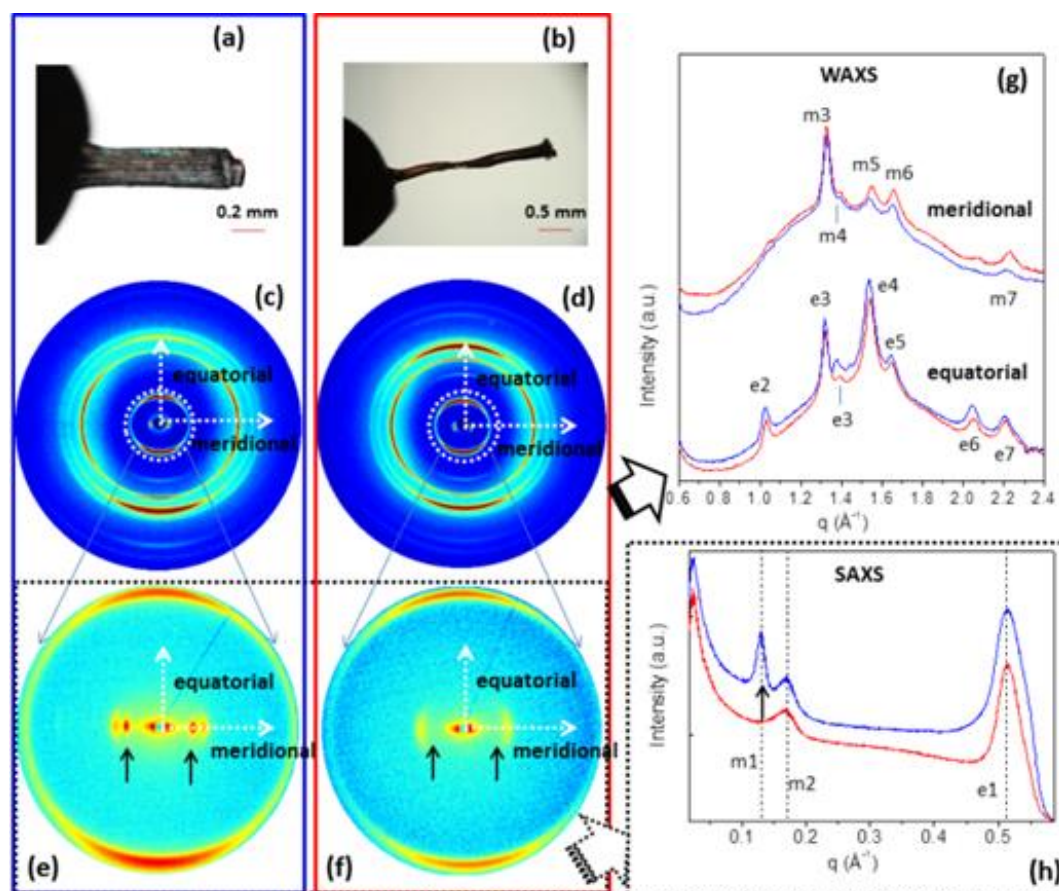


Figure 61: Blue lines refer to empty PEG₈-F6; red lines to NBD/PEG₈-F6. (a) and (b) as prepared fibers; (c) and (d) 2D WAXS data; (e) and (f) 2D SAXS data; (g) 1D WAXS profiles (upper: meridional and lower: equatorial); (h) 1D SAXS profiles.

These observations suggest that the three-dimensional model proposed for the peptide spine PEG₈-F6, which corresponds to anti-parallel β -sheets separated by a dry interface made of interacting Phe side chains,^[16] can be reliably extended to NBD/PEG₈-F6. In particular, the preservation of the equatorial reflection e1 at 12.2\AA , which is indicative of the inter-sheet distance, suggests that the dye is not inserted in the

Section II: PBMs as photoluminescent supramolecular probes

dry interface, in contrast with what has been observed in the complexation of the dye orange G with the cross- β assembly formed by the peptide KLVFFA.^[24]

Table 8: Meridional and equatorial reflections of NBD/PEG₈-F6 measured from WAXS and SAXS data.

Label	q (Å⁻¹)	d (Å) ±0.3 Å
Equatorial Reflections		
e1	0.51	12
e2	1.0	6.1
e3	1.3	4.8
e5	1.4	4.5
e6	1.6	4.1
e7	1.7	3.8
e8	2.1	3.1
e9	2.2	2.8
Meridional Reflections		
m1	0.13	48
m2	0.17	37
m3	1.3	4.8
m4	1.4	4.5
m5	1.6	4.1
m6	1.7	3.8
m7	2.2	2.8

It is likely that, on analogy with the proposed binding of ThT to amyloid-like nanofibers,^[25] the dye may either bind the groove parallel to the fiber axis formed by the side-chain ladders or at the edges of the flat β -sheet surface.

3.7.5 Scanning electron microscopy

Scanning electron microscopy (SEM) images of NBD-filled NSs at different concentration (50 $\mu\text{g}/\text{mL}$, 200 $\mu\text{g}/\text{mL}$ and 2.0 mg/mL) are reported in **Figure 62**. Previous SEM studies on the empty PEG₈-F6 self-assembled NSs indicated a high morphological variability of this aromatic peptide (**Figure 41** and **Figure 42**).²³¹

At low concentration (50 and 200 $\mu\text{g}/\text{mL}$), NBD/PEG₈-F6 forms either amorphous conglomerates or crystalline structures (**Figure 62a** and **62b**), in line with the empty PEG₈-F6 aggregates. On the other hand, at high concentration (2.0 mg/mL) images of NBD containing NSs reveal the presence of branched structures in place of the sheaf of fibers and of long nanostructures (flat or twisted ribbon shape) previously observed for empty NSs.

These branched structures are typically observed for aromatic peptides dissolved in solutions with high ionic strength.

According to the models proposed for these solutions, branched architectures in NBD/PEG₈-F6 could be explained hypothesizing that the some NBD crystals coat the surface of peptide fibers and in correspondence of these nucleation sites, the grown of the branch occurs.

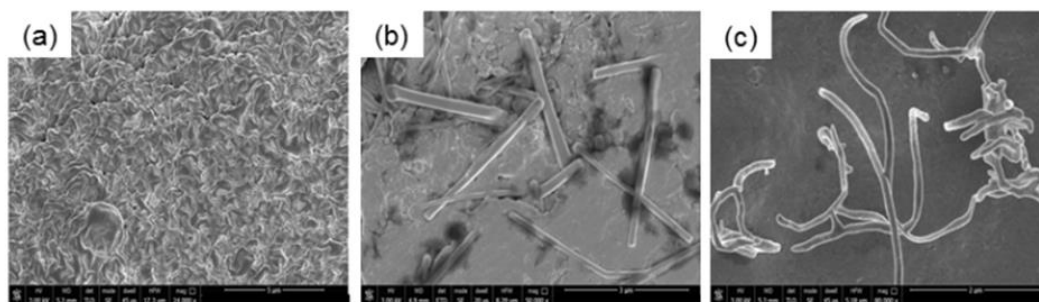


Figure 62: Selected SEM microphotos for NBD-filled PEG₈-F6: a) 50 $\mu\text{g}/\text{mL}$ (24000x, 5 μm scale bar); b) 200 $\mu\text{g}/\text{mL}$ (50000x, 3 μm scale bar), c) 2.0 mg/mL (80000V, 2 μm scale bar)

3.8. Effect of PEG derivatization on PL phenomena

In order to evaluate the effect of the PEG derivatization on the PL phenomena in peptide based NSs, a series of PEGylated hexaphenylalanines (PEG₁₂-F6, PEG₁₈-F6 and PEG₂₄-F6) was synthesized and characterized.²³⁹ These peptide derivatives were obtained by coupling a variable number of amino-hexaalkoxyethylene acid moieties at the N-terminus of the hexaphenylalanine.

The supramolecular behavior of F6-copolymers, both in solution and at the solid state, was investigated by fluorescence, Circular Dichroism (CD), Fourier Transform Infrared spectroscopy (FTIR), Polarized Optical Microscopy (POM), Dynamic Light Scattering (DLS), Scanning Electron Microscopy (SEM), Wide Angle X-ray Scattering (WAXS) both in transmission and reflection (GIWAXS) geometry. Particular attention is given to the effect of PEG polymer length and to the presence of the amide bonds on the supramolecular organization.

The optoelectronic properties of the PEG-series were also studied and compared with PL properties of PEG₈-F6 or NBD/PEG₈-F6 NSs previously reported.²³¹ These investigations pointed out the capability of cross- β nanostructures to exhibit green photoluminescent emission.

3.8.1 Design, synthesis and fluorescence studies

PEGylated hexaphenylalanine conjugates (PEG₁₂-F6, PEG₁₈-F6 and PEG₂₄-F6), schematically represented in **Figure 63a**, were manually synthesized by solid phase method according to the 9-fluorenylmethoxycarbonyl (Fmoc) protocols.²¹⁵

The polymer/peptide derivatives PEG₁₂-F6, PEG₁₈-F6 and PEG₂₄-F6 were obtained in good yield and high purity, coupling respectively, two, three or four units of commercial poly(ethylene glycol) residue using the Fmoc derivative Fmoc-Ahoh-OH, PEG₆, each one containing six ethoxylic repetitions. Coupling reaction of Fmoc-Ahoh-OH was achieved directly in solid phase via carbodiimide activation. This synthetic method, largely used to prepare short PEG conjugates with a molecular weight of 350–800, allows to obtain PEGylated conjugates with monodisperse profiles.^{185,240}

Nullifying the predictable effect of PEG polydispersity, it is possible to obtain amphiphilic peptides with a well-defined hydrophile/lipophile balance (HLB). PEG moiety is expected to enhance the peptide water solubility; nevertheless, due to the high hydrophobicity of phenylalanine residues the three peptides show moderate solubility (~ 20.0 mg/mL).

As predictable, the progressive increase of ethoxylic fragments translates also into fewer values of retention time (t_R) in RP-HPLC for the three polymer/peptide conjugates (**Table 9**).

Section II: PBMs as photoluminescent supramolecular probes

Similarly to the previously studied PEG₈-F6 compound, containing the same F6-aromatic framework, also these peptides show a high tendency to self-assemble.²³¹

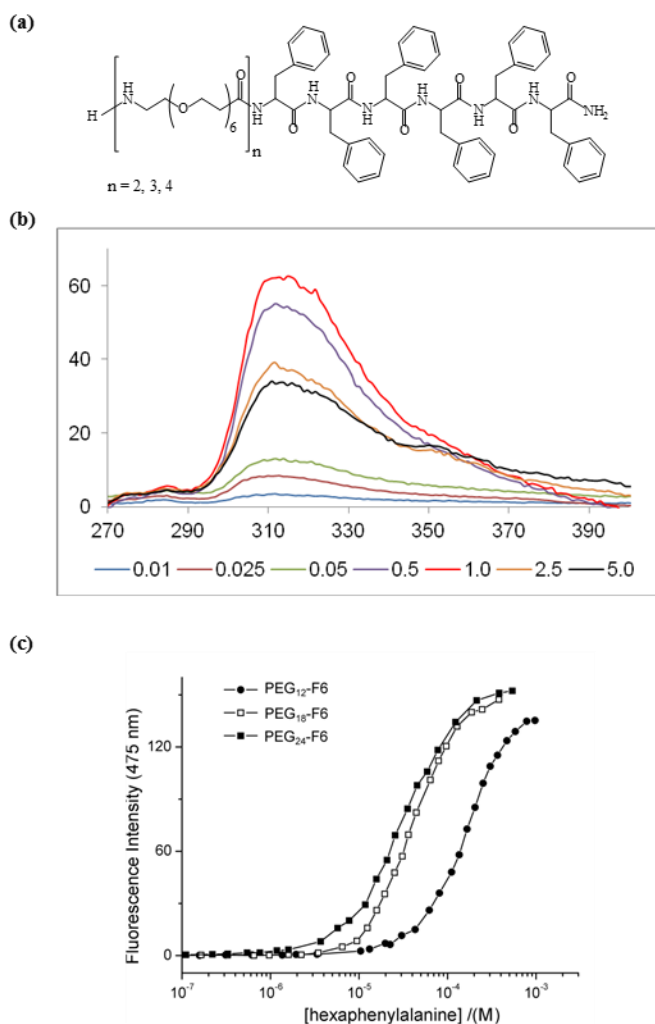


Figure 63: a) Schematic representation of PEGylated hexaphenylalanine PEG₁₂-F6, PEG₁₈-F6 and PEG₂₄-F6. b) Fluorescence emission spectra of PEG₂₄-F6 at several concentrations in 0.01-5.0 mg/mL range. Samples are excited at 257 nm and spectra recorded between 270 and 400 nm. Both PEG₁₂-F6 and PEG₁₈-F6 show the same behavior of PEG₂₄-F6 (data not shown). c) Fluorescence intensity emission of ANS fluorophore at 475 nm vs. concentration of PEG₁₂-F6, PEG₁₈-F6 and PEG₂₄-F6. CAC values are established from the break points.

Section II: PBMs as photoluminescent supramolecular probes

The first evidence on their aggregation phenomena comes from the inspection of the fluorescence spectra, reported in **Figure 63b**, for peptides at different concentrations (between 0.025 and 5.0 mg/mL). Samples were excited at 257 nm, that corresponds to λ_{MAX} of Phe residue, and the emission spectra were recorded between 270 and 400 nm.

All spectra show a weak emission peak at 282 nm, expected for the nude Phe chromophore and a well observable peak centered at 312 nm, typically attributed to Phe excimers, induced by π - π interactions between the aromatic side chain rings. Besides these two peaks, a third one centered around 350-360 nm appears at concentration above 1.0 mg/mL. These peaks (312 and 350) are indicative of a complex supramolecular organization of PEGylated hexaphenylalanines.

An analytical characterization of the aggregation properties of these PEGylated peptides was achieved by the fluorescence-based method that allows evaluating the critical aggregate concentration (CAC). CAC values for the three peptide polymers were established from the graphical break point of the plots in **Figure 63c**.

Table 9: Formula, retention time (R_t) and theoretical molecular weight (MW) of PEGylated hexaphenylalanines. RP-HPLC method and column details are reported in the experimental section. Critical aggregate concentration (CAC) values of PEG-derivatives measured by titration of ANS fluorophore.

Sample	Formula	Rt (min)	M _w (u.m.a.)	CAC (μ M)	CAC (μ g/mL)
PEG ₁₂ -F6	C ₈₄ H ₁₁₅ N ₉ O ₂₀	12.5	1570	38.8	60.9
PEG ₁₈ -F6	C ₉₉ H ₁₄₄ N ₁₀ O ₂₇	11.9	1905	10.7	20.4
PEG ₂₄ -F6	C ₁₁₄ H ₁₇₃ N ₁₁ O ₃₄	11.2	2240	6.2	13.9

CAC values, summarized in **Table 9**, are 60.9, 20.4 and 13.9 μ g/mL for PEG₁₂, PEG₁₈ and PEG₂₄ oligopeptides, respectively. These values suggest a direct dependence of the PEG length on the aggregation tendency: the self-aggregation seems favored in polymers with highest hydrophilicity (PEG₁₂>PEG₁₈>PEG₂₄).

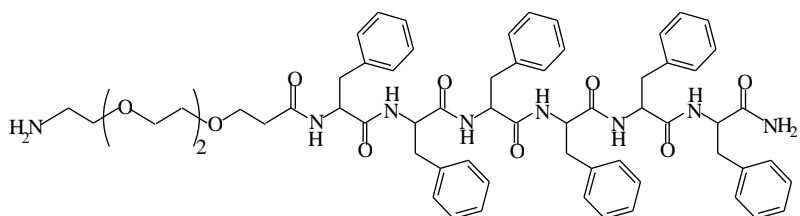
However, in traditional di- or tri-block copolymers, CAC value depends on the hydrophobic/hydrophilic ratio, and the CAC is expected higher for monomers with shorter hydrophilic portions. The observed discrepancy leads to speculate that the self-assembling phenomena in these compounds could be due to more of one contribution. Beyond the aromatic stacking, it is

Section II: PBMs as photoluminescent supramolecular probes

suggest that the formation of additional intramolecular hydrogen bonds between the amide bonds in the PEG chain.

These H-bonds could encourage the self-aggregation of the entire PEG-peptide conjugates. This hypothesis is also supported by the comparison of the CAC value found for PEG₂₄-F6 with others two hexaphenylalanine PEGylated analogues: PEG₈-F6 and PEG_{MW1300}-F6 (**Figure 64a**). The first one, PEG₈-F6, previously characterized by us, contains four amide bonds in PEG fraction as well as PEG₂₄-F6 and exhibits a CAC value of $\sim 10 \mu\text{g/mL}$ ($7.5 \mu\text{M}$), slightly lower than PEG₂₄-F6. Instead, PEG_{MW1300}-F6, with a PEG chain similar to PEG₂₄-F6 but lacking of the amide bonds, self-assembles above a CAC value of $\sim 40 \mu\text{g/mL}$ ($15.2 \mu\text{M}$), that is about 3-fold higher than the CAC value of the analog peptide containing the amide bonds in the PEG chain (**Figure 64b**).

a)



b)

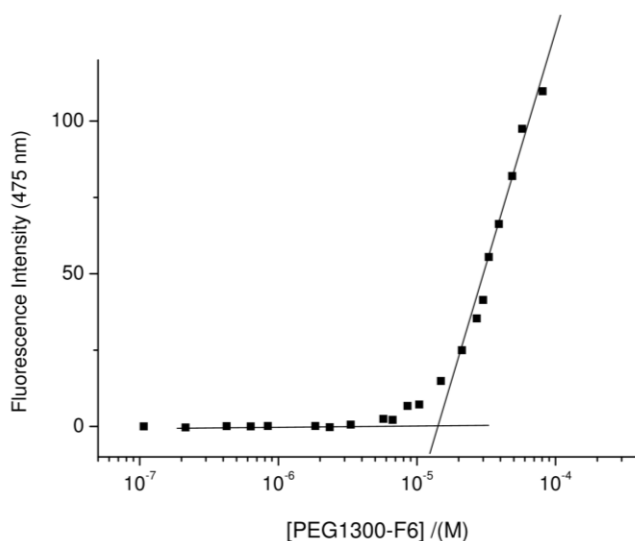


Figure 64: a) Chemical structure of PEG_{MW1300}-F6. b) fluorescence intensity emission of ANS fluorophore at 475 nm vs. concentration of PEG_{MW1300}-F6.

3.8.2 Dynamic Light Scattering

The peptide capability to self-assemble above their CAC value was assessed by DLS technique. DLS studies, previously reported for PEGylated hexaphenylalanine PEG₈-F6, indicated the high kinetic stability of the self-assembled nanostructures and the low incidence of the concentration on their size (**Figure 40**). The same size stability in time was also observed for the series of PEG-peptides here studied (data not shown). The intensity profiles of PEG₁₂, PEG₁₈ and PEG₂₄ oligopeptides in water solution, at 5.0 mg/mL, are reported in **Figure 65**. Intensity profile of PEG₁₂-F6 shows a monomodal distribution with a mean diameter of ~172 nm. On the contrary, both PEG₁₈ and PEG₂₄ derivatives show a bimodal distribution indicating the presence of two aggregate populations, the first centered at 185 nm and the second one at 25 nm.

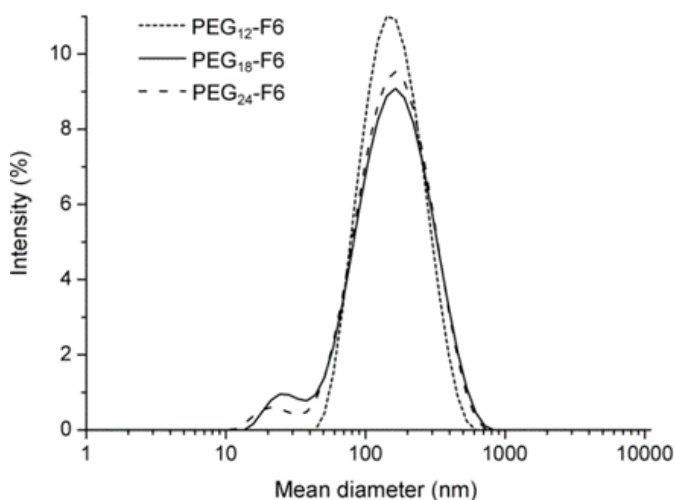


Figure 65: DLS intensity profiles of PEGylated hexaphenylalanine at 5.0 mg/mL in water

3.8.3 Secondary structure characterization

The secondary structure of PEGylated oligopeptides in solution was fully investigated by CD, FTIR and UV-Vis spectroscopies.

Figure 66a shows the CD spectra of the three PEGylated hexaphenylalanine conjugates at 5.0 mg/mL, well-above their CAC value. All the spectra show a maximum centered between 205 and 207 nm, typical of the aromatic side-chains stacking, and a minimum at 227 nm, associated with a β -sheet arrangement.²¹⁶ This dichroic tendency is similar to that previously observed for PEG₈-F6 analog.²³¹ However, a

Section II: PBMs as photoluminescent supramolecular probes

progressive reduction of the intensity of the two peaks can be detected by increasing the PEG length.

The reduction of both peaks confirms the capability of the PEG length to affect the self-aggregation propensity of the hexaphenylalanine and; in agreement with the fluorescence studies, the polymeric peptide containing the PEG₂₄ moiety presents higher tendency to self-aggregate under the same condition of concentration.

The occurrence of β -sheet formation was also confirmed by FTIR spectroscopy in the amide I spectral region and the deconvolution in absorbance for the secondary structure prediction of the FTIR spectra in this region are reported in **Figure 66b** (2.0 mg/mL in water solution). All the F6 derivatives show a similar FTIR spectrum with two peaks at 1638 and 1680 cm⁻¹.

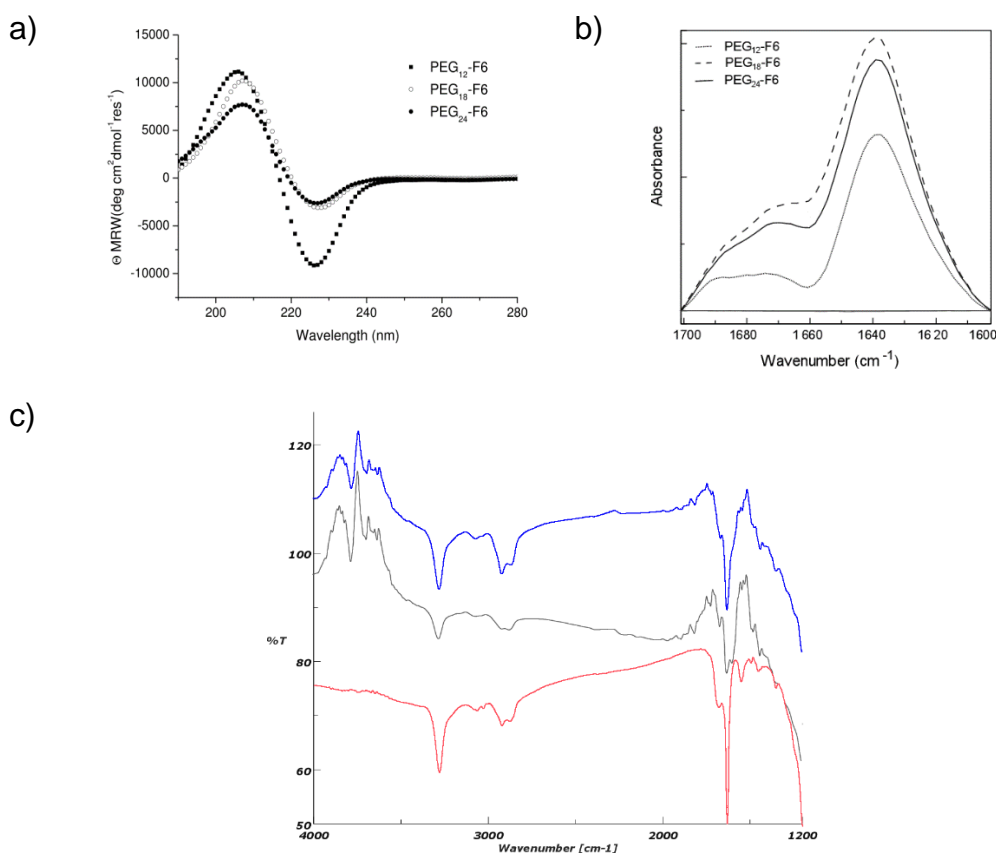


Figure 66: a) Comparison between the CD spectra of PEG₁₂-F6, PEG₁₈-F6 and PEG₂₄-F6. All the sample are 5.0 mg/mL (concentration above CAC); b) FTIR spectra for F6/polymer conjugates at 2.0 mg/mL in the amide I region. c) FTIR spectra of PEG₁₂-F6, PEG₁₈-F6 and PEG₂₄-F6 in blue, black and red, respectively.

Section II: PBMs as photoluminescent supramolecular probes

This profile is typically observed for β -sheet with antiparallel orientation of the β -strands.^{205,206} Moreover, the NH stretching occurring at 3280 cm^{-1} frequency in amide A region (**Figure 66c**), indicates strong intermolecular amide-amide bonds.²⁴¹ The absence of a band around 3400 cm^{-1} and the presence of a band at 1530 cm^{-1} in the amide II region, indicate that all NH groups in PEG₂₄-F6 are involved in tight intermolecular hydrogen-bonding interactions in the fibrillary network.²¹⁷ As previously observed for PEG₈-F6,²³¹ FTIR spectra of these peptides dissolved in HFIP (disaggregating conditions) do not show peaks in the amide I region (data not shown).

All these structural data support the hypothesis of a supramolecular organization in amyloid-like fibrillary nanostructure.

A confirmation on this structural organization was obtained by CR staining assay.²⁰⁹ As expected, UV-Vis spectra show a bathochromic shift of the maximum when the azoic dye is incubated with PEGylated-F6 peptides at 1.0 and 2.5 mg/mL (**Figure 67**) supporting the hypothesis of amyloid-like organization.

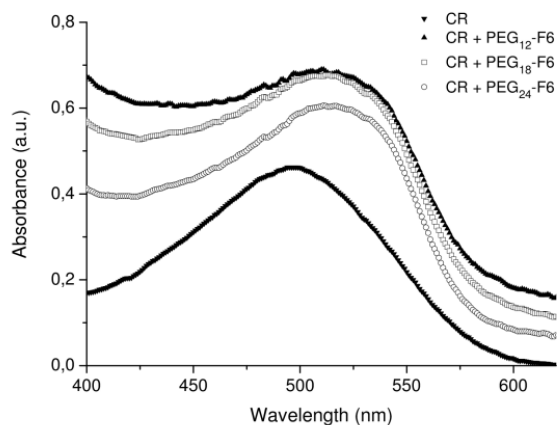


Figure 67: UV-Vis spectra of PEG₁₂-F6, PEG₁₈-F6 and PEG₂₄-F6 at 2.5 mg/mL after incubation with Congo Red; CR spectrum is also reported for comparison.

3.8.4 Wide Angle X-ray Scattering

A deep characterization of the nanostructures at the solid state was performed by WAXS and GIWAXS scattering techniques, in transmission and reflection mode respectively.

Figures 68b,c,d (left panel) display the two-dimensional (2D) WAXS patterns collected on the fibers with PEG of different lengths (PEG₁₂, PEG₁₈ and PEG₂₄, respectively). 2D-WAXS pattern of PEG₈ derivative, previously studied²³¹, is also reported for comparison (**Figure 68a**). The

Section II: PBMs as photoluminescent supramolecular probes

2D patterns, once centered, calibrated and radially folded into 1D profiles, are shown in **Figures 68a,b,c,d** (right panel), respectively. **Figure 68e** shows the same 1D patterns which have been shifted vertically of the same value for sake of clarity. This comparison shows that the diffraction patterns are almost identical, with two relevant peaks occurring at $q = 0.518\text{\AA}^{-1}$ and $q = 1.32\text{\AA}^{-1}$, that we assigned to the equatorial β -sheet distance $d_e = 12.2\pm 0.3\text{\AA}$ and to the meridional β -strands distance of $d_m = 4.8\pm 0.3\text{\AA}$, respectively. The reflection corresponding to $d \sim 4.8\text{\AA}$ could be, in principle, ascribed to the PEG crystallization (4.7\AA).²⁴³ However, the simultaneous presence of the equatorial reflection at $d \sim 12.2\text{\AA}$ is symptomatic of cross- β amyloid structures.

Scaling the diffraction patterns to make them coinciding for the background, as reported in **Figure 68f**, allows to appreciate difference in the intensity of the most represented reflection at $q=0.518\text{\AA}^{-1}$, relevant to the equatorial β -sheet.

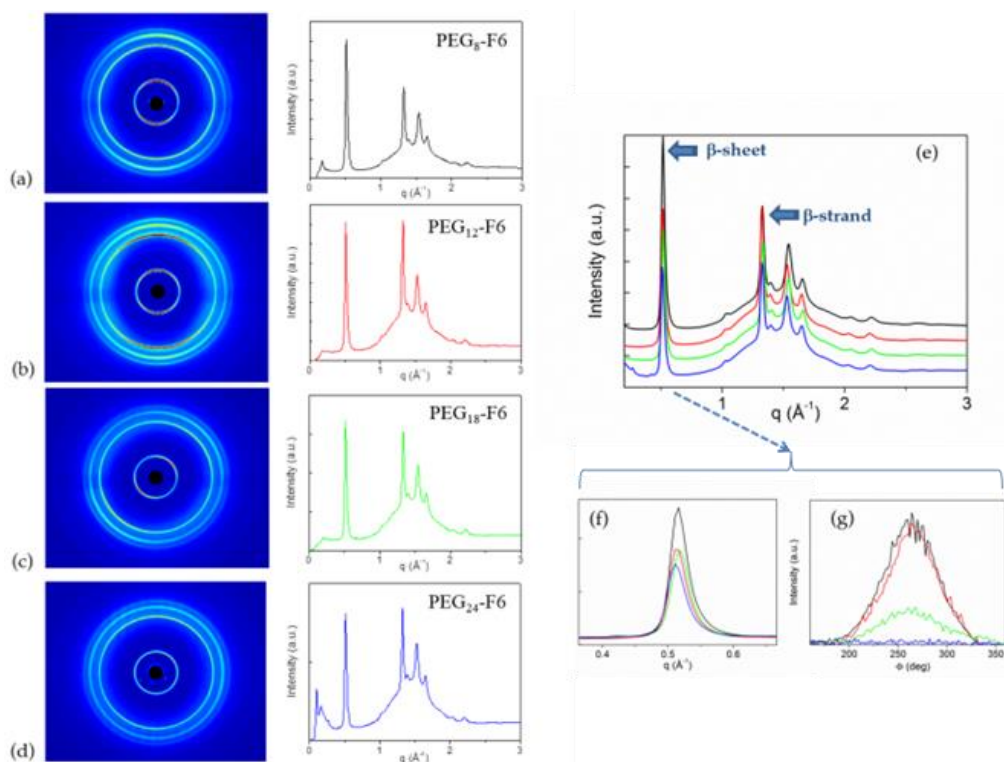


Figure 68: (a,b,c,d) 2D (left panel) and 1D (right panel) WAXS data; (e) 1D WAXS patterns vertically shifted for sake of clarity; (f) detail of the equatorial β -sheet distance at $q=0.518\text{\AA}^{-1}$ ($d_e=12.2\pm 0.3\text{\AA}$); (g) equatorial β -sheet reflection, integrated along the azimuth Φ angle (i.e. along the diffraction circle).

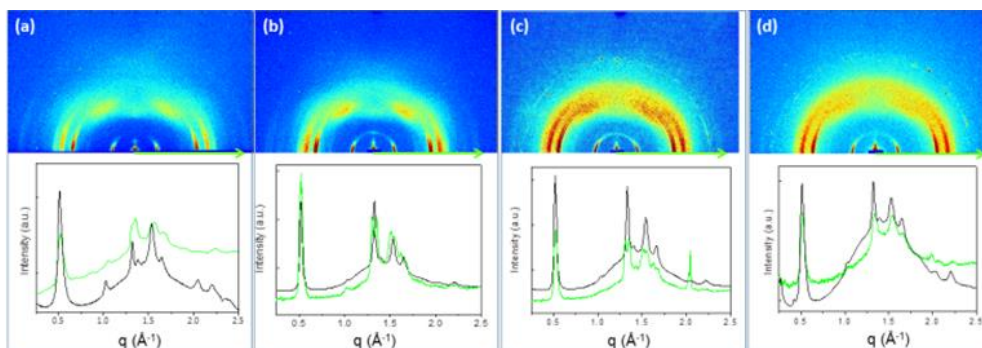


Figure 69: 2D GIWAXS (upper panels) and corresponding 1D GIWAXS data (lower panels, green curves) for PEG₈ (a), PEG₁₂ (b), PEG₁₈ (c) and PEG₂₄ (d) fibers, deposited on silicon substrates. The black profiles in the lower panels are the corresponding WAXS profiles collected for the same samples.

As a result, the most intense peak is registered for PEG₈, then almost equal intensities are found for PEG₁₂ and PEG₁₈ and the lowest intensity for the PEG₂₄ fiber. This difference in intensity can be attributed to the partial effect of PEG crystallization that occurs in proportional way to the PEG length / molecular weight.

Finally, for the same equatorial β -sheet reflection, it was estimated the full-width-at-half-maximum (FWHM) along the azimuth Φ angle (i.e. along the diffraction circle): $\text{FWHM}(\text{PEG}_8) = \text{FWHM}(\text{PEG}_{12}) = 54 \pm 2^\circ$, $\text{FWHM}(\text{PEG}_{18}) = 62 \pm 2^\circ$, $\text{FWHM}(\text{PEG}_{24}) > 180^\circ$ (**Figure 68g**). They reflect a clear increase in the fiber disorder which is maximum for the PEG₂₄ sample where it is not possible to identify any preferred orientation direction of the fiber.

It was excluded that fiber disorder can be attributed to the PEG crystallization. Indeed, polarized optical microscopy images of dried samples at high concentration (5wt%) do not show the spherulite, typical structures of PEG crystallization, but the formation of a liquid crystal phase *via* birefringence (data not shown).

To analyze possible differences in the fiber structure due to the different sample preparation or influences due to the substrate, fibers were deposited on top surface of silicon substrates and studied by GIWAXS.

Figure 59 shows the GIWAXS 2D data of the PEG₈ (a), PEG₁₂ (b), PEG₁₈ (c) and PEG₂₄ (d) fibers, (upper panels) respectively; the corresponding lower panels display the horizontal cut (green line) extracted from each 2D GIWAXS data along the green arrow compared to the relevant meridional WAXS profiles (black line) previously shown in **Figure 68**. The comparison clearly shows the same relevant peaks, occurring at $q = 0.518 \text{ \AA}^{-1}$ (equatorial β -sheet distance $d_e = 12.2 \pm 0.3 \text{ \AA}$) and $q = 1.32 \text{ \AA}^{-1}$ (meridional β -strands of $d_m = 4.8 \pm 0.3 \text{ \AA}$) are measured

either for the fibers studied in transmission (WAXS, **Figure 68**) and reflection (GIWAXS, **Figure 69**) mode, proving that the sample preparation does not modify the atomic arrangement of the fibers. In **Figure.70** the WAXS/GIWAXS characterization of PEG_{MW1300}-F6 is reported. **Figure 70a** compares the optical microscopy of a single fiber of PEG_{MW1300}-F6 to the image of the same material deposited on silicon substrate (**Figure 70b**).

The corresponding 2D WAXS (c) and GIWAXS (d) data are displayed in the same figure with the integrated 1D profiles (e) reported as green (GIWAXS cut of the 2D data, extracted along the green arrow) and black (WAXS) lines. Also in this case the most important reflections, corresponding to the equatorial β -sheet ($d_e=12.2\pm 0.3$ Å) and the meridional β -strands ($d_m=4.8\pm 0.3$ Å) distances, coincide between WAXS and GIWAXS data. In analogy to what measured for the PEG₈, PEG₁₂, PEG₁₈ and PEG₂₄ fibers (see **Figure 68g**), it was estimated also for the PEG_{MW1300}-F6 sample the full-width-at-half-maximum (FWHM) along the azimuth Φ angle, in correspondence of the same equatorial β -sheet reflection (see comparison in **Figure 70f**, where the added magenta profile corresponds to the PEG_{MW1300}-F6 sample).

The FWHM(PEG_{MW1300}) is comparable to what measured for PEG₁₈-F6, thus confirming an effect of the amide bonds in the PEG chain also on the fiber order.

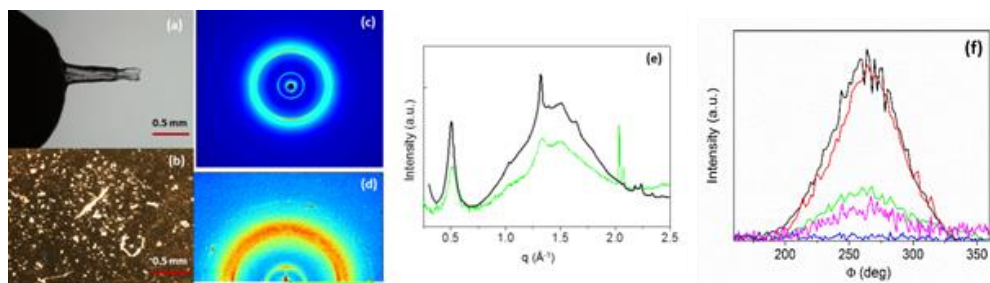


Figure 70: Microscopy of a single PEG_{MW1300}-F6 fiber (a) and the fibers deposited on silicon substrate (b); 2D WAXS data of the single fiber (c); 2D GIWAXS data of the fibers onto a silicon substrate; (e) integrated 1D profiles GIWAXS (green) and WAXS (black). (f) Equatorial β -sheet reflection, integrated along the azimuth Φ angle (i.e. along the diffraction circle). Magenta profile corresponds to the PEG_{MW1300}-F6 sample.

3.8.5 Scanning Electron Microscopy

SEM images of PEGylated F6-peptides at 2.0 mg/mL, reported in **Figure 71**, confirmed their aptitude to self-assemble in supramolecular NSs.

Section II: PBMs as photoluminescent supramolecular probes

Micrographs of PEG₁₂-F6 in **Figure 71a** show braid-like microstructures growing from thin scratches. Instead, PEG₁₈-F6 self-aggregates in sheaf formed by small fibers of 60-500 nm placed side by side (**Figure 71b**). Each fiber has a thickness between 60 and 200 nm. On the contrary, SEM images of PEG₂₄-F6 show ~600-1000 μm long and ~20 μm large nanostructures with a twisted ribbon shape (**Figure 71c,d**). This kind of structures is expected for amyloid peptides functionalized with short PEG chains.²⁴⁰

According to Polarized Optical Microscopy (POM), it is not observed in SEM images the effect of crystallization typically displayed by PEGylated peptides.²¹⁷

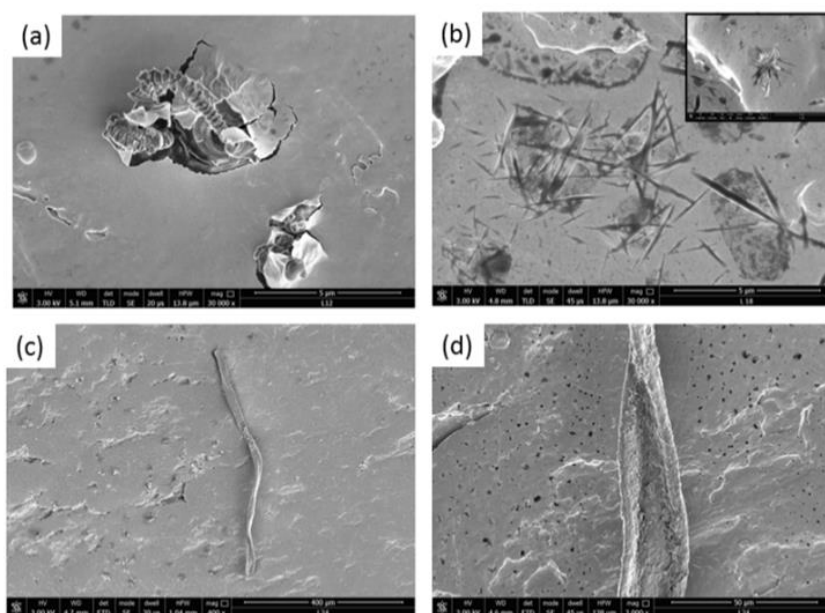


Figure 71: Selected SEM micrographs for PEGylated oligomers: (a) PEG₁₂-F6(30000x, 5 μm scale bar); (b) PEG₁₈-F6 (30000x, 5 μm scale bar); (c) and (d) PEG₂₄-F6 (400x, 400 μm and 3000x, 50 μm scale bar, respectively). In the insert of panel b an additional view of PEG₁₈-F6 (30000x, 5 μm scale bar) on the aluminum stub showing an intricate sheaf of fibers.

The absence of crystallization phenomenon in SEM images confirms further that the continuous rings measured in the WAXS-diffraction pattern are due to the low orientation of PEG₂₄-F6 dried fibers in space. From the comparison of the SEM images of the three PEGylated derivatives, it arises that the PEG length affects the hierarchical organization of the peptide and the elongation of the nanostructure. The trend here observed is opposite to the conventional one shown by Hamley *et al.* for PEGylated amyloid peptides.²¹⁷ However, the fibers

observed for PEG₂₄-F6 are very similar to fibers previously observed for PEG₈-F6, in which the ethoxylic groups is shorter than PEG₂₄-F6, but the number of the amide bonds in PEG moiety is the same. This result suggests once more a deep relationship between the number of the amide bonds and the structural aggregation of these peptides.

3.8.6 Photoluminescence in peptide nanofibers

Fluorescence behavior of PEGylated peptides (PEG₁₂-F6, PEG₁₈-F6 and PEG₂₄-F6) was investigated both in solution (**Figure 72**) and at solid state (**Figure 73**) and it was compared with PEG₈-F6 nanostructures, empty and filled with the NBD dye.

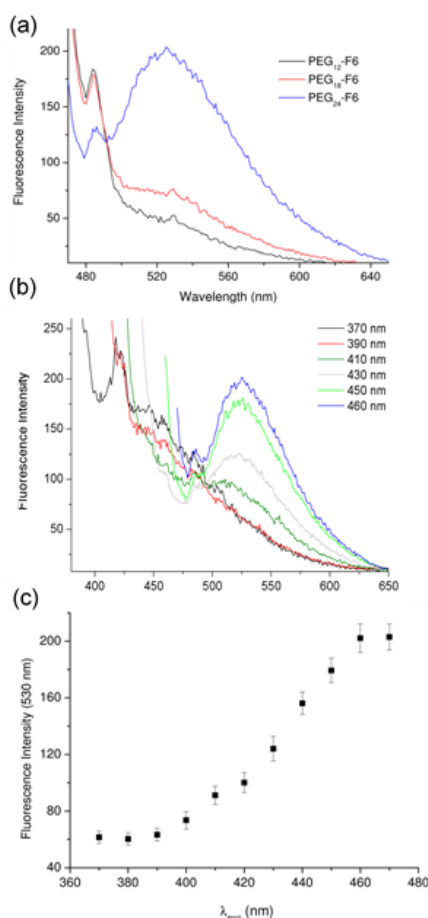


Figure 72: a) PL emission spectra of PEGylated-F6 nanostructures at 10 mg/mL upon excitation at $\lambda_{exc} = 460$ nm. b) Selected PL emission spectra of PEG₂₄-F6 excited at several wavelengths in the range between 370-480 nm. c) Plot of the fluorescence intensity of PEG₂₄-F6 at 530 nm as function as the excitation wavelength.

Section II: PBMs as photoluminescent supramolecular probes

As PEG₈-F6 NSs, also PEG₁₂-F6, PEG₁₈-F6 and PEG₂₄-F6 derivatives, having a high content of β -sheet structures, show optoelectronic properties in water when excited at 370 or at 410 nm. However, beyond the emission peak at 460 nm, an additional PL emission peak at 530 nm can be observed upon excitation of the solutions at 460 nm (**Figure 72a**). This peak at 530 nm is mainly evident for PEG₂₄-F6, whereas it appears to be absent or very weak for PEG₁₂-F6 and PEG₁₈-F6. The green PL emission of PEG₂₄-derivative is well distinguishable also when the peptide solution is excited at different wavelengths (**Figure 72b**). The plot of the fluorescence intensity in the maximum as function as the excitation wavelength is reported in **Figure 72c**.

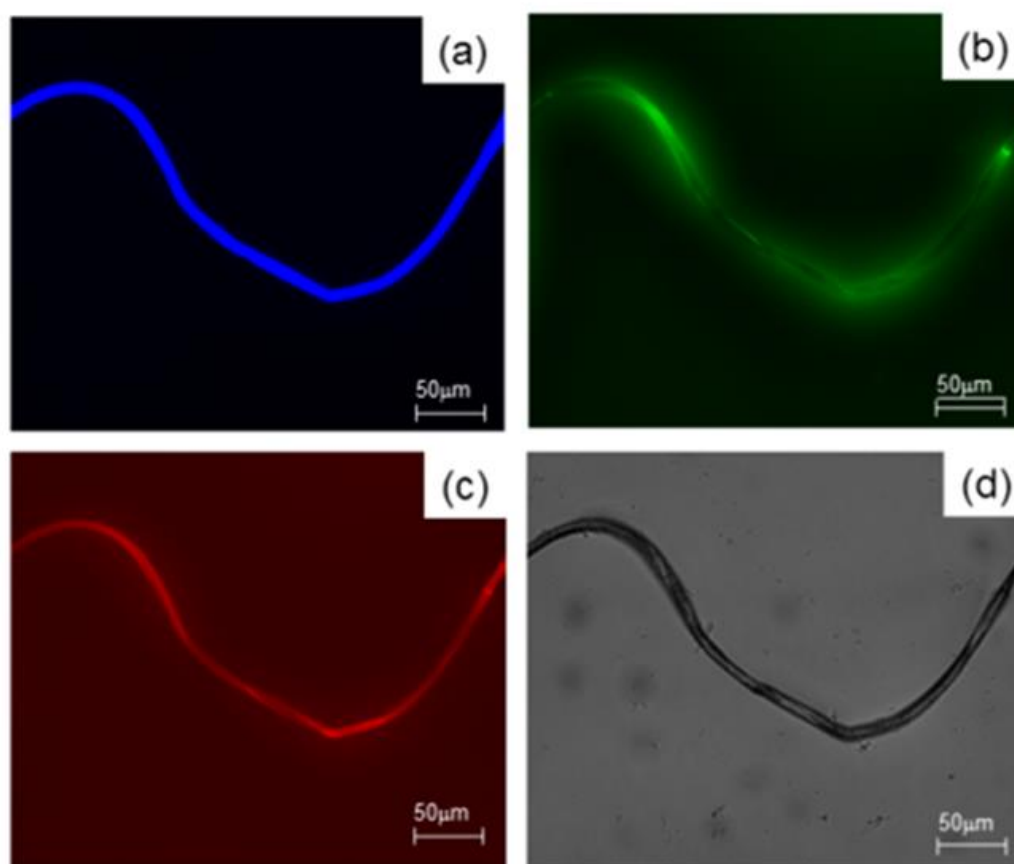


Figure 73: Fluorescence microscopy images of PEG₂₄-F6 at 10 mg/mL, deposited on a clean coverslip glass and slowly dried at room temperature. PL images are obtained by exciting the air dried sample in the spectral region of: (a) DAPI (4',6-diamidino-2-phenylindole; $\lambda_{\text{exc}} = 359$ nm, $\lambda_{\text{em}} = 461$ nm); (b) GFP (Green Fluorescent Protein; $\lambda_{\text{exc}} = 488$ nm, $\lambda_{\text{em}} = 507$ nm); (c) Rho (Rhodamine; $\lambda_{\text{exc}} = 555$ nm, $\lambda_{\text{em}} = 580$ nm); and in the bright fields (d). The scale bar of all the images is 50 μm .

This additional excitation-emission pair of PEG₂₄-F6 can be traced back to the formation of more stable electronic states resulting by the additional contribution of amide non-covalent interactions.

The fluorescence microscopy images of the air-dried samples deposited on a clean coverslip glass are reported in **Figure 72** and **Figure 73**. Due to the wide spectral region observed for the samples in solution, immunofluorescence images at the solid state were observed with different filters (DAPI, GFP and Rho) that able to cover the entire range of excitation and emission wavelengths. Images of PEG₂₄-F6 (**Figure 72**) show the capability of this peptide nanostructure to emit in blue, green, and red fields.

On the other hand, images of PEG₁₂ and PEG₁₈ show a good emission of the NSs only in the blue-field (**Figure 74**).

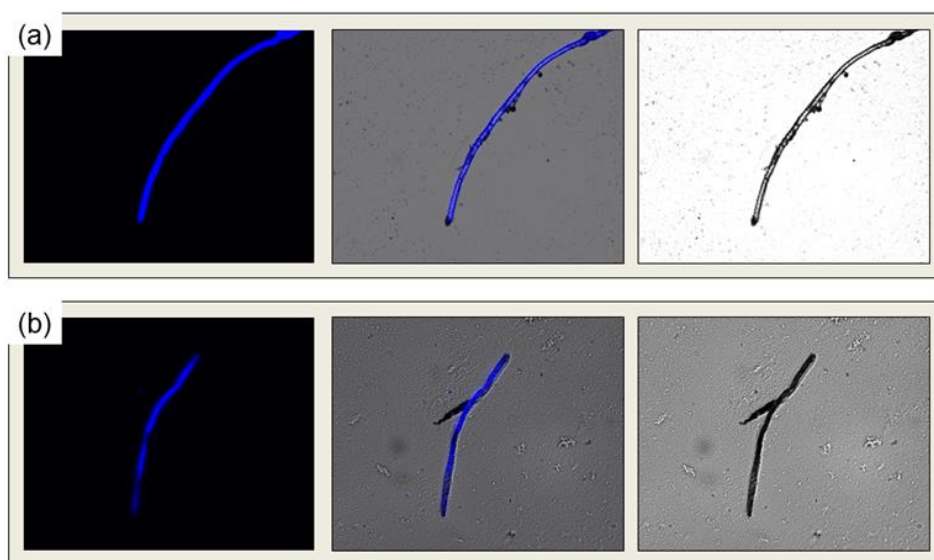


Figure 74: Fluorescence microscopy images of: (a) PEG₁₂-F6 and (b) PEG₁₈-F6 at 10 mg/mL, deposited on a clean coverslip glass and slowly dried at room temperature. PL images are obtained by exciting in the UV-Vis spectral region. Fluorescence images (on the left), bright field images (on the right) and the merge of fluorescence and bright field images (at the center).

These results indicate the capability of these peptides to keep the same optoelectronic properties both in solution and at the solid state. Taking into account the different number of H-bonding donors/acceptors in PEG₂₄-F6 with respect to the others PEGylated analogues we assumed that the distinct PL behavior of these compounds could be, at least in part, due to the different H-bonding potential of these compounds

This hypothesis has been supported through the investigation of the PL properties of PEG_{MW1300}-F6, whose PEG moiety is comparable in size

Section II: PBMs as photoluminescent supramolecular probes

to that PEG₂₄-F6 though lacking the amide groups that could be potentially involved in H-bonding. In line with our suggestion, PEG_{MW1300}-F6 does not give any emission peak at 530 nm in the same experimental condition, while retaining the usual emissions at 370 and 410 nm (**Figure. 75**).

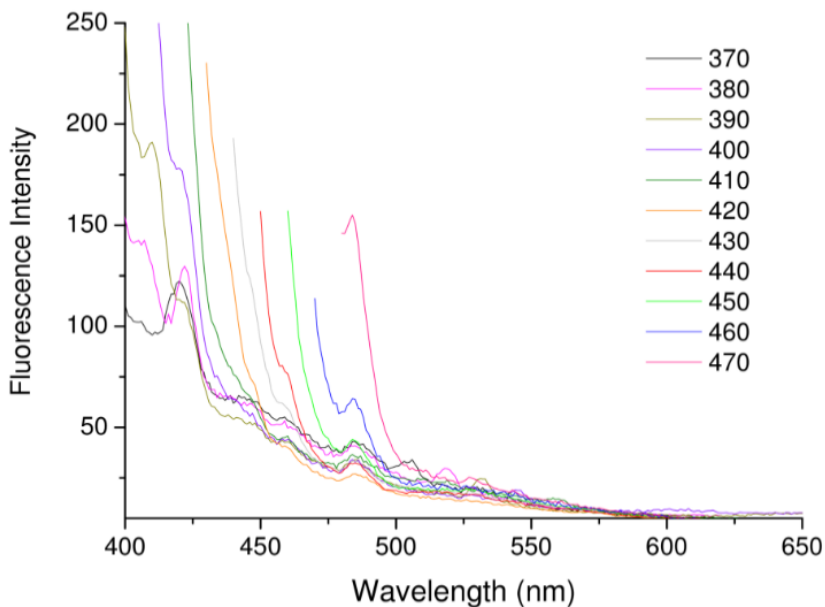
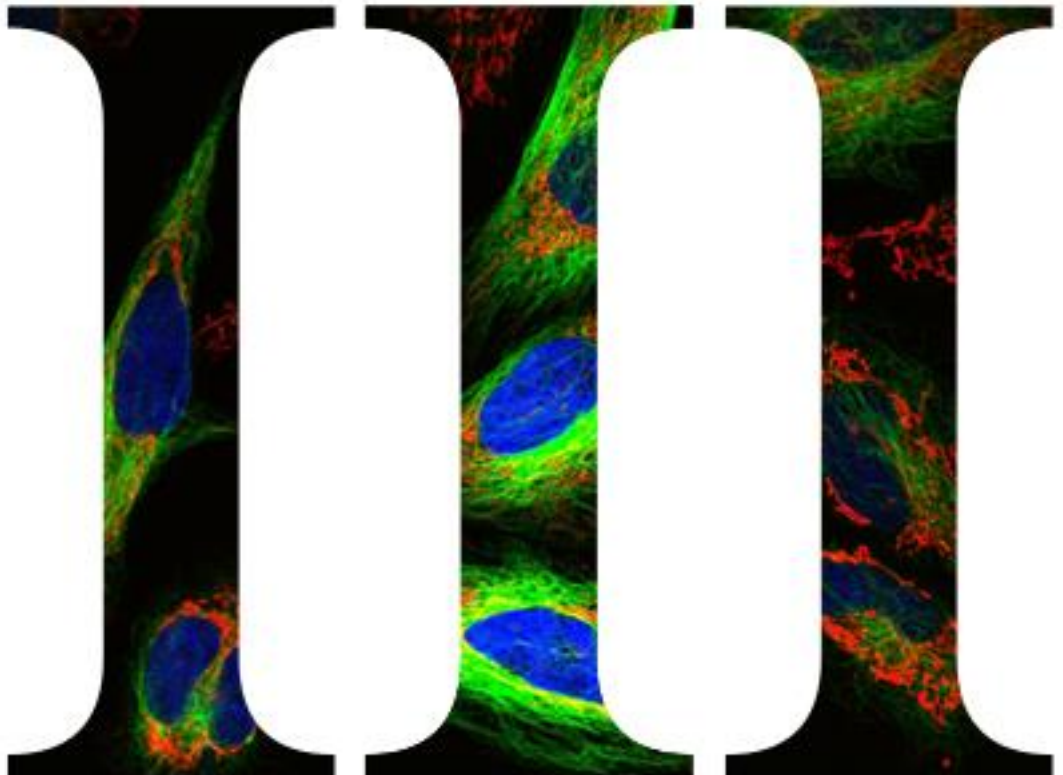


Figure 75: Fluorescence emission spectra of PEG_{MW1300}-F6 in water at 10 mg/mL concentration. Spectra were recorded exciting sample at several wavelength ranged between 370 and 480 nm



Section III

Peptide-based materials obtained by chemical modifications
of homophenylalanine sequences and peptide hydrogels

Carlo Diaferia | University of Naples Federico II | XXX cycle

Section III: PBMs obtained by punctual chemical modifications

3.9 Hexapeptide containing Tyrosine residues

As previously reported, PEG₈-F6 is a polymer-peptide monomer able to self-assemble in fibrillar amyloid like networks.²³¹ This supramolecular behavior was expected for phenylalanine (Phe) containing polypeptides.^{184,184,196}

The impact of this key aromatic amino acid on the supramolecular structural organization was here evaluated by replacing phenylalanine in PEG₈-F6 with tyrosine (Y), another aromatic residue. Similar to its ancestor peptide PEG₈-F6, PEG₈-Y6 (**Figure 75a**) keeps the same molecular architecture composed of an aromatic framework of six amino acid residues and a polymer functionality. In order to evaluate the effect of a partial replacement of Phe with Tyr, we also synthesized PEG₈-(FY)3 (**Figure 75 a**) in which the two aromatic residues are alternated in the sequence. PEG moiety in these peptides is expected to increase their water solubility. Indeed, we observed a clear drop of the water solubility and self-assembling capability for PEG₈-F6 as a consequence of the PEG removal (data not shown).

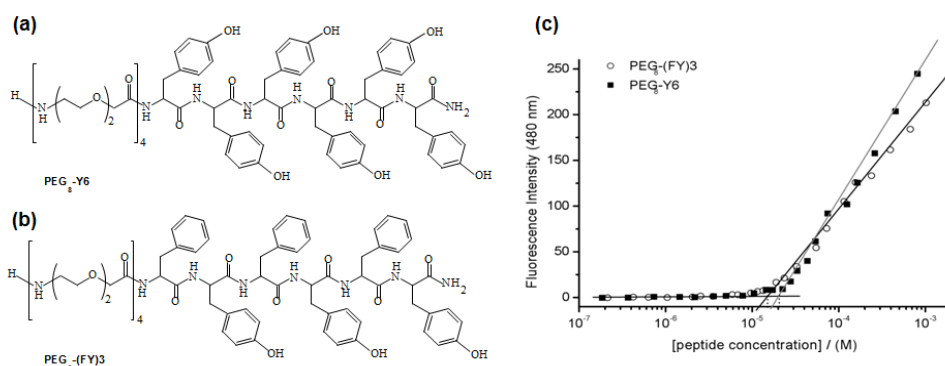


Figure 75: Schematic representation of PEGylated hexapeptides: PEG₈-Y6 (a) and PEG₈-(FY)3 (b). Fluorescence intensity emission of ANS fluorophore titration at 475 nm vs. concentration of PEG₈-Y6 and PEG₈-(FY)3 (c). CAC values are established from the break points.

However, an additional role of PEG in alteration of the structural/functional properties of these systems cannot be excluded. Indeed, it is well-known from the literature that PEG moiety bound at N or C-terminus of short peptides can induce crystallization effects.^{187,240} In order to assess the influence of PEG on the self-assembling process, we also synthesized Y6 and (FY)3, that are two analogues peptides without PEG functionalization.

3.9.1 Synthesis and fluorescence of tyrosinate peptides

All the peptides were synthesized in good yields and high purity according to the standard protocols of the solid phase peptide synthesis (Fmoc/OtBu).²¹⁵ For PEGylated derivatives, PEG moiety was inserted at the N-terminus of the peptide sequences through the sequential coupling of four monodisperse commercial oxyethylene linkers (Fmoc-AdOO-OH, PEG₂).

Differently from PEG₈-F6, which requires a pre-dissolution in 1,1,1,3,3,3-hexafluoro-2-propanol (HFIP),²³¹ PEG-tyrosinate analogues, having additional sites for hydrogen bonding and an increased side chain polarity, present good solubility in water and were directly dissolved in water at the final desired concentration.

Fluorescence spectra of PEG₈-(FY)3 and of PEG₈-Y6 peptides (**Figure 76**) were recorded in water at several concentrations (0.05, 0.1, 0.25, 0.5, 1.0, 2.0, 4.0 and 10 mg/mL). Spectra of PEG₈-(FY)3 were recorded by exciting the peptide at both 257 and 276 nm, that correspond to the absorbance wavelengths for Phe and Tyr chromophores, respectively. On the other hand, PEG₈-Y6 samples were excited only at 276 nm. Independently from the λ_{ex} and from the concentration studied, all the spectra of PEG₈-(FY)3 show only a peak at 305 nm, typically observed for Tyr residue, whereas the peak at 282 nm is absent.

The absence of this peak can easily be explained as a consequence of a RET (Resonance Energy Transfer) phenomenon occurring between Phe and Tyr residues. Beside the peak at 305 nm, two additional peaks at 360 and 376 nm appear for the sample at the highest studied concentration (10 mg/mL). The same peaks were also found in the fluorescence spectrum of PEG₈-Y6 at 10 mg/mL. These peaks were attributed to peptide aggregation phenomena. The critical aggregate concentration (CAC) of PEGylated peptides was achieved by the well-known fluorescence-based method, in which the fluorescent probe, 8-anilinonaphthalene-1-sulfonate ammonium salt (ANS), is titrated with increasing amount of the peptide.⁶³

Critical Aggregation concentration values were established from the graphical break point of the plots in **Figure 76c**.

ANS dye shows a very similar behavior upon titration with PEG₈-(FY)3 and PEG₈-Y6 solutions and the CAC values are $1.5 \cdot 10^{-5}$ M (22.8 $\mu\text{g/mL}$) and $2.0 \cdot 10^{-5}$ M (31.4 $\mu\text{g/mL}$), respectively. These values are of the same order of magnitude and slightly higher than the CAC value previously found for the more hydrophobic hexaphenylalanine analog (7.5 μM , 10 $\mu\text{g/mL}$).²³¹

This result was expected due to the higher hydrophobicity of the phenylalanine with respect to the tyrosine. Moreover, the partial or complete replacement of the phenylalanine residues with the tyrosine

Section III: PBM obtained by punctual chemical modifications

ones does not seem affect significantly the aggregation propensity of the peptide derivative.

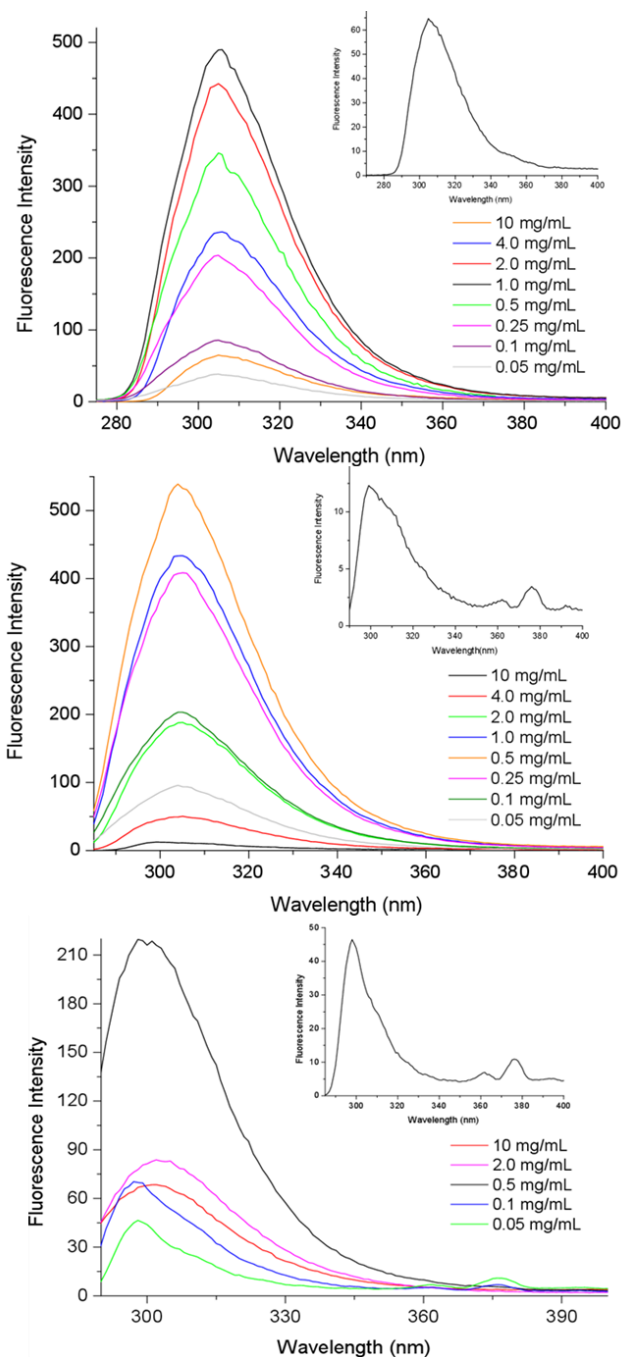


Figure 76: Fluorescence emission spectra of PEG₈-(FY)3 excited at $\lambda_{ex} = 257$ nm (left) and $\lambda_{ex} = 276$ nm (middle) and of PEG₈-Y6 excited $\lambda_{ex} = 276$ nm (right) in 0.05-10 mg/mL concentration range. In the insert, the fluorescence spectrum at 10 mg/mL..

3.9.2 Structural characterization in solution

The structural organization of PEGylated aromatic hexapeptides was investigated by Circular Dichroism (CD) and by Fourier Transform Infrared (FTIR). CD spectra of PEG₈-(FY)3 and PEG₈-Y6 in water at several concentrations (0.1, 1.0, 2.0 and 5.0 mg/mL) are reported in **Figure 77a** and **Figure 77b**.

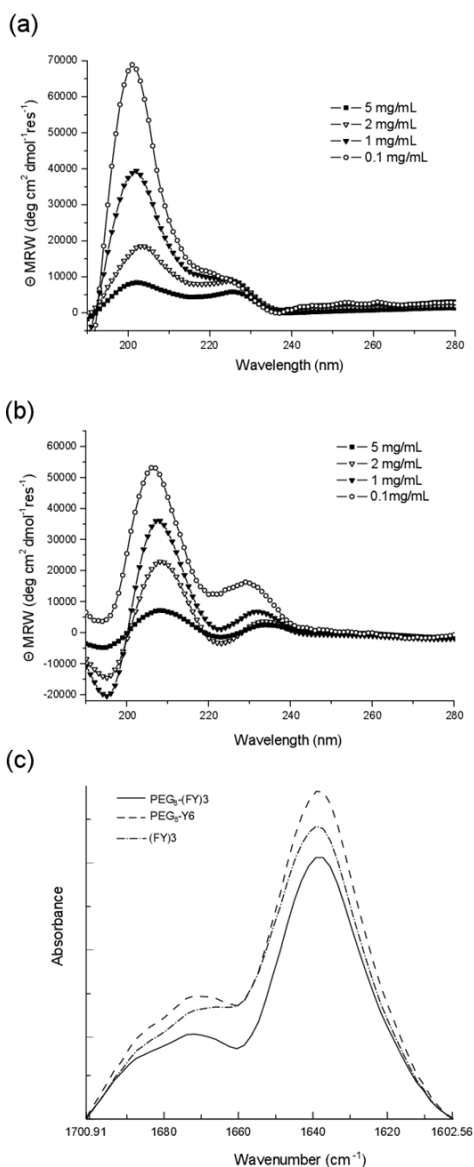


Figure 77: CD spectra of: (a) PEG₈-(FY)3 and (b) PEG₈-Y6 in water at several concentrations (0.1, 1.0, 2.0 and 5.0 mg/mL). (c) FTIR spectra of PEG₈-Y6 and PEG₈-(FY)3 and (FY)3 in water at 5.0 mg/mL in the amide I region.

Section III: PBMs obtained by punctual chemical modifications

All the spectra of PEG₈-(FY)3 show a very similar dichroic tendency with respect to PEG₈-F6 with two maxima at 226 and 202 nm, and a minimum around 235 nm. The two maxima (226 and 202 nm) can be associated with the $n \rightarrow \pi^*$ transition of the peptide bond and to the $\pi \rightarrow \pi^*$ transition of the peptide bond and/or phenyl moieties, respectively. In details, the peak at 202 nm is characteristic of peptides in which an aromatic side-chain stacking occurs, whereas the minimum at 235 nm is associated with a β -sheet secondary structure arrangement.^{203,216}

The decreasing intensity of the peak at 202 nm, as function of concentration, is due to a gradual subtraction and consequent silencing of chromophores in the final spectrum. This evidence confirms a progressive self-aggregation of the peptide derivative driven by aromatic interactions. The other PEGylated peptide, PEG₈-Y6, shows a slightly different CD behavior compared to PEG₈-(FY)3.

In the spectra of PEG₈-Y6, two maxima red shifted at 207 and 230 nm are well detectable. Beyond these two maxima, there is a pronounced minimum at 193 nm, whereas the minimum around 235-240 nm is absent. These spectral differences reflect fine dissimilarities in the secondary structure of the two compounds.

The obtained aggregates were also structurally examined by FTIR spectroscopy in the spectral region of the stretching of amide I (1600-1700 cm^{-1}). FTIR spectra of PEG₈-(FY)3 and PEG₈-Y6 peptides in water solution at 5.0 mg/mL, reported in **Figure 77c**, show a similar profile with two peaks at 1638 and 1680 cm^{-1} . This profile, typically observed for β -sheets with an antiparallel orientation of the β -strands, was previously observed also for PEG₈-F6.²³¹

3.9.3 Structural characterization at the solid state

Self-assembled aromatic peptides and their PEGylated analogues were further characterized at the solid state by Transmission Electron Microscopy (TEM) and WAXS techniques (**Figure 78**).

Selected TEM images of PEG₈-(FY)3 show a continuous network of fibers interconnected by physical cross-link points. The analogue (FY)3, lacking of PEG decoration, showed a smaller amount of fibrils at the same concentration. This result can be related to a less fiber entangling that has as consequence the absence of gelation ability for (FY)3.

WAXS measurements were collected on dried fibers. **Figure 78** shows the microscopic image of the fibers (upper row), the 2D WAXS data (middle row), and the 1D WAXS profiles (lower row). A comparative analysis of these experiments highlights analogies and differences. In all cases, the WAXS data present the typical fiber diffraction pattern with two crossed main axes: the meridional along the fiber direction and

Section III: PBMs obtained by punctual chemical modifications

the equatorial perpendicular to it (see white dotted arrows). The 2D data were integrated along these orthogonal axes and the corresponding 1D profiles, displayed in **Figure 78** (lower row) as red (meridional) and black (equatorial) profiles, present almost the same reflections.

The 0-4 labelled meridional and equatorial peaks were summarized in the **Table 10**, where the diffraction peak at $q=1.29-1.33 \text{ \AA}^{-1}$ ($d=4.7-4.9 \text{ \AA}$) corresponds to the distance between adjacent peptide backbones organized into β -strands along the fiber axis²⁴³ and the diffraction peak at $q=0.49-0.3 \text{ \AA}^{-1}$ ($d=11.9-12.8 \text{ \AA}$) corresponds to the distance between two distinct β -sheets.²⁴⁴

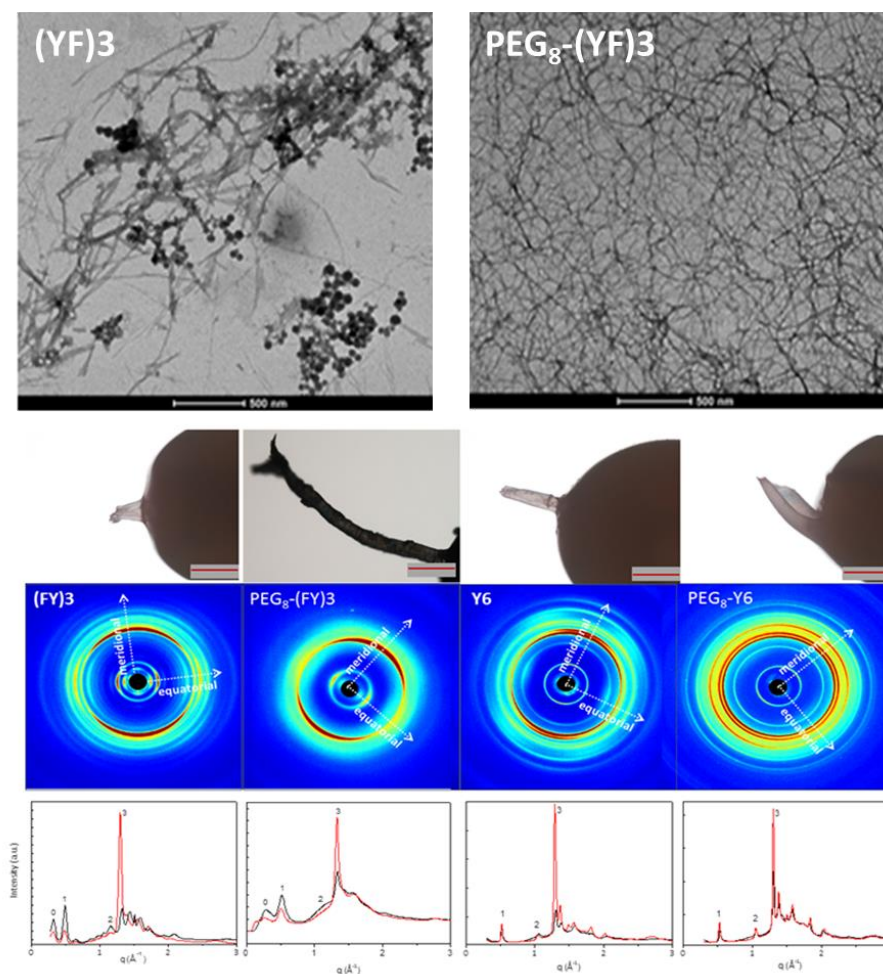


Figure 78: Structural characterization at the solid state. In the top, selected TEM images (YF)3 and PEG₈-(FY)3. Microscopic image of the fibers (upper row), 2D WAXS data (middle row), 1D WAXS meridional/equatorial (red/black) profiles (lower row). The scale bar of the images is 0.5 μm

Table 10: Meridional and equatorial peaks position in q (\AA^{-1}) and corresponding distance $d=2\pi/q$ (\AA).

	(FY)3		PEG ₈ -(FY)3		Y6		PEG ₈ -Y6	
	$q(\text{\AA}^{-1})$	$d(\text{\AA})\pm 0.5$	$q(\text{\AA}^{-1})\pm 0.02$	$d(\text{\AA})\pm 0.5$	$q(\text{\AA}^{-1})\pm 0.02$	$d(\text{\AA})\pm 0.5$	$q(\text{\AA}^{-1})\pm 0.02$	$d(\text{\AA})\pm 0.5$
0	0.32	19.6	0.29	21.5				
1	0.49	12.8	0.52	12.05	0.51	12.3	0.53	11.9
2	1.12	5.6	1.12	5.6	1.05	6.0	1.05	6.0
3	1.33	4.7	1.33	4.7	1.29	4.9	1.29	4.9

It is, however, important to note that the addition of the PEG moiety has different consequences on (FY)3 and Y6 assembly. Indeed, while the (FY)3 fiber are marginally affected by the addition of the PEG, the 2D WAXS diffraction patterns of Y6 and PEG₈-Y6 show significant differences. In particular, the pattern exhibited by PEG₈-Y6 is characterized by the presence of additional circles which are likely produced by the crystallization of PEG.

3.9.4 Molecular modelling and dynamics

In order to gain atomic-level structural data on the peptide moiety of the assemblies formed by Y6 and (FY)3 molecular modelling and molecular dynamics (MD) analyses were performed.

Different models made of one, two, or three β -sheets, each composed of fifty β -strands, were generated taking the crystalline assembly of the hexapeptide KLVFFA fragment as reference.^{198,231}

For the Y6 hexapeptide, models composed by either one or two sheets were considered (Y_ST50_SH1 and Y_ST50_SH2). For the (FY)3 system, which is endowed with a larger sequence complexity, we generated models made of either two or three β -sheets (FY_ST50_SH2 and FY_ST50_SH3).

Representations of the starting models are shown in **Figure 79**. The RMSIP values (data not shown) indicate that all simulations reached a satisfactory level of convergence

Section III: PBMs obtained by punctual chemical modifications

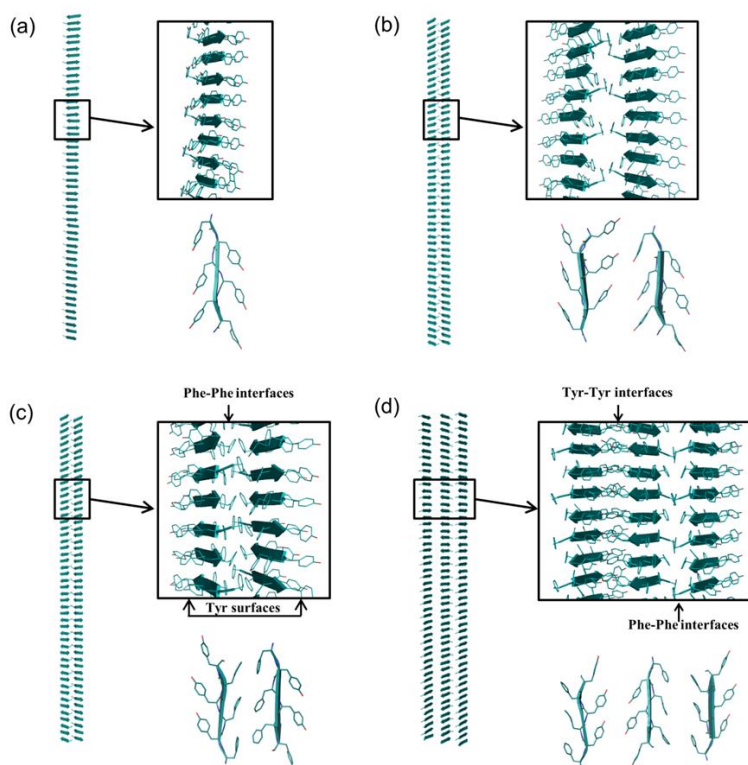


Figure 79: Three-dimensional representations of the starting flat models used in the Molecular Dynamics studies: Y_ST50_SH1 (a), Y_ST50_SH2 (b), FY_ST50_SH2 (c), and FY_ST50_SH3 (d).

3.9.4.1 MD simulations of Y6 system

To gain insights into the ability of a Tyr-rich peptide to adopt β -structures, initial MD investigations were performed considering a single sheet made of fifty β -strands (Y_ST50_SH1, **Figure 79a**).

The evaluation of the geometrical parameters commonly used to assess the structural stability of trajectory structures (RMSD deviations from the starting structure and gyration radius) indicates that the system undergoes a major structural transition in the initial 50 ns of the simulation associated with the overall twisting (**Figure 80**).

Although the secondary structure of the system is rather conserved (**Figure 80c**), significant fluctuations are evident also in the later stages of the trajectory (**Figure 80a,b**). These findings indicate that Y6 has a propensity to adopt β -structures, although the overall structure of the single sheet model is somewhat unstable. Then, it was evaluated the possibility that Y6 could form assemblies through the tight lateral association of Tyr side chains. To this aim, generated a double strand

Section III: PBM's obtained by punctual chemical modifications

model denoted as Y_ST50_SH2 and shown in **Figure 79b** was generated. The inspection of the trajectory frames of the resulting simulation clearly indicates that, after an initial structural transition (0-100 ns), the model reaches a rather stable structural state (**Figure 81**). The analysis of the individual trajectory structures demonstrates that the initial structural transition corresponds to the twisting of the originally flat model (**Figure 81c** and **Figure 79**).

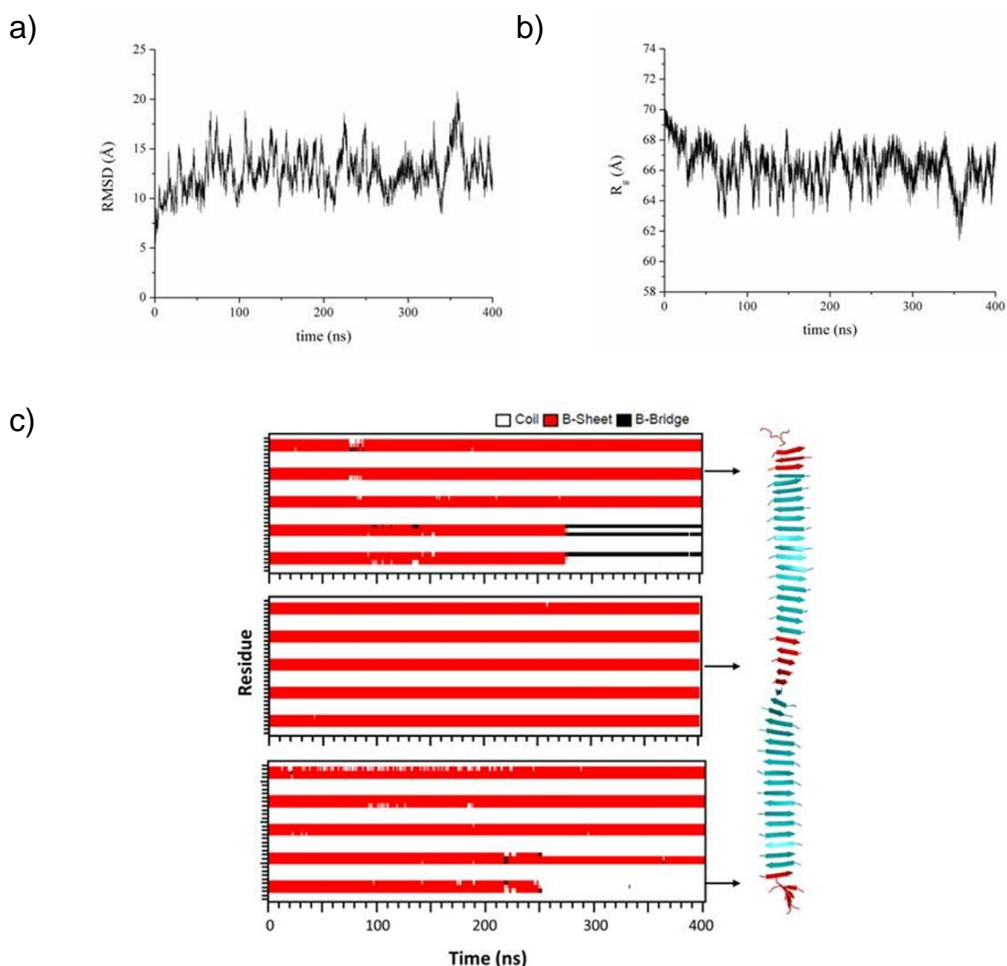


Figure 80. Time evolution of several structural parameters in the MD simulation performed starting from the flat model of Y_ST50_SH1: RMSD values computed on the C α atoms of MD trajectory structures against the starting model (a), gyration radius (b), and secondary structure (c). Secondary structure is reported only for the residues belonging to the central region and to both terminal ends. The average structure, computed in the trajectory region 100-400 ns, is also reported in panel c.

Section III: PBMs obtained by punctual chemical modifications

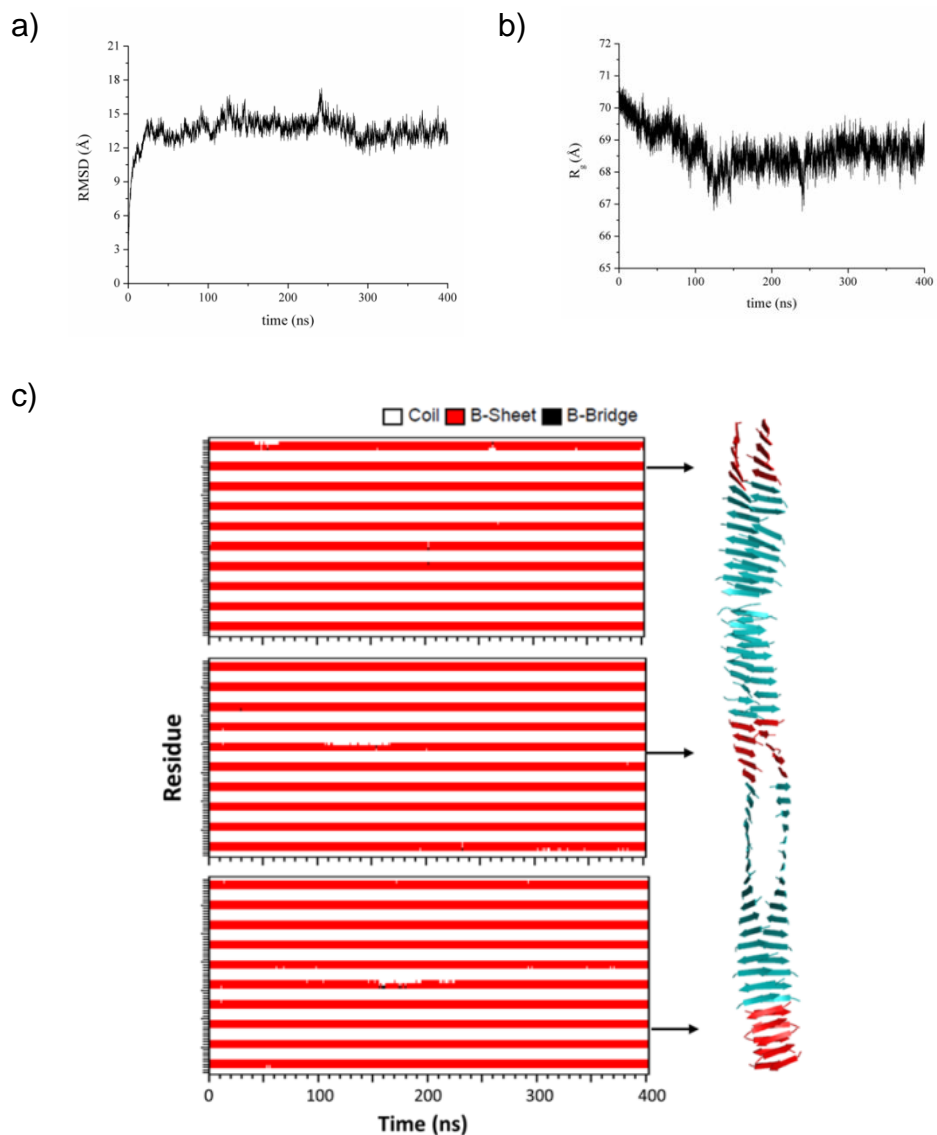


Figure 81: Time evolution of several structural parameters in the MD simulation performed starting from the flat model of Y_ST50_SH2: RMSD values computed on the C α atoms of MD trajectory structures against the starting model (a), gyration radius (b), and secondary structure (c). Secondary structure is reported only for the residues belonging to the central region and to both terminal ends. The average structure, computed in the trajectory region 100-400 ns, is also reported in panel c

Section III: PBMs obtained by punctual chemical modifications

The evaluation of the main chain and side chain flexibility of Y6 residues indicates that Tyr side chains located at the inter-sheet interface are endowed with a limited mobility (**Figure 82**).

It is also worth mentioning that also the flexibility of the solvent exposed residues is rather limited. To unravel the structural determinants that confer stability to this assembly, we evaluated the occurrence of preferred Tyr rotameric states and H-bonding interactions. Interestingly, the structure of the assembly is characterized by an alternation of Y6 peptides in which all Tyr side chains adopt trans states ($\approx 180^\circ$) for the χ_1 dihedral angle with peptides whose residues are in gauche (either $\approx -60^\circ$ or $\approx 60^\circ$) rotameric states (**Figure 82c**). This juxtaposition of the side chains combined with the antiparallel arrangement of the main chain leads to the formation of stacking interactions between Tyr residues of consecutive strands (**Figure 82b**). These stacking intra-sheet interactions also occur for exposed Tyr residues, thus limiting their mobility and somewhat favoring their propensity to form larger Y6 aggregates.

Networks of inter-sheet H-bonds contribute to the overall stability of the Tyr interface (**Figure 82b**). The analysis of other structural periodicities of Y_ST50_SH2 assembly indicates that the distance along the same polypeptide chain between Tyr residues which present the same orientation of the side chain is ≈ 6.5 - 7.0 Å (**Figure 82d**). The inter-sheet distance between facing Tyr residues is approximately 12.5 Å. Notably, these values are in close agreement with the equatorial reflections detected in the WAXS analyses (**Table 10**).

Section III: PBMs obtained by punctual chemical modifications

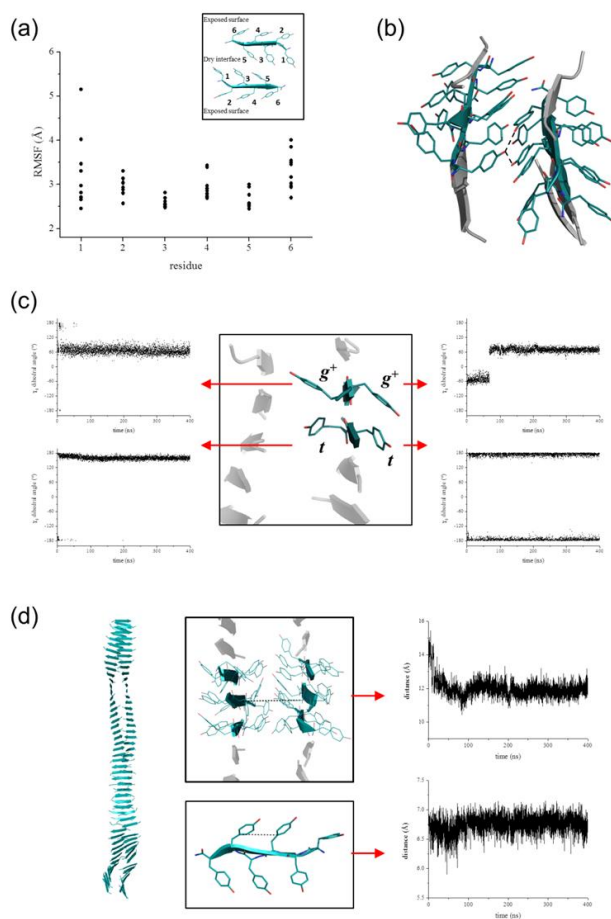


Figure 82. RMSF values of the Y_ST50_SH2 model computed in the equilibrated region of the trajectory (100-400 ns) are shown in panel (a). For clarity only the values of the central ten β -strands are reported. Representative examples of inter-sheet H-bonding interactions are reported in panel (b). Conformations of the Tyr side chains at the exposed and dry interfaces are shown in panel (c). Representative examples of the time evolution of the χ_1 dihedral angle are reported. The time evolution of the distance between two representative C^α atoms of the facing sheets along the trajectory and of the distance along the same polypeptide chain between Tyr residues which present the same orientation of the side chain is reported in panel (d). Time evolution of several structural parameters in the MD simulation performed starting from the flat model of Y_ST50_SH2: RMSD values computed on the C^α atoms of MD trajectory structures against the starting model (a), gyration radius (b), and secondary structure (c). Secondary structure is reported only for the residues belonging to the central region and to both terminal ends. The average structure, computed in the trajectory region 100-400 ns, is also reported in panel c.

3.9.4.2 MD simulations of (FY)3 system

A three-dimensional model for (FY)3 was generated by using a step-wise procedure. As detailed in the methods section, taking into account the elevated hydrophobicity of Phe residues, we preliminarily generated a model composed of two sheets with facing Phe side chains at the dry interface and exposed Tyr side chains (FY_ST50_SH2) (**Figure 79c**). MD simulations carried out on this system clearly indicate that it reaches a stable state after an initial structural transition (0-250 ns) As for Y6, this transition corresponds to the twisting of the model (**Figure 83**).

The inspection of the trajectory structures indicates that, for the Phe moieties, this system recapitulates the structural features of the previously characterized F6 assembly.²³¹

On the other hand, the exposed Tyr residues behave like the exposed residues of Y6 (data not shown).

The ability of the Phe residues of (FY)3 to form a stable apolar interface and the capability of Tyr residues of Y6 to tightly associate led us to generate a three-sheet model characterized by two distinct interfaces: one apolar made of Phe residues and the other more polar made of Tyr residues (**Figure 79d**). MD simulations clearly indicate that this assembly is rather stable as demonstrated by the monitoring of several structural parameters (**Figure 84**).

The analysis of both the apolar and polar interface clearly unravels the basis of their stability. In both of them the alternation of peptides with trans and gauche+ rotameric states of the side chains leads to the formation of stabilizing stacking interactions (**Figure 85b,c**).

At the Phe-interface additional interactions are established by the aromatic rings of facing residues. On the other hand, the Tyr-interface is stabilized by both intra-sheet and inter-sheet H-bonds (**Figure 85b**). As expected, the inter-sheet distances of both Phe- and Tyr-interface are approximately 12.5 Å (**Figure 85d**).

The combination of these two interfaces leads to a model characterized by a periodicity of 21 Å (**Figure 85d**).

These values are in close agreement with those experimentally derived by WAXS (**Figure 78** and **Table 10**).

Section III: PBMs obtained by punctual chemical modifications

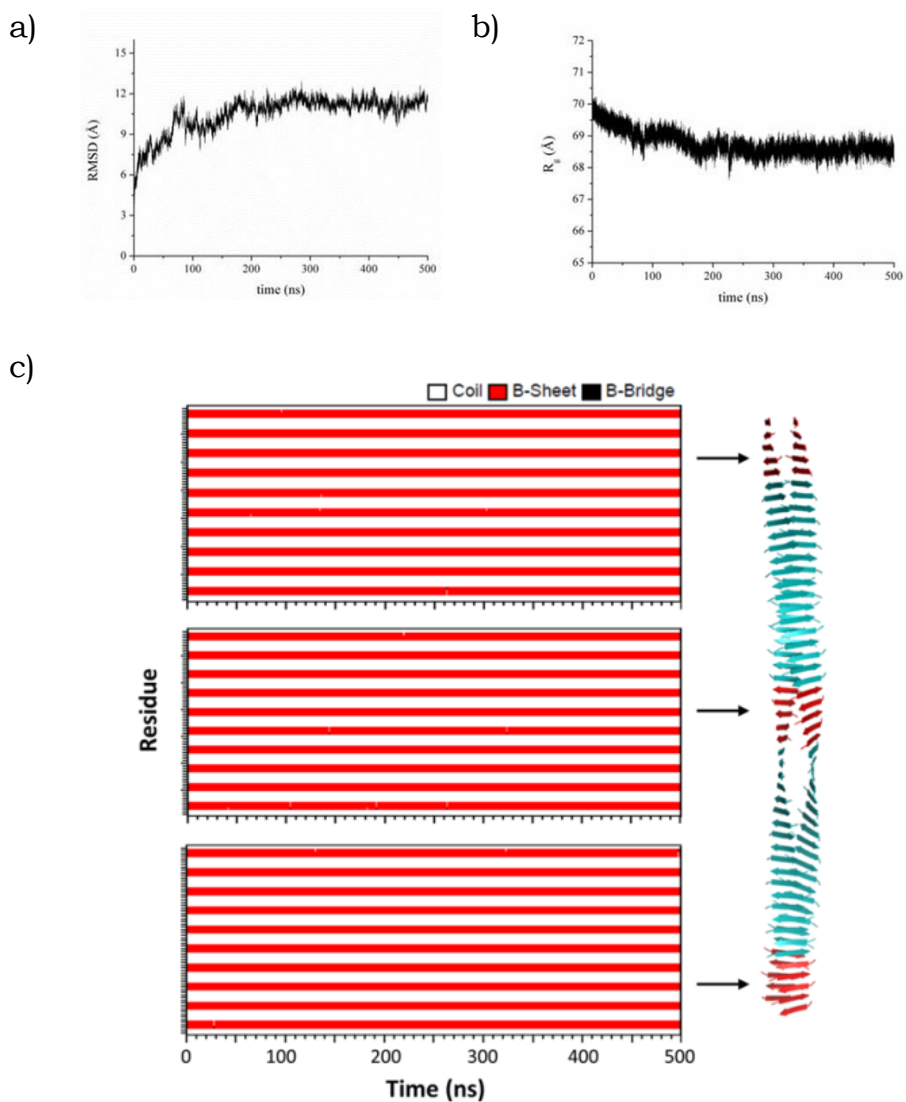


Figure 83. Time evolution of several structural parameters in the MD simulation performed starting from the flat model of FY_ST50_SH2: RMSD values computed on the C^α atoms of MD trajectory structures against the starting model (a), gyration radius (b), and secondary structure (c). Secondary structure is reported only for the residues belonging to the terminal ends and to the central region. The average structure, computed in the equilibrated region of the trajectory (250-500 ns) is reported.

Section III: PBM's obtained by punctual chemical modifications

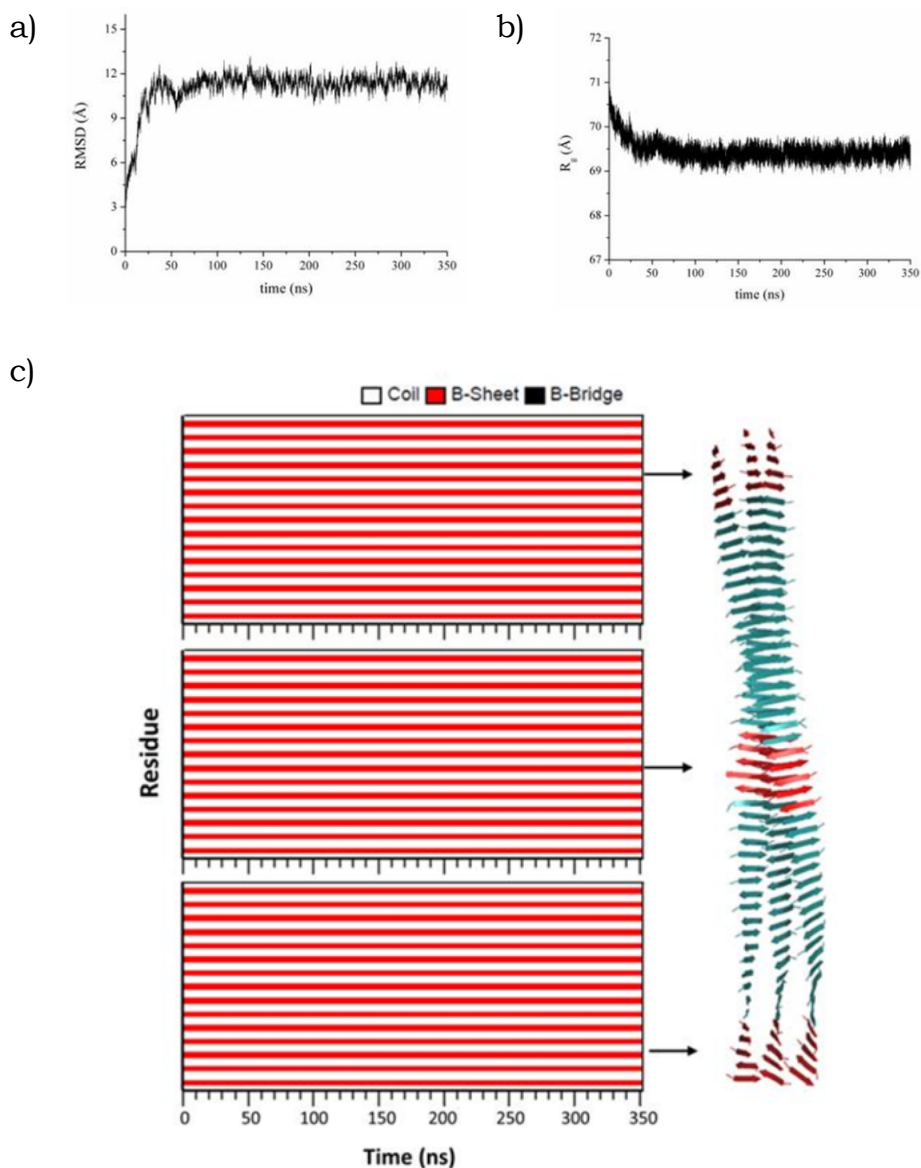


Figure 84. Time evolution of several structural parameters in the MD simulation performed starting from the flat model of FY_ST50_SH3: RMSD values computed on the C^α atoms of MD trajectory structures against the starting model (a), gyration radius (b), and secondary structure (c). Secondary structure is reported only for the residues belonging to the terminal ends and to the central region. The average structure, computed in the equilibrated region of the trajectory (100-3500 ns) is reported.

Section III: PBMs obtained by punctual chemical modifications

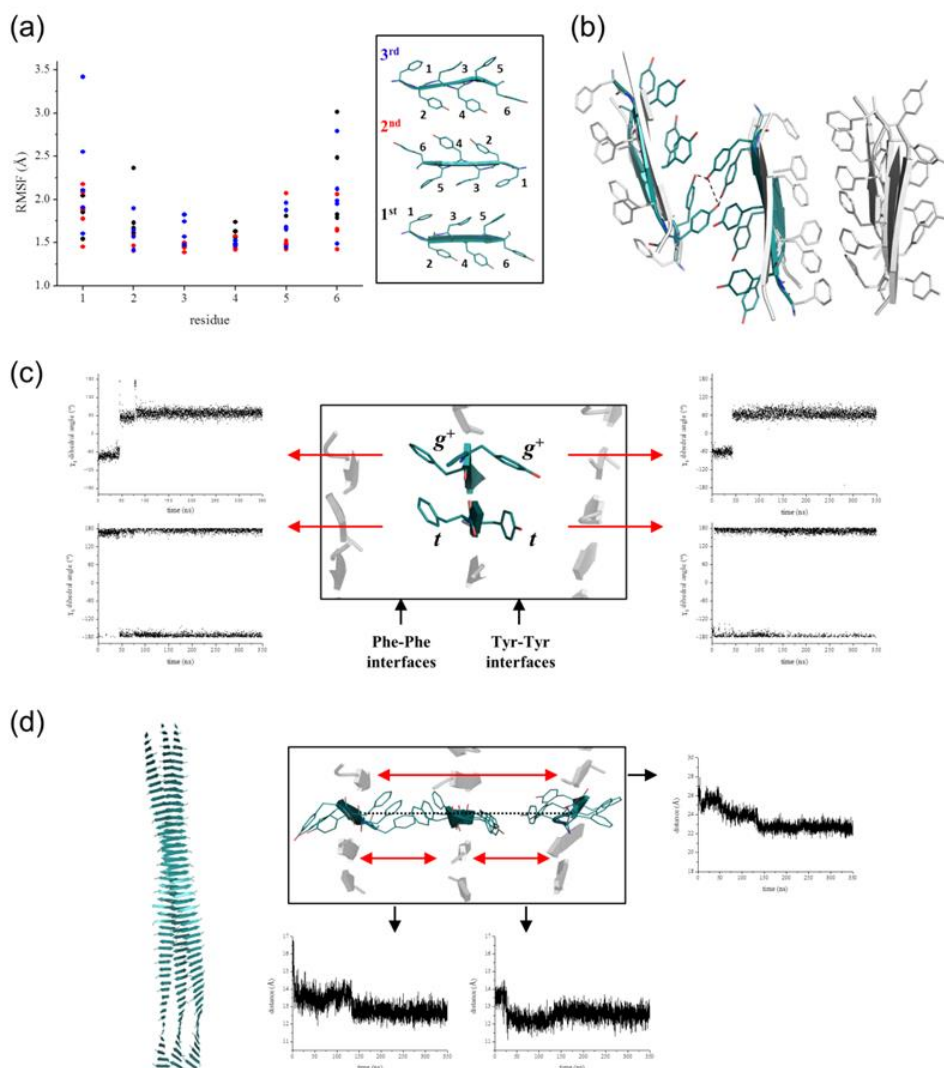


Figure 85. RMSF values of the FY_ST50_SH3model computed in the equilibrated region of the trajectory (100-350 ns) are shown in panel (a). For clarity only the values of the central fifteen β -strands are reported. Representative examples of inter-sheet H-bonding interactions at the Tyr-Tyr interfaces are reported in panel (b). Conformations of the residue side chains are shown in panel (c). Representative examples of the time evolution of the χ_1 dihedral angle are reported. The time evolution of the distance between two representative C^α atoms of the external sheets along the trajectory is reported in panel (d).

3.9.5 PEG₈-(FY)3 gel: rheological characterization

From the qualitative point of view, PEG₈-(FY)3 showed a certain tendency to gelificate in water above a concentration of 0.5wt %.

The monitoring of the stability of the 1.0wt % gel over time indicated that at this concentration the gel maintains its ultrastructure up to 60 days (**Figure 86a**). Although, based on sequence considerations, PEG₈-(FY)3 is expected to have intermediate properties between PEG₈-F6 and PEG₈-Y6, none of these two latter compounds form hydrogels under the same concentration and temperature used to prepare the PEG₈-(FY)3 hydrogel.

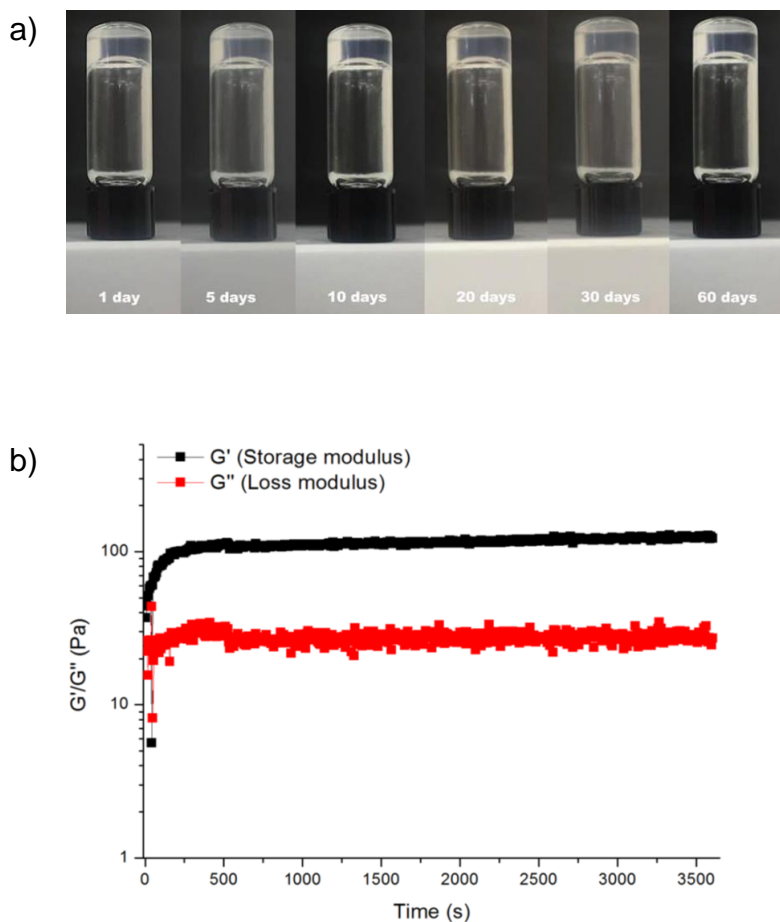


Figure 86: a) Inverted tube test for PEG₈-(FY)3 at 1.0wt % until two months. b) Time sweep (1 hour experiment) for PEG₈-(FY)3 gel at 1.0wt % concentration. Rheological results expressed in terms of storage (G') and loss modulus (G'').

Section III: PBMs obtained by punctual chemical modifications

For the PEG₈-(FY)3 system the PEG moiety is essential for gelification as the peptide (FY)3 peptides, lacking the PEG portion, present a very limited water solubility, also after pre-dissolution in organic solvent, leading to the formation of solid precipitates.

In order to further examine the mechanical properties of the PEG₈-(FY)3 hydrogel, rheological analysis was performed at 1.0wt % concentration. The results of the experiments are reported in terms of storage modulus (G') and of loss modulus (G''). The optimal measurement parameters were defined according to dynamic strain sweep (at a frequency of 1 Hz) and frequency sweep (at 0.1 % strain) oscillatory tests. Time sweep measurement was performed with 1 Hz frequency and 0.1 % strain for a time period of 1 h. G' and G'' time sweep curves are presented **in Figure 86b**. The evidence that the value of storage modulus (G'~100 Pa) is higher than that of the loss one (G''~28 Pa) confirms analytically the gel state of the system, excluding the possibility that the supramolecular material has a high viscose liquid behaviour.²⁴⁵ Furthermore, if compared with other organogelator system, this modulus values point out the weak nature of the self-supporting hydrogel.

3.9.6 In vitro biocompatibility profiles of PEG₈-(FY)3 gel

Biocompatibility of the PEG₈-(FY)3 hydrogel at a concentration of 1.0 wt% was evaluated on Chinese Hamster Ovarian (CHO) cells cultured in Dulbecco's Modified Eagle's medium (DMEM).

The elution test, coupled with MTT viability assay, is an in vitro cytotoxicity study designed to detect the possible presence of toxic material eluted in the media from the gel sample. The DMEM media was incubated with the gel overnight. The extracted media was used to culture CHO cells and the viability was determined after six and twenty-four hours of incubation.

The cell viability, estimated by MTT assay, was certified to be 93 % and 90% for six and twenty-four hours incubation times, respectively (**Figure 87a and 87b**, inserts). Simultaneously, after the treatment with the extracted media, cells were analysed for viability using live-dead staining with fluorescein diacetate (FDA), a cell membrane dye indicating live cells (green), and with propidium iodide (PI), a DNA stain indicating dead cells (red).²⁴⁶ The degree of death was determined by fluorescence microscopy imaging. Fluorescence micrograph (merged in red and green field) for live/dead assay after six hours shows high confluent live cells with no red spots (**Figure 87a**).

A very similar result was detected for the sample with longer incubation (**Figure 87b**).

Section III: PBMs obtained by punctual chemical modifications

The high cytocompatibility detected *in vitro* can be probably attributed to the hydrogel preparation method that, contrarily to others peptide hydrogels, does not require the employment of any organic solvents (like DMSO, HFIP or MeOH).²⁴⁷

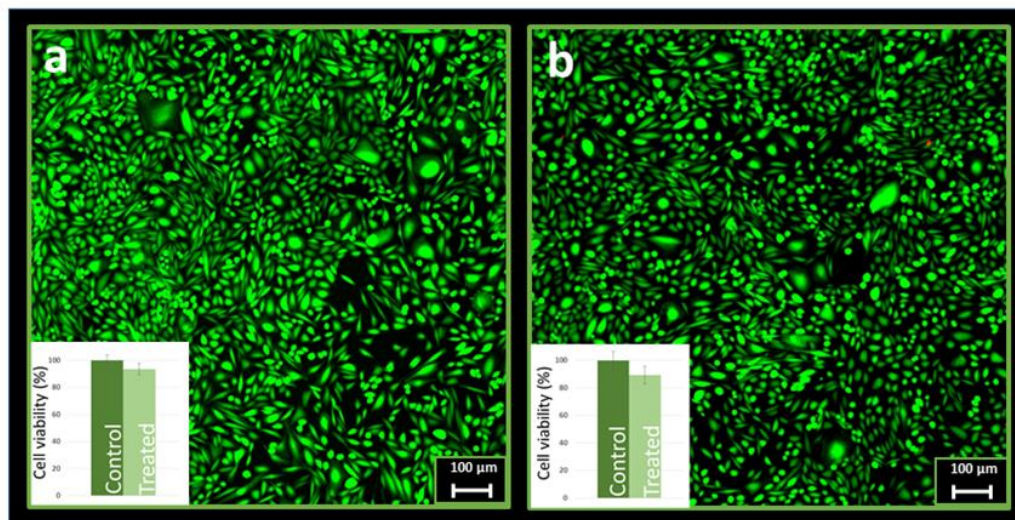


Figure 87: Representative merged image for live/dead assay after six (a) and twenty-four (b) hours incubation of CHO cells with extract media of PEG8-(YF)3 at 1.0wt %. The MTT viability test result are reported in the insert of the two panels.

3.10. Self-assembled tetra-tryptophan based NPs

In order to further investigate the effect of a punctual modification on the supramolecular organization, the synthesis of PEG₆-W4 (**Figure 88a**), a PEG adduct of the tetra-tryptophan (W4) was achieved. In this PEGylated tetra-peptide the Phe residue¹⁹⁹ was replaced with the tryptophan (Trp, W).

W is one of the essential amino acids and represents the key-precursor for biosynthetic pathway of some neurotransmitters and hormones (tryptamine, serotonin and melatonin) and for all the anthranilic compounds (like NAD, acetyl-CoA and B3 vitamin).²⁴⁸

In addition, Trp fulfils an important role in enzymatic chemistry due the possibility to coordinate transition metals by the N- indolic group in active task.²⁴⁹

Section III: PBMs obtained by punctual chemical modifications

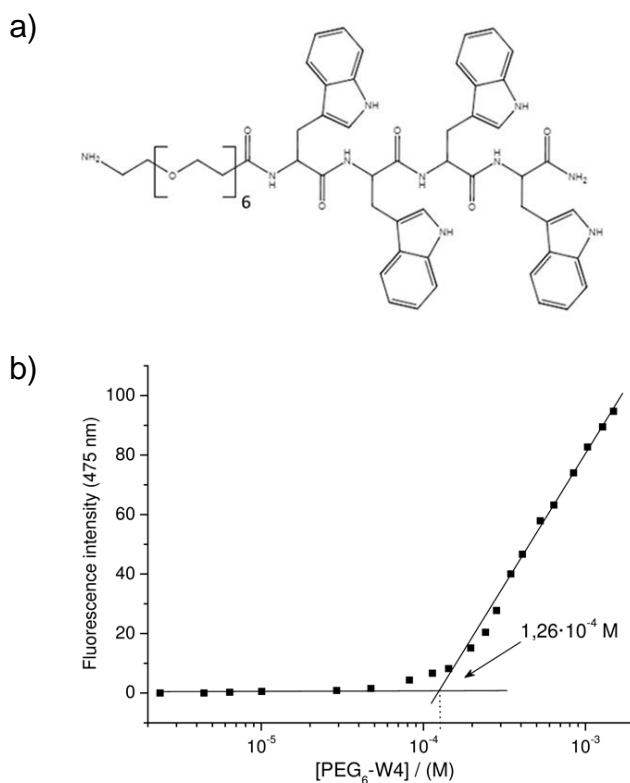


Figure 88. a) Schematic representation of PEG₆-W4 chemical structure, b) Fluorescence intensity emission of ANS fluorophore at 475 nm vs. concentration of PEG₆-W4. The CAC value of the peptide derivative is established from the break points.

3.10.1 Synthesis of PEG₆-W4

PEG₆-W4 was synthesized in solid phase according to the Fmoc (fluorenylmethyloxycarbonyl) standard protocols of the peptide synthesis.²¹⁵

Due to the high hydrophobicity of the sequence, a DMF/NMP 1/1 (v/v) mixture was used as reaction solvent.²⁵⁰

The Boc (tert-Butyloxycarbonyl) protection on the Trp side chain avoided collateral reactions (polymerizations, reduction indol-indoline and alkylation) associated with indole chemistry.²⁵¹ At the end of the synthesis, the pure compound, obtained by RP-HPLC chromatography, was characterized by LC-MS spectrometry and ¹HNMR spectroscopy. (characterization is reported in **Appendix I**)

As expected on the basis of the different solubility of Trp and Phe, PEG₆-W4 presents a smaller water solubility with respect to the previously characterized analogue containing the same number of Phe residues (PEG₆-F4).¹⁹⁹ Indeed, while PEG₆-F4 was directly solubilized

Section III: PBMs obtained by punctual chemical modifications

in water up to 30 mg/mL, tetra-Trp derivative required a preventive dissolution of the peptide powder in HFIP at 100 mg/mL and a subsequent dilution in water up to 10 mg/mL. It is plausible to suppose that the self-organization of the monomers occurs at the water dilution step by aromatic collapse, being HFIP a disintegrative solvent for aromatic compounds.²⁵²

In order to analytically establish the minimal concentration for self-aggregation, CAC was determined using ANS method.^{63,196}

Tracking and plotting the fluorescence intensity as function of the concentration, CAC value for PEG₆-W4 (1.26×10^{-4} M, 126 μ M) was determined in the break point of the graph reported in **Figure 88b**.

The critical concentration found for PEG₆-W4 is about 3-fold higher with respect to the value previously measured for F4-derivative (~ 43 μ M).¹⁹⁹

On the basis of simple consideration on the hydrophilic/hydrophobic balance, a higher self-assembly propensity of Trp homo-sequence is conceivable with respect to Phe one. This unexpected behavior can be related to a worse packaging of W4 consequent to the different Van der Waals volume of Trp and Phe (that are 163 and 135 \AA^3 , respectively).

3.10.2 Secondary structure assignment

A detailed analysis of PEG₆-W4 structure was performed by circular dichroism (CD) and FTIR to unravel the supramolecular organization of PEGylated tetra-tryptophan monomers.

Amide chromophores present in the protein backbone generate characteristic spectra with multiple transitions that can be ascribed to specific secondary structure motifs.²⁵³ CD spectra of PEG₆-W4 solutions, reported in **Figure 89**, show the dichroic signature of the peptide between 280 and 190 nm at several concentrations (0.1, 0.34, 1.35, 3.5 and 5 mg/mL).

For concentration below (0.1 mg/mL) and close to the CAC value (0.34 mg/mL), dichroic trends are dominated by a negative peak (**Figure 89a**). This signal is characterized by a progressive bathochromic shift from 225 nm to 230 nm while increasing concentration that can be attributed to a β -sheet structuration (**Figure 89b**).²⁵⁴

A substantial conformational transition to Trp-zipper organization was detected at higher concentrations (1.35, 3.5 and 5.0 mg/mL).

The structural change is revealed by an intense Trp-Trp exciton-coupled band, resulting in a negative peak at 217 nm and a positive signal at 233 nm with a zero isobestic cross-over point at 224 nm. No differences emerge from the comparison of the CD spectrum profiles at the three analyzed concentrations; however the increase of concentration is associated with a progressive decrease in intensity. This experimental evidence can be related to an increase in the

Section III: PBMs obtained by punctual chemical modifications

concentration of W4 aggregates that progressively subtracts detectable chromophores from the solution. The positive Cotton effect and the 233 nm zero are consistent with a backbone right handed helical twist.^{255,256}

Moreover, the weak peak around 274 nm is indicative of a zipper type arrangement, made it possible by the interaction of Trp chromophores (insert in **Figure 89b**).²⁵⁷ Given these experimental evidences, a Trp-Trp cross-strand indole-mediated interaction can be referenced (or considered) as the stabilizing factor of the supramolecular aggregates and as mechanism for the β -structure organization by hydrophobic collapse.

The β -sheet arrangement of the peptide was further confirmed by FTIR spectroscopy. In **Figure 89c** it is reported the deconvolution in absorbance for the secondary structure prediction of the amide I spectral region (1600-1700 cm^{-1}). FTIR spectrum shows two peaks at 1638 and 1680 cm^{-1} . This profile is normally observed for β -sheet with antiparallel orientation of the β -strands.^{205,206}

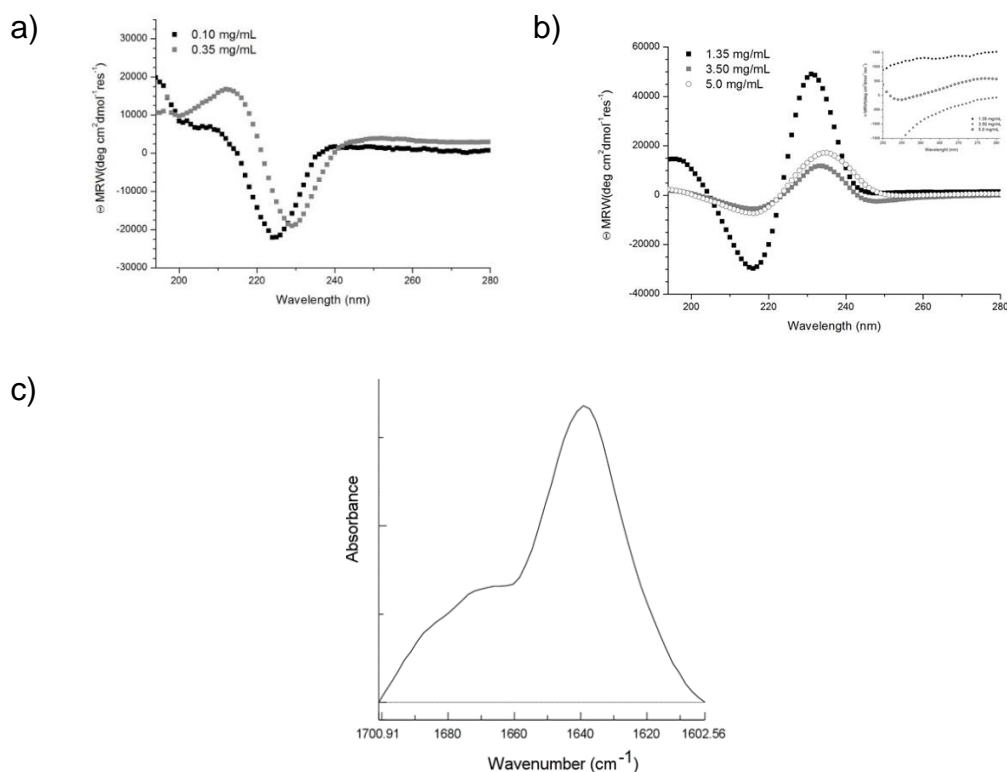


Figure 89. Secondary structure characterization of PEG₆-W4 aromatic peptides: a) CD spectra below (0.1 mg/mL) and close (0.34 mg/mL) to the CAC value, b) CD spectra above the CAC (1.35, 3.5 and 5 mg/mL), c) FTIR spectra at 5.0 mg/mL in the amide I region.

3.10.3 Structural characterization at the solid state

PEGylated tetra-tryptophan nanostructures were also characterized at solid state by WAXS/SAXS and TEM measurements. 2D WAXS data of PEG₆-W4 reported in **Figure 90a** (right) have been collected on the air dried fibers. 2D WAXS data of the PEG₆-F4 are also reported for comparison in **Figure 90a** (left).

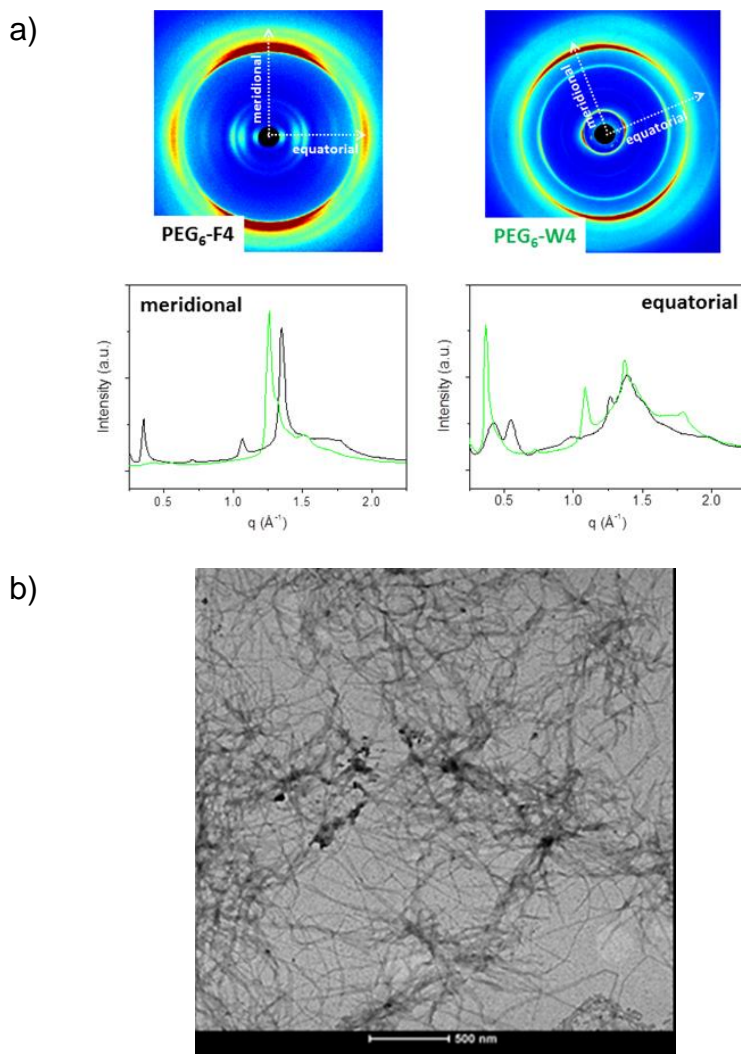


Figure 90. a) 2D WAXS data (upper row) and 1D WAXS meridional and equatorial profiles (lower row). b) Selected TEM images for PEG₆-W4 nanostructures.

Section III: PBMs obtained by punctual chemical modifications

For both the peptides, the WAXS data present the characteristic diffraction pattern of a amyloid-like fiber, with two main axes of symmetry: the meridional axis along the fiber direction and the equatorial axis perpendicular to it.¹²⁴ These axes were marked as white dotted arrows in each figure. The 2D data were integrated along these orthogonal directions and the corresponding 1D profiles were displayed in **Figure 90a** (lower row).

The most intense meridional and equatorial peaks were summarized in **Table 11**, where the diffraction peak at $q=1.26-1.35 \text{ \AA}^{-1}$ ($d=4.6-4.9 \text{ \AA}$) corresponds to the distance between adjacent peptide backbones organized into β -strands along the fiber axis.¹⁹⁹ 2D SAXS data, recorded on the same nanofibers (data not shown) do not display diffraction contributions at the nanoscale, thus indicating the absence of a hierarchical organization of the fiber. The presence of fibers at the solid state was also confirmed by TEM images (5.0 mg/mL), reported in **Figure 90b**.

Table 11: Meridional and equatorial peaks position in $q \text{ (\AA}^{-1}\text{)}$ and corresponding distance $d=2\pi/q \text{ (\AA)}$. The distances between adjacent peptide backbones (β -strands distance) along the fiber axis are marked in bold.

	PEG ₆ -W4		PEG ₆ -F6	
	$q(\text{\AA}^{-1}) \pm 0.02$	$d(\text{\AA}) \pm 0.5$	$q(\text{\AA}^{-1}) \pm 0.02$	$d(\text{\AA}) \pm 0.5$
Meridional	1.35	4.6	1.26	4.9
	--	--	1.23	5.1
	--	--	1.52	4.1
	0.37	17.0	0.42	15.0
Equatorial	--	--	0.56	11.2
	0.72	8.7	0.79	7.9
	1.08	5.8	0.99	6.4
	1.42	3.5	1.42	4.4

3.10.4 Dynamic simulations

In order to gain atomic-level structural information on the peptide spine of the W4 system it were performed MD simulations on different assemblies characterized by a different number of facing β -sheets (two to four) each composed of fifty β -strands (SH2_ST50_W4, SH3_ST50_W4, and SH4_ST50_W4).

Simulations carried out on SH2_ST50_W4 indicate that the system is highly unstable as it rapidly loses its starting structure (data not shown). This behavior is somewhat different from that exhibited by a similar model of the peptide made by six Phe residues (F6).²³¹

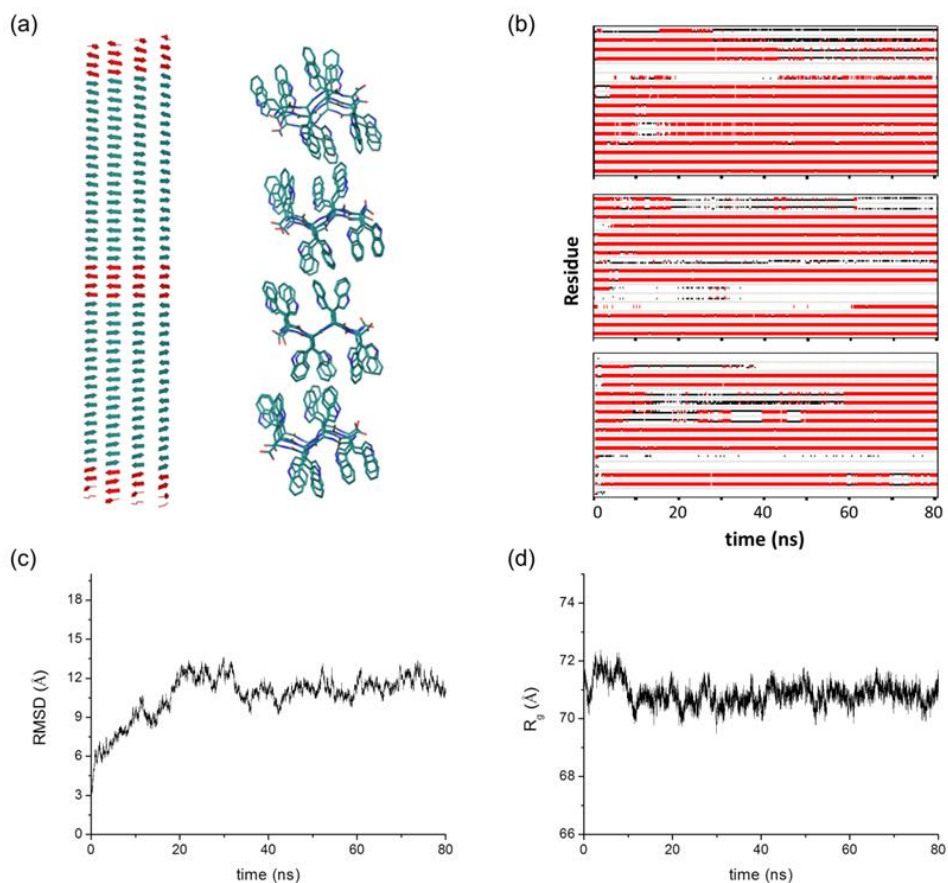


Figure 91: Time evolution of structural parameters in the MD simulation performed starting from the flat model of W4_ST50_SH4: a) two different views of the starting model, b) secondary structure, c) RMSD values computed on the C $^{\alpha}$ atoms of MD trajectory structures against the starting model, and d) gyration radius. Secondary structure is reported only for the residues belonging to the central region and to both terminal ends depicted in red in panel a.

Section III: PBMs obtained by punctual chemical modifications

This observation may be explained by considering the reduced inter-sheet interface of the tetrapeptide W4 compared to the hexapeptide F6. In this framework, we generated larger and more realistic models of the W4 fiber by increasing the number of the β -sheets of the assemblies. Simulation carried out on the system made of three sheets indicates that, although more stable than SH2_ST50_W4, it also undergoes a substantial disassembly (data not shown). On the other hand, the model composed of four β -sheets (SH4_ST50_W4) (**Figure 91a**) is endowed with a significantly higher stability. Indeed, an 80-ns MD simulation indicates that this system, after an initial transition, reaches a stable state that persists in the 20-80 ns interval as highlighted by the gyration radius and the Root Mean Square Deviation (RMSD) values of the trajectory structures against the starting model (**Figures 91c** and **91d**). **Figure 91b** also indicates that this system retains a significant level of secondary structure. It is worth mentioning that the high value (0.79) of the RMSIP calculated on two halves of the equilibrated trajectory (20-50 and 50-80 ns) suggests that the system reached a good level of convergence.

The inspection of the structural and dynamic features of the models detected in the equilibrated region of the trajectory indicates that the major transition of SH4_ST50_W4 corresponds to a twisting of the assembly (**Figure 92a**).

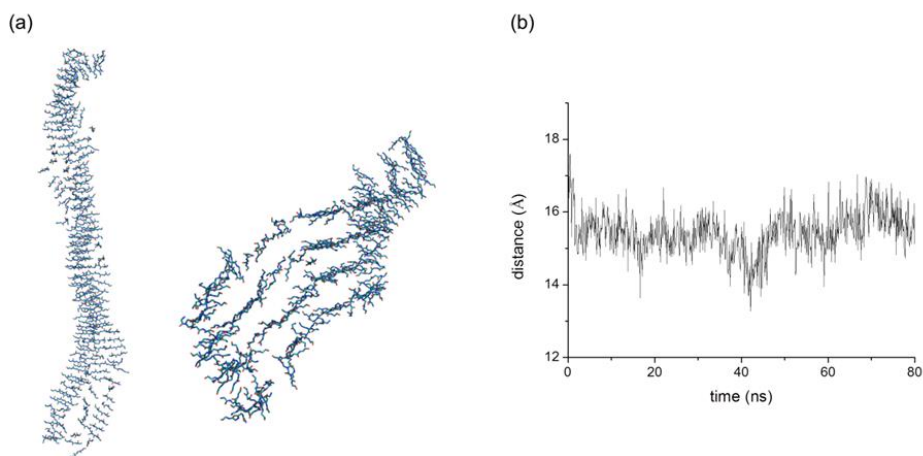


Figure 92. Structural features of W4_ST50_SH4: a) two views of a representative model of the equilibrated portion of the MD trajectory, b) representative example of the time evolution of the inter-sheet distance.

The inspection of the Root Mean Square Fluctuation (RMSF) values indicates that the C α atoms are endowed with a certain level of mobility (**Figure 93a**).

Section III: PBMs obtained by punctual chemical modifications

Notably, the RMSF values corresponding to the atoms of the side chain are comparable to those exhibited by the C α atoms (**Figure 93b**). This finding suggests that the intra-sheet and the inter-sheet interactions between Trp side chains limit their mobility. The analysis of the distances between facing sheets at the dry interface indicates that they are separated by approximately 15.0 Å (**Figure 93b**). This value, although larger than that found for the F6 system,²³¹ is slightly lower than that experimentally derived from the WAXS data (17.0 Å) (**Table 11**). This discrepancy may be ascribed to the finite size of SH4_ST50_W4 that, containing only four sheets, may favour an approaching of facing sheets.

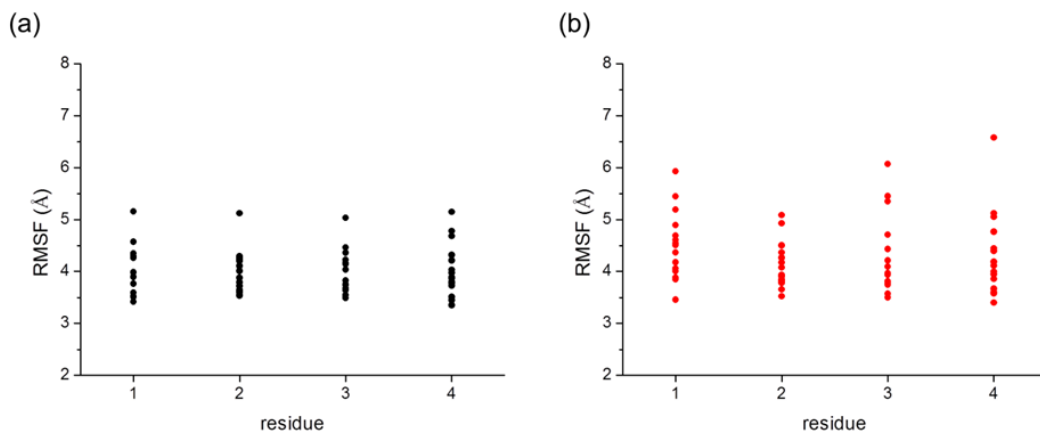


Figure 93: RMSF values computed on C α (a) and on side chain atoms (b) in the equilibrated region of the trajectory.

Section III: PBMs obtained by punctual chemical modifications



Experimental section

Materials, methods,
protocols and experimental details

Carlo Diaferia | University of Naples Federico II | XXX cycle

4.1 Materials and Methods

Protected N^α-Fmoc-amino acid derivatives orthogonally protected in side chain, coupling reagents (HOBt, PyBOP, HATU and DIEA), and Rink amide MBHA (4-methylbenzhydrylamine) resin were purchased from Calbiochem-Novabiochem (Laufelfingen, Switzerland). The Fmoc-21-amino-4,7,10,13,16,19-hexaoxahe-neicosanoic acid [Fmoc-Ahoh-OH, (L₆)] and the Fmoc-8-amino-3,6-dioxaoctanoic acid [Fmoc-AdOO-OH, (L₂)] were purchased from Neosystem (Strasbourg, France). DTPA(OtBu)₄-OH and DOTA(OtBu)₃-OH chelating agents were purchase from Chemateck (Dijon, France).

All other chemicals and fluorophores were commercially available by Sigma-Aldrich, Fluka (Bucks, Switzerland) or LabScan (Stillorgan, Dublin, Ireland) and were used as received unless otherwise stated. All solutions were prepared by weight with doubly distilled water.

Preparative RP-HPLCs were carried out on a LC8 Shimadzu HPLC system (Shimadzu Corporation, Kyoto, Japan) equipped with an UV lambda-Max Model 481 detector using Phenomenex (Torrance, CA) C₁₈ column. Elution solvents are H₂O/0.1%TFA (A) and CH₃CN/0.1% TFA (B).

Purity and univocal identity of the products were assessed by analytical LC-MS analyses by using Finnigan Surveyor MSQ single quadrupole electrospray ionization (Finnigan/Thermo Electron Corporation San Jose, CA), column: C₁₈-Phenomenex eluted with an H₂O/0.1% TFA (A) and CH₃CN/0.1% TFA (B), with a flow of 200 μL⁻¹. Analytical method of analysis are identified as:

Method 1 :	5-70-15	(flow of 200 μL ⁻¹)
Method 2 :	20-80-15	(flow of 200 μL ⁻¹)
Method 3 :	5-70-15	(flow of 1 mL ⁻¹)
Method 4 :	20-80-20	(flow of 1 mL ⁻¹)

Times retentions, molecular mass values and ¹HNMR characterization for all the synthesized compound are collected in the **Appendix 1**.

4.2 Peptide and peptide conjugates synthesis

Standard solid-phase peptide synthesis (SPPS) procedures with (fluorenylmethyloxycarbonyl) Fmoc/OtBu protection strategy were achieved to obtain peptide sequences and conjugates.²¹⁵

The Rink amide MBHA resin (substitution 0.65 mmolg⁻¹) was used as the solid-phase support to provide the peptides as C-terminus amides. Synthesis was per-formed on a scale of 0.2 mmol using N,N-

dimethylformamide (DMF) as solvent. For high hydrophobic sequences, N-methyl-2-pyrrolidone (NMP) was associated to DMF.²⁵⁰

Before starting with the elongation of the peptide, the resin was swelled for 30 min in DMF. Fmoc deprotection steps (two treatment of 7-10 minutes) were realized with a solution of 30% (v/v) piperidine in DMF. Coupling steps were achieved *via* carbodiimide activation by adding 2-fold molar excess of amino acid or PEG fragments, mixed with equimolar amounts of 1-hydroxybenzotriazole (HOBt), benzotriazol-1-yl-oxy-tris-pyrrolidino-phosphonium (PyBop), and a 4-fold molar excess of diisopropylethylamine (DIPEA). Chelating agents and difficult couplings were carried out by using 1-[Bis(dimethylamino)methylene]-1H-1,2,3-triazolo[4,5-b]pyridinium-3-oxid hexafluorophosphate (HATU) as activating agent and DIPEA as base. All couplings were performed twice for 1h.

Selective removal of N-methyltrityl (Mtt) protecting group from the lysine epsilon amine function was realized with a solution of 1% trifluoroacetic acid (TFA)/5% tri-isopropylsilane (TIS) in dichloromethan (DCM).

Qualitative ninhydrine test (called alternatively Kaiser test) was performed in order to check coupling and deprotection steps.²⁵⁸

Final products were fully deprotected and cleaved from the support with the TFA (trifluoroacetic acid)/TIS (triisopropylsilane)/H₂O (92.5/5/2.5 v/v/v) mixture at room temperature for 3 hours. For peptide lacking in side chain protecting group, the cleavage mixture was TFA (trifluoroacetic acid)/ H₂O (95/5) v/v.

Peptides and peptide conjugates were precipitated with ice-cold ethyl ether, dissolved in H₂O/CH₃CN and freeze-dried.

As previously mentioned, the purification of the crude products was carried out by preparative RP-HPLC. Mass spectra and ¹HNMR confirmed the products identity. Full characterization of peptides derivatives is reported in **Appendix I**

4.3 Preparation of peptide solutions and aggregates

Peptide solution and aggregates were prepared using different methodologies according to the solubility of monomers:

- *Direct dissolution in water.* solution of tetraphenylalanines (DOTA-L₆-F4, DTPA-L₆-F4, FF-DOTA-FF and ff-DOTA-FF, as free bases or as Gd complexes) derivatives, dinaphtylalanine peptide conjugates (DOTA-L₆-2NaI₂ and DOTA(Gd)-L₆-2NAL₂), peptide containing tyrosine (PEG₈-Y6, PEG₈-(FY)3) and of PEGylated hexaphenylalanine (PEG₁₂-F6, PEG₁₈-F6 and PEG₂₄-F6) were prepared by dissolving the lyophilized powder in

double-distilled water. If required, samples were sonicated for 15 min at 25°C.

- *Solvent switch method:* this strategy was applied for PEG₈-F6 and PEG₆-W4 derivatives. An initial solution (at 100 mgmL⁻¹) was prepared dissolving the lyophilized peptide powder in 1,1,1,3,3,3-hexafluoro-2-propanol (HFIP). Subsequently, this solution was diluted in water. The organic solvent was removed with N₂ flow.

4.4 UV-Vis peptide quantification

The final solution concentration was analytically assigned by absorbance on a UV/Vis Thermo FisherScientific Inc (Wilmington, Delaware USA) Nanodrop 2000c spectro-photometer equipped with a 1.0 cm quartz cuvette (Hellma). Molar extinction coefficients of peptide conjugates were calculating using the following molar absorptivity (ϵ) and absorption wavelength for single chromophore residue:

<i>L,D</i> -Phenylalanine	$\epsilon_{257} = 195$	$M^{-1}cm^{-1}$
<i>L</i> -2-Naphthylalanine	$\epsilon_{280} = 3035$	$M^{-1}cm^{-1}$
<i>L</i> -Tyrosine	$\epsilon_{275} = 1215$	$M^{-1}cm^{-1}$
<i>L</i> -Tryptophan	$\epsilon_{280} = 5600$	$M^{-1}cm^{-1}$

4.5 Preparation of PEG₈-F6 NBD-filled nanostructure

PEG₈-F6 NSs filled with 4-chloro-7-nitrobenzofurazan (NBD) were prepared according to solvent switch method, by dissolving fluorescent NBD dye and PEG₈-F6 peptide in HFIP. The peptide and NBD concentrations in HFIP were 100 and 10 mg mL⁻¹, respectively. This solution was ten-fold diluted in water, and the organic solvent was removed by a slow nitrogen flow.

Then, the solution was centrifuged for 5 min at 13500 rpm, and the supernatant was purified from free NBD by gel-filtration with a Sephadex G-50 column pre-equilibrated with water.

For the determination of the amount of NBD encapsulated in NSs, a sample was lyophilized and spectroscopically investigated by UV/Vis measurements at $\lambda = 340$ nm on the powder dissolved in CH₃OH. Themolar absorptivity (ϵ) at 340 nm ($9352 M^{-1}cm^{-1}$) was calculated by a calibration curve. The identity of NBD after loading in PEG₈-F6was determined by LC-MS.

4.6 Preparation of gadolinium(III) and lanthanum (III) complexes

The complexation has been carried out by adding 1:1 molar ratio of GdCl_3 or LaCl_3 salts to the aqueous solutions of the DOTA or DTPA derivatives at neutral pH and room temperature. The amount of residual free $\text{Gd}^{3+}/\text{La}^{3+}$ ions was assessed by the orange xylenol UV method²⁵⁹ and complexed by further addition of the corresponding amount of each ligand.

4.7 Fluorescence studies and determination of CAC

Fluorescence spectra and values of critical aggregate concentration (CAC) were obtained by fluorescence measurements. Fluorescence spectra were recorded at room temperature on a Jasco Model FP-750 spectrofluorophotometer in a 1.0 cm path length quartz cell. Equal excitation and emission bandwidths (5 nm) were used throughout the experiments with a recording speed of 125 nm/min and automatic selection of the time constant.

The CAC values were measured by using 8-anilino-1-naphthalene sulfonic acid ammonium salt (ANS)^{260,261} and/or Pyrene (Pyr) as fluorescent probes.²⁰¹

Small aliquots of peptide conjugate in water solutions, were added to 200 μL of aqueous solution of ANS (20 μM) or Pyr (1 μM). Final spectra, to be used for calculations, were obtained after blank correction and adjustment for dilution. The fluorescence intensity of ANS was followed as a function of the peptide concentration. The CAC values were determined by linear least-squares fitting of the fluorescence emission at 475 nm, upon excitation at 350 nm versus peptides derivatives concentration lower and higher than the change of slope. The excitation wavelength of Pyr was settled at 335 nm and spectra were recorded between 350 and 550 nm.

4.8 Circular Dichroism characterization

Far-UV CD spectra of the peptide conjugates were collected at room temperature on a Jasco J-810 spectropolarimeter equipped with a NesLab RTE111 thermal controller unit using a 0.1 mm quartz cell at 25 °C. The spectra of samples at several concentrations were recorded from 280 to 190 nm. Other experimental settings were: scan speed, 10 nm min^{-1} ; sensitivity, 50 mdeg; time constant, 16 s; bandwidth, 1 nm. Each spectrum was obtained by averaging three scans, corrected for the blank and adjusted for dilution. Ellipticities were reported as the

mean residue ellipticity (MRE), which is the ellipticity per mole of peptide divided by the number of amide bond in the building block.

4.9 Fourier Transform Infrared spectroscopy (FT-IR)

FT-IR spectra of samples (always at concentration higher than CAC) were collected on a Jasco FT/IR 4100 spectrometer (Easton, MD) in an attenuated total reflection (ATR) mode and using a Ge single-crystal at a resolution of 4 cm^{-1} . All the spectral data were processed using built-in software. Spectra were collected in transmission mode and then converted in emission. FT-IR spectra were also collected on samples at the solid state. Each sample was recorded with a total of 100 scans with a rate of $2\text{ mm}\cdot\text{s}^{-1}$ against a KBr background.

4.10 Dynamic Light Scattering (DLS):

DLS measurements were carried out using a Zetasizer Nano ZS (Malvern Instruments, Westborough, MA) that employs a 173° backscatter detector. Other instrumental settings (measurement position and attenuator) were automatically regulated by the instrument.

4.11 Congo Red (CR) spectroscopic assay

UV-Vis measurements of Congo Red (CR) alone or in presence of peptide self-assembling derivatives were carried out on Thermo Fisher Scientific Inc (Wilmington, Delaware USA) Nanodrop 2000c spectrophotometer equipped with a 1.0 cm quartz cuvette (Hellma). A stock solution of CR (3.5 mg in 500 μL) was freshly prepared in 10 mM phosphate buffer pH 7.4 and filtered through 0.2 μm syringe immediately prior to use. A small aliquot (5 μL) of this solution was diluted with the buffer at 12.5 μM final concentration and the UV-Vis spectrum was recorded between 400 and 700 nm at room temperature. Appropriate volume of peptide water solution were added to CR solution and samples were incubated for 30 min at room temperature. The spectra were recorded and background subtracted using a Congo Red spectrum in phosphate buffer as reference solution.

4.12 Congo Red staining and polarized optical birefringence assay

Dried film of peptide conjugates was prepared placing 30 μL of the peptide solution (0.25 wt %) in deionized water, onto a glass slide and left drying at room temperature. The air-dried samples were stained with 25 μL of CR solution just prepared adding a saturating amount of

CR in ethanol containing 20% of NaCl saturated water. After deposition, CR extra solution was detached from the glass slide with a filter paper. Fibers containing CR were prepared, according to the method described below in the Wide-Angle X-ray Scattering section, adding 4 μL of CR staining solution to 100 μL of peptide solution (0.25 wt%). Both film and solid fiber were observed under bright field illumination and between crossed polars using a Nikon AZ100 microscope.

4.13 Thioflavin T (ThT) spectroscopic assay

Thioflavin T associates rapidly with β -aggregated peptides giving rise to an enhanced emission at 482 nm.[35] Fluorescence spectrum of an aqueous solution of ThT (25 μM) before and after the addition of tetra-phenylalanine derivatives (2 mg/mL) was recorded at 25°C at regular intervals (each ten minutes) during two hours after the peptide addition into the cuvette. Samples were excited at 450 nm and fluorescence emission spectra were recorded between 460 and 650 nm.

4.14 ^1H NMR spectra and experiments

NMR experiments were acquired in the temperature range of 298–303 K on either a Varian Unity Inova 600 MHz spectrometer provided with a cold probe or a 400 MHz Varian instrument provided with a 5-mm triple resonance probe and z-axis pulsed-field gradients. For identification, peptide conjugates were dissolved in CD_3OD . Chemical shift and assignment are reported in Appendix 1.

For DOTA- L_6 -F2 and DOTA- L_6 -2 NaI_2 and their parental La complexes, samples were dissolved in a mixture $\text{H}_2\text{O}/\text{D}_2\text{O}$ (98% D, Armar Chemicals, Dottingen, Switzerland) 90/10 v/v with a total volume equal to 600 μL . The DOTA- L_6 -F2 was analyzed in the concentration range 0.3 mg/mL (i.e., 0.3 mM)–5.0 mg/mL (i.e., 4.8 mM); for the La-DOTA- L_6 -F2 the examined concentration range was 0.3 mg/mL (i.e., 0.3 mM)–10.0 mg/mL (i.e., 8.5 mM). The 2 NaI_2 compound was analyzed in the concentration range 0.1 mg/mL (i.e., 0.1 mM)–5.0 mg/mL (i.e., 4.4 mM) and La-2 NaI_2 in the range 0.2 mg/mL (i.e., 0.2 mM)–2.5 mg/mL (i.e., 2 mM). 1D [^1H] experiments along with a series of 2D experiments [(i.e., 2D [^1H , ^1H] TOCSY (Total Correlation Spectroscopy)²⁶² (70 ms mixing time), 2D [^1H , ^1H] NOESY (Nuclear Overhauser Enhancement Spectroscopy)²⁶³ (300 ms mixing time), and 2D [^1H , ^1H] ROESY (Rotating frame Overhauser Enhancement Spectroscopy) (200 and 250 ms mixing times)] were recorded. 1D spectra were usually acquired with a relaxation delay d1 of 1.5 s and 32–512 scans; 2D experiments were recorded with 16–64 scans, 128–256 FIDs in t1, 1024 or 2048 data points in t2.

Assignments of the DOTA-L₆-F2 and 2NaI₂-lacking the La (III) ion- were obtained at 1 mM concentration with a canonical protocol²⁶⁴ involving comparison of 2D [¹H, ¹H] TOCSY (70 ms mixing time), and 2D [¹H, ¹H] ROESY(200 ms mixing time). Water suppression was achieved by Excitation Sculpting²⁶⁵ Spectra were processed with VNMRJ (Varian by Agilent Technologies, Italy) and analyzed with NEASY²⁶⁶ comprised in the CARA software package (<http://www.nmr.ch/>).

4.15 Transmission Electron Microscopy (TEM) images.

TEM observations were performed with a transmission electron microscope FEI TECNAI G12 Spirit-Twin (LaB₆ source) equipped with a bottom mounted FEI Eagle-4k CCD camera (Eindhoven, The Netherlands), operating with an acceleration voltage of 120 kV. (LaMest Pozzuoli, Italy). A droplet of the sample solution (5.0 mg/mL) was placed onto a 400 mesh holey-carbon coated copper grid, air-dried for 1 hour, and then negatively stained with phosphotungstic acid in water solution (1wt%). Tomography holder with FEI Eagle 4K CCD camera and Xplore3D software were used to obtain digital images.

4.16 Scanning Electron Microscopy (SEM) images.

Morphological analysis of the nanostructures was carried out using field emission scanning electron microscope (Nova NanoSem 450-FEI). Samples were prepared using different samples concentration. Briefly, the samples were placed on an aluminum stub using a graphite adhesive tape. A thin coat of gold and palladium was sputtered at a current of 20 mA for 90 s. The sputter coated samples were then introduced into the specimen chamber and the images were acquired at an accelerating voltage of 2-5 kV, spot 3, through the Everhart Thornley Detector (ETD) and the Through the Lens Detector (TLD).

4.17 Wide-Angle (WAXS) and Small-Angle X-ray Scattering (SAXS)

Fiber diffraction WAXS and SAXS patterns were recorded from dried fibers prepared by the stretch frame method.²⁴³ Briefly, a droplet (10 μL) of a high concentrated peptide aqueous solution (in the range 1-3 wt %) was suspended between the ends of a wax-coated capillary (spaced 2 mm apart). The droplet was allowed to dry gently at room temperature overnight to obtain oriented fibers. WAXS and SAXS data were collected at the X-ray MicroImaging Laboratory (XMI-L@b) equipped with a Fr-E+ SuperBright rotating anode copper anode microsource (Cu

$K\alpha$, $\lambda=0.15405$ nm, 2475W), a multilayer focusing optics (Confocal Max-Flux; CMF 15-105) and a three-pinhole camera (Rigaku SMAX-3000).²⁶⁷

For WAXS in reflection mode (GIWAXS) some droplets of solutions were deposited on the top surface of Si substrate and left drying at room temperature.

For WAXS data collection an image plate (IP) detector with 100 μm pixel size was placed at 10 cm from the sample and calibrated by means of the Si NIST standard reference material (SRM 640b); for SAXS data collection a Triton 20 gas-filled photon counter detector with ~ 200 μm pixel size was placed at 2.2 m from the sample and calibrated by means of silver behenate. A detailed description of the XMI-L@b performances can be found in Altamura *et al.*²⁶⁷ and Sibillano *et al.*²⁶⁸

4.18 Fluorescence and confocal microscopy

15-20 μL of sample in solution (10 mgmL^{-1}) were deposited on a clean coverslip glass, dried and imaged with fluorescence and confocal microscopies. Immunofluorescence images were taken with a Leica DFC320 video-camera (Leica, Milan, Italy) connected to a LeicaDMRB microscope equipped with 10 V and 40 V objectives and the Image J Software (National Institutes of Health, Bethesda, MD) was used for images analysis. Confocal images were obtained with a Leica TCS-SMD-SP5 confocal microscope ($I_{\text{ex}}=405$ nm and $I_{\text{em}}=490\text{--}510$ nm). 0.8 mm-thick optical slices were acquired with a 63V or 40 V/1.4 NA objective.

4.19 Water proton relaxation measurements

The longitudinal water proton relaxation rates were measured at 25°C by using a Stelar Spinmaster (Stelar, Mede, Pavia, Italy) spectrometer operating at 0.5 T (21.5 MHz Proton Larmor Frequency), by mean of the standard inversion-recovery technique. The temperature was controlled with a Stelar VTC-91 air-flow heater equipped with a copper constantan thermocouple (uncertainty 0.1°C). The proton $1/T_1$ NMRD profiles were measured at 25°C on a fast field-cycling Stelar relaxometer over a continuum of magnetic field strengths from 0.00024 to 0.47 T (corresponding to 0.01-20 MHz proton Larmor frequencies). The relaxometer operates under computer control with an absolute uncertainty in $1/T_1$ of $\pm 1\%$. Additional data points in the range 21.5-70 MHz were obtained on the Stelar Spinmaster spectrometer.

4.20 Rheological characterization of PEG₈-(FY)3 gel

Gels of PEG₈-(FY)3 were prepared at 1.0 wt % concentration by suspending the peptide powder in water. A bath sonication was required for obtain homogeneous self-supporting gels. Inverted and sloping tube tests were performed with a sample volume of 500 μ L. Rheological measurements for 1.0 wt % PEG₈-(FY)3 self-supporting gels were performed on an AR-G2 controlled-stress rheometer (TA Instruments, USA). A parallel plate geometry was used. Oscillatory frequency (0.01-100 Hz) and strain sweep (0.01-100%) at 4°C were conducted with the aim to determine the linear viscoelastic region. Time-sweep oscillatory test was performed for one hour on 300 μ L of fresh gel at temperature of 4°C with 0.1 % strain and 1Hz frequency. All the rheological data were reported in Pascal (Pa) as G' and G'', the storage and loss moduli, respectively.

4.21 *In vitro* cytotoxicity studies

In vitro cytotoxicity was performed for DOTA(Gd)-L₆-F4 and DTPA(Gd)-L₆-F4 aggregates and for PEG₈-(FY)3 gel.

In particular, the cytotoxicity of Gd(III) probes was investigated in a mouse macrophages cell line (J774A.1) and in a mouse embryonic fibroblast cell line (3T3). J774A.1 and 3T3 cells were seeded in DMEM culture medium, enriched with 10% fetal bovine serum and 1% glutamine, at 150,000 and 50,000 cells/well respectively, in 96-well plates the day before the incubation. The cells were incubated for 3 hours (J774A.1) or overnight (3T3) at 37°C with the two Gd-based probes at different concentrations: 0.5, 1, 2, 3 and 5 mg/mL. After the incubation, cells were gently washed and re-incubated for 4 hours with 20 μ L of CellTiter-Blue® reagent for the viability test. The CellTiter-Blue® reagent is a solution containing resazurin, an indicator dye, which has little intrinsic fluorescence with the maximum absorbance at 605 nm. The reagent undergoes a “blue shift” upon reduction of resazurin to resorufin with a maximum peak at 573 nm. The fluorescence produced is proportional to the number of viable cells. The same amount of CellTiter-Blue® reagent was added to triplicate wells without cells (no-cell control) and with untreated cells (control cells) respectively. At the end of the incubation, the fluorescence at 560/590 nm was measured using the fluorometric method. The experiments were carried out in triplicate. Obtained data were analysed subtracting the mean fluorescence value of the culture background from all fluorescence values of experimental wells. The percentage of viable cells was calculated according to the following equation:

Material, methods protocols and experimental details

$$\% \text{ viable cells} = \frac{\text{experimental cells mean value}}{\text{control cells mean value}} \times 100$$

Regarding PEG₈-(FY)3 gels, the *in vitro* biocompatibility profile was studied performing elution test and live/dead assay. The cell line was Chinese Hamster Ovarian (CHO) cells, purchased from ATCC. CHO cell line was cultured in Dulbecco's Modified Eagle's medium (DMEM) supplemented with 100 U mL⁻¹ penicillin, 100 U mL⁻¹ streptomycin, 10% fetal calf serum, and 2 mmol L⁻¹ of L⁻¹ glutamine (all these materials are available at Biological Industries, Israel). The cells were stored in a wall-plate in a 5% CO₂ humidified atmosphere at the temperature of 37 °C. For elution test, 200 μL of PEG₈-(FY)3 gel at 1.0wt % were prepared in sterile condition (with UV-sterilization) and incubated overnight with 1 mL of DMEM (ratio gel-extracting media 1/5 v/v). No color change was detected for the media after the incubation and the tested pH value (7.5-7.8) was suitable for culturing. The efficient gel extraction and permeability was confirmed by its pink coloration. The extracted media was used to grow the cells for 6 hours and, after this time incubation, the viability was determined by MTT test. 20 μL of a MTT solution (5 mg/mL) in phosphate buffer saline (PBS) was added to each well. After 4 hour incubation, 100 μL of DMSO was added to extract the MTT reduced adduct (Formazan). All the samples were shaken for 20 minute to allow a complete dissolution of the precipitated Formazan in DMSO. Absorbance was measured using Tecan Spark plate reader at 570 nm. Background was measure at 680 nm. The viability was expressed as percentage. The live/dead assay was performed using a kit (Sigma Aldrich) containing FDA (6.6 μg/mL) and PI (5 μg/mL). After the addition of the two fluorescent dyes, cells were incubated for ~10 minutes in the same previously reported condition. Labeled cells were immediately viewed using a Nikon Eclipse Tifluorescent microscope and images (reported as merged figure) were captured by a ZylascMOS camera using Nikon Intensilight C-HGFI fluorescent lamp.

4.22 Cellular uptake studies

Ca. 1×10^6 J774A.1 cells, in DMEM medium, were incubated with different concentrations of DOTA(Gd)-L₆-F4 and DTPA(Gd)-L₆-F4 for 3h at 37 °C. After this incubation time, the cells were washed three times with 5 mL ice-cold phosphate-buffered saline (PBS), detached with a scraper and, for the acquisition of the MR images, collected in 50μL of PBS, transferred into glass capillaries that were centrifuged at 1500 rpm for 5 min and placed in an agar phantom. The MR images were acquired by standard T1-weighted spin-echo sequence (TE = 2.6 ms, 16 variable TR ranging from 50 to 8000 ms, NEX = 1, FOV = 1.1x1.1

cm², 1 slice, slice thickness = 1 mm) and recorded on a Bruker Avance300 operating at 7 T. After imaging, the labeled cells were suspended in 200 μ L PBS and sonicated to obtain cell lysates. Gd(III) content was measured by ICP-MS analysis (Element-2; Thermo-Finnigan, Rodano Milan, Italy). The preparation of the samples for ICP-MS analysis has been carried out as follows: i) 150 μ L of each cell lysate was mineralized with 1 mL of concentrated HNO₃ (65% v/v) under microwave heating at 160°C for 40 minutes (Milestone MicroSYNTH Microwave lab station equipped with an optical fiber temperature control and HPR-1000/6M six position high-pressure reactor, Bergamo, Italy); ii) after mineralization, the volume of each sample was brought to 2 mL with ultrapure water and the sample was analyzed by ICP-MS. The calibration curve was obtained using four gadolinium absorption standard solutions (Sigma-Aldrich) in the range 0.005-0.2 μ g/mL. The protein content of cells lysates was determined by the Bradford method using bovine serum albumin as standard.

4.23 Doxorubicin loading and leakage

A DOX solution ($1 \cdot 10^{-4}$ M) was placed in the cuvette and titrated with small amount of DOTA(Gd)-L₆-2NaI₂ peptide conjugate at 50mg/mL. The fluorescence of each sample was monitored on Jasco Model FP-750 spectrofluorophotometer as above described. Excitation wavelength was settled at 480 and UV-Vis spectra were collected between 490 and 700nm. At the end of the titration the DOX filled Gd-2NaI₂ aggregates were 10-fold diluted and the DOX fluorescence was monitored up to 72h. The extent of the DOX leakage was calculated as follows: Leakage (%) = $100 (F_i - F_0) / (F_{100} - F_0)$, where F_i represents the level of fluorescence measured for each time point, whereas F_{100} and F_0 are the fluorescence levels before and after the peptide addition in cuvette, respectively.

4.24 Molecular modelling and molecular dynamics simulation: systems and notations.

A three-dimensional model for the F6 peptide was generated by using the steric zipper structure of the hexapeptide fragment KLVFFA of the amyloid-beta peptide. In particular, the coordinates of the polymorph II (Protein Data Bank entry 3OW9²⁶⁹) refined at 1.80 Å resolution were considered. (**Figure A3 in Appendix II**) Monomers for the analyzed systems were generated using the structure of the hexapeptide fragment by replacing the non-Phe/non-Tyr/non-Trp residues of the model with Phe/Tyr/Trp. The asymmetric unit of this structure contains two copies of the peptide arranged as an antiparallel two-stranded β -

sheet. Steric zipper pairs of β -sheets were built by using the symmetry operations of KLVFFA structure space groups (C2).

Models here investigated were denoted as SH_x_ST_y_AA, where x and y indicate the number of β -sheets and β -strands per sheet, respectively; and AA indicates the number and the type of amino acid residues per chain.

MD simulations were performed using the GROMACS software package 4.5.7²⁷⁰ with the OPLS-AA force field. Starting from these structures, models composed of a single β -sheet made of fifty strands were generated. Steric zipper models were generated through the association of a pair of these sheets using the organization of the KLVFFA in the crystalline state.²⁶⁹ The energy of the structures generated by modeling was initially minimized in vacuo. Minimized models were then immersed in triclinic boxes filled with water molecules (TIP4P water model). Simulations were run by applying periodic boundary conditions. Equilibration of the system was conducted in order to stabilize the temperature (300 K) and the pressure (1 atm.). Energies were initially minimized by fixing the protein atoms and then without restraints. The Particle Mesh Ewald (PME) method (grid spacing of 0.12 nm)²⁷¹ was used to calculate the electrostatic interactions, whereas a cut off of 10 Å was applied to treat Lennard–Jones interactions. The LINCS algorithm was used to constrain bond lengths. Trajectory structures were analyzed by using in-house programs, VMD,²⁷² and GROMACS routine.²⁷⁰ The achievement of an adequate convergence in the MD simulation has been checked by calculating the root-mean-square inner product (RMSIP = 0.82) between the two halves of the equilibrated trajectory (20–60 ns and 60–100 ns).



Conclusion

General resume,
outcomes and final considerations

Conclusions and prospective

5.1 General resume, outcomes and conclusions

Peptide materials based on the aggregation of amphiphilic peptides represent a rapidly growing field within materials science. Diphenylalanine (FF or F2) homodimer has showed stimulating potentialities for the development of novel materials in fabrication, industrial, biological and medical fields. However, due to their very low solubility, research on FF-based compounds as diagnostic tools remains largely unexplored.

According to the design approach used in this thesis, it was demonstrated that water-soluble aromatic peptide building blocks could be prepared by modifying them with PEG moieties or by replacing the Phe amino acid with the more hydrophilic Tyr one. Rational design allowed also a chemical functionalization with chelating agent for MRI application.

According to the characterization, the final functional properties of the supramolecular materials were found be strongly dependent by the chemical entity of the building blocks.

The chemical features of the constituent building blocks affect also the physicochemical properties of the nanomaterials. Organization in β -sheet rich materials generates blue PL phenomenon.

MD simulation and molecular dynamics permitted a better understanding of how inner molecular organization governs the self-aggregation process. These knowledges could allow the engineering of novel supramolecular materials with enhanced functionalities.

A summary of these studies, divided in three fundamental section, is reported.

Supramolecular contrast agents for MRI application can be prepared by self-assembling of a monomer based on FF sequence. They are composed of three different moieties: a hydrophobic peptide region containing an aromatic framework, a hydrophilic portion containing a stable Gd-complex (Gd-DOTA or Gd-DTPA) and a linker (eg. PEG) interposed between the aromatic framework and the Gd-complex. The insertion of the linker permits to increase the solubility and to distance the Gd-complex from the aggregating motif. Indeed, the spatial proximity of the bulk gadolinium complex to the aromatic FF framework causes the loss of the intermolecular π - π interactions.

Results of this thesis demonstrate that the elongation of the peptide framework (F4 in place of F2) could restore the aromatic interactions. Nanostructures prepared according to this strategy showed common structural features ascribable to amyloid like structure rich in antiparallel β -sheet.

As expected for supramolecular MRI CAs, these NSs present enhanced relaxivity properties with respect to the classical contrast agents at low molecular weight (Gd-DOTA and Gd-DTPA). Surprising the T_R values extracted from the fitting procedure are quite short if compared to those usually found for nano-sized aggregates. These low T_R values can be attributed to the occurrence of a quite fast internal motility of the Gd-complexes along the linker spacer with respect to the overall fibril-like structures.

Due to the significant internalization efficiency and to the high relaxivity values, these NSs are able to enhance the MRI cellular response on J774A.1 mouse macrophages cell line in which the cytotoxicity of the fibril nanoaggregates was negligible with an incubation time of 3h in the 0.5-5.0 mg/mL concentration range

Moreover, the different positioning of the chelating agent in to the aromatic framework (at the center or at the N-terminus of the F4-motif) can deeply affect both the structural behavior and the relaxivity properties of the supramolecular CAs.

A lower tendency to self-assemble in derivatives having the Gd-complex positioned at the center of the peptide aromatic framework was detected. Well structured fibrillary and intricate networks, appear at 50 mg/mL. At this concentration relaxivity values are lower ($11 \text{ mM}^{-1}\text{s}^{-1}$) than the relaxivity ones observed for analogues with the Gd-complex at the end of framework.

This decrease is related to major flexibility of the Gd-complex on the supramolecular aggregate. The proposed model well explain as the Gd-DOTA complex, pointing far from the spine of the aggregate, is free to move. Instead, peptide backbone folding in an antiparallel β -arrangement allows the spacial approach of phenyl rings of the C and N termini permitting their T-shape staking.

The replacement of Phe in the homodimer with non coded amino acids (such as 2Nal), having a more extended aromatic ring in its side chain, permit to restore in dipeptide π - π interactions and to prompt self-assembly of Gd-conjugates.

Gd-2Nal₂ peptide derivative begins to self-aggregate at $\sim 0.1 \text{ mg/mL}$ ($75 \mu\text{M}$), forming stable amiloid like NSs when concentration is about 10-fold higher ($\sim 1.0 \text{ mg/mL}$). This CAC value, assessed by fluorescence and proton NMR spectroscopies, is higher than the value (0.076 mg/mL) found for tetraphenylalanine Gd-complex Gd-DOTA-L₆-F4. At the atomic level, the peptide conjugates in the aggregates assume a β sheet secondary structure with an antiparallel orientation of single strands and above 5.0 mg/mL , long fibrillary nanostructures appear. Moreover, above 20 mg/mL , gelification phenomena are observed.

These gels are suitable reservoirs for the encapsulation of anticancer drugs like doxorubicin. The high values of r_{1p} ($12.3 \text{ mM}^{-1}\text{s}^{-1}$ at 20 MHz)

and the capability to encapsulate the doxorubicin anticancer drug suggest a potential use of Gd-2NaI₂ nanostructures as theranostic systems.

However, before an *in vivo* applications of these novel class of theranostic agents, several issues have to be improved. For example, the insertion of structural elements able to confer rigidity to the molecules without to alter their solubility could lead to higher relaxivity values. Moreover, the achievement of lower CAC values could permit lowering the toxicity effects associated to these nanostructures.

According to the literature, photoluminescence (PL) phenomena have been observed in fibrillary networks like amyloid fibrils and in others peptide based nanostructures, with a high content of cross- β structures. On the evidence that containing Phe peptides generate supramolecular systems rich in β -organization, a novel monomer, PEG₈-F6, was designed and synthesized.

As expected, PEG₈-F6 is able to self-organize in NSs, rich in β -sheet structures and show PL upon excitation at 370 or at 410 nm.

However, the intensity of fluorescence emitted by these structures is almost weak and the signal remains confined in the near-Vis region.

The development of biocompatible peptide nanostructures as bioimaging tools requires the improvement of their performance in terms of PL intensity and of wavelength range compatible with *in vivo* applications.

A possible strategy to pursue could be the tight association (encapsulation, binding or absorption) of a small fluorescent dye like NBD to the photoluminescent NS.

The close proximity, at the atomic level, between the dye and the nanostructure should promote the energy transfer. With this goal in the mind, 4-Chloro-7-nitrobenzofurazan (NBD) dye was encapsulated in PEG₈-F6 NSs.

The entrapment of NBD in these NSs effectively causes a red-shift from 460 to 530 nm that was attributed to a FRET phenomenon.

The comparison between the structural data of empty and NBD filled PEG₈-F6 NSs suggests that NBD dye is arranged out from the dry interface of the NS, but it remains close enough to the origin of the PL to accept the energy transfer.

The capability to transfer fluorescence between the NS and the dye is kept even when the dye is covalently bound to the peptide nanostructure. These evidences leave to envisage new stimulating feature applications for dye encapsulating peptides as innovative biomaterials. Encapsulation or conjugation of small molecule dyes in/to NSs, represent an alternative and complementary strategy for the detection of the aggregation process of endogenous proteins, which, in

their physio-pathological form, are known to adopt a cross- β structural motif.

It was also demonstrated that the PEG length and its composition could alter the structural and optoelectronic properties of the final material. These findings arise from the compared study carried out along PEG series peptides (PEG₈-F6, PEG₁₂-F6, PEG₁₈-F6, PEG₂₄-F6, PEG_{MW1300}-F6).

Independently from the PEG length and from the number of amide bonds, all the peptide NSs display cross- β like secondary structure with an antiparallel β -strand arrangement. However, a certain decrease of the fiber order was observed along the series (PEG₈>PEG₁₂>PEG₁₈>PEG₂₄). All the peptide nanostructures exhibit the expected blue-PL emission at 460 nm upon excitation at 370 or at 410 nm.

Beyond this blue fluorescence emission, PEG₂₄-F6 shows an additional green-PL emission at 530 nm when excited at 460 nm.

This different optoelectronic behavior could be plausibly attributed to the higher number of amide bonds along the PEG chain, that may either produce a more extended electron delocalization via hydrogen bonds or a fine re-adjustment of the cross β -structure of the peptide spine.

Due to ample debate on the origins of PL phenomenon, it is not possible to completely exclude that others factors that can affect the PL behavior. The interpretation of the PL properties of PEG₂₄-F6 could represent an interesting challenge for future studies.

The π - π stacking interactions between the side chains of aromatic amino acids were used as one of the main driving force towards to the self-assembling of aromatic oligopeptides or polymer-peptides.

Ad hoc modifications of the peptide sequence or a derivatization of the sequence with PEG chains or with chelating agents can deeply affects the structural organization of the nanostructure.

By a chemical prospective, it was explored and studied the replacement of the Phe residue with the two other coded aromatic amino acids, Trp and Tyr.

As expected on the basis of the different solubility of these three amino acids (Trp, Tyr and Phe), Tyr containing peptides showed a higher solubility with respect to Phe containing peptides and their solubilization was achieved directly in water also at high concentrations.

On the other hand, Trp containing peptide (PEG₆-W4) showed a smaller water solubility with respect to the analog containing the same number of Phe residues (PEG₆-F4).

The structural characterization performed in solution highlights a similar behavior of all the studied peptide derivatives: at micromolar

concentration, these systems share a common mechanism of self-assembling, hypnotized by an aromatic collapse.

The novel peptide conjugates are characterized by the formation of nanostructures, rich in antiparallel β -sheets.

However, at the solid state, significant structural differences were observed for the peptide containing Tyr and Trp. TEM, SEM, WAXS/SAXS studies and MD simulations confirmed these differences. Due to the different sizes of Trp and Phe residues, the distance of the dry interface between the two facing β -sheets of PEG₆-W4 is larger than that observed in PEG₆-F4.

Instead, Tyr have a size similar to the Phe, but the phenolic group in its side chain favors a major number of hydrogen bonding interactions with water molecules or main chain carbonyls with respect to the Phe residue. In Tyr rich peptides (Y6), self-assembly occurs through the tight lateral association of Tyr side chains and networks of inter-sheet H-bonds contribute to the overall stability of the Tyr interface.

However, the more polar and solvated interface with respect F6 oligo peptide partially limits the formation of large ordered fibers. Due to the limited self-assembly tendency, in PEG₈-Y6, PEG moiety is able to induce crystallization effects.

In (FY)3, MD simulations suggest the formation of two well-distinguishable interfaces: a dry interface (Phe-interface) stabilized by inter-sheet π -stacking interaction and a wet interface (Tyr-interface) stabilized by both intra-sheet and inter-sheet H-bonds.

At macroscopic level, only PEG₈-(FY)3 showed stable soft hydrogels above 1.0 wt%.

This evidence can be attributable to the higher tendency of Tyr to establish extended hydrogen bonding networks and to achievement in the molecule of an efficient compromise between hydrophobicity/hydrophilicity.

The good water solubility and the low toxicity of PEG₈-(FY)3 suggest that this polymer-peptide could be fruitfully exploited for generating self-supporting biocompatible hydrogels.

Conclusions and prospective



Appendixes

Characterization data
and supporting informations

Carlo Diaferia | University of Naples Federico II | XXX cycle

6.1 Appendix I

The Appendix I gathers together all the chemical shift and assignment from $^1\text{H-NMR}$ spectroscopy, retention time in HPLC, real and calculated conjugates masses and their molecular formulas.

Some $^1\text{H-NMR}$ spectra, mass spectra and analytical HPLC profiles (channel 210 nm) are reported as identification and characterization examples.

DTPA-F2: $^1\text{H-NMR}$ (CD_3OD) (chemical shifts in δ , CH_3OH as internal standard 3.55) = 7.51-7.42 (m, 10 *CH* aromatic), 4.96-4.86 (m, 2H, *CH* Phe α), 4.65-4.40 (dd, 2H, $\text{R}_2\text{NCH}_2\text{CONHR}$), 3.87 (s, 8H, $\text{R}_2\text{NCH}_2\text{COOH}$), 3.53-3.50 (m, 4H, $\text{R}_2\text{NCH}_2\text{CH}_2\text{NR}_2$), 3.42-3.31 (m, 4H, $\text{R}_2\text{NCH}_2\text{CH}_2\text{NR}_2$), 3.24-2.99 (m, 4H, *CH*₂ Phe β). Retention time in **Method I**, $R_t = 10.34$ min; MS (ESI+): m/z 686.1 calcd. For $\text{C}_{32}\text{H}_{42}\text{N}_6\text{O}_{11}$: $[\text{M}+\text{H}^+] = 687.5$.

DOTA-F2: $^1\text{H-NMR}$ (CD_3OD) (chemical shifts in δ , CH_3OH as internal standard 3.55) = 7.51-7.42 (m, 10 *CH* aromatic), 4.86-4.75 (m, 2H, *CH* Phe α), 3.70 (s, 6H, $\text{R}_2\text{NCH}_2\text{COOH}$), 3.45 (s, 16H, $\text{R}_2\text{N-CH}_2\text{CH}_2\text{NR}_2$), 3.40-3.36 (m, 2H, $\text{R}_2\text{NCH}_2\text{CONH}$), 3.16-2.90 (m, 4H, *CH*₂ Phe β). Retention time in **Method I**, $R_t = 10.65$ min; MS (ESI+): m/z 698.3 calcd. For $\text{C}_{34}\text{H}_{46}\text{N}_6\text{O}_{10}$: $[\text{M}+\text{H}^+] = 698.6$.

DTPA-L₂-F2: $^1\text{H-NMR}$ (CD_3OD) (chemical shifts in δ , CH_3OH as internal standard 3.55) = 7.51-7.42 (m, 10 *CH* aromatic), 4.96-4.86 (m, 2H, *CH* Phe α), 4.55 (s, 2H, $\text{R}_2\text{NCH}_2\text{CONHR}$), 3.87 (s, 8H, $\text{R}_2\text{NCH}_2\text{COOH}$), 3.79 (s, 4H, $\text{OCH}_2\text{CH}_2\text{O}$), 3.75 (t, 2H, $\text{RNHCH}_2\text{CH}_2\text{O}$), 3.65 (s, 2H, OCH_2COR), 3.60 (t, 2H, $\text{RNHCH}_2\text{CH}_2\text{O}$), 3.53-3.50 (m, 4H, $\text{R}_2\text{NCH}_2\text{CH}_2\text{N R}_2$), 3.42-3.31 (m, 4H, $\text{R}_2\text{NCH}_2\text{CH}_2\text{NR}_2$), 3.24-2.99 (m, 4H, *CH*₂ Phe β). Retention time in

Method 1, $R_t = 11.19$ min; MS (ESI+): m/z 831.2 calcd. For $C_{38}H_{53}N_7O_{14}$: $[M+H^+] = 831.7$.

DOTA-L₂-F2: 1H -NMR (CD_3OD) (chemical shifts in δ , CH_3OH as internal standard 3.55) = 7.51-7.42 (m, 10 *CH* aromatic), 4.86-4.75 (m, 2H, *CH* Phe α), 3.79 (s, 4H, OCH_2CH_2O), 3.75 (t, 2H, $RNH-CH_2CH_2O$), 3.70 (s, 6H, R_2NCH_2COOH), 3.65 (s, 2H, OCH_2COR), 3.60 (t, 2H, $RNH-CH_2CH_2O$), 3.45 (s, 16H, $R_2N-CH_2CH_2NR_2$), 3.40-3.36 (m, 2H, R_2NCH_2CONH), 3.16-2.90 (m, 4H, *CH*₂ Phe β). Retention time in **Method 1**, $R_t = 11.42$ min; MS (ESI+): m/z 843.2 calcd. For $C_{40}H_{57}N_7O_{13}$: $[M+H^+] = 843.7$.

DTPA-L₆-F2: 1H -NMR (CD_3OD) (chemical shifts in δ , CH_3OH as internal standard 3.55) = 7.51-7.42 (m, 10 *CH* aromatic), 4.86-4.75 (m, 2H, *CH* Phe α), 4.55 (s, 2H, R_2NCH_2CONHR), 3.87 (s, 8H, R_2NCH_2COOH), 3.80 (s, 22H, OCH_2CH_2O), 3.75 (t, 2H, $RNHCH_2CH_2O$), 3.68 (t, 2H, $RNHCH_2CH_2O$), 3.40-3.32 (m, 6H, $R_2NCH_2CH_2NR_2$), 3.27-3.20 (dd, 2H, $R_2NCH_2CH_2NR_2$), 3.16-2.90 (m, 4H, *CH*₂ Phe β). 2.58 (t, 2H, $NHCOCH_2CH_2$). Retention time in **Method 1**, $R_t = 12.10$ min; MS (ESI+): m/z 1020.0 calcd. For $C_{47}H_{70}N_7O_{18}$: $[M+H^+] = 1020.8$.

DOTA-L₆-F2: 1H -NMR (CD_3OD) (chemical shifts in δ , CH_3OH as internal standard 3.55) = 7.51-7.42 (m, 10 *CH* aromatic), 4.86-4.75 (m, 2H, *CH* Phe α), 3.80 (s, 22H, OCH_2CH_2O), 3.75 (t, 2H, $RNHCH_2CH_2O$), 3.70 (s, 6H, R_2NCH_2COOH), 3.60 (t, 2H, $RNHCH_2CH_2O$), 3.45 (s, 16H, $R_2NCH_2CH_2NR_2$), 3.40-3.36 (m, 2H, R_2NCH_2CONH), 3.16-2.90 (m, 4H, *CH*₂ Phe β), 2.58 (t, 2H, $NHCOCH_2CH_2O$). Retention time in **Method 1**, $R_t = 12.33$ min; MS (ESI+): m/z 1032.8 calcd. For $C_{49}H_{76}N_8O_{16}$: $[M+H^+] = 1233.1$.

L₆-F4: ¹H-NMR (CD₃OD) (chemical shifts in δ, CH₃OH as internal standard 3.55) = 7.51-7.42 (m, 20 CH aromatic), 4.86-4.75 (m, 4H, CH Phe α), 3.80 (s, 22H, OCH₂CH₂O), 3.75 (t, 2H, RNHCH₂CH₂O), 3.60 (t, 2H, RNHCH₂CH₂O), 3.16-2.90 (m, 8H, CH₂ Phe β), 2.58 (t, 2H, NHCOCH₂CH₂O). Retention time in *Method 1*, R_t = 15.30 min; MS (ESI+): m/z 939.5 calcd. For C₅₁H₆₇N₆O₁₁: [M+H⁺] = 939.9

DTPA-L₆-F4: ¹H-NMR (CD₃OD) (chemical shifts in δ, CH₃OH as internal standard 3.55) = 7.51-7.42 (m, 20 CH aromatic), 4.86-4.75 (m, 4H, CH Phe α), 4.55 (s, 2H, R₂NCH₂CONHR), 3.87 (s, 8H, R₂NCH₂COOH), 3.80 (s, 22H, OCH₂CH₂O), 3.75 (t, 2H, RNHCH₂CH₂O), 3.68 (t, 2H, RNHCH₂CH₂O), 3.40-3.32 (m, 6H, R₂NCH₂CH₂NR₂), 3.27-3.20 (dd, 2H, R₂NCH₂CH₂NR₂), 3.16-2.90 (m, 8H, CH₂ Phe β), 2.58 (t, 2H, NHCOCH₂CH₂). Retention time in *Method 1*, R_t = 14.54 min; MS (ESI+): m/z 1314.4 calcd. For C₆₅H₈₈N₉O₂₀: [M+H⁺] = 1315.1

DOTA-L₆-F4: ¹H-NMR (CD₃OD) (chemical shifts in δ, CH₃OH as internal standard 3.55) = 7.51-7.42 (m, 20 CH aromatic), 4.86-4.75 (m, 4H, CH Phe α), 3.80 (s, 22H, OCH₂CH₂O), 3.75 (t, 2H, RNHCH₂CH₂O), 3.70 (s, 6H, R₂NCH₂COOH), 3.60 (t, 2H, RNHCH₂CH₂O), 3.45 (s, 16H, R₂NCH₂CH₂NR₂), 3.40-3.36 (m, 2H, R₂NCH₂CONH), 3.16-2.90 (m, 8H, CH₂ Phe β), 2.58 (t, 2H, NHCOCH₂CH₂O). Retention time in *Method 1*, R_t = 14.59 min; MS (ESI+): m/z 1326.8 calcd. For C₆₅H₈₈N₉O₂₀: [M+H⁺] = 1327.2

DOTA-L₆-(2NaI)₂ [2NaI₂]: ¹H-NMR (CD₃OD) (chemical shifts in δ, CH₃OH as internal standard 3.55) = 7.51-7.42 (m, 10 CH aromatic), 4.86-4.75 (m, 2H, CH Phe α), 3.80 (s, 22H, OCH₂CH₂O), 3.75 (t, 2H, RNHCH₂CH₂O), 3.70 (s, 6H, R₂NCH₂COOH), 3.60 (t, 2H, RNHCH₂CH₂O), 3.45 (s, 16H,

$R_2NCH_2CH_2NR_2$), 3.40-3.36 (m, 2H, R_2NCH_2CONH), 3.16-2.90 (m, 4H, CH_2 Phe β), 2.58 (t, 2H, $NHCOCH_2CH_2O$). Retention time in **Method 1**, $R_t = 14.71$ min; MS (ESI+): m/z 1132.8 calcd. For $C_{57}H_{80}N_8O_{16}$: $[M+H^+] = 1133.8$; $[M+Na^+] = 1155.7$; $[M+2H^+]/2 = 568.1$

FF-AdOO-Lys(DOTA)-AdOO-FF [FF-DOTA-FF] and ff-AdOO-Lys(DOTA)-AdOO-FF [ff-DOTA-FF]: 1H -NMR (CD_3OD) (chemical shifts in δ , CH_3OH as internal standard 3.55) = 7.51-7.42 (m, 20 CH aromatic), 4.98-4.76 (m, 4H, CH Phe α), 4.3 (dd, 1H, CH Lys α), 3.72 (s, 12H, OCH_2CH_2O), 3.70 (s, 6H, R_2NCH_2COOH), 3.68 (t, 4H, $RNH-CH_2CH_2O$), 3.65 (s, 4H, OCH_2COR), 3.45 (s, 16H, $R_2N-CH_2CH_2NR_2$), 3.40-3.36 (m, 2H, R_2NCH_2CONH), 3.36-3.25 (m, 8H, CH_2 Phe β), 3.27-3.20 (dd, 2H, $R_2N-CH_2CH_2NR_2$), 3.1 (m, 2H, CH_2 Lys ϵ), 1.90 (m, 2H, CH_2 Lys β), 1.6 (m, 2H, CH_2 Lys δ), 1.45 (m, 2H, CH_2 Lys γ). Retention time in **Method 1** $R_t = 12.65$ min; MS (ESI+): m/z 1407.5 calcd. For $C_{70}H_{99}N_{13}O_{18}$: $[M+H^+] = 1408.5$

DOTA-L₆-(2NaI)₂ [2NaI₂]: 1HNMR (CD_3OD) (chemical shifts in δ , CH_3OH as internal standard 3.55) = 7.51-7.42 (m, 10 CH aromatic), 4.86-4.75 (m, 2H, CH Phe α), 3.80 (s, 22H, OCH_2CH_2O), 3.75 (t, 2H, $RNHCH_2CH_2O$), 3.70 (s, 6H, R_2NCH_2COOH), 3.60 (t, 2H, $RNHCH_2CH_2O$), 3.45 (s, 16H, $R_2NCH_2CH_2NR_2$), 3.40-3.36 (m, 2H, R_2NCH_2CONH), 3.16-2.90 (m, 4H, CH_2 Phe β), 2.58 (t, 2H, $NHCOCH_2CH_2O$). Retention time in **Method 1** $R_t = 12.17$ min; MS (ESI+): m/z 1132.8 calcd. For $C_{57}H_{80}N_8O_{16}$: $[M+H^+] = 1133.8$; $[M+Na^+] = 1155.7$; $[M+2H^+]/2 = 568.1$.

PEG₈-F6: 1H -NMR (CD_3OD) (chemical shifts in δ , CH_3OH as internal standard 3.55) = 7.51-7.42 (m, 30 CH aromatic), 4.86-4.75 (m, 6H, CH Phe α), 3.80 (s, 16H, OCH_2CH_2O), 3.75 (t, 8H, $RNH-CH_2CH_2O$), 3.65 (s, 8H, OCH_2COR), 3.60 (t, 8H, $RNH-CH_2CH_2O$), 3.16-2.90 (m, 12H, CH_2 Phe β).

Retention time in **Method 2** $R_t = 14.05$ MS (ESI+): m/z 1480.7 calcd. for $C_{78}H_{101}N_{11}O_{18}$: $[M+H^+] = 1480.9$

PEG₁₂-F6: 1H -NMR (CD_3OD) (chemical shifts in δ , CH_3OH as internal standard 3.55) = 7.51-7.42 (m, 30 CH aromatic), 4.86-4.75 (m, 6H, CH Phe α), 3.80 (s, 44H, OCH_2CH_2O), 3.75 (t, 4H, $RNHCH_2CH_2O$), 3.60 (t, 4H, $RNHCH_2CH_2O$), 3.16-2.90 (m, 12H, CH_2 Phe β), 2.58 (t, 4H, $NHCOCH_2CH_2O$). Retention time in **Method 1** $R_t = 12.50$ MS (ESI+): m/z 1570.7 calcd. for $C_{84}H_{115}N_9O_{20}$: $[M+H^+] = 1572.1$

PEG₁₈-F6: 1H -NMR (CD_3OD) (chemical shifts in δ , CH_3OH as internal standard 3.55) = 7.51-7.42 (m, 30 CH aromatic), 4.86-4.75 (m, 6H, CH Phe α), 3.80 (s, 66H, OCH_2CH_2O), 3.75 (t, 6H, $RNHCH_2CH_2O$), 3.60 (t, 6H, $RNHCH_2CH_2O$), 3.16-2.90 (m, 12H, CH_2 Phe β), 2.58 (t, 6H, $NHCOCH_2CH_2O$). Retention time in **Method 1** $R_t = 11.90$ MS (ESI+): m/z 1905.5 calcd. for $C_{99}H_{144}N_{10}O_{27}$: $[M+H^+] = 1906.6$

PEG₂₄-F6: 1H -NMR (CD_3OD) (chemical shifts in δ , CH_3OH as internal standard 3.55) = 7.51-7.42 (m, 30 CH aromatic), 4.86-4.75 (m, 6H, CH Phe α), 3.80 (s, 88H, OCH_2CH_2O), 3.75 (t, 8H, $RNHCH_2CH_2O$), 3.60 (t, 8H, $RNHCH_2CH_2O$), 3.16-2.90 (m, 12H, CH_2 Phe β), 2.58 (t, 8H, $NHCOCH_2CH_2O$) Retention time in **Method 1** $R_t = 11.22$ MS (ESI+): m/z 2240.5 calcd. for $C_{99}H_{144}N_{10}O_{27}$: $[M+H^+] = 2243.0$

Y6: 1H -NMR (CD_3OD) (chemical shifts in δ , CH_3OH as internal standard 3.55) = 7.26-7.14 (m, 6 $CH\delta$ aromatic Tyr), 6.88-6.85 (m, 6 $CH\epsilon$ aromatic Tyr), 4.77-4.58 (m, 6H, CH α of Tyr), 3.28-2.92 (m, 12H, CH_2 β of Tyr). Retention time in **Method 3** $R_t = 13.30$ min, MS (ESI+): m/z 966.1 calcd. for $C_{54}H_{57}N_7O_{12}$: $[M+H^+] = 967.1$

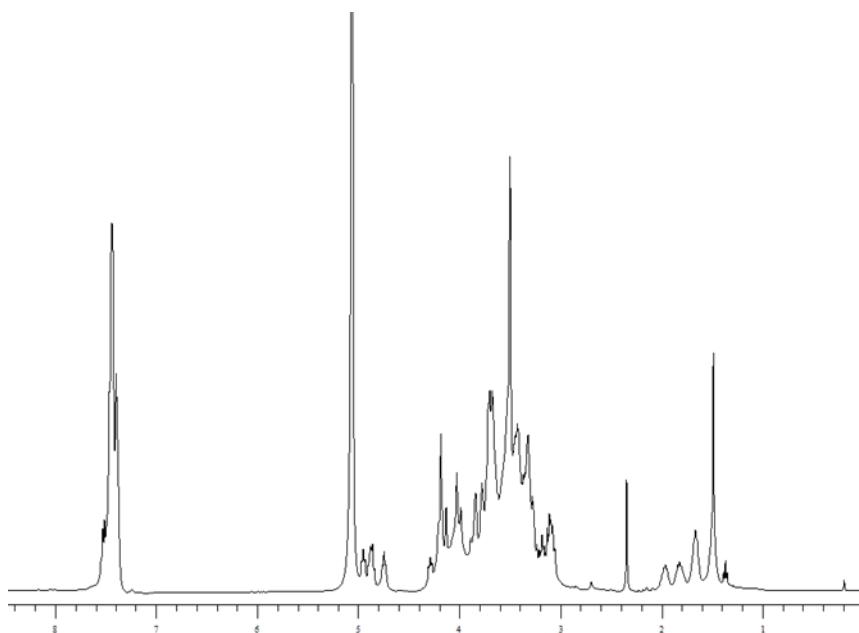
PEG₈-Y6: ¹H-NMR (CD₃OD) (chemical shifts in δ, CH₃OH as internal standard 3.55) = 7.18-7.10 (m, 6 CH δ aromatic Tyr), 6.91-6.82 (m, 6 CH ϵ aromatic Tyr), 4.73-4.51 (m, 6H, CH α Tyr), 3.87 (s, 16H, OCH₂CH₂O), 3.82 (t, 8H, RNH-CH₂CH₂O), 3.74-3.71 (m, 8H, OCH₂COR), 3.63 (t, 8H, RNH-CH₂CH₂O), 3.31-2.92 (m, 12H, CH₂ β of Tyr). Retention time in *Method 3* R_t = 11.56 min, MS (ESI+): m/z 1576.7 calcd. for C₇₈H₁₀₁N₁₁O₂₄: [M+H⁺] = 1577.7

(FY)3: ¹H-NMR (CD₃OD) (chemical shifts in δ, CH₃OH as internal standard 3.55) = 7.48-7.35 (m, 15 CH aromatic Phe), 7.18-7.10 (m, 6 CH δ aromatic Tyr), 6.88-6.85 (m, 6 CH ϵ aromatic Tyr), 4.81-4.54 (m, 6H, CH α of Phe and Tyr), 3.35-2.94 (m, 12H, CH₂ β of Phe and Tyr). Retention time in *Method 3* R_t = 14.52 min, MS (ESI+): m/z 948.1 calcd. for C₅₄H₅₇N₇O₉: [M+H⁺] = 949.1

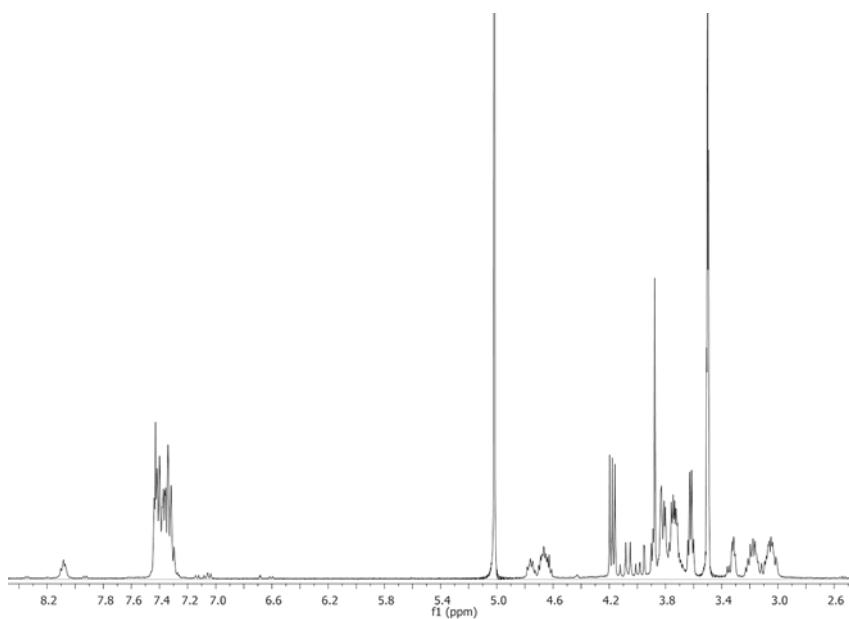
PEG₈-(FY)3: ¹H-NMR (CD₃OD) (chemical shifts in δ, CH₃OH as internal standard 3.55) = 7.48-7.35 (m, 15 CH aromatic Phe), 7.18-7.10 (m, 6 CH δ aromatic Tyr), 6.88-6.85 (m, 6 CH ϵ aromatic Tyr), 4.81-4.54 (m, 6H, CH α of Phe and Tyr), 3.83 (s, 16H, OCH₂CH₂O), 3.80 (t, 8H, RNH-CH₂CH₂O), 3.75-3.72 (m, 8H, OCH₂COR), 3.63 (t, 8H, RNH-CH₂CH₂O), 3.35-2.94 (m, 12H, CH₂ β of Phe and Tyr). Retention time in *Method 3* R_t = 12.21 min, MS (ESI+): m/z 1528.7 calcd. for C₇₈H₁₀₁N₁₁O₂₁: [M+H⁺] = 1526.7

PEG₆-W4: ¹H-NMR (CD₃OD) (chemical shifts in δ, CH₃OH as internal standard 3.55) = 7.51-7.42 (m, 30 CH aromatic), 4.86-4.75 (m, 6H, CH Phe α), 3.80 (s, 16H, OCH₂CH₂O), 3.75 (t, 8H, RNH-CH₂CH₂O), 3.65 (s, 8H, OCH₂COR), 3.60 (t, 8H, RNH-CH₂CH₂O), 3.16-2.90 (m, 12H, CH₂ Phe β). Retention time in *Method 4* R_t = 17.67 min, MS (ESI+): m/z 1096.5 calcd. for C₇₈H₁₀₁N₁₁O₁₈: [M+H⁺] = 1097.6

6.1.2 ^1H NMR spectra

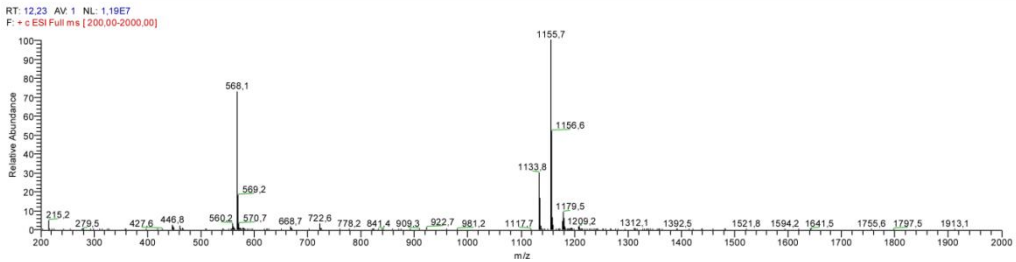
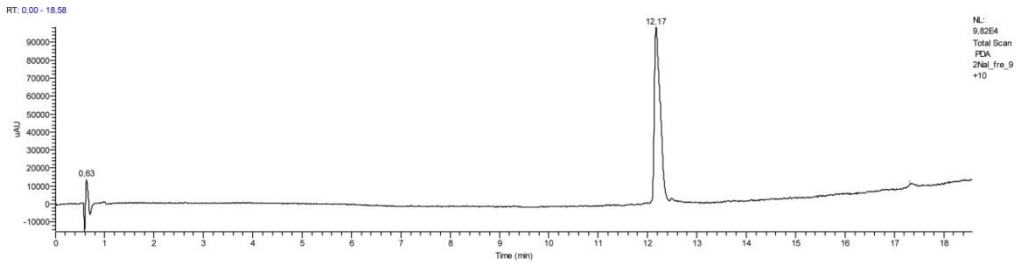


FF-AdOO-Lys(DOTA)-AdOO-FF [FF-DOTA-FF] and ff-AdOO-Lys(DOTA)-AdOO-FF [ff-DOTA-FF]

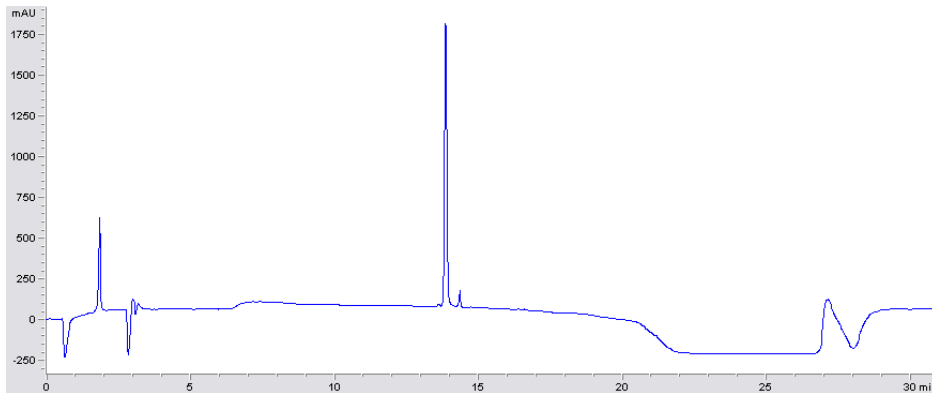


PEG₈-F6

6.1.3 HPLC chromatograms and mass spectrometry



LC-MS spectra for 2NaI₂



(FY)3 Method 3, $R_t=14.52$

6.2 Appendix II

In the Appendix II are collected additional and supporting data for the Result and discussion chapter. Miller indices, d-spacing and unit cell measurements obtained with CLEARER softer for DOTA(Gd)-L₆-F4 and L₆-F4 are inserted in Table A1 and A2.

Biocompatibility study about Gd-2NaI₂ in 10 mM phosphate buffer 0.9 wt.% NaCl was conducted analyzing the HPLC profile of the compound in during the time.

Assignment and chemical shift for protons in of F2-L₆-DOTA and 2NaI₂ and TOCSY/NOESY spectra are reported in Table A3 and A4 and Figure A2, respectively.

Parameter and initial crystal structure for F6 spine are in Table A5 and Figure A3.

Table A1: Miller indices and d-spacings (calculated and observed) for DOTA(Gd)-L₆-F4 fiber determined using the software *CLEARER*. The results provided an orthorhombic unit cell ($\alpha = \beta = \gamma = 90^\circ$), in which the axis values are $a = 4.8 \text{ \AA}$, $b = 29.6 \text{ \AA}$, $c = 56.3 \text{ \AA}$.

Miller Indices			d-Spacings (\AA)	
<i>h</i>	<i>k</i>	<i>l</i>	calculated	observed
0	1	1	26.21967	26.144491
0	2	11	4.8347726	4.8291917
0	2	0	14.817239	14.834262
0	2	3	11.626327	11.547104
0	1	7	7.7571564	7.8169746
0	2	8	6.3534093	6.3533344
0	6	6	4.369945	4.3705463

Table A2: Miller indices and d-spacings (calculated and observed) for L₆-F4 fiber determined using the software CLEARER. The results provided an orthorhombic unit cell ($\alpha = \beta = \gamma = 90^\circ$), in which the axis values are $a = 4.8 \text{ \AA}$, $b = 27.6 \text{ \AA}$, $c = 46.4 \text{ \AA}$.

Miller Indices			d -Spacings (Å)	
<i>h</i>	<i>k</i>	<i>l</i>	calculated	observed
0	1	1	23.725834	23.991104
0	2	1	13.233081	13.298952
0	6	0	4.602433	4.596377
0	7	2	3.8890448	3.8920898
0	2	0	13.8073	13.804399
0	1	4	10.688595	10.701209
0	3	6	5.9187117	5.9088035
0	0	11	4.2153335	4.2161417

Figure A1: Reverse phase HPLC profiles of Gd-2NaI₂ in 10 mM phosphate buffer 0.9 wt.% NaCl at pH 7.4 at time t=0 (a) and t=240 h (b).

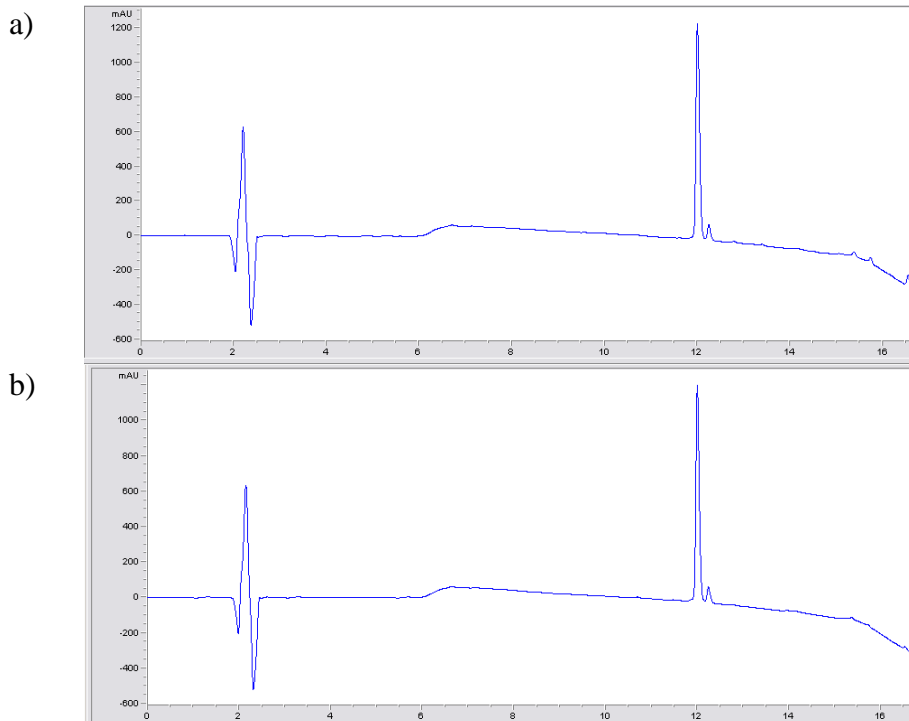


Table A3: Chemical shifts of F2-L₆-DOTA (1mM concentration) at 298 K

F2-L ₆ -DOTA				
	HN	H α	H β	Others
F1	8.12	4.51	2.94-2.87	Aromatics 7.14 7.31
F2	8.17	4.52	3.12-2.88	Aromatics 7.24 7.34 CONH2 7.06-7.00
L6	NHCO CH2 2.43 NHCOCH2 CH2 3.62 NH CH2CH2 3.58, 3.34 NH CH2CH2 8.05 O CH2CH2 O 3.52, 3.57			
DOTA	3.77, 3.33, 3.11			

Table A4: Chemical shifts of 2NaI₂ (1mM concentration) at 298 K.

2NaI ₂				
	HN	H α	H β	Others
NAL1	7.97	4.53	2.94	Aromatics: 7.45, 7.18, 7.75
NAL2	8.15	4.63	3.32-3.00	Aromatics: 7.67, 7.38, 7.85 CONH2 7.10-6.89
L6	NHCOCH ₂ 2.19, 2.12 NHCOCH ₂ CH ₂ 3.40, 3.30 NHCH ₂ CH ₂ 3.52, 3.30 NHCH ₂ CH ₂ 7.98 OCH ₂ CH ₂ O 3.52, 3.57			
DOTA	3.69, 3.24, 3.03			

Figure A2: A) TOCSY 70 (left panel) and ROESY 200 (right panel) spectra of DOTA-L₆-F2 (1 mM concentration). B) TOCSY 70 (left panel) and ROESY 250 (right panel) NMR spectra of 2NaI₂ (1 mM concentration).

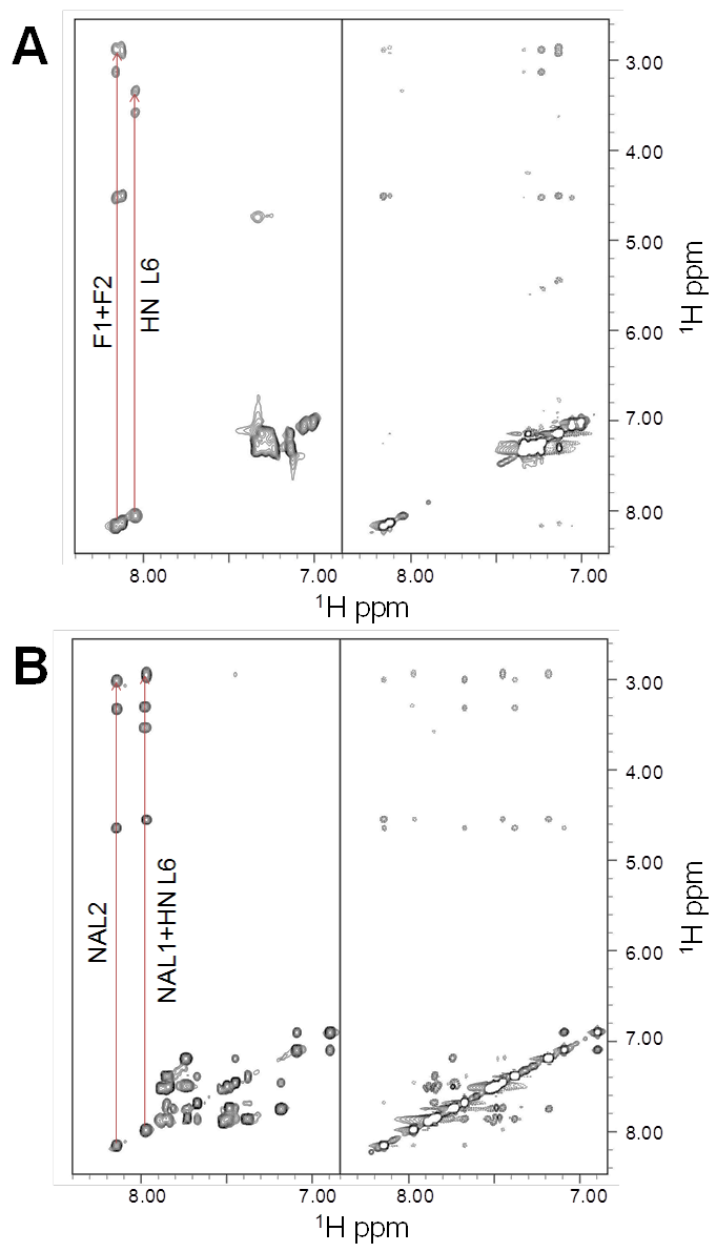
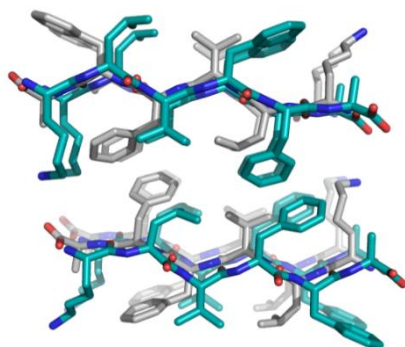


Table A5: MD simulation parameters for F6 spine

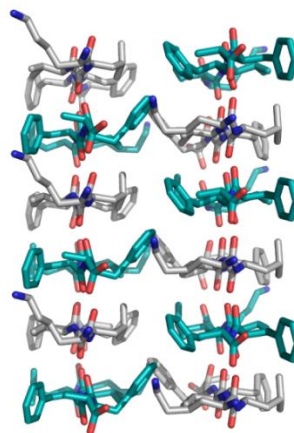
System	Box dimensions (nm³)	Number of water molecules	Timescale (ns)
SH2_ST10_F6	5.384 x 7.644 x 4.916	5641	70
SH2_ST26_F6	4.990 x 14.899 x 4.574	8899	200
SH2_ST50_F6	4.545 x 25.700 x 4.021	11812	100

Figure A3: Generation of the F6 model used in the molecular dynamics studies. Panels (a) and (b) show two different views of the steric zipper structure of the hexapeptide fragment KLVFFA of the amyloid-beta peptide (PDB entry 3OW9). In panel (c) the model in which all side chains were replaced with Phe residues is shown (top view).

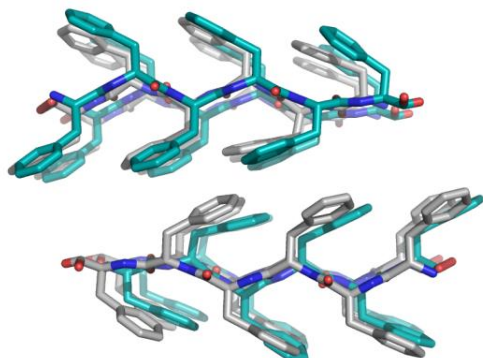
(a)



(b)



(c)





Publications

Full papers and published articles

Carlo Diaferia | University of Naples Federico II | XXX cycle

Peptide Materials Obtained by Aggregation of Polyphenylalanine Conjugates as Gadolinium-Based Magnetic Resonance Imaging Contrast Agents

Carlo Diaferia, Eliana Gianolio, Pasquale Palladino, Francesca Arena, Cinzia Boffa, Giancarlo Morelli, and Antonella Accardo*

Peptide materials based on the aggregation of polyphenylalanine conjugates containing gadolinium complexes and acting as potential contrast agents (CAs) in magnetic resonance imaging (MRI) are described. Monomers contain two (F2) or four (F4) phenylalanine residues for self-assembly, a chelating agent, 1,4,7,10-tetraazacyclododecane-*N,N,N,N*-tetraacetic acid (DOTA) or diethylenetriaminepentaacetic acid (DTPA), for achieving gadolinium coordination, and ethoxy linkers at two (L_2) or six (L_6) poly(ethylene glycol) (PEG) units between the chelating group and the peptide region. Both DOTA and DTPA tetraphenylalanine derivatives, and their gadolinium complexes DOTA(Gd)- L_2 -F4 and DTPA(Gd)- L_2 -F4, are able to self-aggregate at very low concentration. Structural characterization, obtained by circular dichroism and infrared measurements, confirms the amyloid type fibril formation in which an antiparallel peptide alignment is preferred. Amyloid type fibril formation is also observed, in solid state, by transmission electron microscopy images and X-ray diffraction patterns. The relaxivity values of DOTA(Gd)- L_2 -F4 and DTPA(Gd)- L_2 -F4 and their ability to enhance the MRI cellular response on the J774A.1 mouse macrophages cell line indicate that these peptide materials are promising candidate as a new class of supramolecular gadolinium based MRI contrast agents.

1. Introduction

In the last few years an explosion of interest has been focused on the design, synthesis, and characterization of peptide-based materials for nanomedicine and nanoscience.^[1–3] The

Dr. C. Diaferia, Prof. G. Morelli, Dr. A. Accardo
Department of Pharmacy
Research Centre on Bioactive Peptides (CIRPeB)
University of Naples "Federico II" and DFM Scarl
Via Mezzocannone 16, 80134 Naples, Italy
E-mail: antonella.accardo@unina.it

Dr. E. Gianolio, Dr. F. Arena, Dr. C. Boffa
Department of Molecular Biotechnologies and Health Science
University of Turin
Via Nizza 52, 10125 Turin, Italy

Dr. P. Palladino
Department of Chemical Sciences
University of Catania

Viale A. Doria 6, 95124 Catania, Italy
Dr. P. Palladino
I. N. B. Consortium
Viale delle Medaglie D'Oro 305, 00136 Rome, Italy

DOI: 10.1002/adfm.201502458



advancement of knowledge about molecular mechanism and forces that determine the growth of nanometric structures from basic peptide motifs from one side, and the applicative outcome in the obtention of peptide-based nanodevices for electronics, biosensing, coating for tissue engineering and cell adhesion, and drug delivery from the other side, have rapidly reached successful results.^[4]

This has been achieved by mimicking the strategies that nature pursues in the construction of complex supramolecular aggregates, essentially based on self-assembly and bottom-up procedures.

A large number of peptide-based building blocks, comprising cyclic peptides, amphiphile peptides, dendritic peptides, and aromatic dipeptides, have been considered for generating self-assembled nanostructures.^[5–8]

Among the different applications of peptide-based materials, there are several advantages, such as the intrinsic biological

origin, low immunogenicity, biocompatibility, low cost, high stability, ability for specific molecular recognition, long-term storage, and easy handling, that make synthetic peptides useful and versatile building blocks for applications in biomedical field.

The self-aggregation of short peptide sequences can be catalysed by the insertion of nonpeptidic hydrophobic groups, such as aliphatic chains^[9,10] or cholesterol derivatives,^[11] or introducing amino acids able to promote aromatic π -stacking interactions between their side chains, such as phenylalanine, tyrosine, and tryptophan.^[6]

Intense stimulus in this research area was promoted by the identification of some natural self-aggregation patterns, such as diphenylalanine (FF) motif. Diphenylalanine, which constitutes the core recognition motif of Alzheimer's β -amyloid peptide, is able to self-assemble into many different nanostructures from nanotubes to organogels.^[12,13]

FF nanostructures have been investigated for their mechanical, electrochemical, and optical properties. Many studies reported in literature are principally focused on clarifying the physicochemical aspects responsible for array stability in FF nanostructures,^[14–16] whereas only few studies have been devoted in the investigation of FF aggregates for biomedical

Special Issue Article

Journal of
Peptide Science

Received: 13 October 2014

Revised: 25 December 2014

Accepted: 9 January 2015

Published online in Wiley Online Library: 6 March 2015

(wileyonlinelibrary.com) DOI 10.1002/psc.2759



Liposomal doxorubicin doubly functionalized with CCK8 and R8 peptide sequences for selective intracellular drug delivery[‡]

Paola Ringhieri,^a Carlo Diaferia,^a Stefania Galdiero,^a Rosanna Palumbo,^b Giancarlo Morelli^a and Antonella Accardo^{a,*}

A new dual-ligand liposomal doxorubicin delivery system, which couples targeting to enhanced cellular uptake and may lead to a more efficient drug delivery system, is here designed and synthesized. Liposomes based on the composition 1,2-dioleoyl-sn-glycero-3-phosphocholine/1,2-distearoyl-sn-glycero-3-phosphoethanolamine-Peg2000-RB/(C18)₂-L5-SS-CCK8 (87/8/5 mol/mol/mol) were prepared and loaded with doxorubicin. Presence of the two peptides on the external surface is demonstrated by fluorescence resonance energy transfer assay. The combination of the R8 cell-penetrating peptide and of the CCK8 targeting peptide (homing peptide) on the liposome surface is obtained by combining pre-modification and post-modification methods. In the dual-ligand system, the CCK8 peptide is anchored to the liposome surface by using a disulfide bond. This chemical function is inserted in order to promote the selective cleavage of the homing peptide under the reductive conditions expected in proximity of the tumor site, thus allowing targeting and internalization of the liposomal drug. Copyright © 2015 European Peptide Society and John Wiley & Sons, Ltd.

Additional supporting information may be found in the online version of this article at the publisher's website.

Keywords: liposomes; homing peptides; cell-penetrating peptides; click chemistry; drug delivery systems

Introduction

The therapeutic effectiveness of many pharmaceutical compounds currently proposed for the treatment of cancer diseases is low, because a large amount of the administered drug is also delivered to normal tissues. Inefficient delivery reduces the total dose of drug reaching the target and is responsible of severe adverse effects on non-target organs. Consequently, researchers are focusing their attention on the development of novel sophisticated systems able to enhance the therapeutic index of anticancer drugs by improving delivery and allowing the drug to reach the intended target organ at full concentration [1–3]. Recently, several examples of supramolecular systems, including micelles [4,5], liposomes, [6,7] dendrimers [8] and nanoparticles [9,10], loaded with anticancer drugs such as doxorubicin, paclitaxel or cisplatin have been proposed as innovative delivery vehicles. For example, pegylated liposomal doxorubicin (PLD), commercially available as Doxil/Caelyx, is routinely administered in ovarian and metastatic breast cancers [11], and several other liposomal drugs are under development in clinical phases. Although liposomal formulations allow to reduce severe cardiotoxicity associated with free doxorubicin and to increase drug delivery to target cells exploiting the enhanced permeability and retention effect, the therapeutic efficacy of PLD remains low because mainly of poor cell penetration and slow drug release from liposomes [11–13].

In order to accumulate the drug only to target organs and inside malignant cells, new delivery systems based on micelles or

* Correspondence to: Antonella Accardo, Department of Pharmacy and CRPcB, Centro Interuniversitario di Ricerca sul Peptide Bioattivo – University of Naples Federico II, Via Mezzocannone 16, 80134, Naples, Italy. E-mail: antonella.accardo@unina.it

[‡] Special issue of contributions presented at the 14th Naples Workshop on Bioactive Peptides “The renaissance era of peptides in drug discovery”, June 12–14, 2014, Naples.

^a Department of Pharmacy and CRPcB, Centro Interuniversitario di Ricerca sul Peptide Bioattivo – University of Naples Federico II, Via Mezzocannone 16, 80134, Naples, Italy

^b IIR, CNR, Via Mezzocannone 16, 80134, Naples, Italy

Abbreviations: AADQ, 8-aminoo-3,6-dioxoacetic acid; CCKR, cholecystikinin receptor; DCM, dichloromethane; DPEA, N,N-disopropylethylamine; DLS, dynamic light scattering; DMF, dimethylformamide; DOPG, 1,2-dioleoyl-sn-glycero-3-phosphocholine; doxorubicin hydrochloride, (DS, 10S)-10-(4-amino-5-hydroxy-6-methyl-tetrahydro-2H-pyran-2-yl)-6,8,11-trihydroxy-9-(2-hydroxyacetyl)-1-methoxy-7,8,9,10-tetrahydro-tetracene-5,12-dione; DSPE-Peg2000-Mal, 1,2-distearoyl-sn-glycero-3-phosphoethanolamine-N-[maleimide (polyethylene glycol)-2000] (ammonium salt); DTT, dithiothreitol; ESI MS, electrospray ionization-mass spectrometry; FITC, fluorescein isothiocyanate; Fmoc-Pro-CH₂, Fmoc-L-propargylglycine; FRET, fluorescence resonance energy transfer assay; HATU, o-(7-azabenzotriazol-1-yl)-1,1,3,3-tetramethyluronium; HEPES, 4-(2-hydroxyethyl) piperazine-ethanesulfonic acid; HOBt, 1-hydroxybenzotriazole; HPLC, high-performance liquid chromatography; MBHA resin, 4-methylbenzylideneamine resin; Mtt, 4-methylstyryl; N3-Pag(β-COOH) PEG, 14-azido-5-oxo-3,9,12-trioxo-6-azastetradecan-1-ol-ic acid polyethylene glycol; PyBOP, benzotriazol-1-yl-oxytris(pyrrolidino)phosphonium; Rho-PE, 1,2-dioleoyl-sn-glycero-3-phosphoethanolamine-N-(lissamine rhodamine B sulfonyl) (ammonium salt); SFDP-NHS, 3-(2-pyridylidithio)propionic acid N-hydroxysuccinimide ester; SPPS, solid phase peptide synthesis; TFA, trifluoroacetic acid; TIS, trisopropylsilane.

SCIENTIFIC REPORTS

OPEN Self-assembly of PEGylated tetra-phenylalanine derivatives: structural insights from solution and solid state studies

Received: 02 February 2016

Accepted: 04 May 2016

Published: 25 May 2016

Carlo Diaferia^{1,2}, Flavia Anna Mercurio², Cinzia Giannini³, Teresa Sibillano³, Giancarlo Morelli^{1,2}, Marilisa Leone² & Antonella Accardo^{1,2*}

Water soluble fibers of PEGylated tetra-phenylalanine (F4), chemically modified at the N-terminus with the DOTA chelating agent, have been proposed as innovative contrast agent (CA) in Magnetic Resonance Imaging (MRI) upon complexation of the gadolinium ion. An in-depth structural characterization of PEGylated F4-fibers, in presence (DOTA-L₆-F4) and in absence of DOTA (L₆-F4), is reported in solution and at the solid state, by a multiplicity of techniques including CD, FTIR, NMR, DLS, WAXS and SAXS. This study aims to better understand how the aggregation process influences the performance of nanostructures as MRI CAs. Critical aggregation concentrations for L₆-F4 (43 μM) and DOTA-L₆-F4 (75 μM) indicate that self-aggregation process occurs in the same concentration range, independently of the presence of the CA. The driving force for the aggregation is the π-stacking between the side chains of the aromatic framework. CD, FTIR and WAXS measurements indicate an antiparallel β-sheet organization of the monomers in the resulting fibers. Moreover, WAXS and FTIR experiments point out that in solution the nanomaterials retain the same morphology and monomer organizations of the solid state, although the addition of the DOTA chelating agent affects the size and the degree of order of the fibers.

Peptide materials based on the aggregation of amphiphilic peptides represent a rapidly growing field within materials science^{1–3}. They have been considered for several applications in different fields from electronic to nanomedicine. Amphiphilic peptides self-assemble in well-structured supramolecular materials as the result of an intricate network of interactions between hydrophobic and hydrophilic regions. The interaction mode can strongly influence both morphology and properties of the final peptide-based materials. Special interest was recently devoted to peptide self-assembling materials in which aggregation is promoted by aromatic amino acids, such as phenylalanine, tyrosine or tryptophan, where π-stacking interactions occur^{4–6}. To this regard, a paradigmatic example is represented by the diphenylalanine (FF or F2) peptide, which constitutes the core recognition motif of Alzheimer's β-amyloid peptide. FF is able to self-assemble into many different nanostructures from nanotubes to vesicles and organogels. Peptide nanostructures containing the FF motif or more extended aromatic sequences have been investigated for their mechanical, electrochemical and optical properties, and more recently for some nanomedicine applications^{7,8}. Despite the growing literature about FF, only a few examples of new materials obtained by the self-assembling of tetraphenylalanines have been reported until now^{9–12}. In order to get a deeper understanding of the molecular interactions involved in their self-assembly process, theoretical calculations for FFFF (also called F4) and Fmoc-FFFF aggregates have been recently reported⁹. Moreover, a few examples of tetraphenylalanine-polymer conjugates, in which the aromatic framework has been elongated at the N-terminus with addition of polymeric chains, have been proposed. The F4-PEG5000 derivative, synthesized by Hamley and coworkers, is able to self-aggregate in water solution at low concentrations (0.095 wt%), whereas well-developed β-sheet structures occur only at higher concentration¹⁰. Other examples of F4-polymer

¹Department of Pharmacy and CIRPeB, University of Naples "Federico II", via Mezzocannone 16, 80134 Napoli, Italy. ²Institute of Biostructure and Bioimaging (IBB), CNR, via Mezzocannone 16, 80134 Napoli, Italy. ³Institute of Crystallography (IC), CNR, Via Amendola 122, 70126 Bari, Italy. *Present address: Department of Pharmacy, University of Naples "Federico II", Via Mezzocannone, 16 – I-80134 Napoli, Italy. Correspondence and requests for materials should be addressed to A.A. (email: antonella.accardo@unina.it)

Nanotechnology

Hierarchical Analysis of Self-Assembled PEGylated Hexaphenylalanine Photoluminescent Nanostructures

Carlo Diaferia,^[a] Teresa Sibillano,^[b] Nicole Balasco,^[c] Cinzia Giannini,^[b] Valentina Roviello,^[d] Luigi Vitagliano,^[c] Giancarlo Morelli,^[a] and Antonella Accardo*^[a]

Abstract: Despite the growing literature about diphenylalanine-based peptide materials, it still remains a challenge to delineate the theoretical insight into peptide nanostructure formation and the structural features that could permit materials with enhanced properties to be engineered. Herein, we report the synthesis of a novel peptide building block composed of six phenylalanine residues and eight PEG units, PEG₈-F₆. This aromatic peptide self-assembles in water in stable and well-ordered nanostructures with optoelectronic

properties. A variety of techniques, such as fluorescence, FTIR, CD, DLS, SEM, SAXS, and WAXS allowed us to correlate the photoluminescence properties of the self-assembled nanostructures with the structural organization of the peptide building block at the micro- and nanoscale. Finally, a model of hexaphenylalanine in aqueous solution by molecular dynamics simulations is presented to suggest structural and energetic factors controlling the formation of nanostructures.

Introduction

Self-assembly is an increasingly attractive tool for the fabrication of novel nanomaterials.^[1] In this field, self-assembled peptides have received considerable interest because of their intrinsic biocompatibility, relative simple synthesis and preparation, versatility, and functional diversity.^[2] In 2003, diphenylalanine (FF) was identified by Gazit as a recognition motif of the Alzheimer's β -amyloid peptide^[3] and since then it has been extensively studied.^[4] Diphenylalanine homodimers show a very high morphological variability^[5] depending on the experimental preparation conditions, such as solvent,^[6] pH,^[7] or temperature.^[8] Moreover, chemical modifications of the aromatic dipeptide (e.g. the introduction of a thiol group or of a fluorenylmethylloxycarbonyl (Fmoc) group) can alter the self-assembling phenomena.^[9] Nanotubes, nanowires, nanofibrils, spherical vesicles, and organogels are just a few examples of the new peptide materials, based on FF self-assembly. These materials

exhibit mechanical,^[10] electrical,^[11] electrochemical,^[12] or optical (photoluminescence^[13] and optical waveguide^[14]) properties. All these physicochemical characteristics make them suitable for several applications in biology, nanomedicine, and nanofabrication fields (for tissue engineering, drug delivery, bioimaging, and fabrication of biosensors).^[15] Moreover, their high thermal, chemical,^[16] and proteolytic stability^[17] provides them with the features for potential applications in the industrial field. The functional properties of self-assembled materials seem strictly correlated with their morphological features, thus suggesting the existence of a direct relationship between the structural organization of the building blocks and the physicochemical properties of the nanomaterials. For these fundamental reasons, a deep study into the peptide nanostructure formation (control of the morphological diversity, rational modification of the peptide motifs, and prediction for the resulting self-assembled structures) and on the structural features of the nanostructures could permit new materials with enhanced properties to be engineered. Crystallographic studies showed that FF crystals contain ringlike networks with a hexagonal symmetry promoted by head-to-tail hydrogen-bonding interactions between the charged termini of neighboring dipeptides and by the „T-shaped“ contacts between the aromatic side chains.^[18] Molecular dynamic simulations confirmed the formation of open and ringlike peptide networks also for FF peptides in aqueous solution.^[19] Concurrently to these networks, more-complex structures, arranged in parallel or antiparallel β -sheets, were also observed.^[13] Analogous structures characterized by higher stability and peptide-network propensity were observed in the triphenylalanine (FFF) simulations, thus suggesting that stacking interactions could contribute to the stability of the nanostructure. In contrast to FF dipeptide, it was noted that FFF tripeptide forms planar nanostructures.^[20] In-

[a] Dr. C. Diaferia, Prof. G. Morelli, Dr. A. Accardo
Department of Pharmacy Research Centre on Bioactive Peptides (CRPAB)
University of Naples „Federico II“ and DFM Scarl
Via Mezzocampane 16, 80134 Naples (Italy)
E-mail: Antonella.accardo@unina.it

[b] Dr. T. Sibillano, Dr. C. Giannini
Institute of Crystallography (IC), CNR, Via Amendola 122
70126 Bari (Italy)

[c] Dr. N. Balasco, Dr. L. Vitagliano
Institute of Biostuctures and Biomimicry (IBB), CNR
Via Mezzocampane 16, 80134 Naples (Italy)

[d] Dr. V. Roviello
Regional Center of Competence Technologies Scarl
Via Nuova Agnano, 11, 80125 Naples (Italy)

* Supporting Information for this article is available on the WWW under <http://dx.doi.org/10.1002/chem.201604107>.



Gadolinium containing telechelic PEG-polymers end-capped by diphenylalanine motifs as potential supramolecular MRI contrast agents

Carlo Diaferia,^a Eliana Gianolio,^b Antonella Accardo^a and Giancarlo Morelli^{a*}

Telechelic PEG-polymers end-capped by diphenylalanine (FF) motifs and containing a DOTA-Gd complex, bound on a lysine side chain at the centre of peptide moiety, are studied for their assembling properties and for the relaxometric behavior. The observed variations in terms of relaxivity are correlated to the assembling properties of the aggregates by using several techniques: fluorescence, Circular Dichroism (CD) and Fourier Transform Infrared (FTIR) for aggregation tendency and secondary structure determination; Dynamic Light Scattering (DLS) and Transmission Electron Microscopy (TEM) for morphological definition. Self-aggregation in water solution of the peptide conjugates, due to interaction of the phenylalanine frameworks, starts at concentration around 1 mg/ml with a first evidence of the coexistence of fibrillary networks and hydrogels at 10 mg/ml. Definitive presence of well-structured fibrillary networks, dominated by an antiparallel β -sheet arrangement, occurs at 50 mg/ml. At the latter concentration relaxivity values measured at 20 MHz and 298 K, are around $11 \text{ mM}^{-1} \text{ s}^{-1}$, in line with a possible use of these aggregates as MRI contrast agents. Copyright © 2016 European Peptide Society and John Wiley & Sons, Ltd.

Additional supporting information may be found in the online version of this article at the publisher's web site.

Keywords: oligo-phenylalanines; telechelic polymers; MRI contrast agents; nanofibers; self-assembling

Introduction

The self-assembling of hydrophobic, amphiphilic, and aromatic peptides is a promising route for the obtainment of new nanomaterials displaying a wide range of properties and applications [1–3]. Peptide-based self-assembled compounds organized in a high ordered architecture are able to give new functional materials that open application in emerging fields such as optical devices [4], artificial photosynthesis [5], rechargeable batteries [6], biosensors/chips [7], coating for tissue engineering and cell adhesion [8], and healthcare (regenerative medicine and drug delivery) [8,9].

However, the knowledge of the forces that permit to obtain an ordered organization of the nanostructure at micro-scale and nano-scale could help in projecting new peptide based materials for more attractive applications.

Peptide materials based on diphenylalanine (FF) motif [10] and all its analogues (Fmoc-FF, Fmoc-FFF, Boc-FFF, FFFF, Fmoc-FFFF, and polymeric polyethylene oxide, PEO, and polyethylene glycol, PEG conjugates) have been strongly studied for their ability to give a wide range of structures (nanotubes, nanowires, nanofibrils, spherical vesicles, and organogels) with physicochemical properties suitable for several applications in the earlier mentioned emerging fields [11–13]. Many studies reported in literature are principally focused on clarifying the physicochemical aspects responsible for array stability in these nanostructures [14–16] and on the study of relationship between the structural organization of the building blocks, the preparation method of the samples and the physicochemical properties of the nanomaterials [17,18].

However, only few studies have been devoted in the investigation of FF aggregates for biomedical applications, essentially due to their intrinsic low water solubility [19]. To increase their solubility, hydrophilic polymers of appropriate lengths can be bound to the aromatic framework.

We have recently developed new potential Magnetic Resonance Imaging (MRI) contrast agents (CAs) based on diphenylalanine aggregates derivatized with oxoethylene linkers and a chelating agent (DTPA or DOTA) able to complex the paramagnetic gadolinium(III) ion [20]. In particular, tetraphenylalanine peptides modified on the N-terminus with the 21-amino-4,7,10,13,16,19-hexaoxaheneicosanoic acid [Ahh-OH, (L₂₁)] spacer and with the DOTA(Gd) or DTPA(Gd) complexes [DOTA(Gd)-L₂₁-F4 and DTPA(Gd)-L₂₁-F4] self-assemble in water solution, also at low concentration, giving well soluble nanoaggregates. Single peptides in the aggregates are in a beta-sheet conformation with an antiparallel alignment along the fiber axis, and aggregating forces essentially are due to the interactions between phenylalanine aromatic frameworks. Both compounds have been also fully

* Correspondence to: Giancarlo Morelli, Department of Pharmacy, Research Centre on Bioactive Peptides (CIRPEB), University of Naples "Federico II", Via Mezzocannone 16, 80134-Naples, Italy. Email: gmorelli@unina.it

^a Department of Pharmacy, Research Centre on Bioactive Peptides (CIRPEB), University of Naples "Federico II", Via Mezzocannone 16, 80134, Naples, Italy

^b Department of Molecular Biotechnologies and Health Science, University of Turin, Via Nizza 52, 10125, Turin, Italy



Insights into amyloid-like aggregation of H2 region of the C-terminal domain of nucleophosmin

Anna Russo^a, Carlo Diaferia^a, Sara La Manna^a, Cinzia Giannini^b, Teresa Sibillano^b, Antonella Accardo^a, Giancarlo Morelli^a, Ettore Novellino^a, Daniela Marasco^{a,*}

^a Department of Pharmacy, CIRPEB: Centro Interuniversitario di Ricerca sui Peptidi Bioattivi - University of Naples "Federico II", 80134 Naples, Italy
^b Institute of Crystallography (IC), National Research Council, Bari 70125, Italy

ARTICLE INFO

Article history:

Received 2 September 2016
 Received in revised form 29 October 2016
 Accepted 14 November 2016
 Available online 17 November 2016

Keywords:

Misfolding
 Aggregation
 Acute myeloid leukemia
 Wide-angle X-ray scattering

ABSTRACT

Nucleophosmin (NPM1) is a multifunctional protein involved in a variety of biological processes including the pathogenesis of several human malignancies and is the most frequently mutated gene in Acute Myeloid Leukemia (AML). To deepen the role of protein regions in its biological activities, lately we reported on the structural behavior of dissected C-terminal domain (CTD) helical fragments. Unexpectedly the H2 (residues 264–277) and H3 AML-mutated regions showed a remarkable tendency to form amyloid-like assemblies with fibrillar morphology and β -sheet structure that resulted as toxic when exposed to human neuroblastoma cells. More recently NPM1 was found to be highly expressed and toxic in neurons of mouse models of Huntington's disease (HD). Here we investigate the role of each residue in the β -strand aggregation process of H2 region of NPM1 by performing a systematic alanine scan of its sequence and structural and kinetic analyses of aggregation of derived peptides by means of Circular Dichroism (CD) and Thioflavin T (Th-T) assay. These solution state investigations pointed out the crucial role exerted by the basic amyloidogenic stretch of H2 (264–271) and shed light on the initial and main interactions involved in fibril formation: we performed studies on fibrils deriving from the related A α peptides through the analysis of fibrils with birefringence of polarized optical microscopy and wide-angle X-ray scattering (WAXS). This analysis suggested that the presence of branched Ile²⁶⁸ conferred preferential packing patterns that, instead, appeared geometrically hampered by the aromatics side-chain of Phe²⁶⁸. Present investigations could be useful to deepen the knowledge of AML molecular mechanisms and the role of cytoplasmic aggregates of NPM1c+.

© 2016 Elsevier B.V. All rights reserved.

1. Introduction

In processes of protein misfolding the amyloid fibrillation is a unique ordered state governed by specific patterns of molecular interactions and not an specific aggregation on [1,2]. The process that leads to the formation of amyloid aggregates is a heterogeneous multistep reaction with many parallel events [3] and, nevertheless the common structural features of final fibrils [4,5], initiation steps of the aggregation by different proteins can be significantly diverse. Even if the primary sequences do not determine uniquely the structures of final fibrils [6–8], the details

of structural variations can be markedly sequence-dependent [9]. The determination of conformational elements that underlay molecular recognition and self-assembly is crucial to understand amyloid formation [10]. Normally folded proteins can access to amyloidogenic states as a result of thermal fluctuations of the native state [11] or disruption of the quaternary structure [12] and the amyloidogenic state is often considered as an ensemble of native-like conformations with locally unfolded elements [13,14]. The characterization of these amyloidogenic species is crucial to elucidate potential aggregation under native conditions and for *in vivo* aggregation events [15]. Many peptides and proteins convert *in vitro* into highly organized amyloid structures and the investigations of the effects of sequence changes on the aggregation can help the development of therapeutic strategies for amyloid-associated diseases [16].

Nucleophosmin (NPM1, B23, No38 and numatrin) is a multifunctional protein, present in the granular region of nucleoli [17,18], belonging to the nucleoplamin family of nuclear chaperones [19] that shuttles between the nucleus and cytoplasm [20]. In human cells this protein is expressed in three distinct isoforms: B23.1, the longest and the most abundant (294 residues), B23.2 and B23.3 splicing variants lacking the

Abbreviations: TIS, Tris(isopropyl)silane; TFA, Trifluoroacetic acid; DMF, Dimethylformamide; HBTU, 1-H-Benzotriazolium, 1-[bis(dimethylamino)methylene]-Hexafluorophosphate(1-,3-) oxide; HOBt, N-hydroxybenzotriazole; DEA, Diisopropylethylamine; Fmoc, Fluorenylmethoxycarbonyl; HPLC, High Performance Liquid Chromatography; LC-MS, Liquid Chromatography Mass Spectrometry; CD, Circular dichroism; CTD, C-terminal domain; NPM1, Nucleophosmin 1; AML, Acute myeloid leukemia; ThT, Thioflavin T; CR, Congo Red; WAXS, Wide-angle X-ray scattering.

* Corresponding author at: Department of Pharmacy, University "Federico II", Via Mezzocannone, 16, 80134 Naples, Italy.

E-mail address: daniela.marasco@unina.it (D. Marasco).

SCIENTIFIC REPORTS

OPEN

Cross-beta nanostructures based on dinaphthylalanine Gd-conjugates loaded with doxorubicin

Received: 26 October 2016

Accepted: 1 February 2017


Published online: 23 March 2017

Carlo Diaferia¹, Eliana Gianolio², Teresa Sibillano³, Flavia Anna Mercurio⁴, Marilisa Leone⁴, Cinzia Giannini³, Nicole Balasco⁴, Luigi Vitagliano⁴, Giancarlo Morelli³ & Antonella Accardo¹

Very recently we proposed novel di- and tetra-phenylalanine peptides derivatized with gadolinium complexes as potentials supramolecular diagnostic agents for applications in MRI (Magnetic Resonance Imaging). It was observed that in very short FF dipeptide building blocks, the propensity to aggregate decreases significantly after modification with bulky moiety such as Gd-complexes, thus limiting their potential as CAs. We hypothesized that the replacement of the Phe side chain with more extended aromatic groups could improve the self-assembling. Here we describe the synthesis, structural and relaxometric behavior of a novel water soluble self-assembled peptide CA based on 2-naphthylalanine (2Na). The peptide conjugate Gd-DOTA-L₂-(2Na)₂ is able to self-assemble in long fibrillary nanostructures in water solution (up to 1.0 mg/mL). CD and FTIR spectroscopies indicate a β sheet secondary structure with an antiparallel orientation of single strands. All data are in good agreement with WAXS and SAXS characterizations that show the typical "cross- β pattern" for fibrils at the solid state. Molecular modeling indicates the three-dimensional structure of the peptide spine of aggregates is essentially constituted by extended β -sheet motifs stabilized by hydrogen bonds and hydrophobic interactions. The high relaxivity of nanoaggregates ($12.3 \text{ mM}^{-1} \text{ s}^{-1}$ at 20 MHz) and their capability to encapsulate doxorubicin suggest their potential application as supramolecular theranostic agents.

Since its identification as recognition motif of the Alzheimer's β -amyloid peptide, the aromatic homodimer diphenylalanine (FF) has been largely studied for its capability to self-organize into a large variety of nanostructures (NSs) from nanotubes to nanofibrils, vesicles and organogels^{1,2}. The morphological variability of NSs structurally depends on the experimental procedure adopted for their preparation such as the polarity of the solvent³, the pH value⁴ or temperature⁵. In addition, chemical modifications of the aromatic homodimer, including the introduction of a thiol group or of a fluorenylmethyloxycarbonyl (Fmoc) group, can cause variations in the morphology of the aggregate⁶. The morphology of the FF-NSs seems to be determinant for their physicochemical properties. Mechanical, electrochemical and optoelectronic properties of FF-NSs⁷ leave envisage a their potential application in nanofabrication and industrial fields. However, only a few studies have been devoted, until now on their potential abilities in the biomedical field⁸. Moreover, also their applications in the diagnostic field remains unexplored, overall for the low intrinsic water solubility of these derivatives. Very recently we described the first example of supramolecular aggregates based on PEGylated cationic di-phenylalanine and tetra-phenylalanine conjugates as enhanced contrast agents (CAs) for diagnostic applications in Magnetic Resonance Imaging (MRI)⁹. These conjugates contain two (FF or F2) or four (F4) phenylalanine residues for promoting the self-assembly, a branched or linear bifunctional chelating agent such as DOTA (1,4,7,10-tetraazacyclododecane-N,N,N,N-tetraacetic acid) or DTPA (diethylenetriamine penta-acetate), for achieving the kinetically stable and thermodynamically inert coordination of the gadolinium paramagnetic ion and an ethoxylic linker at six PEG units (L₆) between the chelating agent and the oligopeptide. In zwitterionic FF homodimer the self-assembling pathway is driven by head-to-tail hydrogen-bonding between the charged termini of neighbouring dipeptides and "T-shaped" contacts between the amino acid side-chains^{7,8}. On the contrary, in capped uncharged dipeptide FF the loss of the

¹Department of Pharmacy, Research Centre on Bioactive Peptides (CIRPEB), University of Naples "Federico II", Via Mezzocannone 16, 80134, Naples, Italy. ²Department of Molecular Biotechnologies and Health Science, University of Turin, Via Nizza 52, 10125, Turin, Italy. ³Institute of Crystallography (IC), CNR, Via Amendola 122, 70126, Bari, Italy. ⁴Institute of Biostructure and Bioimaging (IBB), CNR, Via Mezzocannone 16, 80134, Naples, Italy. Correspondence and requests for materials should be addressed to A.A. (email: antonella.accardo@unina.it)

 Photoluminescence

Photoluminescent Peptide-Based Nanostructures as FRET Donor for Fluorophore Dye

 Carlo Diaferia,^[a] Teresa Sibillano,^[b] Cinzia Giannini,^[b] Valentina Roviello,^[c] Luigi Vitagliano,^[d] Giancarlo Morelli,^[a] and Antonella Accardo^{*[a]}

Abstract: A great interest has been recently generated by the discovery that peptide-based nanostructures (NSs) endowed with cross- β structure may show interesting photoluminescent (PL) properties. It was shown that NSs formed by PEGylated hexaphenylalanine (PEG_n-F6, PEG = polyethylene glycol) are able to emit at 460 nm when excited at 370 or 410 nm. Here, the possibility to transfer the fluorescence of these PEG_n-F6-based NSs by foster resonance electron transfer (FRET) phenomenon to a fluorescent dye was explored. To achieve this aim, the 4-chloro-7-nitrobenzofuran (NBD) dye was encapsulated in these NSs. Structural data in solution and in solid state, obtained by a variety of techniques (circular dichroism, Fourier-transform infrared spectroscopy, wide-angle X-ray scattering, and small-angle X-ray scatter-

ing), indicated that the organization of the peptide spine of PEG_n-F6 NS, which consists of anti-parallel β -sheets separated by a dry interface made of interacting phenylalanine side chains, was maintained upon NBD encapsulation. The spectroscopic characterization of these NSs clearly showed a red-shift of the emission fluorescence peak both in solution and in solid state. This shift from 460 to 530 nm indicated that a FRET phenomenon from the peptide-based to the fluorophore-encapsulated NS occurred. FRET could also be detected in the PEG_n-F6 conjugate, in which the NBD was covalently bound to the amine of the compound. On the basis of these results, it is suggested that the red-shift of the intrinsic PL of NSs may be exploited in the bio-imaging field.

Introduction

In the last few years an explosion of interest has been focused on peptide-based materials for interdisciplinary nanoscience applications.^[1] There are several advantages for using peptides as building blocks, such as intrinsic biological origin, low cost, high stability, ability for specific molecular recognition, long-term storage, and easy handling. One of the most studied representative building blocks, able to self-assemble in supra-molecular nanostructures (NSs), is the diphenylalanine homodimer (FF).^[2] FF self-assembles in nanotubes that show noteworthy

mechanical rigidity^[3] along with a multiplicity of other chemical and physical functionalities,^[2] making it promising for potential application in nanomedicine,^[4] nanofabrication,^[5] tissue engineering,^[6] bio-imaging,^[6] drug delivery,^[6] and fabrication of biosensors.^[6] However, the low water solubility of these peptide NSs has partially limited their application in nanomedicine. Very recently, we described the first examples of NSs based on PEGylated (PEG = polyethylene glycol) cationic poly-phenylalanines^[7a, 11] or their analogues (di-naphthylalanine)^[7b] for bio-imaging applications. These peptide derivatives contain an aromatic region to allow the self-assembly of the NS, a gadolinium (Gd) complex for applications as *in vivo* contrast agent in magnetic resonance imaging (MRI), and a PEG spacer at different length between the Gd-complex and the peptide moiety. These peptides could be potentially proposed for application in MRI owing to their high uptake and moderately low toxicity on selected cell lines.^[8] In more recent years, a great interest has been generated around peptide-based NSs with interesting photoluminescent (PL) properties. Peptide-based NSs can exhibit blue photoluminescence when excited at a wavelength of 370 or 410 nm. This PL phenomenon has also been observed in FF and FFF NSs upon thermally induced reconstructive phase transition (heating sample at 140–180 °C) as shown by Rosenman and co-workers^[9a, 13] or in amyloid-like fibrils rich in β -sheet structures.^[9c] Some hypotheses on the origin of this PL, such as electron delocalization through hydrogen bonds in the β -sheet-rich structure^[9b] or proton transfer,^[9d] have been proposed until now. We recently reported on

[a] Dr. C. Diaferia, Prof. G. Morelli, Dr. A. Accardo
Department of Pharmacy Research Centre on Bioactive Peptides (CRPdB)
University of Naples "Federico II" and DFM Scat
Via Mezzocoronone 16, 80134 Naples (Italy)
E-mail: Antonella.accardo@unina.it

[b] Dr. T. Sibillano, Dr. C. Giannini
Institute of Crystallography (IC), CNR
Via Amendola 122, 70126 Bari (Italy)

[c] Dr. V. Roviello
Analytical Chemistry for the Environment and CeSMA
(Centro Servizi Metodologici Avanzati)
University of Naples "Federico II"
Corso Nicolangelo Protopsani, 80146, Naples (Italy)

[d] Dr. L. Vitagliano
Institute of Biosturctures and Biomaging (IBB), CNR
Via Mezzocoronone 16, 80134 Naples (Italy)

Supporting Information for this article can be found under:
<https://doi.org/10.1002/chem.201701381>.

Peptide-Polymer Conjugates
Structural Characterization of PEGylated Hexaphenylalanine Nanostructures Exhibiting Green Photoluminescence Emission

 Carlo Diaferia,^[a] Teresa Sibillano,^[b] Davide Altamura,^[b] Valentina Roviello,^[c] Luigi Vitagliano,^[d] Cinzia Giannini,^[b] Giancarlo Morelli,^[a] and Antonella Accardo^{*[a]}

Abstract: Peptides containing aromatic residues are known to exhibit spontaneous phenomena of supramolecular organization into ordered nanostructures (NSs). In this work we studied the structural behavior and optoelectronic properties of new biocompatible materials obtained by the self-assembly of a series of hexaphenylalanines (F6) modified at the N terminus by a PEG chain of different lengths. PEG₁₇-F6, PEG₃₈-F6, and PEG₇₂-F6 peptides were synthesized by coupling sequentially two, three, or four units of amino-carboxy-PEG₆ blocks, each one containing six oxyethylene repetitions. Changes in the length and composition of the PEG

chain were found to modulate the structural organization of the phenylalanine-based nanostructures. An increase in the self-aggregation tendency was observed with longer PEG chains, whereas, independently of the PEG length, the peptide NSs display cross- β -like secondary structures with an antiparallel β -strand arrangement. WAXS/GWAXS diffraction patterns indicate a progressive decrease in fiber order along the series. All the PEG-F6 derivatives present blue photoluminescent (PL) emission at 460 nm, with the adduct with the longest PEG chain (PEG₇₂-F6) showing an additional green emission at 530 nm.

Introduction

Self-assembling peptides are a class of building blocks that undergo spontaneous supramolecular organization into ordered structure on the nanoscale. The ability of peptides to self-assemble, adopting stable secondary conformations, has allowed them to be used in nanotechnology and in materials science as very multifunctional tools.^[1] Superhydrophobic coating,^[2] tissue engineering,^[3] cell culturing,^[4] biosensing,^[5] and drug delivery^[6] are only some of the possible areas of application of peptide-based supramolecular systems. The driving forces that hold up spontaneous aggregations are pinpointed in hydrogen bonds and hydrophobic and aromatic interactions. Peptides

also exhibit versatile features such as resistance to pH^[7] as well as high^[8] or low temperatures,^[9] mutual recognition,^[10] functionality,^[11] high mechanical performance,^[12] and intrinsic biocompatibility.^[13] In addition to these characteristics, the rational design of peptide building blocks and the convenient synthetic procedures of decoration also make it possible to combine self-assembling peptides with a range of other functional moieties (such as lipids,^[14] metallic centers,^[15] and nucleic acid derivatives).^[16] The mix of peptides with synthetic polymers (e.g., poly(ethylene oxide) (PEO),^[17] poly(ethylene glycol) (PEG),^[18] polycaprolactone (PCL),^[19] poly(propylene oxide) (PPO),^[20] or poly(acrylic acid) (PPA)^[21]) allows (generally in amphiphilic blocks) peptide functionality and recognition capability to be synergistically combined with polymer cheapness and responsiveness to obtain new hybrid materials. Since the early 1950s, when Jatzkewitz described the first example of a peptide/polymer conjugate,^[22] several reviews,^[23] communications,^[24] and perspectives^[25] on their synthesis and potential applications have been reported. It has been observed that the conjugation of polymers (with particular reference to PEG chains) to natural or synthetic peptides such as poly(γ -benzyl-L-aspartate),^[26] [(AG)₃EG]₁₀,^[27] DGRFFF,^[28] [(LELL)₆],^[29] and oligo(phenylalanines)^[17] can strongly affect their structural properties. Moreover, owing to the crystallization phenomenon, PEG could inhibit the fibrillation of amyloid peptide sequences (i.e., A β ₁₋₂₀^[30] and A β ₁₋₂₅^[31]), a function not available to the unmodified peptide.

In the last decade, homo-peptides have been identified as the simplest class of self-assembling elements and diphenylalanine (FF) represents the most well-known peptide building block.^[32] Also, tetra- and pentaphenylalanines have been proposed as promising building blocks for future technological

[a] Dr. C. Diaferia, Prof. G. Morelli, Dr. A. Accardo
Department of Pharmacy
Research Centre on Bioactive Peptides (CRPeB)
University of Naples "Federico II" and IFM ScAR
Via Mezzocannone 16, 80134 Naples (Italy)
E-mail: Antonella.accardo@unina.it

[b] Dr. T. Sibillano, Dr. D. Altamura, Dr. C. Giannini
Institute of Crystallography (IC), CNR
Via Amendola 122, 70126 Bari (Italy)

[c] Dr. V. Roviello
Analytical Chemistry for the Environment
and Centro Servizi Metrologici Avanzati
University of Naples "Federico II"
Corso Nicolangelo Protapiscani, 80146, Naples (Italy)

[d] Dr. L. Vitagliano
Institute of Biostructures and Biomaging (IBB), CNR
Via Mezzocannone 16, 80134 Naples (Italy)

Supporting Information and the ORCID identification number(s) for the author(s) of this article can be found under <https://doi.org/10.1002/chem.201703055>.



Nanoscale

Full article

Amyloid-like fibrillary morphology originated by tyrosinate aromatic hexapeptides.

Carlo, Diaferia,^a Nicole Balasco,^{b, c} Teresa Sibillano,^a Moumita Ghosh,[†] Lihl Adler-Abramovich,[†] Cinzia Giannini,^a Luigi Vitagliano,[‡] Giancarlo Morelli,[§] Antonella Accardo

Received 15th September 2017,
Accepted 09th January 2018

DOI: 10.1039/s0000000x

www.rsc.org

Diphenylalanine based nanostructures have attracted great attention in the material science for their functional properties in the nanofabrication, nanomedicine and industrial fields. These properties strongly depend from that hierarchic organization of the nanostructure that in turn can be fine tuned by punctual chemical modifications of the building blocks. Here we investigate how the partial or the complete replacement of the Phe residue with Tyr one (PEG_n-Y6 and PEG_n-[FY]3) in ancestor PEG_n-F6 can alter the structure of the nanomaterial. The effect of the PEG derivatization was also evaluated in peptides lacking of the PEG moiety (Y6 and [FY]3). Both PEG_n-Y6 and PEG_n-[FY]3 self-assemble in water at micromolar concentration in β -sheet rich nanostructures. Instead, WAXS diffraction patterns show significant structural differences between the samples. [FY]3 and Y6 show a 2D WAXS profile typically observed in cross- β amyloid like structures with a meridional and the equatorial reflections at 4.7 and 12.5 Å, respectively. The addition of the PEG moiety at the N-terminus of peptide affects the diffraction pattern of PEG_n-Y6, there are circle typically observed in presence of PEG crystallization. MD simulations are in good agreement with experimental WAXS data. Gelation phenomenon was detected only for PEG_n-[FY]3 above a concentration of 1.0 wt% as confirmed by storage ($G' \sim 100$ Pa) and loss ($G'' \sim 25$ Pa) moduli in rheological studies. The cell viability on CHO cells of this soft hydrogel, estimated by MTT and live/dead assays, was certified to be 90% after 24 hours of incubation.

Introduction

Since the beginning of the last century, nanotechnology has imposed itself as revolutionary scientific area at the interface between different disciplines, which include chemistry, medicine, material science and biology. A large variety of nanoplatforms (NPs) with different morphology, shape, compatibility and functionality have been obtained by opportunely manipulating matter.¹ The need to obtain nanostructures (NSs) with well-defined characteristics of uniformity, purity, size, and chemical compositions brought to the development of many technologies and approaches for their manufacturing.² One of the most common strategy takes advantage of self-assembling phenomena that rely on associations through non-covalent interactions between

monomers.³ Intensive investigations, carried out over the last two decades, have highlighted an extraordinary propensity of proteins, peptides and even single amino acids to form assemblies with well-defined structural, chemical and physical properties.⁴ Protein and peptide self-association has a huge impact in different, apparently unrelated, scientific areas. Indeed, it is commonly believed that protein/peptide self-association generates the molecular species that are causative agents of neurodegenerative diseases.^{5,6} On the other hand, the ability of proteins, peptides and amino acids to form non-covalent, through highly stable, assemblies have been envisaged as an extremely powerful tool to generate innovative entities with widespread applications. Interestingly, being the process of protein/peptide aggregation common to all these studies, there has been a fruitful flow of information from one field to the other. The tendency of these compounds to undergo self-aggregation is obviously linked to the ability of main chain atoms to form hydrogen bonding interactions. A contribution to the formation of these assemblies can also be occasionally provided by electrostatic interactions established by terminal charged groups. In addition to that, it has been well established that also interactions involving side chains may be crucial for these associations. For example, it has been shown that glutamine (Gln) and asparagine (Asn) residues can stabilize amyloid-like aggregates as their side chains can form ladders of hydrogen bonds.^{7,8} Moreover, the suggestion that aromatic side

^aDepartment of Pharmacy, Research Centre on Bioactive Peptides (ORPeB) University of Naples "Federico II" Via Mezzocannone 16, 80134 Naples (Italy)

^bInstitute of Biostructures and Biomaging (IBB), CNR Via Mezzocannone 16, 80134 Naples (Italy)

^cInstitute of Crystallography (IC), CNR Via Amendola 122, 70126 Bari (Italy)

^dDepartment of Oral Biology, The Goldschleger School of Dental Medicine, Sackler Faculty of Medicine, Tel Aviv University, Tel Aviv 69978, Israel

^ee.

Chemistry - A European Journal
Self-assembling of Fmoc-GC Peptide Nucleic Acid dimers into highly fluorescent aggregates
 –Manuscript Draft–

Manuscript Number:	
Article Type:	Full Paper
Corresponding Author:	Alessandra Romanelli, Ph.D Università di Napoli Napoli, ITALY
Corresponding Author E-Mail:	alessandra.romanelli@unina.it
Order of Authors (with Contributor Roles):	Concetta Avitabile Carlo Diaferia Bartolomeo della Ventura Flavia Mercurio Marilisa Leone Valentina Roviello Michele Saviano Raffaele Velotta Giancarlo Morelli Antonella Accardo Alessandra Romanelli, Ph.D
Keywords:	Peptide Nucleic Acids; aggregation; fluorescence; REES; nanosphere
Manuscript Classifications:	Aggregation; Fluorescence; Self-assembly; Time-resolved spectroscopy
Suggested Reviewers:	Majed Chergui majed.chergui@epfl.ch expert in spectroscopy David Andreu-Martinez david.andreu@upf.edu expert in NMR Roberto Corradini roberto.corradini@unipr.it expert in PNA Lihi Adler-Abramovich lihia@tauex.tau.ac.il expert in PNA and peptide aggregation Fernando Formaggio fernando.formaggio@unipd.it expert in peptide, recently involved in studies on mixed systems, composed of peptide and nucleobases.
Opposed Reviewers:	Lorenzo Stella stella@stc.uniroma2.it conflict of interest
Abstract:	Self-assembling of molecules by non-covalent interactions is one of the most attracting topics in supramolecular chemistry. The use of short peptides or modified nucleotides as building blocks of the aggregates is particularly intriguing, as these are very easy to synthesize; moreover subtle changes in the chemical structure of such building blocks may drastically affect the properties of the aggregates. The ability of Peptide Nucleic

Powered by Editorial Manager® and Prodxion Manager® from Aries Systems Corporation

**Structural characterization of self-assembled tetra-tryptophan based nanostructures:
variations on a common theme**

Carlo Diaferia,¹ Nicole Balasco,² Teresa Sibillano,³ Cinzia Giannini,³ Luigi Vitagliano,² Giancarlo Morelli,¹ Antonella Accardo¹

¹Department of Pharmacy, Research Centre on Bioactive Peptides (CIRPeB), University of Naples "Federico II", Via Mezzocannone 16, 80134-Naples, Italy.

²Institute of Biostructures and Bioimaging (IBB), CNR, via Mezzocannone 16, 80134 Naples (Italy)

³Institute of Crystallography (IC), CNR, Via Amendola 122, 70126 Bari (Italy)

Correspondence: Dr. Antonella Accardo, Department of Pharmacy, Research Centre on Bioactive Peptides (CIRPeB), University of Naples "Federico II", Via Mezzocannone 16, 80134-Naples, Italy. E-mail:

antonella.accardo@unina.it; Phone: +39-081-2532045; Fax: +39-081-2536642

Abstract

Over the years, a large number of multidisciplinary investigations has unveiled that self-assembly of short peptides and even of individual amino-acids can generate a variety of different biomaterials. In this framework, we have recently reported that PEG conjugates of short homopeptides, containing aromatic amino-acids such as phenylalanine (Phe, F) and naphthylalanine (Nal), are able to form elongated fibril aggregates having interesting chemical and physical properties. We here extend these analyses by characterizing the self-assembling propensity of PEG₆-W4, a polyethylene glycol (PEG) adduct of the tetra-tryptophan (W4) sequence. A comprehensive structural characterization of PEG₆-W4 was obtained both in solution and at the solid state through the combination of spectroscopic, microscopy, X-ray scattering, and computational techniques. Collectively, these studies demonstrate that this peptide is able to self-assembly in fibrillary networks characterized by a cross β -structure spine. Present findings clearly demonstrate that aromatic residues display a general propensity to induce self-aggregation phenomenon, despite the significant differences of the physicochemical properties at their side chains.

τ_R	<i>Reorientational time</i>
τ_S	<i>Electronic relaxation time</i>
$^1\text{HNMR}$	<i>Hydrogen Nuclear Magnetic Resonance</i>
Å	<i>Angstrom</i>
ADNTs	<i>Aromatic Dipeptide Nanotubes</i>
AdOO	<i>Fmoc-8-amino-3,6-dioxaoctanoic acid</i>
Ahoh	<i>Fmoc-21-amino-4,7,10,13,16,19-hexaoxahe-neicosanoic acid</i>
ANS	<i>8-anilino-1-naphthalene sulfonic acid ammonium salt</i>
Boc	<i>tert-butyloxycarbonyl;</i>
CAC	<i>Critical Aggregation Concentration</i>
CAT	<i>Computer-Assisted Tomography</i>
CAs	<i>Contrast Agents</i>
CD	<i>Circular Dichroism</i>
CR	<i>Congo Red dye</i>
DIPEA	<i>Diisopropylethylamine</i>
DLS	<i>Dynamic Light Scattering</i>
DMF	<i>N,N-dimethylformamide</i>
DOTA	<i>1,4,7,10-tetraazacyclododecane- N,N,N,N- tetraacetic acid</i>
DTPA	<i>diethylenetriaminepentaacetic acid</i>
DOX	<i>Doxorubicin</i>
F	<i>(L)-Phenylalanine</i>
FF	<i>Diphenylalanine homopeptide</i>
Fmoc	<i>9-fluorenylmethyloxycarbonyl</i>
f	<i>(D)-Phenylalanine</i>
FRET	<i>Förster resonance electron transfer</i>
FT-IR	<i>Fourier Transform Infrared</i>
Gd	<i>Gadolinium</i>
HATU	<i>1-[Bis(dimethylamino)methylene]-1H-1,2,3-triazolo[4,5-b]pyridinium-3-oxid hexafluorophosphate</i>
HFIP	<i>1,1,1,3,3,3-hexafluoro-2-isopropanol</i>
HOBT	<i>1-hydroxybenzotriazole</i>
L ₂	<i>Fmoc-8-amino-3,6-dioxaoctanoic acid</i>
L ₆	<i>Fmoc-21-amino-4,7,10,13,16,19-hexaoxahe-neicosanoic acid</i>
LC/MS	<i>Liquid Chromatography-Mass spectrometry</i>
M	<i>Molar</i>
MD	<i>Molecular Dynamics</i>
MEG	<i>Magnetoencephalogram</i>
MRI	<i>Magnetic Resonance Imaging</i>
Mtt	<i>N-methyltrityl</i>
Mw	<i>Molecular weight</i>
NBD	<i>4-Chloro-7-nitrobenzofurazan</i>
NMs	<i>Nanomaterials</i>
NMRD	<i>Nuclear Magnetic Relaxation Dispersion</i>
NMP	<i>N-methyl-2-pyrrolidone</i>

NPs	<i>Nanoplatfoms</i>
PBMs	<i>Peptide-based materials</i>
PEG	<i>Polyethylene glycol</i>
PEG ₂	<i>Fmoc-8-amino-3,6-dioxaoctanoic acid</i>
PEG ₆	<i>Fmoc-21-amino-4,7,10,13,16,19-hexaoxahe-neicosanoic acid</i>
PEO	<i>Polyethylene oxide</i>
PET	<i>Positron Emission Tomography</i>
Phe	<i>Phenylalanine</i>
PL	<i>Photoluminescence</i>
POM	<i>Polarized Optical Microscopy</i>
PyBop	<i>benzotriazol-1-yl-oxy-tris-pyrrolidino-phosphonium</i>
Pyr	<i>Pyrene</i>
r_1	<i>Longitudinal relaxivity</i>
r_2	<i>Transverse relaxivity</i>
R_1^{obs}	<i>Measured Relaxivity</i>
R_{1p}	<i>Relassività del protone dell'acqua</i>
R_t	<i>Ritention time</i>
RP-HPLC	<i>Reverse Phase High Pressure Liquid Cromatography</i>
RMSD	<i>Root Mean Square Deviation</i>
RMSF	<i>Root Mean Square Fluctuation</i>
RMSIP	<i>Root Mean Square Inner Product</i>
SAXS	<i>Small Angle X-Ray Scattering</i>
SEM	<i>Scanning Electron Microscopy</i>
SPIONs	<i>Superparamagnetic iron oxide</i>
SPPS	<i>Solid Phase Peptide Synthesis</i>
T_1	<i>Longitudinal relation time</i>
T_2	<i>Transversal relation time</i>
TEM	<i>Transmission Electron Microscopy</i>
TFA	<i>Trifluoroacetic acid</i>
ThT	<i>Tioflavin T</i>
TIS	<i>tri-isopropylsilane</i>
TMS	<i>Tetrametilsilano</i>
tBu	<i>Tert-butyl</i>
Tyr	<i>(L)-Tyrosine</i>
Trp	<i>(L)-Tryptophan</i>
v/v	<i>Volume/volume concentration</i>
WAXS	<i>Wide Angle X-Ray Scattering</i>
Xe	<i>Xenon</i>
XRD	<i>X-Ray Diffraction</i>

- 1 A.R Kherlopian, T. Song, Q. Duan, M.A. Neimark, M.J. Po, J.K Gohagan, A.F. Laine, *BMC Systems Biology* **2008**, 2, 74-92.
- 2 R. Salzer, *Biomedical Imaging: Principles and Applications* **2015**, John Wiley & Sons Etd.
- 3 M.A. Farruhk, *Functionalized Nanomaterials* **2016**, InTech-Open Access Publisher.
- 4 J. Ramsdem, *Nanotechonology: an introduction 2nd ed.* **2016**, William Andrew, Elvesier.
- 5 T.H. LaBean, *Nature* **2009**, 459, 331-332.
- 6 A.P. Khandhar, P. Keselman, S.J. Kemp, R.M. Ferguson, P.W. Goodwill, S.M. Conolly, K.M. Krishnan, *Nanoscale* **2017**, 9(3), 1299-1306
- 7 X. Huang, R. O'Connor, E.A. Kwizera, *Nanotheranostics* **2017**, 1(1), 80-102.
- 8 R. Cheheltani, R.M. Ezzibdeh, P. Chhour, K. Pulaparathi, J. Kim, M. Jurcova, J.C. Hsu, C. Blundell, H.I. Litt, V.A. Ferrari, H.R. Allcock, C.M. Sehgal, D.P. Cormode, *Biomaterials* **2016**, 102, 87-97.
- 9 E.C. Lin, *Mayo Clin. Proc.* **2010**, 85(12), 1142-1146.
- 10 J. A. Seibert, R.L. Morin, *Pediatr. Radiol.* **2011**, 41(5), 573-581.
- 11 F.A Gallagher, *Clinic Radiol.* **2010**, 65(7), 557-566.
- 12 J. Swanevelde, *Cont. Ed. Anaest. Crit. Care Pain* **2011**, 11(5), 186-192.
- 13 N. Ji, *Neuron* **2014**, 83(6), 1242-1254.
- 14 S.K. Nune, P. Gunda, P.K. Thallapally, Y.Y. Lin, M. L. Forrest, C.J. Berkland, *Expert. Opin. Drug. Deliv.* **2009**, 6(11), 1175-1194.
- 15 I.R. Young, *Methods in Biomedical Magnetic Resonance Imaging and Spectroscopy* **2000**, John Wiley & Sons Ltd., Chichester.
- 16 P.A. Rinck, *Magnetic Resonance in Medicine* **2003**, ABW Wissenschaftsverlag GmbH, Berlin.
- 17 M.F. Tweedle, In: J.-C.G. Bünzli, G.R. Choppin (Eds.), *Lantanide Probes in Life, Chemical and Earth Sciences: Theory and Practice*, **1989**, Elsevier, Amsterdam, 127.
- 18 H.J Weinmann, A. Mühler, B. Radüchel, In: *Biomedical Magnetic Resonance Imaging and Spectroscopy* **2000**, I.R. Young (Ed.), John Wiley & Sons Ltd., Chichester, 705.
- 19 R. Weissleder, M. Papisov, *Rev. Magn. Reson. Med.* **1992**, 4, 1-20.

- 20 L. Banci, I. Bertini, C. Luchinat, *Nuclear and Electronic Relaxation* **1991**, VCH, Weinheim.
- 21 M.F Tweedle, V.M. Runge, *Drugs Future* **1992**, 17, 187-190.
- 22 M. Botta, *Eur. J. Inorg. Chem.* **2000**, 399-407.
- 23 A.J. Peters, J. Huskens, D.J. Raber, *Prog. in NMR Spectrosc.* **1996**, 28, 283-350.
- 24 S.H. Koenig, R.D. Brown III, *Prog. in NMR Spectrosc* **1991**, 22, 487-567.
- 25 R.B. Lauffer, *Chem. Rev.* **1987**, 87, 901-927.
- 26 S. Aime, M. Botta, M. Fasano, E. Terreno, *Chem. Soc. Rev.* **1998**, 27, 19-29.
- 27 S. Aime, M. Botta, M. Fasano, S. Geninatti Crich, E. Terreno, *Coord. Chem. Rev.* **1999**, 321, 185-186.
- 28 L. Helm, A.E. Merbach, *Chem. Rev.* **2001**, 105, 1923-1960.
- 29 K.A. Deal, R. Motekaitis, A.E. Martell, J.M. Welch, *J. Med. Chem.* **1996**, 39, 3096-3106.
- 30 J.H. Freed, *J. Chem. Phys.* **1978**, 68, 4034-4037.
- 31 H. Schmitt-Willich, M. Brehm, C.L.J. Evers, G. Michl, A. Müller-Farnow, O. Petrov, J. Platzek, B. Radüchel, D. Sülzle, *Inorg. Chem.* **1999**, 38, 1134-1144.
- 32 F. Uggeri, S. Aime, P.L. Anelli, M. Botta, M. Brocchetta, C. de Haën, G. Ermondi, M. Grandi, P. Paoli, *Inorg. Chem.* **1995**, 34, 633-642.
- 33 S. Aime, A.S. Batsanov, M. Botta, J.A.K. Howard, D. Parker, K. Senanayake, G. Williams, *Inorg. Chem.* **1994**, 33, 4696-4706.
- 34 A. Mühler, *MAGMA* **1995**, 3, 21-33.
- 35 M. Bottrill, L. Kwok, N.J. Long, *Chem. Soc. Rev.* **2006**, 35, 557-571.
- 36 E. Battistini, E. Gianolio, R. Gref, P. Couvreur, S. Fuzerova, M. Othman, S. Aime, B. Badet, P. Durand, *Chem. Eur. J.* **2008**, 14, 4551-4561.
- 37 S. Aime, M. Botta, E. Garino, S. Geninatti Crich, G. Giovenzana, R. Pagliarin, G. Palmisano, M. Sisti, *Chem. Eur. J.* **2000**, 6, 2609-2617.
- 38 M.P. Lowe, *Aust. J. Chem.* **2002**, 55, 551-556.
- 39 L. Frich, A. Bjornerud, S. Fossheim, T. Tillung, I. Gladhaug, *Magn. Reson. Med.* **2004**, 52, 1302-1309.
- 40 S.R. Zhang, K.C. Wu, A.D. Sherry, *Angew. Chem. Int. Ed.* **1999**, 38, 3192-3194.

- 41 L. Burai, E. Toth, S. Seibig, R. Scopelliti, A.E. Merbach, *Chem. Eur. J.* **2000**, 6, 3761-3770.
- 42 E.L. Que, C.J. Chang, *J. Am. Chem. Soc.* **2006**, 128, 15942-15943.
- 43 P.L. Anelli, I. Bertini, M. Fragai, L. Lattuada, C. Luchinat, G. Parigi, *Eur. J. Inorg. Chem.* **2000**, 625-630.
- 44 W.J.M. Mulder, G.J. Strijkers, A.W. Griffioen, L. van Bloois, G. Molema, G. Storm, G. Koning, K. Nicolay, *Bioconjugate Chem.* **2004**, 15, 799-806.
- 45 S.R. Bull, M.O. Guler, R.E. Bras, T.J. Maede, S.I. Stupp, *Nano Lett.* 2005, 5, 1-4.
- 46 A.W. Bosman, H.M. Janssen, E.W. Meijer, *Chem. Rev.* **1999**, 99, 1665-1688.
- 47 D.L. Ladd, R. Hollister, X. Peng, D. Wei, G. Wu, D. Delecki, R.A. Snow, J.L. Toner, K. Kellar, J. Eck, V.C. Desai, G. Raymond, L.B. Kinter, T.S. Desser, D.L. Rubin, *Bioconjugate Chem.* **1999**, 10, 361-370.
- 48 S. Laus, B. Sitharaman, E. Toth, R.D. Bolskar, L. Helm, L.J. Wilson, A.E. Merbach, *J. Phys. Chem. C* **2007**, 111, 5633-5639.
- 49 K.B. Hartman, S. Laus, R.D. Bolskar, R. Muthupillai, L.M. Helm, E. Toth, A.E. Merbach, L.J. Wilson, *Nano Lett.* **2008**, 8, 415-419.
- 50 S. Geninatti Crich, A. Barge, E. Battistini, C. Cabella, S. Coluccia, D. Longo, V. Mainero, G. Tarone, S. Aime, *J. Biol. Inorg. Chem.* **2005**, 10, 78-86.
- 51 J.R. Lakowicz, *Principles of Fluorescence Spectroscopy*, 3rd edition **2006**, Springer, USA.
- 52 A. Keppler, S. Gendreizig, T. Gronemeyer, H. Pick, H. Vogel, K. Johnsson, *Nat. Biotechnol.* **2003**, 21(1), 86-89.
- 53 X. Fei, Y. Gu, *Prog. Nat. Sci.* **2009**, 19(1), 1-7.
- 54 T. Nagano, *Proc. Jpn. Acad. Ser. B Phys. Biol. Sci.* **2010**, 86(8), 837-847.
- 55 M.Y. Berezin, S. Achilef, *Chem. Rev.* **2010**, 110(5), 2641-2684.
- 56 W. Birmachu, J.K. Reed, *J. Phot. Phot. A: Chem.* **1988**, 2-3, 261-268.
- 57 T. Zimmermann, J. Marrison, K. Hogg, P. O'Toole, *Methods. Mol Biol.* **2014**, 1075, 129-148.
- 58 H. Kambara, K. Nagai, K. Kawamoto, *Electrophoresis* **1992**, 13(1), 542-546.

- 59 T. Repenko, A. Rix, S. Ludwanowski, D. Go, F. Kiessling, W. Lederle, A.J.C. Kuehne, *Nat. Commun.* **2017**, 8,480-488.
- 60 C. Wu, B. Bull, C. Szymanski, K. Christensen, J. McNeill, *ACS Nano* **2008**, 2, 2415-2423.
- 61 M. Carreras, G. Pargament, S. Catz, J. Poderoso, A. Boveris, *FEBS Lett* **1994**, 341, 65-68.
- 62 K. Pu, A.J. Shuhendler, J. Rao, *Angew. Chemie Int. Ed.* **2013**, 52, 10325-10329.
- 63 A. Morisco, A. Accardo, E. Gianolio, D. Tesauro, E. Benedetti, G. Morelli, *J. Pept.Sci.* **2009**, 15(3),242-250.
- 64 A. Accardo, D. Tesauro, L. Aloj, C. Pedone, G. Morelli, *Coordin. Chem. Rev.* **2009**, 253, 2193-2213.
- 65 A. Camposeo, M. Moffa, L. Persano In: A. Macagnano, E. Zampetti, E. Kny E. (eds) *Electrospinning for High Performance Sensors. NanoScience and Technology.* **2015**, Springer.
- 66 C. Li, G. Shi, *J. Photochem. Photobio. C: Photochemi. Rev.* **2014**, 19, 20-34.
- 67 A.M. Smith, N. Shuming, *Acc Chem Res.* **2010**, 43(2), 190-200.
- 68 R. Schirhagl, K. Chang, M. Loretz, C.L. Degen, *Annu. Rev. Phys. Chem.* **2014**, 65, 83-105.
- 69 X. Sun, Y. Lei, *TrAC* **2017**, 87, 169-180.
- 70 F. Gao, *Appl. Phys. Lett.* **2011**, 98, 193105.
- 71 E. Mehdizadeh, A. Rahafrooz, S. Pourkamali, *Nanotechnology* **2014**, 25(31), 315303-315310.
- 72 M. Krivec, A. Roshanghias, A. Abram, A. Binder, *Microelectron. Eng.* **2017**, 176, 1-5.
- 73 A.K. Singh, B.P. Panda, S. Mohanty, S.K. Nayak, *Materials Focus* **2016**, 5(6), 529-536.
- 74 Y. Zhu, J. Moran-Mirabal, *Langmuir* **2016**, 32(42), 11021-11028.
- 75 G.M. Whitesides, B. Grzybowski, *Science* **2002**, 295, 2418-2421.
- 76 T. Taira, S. Yanagisawa, T. Nagano, T. Tsuji, A. Endo, T. Imura, *Colloids Surf. B: Biointerfaces*, **2017**, 156, 382-387.
- 77 W. Huang, J. Yang, Y. Jia, X. Wang, X. Xue, H. Yang, G. Wang, B. Jiang, F. Li, S. Komarneni, *Polymers* **2016**, 8(5), 183-187.
- 78 P. Xing, X. Chu, G. Du, M. Ma, S. Li, A. Hao, *Colloid Polymer Sci.* **2014**, 292(12), 3223-3231.
- 79 A. Klug, *Angew. Chem. Int. Ed. Engl.* **1983**, 22, 565-636.

- 80 K.H. Downing, E. Nogales, *Curr. Opin. Cell. Biol.* **1998**, 10, 16–22.
- 81 E. Nogales, M. Whittaker, R.A. Milligan, K.H. Downing, *Cell* **1999**, 96, 79–88.
- 82 U.B. Sleytr, P. Messner, D. Pum, M. Sa´ra, *Angew. Chem. Int. Ed.* **1999**, 38, 1034–1054.
- 83 L. Sun, C. Zheng, T.J. Webster, *Int. J. Nanomedicine* **2017**, 12, 73–86.
- 84 M.R. Ghadiri, J.R. Granja, R.A. Milligan, D.E. Mcrecree, N. Khazanovich, *Nature* **1993**, 366, 324–327.
- 85 C. Valery, M. Paternostre, B. Robert, T. Gulik-Krzywicki, T. Narayanan, J.C. Dedieu, G. Keller, M.L. Torres, R. Cherif-Cheikh, P. Calvo, F. Artzner, *Proc. Natl. Acad. Sci. U.S.A.* **2003**, 100, 10258–10262.
- 86 K.M. Koss, L.D. Unsworth, *Acta Biomaterialia* **2016**, 44, 2–15.
- 87 C. Tang, F. Qiu, X. Zhao, *J. Nanomaterials* **2013**, 469261, 9 pp.
- 88 Y. Navon, M. Zhou, J.B. Matson, R. Bitton, *Biomacromolecules* **2016**, 17(1), 262–270.
- 89 M. Reches, E. Gazit, *Phy. Biol.* **2006**, 3(1), S10–9.
- 90 M.S.K.S. Liberato, E.R. da Silva, D.R. de Araujo, S. Guha, W.A. Alves, *J. Mater. Chem. B: Materials for Biology and Medicine* **2016**, 4, 1405–1413.
- 91 Z. Yu, F. Tantakitti, L.C. Palmer, S.I. Stupp, *Nano Letters* **2016**, 16(11), 6967–6974.
- 92 Y. Miller, B. Ma, R. Nussinov, *J. Phys. Chem. B* **2015**, 119(2), 482–490.
- 93 K.A. Dill, S.B. Ozkan, M.S. Shell, T.R. Weikl, *Annu. Rev. Biophys.* **2008**, 37, 289–316.
- 94 S. Bhattacharyya, H. Yu, C. Mim, A. Matouschek, *Nat. Rev. Mol. Cel. Bio.* **2014**, 15, 122–133.
- 95 H. Saibil, *Nature Rev. Mol. Cel. Bio.* **2013**, 14, 630–642.
- 96 F. Ursini, K.J. Davies, M. Maiorino, T. Parasassi, A. Sevanian, *Trends Mol. Med.* **2002**, 8(8), 370–374.
- 97 J. Bieschke, Q. Zhang, D.A. Bosco, R.A. Lerner, E.T. Powers, P. Jr Wentworth, J.W. Kelly, *Acc. Chem. Res.* **2006**, 39(9), 611–619.
- 98 E.B. Malolepsza, *Methods Mol. Biol.* **2008**, 443, 297–330.
- 99 S. Dukan, A. Farewell, M. Ballesteros, F. Taddei, M. Radman, T. Nystrom, *Proc. Natl. Acad. Sci. U.S.A.* **2000**, 97(11), 5746–5749.

- 100 R.S. Rajan, R.R. Kopito, *Abstracts of papers of the Am.Chem.Soc.* **2004**, 227, U220.
- 101 D.A. Drummond, C.O. Wilke, *Cell* **2008**, 134(2), 341-352.
- 102 M.L. De Marco, V. Daggett, *Biochemistry* **2007**, 46(11), 3045-3054.
- 103 M.W. van der Kamp, V. Daggett, *Biophys. J.* **2010**, 99(7), 2289-2298.
- 104 L.M. Blancas-Mejía, M. Ramirez-Alvarado, *Annu. Rev. Biochem.* **2013**, 82, 745-774.
- 105 F. Chiti, C.M. Dobson, *Annu. Rev. Biochem.* **2006**, 75, 333-366.
- 106 C. Casalone, G. Zanusso, P. Acutis, S. Ferrari, L. Capucci, F. Tagliavini, S. Monaco, M. Caramelli, *Proc. Natl. Acad. Sci. U.S.A.* **2003**, 101(9), 3065-3070.
- 107 C.M. Dobson, *Philos. Trans. R. Soc. Lond. B. Biol. Sci.* **2001**, 356(1406), 133-145.
- 108 A. Vital, M.H. Cannon, R. Gil, J.J. Hauw, C. Vital, *Neuropathology* **2007**, 27(3), 273-277.
- 109 M. P. Murphy, H. LeVine, *J. Alzheimers Dis.* **2010**, 19(1), 311-323.
- 110 D.P. McGowan, W. van Roon-Mom, H. Holloway, G.P. Bates, L. Mangiarini, G.J. Cooper, R.L. Faull, R.G. Snell, *Neuroscience* **2000**, 100(4), 677-680.
- 111 D.J. Irwin, V.M-Y. Lee, J. Q. Trojanowski, *Nat. Rev. Neurosci.* **2013**, 14(9), 626-636.
- 112 S.C. Shin, J. Robinson-Papp, *Mt. Sinai J. Med.* **2012**, 79(6), 733-748.
- 113 T.P.J. Knowles, R. Mezzenga, *Adv. Mater.* **2016**, 28(31), 6546-6561.
- 114 V.A. Iconomidou, G. Vriend, S.J. Hamodrakas, *FEBS Lett.* **2000**, 479, 141-145.
- 115 . S. Kasai, Y. Ohga, M. Mochizuki, N. Nishi, Y. Kadoya, M. Nomizu, *Biopolymers* **2004**, 76(1), 27-33.
- 116 S.K. Maji, M.H. Perrin, M.R. Sawaya, S. Jessberger, K. Vadodaria, R.A. Rissman, P.S. Singru, K.P. Nilsson, R. Simon, D. Schubert, D. *Science* **2009**, 325, 328-332.
- 117 D.M. Fowler, A.V. Koulov, C. Alory-Jost, M.S. Marks, W.E. Balch, J.W. Kelly, *PLoS Biol.* **2006**, 4, e6
- 118 K. Si, M. Giustetto, A. Etkin, R. Hsu, A.M. Janisiewicz, M.C. Miniaci, J.H. Kim, H. Zhu, E.R. Kandel, *Cell* **2003**, 115, 893-904.
- 119 K. Si, Y.B. Choi, E. White-Grindley, A. Majumdar, E.R. Kandel, *Cell* **2010**, 140, 421-435.

- 120 R.A. Kyle, M.A. Gertz, Amyloid and amyloidosis 1998: proceedings of the VIIIth international symposium on amyloidosis, **1999**, CRC Press.
- 121 F. Chiti, P. Webster, N. Taddei, A. Clark, M. Stefani, G. Ramponi, C.M. Dobson, *Proc. Nat. Acad. Sci. U.S.A.* **1999**, 96(7), 3590-3594.
- 122 L. Jimenez, J.I. Gujjarro, E. Orlova, J. Zurdo, C.M. Dobson, M. Sunde, H.R. Saibil, *EMBO J.* **1999**, 18(4), 815-821.
- 123 M. Sunde, C. Blake, *Adv. Protein Chem.* **1997**, 50, 123-159.
- 124 L.C. Serpell, *Biochim. Biophys. Acta, Mol. Basis Dis.* **2000**, 1502, 16-30.
- 125 R. Orbach, I. Mironi-Harpaz, L. Adler-Abramovich, E. Mossou, E.P. Mitchell, V.T. Forsyth, E. Gazit, D. Seliktar, *Langmuir* **2012**, 28, 2015-2022.
- 126 R. Nelson, D. Eisenberg, *Curr. Opin. Struct. Biol.* **2006**, 16, 260-265.
- 127 R. Nelson, M.R. Sawaya, M. Balbirnie, A.O. Madsen, C. Riek, R. Grothe, D. Eisenberg, *Nature* **2005**, 435, 773-778.
- 128 W.E. Klunk, R.F. Jacob, R.P. Mason, *Analytical Biochemistry* **1999**, 266, 66-76.
- 129 M.R.H. Krebs, E.H.C. Bromley, A.M. Donald, *J. Struct. Biol.* **2005**, 149 (1), 31-37.
- 130 T. Harada, R. Kuroda, *Biopolymers.* **2011**, 95(2), 127-134.
- 131 A.J. Howie, D.B. Brewer, *Micron.* **2009**, 40(3), 285-301.
- 132 J. Seo, W. Hoffmann, S. Warnke, X. Huang, S. Gewinner, W. Schöllkopf, M.T. Bowers, G. von Helden, K. Pagel, *Nature Chemistry* **2017**, 9, 39-44.
- 133 T.R. Jahn, O.S. Makin, K.L. Morris, K.E. Marshall, P. Tian, P. Sikorski, L.C. Serpell, *J Mol Biol.* **2010**, 395(4), 717-727.
- 134 B. Neddenriep, A. Calciano, D. Conti, E. Sauve, M. Paterson, E. Bruno, D.A. Moffet, *Open Biotechnol. J.* **2011**, 23(5), 39-46.
- 135 D. Goyal, S. Shuaib, S. Mann, B. Goyal, *ACS Comb. Sci.* **2017**, 19(2), 55-80.
- 136 K. Tenidis, M. Waldner, J. Bernhagen, W. Fischle, M. Bergmann, M. Weber, M.L. Merkle, W. Voelter, H. Brunner, A. Kapurniotu, *J. Mol. Biol.* **2000**, 295, 1055-1071.

- 137 Y. Mazor, S. Gilead, I. Benhar, E. Gazit, *J. Mol. Biol.* **2002**, 322, 1013-1024.
- 138 M. Reches, Y. Porat, E. Gazit, *J. Biol. Chem.* **2002**, 277, 35475-35480.
- 139 M. Reches, E. Gazit, *Amyloid* **2004**, 11, 81-89.
- 140 J.J. Balbach, Y. Ishii, O.N. Antzutkin, R.D. Leapman, N.W. Rizzo, F. Dyda, J. Reed, R. Tycko, *Biochemistry* **2000**, 39, 13748-13759.
- 141 C. Hilbich, B. Kisters-Woike, J. Reed, C.L. Masters, K. Beyreuther, *J. Mol. Biol.* **1992**, 228, 460-473.
- 142 D. Haldar, A. Banerjee, *Int. J. Pept. Res. Ther.* **2006**, 12, 341-348.
- 143 C.R. Martinez, B.L. Iverson, *Chem. Sci.* **2012**, 3, 2191-2201.
- 144 M. Reches, E. Gazit, *Science* **2003**, 300(5619), 625-627.
- 145 M.F. Perutz, J.T. Finch, J. Berriman, A. Lesk, *Proc. Natl. Acad. Sci. U.S.A.* **2002**, 99(8), 5591-5595.
- 146 M. Reches, E. Gazit, *Nano Letters* **2004**, 4(4), 581-585.
- 147 C. Guo, Y. Luo, R. Zihou, G. Wei, *ACS Nano* **2012**, 6, 3907-3918.
- 148 M. Reches, E. Gazit, *Isr. J. Chem.* **2005**, 45, 363-371.
- 149 88. I. Azuri, L. Abramovich, E. Gazit, O. Hod, L. Kronik, *J. Am. Chem. Soc.* **2014**, 136, 963-969.
- 150 C.H. Görbitz, *Chem. Commun.* **2006**, 22, 2332-2334.
- 151 C.H. Görbitz, *Chem. Eur. J.* **2001**, 7, 5153-5159.
- 152 R.F. Silva, D.R. Araujo, E.R. Silva, R.A. Ando, W.A. Alves, *Langmuir* **2013**, 29, 10205-10212.
- 153 L. Adler-Abramovich, M. Reches, V.L. Sedman, A. Stephanie, S.J.B. Tendler, E. Gazit, *Langmuir* **2006**, 22(3), 1313-1320.
- 154 N. Kol, L. Adler-Abramovich, D. Barlam, R.Z. Shneck, E. Gazit, I. Rouso, *Nano Letters*, **2005**, 5(7), 1343-1346.
- 155 L. Niu, X. Chen, S. Allen, S.J.B. Tendler, *Langmuir* **2007**, 23, 7443-7446.
- 156 95. K.B. Andersen, J. Castillo-Leon, M. Hedstromb, W.E. Svendsen, *Nanoscale* **2011**, 3, 994-998.
- 157 J.S. Lee, I. Yoon, J. Kim, H. Ihee, B. Kim, C. B. Park, *Angew. Chem. In. Ed.* **2010**, 50, 1164-1167.
- 158 S. Vasileva, P. Zelenovskiya, D. Vasileva, A. Nuraeva, V. Ya Shura, A.L. Kholkin, *J. Phys. Chem. Solids* **2016**, 93, 68-72.
- 159 V. Nguyen, R. Zhu, K. Jenkins, R. Yang, *Nature Communications* **2016**, 7, 13566.

- 160 Y. Song, S.R. Challa, C.J. Medforth, Y. Qiu, R.K. Watt, D. Peña, J.E. Miller, F. van Swol, J.A. Shelnutt, *Chem. Commun.* **2004**, 9, 1044-1045.
- 161 N.I. Sax, *Dangerous properties of industrial materials. 6th ed.* **1984**, Van Nostrand Reinhold New York.
- 162 T.O. Mason, D.Y. Chirgadze, A. Levin, L. Adler-Abramovich, E. Gazit, T.P.J. Knowles, A.K. Buell, *ACS Nano* **2014**, 8(2), 1243-1253.
- 163 J. Castillo-León, R. Rodriguez-Trujillo, S. Gauthier, A.C.Ø. Jensen, W.E. Svendsen, *Microelectron. Eng.* **2011**, 88(8), 1685-1688.
- 164 L. Adler-Abramovich, D. Aronov, P. Beker, M. Yevnin, S. Stempler, G. Rosenman, E. Gazit, *Nature Nanotechnology* **2009**, 4, 849-854.
- 165 J. Ryu, C.B. Park, *Adv. Mater.* **2008**, 20, 3754-3758.
- 166 G. Singh, A.M. Bittner, S. Loscher, N. Malinowski, K. Kern, *Adv. Mater.* **2008**, 20, 2332-2336.
- 167 L. Adler-Abramovich, E. Gazit, *J. Pep. Sci.* **2007**, 14, 217-223.
- 168 M. Dimaki, P. Bøggild, *Physica status solidi (a)* **2006**, 203, 1088-1093.
- 169 D. Whang, S. Jin, Y. Wu, C.M. Lieber, *Nano Letters* **2003**, 3, 1255-1259.
- 170 W. Zhanga, C. Gao, *J. Mater. Chem. A* **2017**, in press.
- 171 M.S. Lin, L.Y. Chen, H.T. Tsai, S.S. Wang, Y. Chang, A. Higuchi, W.Y. Chen, *Langmuir* **2008**, 24(11), 5802-5808.
- 172 X.H. Yan, Y. Cui, Q. He, K.W. Wang, J.B. Li, W.H. Mu, B.L. Wang, Z.C. Ou-yang, *Chem. Eur. J.* **2008**, 14(19), 5974-5980.
- 173 G. Demirel, R. Malvadkar, R.C. Demirel, *Langmuir* **2010**, 26, 1460-1463.
- 174 X. Yan, Q. He, K. Wang, L. Duan, Y. Cui, J. Li, *Angew Chem. Int. Ed.* **2007**, 46, 2431-2434.
- 175 A.M. Smith, R.J. Williams, C. Tang, P. Coppo, R.F. Collins, M.L. Turner, A. Saiani, R.V. Ulijn, *Adv. Mater.* **2007**, 20, 37-41.
- 176 A. Mahler, M. Reches, M. Rechter, S. Cohan, E. Gazit, *Adv. Mater.* **2006**, 18, 1365-1370.
- 177 S. Yuran, Y. Razvag, M. Reches, *ACS Nano* **2012**, 6(11), 9559-9566.
- 178 A.D. Martin, J.P. Wojciechowski, A.B. Robinson, C. Heu, C.J. Garvey, J. Ratcliffe, L.J. Waddington, J. Gardiner, P. Thordarson, *Sci. Rep.* **2017**, 7, 43947.

- 179 M. Pellach, S. Mondal, L.J.W. Shimon, L. Adler-Abramovich, L. Buzhansky, E. Gazit, *Chem. Mater.* **2016**, 28(12), 4341-4348.
- 180 P. Tamamis, L. Adler-Abramovich, M. Reches, K. Marshall, P. Sikorski, L.C Serpell, E. Gazit, G. Archontis, *Biophys. J.* **2009**, 96(12), 5020-5029.
- 181 E. Mayans, J. Casanovas, A.M. Gil, A.I. Jimenez, C. Cativiela, J. Puiggali, C. Aleman, *Langmuir* **2017**, 33(16), 4036-4048.
- 182 E. Mayans, G. Ballano, J. Casanovas, A. Diaz, M.M. Perez-Madrigal, F. Estrany, J. Puiggali, C. Cativiela, C. Aleman, *Chem. Eur. J.* **2015**, 21(47), 16895-16905.
- 183 Z. Arnon, L. Adler-Abramovich, A. Levin, E. Gazit, *Isr. J. Chem.* **2015**, 55(6-7), 756-762.
- 184 N. Tzokova, C.M. Fernyhough, M.F. Butler, S.P. Armes, A.J. Ryan, P.D. Topham, D.J. Adams, *Langmuir* **2009**, 25(18), 11082-11089.
- 185 H-A. Klok, *Macromolecules* **2009**, 42, 7990-8000.
- 186 N. Tzokova, C.M. Fernyhough, P.D. Topham, N. Sandon, D.J. Adams, M.F. Butler, S.P. Armes, A.J. Ryan, *Langmuir* **2009**, 25(18), 2479-2485.
- 187 V. Castelletto, I.W. Hamley, *Biophys Chem.* 2009, 141, 169-174.
- 188 I. O. Matos, W.A. Alves, *ACS Applied Mat. Interf.* **2011**, 3(11), 4437-4443.
- 189 S. Kogikoski, C.P. Sousa, M.S. Liberato, T. Andrade-Filho, T. Prieto, F.F. Ferreira, A.R. Rocha, S. Guha, W. Alves, *Phys. Chem. Chem. Phys.* **2016**, 18(4), 3223-3233.
- 190 N. Even, L. Adler-Abramovich, L. Buzhansky, H. Dodiuk, E. Gazit, *Small* **2011**, 7(8), 1007-1011.
- 191 Y. Ikezoe, G. Washino, T. Uemura, S. Kitagawa, H. Matsui, *Nat. Mater.* **2012**, 11, 1081-1085.
- 192 H. Yan, P. Zhu, J. Li, *Chem. Soc. Rev.* **2010**, 39, 1877-1890.
- 193 J. Ryu, S.Y. Lim, C.B. Park, *Adv. Mater.* **2009**, 21, 1577-1581
- 194 T. Yuan T, J. Fei, Y. Xu Y, X. Yang, J. Li, *Macromol. Rapid Commun.* **2017**, 10.1002/marc.201700408.
- 195 J.R. Mart, D. Rachel, M.M. Osborne, M. Stevens, R.V. Ulijn, *Soft Matter* **2006**, 2, 822-835.
- 196 C. Diaferia, E. Gianolio, P. Palladino, F. Arena, C. Boffa, G. Morelli, A. Accardo, *Adv. Funct. Mater* **2015**; 25(45),7003-7016.

- 197 C. Diaferia, E. Gianolio, A. Accardo, G. Morelli, *J. Pept. Sci.* **2017**, 23(2), 122-130.
- 198 C. Diaferia, E. Gianolio, T. Sibillano, F.A. Mercurio, M. Leone, C. Giannini, N. Balasco, L. Vitagliano, G. Morelli, A. Accardo, *Sci. Rep.* **2017**, 7, 307.
- 199 C. Diaferia, F.A. Mercurio, C. Giannini, T. Sibillano, G. Morelli, M. Leone, A. Accardo, *Sci. Rep.* **2016**; 6, 26638.
- 200 A. Accardo, A. Morisco, E. Gianolio, D. Tesauro, G. Mangiapia, A. Radulescu, A. Brandt, G. Morelli, *J. Pept. Sci.* **2011**, 17, 154-162.
- 201 jima, *J. Lumin.* **1976**, 11, 429-432.
- 202 A. Accardo, D. Tesauro, G. Mangiapia, C. Pedone, G. Morelli, *Biopolymers (Pept. Sci.)* **2007**, 88(2), 115-121.
- 203 R. Huang, R. Su, W. Qi, J. Zhao, Z. He, *Nanotechnology* **2011**, 22, 245609-245615.
- 204 S.D. Moran, M.T. Zanni, *J. Phys. Chem. Lett.* **2014**, 5, 1984-1993.
- 205 H.A. Behanna, J.J.J.M. Donners, A.C. Gordon, S.I. Stupp, *J. Am. Chem. Soc.* **2005**, 127, 1193-1200.
- 206 R. Huang, W. Qi, L. Feng, R. Su, Z. He, *Soft Matter* **2011**, 7, 6222-6230.
- 207 L.C. Serpell, *Biochim. Biophys. Acta, Mol. Basis Dis.* **2000**, 1502, 16-30.
- 208 M. Biancalana, S. Koide, *Biochim. Biophys. Acta.* **2010**, 1804(7), 1405-1412.
- 209 C. Wu, J. Scott, J.E. Schea, *Biophys J.* **2012**, 103(3), 550-557.
- 210 S.O. Makin, P. Sikorski, L.C. Serpell, *J. Appl. Cryst.* **2007**, 40, 966-972.
- 211 I. Solomon, *Phys. Rev.* **1955**, 99, 559-565.
- 212 P. Caravan, J.J. Ellison, T.J. McMurry, R.B. Lauffer, *Chem. Rev.* **1999**, 99, 2293-2352.
- 213 W.T. Truong, Y. Su, D. Gloria, F. Braet, P. Thordarson, *Biomaterials Sciences* **2015**, 3, 298-307.
- 214 E. Gianolio, F. Arena, G.J. Strijkers, K. Nicolay, A. Högset, S. Aime, *Magn. Reson. Med.* **2011**, 65(1), 212-219.
- 215 W.C. Chang, P.D. White, *Fmoc solid phase peptide synthesis, a practical approach.* **2000** Oxford University Press: New York, USA.
- 216 H. Yang, S. Yang, J. Kong, A. Dong, S. Yu, *Nat Protocols* **2015**, 10, 382-396.
- 217 V. Castelletto, G.E. Newby, D.H. Merlino, I.W. Hamley, D. Liu, L. Noirez, *Polym. Chem.* **2010**, 1, 453-459.

- 218 D.V. Unverferth, R.D. Magorien, C.V. Leier, S.P. Balcerzak, *Cancer Treat. Rew.* **1982**, 9(2), 149-164.
- 219 C.L. Chin, W.M. Whelan, I. A. Vitkin, In: *Optical Fiber Sensors for Biomedical Applications* **2010** A. Welch, M. van Gemert (eds) Springer, Dordrecht.
- 220 S.T. Parker, P. Domachuk, J. Amsden, J. Bressner, J.A. Lewis, D.L. Kaplan, F.G. Omenetto, *Adv. Mater.* **2009**, 21, 1-5.
- 221 N. Huang, J. Voros, S.M de Paul, N.D. Spencer, *Langmuir* **2002**, 18, 220-230.
- 222 A. Jain, A.H.J. Yang, D. Erickson, *Optics Lett.* **2012**, 37(9), 1472-1474.
- 223 N. Amdusky, M. Molotoskii, D. Aronov, L. Adler-Abramovoch, E. Gazit, G. Rosenman, *Nano Lett.* **2009**, 9(9), 3111-3115.
- 224 A. Handelman, A. Natan, G. Rosenman, *J. Pept. Sci.* **2014**, 20, 487-493.
- 225 A. Handelman, N. Kuritz, A. Natan, G. Rosenman, *Langmuir* **2016**, 32(12), 2847-2862.
- 226 A. Handelman, S. Lavrov, A. Kundryavtsev, A. Khatchaturiants, Y. Rosemberg, E. Mishina, G. Rosenman, *Adv. Optical Mat.* **2013**, 1, 875-884.
- 227 L.L. del Mercato, P.P. Pompa, G. Maruccio, A. Della Torre, S. Sabella, A.M Tamburro, R. Cingolani, R. Rinaldi, *Proc. Natl. Acad. Sci. U.S.A.* **2007**, 104(46), 18019-18024.
- 228 O. Tcherkasskaya, *Protein Sci.* **2007**, 16, 561-571.
- 229 P. Hanczyc, M. Samoc, B. Norden, *Nat. Photonics* **2013**, 7, 969-972.
- 230 D. Pinotsi, L. Grisanti, P. Mahou, R. Gebauer, C.F. Kaminski, A. Hassanali, G.S. Kaminski Schierle, *J. Am. Chem. Soc.* **2016**, 138, 3046-3057.
- 231 C. Diaferia, T. Sibillano, C. Giannini, V. Roviello, L. Vitagliano, G. Morelli, A. Accardo, *Chem. Eur. J.* **2017**, 23(36), 8741-8748.
- 232 D. Eisenberg, M. Jucker, *Cell* **2012**, 148(6), 1188-1203.
- 233 S. Burkoth, T.L.S. Benzinger, D.N.M. Jones, K. Hallenga, S.C. Meredith, D.G. Lynn, *J. Am. Chem. Soc.* **1998**, 120(30), 7655-7656.
- 234 T.S. Burkoth, T.L.S. Benzinger, V. Urban, D.G. Lynn, S.C. Meredith, P. Thiyagarajan, *J. Am. Chem. Soc.* **1999**, 121(32), 7429-7430.

- 235 V. Castelletto, G. Cheng, S. Furzeland, D. Atkins, I.W. Hamley, *Soft Matter* **2012**, 8, 5434-5438.
- 236 A.V. Semenyuk, D.I. Svergun, *J. Appl. Cryst.* **1991**, 24, 537-540.
- 237 G. Cattani, L. Vogeley, P.B. Crowley, *Nature Chemistry* **2015**, 7, 823-828.
- 238 T.J. van Ham, A. Esposito, J.R. Kumita, S.T. Hsu, G.S. Kaminski, C.F. Kaminski, C.M. Dobson, E.A. Nollen, C.W. Bertoncini, *Mol. Biol.* **2010**, 395(3), 627-42.
- 239 C. Diaferia, T. Sibillano, D. Altamura, V. Roviello, L. Vitagliano, C. Giannini, G. Morelli, A. Accardo, *Chem. Eur. J.* **2017**, 22(46), 16586-16597.
- 240 I.W. Hamley, *Biomacromolecules* **2014**, 15, 1543-1549.
- 241 J. Kong, S. Yu, *Acta Bioch. Biophys. Sinica* 2007, 39(8), 549-559.
- 242 Takahashi, Y. Tadokoro, H. *Macromolecules* **1973**, 6, 672-65.
- 243 M. Sunde, L.C. Serpell, M. Bartlam, P.E. Fraser, M.B. Pepys, C.C. Blake, *J Mol Biol.* **1997**, 273, 729-739.
- 244 N.A. Dudukovic, C.F. Zukoski, *Soft Matter* **2015**, 11, 7663-7673.
- 245 S.R. Raghavan, B.H. Cipriano, R.G. Weiss, **2005** P.Terech P. (eds.), Springer, , Chapter 8, 233-244.
- 246 Z. Huang, C. Cheng, J. Wang, H. Wei, X. Liu, X. Yan, Y. Zhou, Y. Liu and S. Yang, *Cell Physiol Biochem*, 2017, 41, 1572-1583.
- 247 41.N. A. Dudukovic and C. F. Zukoski, *Langmuir*, 2014, 30, 4493-4500.
- 248 W. Heine, M. Radke, K. D. Wutzke, *Amino Acids* **1995**, 9(3), 91-205.
- 249 Y. Shimazaki, T. Yajima, O.Yamauchi, *J. Inorg. Biochem.* **2015**, 148, 105-115.
- 250 S.C. Vigil-Cruz, A.M. Peck, J.V. Aldrich, **2006** *Understanding biology using peptides: proceedings of the 19th American peptide symposium* (S. E. Blondelle, Ed.), Vol. 9, Springer.
- 251 A. Isidro-Llobet, M.A. Alvarez, F. Albericio, *Chem. Rev.* **2009**, 109, 2455-2504.
- 252 S.M.M. Reddy, G. Shanmugam, A.B. Mandal, *Org. Biomol. Chem.* **2014**, 12, 6181-6189.
- 253 N.J. Greenfield, *Proc. Natl. Acad. Sci. U.S.A.* **2006**, 1(6), 2876-2890.
- 254 W.C. Johnson, *Proteins* **1999**, 35, 307-312.

- 255 V.R. Naidu, M.C. Kim, J. Suk, H.J. Kim, M. Lee, E. Sim, K.S. Jeong, *Org. Lett.* **2008**, 10, 5373-5376.
- 256 V. Haridas, S. Sadanandan, S. Dhawan, R. Mishra, I. Jain, G. Goel, Y. Huc, S. Patel, *Org. Biomol. Chem.* **2017**, 15, 1661-1669.
- 257 W.W. Streicher, G.I. Makhatadze, *J. Am. Chem. Soc.* **2006**, 128, 30-31.
- 258 I. Coin, M. Beyermann, M. Bienert, *Protocol Exchange* **2007**, 10.1038/nprot.2007.461
- 259 A. Barge, G. Cravotto, E. Gianolio, F. Fedeli, *Contrast Media Mol. Imaging* **2006**, 1, 184-188.
- 260 K.S. Birdi, H.N. Singh, S.U. Dalsager, *J. Phys. Chem.* **1979**, 83, 2733-2737.
- 261 E. De Vendittis, G. Palumbo, G. Parlato, V. Bocchini, *Anal. Biochem.* **1981**, 115, 278-286.
- 262 C.G.O. Griesinger, K. Wuethrich, R.R. Ernst, *J. Am. Chem. Soc.* **1988**, 110, 7870-7872.
- 263 A.R.R.E. Kumar, K. Wuthrich, *Biochem. Biophys. Res. Commun.*, **1980**, 95, 1-6.
- 264 K. Wuthrich, *NMR of proteins and nucleic acids* **1986**.
- 265 T.L. Hwang, A.J. Shaka, *J Magn Reson Ser A* 1995, 112, 275-279.
- 266 L. Tei, *Chem Eur J.* 2010, 16, 8080-8087.
- 267 D. Altamura, R. Lassandro, F.A. Vittoria, L. De Caro, D. Siliqi, M. Ladisa, C. Giannini, *J. Appl. Cryst.* **2012**, 45(4), 869-873.
- 268 T. Sibillano, L. De Caro, D. Altamura, D. Siliqi, M. Ramella, F. Boccafoschi, G. Ciasca, G. Campi, L. Tirinato, E. Di Fabrizio, C. Giannini, *Sci. Rep.* **2014**, 4, 6985.
- 269 D. Van Der Spoel, E. Lindahl, B. Hess, G. Groenhof, A.E. Mark, H.J. Berendsen, *J. Comput. Chem.* **2005**, 26(16), 1701-1718.
- 270 V. Van Der Spoel, E. Lindahl, B. Hess, G. Groenhof, A.E. Mark, H.J. Berendsen, *J. Comput. Chem.* **2005**, 26(16), 1701-1718.
- 271 T.A. Darden, D.M. York, L.G. Pedersen, *J. Chem. Phys.* **1993**, 98(12), 10089-10092.
- 272 W. Humphrey, A. Dalke, K. Schulten, *J. Mol. Graph.* **1996**, 14(1), 27-38.

Peptide Materials Obtained by Aggregation of Polyphenylalanine Conjugates as Gadolinium-Based Magnetic Resonance Imaging Contrast Agents

Carlo Diaferia, Eliana Gianolio, Pasquale Palladino, Francesca Arena, Cinzia Boffa, Giancarlo Morelli, and Antonella Accardo*

Peptide materials based on the aggregation of polyphenylalanine conjugates containing gadolinium complexes and acting as potential contrast agents (CAs) in magnetic resonance imaging (MRI) are described. Monomers contain two (F2) or four (F4) phenylalanine residues for self-assembly, a chelating agent, 1,4,7,10-tetraazacyclododecane-*N,N,N,N*-tetraacetic acid (DOTA) or diethylenetriaminepentaacetic acid (DTPA), for achieving gadolinium coordination, and ethoxylic linkers at two (L₂) or six (L₆) poly(ethylene glycol) (PEG) units between the chelating group and the peptide region. Both DOTA and DTPA tetraphenylalanine derivatives, and their gadolinium complexes DOTA(Gd)-L₆-F4 and DTPA(Gd)-L₆-F4, are able to self-aggregate at very low concentration. Structural characterization, obtained by circular dichroism and infrared measurements, confirms the amyloid type fibril formation in which an antiparallel peptide alignment is preferred. Amyloid type fibril formation is also observed, in solid state, by transmission electron microscopy images and X-ray diffraction patterns. The relaxivity values of DOTA(Gd)-L₆-F4 and DTPA(Gd)-L₆-F4 and their ability to enhance the MRI cellular response on the J774A.1 mouse macrophages cell line indicate that these peptide materials are promising candidate as a new class of supramolecular gadolinium based MRI contrast agents.

1. Introduction

In the last few years an explosion of interest has been focused on the design, synthesis, and characterization of peptide-based materials for nanomedicine and nanoscience.^[1–3] The

advancement of knowledge about molecular mechanism and forces that determine the growth of nanometric structures from basic peptide motifs from one side, and the applicative outcome in the obtainment of peptide-based nanodevices for electronics, biosensing, coating for tissue engineering and cell adhesion, and drug delivery from the other side, have rapidly reached successful results.^[4]

This has been achieved by mimicking the strategies that nature pursues in the construction of complex supramolecular aggregates, essentially based on self-assembly and bottom-up procedures.

A large number of peptide-based building blocks, comprising cyclic peptides, amphiphile peptides, dendritic peptides, and aromatic dipeptides, have been considered for generating self-assembled nanostructures.^[5–8]

Among the different applications of peptide-based materials, there are several advantages, such as the intrinsic biological origin, low immunogenicity, biocompatibility, low cost, high stability, ability for specific molecular recognition, long-term storage, and easy handling, that make synthetic peptides useful and versatile building blocks for applications in biomedical field.

The self-aggregation of short peptide sequences can be catalysed by the insertion of nonpeptidic hydrophobic groups, such as aliphatic chains^[9,10] or cholesterol derivatives,^[11] or introducing amino acids able to promote aromatic π -stacking interactions between their side chains, such as phenylalanine, tyrosine, and tryptophan.^[6]

Intense stimulus in this research area was promoted by the identification of some natural self-aggregation patterns, such as diphenylalanine (FF) motive. Diphenylalanine, which constitutes the core recognition motif of Alzheimer's β -amyloid peptide, is able to self-assemble into many different nanostructures from nanotubes to organogels.^[12,13]

FF nanostructures have been investigated for their mechanical, electrochemical, and optical properties. Many studies reported in literature are principally focused on clarifying the physicochemical aspects responsible for array stability in FF nanostructures,^[14–16] whereas only few studies have been devoted in the investigation of FF aggregates for biomedical

Dr. C. Diaferia, Prof. G. Morelli, Dr. A. Accardo
Department of Pharmacy
Research Centre on Bioactive Peptides (CIRPeB)
University of Naples "Federico II" and DFM Scarl
Via Mezzocannone 16, 80134 Naples, Italy
E-mail: antonella.accardo@unina.it



Dr. E. Gianolio, Dr. F. Arena, Dr. C. Boffa
Department of Molecular Biotechnologies and Health Science
University of Turin
Via Nizza 52, 10125 Turin, Italy

Dr. P. Palladino
Department of Chemical Sciences
University of Catania
Viale A. Doria 6, 95124 Catania, Italy

Dr. P. Palladino
I. N. B. B. Consortium
Viale delle Medaglie D'Oro 305, 00136 Rome, Italy

DOI: 10.1002/adfm.201502458

applications,^[17–19] essentially due to their intrinsic low water solubility.^[20]

Very recently two examples of cationic diphenylalanine based microtubes (FF-MTs) and nanoparticles (CDPNCs) have been reported as potential vehicles for drug delivery.^[21,22] However, research on FF-based compounds as diagnostic tools remains largely unexplored. Here, we describe new peptide materials based on poly-phenylalanine conjugates as potential contrast agents in magnetic resonance imaging (MRI).

The paramagnetic gadolinium complexes currently used in clinical diagnosis as MRI contrast agents are essentially low molecular weight compounds that rapidly equilibrate between the intra- and extravascular spaces after intravenous administration. However, gadolinium-based supramolecular aggregates, such as micelles,^[23,24] liposomes,^[25,26] and peptide amphiphile nanofibers^[27,28] have been proposed as MRI contrast agents in order to obtain enhanced contrast efficacy and different pharmacokinetic behavior.^[29,30] It is known, in fact, that the ability of a MRI contrast agent to act as water proton relaxation agent is proportional to its molecular weight.^[29,30]

Here we report the aggregation properties of phenylalanine derivatives displayed in **Figure 1A**, together with their relaxometric behavior, cytotoxicity, and cellular uptake in J774A.1 and 3T3 cells.

2. Results and Discussion

2.1. Design, Synthesis, and Aggregation Behavior

Various aromatic amino acids (phenylalanine, tryptophan, and tyrosine) and other aromatic moieties (naphthalene, azobenzene, and pyrene) have been proposed as building block for the synthesis of new nanomaterials. The structural properties of the resulting materials strongly depend from several parameters including hydrophilicity/hydrophobicity and extent of the

aromatic ring. The self-assembling peptide derivatives here proposed as MRI contrast agents are based on poly-phenylalanine conjugates. Poly-phenylalanine conjugates, schematically represented in **Figure 1A**, contain two (F2) or four (F4) phenylalanine residues for self-assembly, a bifunctional chelating agent, 1,4,7,10-tetraazacyclododecane-*N,N,N,N*-tetraacetic acid (DOTA) or diethylenetriaminepentaacetic acid (DTPA), for achieving gadolinium coordination and an ethoxylic linker consisting of two (L_2) or six (L_6) PEG units between the chelating group and peptide region. All compounds were obtained by Fmoc/tBu solid phase synthesis in good yield and high purity. The relative simple self-organization of di-phenylalanine depends on a combination of two kinds of not covalent interactions: i) head-to-tail backbone hydrogen bonds and ii) π - π stacking between the aromatic ring of side chains.^[14] Hydrogen bonds and π - π stacking are weak not covalent interactions that occur only if mutual guidance and directionality of the counterparts are kept. As a consequence, any modification of the peptide requires a careful design. First of all, it is well known that chemical modifications of Phe–Phe homo-dimer at C or N-terminus may destroy the head-to-tail intermolecular hydrogen bonds, whereas π - π intermolecular interaction of the aromatic framework should be kept. However, independently from the chelating agent used, di-phenylalanine conjugates DOTA(Gd)-F2 and DTPA(Gd)-F2 here reported do not show propensity to aggregate in water solution (data not shown), probably due to the steric hindrance of the bulk gadolinium complex, even with the insertion of L_2 ethoxylic spacer between the peptide framework and the chelating agent.

Differently, UV-vis and fluorescence measurements suggest a weak aggregation tendency for DOTA- L_6 -F2 and DTPA- L_6 -F2 conjugates, in which L_2 spacer is replaced with L_6 spacer at six ethoxylic units (**Figure 1A**). UV-vis spectra show the typical maximum of Phe residue at 257 nm ($n \rightarrow \pi$ transition of the aromatic residue), and another maximum at 282 nm, distinctive of the Phe excimer formation (data not shown).^[31] Accordingly,

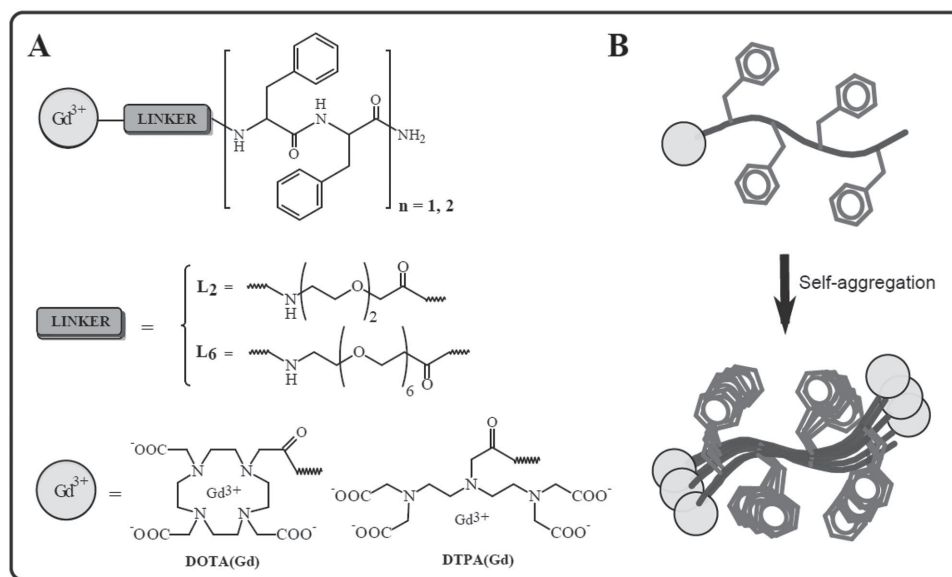


Figure 1. A) Schematic representation of diphenylalanine or tetraphenylalanine conjugates, obtained using L_2 or L_6 polyethoxylic linkers and the DTPA(Gd) or DOTA(Gd) gadolinium complexes. B) Putative aggregation pattern for polyphenylalanine conjugates.

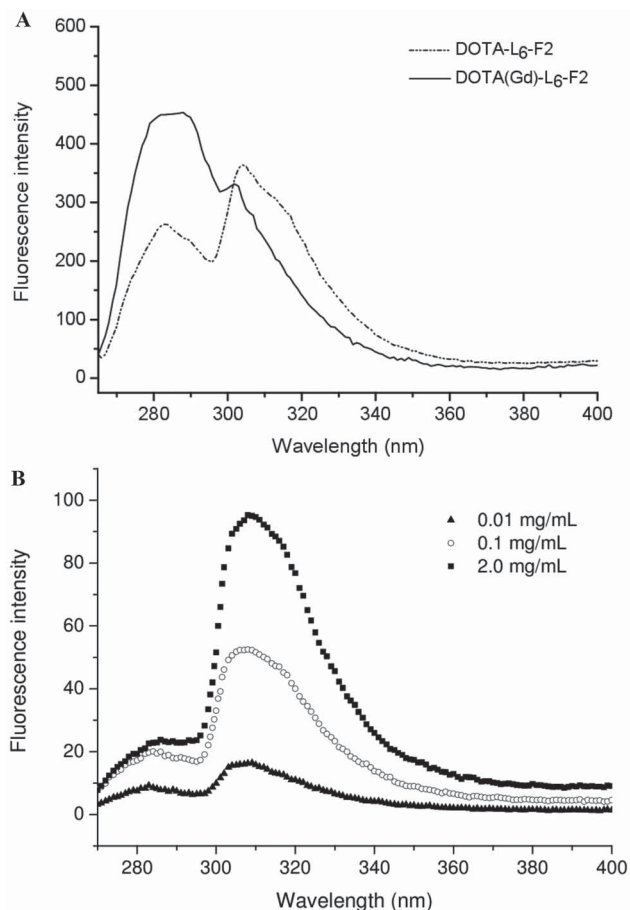


Figure 2. Fluorescence spectra of A) DOTA-L₆-F₂ and its gadolinium complex DOTA(Gd)-L₆-F₂ in water solution at 2.0 mg mL⁻¹ and B) DOTA(Gd)-L₆-F₄ tetra-phenylalanine at a concentration of 0.01, 0.1, and 2.0 mg mL⁻¹. All emission spectra were recorded at 25 °C between 265 and 400 nm with excitation at 258 nm.

fluorescence spectrum of DOTA-L₆-F₂ at 2.0 mg mL⁻¹ reported in **Figure 2A** clearly shows the monomer emission at 282 nm and the conspicuous excimer emission around 310 nm.^[32] However, the emission peak of phenylalanine excimer almost disappears after the gadolinium complexation (see **Figure 2A**).

The same behavior is also displayed by DTPA-L₆-F₂. This outcome could be attributed to the higher steric effect of gadolinium complex with respect to the chelating agent as free base. In order to restore the interactions between the phenylalanine side chains, the peptide framework was reinforced by increasing the number of the phenylalanine residues from two to four, keeping unaltered the length of the spacer. These optimized conjugates DOTA(Gd)-L₆-F₄ and DTPA(Gd)-L₆-F₄ show high water solubility: their solutions appear perfectly clear up to 35 mg mL⁻¹; whereas higher concentration (50 mg mL⁻¹) leads to a hydrogel formation. The same behavior is also observed for L₆-F₄ derivative lacking of chelating agent at the N-terminus. Fluorescence spectra of DOTA(Gd)-L₆-F₄ at three different concentrations (0.01, 0.1, and 2.0 mg mL⁻¹) reported in **Figure 2B** show both the Phe (λ_{282}) and its excimer (λ_{310}) emission peaks, thus confirming the high propensity of the complex to aggregate, also at low concentration. Furthermore, by increasing the

concentration of DOTA(Gd)-L₆-F₄ from 0.01 to 2.0 mg mL⁻¹, a progressive increase (from 1.7 to 4.0) of the ratio between the fluorescence intensities at λ_{310} and λ_{282} is observed. The potential of nanosized supramolecular systems in the field of drug delivery and diagnostic biomedical applications has been investigated from many years. In particular, if MRI diagnostic systems are considered, the possibility to exploit large-sized macromolecules is favourable also from the contrast efficiency point of view. For this reason, on the basis of the preliminary aggregation data, the Gd-complexes of the tetra-phenylalanine conjugates, endowed with the highest propensity to aggregation, were selected to be further investigated for a relaxometric and structural characterization. Moreover, their cytotoxicity and cellular uptake capacity were investigated in J774A.1 and 3T3 cell lines.

2.2. Fluorescence Spectroscopy

Critical aggregate concentration (CAC) values of tetraphenylalanine derivatives as free basis or as gadolinium complexes were quantitatively estimated with a fluorescence-based method using 8-anilinoanthracene-1-sulfonate (ANS) as probe. ANS fluorophore gives fluorescence emission at 460–480 nm only in a hydrophobic environment, such as in the micelle core.^[33] The fluorescence intensity of an ANS solutions (20×10^{-6} M in water) at 475 nm as function of tetra-phenylalanine derivatives concentration are reported in **Figure 3**, and the CAC values of the aggregates were determined at the break point (**Table 1**). During the titration experiment, the fluorescence emission of DOTA-L₆-F₄ remains unchanged until 75×10^{-6} M (≈ 0.099 mg mL⁻¹), whereas an increase in the signal at 475 nm was detected above this concentration value, indicating the self-organization of the tetraphenylalanine derivative (**Figure 3A**). Usually, in the molecules containing chelating agents, aggregation properties can be influenced by two different phenomena: electrostatic repulsions and/or steric hindrance.^[29] However, only a slight decrease in the CAC value is observed after the gadolinium complexation that reduces the negative charge from -3 to 0 (CAC = 0.076 mg mL⁻¹ for DOTA(Gd)-L₆-F₄). On the contrary, a significant change has been observed when DOTA is replaced by the branched chelator DTPA (CAC = 0.59 mg mL⁻¹) or by its gadolinium complex DTPA(Gd) (CAC = 0.51 mg mL⁻¹) (see **Figure 3B** and **Table 1**). These results suggest that the influence of electrostatic repulsions is almost negligible, whereas the replacement of the macrocycle DOTA with the branched and bulky DTPA produces an increase of the CAC values.

Aggregation of tetraphenylalanine derivatives was also investigated by monitoring fluorescence behavior of pyrene (Pyr). 1×10^{-6} M Pyr solution was titrated by adding increasing amounts of tetraphenylalanine derivatives. Fluorescence spectra of Pyr/DOTA(Gd)-L₆-F₄ solutions are reported in **Figure 4A,B**. Pyr is a poorly soluble water molecule that shows an emission spectrum in water with five vibrational bands when excited at $\lambda = 335$ nm: the first (I_1 at 373 nm) and the third (I_3 at 383 nm) of them are strongly affected by the polarity of the surrounding environment. Moreover, at high concentration Pyr gives stacking phenomena resulting in excimer's formation that can be diagnosed by the appearance of a maximum at around 480 nm.^[10]

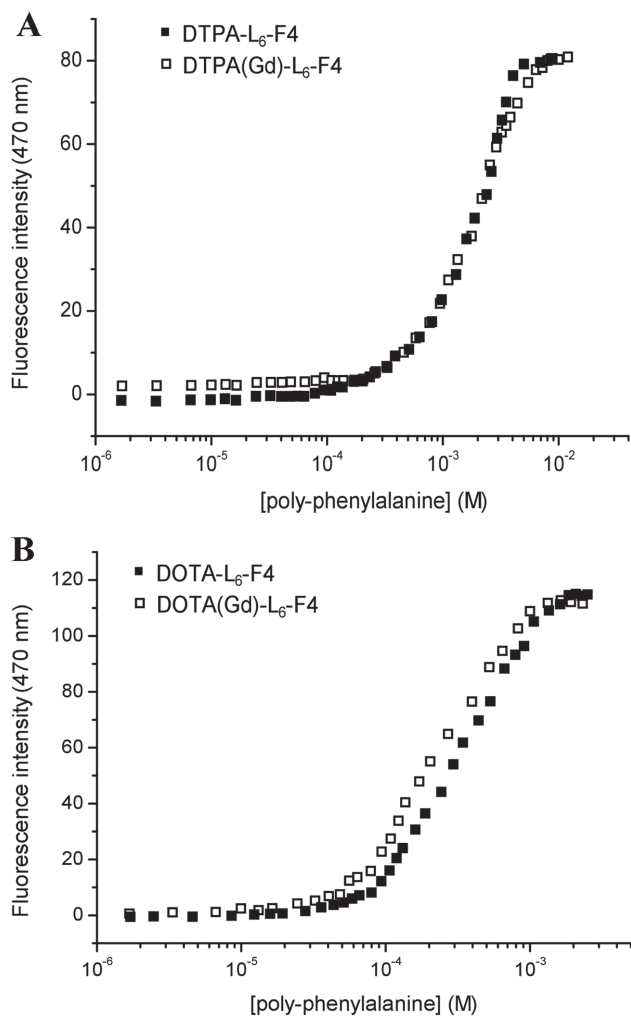


Figure 3. Fluorescence intensity emission of the ANS fluorophore at 475 nm versus the concentration of A) DTPA-L₆-F4 and B) DOTA-L₆-F4 as free bases or as gadolinium complexes. CAC values are established from the break points.

The addition of small amounts of DOTA(Gd)-L₆-F4 to Pyr solution causes a progressive decrease of fluorescence signal (Figure 4A). This effect was observed until concentration 14.3×10^{-6} M of tetra-phenylalanine derivative, in which Pyr/DOTA(Gd)-L₆-F4 molar ratio is 1/10. On the contrary, at concentration of 167×10^{-6} M and higher, an increase of the fluorescence intensities occurs. These data indicate that the aggregation phenomenon occurs at concentration within the 14.3×10^{-6} M to 167×10^{-6} M range, in agreement with the CAC

Table 1. Critical aggregate concentration (CAC) values of tetraphenylalanine derivatives measured by titration of the ANS fluorophore.

Sample	CAC [M]	CAC [mg mL ⁻¹]
DOTA-L ₆ -F4	7.5×10^{-5}	9.9×10^{-2}
DOTA(Gd)-L ₆ -F4	5.1×10^{-5}	7.6×10^{-2}
DTPA-L ₆ -F4	4.5×10^{-4}	59×10^{-2}
DTPA(Gd)-L ₆ -F4	3.5×10^{-4}	51×10^{-2}

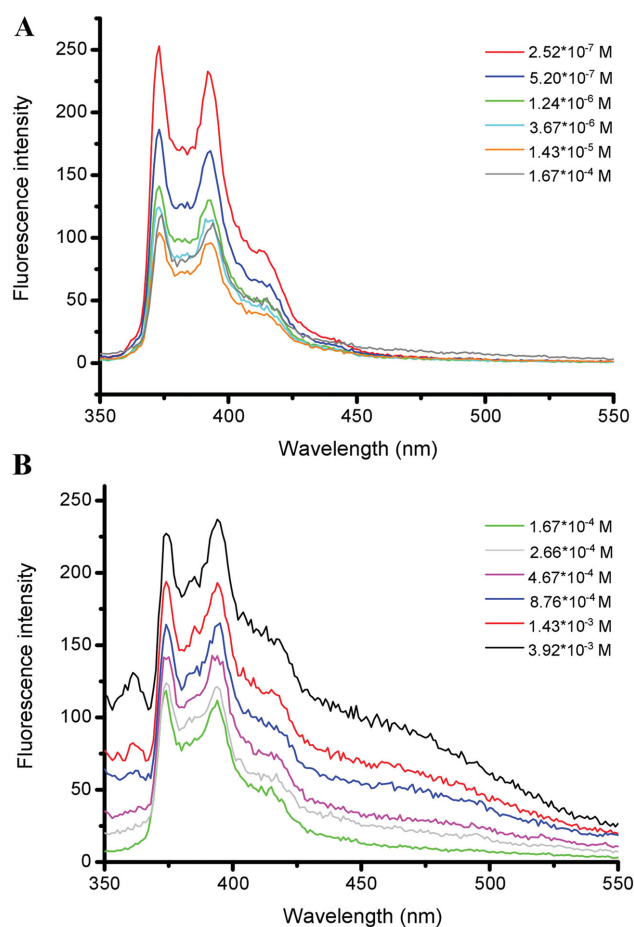


Figure 4. Fluorescence spectra of a 1×10^{-6} M pyrene solution titrated with DOTA(Gd)-L₆-F4. Pyr emission spectra were recorded at 25 °C between 350 and 550 nm with excitation at 335 nm.

value (51×10^{-6} M) found by ANS titration, suggesting that when DOTA(Gd)-L₆-F4 concentration is lower than 14.3×10^{-6} M, the predominant effect is a quenching due to the aromatic stacking between phenylalanine residues and pyrene, whereas above this concentration, a fluorescence resonance energy transfer (FRET) effect occurs in which tetra-phenylalanines, in their aggregated form, act as donor for pyrene.

2.3. Secondary Structure

The secondary structure of DOTA-L₆-F4 and DTPA-L₆-F4 peptide derivatives, as free bases or as gadolinium complexes, was assessed using circular dichroism (CD in Figure 5 and Figures S1–S5, Supporting Information) and Fourier transform infrared spectroscopies (FTIR in Figure 6A).

CD spectra of solutions at several concentrations were recorded between 280 and 195 nm. CD spectra at concentrations below or close to CAC values clearly show two maxima around 205 and 220 nm, due to aromatic side-chains stacking, and pronounced minimum at 232 nm, which can be associated with a β -structure.^[31,34] Significant conformational transition was observed at higher concentrations, where the

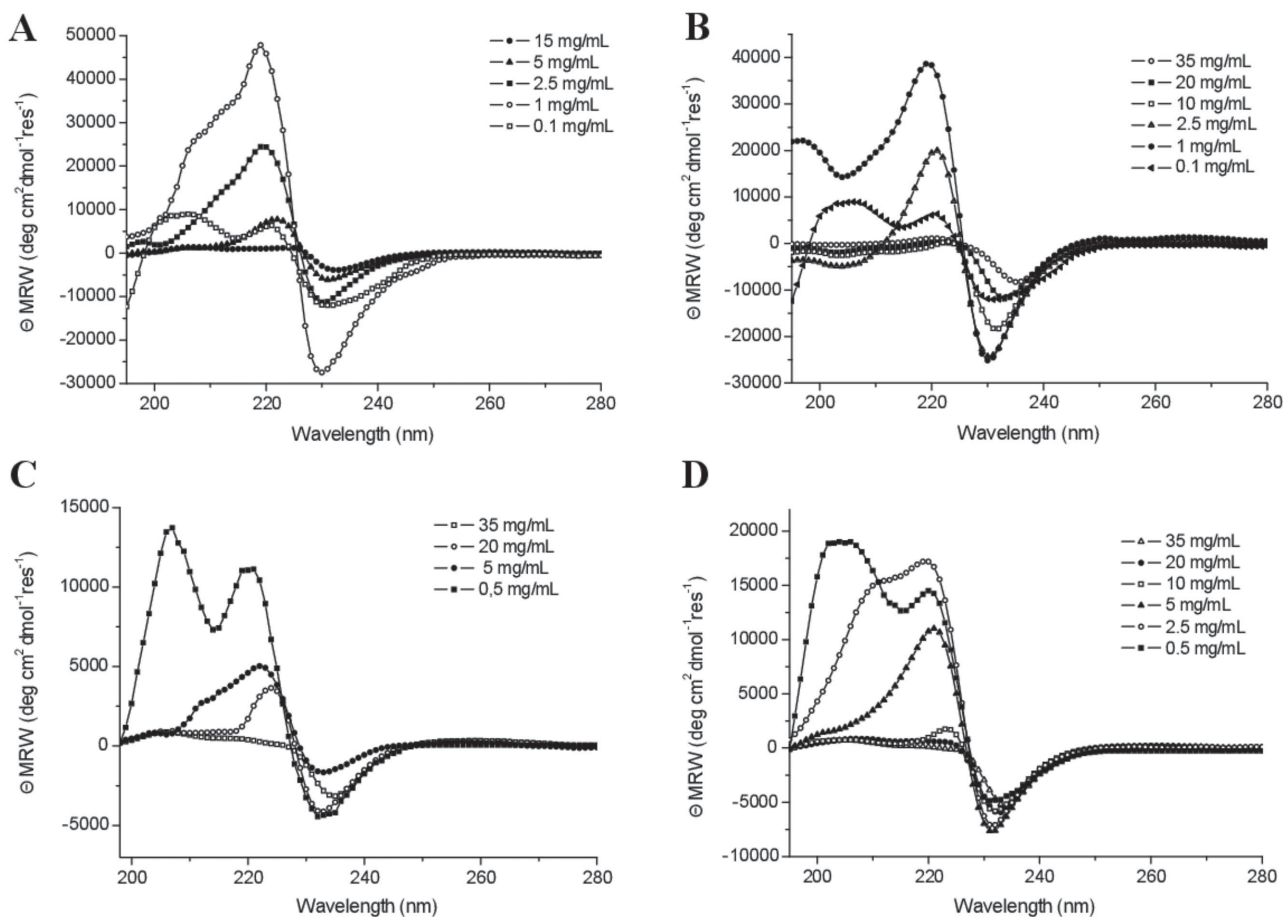


Figure 5. Selected Far-UV CD spectra of A) DOTA-L₆-F₄, B) DOTA(Gd)-L₆-F₄, C) DTPA-L₆-F₄, and D) DTPA(Gd)-L₆-F₄ in a concentration range of 0.1–35 mg mL⁻¹.

main minimum at 230 nm and the absence of the maxima above reported can be interpreted as a signature for the dominant β -sheet arrangements.^[31,34] From the inspection of Figure 5, the CD spectra of peptide derivatives show similar trend irrespective of chelating agent. However, the conformational transition described above was detected at higher concentration for DTPA-L₆-F₄ than DOTA-L₆-F₄, in agreement with the difference in CAC values between these conjugates. Dichroic tendency of DOTA(Gd)-L₆-F₄ at 20 mg mL⁻¹ (well above the CAC value determined by fluorescence) was also evaluated as function of the temperature between 10 and 80 °C. At low temperature, it was observed a distinct minimum around 235 nm, typical of the polyphenylalanine in β -aggregate form (Figure S5A, Supporting Information). By increasing the temperature, the shape of the spectra remains unchanged, but a progressive decrease of the signal intensities with a red-shift effect occurs probably due to a progressive unfolding of the peptide conjugate with higher molecular mobility. However, the conformational features are kept almost until 80 °C, thus indicating a good thermal stability of the aggregate.^[35] The integrity of the gadolinium complex in DOTA(Gd)-L₆-F₄ at the final temperature (80 °C) was confirmed by the mass peak reported in Figure S5B of the Supporting Information.

IR spectroscopy is often employed to probe the secondary structure assumed by di- or tetraphenylalanine derivatives.^[17,36] Usually, the attention is focused on the amide I bands able to provide information on the secondary structure adopted. FTIR spectra in the amide I region are shown in Figure 6A for DTPA(Gd)-L₆-F₄ and DOTA(Gd)-L₆-F₄ solutions at 2.0 mg mL⁻¹. Both the spectra show a principal peak at 1637 cm⁻¹ and a minor peak at 1680 cm⁻¹. The peak at 1637 cm⁻¹ is strongly indicative of β -sheet formation, whereas the fewer intensity of the second peak at 1680 cm⁻¹ is indicative of an antiparallel orientation of the β -sheets.^[37] FTIR spectra were also recorded on a dried film of DTPA(Gd)-L₆-F₄ and DOTA(Gd)-L₆-F₄ (see Figure S6, Supporting Information). These spectra reported a similar profile with respect to samples in solution.

Amyloid type fibril formation was also confirmed by using the typical Thioflavin T and Congo Red spectroscopic assays. Fluorescence spectra of ThT, before and after the addition of DOTA-L₆-F₄, are reported in Figure S7 of the Supporting Information. Spectra of DOTA-L₆-F₄ and its gadolinium complex in absence of ThT are also reported for comparison.

As shown in Figure S7 of the Supporting Information, DOTA(Gd)-L₆-F₄ gadolinium complex alone gives an emission peak in the same region in which the emission of ThT- β aggregate is expected.

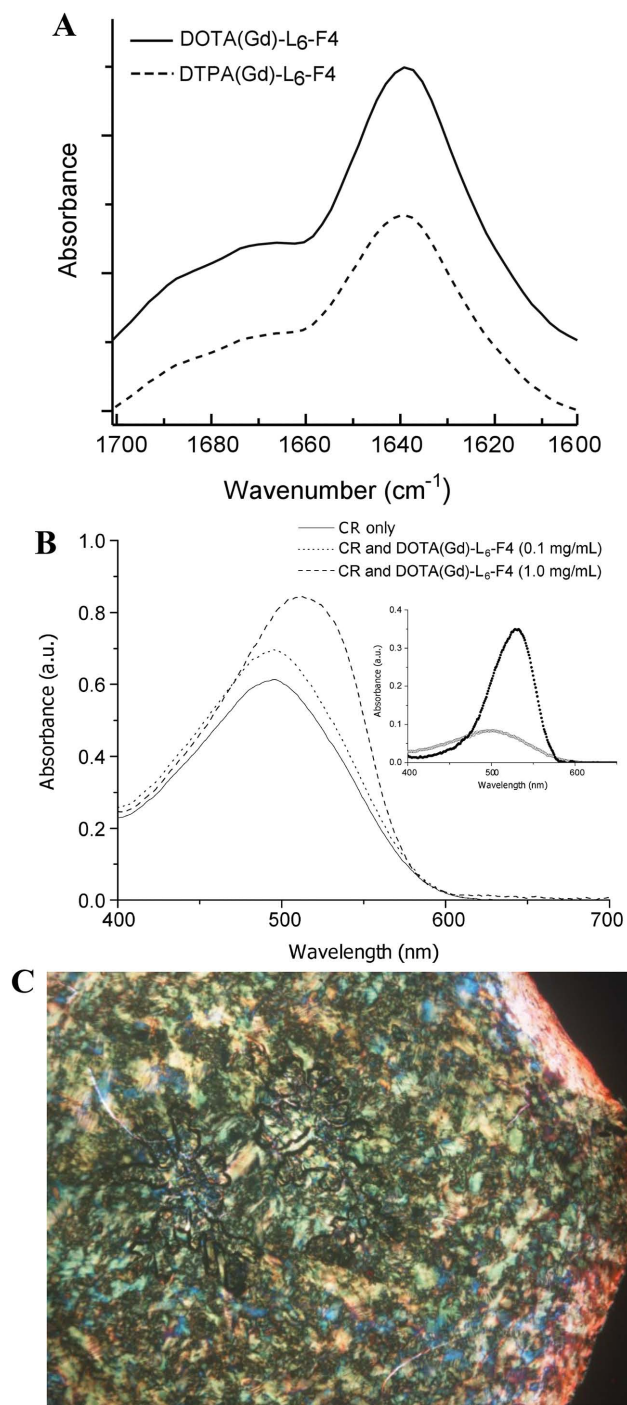


Figure 6. A) FTIR spectra of DOTA(Gd)-L₆-F4 and DTPA(Gd)-L₆-F4 in the amide I region at 2.0 mg mL⁻¹ concentration. B) The UV-vis spectra of DOTA(Gd)-L₆-F4, stained with Congo Red, at 0.1 and 1.0 mg mL⁻¹. The spectrum of Congo Red is also reported for comparison. Insets: The spectra of DOTA(Gd)-L₆-F4 0.1 mg (○) and 1.0 mg mL⁻¹ (●) after the subtraction of the CR spectrum. C) Polarized optical microscopy image of dried DOTA(Gd)-L₆-F4 on a glass microscopy slide stained with Congo Red solution.

As a consequence, in this sample we cannot attribute the peak at 482 nm to the interaction between ThT and the tetra-phenylalanine aggregate. On the contrary, in its uncomplexed form, DOTA chelating agent did not provide fluorescence

signals. The sudden appearance of an emission peak at 482 nm after the addition of DOTA-L₆-F4 (2.0 mg mL⁻¹ as final concentration) indicates unambiguously the binding of the ThT to the peptide derivatives.^[38] The fluorescence signal remains unchanged until 2 h from the incubation, thus confirming the immediate interaction of ThT with peptides. The same behavior was also observed for tetra-phenylalanine analogues containing DTPA chelating agent and its gadolinium complex (data not shown). According to the ThT assay, Congo Red staining (both UV-vis spectroscopy and polarized optical microscopy) confirms the amyloid type fibril formation. UV-vis spectra, reported in Figure 6B, show the spectral shift of the conventional CR band from 488 to 540 nm after the addition of DOTA(Gd)-L₆-F4 in the cuvette for two different concentrations (0.1 and 1.0 mg mL⁻¹). At the same time, air-dried films of gadolinium poly-phenylalanine derivatives stained with Congo Red and tetra-phenylalanine peptide dried fibers containing CR exhibit intense green birefringence when imaged with polarized optical microscopy (see Figure 6C and Figure S8, Supporting Information).

2.4. TEM and X-Ray Diffraction

The morphology of the self-assembled nanostructures was also assessed by TEM and X-ray diffraction. Selected images of DTPA(Gd)-L₆-F4 and DOTA(Gd)-L₆-F4 gadolinium complexes in water solution at 5.0 mg mL⁻¹ show the presence of long nanofibers with a minimum thickness around 10 nm (Figure 7). The recorded XRD patterns from DOTA(Gd)-L₆-F4 and L₆-F4 peptide dried stalks are shown in Figure 8A,B, respectively.

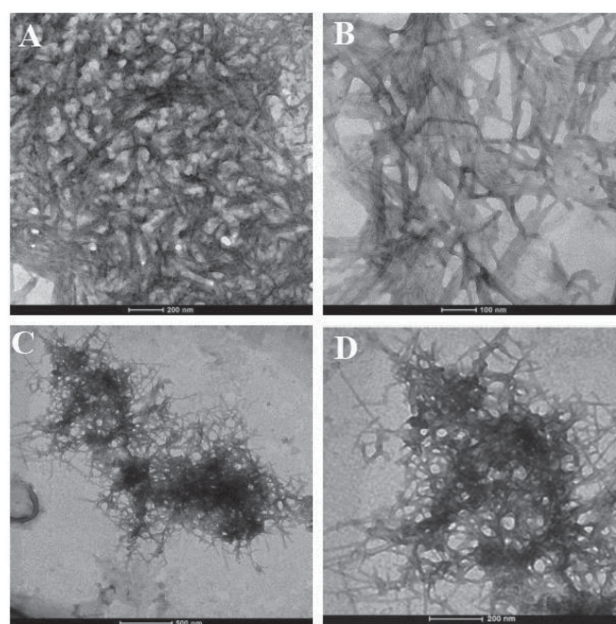


Figure 7. Selected TEM images for A,B) DOTA(Gd)-L₆-F4 at 5.0 mg mL⁻¹ and C,D) DTPA(Gd)-L₆-F4 at 5.0 mg mL⁻¹. Scale bars are 200 nm for (A,D), 100 nm for (B), and 500 nm for (C).

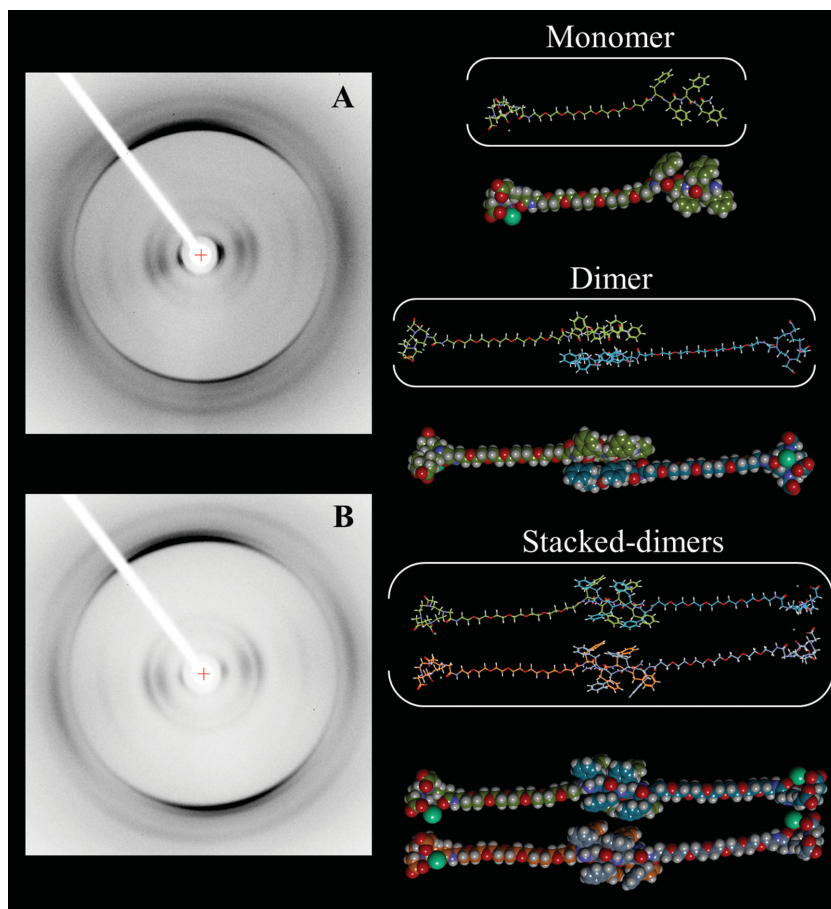


Figure 8. Selected X-ray fiber diffraction for A) DOTA- L_6 -F4 and B) L_6 -F4. The patterns show the diffraction features associated with the β -structure. Based on our experimental results, on the right side, a model of DOTA(Gd)- L_6 -F4 as monomer, dimer and stacked-dimers is reported.

Miller indices and d-spacings for both fiber types were determined using the software *CLEARER* and are reported in Tables S1 and S2 of the Supporting Information. As clearly indicated from the diffraction pattern, the structural arrangement of the pegylated cationic tetra-phenylalanine was not significantly affected from the functionalization of the N-terminus with the DOTA (or DTPA, data not shown) chelating agents. Both the X-ray diffractions show the typical “cross- β ” diffraction pattern of amyloid fibers, with a Bragg spacing of 4.8–4.9 Å along the meridian, generally attributed to the interchain distance between the hydrogen-bonded strands oriented perpendicularly to the fiber axis, and a more diffuse periodicity of ≈ 10 Å in the equatorial direction, usually ascribed to the staking of these β -sheets perpendicularly to the fiber axis.^[39,40] These XRD results are in agreement with the above reported CD (Figure 5) and IR data (Figure 6A and Figure S6, Supporting Information) indicating a β -sheet conformation of DOTA(Gd)- L_6 -F4 in a dried film. In Figure 8 it is also reported a simplified model in extended conformation of DOTA(Gd)- L_6 -F4 based on our experimental results to better appreciate the monomer dimension (about 50 Å), the antiparallel two-stranded β -disposition of the dimer with the fiber axis pointing up the plane of the paper, and the stacked-dimers with the fiber axis pointing toward the observer.

2.5. Relaxometry

Gd-complexes are used as positive MRI contrast agents (CAs) as they are able to strongly enhance the water protons relaxation rate in aqueous solutions thanks to the magnetic dipolar interaction between unpaired electrons on the gadolinium ions and the water protons. Their efficacy as MRI CAs is thus measured on the basis of this ability, which is usually defined as longitudinal “relaxivity” (r_{1p}) and is referred to the water proton relaxation rate of a solution containing one millimolar concentration of the Gd-complex.

The relaxivity of a Gd-containing system depends on the complex interplay among structural, dynamic, and electronic parameters.^[41] At the frequencies most commonly used in commercial tomographs (20–60 MHz), r_{1p} is generally determined by the reorientational correlation time (τ_R) of the chelate so that high molecular weight systems display higher relaxivity. Based on this property, it is possible to follow the occurrence of an aggregation process involving a Gd-complex through the measure of the water proton longitudinal relaxation rate of its aqueous solution. The relaxivities of DOTA(Gd)- L_6 -F4 and DTPA(Gd)- L_6 -F4, measured at 21.5 MHz (0.5 T) and 298 K as a function of the complex concentration, are reported in Figure 9A. The observed progressive enhancement in relaxivity is indicative of the self-aggregation of the two Gd-complexes. The inset in Figure 9A shows an amplification of the graph at low concentration values from which it is possible to observe that DTPA(Gd)- L_6 -F4 starts to aggregate at higher concentrations than DOTA(Gd)- L_6 -F4, reflecting the CAC values determined by fluorescence spectroscopy.

The analysis of the magnetic field dependence of the relaxivity, obtained through the registration of the so-called nuclear magnetic resonance dispersion (NMRD) profiles, allows the determination of the principal parameters characterising the relaxivity of a Gd(III) chelate. The NMRD profiles of DOTA(Gd)- L_6 -F4 and DTPA(Gd)- L_6 -F4, measured at 40 mg mL⁻¹ concentration, are reported in Figure 9B. The shape of both the profiles, with the characteristic peak of relaxivity in the region of Proton Larmor Frequencies 10–70 MHz, is a clear indication that, at this concentration, the Gd-complexes are in an aggregated form. Data were fitted to the conventional Solomon–Bloembergen–Morgan theory^[42,43] and the relative fitting parameters are reported in Table 2.

The high field relaxivity of the two complexes are quite similar, being, at 20 MHz, 14.8×10^{-3} and $14.0 \times 10^{-3} \text{ M}^{-1} \text{ s}^{-1}$ for DOTA(Gd)- L_6 -F4 and DTPA(Gd)- L_6 -F4, respectively. The τ_R values found for the two complexes are in fact very close. On the other hand, the big difference in relaxivity observed in the low field region has to be ascribed to the difference in the electronic

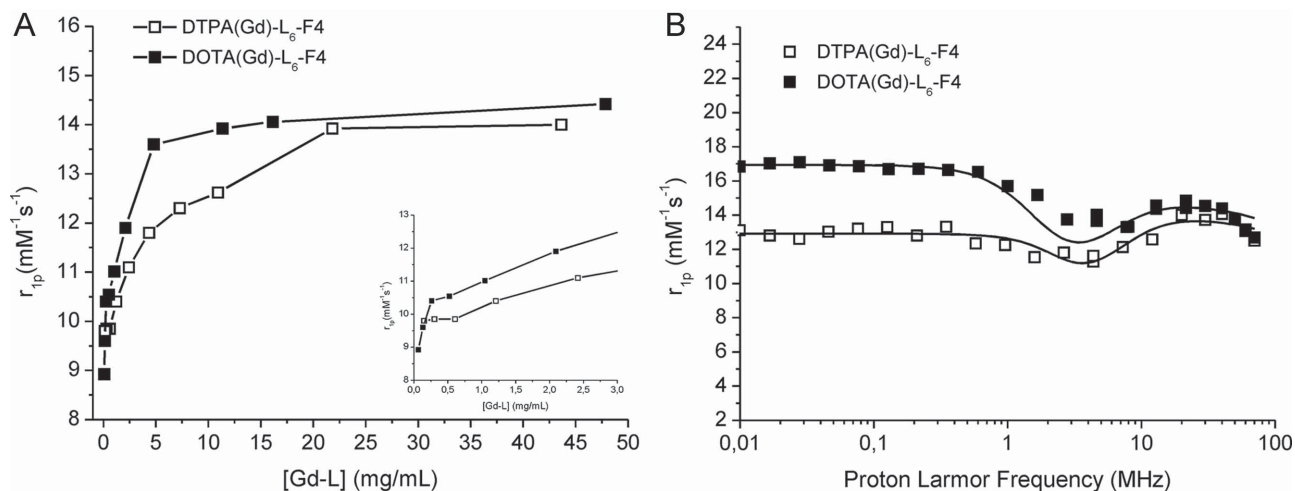


Figure 9. A) Longitudinal proton relaxivity of DOTA(Gd)-L₆-F4 and DTPA(Gd)-L₆-F4 measured at 21.5 MHz (0.5 T) and 298 K as a function of the concentration of the poly-phenylalanine Gd-complexes. B) Nuclear magnetic resonance dispersion (NMRD) profiles of the 40 mg mL^{-1} aqueous solutions of the two polyphenylalanine Gd-complexes at 298 K. The data refer to $1 \times 10^{-3} \text{ M}$ concentration of the paramagnetic complexes.

relaxation time (τ_{s0}) of the two Gd-complexes (Table 2). It is in fact known, that highly symmetric and rigid DOTA-type chelates generally have longer τ_{s0} values than DTPA-like, and this physically translates to a higher low-field relaxivity.^[44] It is worth to note that the τ_R values extracted from the fitting procedure for DOTA(Gd)-L₆-F4 and DTPA(Gd)-L₆-F4 in the aggregated form are quite short if compared to those usually found for nanosized aggregates (1–30 ns). Likely, this finding can be explained with the occurrence of a quite fast internal motility of the Gd-complexes along the linker spacer with respect to the overall fibril-like structures, as evidenced in the model arrangement proposed in Figure 8.

2.6. Cytotoxicity and MRI Evaluation of the Cellular Uptake

The cytotoxicity of the fibril nanoaggregates of DOTA(Gd)-L₆-F4 and DTPA(Gd)-L₆-F4 has been initially tested in the mouse embryonic fibroblast cell line 3T3 in the concentration range 0.5–5.0 mg mL^{-1} (Figure 10A). With a view to the subsequent experiments on the evaluation of the MRI cellular response, given that the particles, in this preliminary stage, are not functionalized for a target-specific cellular internalization, it was necessary to push the uptake experiment with an overnight incubation. The cytotoxicity assay revealed a significant reduction in

fibroblast viability along with the increase of the Gd-complexes concentration, with a higher effect in the case of DOTA(Gd)-L₆-F4 particles. The cytotoxicity appears to be higher than that reported in the case of analogous di-phenylalanine microtubes in the same cell line^[21] because of the longer incubation time (overnight in our experiments vs 2 h in the literature data.^[21]

A recent work on the assessment of the cellular response to dissolution and degradation products from self-assembled Fmoc-FF gels revealed that the critical factor affecting cell viability is the time a gel is allowed to degrade and leach into the media.^[45] We thought that a way to elude a long incubation time while maintaining a sufficient amount of internalized probes to test their ability to enhance the MRI cellular response would be to use a macrophagic cell line which attitude is to phagocytize a huge amounts of particles in short times. Thus, the cytotoxicity of the fibril nanoaggregates of DOTA(Gd)-L₆-F4 and DTPA(Gd)-L₆-F4 was investigated in J774A.1 mouse macrophages (Figure 10B) in the same concentration range (0.5–5.0 mg mL^{-1}) but with an incubation time of 3 h. In this case, the treated cells showed the same viability of the control cells even at the higher concentrations. Next, the uptake efficiency of DOTA(Gd)-L₆-F4 and DTPA(Gd)-L₆-F4 nanoaggregates and their efficacy in enhancing the MR-signal upon internalization, were investigated in J774A.1 cells and compared to those of the parents Gd-DOTA (Dotarem, Guerbert

Table 2 Main relaxometric parameters derived from fitting of NMRD profiles at 21.5 MHz reported in Figure 10B.

System	$r_{1p}^a)$ [$\times 10^{-3} \text{ M}^{-1} \text{ s}^{-1}$]	$\Delta^2)^b)$ [s^{-2}]	$\tau_V^c)$ [ps]	$\tau_{s0}^d)$ [ps]	$\tau_R^e)$ [ps]
DOTA(Gd)-L ₆ -F4	14.8	8.0×10^{18}	49	212	490
DTPA(Gd)-L ₆ -F4	14.0	1.25×10^{19}	52	127	457

^{a)}On carrying out the fitting procedure, some parameters were fixed to reasonable values: $r_{\text{Gd-H}}$ (distance between Gd and protons of the inner sphere water molecule) = 3.1 Å; a (distance of minimum approach of solvent water molecules to Gd^{3+} ion) = 3.8 Å; D (solvent diffusion coefficient) = $2.2 \times 10^{-5} \text{ cm}^2 \text{ s}^{-1}$; ^{b)}Squared mean transient zero-field splitting (ZFS) energy; ^{c)}Correlation time for the collision-related modulation of the ZFS Hamiltonian; ^{d)}Electronic relaxation time at zero field (calculated as $1/\tau_{s0} = 12\Delta^2 \times \tau_e$); ^{e)}Reorientational correlation time.

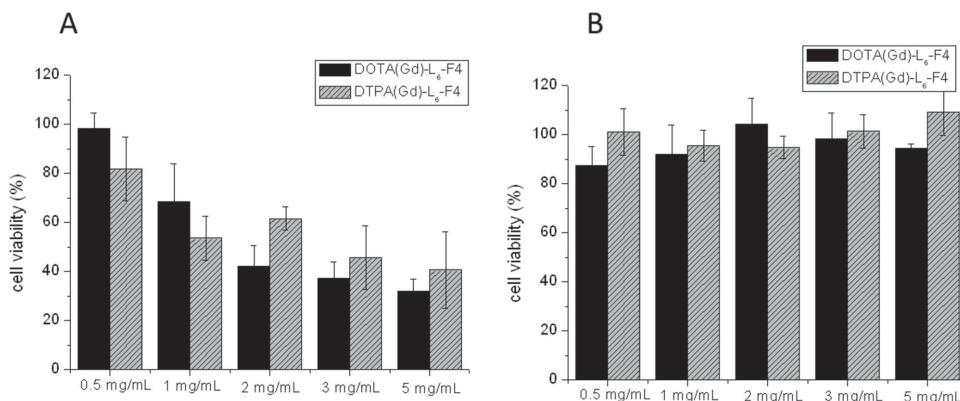


Figure 10. Cell viability percentage, evaluated by a CellTiter-Blue reagent test, after A) overnight treatment of the 3T3 fibroblasts and B) 3 h treatment of J774A.1 macrophages with various concentrations of DOTA(Gd)-L₆-F4 and DTPA(Gd)-L₆-F4. Data are expressed as the mean \pm SD ($n = 3$).

SA, France) and Gd-DTPA (Magnevist, Schering AG, Germany) complexes. The cells were incubated with increasing concentrations of DOTA(Gd)-L₆-F4 and DTPA(Gd)-L₆-F4 for 3 h at 37 °C and the amount of internalized gadolinium determined through ICP-MS analysis (Figure 11A).

Both the tetraphenylalanine functionalized Gd-complexes, being under the form of aggregates, displayed internalization efficiency far higher than that of the control complexes. The cellular MRI-signal response to labelling with the Gd-complexes was investigated at 7.1 T (Figure 11B). The T_{1w} images of the cellular pellets, and the corresponding R_1 ($1/T_1$) values, reflect the trend of higher cellular internalization for F4-Gd complexes displayed in Figure 11A, being the signal intensity remarkably higher than that observed when J774A.1 cells were incubated with Gd-DOTA and Gd-DTPA. The comparison between the two F4-Gd complexes reveals a higher efficiency of DOTA(Gd)-L₆-F4 in enhancing the water proton MR-signal with respect to DTPA(Gd)-L₆-F4. The reason for this, likely, relies in the different aggregation state of the two Gd-complexes in the concentration used for this experiment. Both at 1.5×10^{-3} and $3.5 \times 10^{-3} \text{ M}^{-1}$ (corresponding to 2.0 and 5.0 mg mL^{-1}), in fact, as can be appreciated in Figure 9A, DOTA(Gd)-L₆-F4 is endowed with an higher relaxivity due to its higher aggregation tendency,

while for DTPA(Gd)-L₆-F4 the relaxivity is lower. An accurate analysis of the observed relaxation rates of the pellets of cells, incubated with DOTA(Gd)-L₆-F4 and DTPA(Gd)-L₆-F4 with reference to the amount of internalized Gd-complexes, reveals that the increase in the uptake extent observed by passing from 1.5×10^{-3} to $3.5 \times 10^{-3} \text{ M}^{-1}$ concentration in the incubation media, is not accompanied by the corresponding enhancement in the relaxation rate (signal intensity) for each Gd-containing system. This behavior can be explained on the basis of the previously observed “quenching” effect on the relaxivity taking place when cells are labelled with high amounts of Gd-complexes and is related to the confinement of the probe in the sub-cellular or cellular compartments.^[46,47] The MRI contrast effect is not limited by insufficient loading with paramagnetic material, but by the exchange rate of water molecules across the endosomal or cellular membrane.

3. Conclusions

The synthesis and the structural characterization of novel potential MRI contrast agents based on the aggregation of polyphenylalanine conjugates have been reported. The insertion of

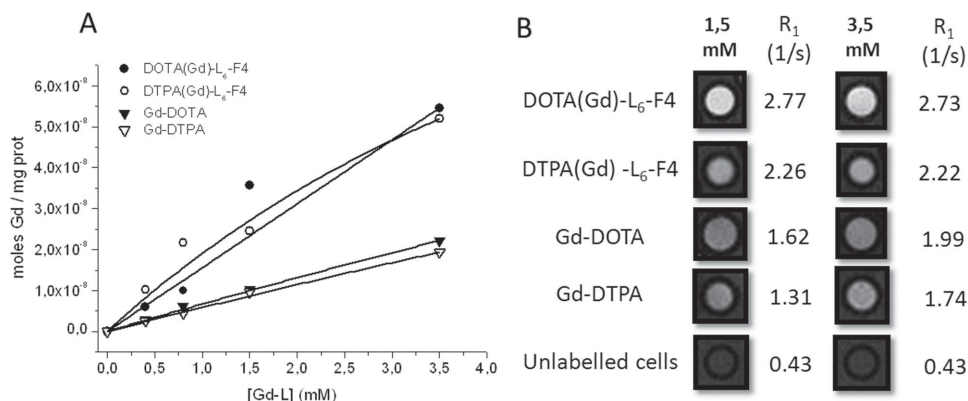


Figure 11. A) Amount of internalized gadolinium ions, evaluated by ICP-MS, in J774A.1 cells incubated with increasing concentrations of DOTA(Gd)-L₆-F4, DTPA(Gd)-L₆-F4, Gd-DOTA, and Gd-DTPA for 3 h. B) T_1 -weighted MR-images, and relative observed relaxation rates, of pellets of J774A.1 cells labelled with 1.5 and $3.5 \times 10^{-3} \text{ M}$ DOTA(Gd)-L₆-F4, DTPA(Gd)-L₆-F4, Gd-DOTA, and Gd-DTPA.

a DTPA or a DOTA gadolinium complex on the N-terminus FF homodimer destroys both the head-to-tail interaction and the π - π intermolecular interaction of the aromatic framework. This effect can be probably attributed to the steric hindrance of the gadolinium complex. Hence, the peptide framework was reinforced by increasing the number of the phenylalanine residues from two to four. Both the DOTA and DTPA tetraphenylalanine derivatives are able to self-aggregate at very low concentration, also after gadolinium coordination. Moreover, Gd(III) complexes are completely soluble in water, whereas a previously reported N-terminus-methoxy and C-terminus-ethyl protected F4-L₇ derivative showed a poor water solubility.^[36] The structural characterization aimed to define the secondary structure of the peptide fragment confirms the amyloid type fibril formation in which, as expected, an antiparallel alignment is preferred. Amyloid type fibril formation was also confirmed by TEM images and X-ray diffraction patterns. Moreover, the self-aggregation of DOTA(Gd)-L₆-F4 and DTPA(Gd)-L₆-F4 has been proved by the progressive enhancement in relaxivity observed increasing the Gd complex concentration and by the typical shape of the NMRD profiles in the region of Proton Larmor Frequencies 10–70 MHz. The relaxivity values of the two complexes at 20 MHz are 14.8×10^{-3} and $14.0 \times 10^{-3} \text{ M}^{-1} \text{ s}^{-1}$ for DOTA(Gd)-L₆-F4 and DTPA(Gd)-L₆-F4, respectively. These values are higher than the classical contrast agents at low molecular weight. On the other hand, these values are comparable or lower than many examples of Gd(III)-based micelle or liposome contrast agents.^[23–30] Surprising the τ_R values extracted from the fitting procedure are quite short if compared to those usually found for nano-sized aggregates (1–30 ns). In our opinion, these low τ_R values can be attributed to the occurrence of a quite fast internal motility of the Gd-complexes along the linker spacer with respect to the overall fibril-like structures. Preliminary studies aimed to define the ability of DOTA(Gd)-L₆-F4 and DTPA(Gd)-L₆-F4 to enhance the MRI cellular response was achieved on J774A.1 mouse macrophages cell line in which the cytotoxicity of the fibril nanoaggregates was negligible with an incubation time of 3 h in 0.5–5.0 mg mL⁻¹ concentration range. The in vitro MRI behavior of nanoaggregates was also compared to those of the parents Gd-DOTA and Gd-DTPA complexes. Both the tetra-phenylalanine Gd-complexes showed a significant internalization efficiency and a remarkably enhance of the water proton MR-signal with respect to the control complexes. Moreover, the higher efficiency of DOTA(Gd)-L₆-F4 in enhancing the water proton MR-signal with respect to DTPA(Gd)-L₆-F4 probably reflects the different aggregation state of the two Gd-complexes in the concentration used for this experiment. At the best of our knowledge, this is the first example of aromatic framework based nanoaggregates as MRI contrast agent. However, several issues have to improve before their in vivo applications as diagnostic tools. For example, the insertion of structural elements able to confer rigidity to the molecules without to alter their solubility could lead to higher relaxivity values. At the same time, synthetic modifications of the peptide framework, e.g., the replacement of natural amino acids with uncoded ones, could improve the stability of the fibrillary aggregates, thus reducing the extent of degradation products that are invoked as the critical factor affecting cell viability into the cellular media.

4. Materials and Methods

Protected N α -Fmoc-amino acid derivatives, coupling reagents, and Rink amide MBHA (4-methylbenzhydrylamine) resin were purchased from Calbiochem-Novabiochem (Laufelfingen, Switzerland). The Fmoc-21-amino-4,7,10,13,16,19-hexaoxaheptanoic acid [Fmoc-Ahoh-OH, (L₆)] and the Fmoc-8-amino-3,6-dioxaoctanoic acid [Fmoc-AdOO-OH, (L₂)] were purchased from Neosystem (Strasbourg, France). DTPA(OtBu)₄-OH and DOTA(OtBu)₃-OH chelating agents were purchased from Chemateck (Dijon, France). All other chemicals were commercially available by Sigma-Aldrich (Milan, Italy) or Fluka (Bucks, Switzerland) or LabScan (Stillorgan, Dublin, Ireland) and were used as received unless otherwise stated. All solutions were prepared by weight with doubly distilled water. Preparative RP-HPLCs were carried out on a LC8 Shimadzu HPLC system (Shimadzu Corporation, Kyoto, Japan) equipped with an UV lambda-Max Model 481 detector using Phenomenex (Torrance, CA) C18 column. Elution solvents are H₂O/0.1% TFA (A) and CH₃CN/0.1% TFA (B), from 5% to 70% over 30 min at 20 mL min⁻¹ flow rate. Purity and identity of the products were assessed by analytical LC-MS analyses by using Finnigan Surveyor MSQ single quadrupole electrospray ionization (Finnigan/Thermo Electron Corporation San Jose, CA), column: C18-Phenomenex eluted with an H₂O/0.1% TFA (A) and CH₃CN/0.1% TFA (B) from 5% to 70% over 15 min at 200 $\mu\text{L min}^{-1}$ flow rate.

Synthesis of Peptide Derivatives: Peptides and peptide conjugates were synthesized by using standard solid-phase 9-fluorenylmethoxycarbonyl (Fmoc) procedures. The Rink amide MBHA resin (substitution 0.65 mmol g⁻¹) was used as the solid phase support to provide the peptides as C-terminus amide, and synthesis was performed on a scale of 0.2 mmol. The resin was swelled in DMF for 30 min and the Fmoc deprotection reaction (10 min) was performed twice with 30% (v/v) piperidine in DMF. The amino acid coupling was achieved by adding twofold molar excess of amino acid, mixed with equimolar amounts of 1-hydroxybenzotriazole (HOBt), benzotriazol-1-yl-oxy-tris-pyrrolidino-phosphonium (PyBop), and fourfold molar excess of diisopropylethylamine (DIPEA) in DMF. All couplings were performed twice for 1 h. Chelating agents and the ethoxylic spacers (Fmoc-AdOO-OH and Fmoc-Ahoh-OH) were coupled as previously described.^[48,49] Peptides were fully deprotected and from the resin with the TFA (trifluoroacetic acid)/ TIS (triisopropylsilane)/ H₂O (95.5/2.0/2.5 v/v/v) mixture at room temperature. Peptides and peptide conjugates were precipitated with ice-cold ethyl ether, dissolved in H₂O/CH₃CN and freeze-dried. The purification of the crude products was carried out by RP-HPLC. Mass spectra confirm the products identity. Retention times (R_t) and molecular weight (M_w) of the peptide derivatives are reported in Table 3.

DTPA-F2: ¹H-NMR (CD₃OD) (chemical shifts in δ , CH₃OH as internal standard 3.55) = 7.51–7.42 (m, 10 CH aromatic), 4.96–4.86 (m, 2H, CH Phe α), 4.65–4.61 (d, J = 16 Hz, 1H, R₂NCH₂CONHR), 4.44–4.40 (d, J = 16 Hz, 1H, R₂NCH₂CONHR), 3.87 (s, 8H, R₂NCH₂COOH), 3.53–3.50 (m, 4H, R₂NCH₂CH₂NR₂), 3.42–3.31 (m, 4H, R₂NCH₂CH₂NR₂), 3.24–2.99 (m, 4H, CH₂ Phe β).

Table 3. Retention time (R_t) and theoretical molecular weight (M_w) of investigated polyphenylalanine conjugates. RP-HPLC method and column details are reported in the Materials and Methods Section.

Sample	Formula	R_t [min]	M_w [u.m.a.]
DTPA-F2	$C_{32}H_{42}N_6O_{11}$	10.34	686
DOTA-F2	$C_{34}H_{46}N_6O_{10}$	10.65	698
DTPA-L ₂ -F2	$C_{38}H_{53}N_7O_{14}$	11.19	831
DOTA-L ₂ -F2	$C_{40}H_{57}N_7O_{13}$	11.42	843
DTPA-L ₆ -F2	$C_{47}H_{70}N_7O_{18}$	12.10	1020
DOTA-L ₆ -F2	$C_{49}H_{76}N_8O_{16}$	12.33	1032
L ₆ -F4	$C_{51}H_{67}N_6O_{11}$	15.30	939
DTPA-L ₆ -F4	$C_{65}H_{88}N_9O_{20}$	14.54	1314
DOTA-L ₆ -F4	$C_{67}H_{94}N_{10}O_{18}$	14.59	1326

DOTA-F2: 1H -NMR (CD_3OD) (chemical shifts in δ , CH_3OH as internal standard 3.55) = 7.51-7.42 (m, 10 CH aromatic), 4.86-4.75 (m, 2H, CH Phe α), 3.70 (s, 6H, R_2NCH_2COOH), 3.45 (s, 16H, $R_2N-CH_2CH_2NR_2$), 3.40-3.36 (m, 2H, R_2NCH_2CONH), 3.16-2.90 (m, 4H, CH_2 Phe β).

DTPA-L₂-F2: 1H -NMR (CD_3OD) (chemical shifts in δ , CH_3OH as internal standard 3.55) = 7.51-7.42 (m, 10 CH aromatic), 4.96-4.86 (m, 2H, CH Phe α), 4.55 (s, 2H, R_2NCH_2CONHR), 3.87 (s, 8H, R_2NCH_2COOH), 3.79 (s, 4H, OCH_2CH_2O), 3.75 (t, $J = 4$ Hz, 2H, $RNHCH_2CH_2O$), 3.65 (s, 2H, OCH_2COR), 3.60 (t, $J = 7$ Hz, 2H, $RNHCH_2CH_2O$), 3.53-3.50 (m, 4H, $R_2NCH_2CH_2N$ R_2), 3.42-3.31 (m, 4H, $R_2NCH_2CH_2NR_2$), 3.24-2.99 (m, 4H, CH_2 Phe β).

DOTA-L₂-F2: 1H -NMR (CD_3OD) (chemical shifts in δ , CH_3OH as internal standard 3.55) = 7.51-7.42 (m, 10 CH aromatic), 4.86-4.75 (m, 2H, CH Phe α), 3.79 (s, 4H, OCH_2CH_2O), 3.75 (t, $J = 4$ Hz, 2H, $RNH-CH_2CH_2O$), 3.70 (s, 6H, R_2NCH_2COOH), 3.65 (s, 2H, OCH_2COR), 3.60 (t, $J = 6$ Hz, 2H, $RNH-CH_2CH_2O$), 3.45 (s, 16H, $R_2N-CH_2CH_2NR_2$), 3.40-3.36 (m, 2H, R_2NCH_2CONH), 3.16-2.90 (m, 4H, CH_2 Phe β).

DTPA-L₆-F2: 1H -NMR (CD_3OD) (chemical shifts in δ , CH_3OH as internal standard 3.55) = 7.51-7.42 (m, 10 CH aromatic), 4.86-4.75 (m, 2H, CH Phe α), 4.55 (s, 2H, R_2NCH_2CONHR), 3.87 (s, 8H, R_2NCH_2COOH), 3.80 (s, 22H, OCH_2CH_2O), 3.75 (t, $J = 8$ Hz, 2H, $RNHCH_2CH_2O$), 3.68 (t, $J = 7$ Hz, 2H, $RNHCH_2CH_2O$), 3.40-3.32 (m, 6H, $R_2NCH_2CH_2NR_2$), 3.27-3.20 (dd, $J = 7$ Hz, $J = 14$ Hz, 2H, $R_2NCH_2CH_2NR_2$), 3.16-2.90 (m, 4H, CH_2 Phe β). 2.58 (t, $J = 6$ Hz, 2H, $NHCOCH_2CH_2O$).

DOTA-L₆-F2: 1H -NMR (CD_3OD) (chemical shifts in δ , CH_3OH as internal standard 3.55) = 7.51-7.42 (m, 10 CH aromatic), 4.86-4.75 (m, 2H, CH Phe α), 3.80 (s, 22H, OCH_2CH_2O), 3.75 (t, $J = 4$ Hz, 2H, $RNHCH_2CH_2O$), 3.70 (s, 6H, R_2NCH_2COOH), 3.60 (t, $J = 6$ Hz, 2H, $RNHCH_2CH_2O$), 3.45 (s, 16H, $R_2NCH_2CH_2NR_2$), 3.40-3.36 (m, 2H, R_2NCH_2CONH), 3.16-2.90 (m, 4H, CH_2 Phe β), 2.58 (t, $J = 6$ Hz, 2H, $NHCOCH_2CH_2O$).

L₆-F4: 1H -NMR (CD_3OD) (chemical shifts in δ , CH_3OH as internal standard 3.55) = 7.51-7.42 (m, 20 CH aromatic), 4.86-4.75 (m, 4H, CH Phe α), 3.80 (s, 22H, OCH_2CH_2O), 3.75 (t, $J = 4$ Hz, 2H, $RNHCH_2CH_2O$), 3.60 (t, $J = 6$ Hz, 2H,

$RNHCH_2CH_2O$), 3.16-2.90 (m, 8H, CH_2 Phe β), 2.58 (t, $J = 6$ Hz, 2H, $NHCOCH_2CH_2O$).

DTPA-L₆-F4: 1H -NMR (CD_3OD) (chemical shifts in δ , CH_3OH as internal standard 3.55) = 7.51-7.42 (m, 20 CH aromatic), 4.86-4.75 (m, 4H, CH Phe α), 4.55 (s, 2H, R_2NCH_2CONHR), 3.87 (s, 8H, R_2NCH_2COOH), 3.80 (s, 22H, OCH_2CH_2O), 3.75 (t, $J = 4$ Hz, 2H, $RNHCH_2CH_2O$), 3.68 (t, $J = 6$ Hz, 2H, $RNHCH_2CH_2O$), 3.40-3.32 (m, 6H, $R_2NCH_2CH_2NR_2$), 3.27-3.20 (dd, $J = 7$ Hz, $J = 14$ Hz, 2H, $R_2NCH_2CH_2NR_2$), 3.16-2.90 (m, 8H, CH_2 Phe β), 2.58 (t, $J = 6$ Hz, 2H, $NHCOCH_2CH_2O$).

DOTA-L₆-F4: 1H -NMR (CD_3OD) (chemical shifts in δ , CH_3OH as internal standard 3.55) = 7.51-7.42 (m, 20 CH aromatic), 4.86-4.75 (m, 4H, CH Phe α), 3.80 (s, 22H, OCH_2CH_2O), 3.75 (t, $J = 4$ Hz, 2H, $RNHCH_2CH_2O$), 3.70 (s, 6H, R_2NCH_2COOH), 3.60 (t, $J = 6$ Hz, 2H, $RNHCH_2CH_2O$), 3.45 (s, 16H, $R_2NCH_2CH_2NR_2$), 3.40-3.36 (m, 2H, R_2NCH_2CONH), 3.16-2.90 (m, 8H, CH_2 Phe β), 2.58 (t, $J = 6$ Hz, 2H, $NHCOCH_2CH_2O$).

Preparation of Gadolinium Complexes: The complexation has been carried out by adding 1:1 molar ratio of $GdCl_3$ to the aqueous solutions of the DOTA or DTPA derivatives at neutral pH and room temperature. The amount of residual free Gd^{3+} ions was assessed by the orange xylenol UV method^[50] and complexed by further addition of the corresponding amount of each ligand.

Fluorescence Studies: The values of critical aggregate concentration (CAC) were obtained by fluorescence measurements. Fluorescence spectra were recorded at room temperature on a Jasco Model FP-750 spectrofluorophotometer in a 1.0 cm path length quartz cell. Equal excitation and emission bandwidths (5 nm) were used throughout the experiments with a recording speed of 125 nm min^{-1} and automatic selection of the time constant. The CAC values were measured by using 8-anilino-1-naphthalene sulfonic acid ammonium salt (ANS)^[51,52] and pyrene (Pyr) as fluorescent probes.^[53]

Small aliquots of peptide conjugate in water solutions, as free bases or as gadolinium complexes, were added to 1.0 mL of aqueous solution of ANS (20×10^{-6} M) or Pyr (1×10^{-6} M). Final spectra, to be used for calculations, were obtained after blank correction and adjustment for dilution. The fluorescence intensity of ANS was followed as a function of the peptide concentration. The CAC values were determined by linear least-squares fitting of the fluorescence emission at 470 nm, upon excitation at 350 nm versus the polyphenylalanine concentration lower and higher than the change of slope. The excitation wavelength of Pyr was settled at 335 nm and spectra were recorded between 350 and 550 nm.

Thioflavin T (ThT) Spectroscopic Assay: Aggregation behavior of DOTA-L₆-F4 and DTPA-L₆-F4 as free bases or as gadolinium complexes was assessed by using Thioflavin T (ThT). Thioflavin T associates rapidly with β -aggregated peptides giving rise to an enhanced emission at 482 nm.^[54] Fluorescence spectrum of an aqueous solution of ThT (25×10^{-6} M) before and after the addition of tetraphenylalanine derivatives (2 mg mL^{-1}) was recorded at 25 °C at regular intervals (each 10 min) during 2 h after the peptide addition into the cuvette. Samples were excited at 450 nm and fluorescence emission spectra were recorded between 460 and 650 nm.

Congo Red Spectroscopic Assay: UV-vis measurements of Congo Red (CR) alone or in presence of poly-phenylalanine

derivatives were carried out on Thermo Fisher Scientific Inc (Wilmington, Delaware, USA) Nanodrop 2000c spectrophotometer equipped with a 1.0 cm quartz cuvette (Hellma). A stock solution of CR (3.5 mg in 500 μL) was freshly prepared in 10×10^{-3} M phosphate buffer pH 7.4 and filtered through 0.2 μm syringe immediately prior to use. A small aliquot (5 μL) of this solution was diluted with the buffer at 12.5×10^{-6} M final concentration and the UV-vis spectrum was recorded between 400 and 700 nm at room temperature. 50 μL of DTPA(Gd)-L₆-F4 or DOTA(Gd)-L₆-F4 (20 mg mL⁻¹) were added to CR solution and samples were incubated for 30 min at room temperature. The spectra were recorded and background subtracted using a Congo Red spectrum in phosphate buffer as reference solution.

Circular Dichroism: Far-UV CD spectra of the peptide conjugates in aqueous solution were collected on a Jasco J-810 spectropolarimeter equipped with a NesLab RTE111 thermal controller unit using a 0.1 mm quartz cell at 25 °C. The spectra of samples at several concentrations (35, 20, 15, 10, 5, 2.0, 1.0, 0.5, and 0.1 mg mL⁻¹) are recorded from 280 to 195 nm. Other experimental settings were: scan speed, 10 nm min⁻¹; sensitivity, 50 mdeg; time constant, 16 s; bandwidth, 1 nm. Each spectrum was obtained by averaging three scans and corrected for the blank. Here Θ represents the mean residue ellipticity (MRE), i.e., the ellipticity per mole of peptide divided by the number of amino acid residues in the peptide. Thermal profiles (CD vs temperature, in the 10–80 °C range) of the tetraphenylalanine derivatives at 20 mg mL⁻¹ were recorded every 10 °C, equilibrating for 10 min before next measurement.

Fourier Transform Infrared Spectroscopy (FTIR): FTIR spectra of samples (2.0 mg mL⁻¹) were collected on a Jasco FT/IR 4100 spectrometer (Easton, MD) in an attenuated total reflection (ATR) mode and using a Ge single-crystal at a resolution of 4 cm⁻¹. All the spectral data were processed using built-in software. Spectra were collected in transmission mode and then converted in emission. Each sample was recorded with a total of 100 scans with a rate of 2 mm s⁻¹ against a KBr background.

Transmission Electron Microscopy (TEM) Images: TEM observation were performed with a transmission electron microscope FEI TECNAI G12 Spirit-Twin (LaB6 source) equipped with a bottom mounted FEI Eagle-4k CCD camera (Eindhoven, The Netherlands), operating with an acceleration voltage of 120 kV (LaMest Pozzuoli, Italy). A droplet of the sample solution (5 mg mL⁻¹) was placed onto a 400 mesh holey-carbon coated copper grid, air-dried for 1 h, and then negatively stained with phosphotungstic acid in water solution (1 wt%). Tomography holder with FEI Eagle 4K CCD camera and Xplore 3D software were used to obtain digital images.

X-ray Fiber Diffraction (XRD): Diffraction patterns were obtained for stalks prepared by the stretch frame method.^[55] Briefly, a droplet (10 μL) of peptide aqueous solution (3 wt%) was suspended between the ends of a wax-coated capillary (spaced 2 mm apart). The droplet was allowed to dry gently at room temperatures overnight to obtain oriented fibers. The stalk was mounted vertically onto the four axis goniometer of an R-AXIS IV++ X-ray diffractometer (Rigaku) equipped with a rotating anode generator. The XRD data were collected using a Saturn 944 CCD camera (CuK α high intensity X-ray microfocus source, $\lambda = 1.5418$ Å). The specimen-to-film distance was set at 90 mm and the exposure time was set to 60 s. The X-ray

patterns were processed using the analysis and simulation CLEARER software.^[56]

Congo Red Staining and Polarized Optical Microscopy: Dried film of polyphenylalanine was obtained placing 10 μL of the peptide aqueous solution (3 wt%) onto a glass slide and left drying at room temperature. Then, the air-dried samples were stained with 150 μL of freshly prepared CR solution, obtained adding a saturating amount of CR in ethanol containing 20% of NaCl saturated water. After the application of the CR solution, the excess was rapidly removed from the glass slide with a filter paper. CR containing fibers were prepared, as above described with stretch frame method, adding 2 μL of CR staining solution to 50 μL of poly-phenylalanine solution. Samples dried on glass slide or CR containing fibers were observed under bright field illumination and between crossed polars using a Nikon AZ100 microscope.

Water Proton Relaxation Measurements: The longitudinal water proton relaxation rates were measured at 25 °C by using a Stelar Spinmaster (Stelar, Mede, Pavia, Italy) spectrometer operating at 0.5 T (21.5 MHz Proton Larmor Frequency), by mean of the standard inversion-recovery technique. The temperature was controlled with a Stelar VTC-91 air-flow heater equipped with a copper constantan thermocouple (uncertainty 0.1 °C). The proton 1/T₁ NMRD profiles were measured at 25 °C on a fast field-cycling Stelar relaxometer over a continuum of magnetic field strengths from 0.00024 to 0.47 T (corresponding to 0.01–20 MHz proton Larmor frequencies). The relaxometer operates under computer control with an absolute uncertainty in 1/T₁ of $\pm 1\%$. Additional data points in the range 21.5–70 MHz were obtained on the Stelar Spinmaster spectrometer. The concentration of the solutions used for the relaxometric characterization was determined according to a previously reported relaxometric method.^[57] Data were fitted to the conventional Solomon–Bloembergen–Morgan theory.

Cytotoxicity Studies: The cytotoxicity of DOTA(Gd)-L₆-F4 and DTPA(Gd)-L₆-F4 probes was investigated in a mouse macrophages cell line (J774A.1) and in a mouse embryonic fibroblast cell line (3T3). J774A.1 and 3T3 cells were seeded in DMEM culture medium, enriched with 10% fetal bovine serum and 1% glutamine, at 150 000 and 50 000 cells per well, respectively, in 96-well plates the day before the incubation. The cells were incubated for 3 h (J774A.1) or overnight (3T3) at 37 °C with the two Gd-based probes at different concentrations: 0.5, 1, 2, 3, and 5 mg mL⁻¹. After the incubation, cells were gently washed and re-incubated for 4 h with 20 μL of CellTiter-Blue reagent for the viability test. The CellTiter-Blue reagent is a solution containing resazurin, an indicator dye, which has little intrinsic fluorescence with the maximum absorbance at 605 nm. The reagent undergoes a “blue shift” upon reduction of resazurin to resorufin with a maximum peak at 573 nm. The fluorescence produced is proportional to the number of viable cells. The same amount of CellTiter-Blue reagent was added to triplicate wells without cells (no-cell control) and with untreated cells (control cells), respectively. At the end of the incubation, the fluorescence at 560/590 nm was measured using the fluorometric method. The experiments were carried out in triplicate. Obtained data were analysed subtracting the mean fluorescence value of the culture background from all fluorescence values of

experimental wells. The percentage of viable cells was calculated according to the following equation:

$$\% \text{ viable cell} = \frac{\text{experimental cells mean value}}{\text{control cells mean value}} \times 100 \quad (1)$$

Cellular Uptake Studies: Approximately 1×10^6 J774A.1 cells, in DMEM medium, were incubated with different concentrations of DOTA(Gd)-L₆-F4 and DTPA(Gd)-L₆-F4 for 3 h at 37 °C. After this incubation time, the cells were washed three times with 5 mL ice-cold phosphate-buffered saline (PBS), detached with a scraper and, for the acquisition of the MR images, collected in 50 µL of PBS, transferred into glass capillaries that were centrifuged at 1500 rpm for 5 min and placed in an agar phantom. The MR images were acquired by standard T₁-weighted spin-echo sequence (TE = 2.6 ms, 16 variable TR ranging from 50 to 8000 ms, NEX = 1, FOV = 1.1×1.1 cm², 1 slice, slice thickness = 1 mm) and recorded on a Bruker Avance300 operating at 7 T. After imaging, the labeled cells were suspended in 200 µL PBS and sonicated to obtain cell lysates. Gd(III) content was measured by ICP-MS analysis (Element-2; Thermo-Finnigan, Rodano Milan, Italy). The preparation of the samples for ICP-MS analysis has been carried out as follows: i) 150 µL of each cell lysate was mineralized with 1 mL of concentrated HNO₃ (65% v/v) under microwave heating at 160 °C for 40 min (Milestone MicroSYNTH Microwave lab station equipped with an optical fiber temperature control and HPR-1000/6M six position high-pressure reactor, Bergamo, Italy); ii) after mineralization, the volume of each sample was brought to 2 mL with ultrapure water and the sample was analyzed by ICP-MS. The calibration curve was obtained using four gadolinium absorption standard solutions (Sigma-Aldrich) in the range 0.005–0.2 µg mL⁻¹. The protein content of cells lysates was determined by the Bradford method using bovine serum albumin as standard.

Supporting Information

Supporting Information is available from the Wiley Online Library or from the author.

Acknowledgements

The authors are indebted with the Italian Minister for Research (M.I.U.R.) for financial support under FIRB “RENAME” RBAP114AMK and PRIN 2012SK7ASN projects. The authors thank Mr. Leopoldo Zona and Giosuè Sorrentino for technical support.

Received: June 16, 2015

Revised: September 17, 2015

Published online: October 21, 2015

- [1] S. I. Stupp, *Nano Lett.* **2010**, *10*, 4783.
 [2] S. Cavalli, F. Albericio, A. Kros, *Chem. Soc. Rev.* **2010**, *39*, 241.
 [3] K. Morris, L. Serpell, *Chem. Soc. Rev.* **2010**, *39*, 3445.
 [4] S. J. Rymer, S. J. B. Tendler, C. Bosquillon, C. Washington, C. J. Roberts, *Ther. Delivery* **2011**, *2*, 1043.
 [5] H. Cui, M. J. Webber, S. I. Stupp, *Biopolymers* **2010**, *94*, 1.
 [6] S. Fleming, R. V. Ulijn, *Chem. Soc. Rev.* **2014**, *43*, 8150.
 [7] I. W. Hamley, *Angew. Chem. Int. Ed.* **2014**, *53*, 6866.
 [8] T. P. Carberry, R. Tarallo, A. Falanga, E. Finamore, M. Galdiero, M. Weck, S. Galdiero, *Chem. Eur. J.* **2012**, *18*, 13678.
 [9] D. Tesauro, A. Accardo, E. Gianolio, L. Paduano, J. Teixeira, K. Schillen, S. Aime, G. Morelli, *ChemBioChem* **2007**, *8*, 950.
 [10] A. Accardo, D. Tesauro, G. Mangiapia, C. Pedone, G. Morelli, *Biopolymers* **2007**, *88*, 115.
 [11] T. Ji, Y. Ding, Y. Zhao, J. Wang, H. Qin, X. Liu, J. Lang, R. Zhao, Y. Zhang, J. Shi, N. Tao, Z. Qin, G. Nie, *Adv. Mater.* **2015**, *27*, 1865.
 [12] M. Reches, E. Gazit, *Science* **2003**, *300*, 625.
 [13] X. Yan, P. Zhu, J. Li, *Chem. Soc. Rev.* **2010**, *39*, 1877.
 [14] I. Azuri, L. Adler-Abramovich, E. Gazit, O. Hod, L. Kronik, *J. Am. Chem. Soc.* **2014**, *136*, 963.
 [15] P. Tamamis, L. Adler-Abramovich, M. Reches, K. Marshall, P. Sikorski, L. Serpell, E. Gazit, G. Archontis, *Biophys. J.* **2009**, *96*, 5020.
 [16] C. Guo, Y. Luo, R. Zhou, G. Wei, *ACS Nano* **2012**, *6*, 3907.
 [17] R. Huang, W. Qi, L. Feng, R. Su, Z. He, *Soft Matter* **2011**, *7*, 6222.
 [18] N. Gour, D. Kedracki, I. Safir, K. X. Ngo, C. Vebert-Nardin, *Chem. Commun.* **2012**, *48*, 5440.
 [19] M. I. Souza, Y. M. Jaques, G. P. de Andrade, A. O. Ribeiro, E. R. da Silva, E. E. Fileti, É. d. S. Ávila, M. V. B. Pinheiro, K. Krambrock, W. A. Alves, *J. Phys. Chem. B* **2013**, *117*, 2605.
 [20] T. O. Mason, D. Y. Chirgadze, A. Levin, L. Adler-Abramovich, E. Gazit, T. P. J. Knowles, A. K. Buell, *ACS Nano* **2014**, *8*, 1243.
 [21] R. F. Silva, D. R. Araújo, E. R. Silva, R. A. Ando, W. A. Alves, *Langmuir* **2013**, *29*, 10205.
 [22] H. Zang, J. Fei, X. Yan, A. Wang, J. Li, *Adv. Funct. Mater.* **2015**, *25*, 1193.
 [23] A. Accardo, D. Tesauro, G. Morelli, E. Gianolio, S. Aime, M. Vaccaro, G. Mangiapia, L. Paduano, K. Schillén, *J. Biol. Inorg. Chem.* **2007**, *12*, 267.
 [24] S. Torres, M. I. M. Prata, A. C. Santos, J. P. Andre, J. A. Martins, L. Helm, E. Toth, M. L. Garcia-Martin, T. B. Rodrigues, P. Lopez-Larrubia, S. Cerdán, C. F. G. C. Geraldes, *NMR Biomed.* **2008**, *21*, 322.
 [25] E. Torres, F. Mainini, R. Napolitano, F. Fedeli, R. Cavalli, S. Aime, E. Terreno, *J. Controlled Release* **2011**, *154*, 196.
 [26] M. Vaccaro, G. Mangiapia, L. Paduano, E. Gianolio, A. Accardo, D. Tesauro, G. Morelli, *ChemPhysChem* **2007**, *8*, 2526.
 [27] A. T. Preslar, G. Parigi, M. T. McClendon, S. S. Sefick, T. J. Moyer, C. R. Haney, E. A. Waters, K. W. MacRenaris, C. Luchinat, S. I. Stupp, T. J. Meade, *ACS Nano* **2014**, *8*, 7325.
 [28] S. R. Bull, M. O. Guler, R. E. Bras, T. J. Meade, S. I. Stupp, *Nano Lett.* **2005**, *5*, 1.
 [29] S. Aime, D. Delli Castelli, S. Geninatti Crich, E. Gianolio, E. Terreno, *Acc. Chem. Res.* **2009**, *42*, 822.
 [30] A. Accardo, D. Tesauro, L. Aloj, C. Pedone, G. Morelli, *Coord. Chem. Rev.* **2009**, *253*, 2193.
 [31] V. Castelletto, I. W. Hamley, *Biophys. Chem.* **2009**, *141*, 169.
 [32] M. R. Nilsson, *Methods* **2004**, *34*, 151.
 [33] A. Morisco, A. Accardo, E. Gianolio, D. Tesauro, E. Benedetti, G. Morelli, *J. Pept. Sci.* **2009**, *15*, 242.
 [34] N. Tzokova, C. M. Fernyhough, M. F. Butler, S. P. Armes, A. J. Ryan, P. D. Topham, D. J. Adams, *Langmuir* **2009**, *25*, 11082.
 [35] R. Huang, R. Su, W. Qi, J. Zhao, Z. He, *Nanotechnology* **2011**, *22*, 245609.
 [36] N. Tzokova, C. M. Fernyhough, P. D. Topham, N. Sandon, D. J. Adams, M. F. Butler, S. P. Armes, A. J. Ryan, *Langmuir* **2009**, *25*, 2479.
 [37] S. D. Moran, M. T. Zanni, *J. Phys. Chem. Lett.* **2014**, *5*, 1984.
 [38] H. A. Behanna, J. J. M. Donners, A. C. Gordon, S. I. Stupp, *J. Am. Chem. Soc.* **2005**, *127*, 1193.
 [39] L. C. Serpell, *Biochim. Biophys. Acta, Mol. Basis Dis.* **2000**, *1502*, 16.

- [40] R. Orbach, I. Mironi-Harpaz, L. Adler-Abramovich, E. Mossou, E. P. Mitchell, V. T. Forsyth, E. Gazit, D. Seliktar, *Langmuir* **2012**, *28*, 2015.
- [41] S. Aime, S. Geninatti Crich, E. Gianolio, G. B. Giovenzana, L. Tei, E. Terreno, *Coord. Chem. Rev.* **2006**, *250*, 1562.
- [42] N. Blombergen, *J. Chem. Phys.* **1957**, *27*, 572.
- [43] I. Solomon, *Phys. Rev.* **1955**, *99*, 559.
- [44] P. Caravan, J. J. Ellison, T. J. McMurry, R. B. Lauffer, *Chem. Rev.* **1999**, *99*, 2293.
- [45] W. T. Truong, Y. Su, D. Gloria, F. Braet, P. Thordarson, *Biomater. Sci.* **2015**, *3*, 298.
- [46] E. Gianolio, F. Arena, G. J. Strijkers, K. Nicolay, A. Högset, S. Aime, *Magn. Reson. Med.* **2011**, *65*, 212.
- [47] E. Di Gregorio, G. Ferrauto, E. Gianolio, S. Aime, *Contrast Media Mol. Imaging* **2013**, *8*, 475.
- [48] A. Accardo, A. Morisco, E. Gianolio, D. Tesauero, G. Mangiapia, A. Radulescu, A. Brandt, G. Morelli, *J. Pept. Sci.* **2011**, *17*, 154.
- [49] A. Accardo, P. Ringhieri, R. Palumbo, G. Morelli, *Biopolymers* **2014**, *102*, 304.
- [50] A. Barge, G. Cravotto, E. Gianolio, F. Fedeli, *Contrast Media Mol. Imaging* **2006**, *1*, 184.
- [51] K. S. Birdi, H. N. Singh, S. U. Dalsager, *J. Phys. Chem.* **1979**, *83*, 2733.
- [52] E. De Vendittis, G. Palumbo, G. Parlato, V. Bocchini, *Anal. Biochem.* **1981**, *115*, 278.
- [53] A. Nakajima, *J. Lumin.* **1976**, *11*, 429.
- [54] H. LeVine III, *Protein Sci.* **1993**, *2*, 404.
- [55] M. Sunde, L. C. Serpell, M. Bartlam, P. E. Fraser, M. B. Pepys, C. C. F. Blake, *J. Mol. Biol.* **1997**, *273*, 729.
- [56] S. O. Makin, P. Sikorski, L. C. Serpell, *J. Appl. Cryst.* **2007**, *40*, 966.
- [57] F. Arena, J. B. Singh, E. Gianolio, R. Stefania, S. Aime, *Bioconj. Chem.* **2011**, *22*, 2625.



Liposomal doxorubicin doubly functionalized with CCK8 and R8 peptide sequences for selective intracellular drug delivery[‡]

Paola Ringhieri,^a Carlo Diaferia,^a Stefania Galdiero,^a Rosanna Palumbo,^b Giancarlo Morelli^a and Antonella Accardo^{a*}

A new dual-ligand liposomal doxorubicin delivery system, which couples targeting to enhanced cellular uptake and may lead to a more efficient drug delivery system, is here designed and synthesized. Liposomes based on the composition 1,2-dioleoyl-sn-glycero-3-phosphocholine/1,2-distearoyl-sn-glycero-3-phosphoethanolamine-Peg2000-R8/(C18)₂-L5-SS-CCK8 (87/8/5 mol/mol/mol) were prepared and loaded with doxorubicin. Presence of the two peptides on the external surface is demonstrated by fluorescence resonance energy transfer assay. The combination of the R8 cell-penetrating peptide and of the CCK8 targeting peptide (homing peptide) on the liposome surface is obtained by combining pre-modification and post-modification methods. In the dual-ligand system, the CCK8 peptide is anchored to the liposome surface by using a disulfide bond. This chemical function is inserted in order to promote the selective cleavage of the homing peptide under the reductive conditions expected in proximity of the tumor site, thus allowing targeting and internalization of the liposomal drug. Copyright © 2015 European Peptide Society and John Wiley & Sons, Ltd.

Additional supporting information may be found in the online version of this article at the publisher's web site.

Keywords: liposomes; homing peptides; cell-penetrating peptides; click chemistry; drug delivery systems

Introduction

The therapeutic effectiveness of many pharmaceutical compounds currently proposed for the treatment of cancer diseases is low, because a large amount of the administered drug is also delivered to normal tissues. Inefficient delivery reduces the total dose of drug reaching the target and is responsible of severe adverse effects on non-target organs. Consequently, researchers are focusing their attention on the development of novel sophisticated systems able to enhance the therapeutic index of anticancer drugs by improving delivery and allowing the drug to reach the intended target organ at full concentration [1–3]. Recently, several examples of supramolecular systems, including micelles [4,5], liposomes, [6,7] dendrimers [8] and nanoparticles [9,10], loaded with anticancer drugs such as doxorubicin, paclitaxel or cisplatin have been proposed as innovative delivery vehicles. For example, pegylated liposomal doxorubicin (PLD), commercially available as Doxil/Caelyx, is routinely administered in ovarian and metastatic breast cancers [11], and several other liposomal drugs are under development in clinical phases. Although liposomal formulations allow to reduce severe cardiotoxicity associated with free doxorubicin and to increase drug delivery to target cells exploiting the enhanced permeability and retention effect, the therapeutic efficacy of PLD remains low because mainly of poor cell penetration and slow drug release from liposomes [11–13].

In order to accumulate the drug only to target organs and inside malignant cells, new delivery systems based on micelles or

* Correspondence to: Antonella Accardo, Department of Pharmacy and CIRPeB, Centro Interuniversitario di Ricerca sui Peptidi Bioattivi – University of Naples 'Federico II', Via Mezzocannone 16, 80134, Naples, Italy. E-mail: antonella.accardo@unina.it

[‡] Special issue of contributions presented at the 14th Naples Workshop on Bioactive Peptides "The renaissance era of peptides in drug discovery", June 12–14, 2014, Naples.

^a Department of Pharmacy and CIRPeB, Centro Interuniversitario di Ricerca sui Peptidi Bioattivi – University of Naples 'Federico II', Via Mezzocannone 16, 80134, Naples, Italy

^b IBB, CNR, Via Mezzocannone 16, 80134, Naples, Italy

Abbreviations: AdOO, 8-amino-3,6-dioxaoctanoic acid; CCK-R, cholecystokinin receptor; DCM, dichloromethane; DIPEA, N,N-diisopropylethylamine; DLS, dynamic light scattering; DMF, dimethylformamide; DOPG, 1,2-dioleoyl-sn-glycero-3-phosphocholine; doxorubicin hydrochloride, (8S,10S)-10-(4-amino-5-hydroxy-6-methyl-tetrahydro-2H-pyran-2-yloxy)-6,8,11-trihydroxy-8-(2-hydroxyacetyl)-1-methoxy-7,8,9,10-tetrahydro-tetracene-5,12-dione; DSPE-Peg2000-Mal, 1,2-distearoyl-sn-glycero-3-phosphoethanolamine-N-[maleimide(polyethylene glycol)-2000] (ammonium salt); DTT, dithiothreitol; ESI MS, electrospray ionization-mass spectrometry; FITC, fluorescein isothiocyanate; Fmoc-Pra-OH, Fmoc-L-propargylglycine; FRET, fluorescence resonance energy transfer assay; HATU, o-(7-azabenzotriazol-1-yl)-1,1,3,3-tetramethyluronium; HEPES, 4-(2-hydroxyethyl) piperazine-ethanesulfonic acid; HOBt, 1-hydroxybenzotriazole; HPLC, high-performance liquid chromatography; MBHA resin, 4-methylbenzhydrylamine resin; Mtt, 4-methyltrityl; N3-Peg(9)-COOH PEG, 14-azido-5-oxo-3,9,12-trioxo-6-azatetradecan-1-oic acid; polyethylene glycol; PyBOP, benzotriazol-1-yl-oxytris(pyrrolidino)phosphonium; Rho-PE, 1,2-dioleoyl-sn-glycero-3-phosphoethanolamine-N-(lissamine rhodamine B sulfonyle) (ammonium salt); SPDP-NHS, 3-(2-pyridylidithio)propionic acid N-hydroxysuccinimide ester; SPPS, solid-phase peptide synthesis; TFA, trifluoroacetic acid; TIS, triisopropylsilane.

liposomes externally modified with bioactive ligands, such as peptides, have been recently proposed.

Two different strategies have been followed: the first is based on the use of bioactive peptides able to target the entire system on receptors overexpressed by cancer cells, while the second exploits cell-penetrating peptides (CPPs) to allow cell penetration of the full delivery system that releases the drug in the inner cell compartments [14]. Examples of the first strategies are micelles and liposomes externally modified with homing peptides (HPs) [15,16], while examples of the second strategy are nanosystems modified with CPPs [17–19]. In both cases, peptides should remain well exposed on the external surface of the delivery system and should maintain the right conformation to perform their biological functions. Therefore, different strategies have been developed to efficiently bind the peptide sequence to the supramolecular aggregate surface and to study the conformational and structural properties of the exposed peptide along with that of the entire aggregate.

Hence, in order to couple the targeting properties of a HP with the cell-penetrating efficacy of a peptide sequence, we describe the preparation of a prototype of a 1,2-dioleoyl-sn-glycero-3-phosphocholine (DOPG)-based liposomal doxorubicin delivery system externally functionalized with two different peptides (Figure 1).

CCK8 has been chosen as HP, while the well-known polyarginine-based sequence (octa-arginine, R8) as CCP. The C-terminal cholecystokinin octapeptide amide (CCK 26-33 or CCK8) [20] displays high affinity and selectivity for CCK2-R cholecystokinin receptor, whereas the same peptide in its sulfated form (sCCK8) presents high affinity for both CCK1-R and CCK2-R cholecystokinin receptors [21,22]. Both cholecystokinin receptors are normally present on the cell surface, but result overexpressed in many malignant transformations: CCK1-R is overexpressed by pancreatic cancer cells while CCK2-R is found in small cell lung cancer, colon and gastric cancers, medullary thyroid carcinomas, astrocytomas and stromal ovarian tumors [23]. The high specificity of the CCK8 peptide toward the

cholecystokinin receptors is also kept when the peptide sequence is modified at the N-terminus with chelating agents [24] or alkyl chains [25,26] allowing the development of target selective contrast agents or cargo systems for selective drug delivery, respectively.

CPPs provide a promising solution to the problems commonly related with drug delivery of conventional cancer chemotherapeutics. CPPs are peptide sequences that, interacting with charged phospholipids on the outer surface of the cell membrane and destabilizing the bilayer, assist the intracellular delivery of various biomolecules including proteins, small molecules, nucleic acids therapeutics and liposomes [27,28]. R8 is a well-known CPP able to promote delivery of a cargo into the cytoplasm [29,30]. The two peptides were bound to the liposomal surface using two different strategies: pre-liposome formulation and post-liposome formulation methods.

In the design of the dual-ligand system, the CCK8 peptide was anchored to the liposome surface by using a disulfide bond. This chemical function was inserted in order to promote the selective cleavage of the HP under the reductive conditions expected in proximity of the tumor site [31].

In fact, in our strategy, the dual-peptide cargo should reach the overexpressed receptors present on tumor site driven by the homing CCK8 peptide; then, the reductive conditions should free the liposomal vehicle that is subsequently internalized in the target cell by means of the R8 peptide. As a consequence, doxorubicin should be released only in the target cells, as schematized in Figure 1.

Materials and Methods

Fmoc-protected amino acid derivatives, coupling reagents and Rink amide p-methylbenzhydrylamine 4-methylbenzhydrylamine resin (MBHA resin) were purchased from Calbiochem-Novabiochem

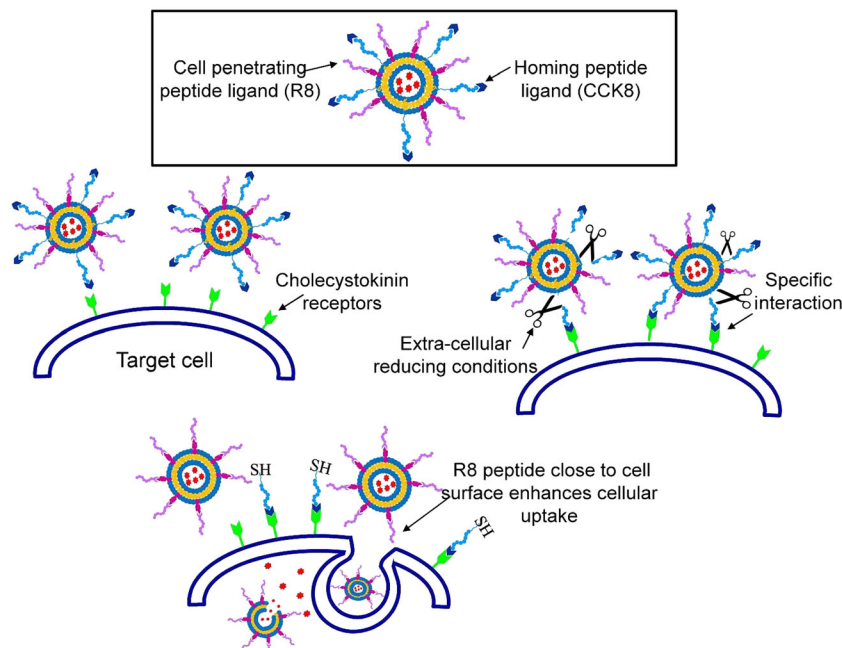


Figure 1. Schematic representation of a liposomal doxorubicin simultaneously functionalized with CCK8 homing peptide ligand and R8 cell-penetrating peptide ligand (DOPG/DSPE-Peg2000-R8/(C18)₂-L5-SS-CCK8, 87/8/5 mol/mol/mol, Doxo-loaded liposomes), and, below, the sketch of a presumed mechanism for cellular uptake and internalization. The first step concerns the selective binding between the CCK8 homing peptides on the liposome surface and the cholecystokinin receptors. In a second step, the cleavage of the thiol bond, under the reducing conditions expected in proximity of the tumor site, should free the liposomal vehicle that, in a third step, is internalized in the target cell by means of the R8 peptide.

(Laufelfingen, Switzerland). Fmoc-L-propargylglycine (Fmoc-Pra-OH) was purchased from Neosystem (Strasbourg, France). N3-Peg(9)-COOH was purchased by Iris Biotech GmbH (Marktredwitz, Germany). Doxorubicin hydrochloride, fluorescein isothiocyanate (FITC) isomer I and 3-(2-pyridyldithio)propionic acid *N*-hydroxysuccinimide ester (SPDP-NHS) were purchased from Sigma-Aldrich (Milan, Italy). DOPG, DSPE-Peg2000-Mal (**4**) and Rho-PE were purchased by Avanti Polar Lipids (Alabaster, AL, USA). *N,N*-dioctadecylsuccinamic acid was synthesized according to a published procedure [32]. All other chemicals were commercially available by Sigma-Aldrich and were used as received, unless otherwise stated. UV-Vis measurements were carried out on Thermo Fisher Scientific Inc (Wilmington, Delaware USA) Nanodrop 2000c spectrophotometer equipped with a 1.0 cm quartz cuvette (Hellma). The fluorescence emission spectra were recorded using a Jasco Model FP-750 spectrofluorimeter (Easton, MD) equipped with a Peltier temperature controller in 1.0 cm path length quartz cell at 25 °C. ¹H NMR spectra were recorded on a Varian 400 MHz spectrometer (Palo Alto, CA).

Solid-Phase Synthesis

Azide-Peg9-Lys(C(O)CH₂CH₂C(O)N-(C₁₈H₃₇)₂)-amide ((C₁₈)₂-Peg9-N3) (**3**) was synthesized according to the experimental procedures elsewhere reported [33].

Synthesis of the Octa-Arginine Derivatives

Fmoc-R8-OH was synthesized according to standard solid-phase techniques with Fmoc/tBu procedures by using a Syro I MultiSynThec GmbH (Wullener, Germany) automatic synthesizer. The Rink amide MBHA resin (substitution 0.65 mmol/g, scale 0.5 mmol, 0.770 g) was used as solid-phase support. Peptide chain was elongated by sequential addition of Fmoc-AA-OH with benzotriazol-1-yl-oxytris(pyrrolidino)phosphonium/1-hydroxybenzotriazole/*N,N*-diisopropylethylamine (PyBOP/HOBt/DIPEA) (1 : 1 : 2) as coupling reagents, in dimethylformamide (DMF) in pre-activation mode. After each coupling, the Fmoc protecting group was removed from the N-terminus by treating the peptidyl resin with few milliliters of DMF/piperidine solution (70/30 v/v). Each coupling was performed twice for 1 h. Then, the peptide-resin was shared in four reactors (each one containing 0.1 mmol of peptide-resin), and the syntheses were completed manually to obtain the R8-Pra (**2a**) and R8-Cys (**2b**) peptide derivatives or their fluorescent analogues R8PraFITC (**2c**) and R8CysFITC (**2d**). The FITC coupling was performed overnight at room temperature by using *o*-(7-azabenzotriazol-1-yl)-1,1,3,3-tetramethyluronium/DIPEA (1/2 with respect to FITC) as activating agents. Peptides were fully deprotected and cleaved from the resin with trifluoroacetic acid (TFA) with 2.5% (v/v) water, 2.0% (v/v) anisole, 2.0% (v/v) thioanisole as scavengers, at room temperature, and then precipitated with ice-cold ethyl ether, filtered, dissolved in water and lyophilized. The crude peptides were purified by reversed-phase high-performance liquid chromatography (RP-HPLC) on a LC8 Shimadzu HPLC system (Shimadzu Corporation, Kyoto, Japan) equipped with a UV Lambda-Max Model 481 detector using a Phenomenex (Torrance, CA) C18 (300 Å, 250 × 21.20 mm, 5 μ) column eluted with H₂O/0.1% TFA (A) and CH₃CN/0.1% TFA (B) from 5 to 70% over 30 min at a flow rate of 20 ml/min. Purity and identity were assessed by analytical LC-MS analyses by using Finnigan Surveyor MSQ single quadrupole electrospray ionization (Finnigan/Thermo Electron Corporation San Jose, CA), column: C18-Phenomenex eluted with

H₂O/0.1% TFA (A) and CH₃CN/0.1% TFA (B) from 5 to 70% over 15 min at 250 μl/min flow rate. The final yields of purified peptides ranged between 60 and 80%. Characteristics of the peptides (formula and molecular mass) are collected in Table 1.

Synthesis of CCK8 Derivatives

(C₁₈)₂-L5-SPDP (**5**)

(C₁₈)₂-L5-SPDP monomer was synthesized on solid phase by using standard Fmoc protocols. The amphiphilic monomer was synthesized on Rink amide MBHA resin (substitution 0.65 mmol/g, 0.2 mmol, 0.308 g). The Fmoc protecting group on the resin was removed by a DMF/piperidine (70 : 30) mixture. All coupling reactions were activated by using PyBOP/HOBt/DIPEA (1/1/2) in DMF. Fmoc-Lys(Mtt)-OH (0.50 g, 0.8 mmol) was coupled on the resin for 1 h. The solution was filtered, and the resin was washed several times with dichloromethane (DCM); the Mtt protecting group on the N^ε amino function of the lysine was removed by various treatment of 2 min each, with a DCM/triisopropylsilane (TIS)/TFA (94 : 5 : 1 v/v/v) mixture. This procedure was repeated until the solution became colorless. The resin was washed three times with DCM and three times with DMF. After the Mtt removal, 0.498 g of *N,N*-dioctadecylsuccinamic acid (0.8 mmol) were coupled for 1 h as previously described [34]. Then, the Fmoc protecting group from the main chain was removed, and five Fmoc-8-amino-3,6-dioxaoctanoic acid (AdOO)-OH ethoxylic linkers (two equivalents for each coupling) were sequentially coupled under standard condition in DMF for 1 h. After the Fmoc removal from the N^ε-terminus of the last ethoxylic linker, two equivalents of heterobifunctional peptide crosslinker SPDP-NHS and four equivalents of DIPEA were added in DMF for 1 h to the resin. The crude product was cleaved from the resin by treatment under stirring for 2 h with 5 ml of a TFA solution containing TIS (2.5%) and water (2.5%). The product was slowly precipitated at 0 °C by adding water dropwise, washed several times with small portions of water and lyophilized. The white solid was recrystallized from MeOH/H₂O and recovered with high yields (>80%). The product was identified by mass spectra [electrospray ionization (ESI)] and NMR spectroscopy. ¹H NMR spectrum was recorded on a Varian 400 MHz spectrometer (Palo Alto, CA).

¹H NMR (400 MHz, CDCl₃) (chemical shifts in δ, CDCl₃ internal standard = 7.26) = 8.50 (d, 1H, H aromatic), 7.6 (m, 2H, H aromatic), 7.1 (m, 1H H aromatic), 4.4 (m, 1H, CH Lys^α), 4.04 (m, 1H, OCH₂CONH), 3.67 (s, 20H, OCH₂CH₂O), 3.59 (m, 10H OCH₂CH₂N), 3.25–3.20 (m, 14H, N-CH₂), 3.2 (m, 2H, CH₂ Lys^β), 2.80 (m, 2H SCH₂), 2.64–2.49 (m, 4H, NHCOCH₂CH₂CO), 1.74 (m, 2H, CH₂Lys^β),

Table 1. Characteristics of investigated peptides and lipopeptides

Peptide	Formula	Molecular mass [g/mol]	
		Calculated	Determined
R8-Pra (2a)	C ₅₃ H ₁₀₃ N ₃ O ₉	1360.64	1361.62
R8-Cys (2b)	C ₅₁ H ₁₀₃ N ₃ O ₉ S	1367.60	1368.6
R8-Pra-βAla-FITC (2c)	C ₇₇ H ₁₁₈ N ₃ O ₁₄ S	1802.22	902.1
R8-Cys-βAla-FITC (2d)	C ₇₅ H ₁₁₈ N ₃ O ₁₄ S ₂	1810.21	906.1
(C ₁₈) ₂ -Peg9-N3 (3)	C ₆₈ H ₁₃₂ N ₈ O ₁₄	1284.5	1285.6
(C ₁₈) ₂ -L5-SPDP (5)	C ₈₃ H ₁₅₄ N ₁₀ O ₁₉ S ₂	1673.0	1674.1
(C ₁₈) ₂ -L5-SS-CCK8 (1)	C ₁₃₂ H ₂₁₉ N ₂₁ O ₃₃ S ₄	2753.6	918.7

1.55 (m, 2H, $\text{CH}_2\text{Lys}^\gamma$), 1.45 (m, 2H, $\text{CH}_2\text{Lys}^\gamma$), 1.40 (m, 4H, RCH_2CH_3), 1.25 (m, 60 CH_2 aliphatic), 0.88 (t, 6H, CH_3).

(C18)₂-L5-SS-CCK8 (1)

Fmoc-Cys(Trt)-CCK8 peptide was synthesized on Rink amide MBHA resin (substitution 0.65 mmol/g, scale of 50 μmol) by using automatic synthesizer as described in the preceding texts. Fmoc and Trt protecting groups from the N^α-terminus and the N^ε-terminus of the cysteine residue were removed with DMF/piperidine (70/30) and DCM/TIS/TFA (94/5/1), respectively. Then, the resin was washed several times with DCM and DFM, and (C18)₂-L5-SPDP (5) amphiphile (1 equiv.) was coupled in DMF over weekend. The crude product was cleaved from the resin as previously described for (C18)₂-L5-SPDP (5). Purity and identity were assessed by analytical LC-MS analyses as previously reported.

Liposome Preparation and Structural Characterization

All liposomal solutions were prepared in 10 mM 4-2-hydroxyethyl piperazine-ethanesulfonic acid (HEPES) buffer at pH 7.4 by using the thin film method. Briefly, the amphiphiles were dissolved in a small amount of MeOH/ CHCl_3 (50/50); subsequently, a thin film of amphiphiles was obtained by evaporating the solvent by slowly rotating the tube containing the solution under a stream of nitrogen. Lipid film was hydrated in HEPES buffer, sonicated for 30 min and extruded 10 times at room temperature, using a thermobarrel extruder system (Northern Lipids Inc, Vancouver, BC, Canada) under nitrogen through a polycarbonate membrane (Nucleopore Track Membrane 25 mm, Whatman, Brentford, UK) with 0.1 μm pore size.

DOPG/(C18)₂-Peg9-N3/(C18)₂-L5-SS-CCK8 and DOPG/DSPE-Peg2000-Mal/(C18)₂-L5-SS-CCK8 (both at 87:8:5 molar ratio) liposomes were prepared, according to pre-liposome formulation method, as previously described, by including the CCK8 amphiphilic derivative in liposome formulation.

Fluorescent-labeled liposomes were prepared by adding 1% mol of Rho-PE in the phospholipid mixture, during the lipid film preparation.

Hydrodynamic radii (R_H), polydispersity index (PI) and zeta potential (ζ) of liposomes were measured by dynamic light scattering (DLS). DLS measurements were carried out using a Zetasizer Nano ZS (Malvern Instruments, Westborough, MA) that employs a 173° backscatter detector. Other instrumental settings are measurement position (mm): 4.65, attenuator: 8, temperature 25 °C and cell: disposable sizing cuvette. Before starting with DLS measurements, samples previously prepared were diluted at final concentration of $2.0 \cdot 10^{-4}$ M and centrifuged at room temperature at 13 000 rpm for 5 min. For each formulation, R_H and PI were calculated as the mean of three measurements on three different batches.

Doxorubicin Loading

Doxorubicin was remote-loaded in liposomes, by using the well-assessed ammonium sulfate gradient method [35]. Briefly, a liposomal solution (10 mM) was prepared as previously reported in 250 mM $(\text{NH}_4)_2\text{SO}_4$ solution at pH 5.5. After preparation, the outer solution was removed by gel filtration, eluting liposomes on a Sephadex G-50 (Amersham Biosciences) column pre-equilibrated with HEPES buffer. After filtration, liposomes were immediately incubated with doxorubicin and stirred for 1 h at 60 °C. The drug weight/lipid weight ratio chosen for the incubation was 0.2. Unloaded doxorubicin was subsequently separated from loaded doxorubicin by gel filtration on a Sephadex column. The amount

of doxorubicin loaded in the inner compartment of liposomes was determined by UV-Vis spectroscopy using calibration curves obtained by measuring absorbance at $\lambda = 480$ nm. The drug loading content (DLC%), defined as the weight ratio of encapsulated doxorubicin vs the amphiphilic molecules forming liposomes) was quantified by subtraction of the amount of removed doxorubicin from the total amount of loaded doxorubicin.

Post-Liposomal Modification

Two post-liposomal modification strategies were used to bind R8 peptide on the outer liposome surface: copper-catalyzed azide-alkyne cycloaddition (CuAAC) and the reaction between maleimide and sulfhydryl group (–SH).

For CuAAC reaction-mixed liposomes, DOPG/(C18)₂-Peg9-N3 (at 92:8 molar ratio) and DOPG/(C18)₂-Peg9-N3/(C18)₂-L5-SS-CCK8 (at 87:8:5 molar ratio) were prepared at $1 \cdot 10^{-3}$ M lipid concentration in 10 mM HEPES buffer at pH 7.4. Then, 1.0 equiv. of the peptide derivative (R8-Pra (2a) or R8PraFITC (2c)), 2.0 equivs. of sodium ascorbate and 0.5 equivs. of CuCl_2 with respect to the azido moiety were added. The reaction mixture was stirred at 40 °C for 30 min and successively stored overnight at room temperature. Free peptide and copper ions were removed by gel filtration chromatography by using Sephadex G-50 column. For reaction between maleimide and sulfhydryl group (–SH) mixed liposomes, DOPG/DSPE-Peg2000-Mal (at 92:8 molar ratio) and DOPG/DSPE-Peg2000-Mal/(C18)₂-L5-SS-CCK8 (at 87:8:5 molar ratio) were prepared at $1 \cdot 10^{-3}$ M lipid concentration in 10 mM HEPES buffer at pH 7.4. Then, 110 μl of a stock solution (1 mg/ml in HEPES) of the peptide derivative (R8-Cys (2b) or R8CysFITC (2d)) was added, and the reaction was left under stirring at room temperature for 1 h. Free peptide was eliminated as described in the preceding texts. The amount of the unreacted fluorescent peptide was spectroscopically estimated using UV-Vis measurements at $\lambda = 490$ nm.

Fluorescence Resonance Energy Transfer

R8 conjugation on the outer liposomal surface was monitored using the fluorescence resonance energy transfer assay (FRET). According to the experimental procedures described in the previous section, CuAAC and maleimido reactions were carried out on DOPG liposomes made fluorescent by adding 1 mol% of Rho-PE during the formulation. After reactions, liposomes were purified by gel filtration in order to remove unbound peptide derivatives. Fluorescence spectra of liposomal solutions before and after the reactions were recorded at room temperature. Equal excitation and emission bandwidths were used throughout the experiments, with a recording speed of 125 nm/min and automatic selection of the time constant. Excitation wavelengths of FITC and Rho were set at 490 and 520 nm, respectively. Emission spectra of samples were recorded between 500 and 700 nm.

Fluorescence Spectroscopy

Emission spectra of tryptophane were recorded in 290–450 nm range exciting at 280 nm the solutions at a CCK8 concentration of $1.0 \cdot 10^{-5}$ M. Equal excitation and emission bandwidths were used throughout the experiments, with a recording speed of 125 nm/min and automatic selection of the time constant.

DTT Reductive Cleavage

The reductive cleavage of the disulfide bond of (C18)₂-L5-SS-CCK8 (**1**) monomer in the dual-ligand-based liposomes (DOPG/(C18)₂-L5-SS-CCK8/R8) was performed adding 750 μ l of 100 mM dithiothreitol (DTT) solution to 3.0 ml of 1 mM liposomes. Reaction was stirred under a nitrogen atmosphere for 2 h at room temperature. Then, liposomes were eluted on Sephadex G-50 column pre-equilibrated with HEPES buffer, and free peptide detached from the liposome was identified by LC-MS spectrometry.

Cell Culture and Flow Cytometry

Cellular uptake of liposomes (LP, R8-LP, CCK8-LP and R8/CCK8-LP) was studied by flow cytometry on A431 cells overexpressing the CCK2-R by stable transfection [36]. Cells were cultured as an exponential growing sub-confluent monolayer on 100 mm plates in DMEM supplemented with 10% FCS, 2 mM L-glutamine and 250 mg/ml G418 in a humidified atmosphere containing 5% CO₂ at 37 °C. Cell aliquots (3·10⁵) were incubated with 0.1 mM liposomes (1 μ M Rho-PE) at RT for 30 min. After the incubation, cells were washed and permeabilized with 0.1% Triton X-100 in 33 mM sodium citrate and analyzed with a flow cytometer equipped with a 488 nm argon laser (FACScan, Becton Dickinson, CA, USA). A total of 30 000 events per sample were collected. Values of fluorescence intensity were obtained from histogram statistic of CellQuest software.

Results and Discussion

Dual-ligand DOPG-based liposomes were prepared using simultaneously two different strategies of functionalization (pre-liposomal and post-liposomal formulation methods). The CCK8 HP was introduced on the outer liposomal surface, according to the pre-liposome formulation method, by inserting its amphiphilic derivative ((C18)₂-L5-SS-CCK8 (**1**), shown in Figure 2A), directly during the liposome formulation step. The (C18)₂-L5-SS-CCK8 (**1**) amphiphile contains the CCK8 sequence, modified at N-terminus with two saturated alkyl chains at 18 carbon atoms, a polyethoxylic spacer and a cleavable disulfide bond between the CCK8 and alkyl moiety. The polyethoxylic spacer was used both to improve the bioavailability of the peptide on the outer liposomal surface and to increase the intrinsic water solubility of the amphiphilic peptide. On the other hand, a disulfide bond was inserted in order to promote a selective cleavage of the CCK8 under the reductive conditions expected in proximity of tumor sites.

The post-liposomal formulation method was used to bind the CPP, R8, to the liposome surface. This coupling strategy involves the insertion onto the liposomal surface of an appropriate functional group able to selectively react with the peptide derivative. Several functional groups such as (i) azides for Cu(I)-catalyzed Huisgen cycloaddition (CuAAC), (ii) biotin for non-covalent interaction with avidin (iii) amines for the amine-*N*-hydroxysuccinimide coupling method, (iv) maleimide for Michael addition or (v) triphosphines for Staudinger ligation are ordinarily used [37]. The synthetic approach should be conveniently selected in order to increase the reproducibility and the yield of the coupling reaction. In order to perform the selective coupling of the R8 peptide on the liposomal surface, both Michael addition and Huisgen cycloaddition strategies were investigated. For Huisgen cycloaddition, R8-Pra derivative (Figure 2B – compound **2a**) and (C18)₂-Peg9-N3 (Figure 2C, compound **3**) were used, whereas for Michael addition,

R8-Cys (Figure 2B – compound **2b**) and DSPE-Peg2000-Mal (Figure 2D, compound **4**) were employed.

Peptide Syntheses

Both peptide derivatives and peptide amphiphiles (refer to Figure 2) were synthesized by solid-phase methods according to standard solid-phase peptide synthesis (SPPS) protocols with Fmoc/tBu chemistry. The synthesis of the cleavable peptide amphiphile (C18)₂-L5-SS-CCK8 (**1**) was achieved in two stages. In the first one, the (C18)₂-L5-SPDP (**5**) amphiphilic monomer (Figure 3A) was synthesized on the Rink amide resin according to the modified protocol sketched in Figure 3B. Fmoc-Lys(Mtt)-OH, in which the two amino functions are orthogonally protected, was anchored to the solid support. After removal of the Mtt group from the N^ε of the lysine, the fragment containing the two alkyl chains was condensed using *N,N*-dioctadecylsuccinamic acid. Then, the Fmoc protecting group on the principal chain was removed, and five ethoxylic linkers and the SPDP-NHS crosslinker were sequentially introduced. SPDP-NHS is an amino and thiol (sulfhydryl) reactive heterobifunctional peptide crosslinker that contains an NHS reactive moiety able to react with primary amines and a pyridinyldisulfide group able to react with sulfhydryl groups to yield a reversible disulfide bond. NHS group was hence used to bind crosslinker at the last ethoxylic linker. At the end of the synthesis, the amphiphilic derivative was cleaved from the resin under acidic conditions, precipitated by adding cold water dropwise. The crude product was dissolved in H₂O/acetonitrile mixture and lyophilized, and its identity was confirmed by ESI mass spectrometry and ¹H NMR characterization. In the second stage, Fmoc-Cys(Trt)-CCK8 was synthesized on the Rink amide resin, and after removal of Trt and Fmoc protecting groups of the cysteine, the crude monomer (C18)₂-L5-SPDP (**5**) was added to the peptidyl resin and left under stirring for 48 h at room temperature. SPDP pyridinyldisulfide group reacts with the SH group of the cysteine residue at the N-terminus of the CCK8 peptide to yield a reversible disulfide bond.

R8-Pra and R8-Cys peptides (compounds **2a** and **2b** in Figure 2B) and their fluoresceinate analogues R8PraFITC and R8CysFITC (compounds **2c** and **2d** in Figure 2B) were obtained by SPPS and subsequently purified by RP-HPLC. In details, peptide derivatives were prepared by adding an L-propargylglycine or a cysteine residue at the N-terminus of the peptide sequence. For the syntheses of their fluoresceinate derivatives, the Fmoc protecting group from the principal chain was removed and Fmoc- β -Ala-OH and FITC-isothiocyanate were coupled in sequence. The β -alanine residue was introduced before the coupling step of FITC chromophore to avoid classical FITC elimination by the Edman degradation mechanism [38]. All the R8 peptide derivatives previously described were obtained in good yields and high purity (HPLC profiles are reported as Supplementary Materials). Parameters of peptide derivatives are reported in Table 1.

Preparation of Dual-Ligand Liposomes

Untargeted and targeted DOPG-based liposomes containing the CCK8 derivative were prepared in 10 mM HEPES buffer at pH 7.4 using the thin film method (Figure 4). Lipid films were hydrated in HEPES buffer, sonicated and extruded under nitrogen. Subsequently, the functionalization of pre-formed liposomes with R8 peptide was carried out using the Cu(I)-catalyzed Huisgen cycloaddition. This reaction presents several advantages such as rapidity, versatility and high product yields. Moreover, several examples of liposome functionalization by click reaction in the presence of

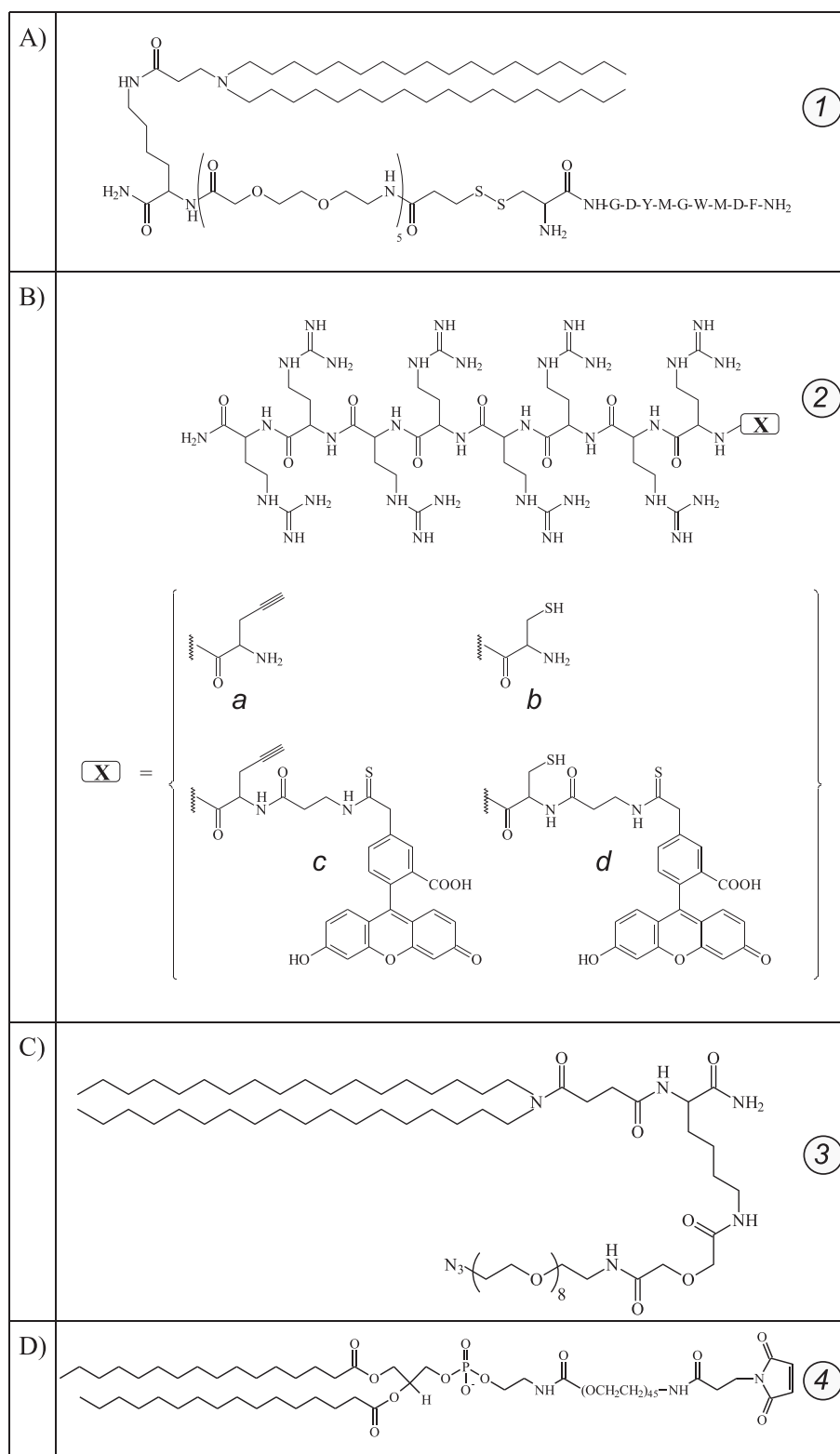


Figure 2. Schematic representation of (A) $(C18)_2$ -L5-SS-Cys-CCK8 (**1**) amphiphilic monomer; (B) R8 peptide derivatives R8-Pra (**2a**) and R8-Cys (**2b**) and their fluorescein analogues R8PraFITC (**2c**) and R8CysFITC (**2d**); (C) $(C18)_2$ -Peg9-N3 (**3**) amphiphilic monomer functionalized with azido group and (D) DSPE-Peg2000-Mal (**4**) phospholipid derivatized with maleimido reactive group.

disulfide bonds are also reported [39,40]. Anyway, several evidences of the ability of ascorbate to reduce disulfide bridges in a mixture containing physiological low-molecular weight disulfides (GS-SG, CyS-S and CyS-SGly) [41] or in proteins (tubulin, tau and

microtubule-associated protein-2) [42], in function of the incubation time, have been recently reported. These evidences pose doubts about the feasibility of the functionalization of liposomes, containing S-S bonds, using reactions that require the addition of

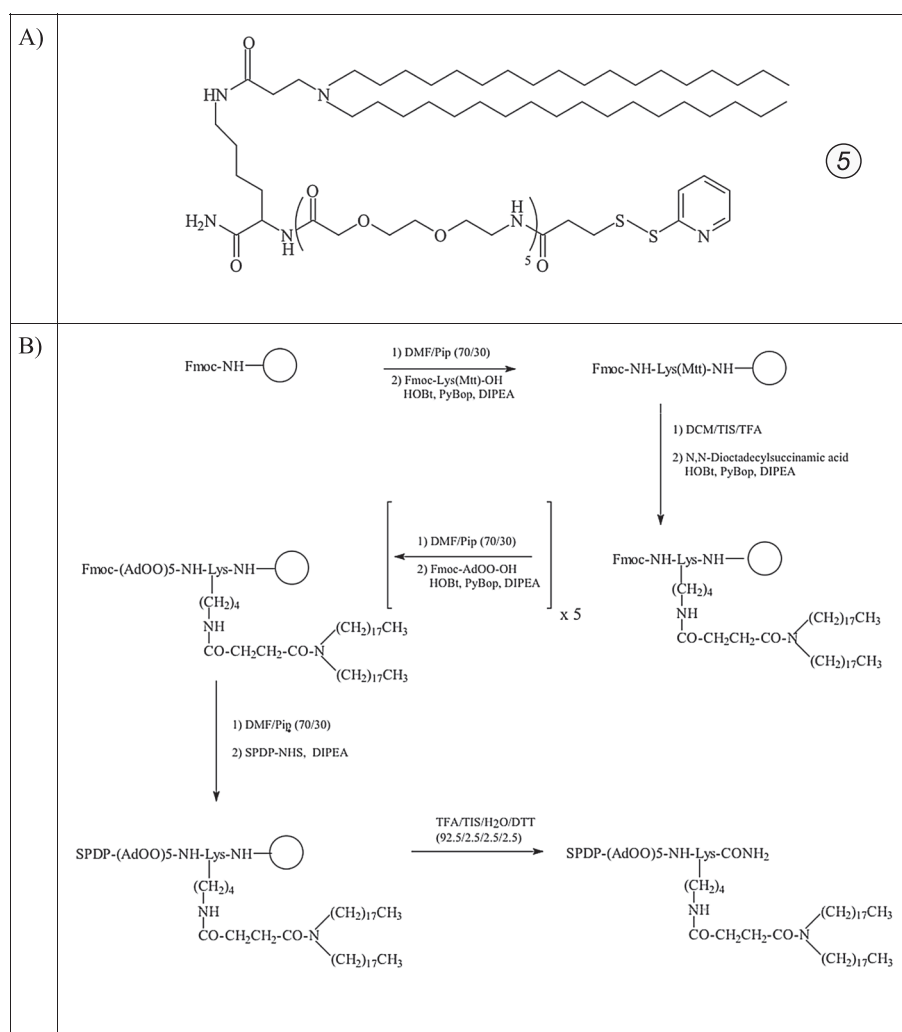


Figure 3. (A) Schematic representation of the synthetic monomer (C18)₂-L5-SPDP (**5**). (B) Scheme for the solid-phase synthesis of the (C18)₂-L5-SPDP (**5**) monomer. The Rink amide resin is represented as an empty circle. Fmoc, 9-fluorenylmethoxycarbonyl; Pip, piperidine; Mtt, 4-methyltrityl; DCM, dichloromethane; DIPEA, *N,N*-diisopropylethylamine; DTT, dithiothreitol; Fmoc-AdOO-OH, Fmoc-8-amino-3,6-dioxaoctanoic acid; HOBt, 1-hydroxybenzotriazole; PyBOP, benzotriazole-1-yl-oxytrispyrrolidinophosphonium hexafluorophosphonate; TFA, trifluoroacetic acid; TIS, triisopropylsilane.

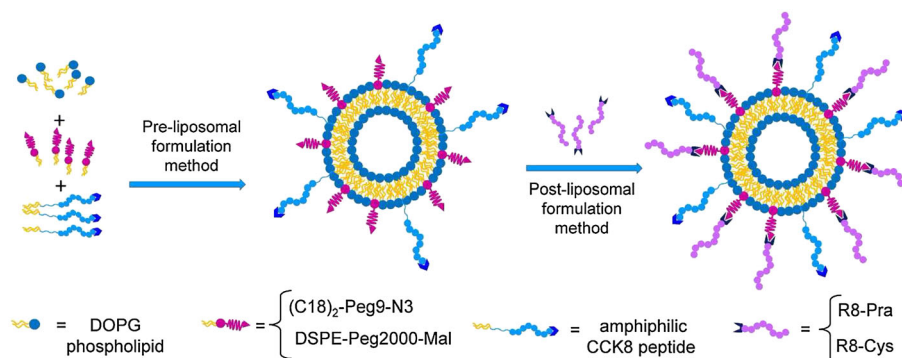


Figure 4. Schematic representation of the procedure used to prepare the dual-ligand liposomes. CCK8 liposomes containing few amounts of azido or maleimido moieties ((C18)₂-Peg9-N3 (**3**) or DSPE-Peg2000-Mal (**4**)) were obtained by the film method. Subsequently, liposomes were externally functionalized with R8 cell-penetrating peptide by CuAAC or Michael addition.

ascorbate, such as click chemistry procedures. Thus, at the end of the click chemistry reaction, we investigated the integrity of the disulfide bond by LC-MS and fluorescence spectroscopy. Liposomes were purified with a Sephadex G-50 gel filtration column and the

elutes characterized. Only few amounts of the unreacted R8-Pra (**2a**) peptide were found, indicating that R8 peptide was covalently bound on the liposomal surface, but chromatographic and ESI spectroscopy analyses (refer to Figure 5A) showed a peak at

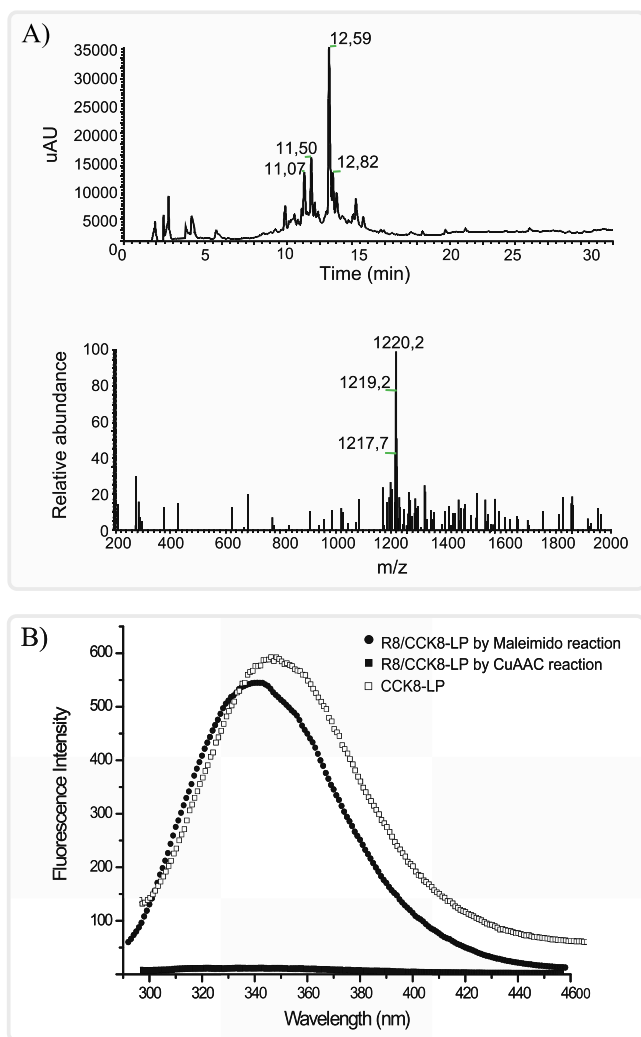


Figure 5. (A) Chromatographic and ESI spectroscopy analyses of gel filtration elute after click chemistry reaction; peak at 12.59 min is attributable to the reduced CCK8-Cys peptide fragment. (B) Fluorescence spectra of tryptophan residue of CCK8 liposomes after post-liposomal formulation strategy by CuAAC and maleimido reaction at 25 °C and $1.0 \cdot 10^{-5}$ M CCK8 concentration. Spectrum of CCK8 liposomes before reactions is also reported for comparison. Spectra were excited at 280 nm and recorded between 290 and 450 nm.

12.59 min with a mass profile attributable to the reduced CCK8-Cys peptide fragment. Moreover, the comparison of the tryptophan fluorescence spectra recorded on the liposomal suspension before and after the reaction showed a dramatic decrease of the emission peak of the indole group at 360 nm. Our results further support the view that the addition of the ascorbate causes the reductive cleavage of the CCK8 from the liposomal surface (Figure 5B) during the click chemistry reaction. As a consequence, Michael addition seemed to be the most suitable alternative strategy for the peptide functionalization of the liposomal surface. According to this procedure, $(C18)_2$ -Peg9-N3 (**3**) monomer was replaced with an equivalent amount of DSPE-Peg2000-Mal (**4**) (8% mol/mol) in the liposome formulation step. Maleimide group is widely employed in bioconjugation reactions for its specificity for thiols, fast aqueous reaction kinetics, lack of byproducts and the ability to form a stable thioether bond. The pre-formed liposomes DOPG/DSPE-Peg2000-Mal/ $(C18)_2$ -L5-SS-CCK8 were reacted with the R8-Cys for 1 h at room temperature at pH 7.4 to give DOPG/DSPE-Peg2000-R8/ $(C18)_2$ -L5-

SS-CCK8 (87/8/5 mol/mol/mol) liposomes; then liposomes were separated from unreacted peptide by gel filtration. Both fluorescence spectroscopy (refer to Figure 5B) and LC-MS analyses indicated that no side reaction involving the CCK8 cleavable monomer occurs during the reaction confirming the efficiency of this procedure compared with the strategy involving click chemistry.

Fluorescence Resonance Energy Transfer (FRET)

Post-liposomal formulation using maleimido or CuAAC reactives were also studied by using FRET. For the experimental procedures, liposomes were doped with 1% (molar ratio) of Rho-PE and R8 peptide was labeled with FITC fluorophore (R8CysFITC or R8PraFITC, indicated as compound **2c** and **2d** in Figure 2B). FITC and rhodamine (Rho) is a well-known donor-acceptor couple. FITC fluorophore absorbs at 490 nm and emits at 520 nm, whereas rhodamine absorbs at 520 and emits at 590 nm. When the FITC derivative is covalently bound on the liposomal surface, acceptor and donor are spatially close to each other and the rhodamine absorbs light at the donor emission wavelength. Fluorescence spectra of Rho-PE-labeled liposomes before (Rho/CCK8-LP) and after (Rho/R8CysFITC/CCK8-LP) functionalization with R8-FITC derivative were recorded after gel filtration of liposomes performed to remove unbound peptide derivatives. Spectra are reported in Figure 6A. Fluorescence spectrum of unlabeled liposomes plus R8CysFITC (**2d**) peptide (R8CysFITC + CCK8-LP), at the same FITC concentration, is also reported for comparison. The fluorescence spectrum of this formulation shows a peak centered at 520 nm as a result of the emission of FITC, whereas liposomes doped with Rho-PE show a peak at 590 nm. After the post-modification reaction, the intensity of the peak at 590 nm associated with Rho emission increases, whereas

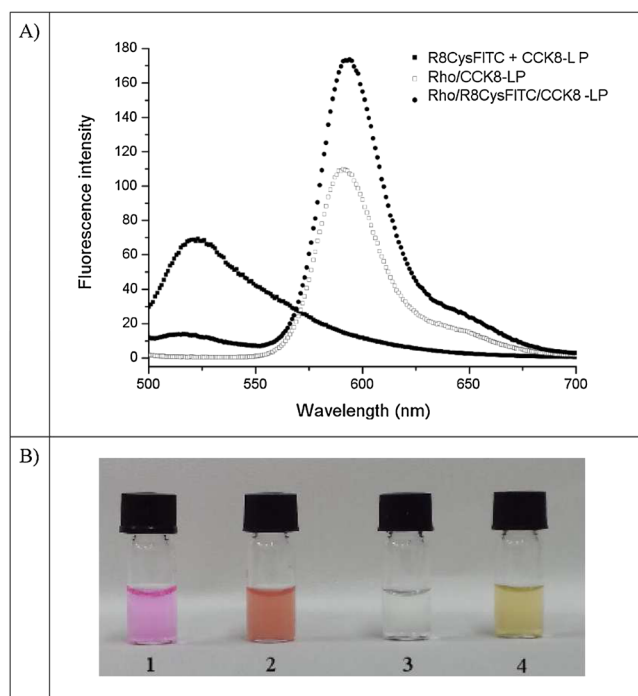


Figure 6. (A) Fluorescence measurements of Rho-PE-labeled liposomes before and after Michael reaction. Fluorescence spectrum of unlabeled liposomes in the presence of R8-FITC not covalently bound (emission peak at 520 nm), at the same concentration, is also reported for comparison. (B) Unlabeled and labeled rhodamine CCK8 liposomes before (vials 1 and 2) and after (vials 3 and 4) conjugation of R8-FITC by post-liposomal formulation.

the intensity of the peak at 520 nm, corresponding to the FITC emission, decreases. This behavior indicates that a covalent bond occurs between the R8-FITC derivative and the functional group on the liposomal surface. As a consequence of the post-formulation reaction, a visible colorimetric change attributable to FRET phenomenon between FITC donor fluorophore and Rho acceptor can be also observed in liposomal solution (refer to Figure 6B).

Structural Characterization

Size, diffusion coefficients and PI of DOPG-based liposomes, before and after post-liposomal formulation reaction with R8 peptide, were measured by DLS at $\theta = 173^\circ$, and data are reported in Table 2. According to literature, mean diameter of DOPG liposomes containing small amount of (C18)₂-Peg9-N3 (**3**) monomer or of DSPE-Peg2000-Mal (**4**) phospholipid is ≈ 90 nm. The introduction of the (C18)₂-L5-SS-CCK8 (**1**) peptide amphiphile (5% mol/mol) does not cause significant variations in the size of the liposomes. On the contrary, an increase of about 25% in diameter (from 91 to 122 nm) is observed after post-liposomal modification with R8 peptide, as reported in Table 2 and depicted in Figure 7. This result can be attributed to the R8 peptide, in which the eight arginine residues at pH 7.4 are in their protonated form. The high number of positive charges probably produces a distancing of the peptide from the outer shell of the liposomes with a consequent increase of the aggregate size.

Doxorubicin Loading

The anticancer drug doxorubicin (Doxo) was loaded into mixed liposomes DOPG/DSPE-Peg2000-Mal (92/8 mol/mol) and DOPG/DSPE-Peg2000-Mal/(C18)₂-L5-SS-CCK8 (87/8/5 mol/mol/

mol) using the well-known ammonium gradient method [35]. The initial amount of doxorubicin used to perform the loading was drug(wt)/lipid(wt) ratio of 0.200. Free Doxo was eliminated by gel filtration. The Doxo loading content (DLC), defined as the weight ratio of the encapsulated Doxo versus the amount of the amphiphilic molecules, was calculated by fluorescence measurements with subtraction of the amount of free doxorubicin, eluted by gel filtration, from the total amount of initial doxorubicin. DLC values were 0.090 for both liposomal formulations and correspond to 90% of the starting doxorubicin. The Doxo loading does not influence the post-liposomal modification with R8 peptide derivatives as evidenced by experiments of liposome functionalization with R8 derivatives according to the maleimido method (data not shown).

Even if, in principle, doxorubicin loading could be efficiently performed on CCK8-labeled liposomes (CCK8-LP) or on the dual-peptide liposomes (R8/CCK8-LP), we proved that the strategy based on the following steps: (i) liposome formulation with the CCK8 peptide derivative; (ii) Doxo loading and (iii) R8 labelling by maleimido reaction, seems a straightforward way to prepare doxorubicin encapsulated dual-labeled liposomes.

DTT Reductive Cleavage

Reductive conditions expected on tumor cells were simulated by adding DTT reductive agent on liposomes. Reaction was stirred under a nitrogen atmosphere for 2 h at room temperature. Then, liposomes were eluted on gel filtration, and possible products of the reductive cleavage were examined by LC-MS spectrometry. The chromatographic profile of the elute shows a retention peak at 12.59 min with a mass of 1220 Da, exactly superimposable to the LC-MS previously reported for the CuAAC post-formulation reaction (refer to Figure 5A). This LC-MS profile, corresponding to the CCK8-Cys peptide, indicates that by treating our liposomal solution (R8/CCK8-LP) with DTT, disulfide bonds between CCK8 peptide fragment and the liposomal surface have been reduced. On the other hand, any presence of the octa-arginine peptide was found in the elutes, thus suggesting that the thioether linkage used to anchor R8 on liposomes is completely stable under this reductive condition.

Flow Cytometric Analysis

The cell labeling efficiency of each liposomal formulation on A431 cell line was assessed by using flow cytometry analysis at room temperature. Liposomes were made fluorescent by insertion of a small amount of Rho-PE. CCK8 liposomes should bind the receptor

Table 2. Structural parameters of liposomes: diffusion coefficients (D), mean diameter and polydispersity index (PI)

Systems	$D \cdot 10^{-12} / \text{m}^2/\text{s}$	Diameter (nm) \pm SD	PI
LP	2.7 ± 1.3	91 ± 43	0.25
R8-LP	2.0 ± 0.8	122 ± 46	0.22
CCK8-LP	2.68 ± 0.5	92 ± 16	0.20
R8/CCK8-LP	2.02 ± 1.4	122 ± 86	0.22

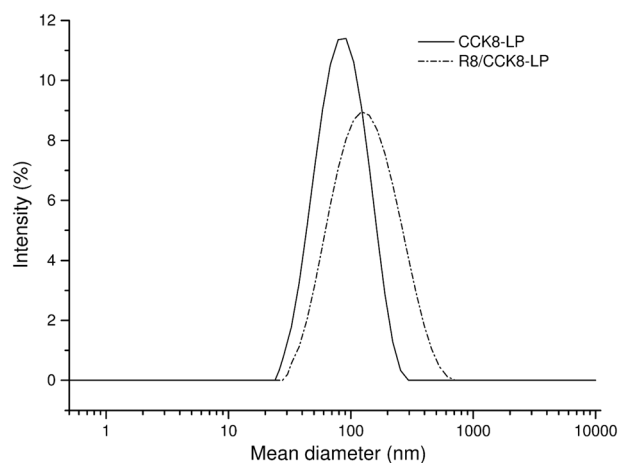


Figure 7. DLS spectra of DOPG/DSPE-Peg2000-Mal/(C18)₂-L5-SS-CCK8 liposomes before and after thioether linkage at 25 °C and $1.0 \cdot 10^{-4}$ M concentration.

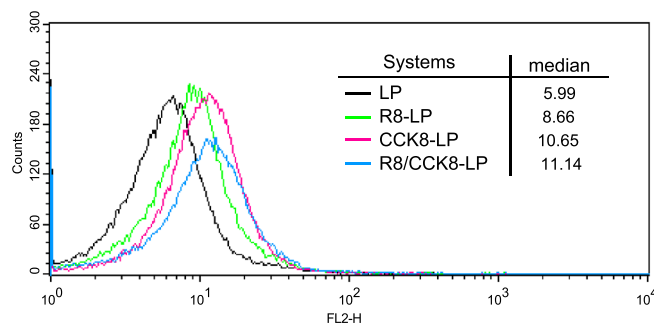


Figure 8. Representative flow cytometry histograms illustrating liposomes binding to A431 cells. Measurements were performed at least three times, and typical results are showed.

remaining confined on the outer of the cell, whereas R8, acting as CPP, should promote the liposome entering in the cells by using an endocytosis mechanism. After incubation with liposomes for 30 min, cells were treated with a permeabilizing agent in order to take in account the total fluorescence (internalized and bound). Flow cytometry histograms illustrating liposomes binding to A431 cells are shown in Figure 8 as preliminary binding results. Values of median of the fluorescence intensity are also reported in the figure insert. Liposomes externally modified with both HP (CCK8) and CPP (R8) peptides showed a slightly higher fluorescence intensity than the R8-LPs and CCK8-LPs in which only one peptide is bound and higher than the untargeted LPs. This result suggests a synergic effect of the two peptides.

Conclusions

Even if the preparation of liposomes derivatized with two different peptides has been already described [2,43,44], we have here reported on the feasibility of a dual peptide-ligand liposome (DOPG/DSPE-Peg2000-R8/(C18)₂-L5-SS-CCK8, 87/8/5 mol/mol/mol) loaded with doxorubicin and containing a disulfide bond between the liposome surface and one of the two external peptides. The presence of the disulfide bond prevents the use of click chemistry reaction and forces to develop appropriate synthetic strategies for the obtainment of liposomes modified with two different peptides in a stable manner. In our case, the CCK8 peptide linked to an hydrophilic moiety thought that the disulfide bond is incorporated in liposome during formulation, according to the pre-liposomal formulation strategy, while the R8 peptide derivative is coupled by using the Michael addition method, following the post-liposomal formulation approach. A complete characterization by different spectroscopic methods confirms the obtainment of liposomes in which both peptides are durably linked to the external liposome surface, while reducing conditions, used to simulate tumor environment, efficiently cut the disulfide bond between CCK8 peptide and the R8 liposome. Doxorubicin is efficiently loaded in the inner water liposome compartment, independently by the peptide(s) presence, leaving unaltered liposome structural parameters. The obtained doxorubicin-loaded liposomes could target cancer cells overexpressing CCK receptors driven by the CCK8 HP; therefore, reductive conditions free the liposomes that could internalize by means of the R8 CPP, thus releasing the active drug only in the target tumor cells.

Acknowledgements

We are indebted with the Italian Minister for Research (M.I.U.R.) for financial support under FIRB 'RENAME' RBAP114AMK projects. The authors thank Mr. Leopoldo Zona for technical assistance in NMR experiments.

References

- Martinez JO, Evangelopoulos M, Karun V, Shegog E, Wang JA, Liu X, Ferrari M, Boada C, Tasciotti E. The effect of multistage nanovector targeting of VEGFR2 positive tumor endothelia on cell adhesion and local payload accumulation. *Biomaterials* 2014; **35**(37): 9824–9832.
- Mei L, Fu L, Shi K, Zang Q, Liu Y, Tang J, Gao H, Zang Z, He Q. Increased tumor targeted delivery using a multistage liposome system functionalized with RGD, TAT and cleavable PEG. *Int. J. Pharm.* 2014; **468**(1–2): 26–38.
- Accardo A, Salsano G, Morisco A, Aurilio M, Parisi A, Maione F, Cicala C, Tesaro D, Aloj L, De Rosa G, Morelli G. Peptide-modified liposomes for selective targeting of bombesin receptors overexpressed by cancer cells: a potential theranostic agent. *Int. J. Nanomed.* 2012; **7**: 2007–2017.
- Morisco A, Accardo A, Tesaro D, Palumbo R, Benedetti E, Morelli G. Peptide-labeled supramolecular aggregates as selective doxorubicin carriers for delivery to tumor cells. *Biopolymers (Pept. Sci.)* 2011; **96**(1): 88–96.
- Ringhieri P, Iannitti R, Nardon C, Palumbo R, Fregona D, Morelli G, Accardo A. Target selective micelles for bombesin receptors incorporating Au(III)-dithiocarbamate complexes. *Int. J. Pharm.* 2014; **473**(1–2): 194–202.
- Tarallo R, Accardo A, Falanga A, Guarnieri D, Vitiello G, Netti P, D'Errico G, Morelli G, Galdiero S. Clickable functionalization of liposomes with the gH625 peptide from Herpes simplex virus type I for intracellular drug delivery. *Chem. Eur. J.* 2011; **17**(45): 12659–12668.
- Wang Y, Zhou J, Qiu L, Wang X, Chen L, Liu T, Di W. Cisplatin-alginate conjugate liposomes for targeted delivery to EGFR-positive ovarian cancer cells. *Biomaterials* 2014; **35**(14): 4297–4309.
- Carberry TP, Tarallo R, Falanga A, Finamore E, Galdiero M, Weck M, Galdiero S. Dendrimer functionalization with a membrane-interacting domain of herpes simplex virus type 1: towards intracellular delivery. *Chem. Eur. J.* 2012; **18**: 13678–13685.
- Lee Y, Graeser R, Kratz F, Geckeler KE. Paclitaxel-loaded polymer nanoparticles for the reversal of multidrug resistance in breast cancer cells. *Adv. Funct. Mater.* 2011; **21**: 4211–4218.
- Falanga A, Vitiello MT, Cantisani M, Tarallo R, Guarnieri D, Mignogna E, Netti P, Pedone C, Galdiero M, Galdiero S. A peptide derived from herpes simplex virus type 1 glycoprotein H: membrane translocation and applications to the delivery of quantum dots. *Nanomedicine* 2011; **7**: 925–934.
- Judson I, Radford JA, Harris M, Blay JY, van Hoesel Q, le Cesne A, van Oosterom AT, Clemons MJ, Kambay C, Hermans C, Whittaker J, Donato di Paola E, Verweij J, Nielsen S. Randomised phase II trial of pegylated liposomal doxorubicin (DOXIL/CAELYX) versus doxorubicin in the treatment of advanced or metastatic soft tissue sarcoma: a study by the EORTC Soft Tissue and Bone Sarcoma Group. *Eur. J. Cancer* 2001; **37**: 870–877.
- Duggan ST, Keating GM. Pegylated liposomal doxorubicin: a review of its use in metastatic breast cancer, ovarian cancer, multiple myeloma and AIDS related Kaposi's sarcoma. *Drugs* 2011; **71**: 2531–2558.
- O'Brien ME, Wigler N, Inbar M, Rosso R, Grischke E, Santoro A, Catane R, Kieback DG, Tomczak S, Ackland SP, Orlandi F, Mellars L, Alland L, Tendler C. Reduced cardiotoxicity and comparable efficacy in a phase III trial of pegylated liposomal doxorubicin HCl (CAELYX/Doxil) versus conventional doxorubicin for first-line treatment of metastatic breast cancer. *Ann. Oncol.* 2004; **15**: 440–449.
- Yang ZZ, Li JQ, Wang ZZ, Dong DW, Qi XR. Tumor-targeting dual peptides-modified cationic liposomes for delivery of siRNA and docetaxel to gliomas. *Biomaterials* 2014; **35**(19): 5226–5239.
- Yu MK, Park J, Jon S. Targeting strategies for multifunctional nanoparticles in cancer imaging and therapy. *Theranostic* 2012; **2**(1): 3–44.
- Accardo A, Tesaro D, Morelli G. Peptide-based targeting strategies for simultaneous imaging and therapy with nanovectors. *Polym. J.* 2013; **45**(5): 481–493.
- Copolovici DM, Langel K, Eriste E, Langel U. Cell-penetrating peptides: design, synthesis, and applications. *ACS Nano* 2014; **8**(3): 1972–1994.
- Guarnieri D, Falanga A, Muscetti O, Tarallo R, Fusco S, Galdiero M, Galdiero S, Netti PA. Shuttle-mediated nanoparticle delivery to the blood-brain barrier. *Small* 2013; **9**(6): 853–862.
- Yang Y, Yang Y, Xie X, Cai X, Zhang H, Gong W, Wang Z, Mei X. PEGylated liposomes with NGR ligand and heat-activable cell-penetrating peptide-doxorubicin conjugate for tumor-specific therapy. *Biomaterials* 2014; **35**(14): 4368–4381.
- Silvente-Poirot S, Dufresne M, Vaysse N, Fourmy D. The peripheral cholecystokinin receptors. *Eur. J. Biochem.* 1993; **215**: 513–529.
- Wank SA. Cholecystokinin receptors. *Am. J. Physiol.* 1995; **269**: G628.
- Laverman P, Behe M, Oyen WJG, Willems PHGM, Corstens FHM, Behr TM, Boerman OC. Two technetium-99m-labeled cholecystokinin-8 (CCK8) peptides for scintigraphic imaging of CCK receptors. *Bioconjugate Chem.* 2004; **15**: 561–568.
- Reubi JC, Schaer JC, Waser B. Cholecystokinin(CCK)-A and CCK-B/gastrin receptors in human tumors. *Cancer Res.* 1997; **57**: 1377–1386.
- Tornesello AL, Aurilio M, Accardo A, Tarallo L, Barbieri A, Arra C, Tesaro D, Morelli G, Aloj L. Gastrin and cholecystokinin peptide-based radiopharmaceuticals: an in vivo and in vitro comparison. *J. Pept. Sci.* 2011; **17**(5): 405–412.

- 25 Accardo A, Tesauo D, Mangiapia G, Pedone C, Morelli G. Nanostructures by self-assembling peptide amphiphile as potential selective drug carriers. *Biopolymers (Pept. Sci.)* 2007; **88**: 115–121.
- 26 Accardo A, Tesauo D, Aloj L, Tarallo L, Arra C, Mangiapia G, Vaccaro M, Pedone C, Paduano L, Morelli G. Peptide containing aggregates as selective nanocarriers for therapeutics. *ChemMedChem* 2008; **3**(4): 594–602.
- 27 Nakase I, Akita H, Kogure K, Graslund A, Langel U, Harashima H, Futaki S. Efficient intracellular delivery of nucleic acid pharmaceuticals using cell-penetrating peptides. *Acc. Chem. Res.* 2012; **45**(7): 1132–1139.
- 28 Galdiero S, Vitiello M, Falanga A, Cantisani M, Incoronato N, Galdiero M. Intracellular delivery: exploiting viral membranotropic peptides. *Curr. Drug Metab.* 2012; **13**: 93–104.
- 29 Biswas S, Deshpande PP, Perche F, Dodwadkar NS, Sane SD, Torchilin VP. Octa-arginine-modified pegylated liposomal doxorubicin: an effective treatment strategy for non-small cell lung cancer. *Cancer Lett.* 2013; **335**(1): 191–200.
- 30 Futaki S, Suzuki T, Ohashi W, Yagami T, Tanaka S, Ueda K, Sugiura Y. Arginine-rich peptides: an abundant source of membrane permeable peptides having potential as carriers for intracellular protein delivery. *J. Biol. Chem.* 2001; **276**: 5836–5840.
- 31 Sawant RM, Hurley JP, Salmaso S, Kale A, Tolcheva E, Levchenko TS, Torchilin VP. "SMART" drug delivery systems: double-targeted pH-responsive pharmaceutical nanocarriers. *Bioconjugate Chem.* 2006; **17**: 943–949.
- 32 Schmitt L, Dietrich C, Tampe R. Synthesis and characterization of chelator-lipids for reversible immobilization of engineered proteins at self-assembled lipid interfaces. *J. Am. Chem. Soc.* 1994; **116**: 8485–8491.
- 33 Accardo A, Ringhieri P, Tesauo D, Morelli G. Liposomes derivatized with tetra-branched neurotensin peptides via click chemistry reactions. *New J. Chem.* 2013; **37**: 3528–3534.
- 34 Tesauo D, Accardo A, Gianolio E, Paduano L, Teixeira J, Schillén K, Aime S, Morelli G. Peptide derivatized lamellar aggregates as target-specific MRI contrast agents. *Chem. Bio. Chem.* 2007; **8**(8): 950–955.
- 35 Fritze A, Hens F, Kimpfler A, Schubert R, Peschka-Süss R. Remote loading of doxorubicin into liposomes driven by a transmembrane phosphate gradient. *BBA Biomembrane.* 2006; **1758**: 1633–1640.
- 36 Aloj L, Panico M, Caracò C, Del Vecchio S, Arra C, Affuso A, Accardo A, Mansi R, Tesauo D, De Luca S, Pedone C, Visentin R, Mazzi U, Morelli G, Salvatore M. In vitro and in vivo characterization of Indium-111 and Technetium-99m labeled CCK8 derivatives for CCK-B receptor imaging. *Cancer Biother. Radiopharm.* 2004; **19**: 91–96.
- 37 Feldborg LN, Jølcck RI, Andresen TL. Quantitative evaluation of bioorthogonal chemistries for surface functionalization of nanoparticles. *Bioconjugate Chem.* 2012; **23**: 2444–2450.
- 38 Jullian M, Hernandez A, Maurras A, Puget K, Amblard M, Martinez J, Subra G. N-Terminus FITC labeling of peptides on solid support: the truth behind the spacer. *Tetrahedron Lett.* 2009; **50**: 260–263.
- 39 Li X, Zhao Y. Protection/deprotection of surface activity and its applications in the controlled release of liposomal contents. *Langmuir* 2012; **28**(9): 4152–4159.
- 40 Zhang S, Zhao Y. Controlled release from cleavable polymerized liposomes upon redox and pH stimulation. *Bioconjugate Chem.* 2011; **22**(4): 523–528.
- 41 Giustarini D, Dalle-Donne I, Colombo R, Milzani A, Rossi R. Is ascorbate able to reduce disulfide bridges? A cautionary note. *Nitric Oxide* 2008; **19**: 252–258.
- 42 Landino LM, Koumas MT, Mason CE, Alston JA. Ascorbic acid reduction of microtubule protein disulfides and its relevance to protein S-nitrosylation assays. *Biochem. Biophys. Res. Commun.* 2006; **340**: 347–352.
- 43 Markoutsas E, Papadia K, Giannou AD, Spella M, Cagnotto A, Salmons M, Stathopoulos GT, Antimisiaris SG. Mono and dually decorated nanoliposomes for brain targeting, in vitro and in vivo studies. *Pharm. Res.* 2014; **31**: 1275–1289.
- 44 Takara K, Hatakejama H, Kibria G, Ohga N, Hida K, Harashima H. Size-controlled, dual-ligand modified liposomes that target the tumor vasculature show promise for use in drug-resistant cancer therapy. *J. Control. Rel.* 2012; **162**: 225–232.

Supporting Information

Additional supporting information may be found in the online version of this article at the publisher's web site.

SCIENTIFIC REPORTS



OPEN

Self-assembly of PEGylated tetra-phenylalanine derivatives: structural insights from solution and solid state studies

Received: 02 February 2016

Accepted: 04 May 2016

Published: 25 May 2016

Carlo Diaferia^{1,2}, Flavia Anna Mercurio², Cinzia Giannini³, Teresa Sibillano³, Giancarlo Morelli^{1,2}, Marilisa Leone² & Antonella Accardo^{1,2,*}

Water soluble fibers of PEGylated tetra-phenylalanine (F4), chemically modified at the N-terminus with the DOTA chelating agent, have been proposed as innovative contrast agent (CA) in Magnetic Resonance Imaging (MRI) upon complexation of the gadolinium ion. An in-depth structural characterization of PEGylated F4-fibers, in presence (DOTA-L₆-F4) and in absence of DOTA (L₆-F4), is reported in solution and at the solid state, by a multiplicity of techniques including CD, FTIR, NMR, DLS, WAXS and SAXS. This study aims to better understand how the aggregation process influences the performance of nanostructures as MRI CAs. Critical aggregation concentrations for L₆-F4 (43 μM) and DOTA-L₆-F4 (75 μM) indicate that self-aggregation process occurs in the same concentration range, independently of the presence of the CA. The driving force for the aggregation is the π -stacking between the side chains of the aromatic framework. CD, FTIR and WAXS measurements indicate an antiparallel β -sheet organization of the monomers in the resulting fibers. Moreover, WAXS and FTIR experiments point out that in solution the nanomaterials retain the same morphology and monomer organizations of the solid state, although the addition of the DOTA chelating agent affects the size and the degree of order of the fibers.

Peptide materials based on the aggregation of amphiphilic peptides represent a rapidly growing field within materials science^{1–3}. They have been considered for several applications in different fields from electronic to nanomedicine. Amphiphilic peptides self-assemble in well-structured supramolecular materials as the result of an intricate network of interactions between hydrophobic and hydrophilic regions. The interaction mode can strongly influence both morphology and properties of the final peptide-based materials. Special interest was recently devoted to peptide self-assembling materials in which aggregation is promoted by aromatic amino acids, such as phenylalanine, tyrosine or tryptophan, where π -stacking interactions occur^{4–6}. To this regard, a paradigmatic example is represented by the diphenylalanine (FF or F2) peptide, which constitutes the core recognition motif of Alzheimer's β -amyloid peptide. FF is able to self-assemble into many different nanostructures from nanotubes to vesicles and organogels. Peptide nanostructures containing the FF motif or more extended aromatic sequences have been investigated for their mechanical, electrochemical and optical properties, and more recently for some nanomedicine applications^{7,8}. Despite the growing literature about FF, only a few examples of new materials obtained by the self-assembling of tetraphenylalanines have been reported until now^{9–12}. In order to get a deeper understanding of the molecular interactions involved in their self-assembly process, theoretical calculations for FFFF (also called F4) and Fmoc-FFFF aggregates have been recently reported⁹. Moreover, a few examples of tetraphenylalanine-polymer conjugates, in which the aromatic framework has been elongated at the N-terminus with addition of polymeric chains, have been proposed. The F4-PEG5000 derivative, synthesized by Hamley and coworkers, is able to self-aggregate in water solution at low concentrations (0.095 wt.%), whereas well-developed β -sheet structures occur only at higher concentration¹⁰. Others examples of F4-polymer

¹Department of Pharmacy and CIRPeB, University of Naples "Federico II", via Mezzocannone 16, 80134 Napoli, Italy. ²Institute of Biostructure and Bioimaging (IBB), CNR, via Mezzocannone 16, 80134 Napoli, Italy. ³Institute of Crystallography (IC), CNR, Via Amendola 122, 70126 Bari, Italy. *Present address: Department of Pharmacy, University of Naples "Federico II", Via Mezzocannone, 16 – I-80134 Napoli, Italy. Correspondence and requests for materials should be addressed to A.A. (email: antonella.accardo@unina.it)

conjugates (mPEO-F4-OEt), containing variable length of PEO chain (350, 1200 and 1800 Da) were synthesized by a click-chemistry reaction between an alkyne modified tetraphenylalanine (alkyne-F4-OEt) and the azide-terminated PEO oligomer (mPEO-N₃). In a water/tetrahydrofuran mixture, mPEO-F4-OEt self-assembles initially in nanotubes (between 2 and 10 mg/mL) and successively, at higher concentration, the entanglement between adjacent nanotubes leads to the hydrogel formation¹¹. The length of the hydrophilic block PEO influences significantly the assembling process by favouring fibers formation and worm-like micelles¹². Very recently, we proposed the first example of PEGylated di-phenylalanine [DOTA(Gd)-L₆-F2 and DTPA(Gd)-L₆-F2] and tetra-phenylalanine [DOTA(Gd)-L₆-F4 and DTPA(Gd)-L₆-F4] conjugates as potential MRI CAs¹³. These conjugates contain two (F2) or four (F4) phenylalanine residues for self-assembly, a chelating agent, DOTA (1,4,7,10-tetraazacyclododecane-N,N,N,N-tetraacetic acid) or DTPA (diethylenetriamine pentaacetate), for achieving gadolinium coordination and an ethoxylic linker at six PEG units (L₆) between the chelating group and the peptide region. All of these phenylalanine conjugates have been structurally characterized by CD, FTIR, fluorescence spectroscopies and X-ray diffraction on the dried fibers. Due to the steric hindrance of the bulk gadolinium complex, F2 conjugates were not able to keep their propensity to aggregate in water solution. On the contrary F4 adducts, with a more extended aromatic framework, kept their capability to aggregate after the synthetic modification with the Gd-complex. The replacement of the paramagnetic Gd(III) ion with others radioactive metal ions (¹¹¹In, ^{67/68}Ga) could open novel perspective for these nanostructures in others diagnostic fields. As an alternative, the chelating agent could be also replaced with an active pharmaceutical ingredient (API). However, at the best of our knowledge, until now it has not been fully explored how modifications on the flexible PEG chain could affect the molecular interactions governing the overall structural organization of the conjugates in aqueous solution. To this aim, here we report an in-depth comparative structural study of PEGylated tetra-phenylalanine nanostructures, in presence (DOTA-L₆-F4) and in absence of DOTA (L₆-F4), in solution and at the solid state. The work relies on a multidisciplinary approach including a variety of techniques such as Circular Dichroism (CD), Fourier Transform Infrared (FTIR), Dynamic Light Scattering (DLS), NMR, Wide-Angle (WAXS) and Small-Angle X-ray Scattering (SAXS). The combination of these techniques allows a full characterization of nanostructures both at the solid-state and in solution, clarifying their molecular organization also in solution at concentrations useful for MRI applications. These findings can help to improve the performance of poly-phenylalanine conjugates as contrast agents.

Results and Discussion

Synthesis and fluorescence spectroscopy. PEGylated tetra-phenylalanine derivatives, L₆-F4 and DOTA-L₆-F4, are schematically reported in Fig. 1A. In DOTA-L₆-F4, the DOTA bifunctional chelating agent, added at the N-terminus of the PEG moiety, can allow kinetically and thermodynamically stable coordination of radioactive or paramagnetic metal ions (¹¹¹In, ^{67/68}Ga, Gd(III)) for diagnostic applications in Nuclear Medicine or Magnetic Resonance Imaging^{14,15}. Both peptides were obtained by Fmoc/tBu solid phase synthesis and subsequently purified by RP-HPLC chromatography. Critical aggregate concentration (CAC) values of L₆-F4 and DOTA-L₆-F4 were determined with a fluorescence-based method, in which 8-anilino-1-naphthalene-1-sulfonate ammonium salt (ANS) was used as fluorescent probe. Fluorescence emission of ANS is commonly observed at 460–480 nm only when this fluorophore is surrounded by a hydrophobic environment, such as in the micelle core^{16,17}. The fluorescence intensity of an ANS solution (20 μM in aqueous solution) at 470 nm, as function of both tetra-phenylalanines concentration, is reported in Fig. 1B. The CAC values determined by Fig. 1B are 75 μM (~0.099 mg/mL) and 43 μM (~0.040 mg/mL) for DOTA-L₆-F4 and L₆-F4, respectively. For L₆-F4 the CAC value is in good agreement with that of ~167 μM, 0.095 wt.%, previously measured by Hamley *et al.*, through pyrene fluorescence assays, for another PEGylated tetra-phenylalanine (F4-PEG5000)¹⁰. As expected, the CAC of L₆-F4 is slightly lower than the CAC of F4-PEG5000, in which the hydrophobic/hydrophilic ratio is more unbalanced towards hydrophilic share. Moreover, the CAC values for L₆-F4 and DOTA-L₆-F4 are quite similar, thus indicating that the self-aggregation process occurs in the same range of concentration, independently of the presence of the chelating agent at the N-terminus. Undoubtedly, the driving force for the aggregation is the π-stacking between the side chains of the aromatic framework. In this perspective, it does not surprise that the two peptides, containing the same aromatic portion, show a very close CAC value. However, it is also well-known that chelating agents such as DOTA and DTPA, can cause a steric and/or electrostatic hindrance, thus providing an increase of the CAC value^{13,18}. In our case, we can ascribe the low incidence of DOTA macrocycle on the fibrillary process in presence of the PEG chain; the latter being long enough to act as a spacer between the chelating agent and the aromatic framework.

NMR spectroscopy. NMR spectroscopy was implemented to better investigate the conformational properties of DOTA-L₆-F4 in solution. Due to the high tendency of the compound to aggregate, experiments at different concentrations were conducted to get an estimate of the critical aggregation concentration (CAC). 1D [¹H] experiments were first acquired (Fig. 1C). At a concentration equal to 0.9 mg/mL (680 μM) or higher, aggregation phenomena resulted so relevant that extensive line broadening dominated the NMR spectra causing loss of signal intensity (Fig. 1C). The sensitivity of the NMR experiments highly improved by lowering the concentration from 0.9 mg/mL (680 μM) to 0.3 mg/mL (230 μM). A further dilution to 0.15 mg/mL (110 μM) caused only a slight enhancement of the spectrum. These results allowed us to set the CAC below 0.15 mg/mL. In addition, this aggregation propensity was confirmed by means of 2D [¹H, ¹H] spectroscopy. 2D [¹H, ¹H] NOESY experiments¹⁹ were collected at three different concentrations (Fig. 2): spectra of diluted F4-L₆-DOTA samples (concentrations equal or below 110 μM) (Fig. 2A) contained only a few cross-peaks and reflected the almost complete absence of aggregation phenomena and the presence in solution of small, fast tumbling flexible species (Fig. 2A). On the contrary, at a concentration equal to 1.25 mg/mL (0.94 mM), NOESY spectra were characterized by extensive signal enlargement, due to the occurrence of large size aggregates in solution (Fig. 2B). The consequent low signal

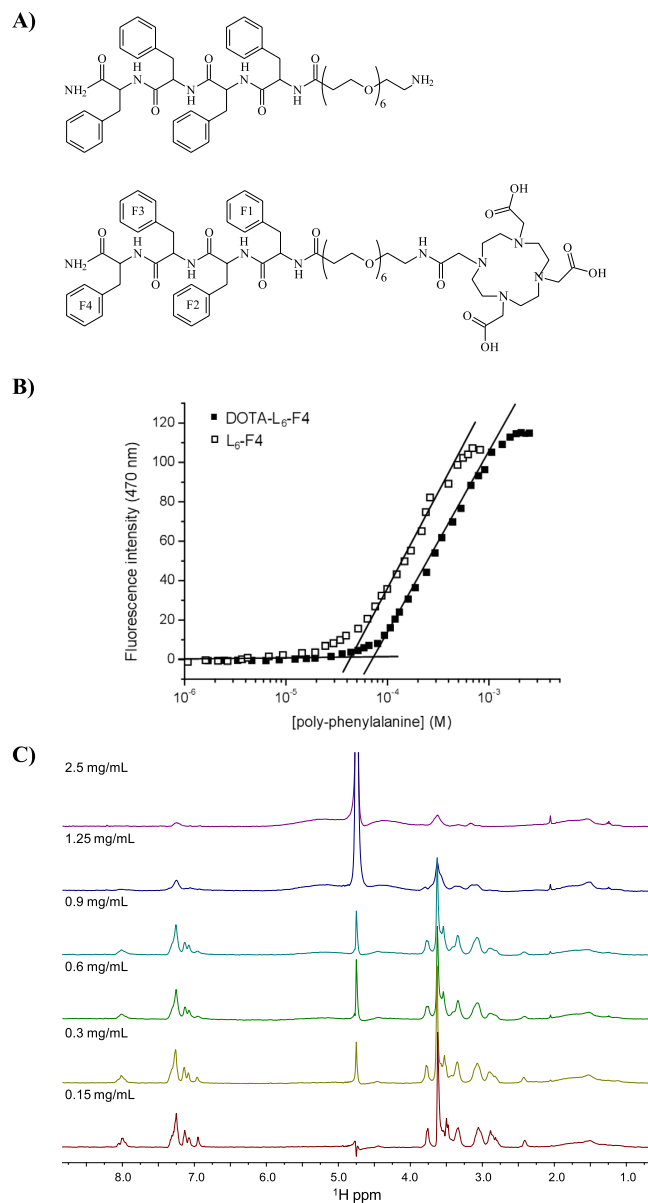


Figure 1. (A) Schematic representation of L₆-F4 and DOTA-L₆-F4 derivatives. (B) Fluorescence intensity emission of ANS fluorophore at 470 nm vs. concentration of L₆-F4 and DOTA-L₆-F4, CAC values are established from the break points. (C) 1D ¹H NMR spectra of DOTA-L₆-F4 recorded at 400 MHz and 298 K with samples dissolved in H₂O/D₂O 90/10 v/v at different concentrations.

intensity, caused by high aggregation levels, did not allow conducting a detailed structural characterization of the concentrated DOTA-L₆-F4 samples containing large size aggregates.

To get insights into the secondary structure elements characterizing small size aggregates formed by DOTA-L₆-F4, NMR spectra were recorded at concentrations between 300 and 500 μM, because under these experimental conditions good quality solution NMR spectra could be collected (Fig. 2C). Proton resonance assignments for DOTA-L₆-F4 were obtained by means of a canonical protocol based on comparison of 2D TOCSY and NOESY experiments²⁰ (Supporting Table S1). Sequential assignments for the four phenylalanine residues were further confirmed by means of heteronuclear 2D and 3D experiments (Figs 3 and 4) recorded with double labeled ¹⁵N/¹³C DOTA-L₆-F4 containing either selective F(2,4) or uniformly F(1,2,3,4) labeling.

The H_N chemical shifts for the four phenylalanine residues are distributed in a very narrow chemical shift range centered around 8 ppm, while, H_α protons resonate at almost identical chemical shifts (Fig. 3 and Table S1). Differences between observed H_α chemical shifts and random coil values were small (Supporting Figure S1)²¹, thus indicating that at the concentration used to run the experiments (i.e., 0.3–0.5 mM range) random coil species were prevalent. Extensive chemical shifts degeneracy could be revealed also for ¹³C_α, ¹³C_β and aromatic carbon atoms of the four phenylalanine residues (Fig. 4). Previous studies have demonstrated that, in the solid state, DOTA-L₆-F4 forms ordered aggregates, characterized by an antiparallel β-sheet structure¹³. We carefully analyzed

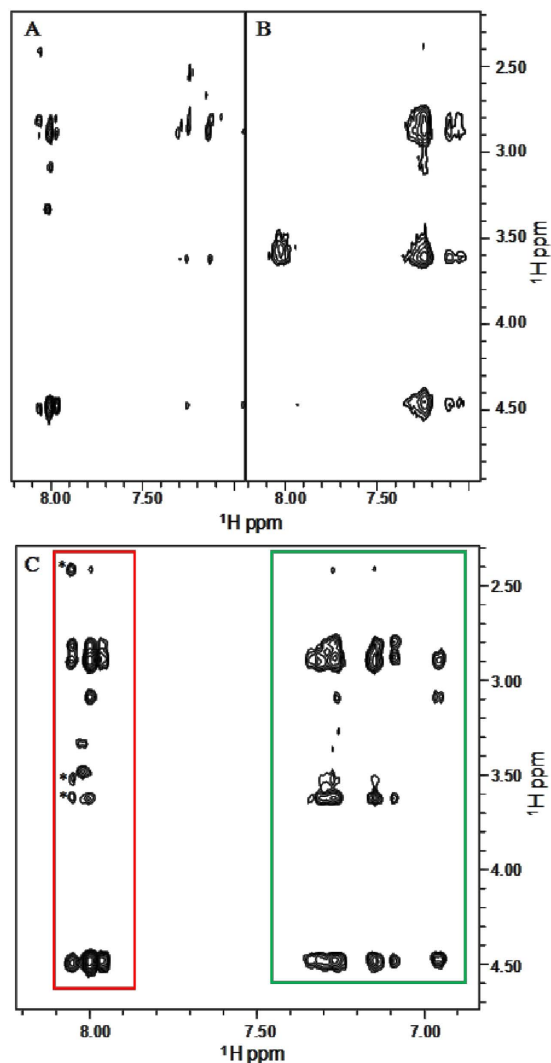


Figure 2. Comparison of 2D ^1H , ^1H NOESY 300 spectra of DOTA- L_6 -F4 at concentrations equal to 0.11 mM (0.15 mg/mL) (A) and 0.94 mM (1.25 mg/mL) (B). 2D NOESY 300 spectrum of DOTA- L_6 -F4 (0.34 mM, 0.45 mg/mL) (C). NOE contacts involving H_N protons with side chain protons are included in the red rectangle whereas correlations arising from aromatic protons are incorporated in the green box. The * indicates a correlation between the H_N amide proton of F1 and close linker (L_6) protons (C).

2D ^1H , ^1H NOESY (Fig. 2C), 3D ^{15}N resolved- ^1H , ^1H NOESY-HSQC (250 ms mixing time) (Fig. 3B), and 3D ^{13}C resolved- ^1H , ^1H NOESY-HSQC (200 ms mixing time) (Fig. 4B), trying to confirm the presence of such ordered species in the solution state. However, as already specified, at the concentrations exploited by NMR, the aggregation level was possibly low and the equilibrium between ordered and disordered species in solution was moved towards the latter forms as clearly indicated by H_α CSD values (Figure S1)²¹.

It's also worth noting that Zanuy and coworkers²² have previously reported a computational conformational study on polyphenylalanine containing peptides and on their PEG adducts. Theoretical quantum mechanical calculations indicated a low tendency of the isolated tetra-phenylalanine (F4) peptide to adopt a fully extended β -conformation whereas pointed out the highest stability of ribbon-like organizations, made up of regular propagation of γ -turns motives through residues 1 to 4, or helical-like structures composed of alternated repetitions of canonical and reverse γ -turns²². Once the PEG unit was added to the F4 peptide, molecular dynamics simulations performed in water starting from a fully extended F4 conformation, indicated that the peptide unit of the resulting material tended to maintain the conformational preferences of the isolated F4 portion and thus to assume a more folded structural organization similar to the pseudo-ribbon or helical arrangements described above. However, this previous computational analysis²² was carried out on monomeric peptide units without taking into account aggregation effects in solution, that even at low extent, may indeed stabilize the fully extended structures.

For our DOTA- L_6 -F4 compound, chemical shifts degeneracy among atoms in the four phenylalanine residues made also impossible to unambiguously distinguish intra- from inter-molecular contacts as well as intra- from inter-residue NOEs (Figs 3B and 4B) that could have clearly witnessed the presence of an organized β -structure. Nevertheless, we can only realistically speculate that the DOTA- L_6 -F4 molecules preferentially adopt an extended

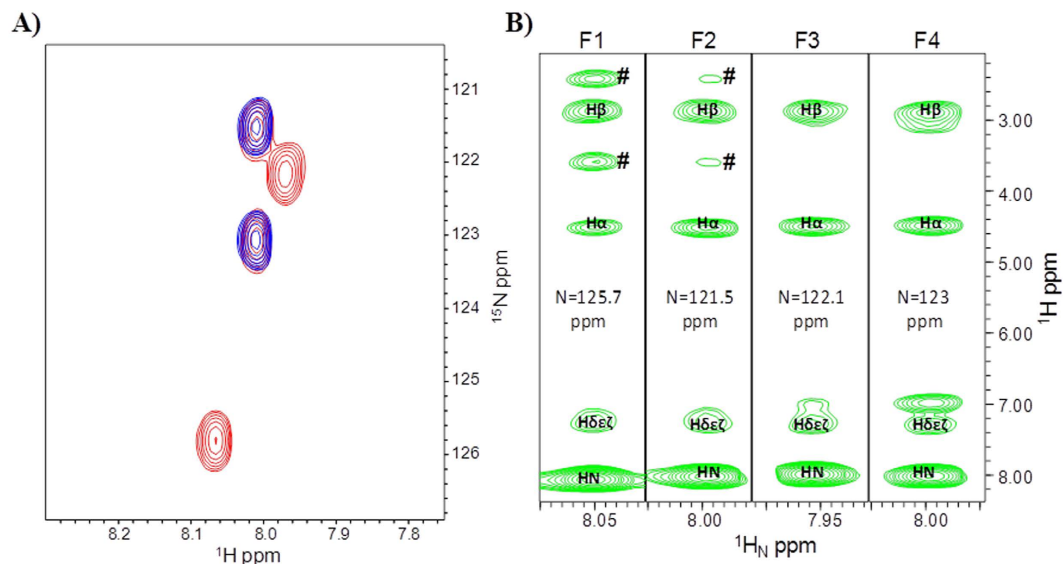


Figure 3. Overlay of $[^1\text{H}, ^{15}\text{N}]$ HSQC spectra of DOTA- L_6 -F4 (100 μM concentration) with $^{15}\text{N}/^{13}\text{C}$ double-labeled F(1,2,3,4) (red) or F(2,4) (blue) (A). Strips from $^1\text{H}/^{15}\text{N}$ slices of the 3D ^{15}N resolved- $[^1\text{H}, ^1\text{H}]$ NOESY-HSQC spectrum of $^{15}\text{N}, ^{13}\text{C}$ F(1,2,3,4) labeled DOTA- L_6 -F4 (500 μM concentration). Each strip corresponds to a single Phe residue as indicated at the top of each slice. Aromatic protons are reported as $\text{H}\delta\epsilon\zeta$. The # highlights unambiguous NOEs between the backbone H_N of F1 and F2 and the closest $-\text{NHCOCH}_2\text{CH}_2\text{O}-$ protons of the L_6 linker portion (B). Spectra were recorded at 600 MHz and 298 K.

structure. Indeed, NOE effects between linker L_6 protons and phenylalanine atoms are limited to short range contact involving primarily F1 and the closest $-\text{NHCOCH}_2\text{CH}_2\text{O}-$ protons of the linker L_6 (Figs 1A and 2C). 2D $[^1\text{H}, ^1\text{H}]$ spectra were recorded also to compare the conformational behavior of DOTA- L_6 -F4 and L_6 -F4 (Supporting Figures S2). In detail, no chemical shifts changes in the 4F- portion of the two molecules could be revealed by analysis of TOCSY spectra (Figure S2). This indicates that the addition of a chelating agent -like DOTA- does not influence the conformational behavior.

DLS characterization. Hydrodynamic radii (R_H) and diffusion coefficients (D) of L_6 -F4 and DOTA- L_6 -F4 in water solution were measured by DLS at 2.0 mg/mL. Both samples show a mono-modal distribution due to translational diffusion process of nanostructures (data not shown). The time correlation functions of the scattered intensity $g(2)(t)-1$ for both tetra-phenylalanine derivatives are reported in Supporting Figure S3A. DLS measurements for L_6 -F4 and DOTA- L_6 -F4 nanostructures at different concentrations (2.0, 5.0 and 10 mg/mL) were also performed in order to investigate the effect of the concentration on the size of nanostructures and the intensity correlation functions for L_6 -F4 are reported in Figure S3B.

Data reveal a translation of the correlation function for DOTA- L_6 -F4 at longer decay time with respect to L_6 -F4, with apparent translational diffusion coefficients $D = (1.8 \pm 0.1) \times 10^{-12}$ and $(7.2 \pm 0.3) \times 10^{-12} \text{ m}^2 \text{ s}^{-1}$ respectively. These data were directly correlated to the apparent hydrodynamic radii (77 and 300 nm for L_6 -F4 and for DOTA- L_6 -F4) through the Stokes-Einstein equation. These R_H values are compatible with supramolecular aggregates with elongated shape²³ such as open bilayers, worm-like micelles or nanofibers as in this case. The slower motion of DOTA- L_6 -F4 with respect to L_6 -F4 suggests that, at a similar concentration, nanostructures containing the DOTA chelating agent have a higher propensity to self-aggregate, with respect to the corresponding derivative in absence of DOTA. This hypothesis is also supported by the DLS analysis of nanostructures at different concentration (Figure S3B).

Secondary structure. Structural characterization of these nanostructures by NMR spectroscopy fails in a range of concentration above 500 μM . In order to deeply investigate the aggregation properties in this range of concentrations, we studied the secondary structure of these peptide derivatives by CD and FTIR spectroscopies. CD spectra of L_6 -F4 in solution, recorded between 280 and 195 nm, are reported in Fig. 5A. For comparison, the dichroic tendency of DOTA- L_6 -F4, previously studied by us¹³ in the same experimental conditions and concentrations has been also reported. CD spectra of PEGylated tetra-phenylalanine L_6 -F4, at concentrations close to the CAC value (0.1 mg/mL), show two maxima (at 205 and 220 nm) and a minimum at 232 nm. The two maxima can be attributed to aromatic side-chains stacking, whereas the minimum can be associated with a β -structure¹³. Significant variations of the dichroic signal can be observed at 5 mg/mL, which corresponds to a concentration higher than the CAC value: the main minimum at 230 nm and the complete absence of the maximum at 205 nm can be ascribed to a dominant β -sheet arrangement¹⁰⁻¹². For each concentration, CD spectra of tetra-phenylalanine in presence of the DOTA macrocycle did not show significant differences in the dichroic tendency. However, according to literature¹¹, the spectrum of L_6 -F4 at 0.1 mg/mL shows a higher intensity of the maximum at 205 nm with respect to DOTA- L_6 -F4. However, the spectra of the two aromatic molecules here described show high

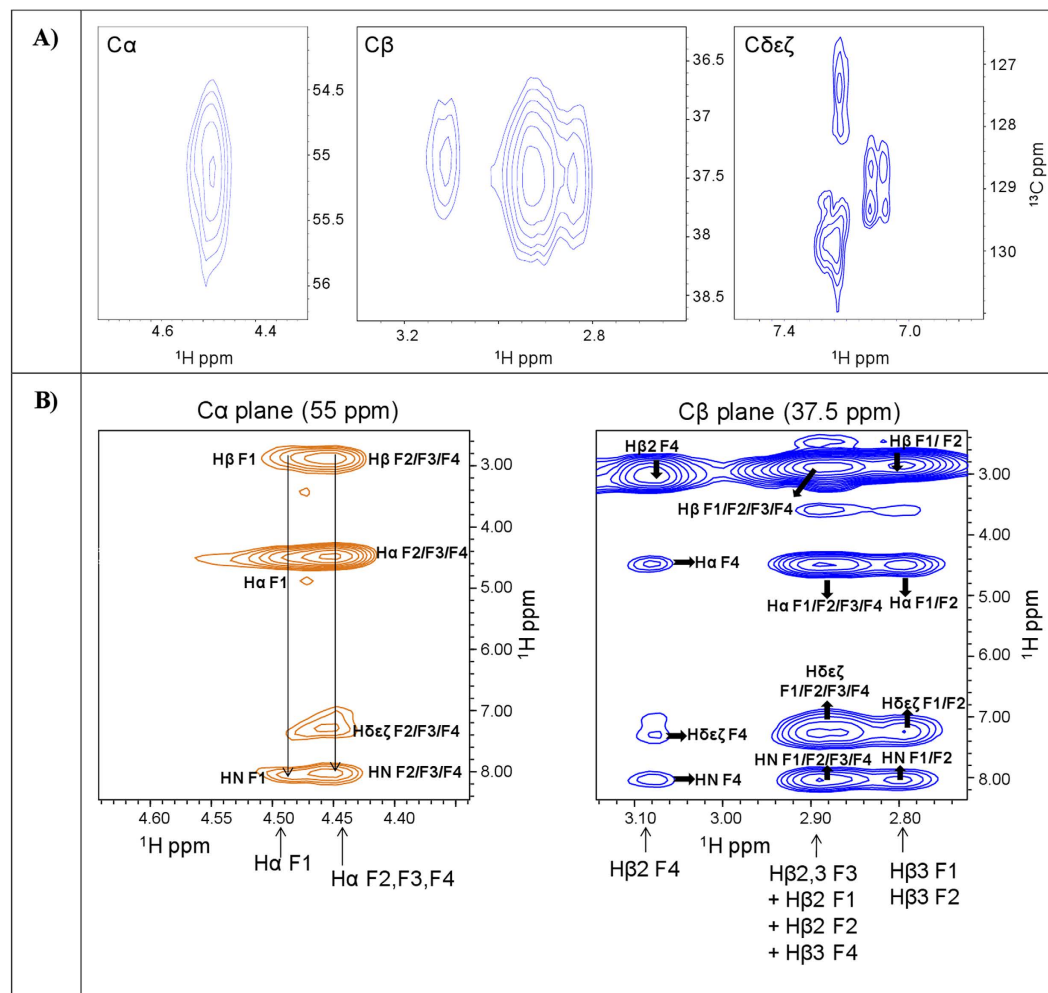


Figure 4. ^1H , ^{13}C HSQC spectra of DOTA- L_6 -F4 (100 μM), recorded with a sample containing $^{15}\text{N}/^{13}\text{C}$ double-labeled F(1,2,3,4) (A). The $\text{C}\alpha$, $\text{C}\beta$ and aromatic region of the ^1H , ^{13}C HSQC spectrum are reported in the left, middle and right panels respectively (B). A few ^1H , $^1\text{H}\alpha$ (left side) and ^1H , $^1\text{H}\beta$ (right side) strips from the 3D ^{13}C resolved- ^1H , ^1H NOESY-HSQC spectrum of double $^{15}\text{N}/^{13}\text{C}$ F(1,2,3,4) labeled DOTA- L_6 -F4 are shown. Assignments are reported for each Phe residue.

similitude, thus suggesting that the addition of the chelating agent at the N-terminus of the sequence does not affect their assembling properties in solution. Further information on the secondary structure adopted by L_6 -F4 and DOTA- L_6 -F4 in solution (2.0 mg/mL) was obtained using FTIR spectroscopy in the amide I region (see Fig. 5B). Both spectra show two peaks at 1637 cm^{-1} and 1680 cm^{-1} , respectively. The peak at 1637 cm^{-1} is strongly indicative of β -sheet formation, whereas the lower intensity of the second peak at 1680 cm^{-1} is indicative of an antiparallel orientation of the β -sheets²⁴. FTIR spectra recorded on dried film of both peptides showed a similar profile with respect to samples in solution (data not shown).

Wide-Angle and Small-Angle X-ray Scattering. Figure 6(A,B) present the two-dimensional (2D) WAXS pattern collected on the L_6 -F4 and DOTA- L_6 -F4 dried samples, respectively. The 2D patterns, once centered, calibrated and radially folded into 1D profiles by integrating along the azimuth, are displayed in Fig. 6(C,D) in the $0.8\text{--}1.8\text{ \AA}^{-1}$ and $0.08\text{--}0.8\text{ \AA}^{-1}$ q-ranges, respectively (black corresponding to the L_6 -F4 and red to DOTA- L_6 -F4). The 2D patterns both display the typical cross- β fiber diffraction pattern which contains, along the meridional and equatorial directions, the following fingerprints:

i) the meridional reflection at $d_{31} = 4.9 \pm 0.3\text{ \AA}$, marked by the white arrow in Fig. 6(A,B), which corresponds to the highest peak in Fig. 6(C). The meridional reflections are due to the separation between adjacent peptide backbones organized into β -strands along the fiber axis. In the meridional direction we have not measured any diffraction reflection at $2d_{31} = 9.8\text{ \AA}$. This absence could be either due to the predominance of parallel β -strands organization or to the 2_1 symmetry of antiparallel β sheets²⁵. However, the presence of the peak at 1680 cm^{-1} in the FTIR spectra, recorded on both tetra-phenylalanines in solution (Fig. 5) and dried sample, led us to hypothesize an antiparallel β sheet with 2_1 symmetry.

ii) A series of equatorial reflections were marked by the dotted lines labelled as 1, 2, 3, 4, 5. The most intense equatorial lines (1, 2, 3) correspond to the spacing: $d_1 = 31 \pm 1\text{ \AA}$, $d_2 = 15 \pm 1\text{ \AA} = d_1/2$, $d_3 = 11 \pm 0.3\text{ \AA}$, indicating

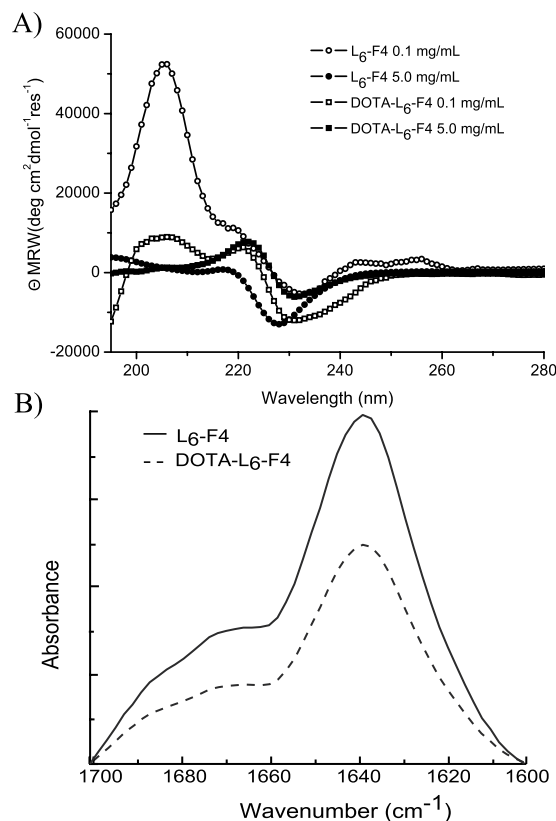


Figure 5. Spectroscopic characterization of L₆-F4 and DOTA-L₆-F4 peptide derivatives by CD and FTIR. (A) Far-UV CD spectra of both peptides in aqueous solution at (5.0 and 0.1 mg/mL) recorded between 280 and 195 nm; (B) FTIR spectra in the amide I region at 2.0 mg/mL concentration.

the presence of a lamellar phase along the fiber cross-section. Only in the case of the DOTA-L₆-F4, another equatorial reflection is measured at very small q value, labelled as 0 in the red pattern of Fig. 6D. This reflection corresponds to a spacing $d_0 = 54 \pm 4 \text{ \AA}$, although this evaluation is less accurate being the reflection on the tail of the primary beam. The d_0 and d_1 could match with the lengths of the backbones for the DOTA-L₆-F4 and L₆-F4, respectively (<http://pubchem.ncbi.nlm.nih.gov>), taking into account a possible folding of the PEG chain.

iii) For both samples the 2D WAXS data are due to oriented fibers, as evidenced by the presence of arcs instead of fully rings. Diffraction patterns, made up of longer arcs, indicate higher fiber disorder (mosaicity effect). Indeed, Figure S4 of the Supporting Information displays four fiber diffraction 2D patterns, simulated by the *CLEARER* program²⁶, for increasing fiber disorder: 0.1 rad (5.7°) in (A), 0.2 rad (11.4°) in (B), 0.5 rad (28.6°) in (C) and 0.75 rad (43°) in (D). The longer arcs of the L₆-F4 sample with respect to the DOTA-L₆-F4 prove the presence of a larger disorder for the L₆-F4 sample. Comparing with the simulated patterns, data registered for the DOTA-L₆-F4 can be well described by a fiber disorder as small as 0.1 rad, while for the L₆-F4 sample the longer arcs can be explained by a disorder of about 0.2 rad. This is confirmed also by the full-width-at-half-maximum of the meridional and equatorial peaks which decreases for the DOTA-L₆-F4, proving how the additional DOTA produces fibers with a higher order degree. It is worth noting that a very large disorder in the fiber would cause the diffraction pattern to lose the typical characteristic arcs which degenerate in the full rings of a powder-like sample (Figure S4D). This behavior was observed by Hamley *et al.*¹⁰ for F4-PEG5000, in which the long PEG moiety causes crystallization effects.

2D SAXS data were also collected on the same L₆-F4 and DOTA-L₆-F4 dried fibers and shown in Figure S5A,B of the Supporting Information, respectively. The data were centered, calibrated and folded in the 1D patterns of Fig. 5C,D, respectively. The SAXS data confirm and reinforce the previous findings. Indeed, while the L₆-F4 sample does not present any SAXS diffraction, the pattern registered on DOTA-L₆-F4 clearly shows fiber diffraction partial rings. This is a distinct indication that the DOTA chelating agent increases the fiber order, extending it from atomic to nanoscale.

Finally, Fig. 7(A,B) show the WAXS profiles collected on the L₆-F4 and DOTA-L₆-F4 solutions (25 mg/mL), respectively, after subtraction of the water contribution (red profiles). In each of them the pattern was compared with the analogous measured in the dried samples (black profiles). The comparison allows identifying exactly the same fingerprints measured for the dried fibers, bringing to the same conclusions. Also in the case of solutions the DOTA-L₆-F4 sample shows sharpest peaks, with respect to the L₆-F4 one, and therefore a more ordered lattice.

Structure and relaxometric properties. DOTA-L₆-F4, and its analogue DTPA-L₆-F4, have been previously complexed with the paramagnetic gadolinium ion and studied for their relaxometric behavior with the aim

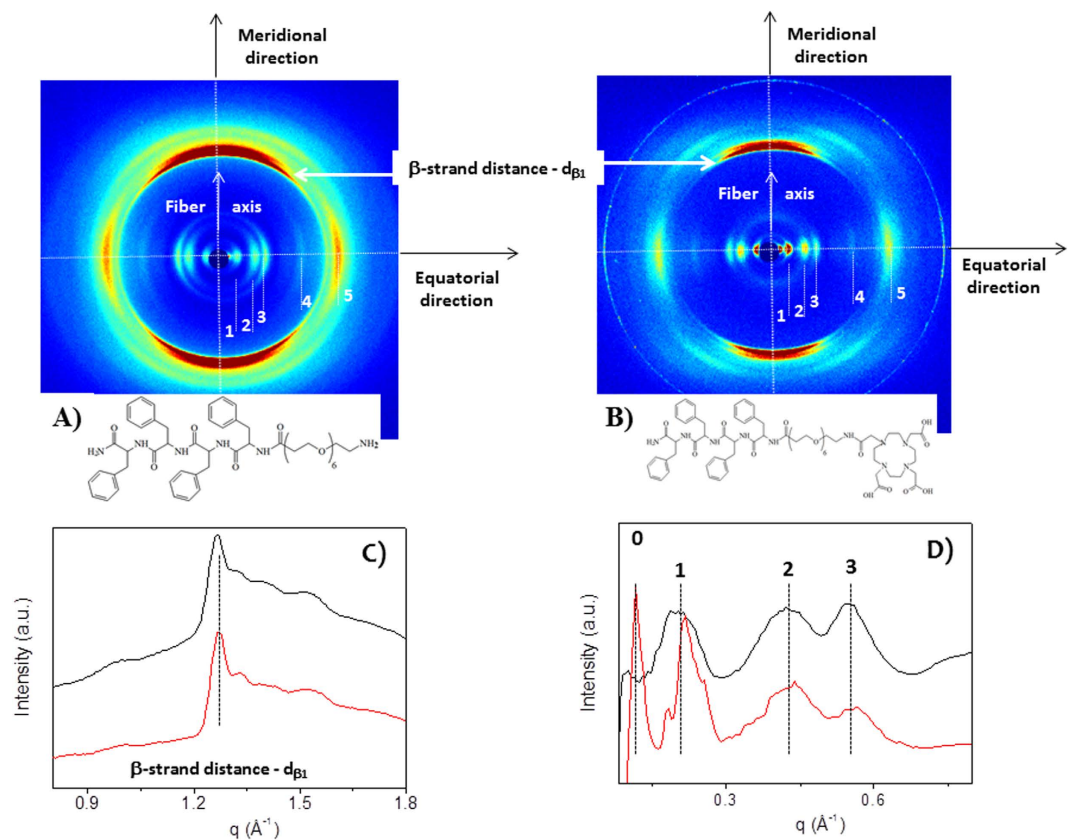


Figure 6. (A,B) show the two-dimensional (2D) WAXS pattern collected on the L₆-F4 and DOTA-L₆-F4 dried samples, respectively; (C,D) show the 1D profiles corresponding to the L₆-F4 (black) and DOTA-L₆-F4 (red).

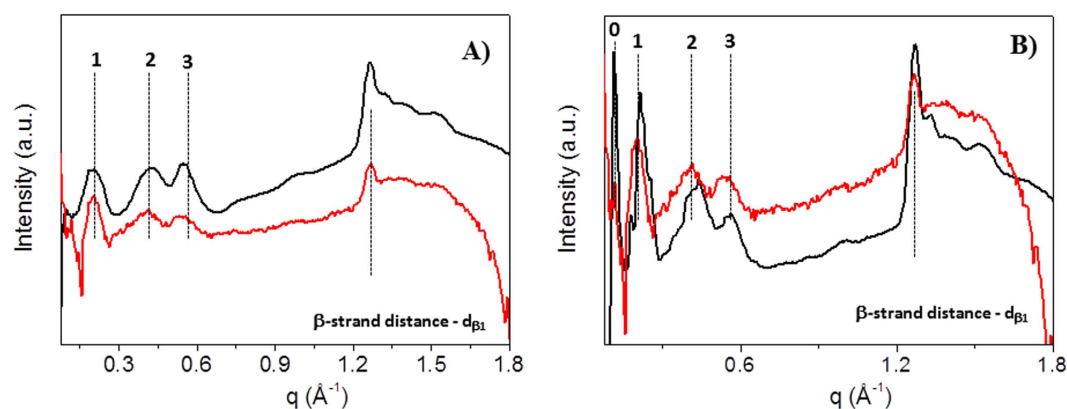


Figure 7. (A,B) show the WAXS profiles, displayed in red, collected on the L₆-F4 and DOTA-L₆-F4 solutions (25 mg/mL) to be compared with the profiles obtained on the analogous dried samples (black line).

to be used as positive MRI contrast agents (CAs)¹³. In principle, the efficacy of a MRI CAs depends on the ability to enhance the water protons relaxation rate in aqueous solutions due to the magnetic dipolar interaction between unpaired electrons on the gadolinium ions and the water protons, which is usually defined as longitudinal “relaxivity” (r_{1p}) and is referred to the water proton relaxation rate of a solution containing the Gd-complex at one millimolar concentration. The relaxivity of a Gd-containing system depends on the complex interplay of structural, dynamic and electronic parameters. At the frequencies most commonly used in commercial tomographs (20–60 MHz), r_{1p} is generally determined by the reorientational correlation time (τ_R) of the chelate so that high molecular weight systems display higher relaxivity. Moreover, when the gadolinium containing adduct is organized in a supramolecular structure with a well-defined three-dimensional order, slow reorientational correlation times and, consequently, high relaxivity values are expected.

This is the case for DOTA(Gd)-L₆-F4, and its analogue DTPA(Gd)-L₆-F4 that present relaxivity values, measured at 21.5 MHz (0.5 T) and 298 K, of 14.8 and 14.0 mM⁻¹s⁻¹, respectively¹³. These values, that are about three times higher the ones measured for the free monomeric DOTA(Gd) and DTPA(Gd) complexes in water solutions under the same experimental conditions, could be related to the structural organization observed for DOTA-L₆-F4. Under the experimental conditions of the MRI studies, DOTA-L₆-F4 monomers aggregate in well-ordered and very stable fibers and the driving force of aggregation is represented by the π -stacking contacts between the side chains of the aromatic framework. CD, FTIR, NMR and WAXS measurements, here reported, confirm the capability of the monomers to self-aggregate in fibers with an antiparallel β -sheet organization both in solution and at the solid state. In particular, NMR and WAXS results highlight the presence of highly stable nanofibers yet in solution, thus suggesting a potential application of these compounds as MRI contrast agents. Moreover, the herein reported in deep physicochemical characterization of these materials allows to unequivocally define the structural parameters characterizing the fibers, such as the inter-planar distances and the L6 folding around the fibers. The knowledge of these parameters can help clarifying important aspects to improve the performances of the final MRI contrast agent, in term of relaxivity values. For example, the mobility of the DOTA chelating agent along the linker spacer, with respect to the overall fibril-like structure, influences the τ_R values that result quite short if compared to those usually found for nano-sized aggregates^{27,28}. Our data clearly indicate that to enhance the performances of DOTA(Gd)-L₆-F4 fibers as MRI contrast agents, an increase of the rigidity of the DOTA moiety, pending from the fiber organization of DOTA-L₆-F4 should be achieved.

Conclusions

Extraordinary interest was recently devoted to peptide materials containing aromatic amino acids in which the aggregation process is promoted by π -stacking interactions. Very recently, we proposed novel PEGylated-F4 fibers, highly soluble in water solution, as potential CAs in MRI. The PEGylated-F4 was chemically modified at the N-terminus with branched DTPA or macrocyclic DOTA chelating agents, both of them able to allow kinetically and thermodynamically stable coordination of metal ions for diagnostic purpose. The comparative structural study of PEGylated tetra-phenylalanine fibers, in presence (DOTA-L₆-F4) and in absence of DOTA (L₆-F4), points out the high similitude between the resulting nanomaterials. Both nanofibers show an antiparallel β -sheets organization, although in DOTA-L₆-F4 fibers an increase in the size and in the order degree was observed. This result suggests the low incidence of the DOTA macrocycle on the β -sheets organization, as a consequence of the PEG chain, the latter being long enough to place a distance between the chelating agent and the aromatic framework. Nevertheless it remains to understand, at the molecular level, what is the rationale for the higher inner order of DOTA-L₆-F4 nanostructures with respect to L₆-F4 ones. The organization in well-ordered and stable fibers of the DOTA-L₆-F4 monomers, observed by comparing structural data from a multiplicity of experimental techniques (CD, FTIR, NMR, DLS, WAXS and SAXS) is responsible of the three-fold increase in the relaxivity value of DOTA(Gd) complex. As a consequence, a potential use of these nanofibers as MRI contrast agent can be realistically envisioned. On the other hand, the structural characterization here reported confirms and reinforces our previous hypothesis about the high flexibility of the DOTA moiety, bound to a quite long PEG chain. A more rigid organization should be advantageous to increase the relaxometric performance of the contrast agent. Despite this issue remains to be improved, the structural similitude of these nanofibers with the fibrillary oligomers (A β O) or plaques commonly observed during the progression of several neurodegenerative disorders (Alzheimer's, Parkinson's and prion-related diseases) open new perspectives towards the development of diagnostic tools for their early detection. Moreover, we can realistically suppose that the replacement of DOTA with another active pharmaceutical ingredient, characterized by a comparable steric and electrostatic hindrance, would not cause significant structural differences. Based on these findings we can conclude that L₆-F4, for its handy preparation and high water solubility, can represent a promising building block for the synthesis of novel materials for therapeutic or diagnostic applications.

Materials and Methods

Peptide synthesis. L₆-F4 and DOTA-L₆-F4 peptides were synthesized by solid phase synthesis and purified by RP-HPLC chromatography, according to the procedure previously described¹³. Similarly, double labeled ¹⁵N/¹³C DOTA-L₆-F4 containing either selective (Phe 2,4) or uniformly Phe(1,2,3,4) labeling were synthesized by replacing Fmoc-Phe-OH with Fmoc-Phe-OH-¹³C₉, ¹⁵N. Double labeled phenylalanine was purchased by Sigma Aldrich (Milan, Italy).

Fluorescence studies. CAC values were obtained by fluorescence measurements. Fluorescence spectra were recorded at room temperature on a Jasco Model FP-750 spectrofluorophotometer in a 1.0 cm path length quartz cell. Equal excitation and emission bandwidths (5 nm) were used throughout the experiments with a recording speed of 125 nm/min and automatic selection of the time constant. The CAC values were measured by using 8-anilino-1-naphthalene sulfonic acid ammonium salt (ANS) as fluorescent probe^{29,30}. Small aliquots of peptide derivatives in water solutions were added to 1.0 mL of aqueous solution of ANS (20 μ M). Final spectra, to be used for calculations, were obtained after blank correction and adjustment for dilution. The ANS fluorescence intensity was followed as a function of the peptide concentration. The CAC values were determined, upon excitation at 350 nm, by linear least-squares fitting of the fluorescence emission at 470 nm versus the poly-phenylalanine concentration, as the crossing point between the changes of slope.

NMR experiments. NMR experiments were acquired at 298 K on either a Varian Unity Inova 600 MHz spectrometer equipped with a cold probe or a 400 MHz Varian instrument provided with a 5-mm triple resonance probe and z-axis pulsed-field gradients. All samples were dissolved in a mixture H₂O/D₂O (98% D₂O, Armar Chemicals, Dottingen, Switzerland) 90/10 v/v with a total volume equal to 600 μ L. The L₆-F4 sample

(0.05–1.5 mM concentration range) was analyzed through a set of 2D experiments: 2D [^1H , ^1H] TOCSY³¹ (70 ms mixing time), 2D [^1H , ^1H] NOESY¹⁹ (300 ms mixing time), and 2D [^1H , ^1H] ROESY (Rotating frame Overhauser Enhancement Spectroscopy)³² (150 and 250 ms mixing times). For the DOTA conjugated molecule DOTA-L₆-F4 1D [^1H] experiments were registered at the following concentrations: 1.9, 0.9, 0.7, 0.4, 0.2, 0.1 mM; whereas 2D [^1H , ^1H] TOCSY (70 ms mixing time), and 2D [^1H , ^1H] NOESY (300 ms mixing time) were acquired at 0.1, 0.3, and 0.9 mM.

1D spectra were usually acquired with a relaxation delay d_1 of 1.5 s and 32–512 scans; 2D experiments were recorded with 16–64 scans, 128–256 FIDs in t_1 , 1024 or 2048 data points in t_2 . Further 3D and 2D heteronuclear correlation experiments^{33,34} (i.e., 2D [^1H , ^{15}N] HSQC (Heteronuclear Single Quantum Correlation Spectroscopy), and 2D [^1H , ^{13}C] HSQC, 3D ^{15}N resolved- ^1H , ^1H] NOESY-HSQC (250 ms mixing time), 3D ^{13}C resolved- ^1H , ^1H] NOESY-HSQC (200 ms mixing time), were set up with two different $^{15}\text{N}/^{13}\text{C}$ Phe labeled DOTA-L₆-F4 samples (concentration range 0.1–1 mM): sample A) containing all phenylalanine residues uniformly labeled with ^{13}C and ^{15}N and sample B) containing instead only $^{15}\text{N}/^{13}\text{C}$ double labeled F2 and F4 (Fig. 1A). The process of proton resonance assignment was performed by following a canonical protocol based on comparison of TOCSY, NOESY and ROESY experiments (See Table S1)²⁰.

Water suppression was achieved by Excitation Sculpting³⁵. Spectra were processed with VNMRJ (Varian by Agilent Technologies, Italy) and analyzed with NEASY³⁶ comprised in the CARS software package (<http://www.nmr.ch/>). 2D HSQC spectra were compared with the program Sparky (T. D. Goddard and D. G. Kneller, SPARKY 3, University of California, San Francisco). Chemical shift deviations from random coil values for H_α protons (CSD) were calculated with the protocol suggested by Kjaergaard and collaborators by keeping into account the influence of neighboring amino acids^{21,37,38}.

DLS measurements. Hydrodynamic radii (R_H) and diffusion coefficients (D) of tetra-phenylalanine nanostructures were measured by Dynamic Light Scattering technique (DLS). DLS measurements were carried out using a Zetasizer Nano ZS (Malvern Instruments, Westborough, MA) that employs a 173° backscatter detector. Other instrumental settings are measurement position (mm): 4.65; attenuator: 8; temperature: 25 °C; cell: disposable sizing cuvette. DLS measurements in triplicate were carried out on aqueous samples at 2.0 mg/mL, after centrifugation at room temperature at 13,000 rpm for 5 minutes.

Circular Dichroism. Far-UV CD spectra of the peptide derivatives in aqueous solution were collected on a Jasco J-810 spectropolarimeter equipped with a NesLab RTE111 thermal controller unit using a 0.1 mm quartz cell at 25 °C. The spectra of samples at (0.1 and 5.0 mg/mL) are recorded from 280 to 195 nm. Other experimental settings were: scan speed = 10 nm/min; sensitivity = 50 mdeg; time constant = 16 s; bandwidth = 1 nm. Each spectrum was obtained by averaging three scans and corrected for the blank. Here Θ represents the mean residue ellipticity (MRE), i.e. the ellipticity per mole of peptide divided by the number of amino acid residues in the peptide.

Fourier Transform Infrared spectroscopy (FTIR). FTIR spectra of samples dried film (2.0 mg/mL) or in solution (2.0 mg/mL) were collected on a Jasco FT/IR 4100 spectrometer (Easton, MD) in an attenuated total reflection (ATR) mode and using a Ge single-crystal at a resolution of 4 cm^{-1} . All the spectral data were processed using built-in software. Spectra were collected in transmission mode and then converted in emission. Each sample was recorded with a total of 100 scans with a rate of 2 $\text{mm}\cdot\text{s}^{-1}$ against a KBr background.

Wide-Angle and Small-Angle X-ray Scattering. Fiber diffraction WAXS and SAXS patterns were recorded from dried fibers; WAXS data were measured from water diluted peptide solutions (10–25 mg/mL). Stalks were prepared by the stretch frame method³⁹. Briefly, a droplet (10 μL) of peptide aqueous solution (3 wt%) was suspended between the ends of a wax-coated capillary (spaced 2 mm apart). The droplet was allowed to dry gently at room temperature overnight to obtain oriented fibers. Peptide solutions were loaded into Lindemann capillaries and measured, in the same experimental conditions adopted for the dried fibers, at room temperature. WAXS/SAXS data were collected at the X-ray MicroImaging Laboratory (XMI-L@b) equipped with a Fr-E+ SuperBright rotating anode copper anode microsource ($\text{Cu K}\alpha$, $\lambda = 0.15405 \text{ nm}$, 2475 W), a multilayer focusing optics (Confocal Max-Flux; CMF 15–105) and a SAXS/WAXS three-pinhole camera (Rigaku SMAX-3000)⁴⁰. For WAXS data collection an image plate (IP) detector with 100 μm pixel size was placed at 8.5 cm from the sample and calibrated by means of the Si NIST standard reference material (SRM 640 b); for SAXS data collection a Triton 20 gas-filled photon counter detector with 200 μm pixel size was placed at 2.2 m from the sample and calibrated by means of silver behenate. A detailed description of the XMI-L@b performances can be found in Altamura *et al.*⁴⁰ and Sibillano *et al.*⁴¹.

References

- Stupp, S. I. Self-assembly and biomaterials. *Nano Letters* **10**(12), 4783–4786 (2010).
- Cavalli, S., Albericio, F. & Kros, A. Amphiphilic peptides and their cross-disciplinary role as building blocks for nanoscience. *Chem. Soc. Rev.* **39**, 241–263 (2010).
- Morris, K. & Serpell, L. C. From natural to designer self-assembling biopolymers, the structural characterization of fibrous proteins & peptides using fibre diffraction. *Chem. Soc. Rev.* **39**, 3445–3453 (2010).
- Fleming, S. & Ulijn, R. V. Design of nanostructures based on aromatic peptide amphiphiles. *Chem. Soc. Rev.* **43**(23), 8150–8177 (2014).
- Hamley, I. W. Peptide nanotubes. *Angew. Chem. Int. Ed.* **53**, 6866–6881 (2014).
- Jayawarna, V. & Ulijn, R. V. In *Supramolecular Chemistry: From Molecules to Nanomaterials*. (Eds Gale *et al.*), Ch. 7, 3525–3539 (Wiley, 2012).
- Reches, M. & Gazit, E. Casting metal nanowires within discrete self-assembled peptide nanotubes. *Science* **300**(5619), 625–627 (2003).

8. Yan, X., Zhu, P. & Li, J. Self-assembly and application of diphenylalanine-based nanostructures. *Chem. Soc. Rev.* **39**(6), 1877–1890 (2010).
9. Mayans, E. *et al.* Self-assembly of tetraphenylalanine peptides. *Chem. Eur. J.* **21**(47), 16895–16905 (2015).
10. Castelletto, V. & Hamley, I. W. Self assembly of a model amphiphilic phenylalanine peptide/polyethylene glycol block copolymer in aqueous solution. *Biophys. Chem.* **141**(2–3), 169–174 (2009).
11. Tzokova, N., Armes, S. P. & Ryan, A. J. *et al.* Soft hydrogels from nanotubes of poly(ethylene oxide)-tetraphenylalanine conjugates prepared by click chemistry. *Langmuir* **25**(4), 2479–2785 (2009).
12. Tzokova, N. *et al.* The effect of PEO length on the self-assembly of poly(ethylene oxide)-tetrapeptide conjugates prepared by “click” chemistry. *Langmuir* **25**, 11082–11089 (2009).
13. Diaferia, C. *et al.* Peptide materials obtained by aggregation of polyphenylalanine conjugates as gadolinium-based magnetic resonance imaging contrast agents. *Adv Funct. Mater.* **25**, 7003–7016 (2015).
14. Accardo, A. *et al.* Peptide modified nanocarriers for selective targeting of bombesin receptors. *Mol. BioSyst.* **6**, 878–887 (2010).
15. Accardo, A., Tesaro, D., Mangiapia, G., Pedone, C. & Morelli, G. Nanostructures by self-assembling peptide amphiphile as potential selective drug carriers. *Biopolymers (Peptide Science)* **88**(2), 115–121 (2007).
16. Caravan, P., Ellison, J. J., McMurry, T. J. & Laufer, R. B. Gadolinium(III) chelates as MRI contrast agents: structure, dynamics, and applications. *Chem Rev.* **99**(9), 2293–2352 (1999).
17. Morisco, A. *et al.* Micelles derivatized with octreotide as potential target-selective contrast agents in MRI. *J. Pept. Sci.* **15**, 242–250 (2009).
18. Accardo, A. *et al.* Nanoparticles containing octreotide peptides and gadolinium complexes for MRI applications. *J. Pept. Sci.* **17**(2), 154–162 (2011).
19. Kumar, A., Ernst, R. R. & Wuthrich, K. A two-dimensional nuclear Overhauser enhancement (2D NOE) experiment for the elucidation of complete proton-proton cross-relaxation networks in biological macromolecules. *Biochem. Biophys. Res. Commun.* **95**, 1–6 (1980).
20. Wuthrich, K. *NMR of proteins and nucleic acids.* (ed Wiley) (New York, 1988).
21. Kjaergaard, M. & Poulsen, F. M. Sequence correction of random coil chemical shifts: correlation between neighbor correction factors and changes in the Ramachandran distribution. *J. Biomol. NMR* **50**(2), 157–165 (2011).
22. Zanuy, D., Hamley, I. W. & Aleman, C. Model Modeling the tetraphenylalanine-PEG hybrid amphiphile: from DFT calculations on the peptide to molecular dynamics simulations on the conjugate. *J. Phys Chem B* **115**(28), 8937–46 (2011).
23. Jonstromer, M., Johnsson, B. & Lindman, B. Self-diffusion in nonionic surfactant-water systems. *J. Phys. Chem.* **95**, 3293–3300 (1991).
24. Moran, S. D. & Zanni, M. T. How to get insight into amyloid structure and formation from infrared spectroscopy. *J. Phys. Chem. Lett.* **5**(11), 1984–1993 (2014).
25. Serpell, L. C., Fraser, P. E. & Sunde, M. X-ray Diffraction of Amyloid Fibrils. *Methods Enzymol.* **309**, 526–536 (1999).
26. Makin, S. O., Sikorski, P. & Serpell, L. C. CLEARER: a new tool for the analysis of X-ray fiber diffraction patterns and diffraction simulation from atomic structural models. *J. Appl. Cryst.* **40**, 966–972 (2007).
27. Vaccaro, M. *et al.* Peptides and gd complexes containing colloidal assemblies as tumor-specific contrast agents in MRI: physicochemical characterization. *Biophys J.* **93**(5), 1736–1746 (2007).
28. Tesaro, D. *et al.* Peptide derivatized lamellar aggregates as target-specific MRI contrast agents. *ChemBioChem* **8**(8), 950–955 (2007).
29. Birdi, K. S., Singh, H. N. & Dalsager, S. U. Interaction of ionic micelles with the hydrophobic fluorescent probe 1-anilino-8-naphthalenesulfonate. *J. Phys. Chem.* **83**, 2733–2737 (1979).
30. De Vendittis, E., Palumbo, G., Parlato, G. & Bocchini, V. A fluorimetric method for the estimation of the critical micelle concentration of surfactants. *Anal. Biochem.* **115**(2), 278–286 (1981).
31. Griesinger, C., Otting, G., Wuthrich, K. & Ernst, R. R. Clean TOCSY for proton spin system identification in macromolecules. *J. Am. Chem. Soc.* **110**(23), 7870–7872 (1988).
32. Bax, A. & Davis, D. G. Practical aspects of two-dimensional transverse NOE spectroscopy. *J. Magn. Reson.* **63**, 207–213 (1985).
33. Talluri, S. & Wagner, G. An optimized 3D NOESY-HSQC. *J. Magn. Reson. Series B.* **112**(2), 200–205 (1996).
34. Wilker, W., Leibfritz, D., Kerssebaum, R. & Bermel, W. Gradient selection in inverse heteronuclear correlation spectroscopy. *Magn. Reson. Chem.* **31**(3), 287–292 (1993).
35. Hwang, T. L. & Shaka, A. J. Water suppression that works. Excitation sculpting using arbitrary waveforms and pulsed field gradients. *J. Magn. Reson. Series A* **112**(2), 275–279 (1995).
36. Bartels, C., Xia, T., Billeter, M., Gunthert, P. & Wuthrich, K. The program XEASY for computer-supported NMR spectral analysis of biological macromolecules. *J. Biomol. NMR* **6**(1), 1–10 (1995).
37. Kjaergaard, M., Brander, S. & Poulsen, F. M. Random coil chemical shifts for intrinsically disordered proteins: Effects of temperature and pH. *J. Biomol. NMR* **49**(2), 139–149 (2011).
38. Schwarzhinger, S. *et al.* Sequence-dependent correction of random coil NMR chemical shifts. *J. Am. Chem. Soc.* **123**(13), 2970–2978 (2001).
39. Sunde, M. *et al.* Common core structure of amyloid fibrils by synchrotron X-ray diffraction. *J. Mol. Biol.* **273**, 729–739 (1997).
40. Altamura, D. *et al.* X-ray microimaging laboratory (XMI-LAB). *J. Appl. Cryst.* **45**(4), 869–873 (2012).
41. Sibillano, T. *et al.* An optimized table-top small-angle X-ray scattering set-up for the nanoscale structural analysis of soft matter. *Sci. Rep.* **4**(6985), 1–7 (2014).

Acknowledgements

We are indebted with the Italian Minister for Research (M.I.U.R.) for financial support under FIRB ‘RINAME’ RBAP114AMK project. The authors thank Leopoldo Zona for excellent technical assistance.

Author Contributions

C.D. synthesized peptide conjugates, C.D. and A.A. performed CAC, C.D., DLS and FTIR experiments. A.A. and G.M. analyzed fluorescence, C.D., DLS and FTIR data. M.L. and F.A.M. recorded and analyzed solution NMR experiments. T.S. and C.G. realized WAXS and SAXS experiments and analyzed SAXS and WAXS data. A.A., C.G. and M.L. discussed the results and wrote the paper in close collaboration with all the authors.

Additional Information

Supplementary information accompanies this paper at <http://www.nature.com/srep>

Competing financial interests: The authors declare no competing financial interests.

How to cite this article: Diaferia, C. *et al.* Self-assembly of PEGylated tetra-phenylalanine derivatives: structural insights from solution and solid state studies. *Sci. Rep.* **6**, 26638; doi: 10.1038/srep26638 (2016).



This work is licensed under a Creative Commons Attribution 4.0 International License. The images or other third party material in this article are included in the article's Creative Commons license, unless indicated otherwise in the credit line; if the material is not included under the Creative Commons license, users will need to obtain permission from the license holder to reproduce the material. To view a copy of this license, visit <http://creativecommons.org/licenses/by/4.0/>

Nanotechnology

Hierarchical Analysis of Self-Assembled PEGylated Hexaphenylalanine Photoluminescent Nanostructures

Carlo Diaferia,^[a] Teresa Sibillano,^[b] Nicole Balasco,^[c] Cinzia Giannini,^[b] Valentina Roviello,^[d] Luigi Vitagliano,^[c] Giancarlo Morelli,^[a] and Antonella Accardo^{*[a]}

Abstract: Despite the growing literature about diphenylalanine-based peptide materials, it still remains a challenge to delineate the theoretical insight into peptide nanostructure formation and the structural features that could permit materials with enhanced properties to be engineered. Herein, we report the synthesis of a novel peptide building block composed of six phenylalanine residues and eight PEG units, PEG₈-F6. This aromatic peptide self-assembles in water in stable and well-ordered nanostructures with optoelectronic

properties. A variety of techniques, such as fluorescence, FTIR, CD, DLS, SEM, SAXS, and WAXS allowed us to correlate the photoluminescence properties of the self-assembled nanostructures with the structural organization of the peptide building block at the micro- and nanoscale. Finally, a model of hexaphenylalanine in aqueous solution by molecular dynamics simulations is presented to suggest structural and energetic factors controlling the formation of nanostructures.

Introduction

Self-assembly is an increasingly attractive tool for the fabrication of novel nanomaterials.^[1] In this field, self-assembled peptides have received considerable interest because of their intrinsic biocompatibility, relative simple synthesis and preparation, versatility, and functional diversity.^[2] In 2003, diphenylalanine (FF) was identified by Gazit as a recognition motif of the Alzheimer's β -amyloid peptide^[3] and since then it has been extensively studied.^[4] Diphenylalanine homodimers show a very high morphological variability^[5] depending on the experimental preparation conditions, such as solvent,^[6] pH,^[7] or temperature.^[8] Moreover, chemical modifications of the aromatic dipeptide (e.g. the introduction of a thiol group or of a fluorenylmethyloxycarbonyl (Fmoc) group) can alter the self-assembling phenomena.^[5] Nanotubes, nanowires, nanofibrils, spherical vesicles, and organogels are just a few examples of the new peptide materials, based on FF self-assembly. These materials

exhibit mechanical,^[9] electrical,^[10] electrochemical,^[11] or optical (photoluminescence^[12] and optical waveguide^[13]) properties. All these physicochemical characteristics make them suitable for several applications in biology, nanomedicine, and nanofabrication fields (for tissue engineering, drug delivery, bioimaging, and fabrication of biosensors).^[5] Moreover, their high thermal, chemical,^[14] and proteolytic stability^[15] provides them with the features for potential applications in the industrial field. The functional properties of self-assembled materials seem strictly correlated with their morphological features, thus suggesting the existence of a direct relationship between the structural organization of the building blocks and the physicochemical properties of the nanomaterials. For these fundamental reasons, a deep study into the peptide nanostructure formation (control of the morphological diversity, rational modification of the peptide motifs, and prediction for the resulting self-assembled structures) and on the structural features of the nanostructures could permit new materials with enhanced properties to be engineered. Crystallographic studies showed that FF crystals contain ringlike networks with a hexagonal symmetry, promoted by head-to-tail hydrogen-bonding interactions between the charged termini of neighboring dipeptides and by the „T-shaped“ contacts between the aromatic side chains.^[16] Molecular dynamic simulations confirmed the formation of open and ringlike peptide networks also for FF peptides in aqueous solution.^[17] Concurrently to these networks, more-complex structures, arranged in parallel or antiparallel β -sheets, were also observed.^[17] Analogous structures characterized by higher stability and peptide-network propensity were observed in the triphenylalanine (FFF) simulations, thus suggesting that stacking interactions could contribute to the stability of the nanostructure. In contrast to FF dipeptide, it was noted that FFF tripeptide forms planar nanostructures.^[18] In-

[a] Dr. C. Diaferia, Prof. G. Morelli, Dr. A. Accardo
Department of Pharmacy, Research Centre on Bioactive Peptides (CIRPeB)
University of Naples „Federico II“ and DFM Scarl
Via Mezzocannone 16, 80134 Naples (Italy)
E-mail: Antonella.accardo@unina.it

[b] Dr. T. Sibillano, Dr. C. Giannini
Institute of Crystallography (IC), CNR, Via Amendola 122
70126 Bari (Italy)

[c] Dr. N. Balasco, Dr. L. Vitagliano
Institute of Biostructures and Bioimaging (IBB), CNR
Via Mezzocannone 16, 80134 Naples (Italy)

[d] Dr. V. Roviello
Regional Center of Competence Technologies Scarl
Via Nuova Agnano, 11, 80125 Naples (Italy)

Supporting information for this article is available on the WWW under <http://dx.doi.org/10.1002/chem.201604107>.

stead, a different aggregative behavior was observed for its analogues Fmoc-FFF and Boc-FFF that preferentially gives formation of nanosphere^[19] and hydrogels, respectively.^[20] Despite the growing literature about FF, only a few examples of nano-materials obtained by the self-assembling of others aromatic analogues (naphthylalanine, tyrosine, tryptophan) or of long polyphenylalanines have been reported until now.^[21] In order to get a deeper understanding of the molecular interactions involved in their self-assembly process, theoretical calculations for tetraphenylalanine (FFFF or F4) and Fmoc-FFFF aggregates have been recently reported.^[21] Analogously hybrid materials, in which the aromatic framework is chemically modified with polymeric chains (polyethylene glycol, polycaprolactone or polyethylene oxide) remain largely unexplored. Some examples of F4-polymer conjugates, containing PEO or PEG chains with a variable length, have been synthesized, and their aggregation properties in water or in water/tetrahydrofuran mixtures have been described. Very recently, we proposed PEGylated-F4 functionalized with contrast agents for potential diagnostic applications in magnetic resonance imaging.^[21e] The longer Phe-based building block reported until now is the pentaphenylalanine, which, thanks to its high hydrophobicity, displayed interesting properties for the surface coating.^[22] With the aim of improving the knowledge in this field, at the molecular level, we herein investigate the effect of the elongation of the aromatic framework in the aggregation process. We have synthesized a novel peptide building block composed of six phenylalanine residues and eight PEG units (PEG₈-F6) (see Figure 1 a). PEG₈-F6 is able to aggregate in water in nanostructures producing novel β -rich peptide materials. The photoluminescence (PL) properties of the self-assembled material are investigated and correlated with the structural organization of the peptide building block at the micro- and nanoscale. A variety of techniques, such as fluorescence, FTIR, CD, DLS, SEM, SAXS, and WAXS has allowed us to 1) investigate the aggregation behavior, 2) study the secondary structure, and 3) visualize the morphology of the final aggregates. Finally, a model of hexaphenylalanine in aqueous solution by molecular dynamics (MD) simulations is presented to suggest structural and energetic factors controlling the formation of nanostructures.

Results and Discussion

Synthesis and fluorescence spectroscopy

PEGylated hexaphenylalanine PEG₈-F6, reported in Figure 1 a, was obtained by Fmoc/*t*Bu solid-phase synthesis in good yield and high purity. LCMS and ¹H NMR are reported in Figure S1, Supporting Information. PEG₈-F6 is formed by two blocks: an aromatic one, formed by the repetition of six phenylalanine residues (F6), and a hydrophilic one composed of eight ethoxylic repetitions, here indicated as PEG₈ (MW ~ 600 Da). This PEG chain was coupled at the N-terminus of the peptide sequence.

The PEG chain was inserted with the aim of producing a water-soluble material for a large field of applications and does not preclude its potential usage in nanomedicine for the delivery of drugs or contrast agents. Nonetheless, PEG₈-F6

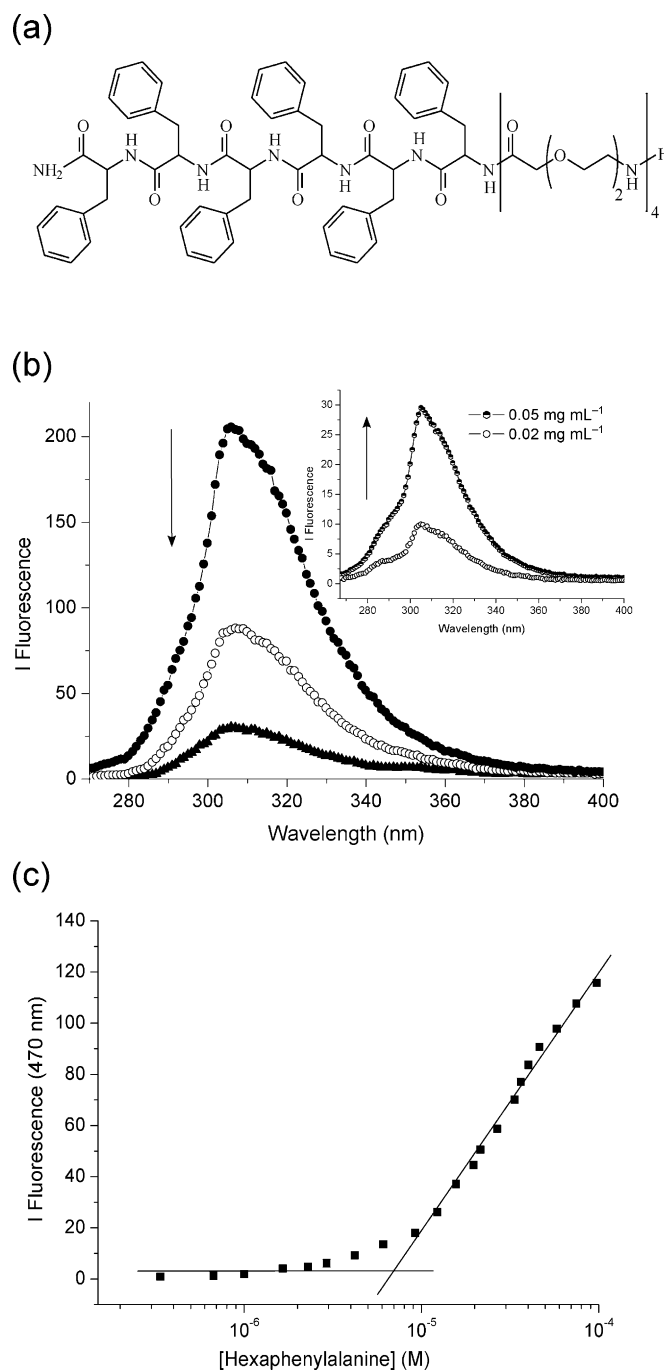


Figure 1. a) Schematic representation of hexaphenylalanine PEG₈-F6. b) Fluorescence spectra of PEG₈-F6 in water solution at 0.1 (●), 1.0 (○), and 2.5 mg mL⁻¹ (▲). In the insert, fluorescence spectra of PEG₈-F6 at 0.02 and 0.05 mg mL⁻¹. All emission spectra were recorded at 25 °C between 265 and 400 nm with an excitation at 258 nm. c) Fluorescence intensity emission of ANS fluorophore at 470 nm versus concentration of PEG₈-F6. CAC values are established from the break point.

shows very limited solubility in water, whereas it shows an excellent solubility in 1,1,1,3,3,3-hexafluoro-2-propanol (HFIP). After dissolution, the peptide solution appeared to clear up to a concentration of 100 mg mL⁻¹. According to the procedure described for cationic diphenylalanine, this stock solution in HFIP was diluted five-fold in water. After dilution and removal

of HFIP, the peptide solution remains perfectly limpid until 20 mg mL^{-1} . The UV/Vis spectrum of PEG₈-F6, reported in Figure S2, Supporting Information, shows the typical spectral profile of Phe residue (*B* band). The tendency of PEG₈-F6 to self-aggregate was evaluated with fluorescence spectroscopy, by exciting the sample at 257 nm (Figure 1 b). At all the concentrations here studied, the expected emission peak at 282 nm, ascribed to the phenylalanine residue, appears weakly outlined, whereas it is well observable that the peak at 310 nm is typical of π -stacking phenomena observed during the excimer Phe formation. This result suggests the high tendency of PEGylated peptide PEG₈-F6 to self-aggregate and indicates that the critical aggregate concentration (CAC) value of this compound is lower than 0.02 mg mL^{-1} . However, two different trends can be identified for the maximum as a function of the concentration. At very low concentrations (0.02 and 0.05 mg mL^{-1}), the fluorescence intensity at 310 nm increases gradually, whereas at high concentrations (0.1 , 1.0 , and 2.5 mg mL^{-1}) an opposite behavior was observed. The decrease of the signal intensity for concentrations above 0.1 mg mL^{-1} can be attributed to quenching that arises from the stacking of the aromatic rings. A more accurate determination of the critical aggregation concentration (CAC) was carried out by using a fluorescence-based method, in which 8-anilino-naphthalene-1-sulfonate ammonium salt (ANS) was used as the fluorescent probe.

It is well-known that ANS fluorophore is able to emit in the range of 460–480 nm only when it is surrounded by a hydrophobic environment, such as in the micelle core.^[23] On the contrary, no fluorescence intensity is observed in water solution. Figure 2 reports the fluorescence intensity of an ANS solution ($20 \mu\text{M}$ in cuvette) at 470 nm, as a function of hexaphenylalanine concentration. From the graphical break point, the CAC value ($7.5 \mu\text{M}$, 0.01 mg mL^{-1}) can be established ($7.5 \mu\text{M}$, 0.01 mg mL^{-1}). This value is significantly lower (around one order of magnitude) than the value found for the polymeric tetraphenylalanine analogues previously studied.^[21b-e] In detail, all the polymeric F4-peptides showed CAC values ranging between 43 and $167 \mu\text{M}$.

As expected, the elongation of the aromatic framework from four to six F residues permits the CAC value to be reduced and in turn to increase the stability of the aggregate upon dilution.

Structural characterization: Secondary structure

Secondary structure of PEGylated hexapeptide in water solution was assessed by CD and FTIR spectroscopies. These spectroscopic methods are typically employed for monitoring the conformational behavior of peptide-based nanostructures and mainly for revealing secondary structural features, such as β -sheet structures, accompanying the formation of amyloid fibers.

CD spectra of PEG₈-F6 at 0.1 , 1.0 , and 10.0 mg mL^{-1} , well above the CAC value, were recorded between 280 and 195 nm and the dichroic behavior was reported in Figure 2a. Due to the very low CAC value of this aromatic derivative, we were not able to record CD spectra of acceptable quality for solution concentration below CAC ($<0.01 \text{ mg mL}^{-1}$). All the spectra

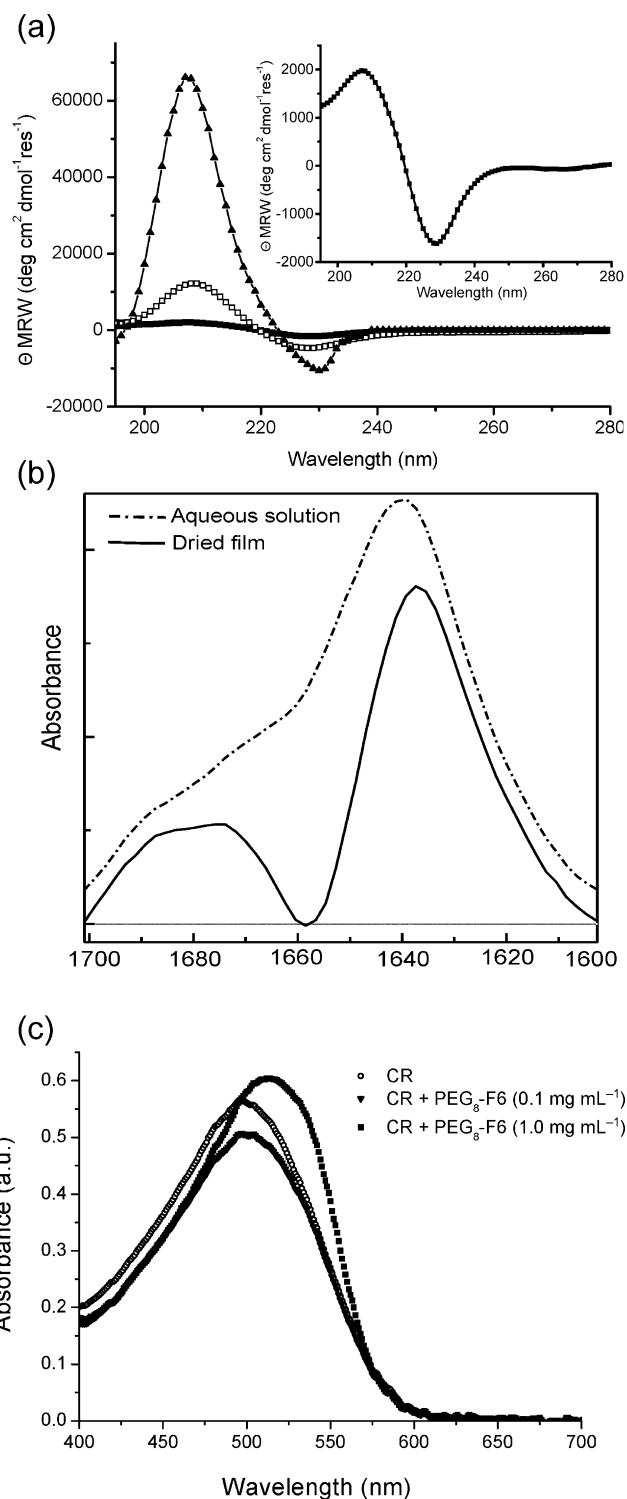


Figure 2. Spectroscopic characterization of PEG₈-F6 by CD and FTIR. a) Far-UV CD spectra of hexaphenylalanine in aqueous solution at 0.1 mg mL^{-1} (\blacktriangle), 1.0 mg mL^{-1} (\square), and 10.0 mg mL^{-1} (\blacksquare). Spectra are recorded between 280 and 195 nm. In the insert, a zoom of the PEG₈-F6 spectrum at 10 mg mL^{-1} is presented. b) FTIR spectra of PEG₈-F6 in solution and at the solid state, in the amide I region. c) UV/Vis spectra of PEG₈-F6, stained with Congo Red at 0.1 and 1.0 mg mL^{-1} . The spectrum of Congo Red is also reported for comparison.

show two peaks: a maximum around 205 nm, attributable to aromatic side-chain stacking, and a minimum around 230 nm,

associated with a β -structure. However, the relative ratio between the intensity of the two peaks decreases progressively as function of the concentration (from 5.8 to 1.2). This decrease indicates the progressive formation of supramolecular aggregates in solution.

According to CD data, the presence of β -sheet structures is supported by FTIR analysis in the region of the amide I vibrational band (1600–1700 cm^{-1}). This region is considered the most sensitive spectral region for the revelation of secondary peptide arrangement.^[24] FTIR spectra for PEG₈-F6, as a dried film or in solution (2.0 mg mL^{-1}), are reported in Figure 2b. Both spectra show a dominant peak at 1637 and 1640 cm^{-1} for the dried film and sample in solution, respectively. Peaks at these wavenumbers are strongly indicative of β -sheet formation. In addition, both spectra show a secondary broad peak at around 1680 cm^{-1} that appears better defined for the solid-state sample (1672 cm^{-1}). The occurrence of this peak indicates an antiparallel orientation of the β -sheet. The FTIR spectrum of PEG₈-F6 also shows a peak at 3280 cm^{-1} corresponding to the NH stretching in fibrillary assembly (see Figure S3, Supporting Information) As expected, in HFIP the FTIR spectrum does not present peaks in the amide I region, thus confirming the disaggregation of PEG₈-F6 in this solvent (data not shown).

Congo Red spectroscopic assay

Further confirmation of PEG₈-F6's ability to aggregate in amyloid-like fibers was obtained with a Congo Red (CR) staining assay. CR is an azoic dye, frequently used as an indicator of the occurrence of amyloid like fibrils.^[25] UV/Vis spectra of CR alone and after incubation with 0.1 or 1.0 mg mL^{-1} of peptide are reported in Figure 2c. As expected, CR absorbs at 490 nm, whereas a spectral shift of the CR band from 490 to 540 nm was observed for solutions containing 1.0 mg mL^{-1} . Instead, only a negligible shift can be invoked for the sample containing 0.1 mg mL^{-1} of PEG₈-F6. At the same time, air-dried film and solid-state PEG₈-F6 were stained with Congo Red and visualized by optical microscopy under cross-polarized light. From the inspection of Figure 3, both air-dried film (Figure 3a) and solid-state sample (Figure 3c) exhibit the characteristic blue–green birefringence.

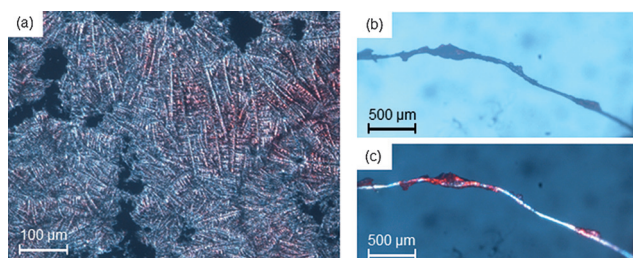


Figure 3. Polarized optical microscopy: a) images of PEG₈-F6 dried onto a glass slide and stained with Congo Red solution; b,c) PEG₈-F6 fibers stained with CR and observed with a Nikon microscope under bright-field illumination and between crossed polars, respectively.

Dynamic light scattering (DLS)

DLS measurements were performed in order to reveal the presence of peptide aggregation in solution and to monitor the system evolution as a function of the concentration and time.

The intensity profiles of PEG₈-F6 in water solution, in the 0.05–5.0 mg mL^{-1} range, are reported in Figure 4 and structural data (mean diameter and diffusion coefficients, D) are collected in Table 1.

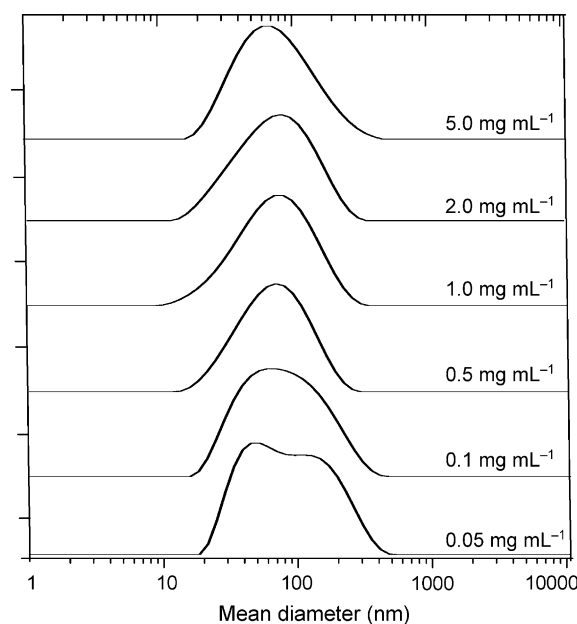


Figure 4. Mean diameter distribution as function of the concentration.

Table 1. Mean diameter and diffusion coefficient for PEG₈-F6 in water at different concentration. Each measure is in triplicate.

PEG ₈ -F6 concentration [mg mL^{-1}]	Mean diameter [nm]	$D \times 10^{-12}$ [$\text{m}^2 \text{s}^{-1}$]
5.0	56.87 ± 0.48	8.66 ± 0.08
2.0	56.70 ± 0.15	8.68 ± 0.04
1.0	56.93 ± 0.63	8.65 ± 0.08
0.5	58.81 ± 0.61	8.37 ± 0.09
0.1	67.84 ± 2.13	7.28 ± 0.22
0.05	74.52 ± 0.77	6.60 ± 0.06

From the inspection of Figure 4, monomodal and bimodal distributions were observed for peptide solutions at high concentration (until 0.5 mg mL^{-1}) and low concentration (0.1 and 0.05 mg mL^{-1}), respectively. These results indicate that PEG₈-F6 nanostructures remain stable upon dilution until 0.5 mg mL^{-1} . Below this concentration a second population arises. At the same time, the size of the nanostructures in solution remains unaltered for up to one month (data not shown). It is well-known that β -sheet-rich peptides tend to aggregate, according to their kinetics, in oligomers, protofibrils, and finally in fibers.^[26] However, PEGylation of amyloid fragments, such as

A β (10-35) peptide induces the inhibition of the fibrillation process, as compared to the peptide alone.^[27]

Scanning electron microscopy

Scanning electron microscopy (SEM) images confirmed the capability of the aromatic peptide to assemble with a high morphological variability (Figure 5). PEG₈-F6 self-assembles at very low concentration (0.05 mg mL⁻¹) giving several amorphous conglomerates (Figure 5a and b). These data are in good

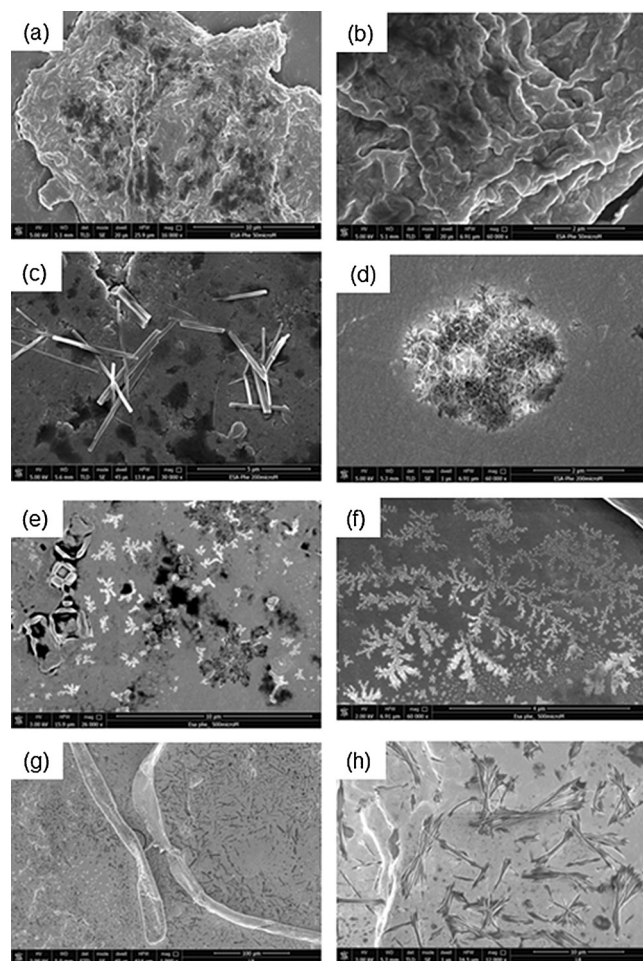


Figure 5. Selected SEM microphotographs for PEG₈-F6: a,b) 50 µg mL⁻¹ (16000 \times , 10 µm and 60000 \times , 2 µm scale bar, respectively); c,d) 0.2 mg mL⁻¹ (30000 \times , 5 µm and 60000 \times , 2 µm scale bar, respectively), e, f) 0.5 mg mL⁻¹ (26000 \times , 10 µm and 60000 \times , 4 µm scale bar, respectively), g,h) 2 mg mL⁻¹ (1000 \times , 100 µm and 12000 \times , 10 µm scale bar, respectively).

agreement with the critical aggregation concentration experimentally determined (\sim 0.01 mg mL⁻¹). The increase of the concentration causes changes of the morphology to give long and well-ordered nanostructures at 2 mg mL⁻¹ (Figure 5). At 0.2 mg mL⁻¹, crystallization effects are observed (Figure 5c and d). In FF dipeptide, the crystal structure is due to hydrogen-bonded head-to-tail chains, which form hydrophilic channels embedded in a hydrophobic matrix created by the peptide side chains. However, in this case, in which head-to-tail interac-

tions are absent, the crystallization can be attributed to the PEG chain on the N-terminus. At 0.5 mg mL⁻¹, formation of highly ordered tree-like multibranch nanostructures is shown. Several nucleation centers are visible on these multibranch nanostructures (Figure 5e and f). Finally, at 1.0 and 2.0 mg mL⁻¹, small conglomerated fibers and very long nanostructures can be observed together on the plate (Figure 5g and h). Many sheafs of fibers with variable length (between 1.5 and 12.5 µm) and thickness (between 250 and 5000 nm) appear. Each sheaf is formed by small fibers of 65–350 nm width, placed side by side. Beside them, also the long nanostructures (from 150 to 4000 µm) present a high morphological variability: some nanostructures with a flat ribbon shape (Figures S4a and S4c, Supporting Information) and others with a twisted ribbon shape (Figures S4b and S4d, Supporting Information). Twisted ribbons are expected for amyloid peptides functionalized with short PEG chains.^[28]

In tubular nanoaggregates (Figures S4a and S4c, Supporting Information), the width maintains a homogeneous size (\sim 10–15 µm) along its full length, whereas in the twisted nanostructures thickness changes of 20 µm are measured along the different parts of the aggregate. From these images we can realistically speculate that above 1.0 or 2.0 mg mL⁻¹, the small fibers begin to collapse to give stacks. These stacks aggregate beyond in long nanostructures. DLS and SEM measures indicate different sizes for self-assembled PEG₈-F6 at the same concentration (for instance at 2.0 mg mL⁻¹). However, this mismatch depends on different physical states of the sample, which is in solution and at the solid state for DLS and SEM, respectively.

Wide- and small-angle X-ray scattering

To gain better insight into the assembly process and molecular organizations, we prepared ordered fibers by the stretch frame method^[29] and acquired wide- and small-angle X-ray scattering (WAXS/SAXS) data. Figure 6a shows PEG₈-F6 dried fibers as placed under the micro-focused X-ray beam. Four different regions were explored, at a relative distance of 0.2 mm, marked as 1 (red), 2 (green), 3 (blue), and 4 (orange) in Figure 6a, to control the lateral homogeneity of the fiber. The WAXS and SAXS detectors, placed at 10 mm and 2.2 m from the sample (see Figure 6b), allowed us to collect the diffraction in two different slightly overlapped Δq ranges: $\Delta q(\text{WAXS})=0.006\text{--}2.5 \text{ \AA}^{-1}$ and $\Delta q(\text{SAXS})=0.007\text{--}0.189 \text{ \AA}^{-1}$. The 2D WAXS and SAXS diffraction patterns are displayed for each sample position in Figure 6a.

Several diffraction peaks were measured either along the meridional (along the fiber) and equatorial direction (perpendicular to the fiber) and no difference was found moving across the different positions, proving a high lateral homogeneity of the fiber, either at the atomic- (WAXS) or at the nano-scale (SAXS). The 2D WAXS and SAXS patterns were centered, calibrated, and folded into 1D profiles, by integrating along the equatorial and meridional directions (white arrows) of Figure 7a and b, respectively. The corresponding 1D patterns were reported, as blue (SAXS) and black (WAXS) profiles, in Fig-

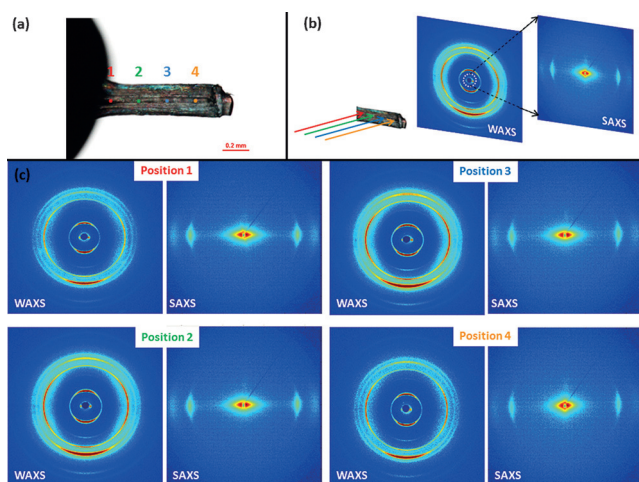


Figure 6. a) PEG₆-F6 sample, as placed under the micro-focused X-ray beam, with the regions explored marked in red (1), green (2), blue (3), and orange (4), placed at a relative distance of 0.2 mm; b) WAXS and SAXS data with different slightly overlapped Δq ranges: $\Delta q(\text{WAXS}) = 0.006\text{--}2.5 \text{ \AA}^{-1}$ and $\Delta q(\text{SAXS}) = 0.007\text{--}0.189 \text{ \AA}^{-1}$; c) 2D WAXS and SAXS diffraction patterns collected for each sample position in (a).

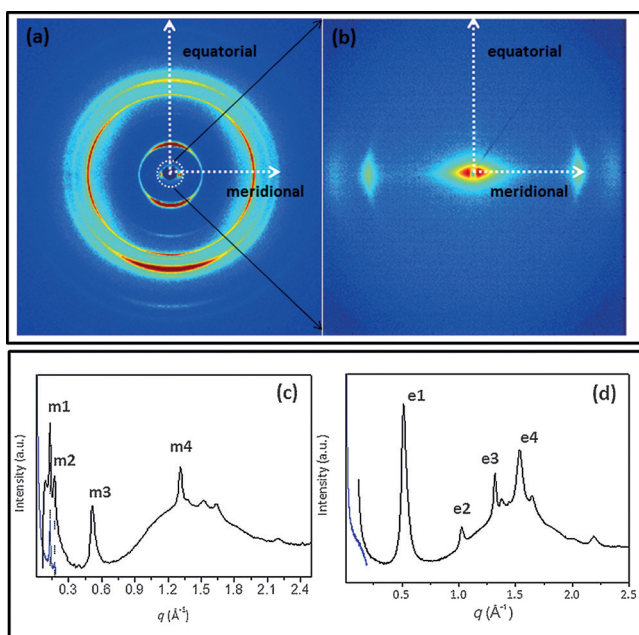


Figure 7. a) 2D WAXS and b) SAXS patterns, recorded for sample position 3; c) meridional and d) equatorial 1D SAXS (blue) and WAXS (black) as obtained once the 2D WAXS (a) and SAXS patterns (b) are centered, calibrated, and folded into uni-dimensional (1D) profiles by integrating along the equatorial and meridional directions (white arrows).

ure 7c and d for the meridional and equatorial direction, respectively. Table 2 summarizes the peak positions (in q) of the most intense SAXS and WAXS peaks, measured along the equatorial and meridional directions. The same meridional reflections were measured either in SAXS and WAXS, marked as m1 and m2 in Figure 7c. No equatorial SAXS peak was detected in the explored range. Therefore, the equatorial profile contains only morphological information.

Table 2. Equatorial and meridional reflections for PEG ₆ -F6 fibers.		
Meridional reflections		
Label	q [\AA^{-1}]	d [\AA]
m1	0.132	48.0
m2	0.171	37.0
m3	0.514	12.2
m4 (β strand)	1.32	4.8
Equatorial reflections		
e1	0.514	12.2
e2	1.026	6.1
e3 (β strand)	1.319	4.8
e4	1.536	4.1

The experimental data were fitted with the GNOM program,^[30] as reported in Figure S5a (Supporting Information, dotted curve corresponds to the experimental data, red line to the fitted profile). The pair distribution function extracted by this analysis, reported in Figure S5b (Supporting Information), is a typical distribution of elongated scattering objects. The gyration radius, determined by this analysis, is $Rg = 69 \pm 1 \text{ nm}$. The diffraction peak positions in Table 2 were converted in lattice spacings (d). Three relevant distances can be distinguished: the typical β -strands distance at $d_{m4} = 4.8 \pm 0.3 \text{ \AA}$, more represented along the meridional direction; the sharp peak at $d_{e1} = 12.2 \pm 0.3 \text{ \AA}$, with its replica at half lattice spacing ($d_{e2} = 6.1 \pm 0.3 \text{ \AA}$), which corresponds to the β -sheet distance; and the meridional peak at $d_{m1} = 48 \pm 0.3 \text{ \AA}$, which corresponds to 10-times the β -strands distance. This meridional reflection with the spacing of 48 \AA may be indicative of additional regularities along this direction. The presence of a clear fiber diffraction pattern either in SAXS and in WAXS is fingerprint of a hierarchical organization of the molecules in fibers from the atomic to the nanoscale, the latter footprint of the quaternary level of the fiber.

Photoluminescence in peptide nanostructures

Recently, Rosenman et al. have described the appearance of blue/green photoluminescence (PL) in FF and FFF nanostructures, upon the thermally induced phase.^[12b,31] This PL phenomenon has been observed by exciting self-assembled oligopeptides at 370 or 410 nm, only after heating the sample at 140–180 °C, as a consequence of an irreversible reconstructive phase transition in the nanostructure.^[12b,31] A similar effect of PL has been also observed for amyloid-like fibrils^[32] considering the nanofiber morphology with antiparallel β -sheet structures. The origin of this fluorescence is truly attributed to the electron delocalization through hydrogen bonds in the β -sheet-rich structures. According to these findings, also our PEG₆-F6 nanoaggregates that contain a high content of β -sheet structures exhibit optoelectronic PL properties in water solution when excited in the same spectral region to those that have been studied recently by Rosenman^[12b,31] (see Figure 8).

PEG₆-F6 at a concentration of 10 mg mL⁻¹ shows a blue PL between 420–460 nm when the sample is excited at a wave-

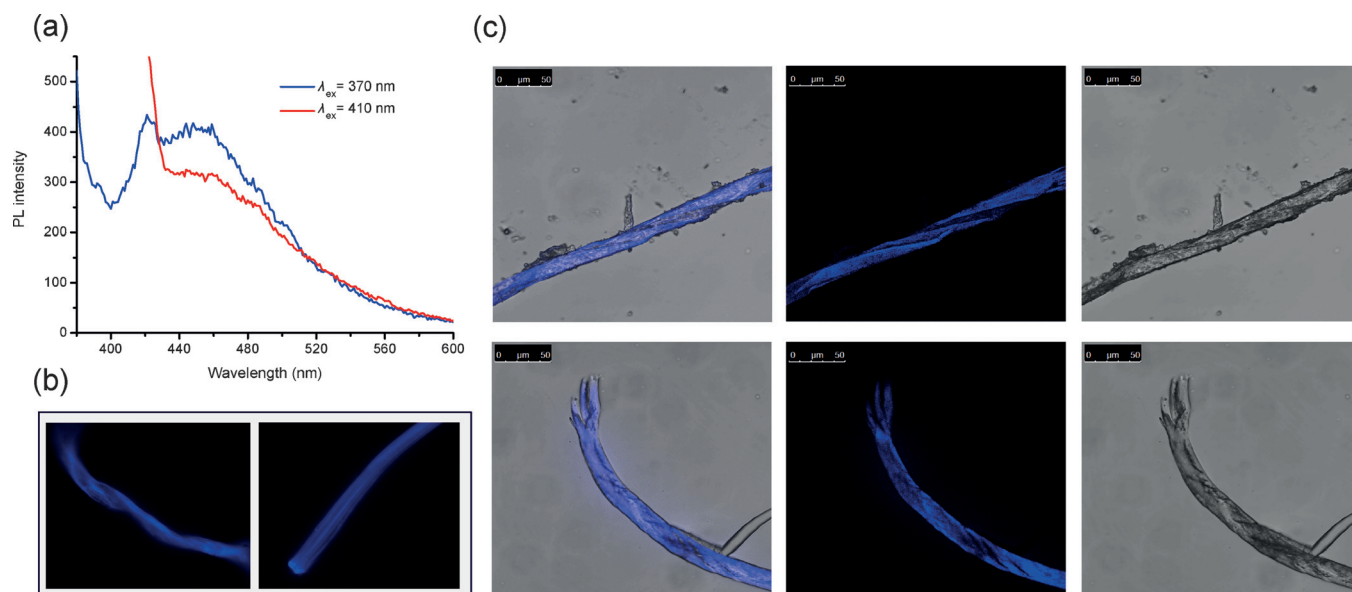


Figure 8. PL of PEG₈-F6 nanostructures at 10 mg mL⁻¹. a) Blue PL emission spectra for the sample in solution upon excitation at ~370 nm (blue line) and at ~410 nm (red line). b) Fluorescence microscopy images of a dried film of PEG₈-F6 obtained by exciting in the UV spectral region (DAPI filter). c) Confocal microscopy images of a dried film of PEG₈-F6: Fluorescence images (on the left), bright field images (on the right) and the merge of fluorescence and bright field images (at the center). Scale bar = 50 μm.

length of 370 or 410 nm. The narrow peak at $\lambda = 420$ nm that appears upon excitation at 370 nm can be associated to the Raman scattering in water.^[33] PEG₈-F6 keeps a PL effect also in the solid state. Figure 8 reports the immunofluorescence and confocal images of the sample deposited on a clean coverslip glass and slowly dried at room temperature.

Molecular modeling and dynamics

To gain insights into the atomic structure of these supramolecular aggregates, we performed molecular dynamics simulations. Although, in principle, PEG moieties could influence the PEG₈-F6 structure, we assumed that the self-assembling is essentially dictated by the aromatic peptide region, as PEG is completely disordered, even in the crystal state, in the only 3D structure available of a highly PEGylated protein.^[34] Accordingly, MD simulations were performed on distinct F6 models generated using the steric zipper structure of the KLVFFA hexapeptide as the template (see Materials and Methods and Table S1 for modeling and notations, Supporting Information). These assemblies were characterized by a different number of β -strands per β -sheet. Models here investigated were denoted as SH_x-ST_y-F6, in which x and y indicate the number of β -sheets and β -strands per sheet, respectively; F6 indicates the number of Phe residues per chain. Preliminary simulations carried out on the smaller systems (SH2-ST10-F6 and SH2-ST26-F6) suggested that these steric zipper models were rather stable in the simulation timescale (data not shown). However, to reduce the impact of the assembly termination effects, most extensive analyses were conducted on the larger SH2-ST50-F6 system (Figure 9a). The inspection of the root mean square values (RMSD) of SH2-ST50-F6 trajectory structures versus the initial structure clearly shows that the starting model undergoes

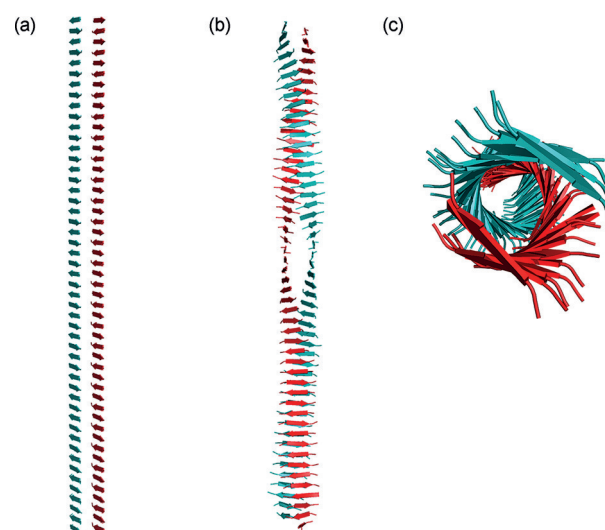


Figure 9. Evolution of the SH2-ST50-F6 model during the simulation. Panel (a) shows the starting flat model, whereas panels (b) and (c) show two different views of the average structure calculated in the equilibrated region of the trajectory.

a major transition during the simulation (Figure S6a,b, Supporting Information). The analysis of the evolution of the trajectory also indicates that the structural transition is followed by states characterized by rather constant RMSD values (Figure S6a, Supporting Information). This behavior suggests that the system adopts a novel structural state in the equilibrated region of the trajectory (20–100 ns). This transition is also coupled with a significant variation of the assembly gyration radius (Figure S6b, Supporting Information). Notably, the secondary structure of SH2-ST50-F6 is well preserved in the simu-

lation (Figure S6c, Supporting Information). The visual analysis of trajectory structures clearly indicates that the initially flat SH2_ST50_F6 β -sheet motif undergoes a significant twist.

This is also evident when the average structure calculated in the equilibrated region of the trajectory is visualized (Figure 9b,c). This behavior has been observed for several other peptides forming cross-beta structures.^[35] It has been suggested that the β -sheet twisting is better suited for fiber formation, whereas the growth of single crystals forces the β -sheets to adopt flat states^[35] However, no twisting has been observed for the Gln homopeptides.^[36] In this latter case, the strong interdigitation of the Gln side chains has likely prevented the β -sheet twisting.

The analysis of the evolution of the intersheet distance shows that the two facing sheets are more separated in the equilibrated region compared to their relative position in the KLVFFA structure (Figure 10). Indeed, in the starting crystallographic KLVFFA structure, the distances between facing C $^{\alpha}$

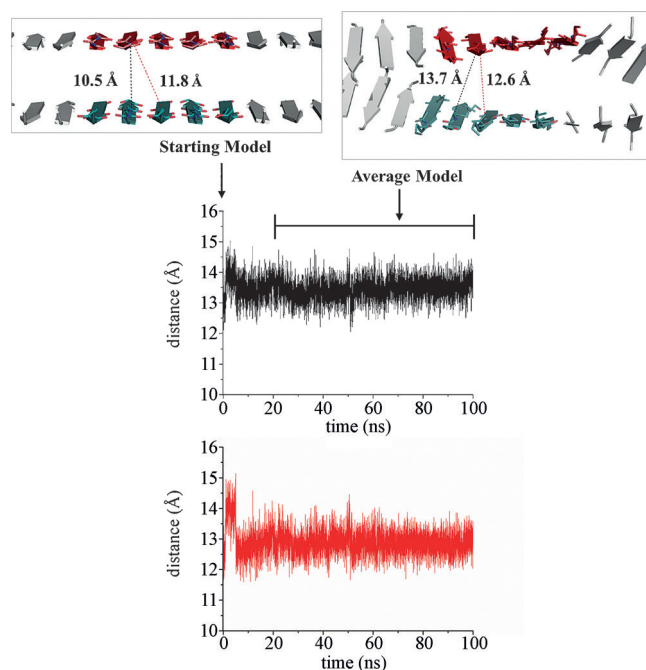


Figure 10. Evolution of the distance between two representative C $^{\alpha}$ atoms of the facing sheets along the trajectory. The values of the monitored distances for both the flat starting model and the twisted average structure are shown in the insets.

atoms belonging to the two distinct β -sheets are on average 10.5 Å (range 9.4–11.6 Å). The modeling in this scaffold of the F6 homopeptide produces some steric hindrance. As a consequence, we observe an increase of the β -sheet separation during the simulation (Figure 10). The shortest distances between C $^{\alpha}$ atoms of the two β -sheets are approximately 12.5 Å. This indicates a close agreement between the intersheet distance of the equilibrated model and the WAXS data. The good agreement between the resulting model and the experimental WAXS data corroborate our assumption that the PEG moiety has a limited impact on PEG₆-F6 structure, which is essentially

dictated by the peptide region. The structural transition occurring in the simulation leads to the staggering of the facing strands of the two β -sheets along the fiber axis.

The examination of the flexibility of this novel state, carried out by computing root mean square fluctuation (RMSF) values, demonstrates that, with the exception of terminal residues within each strand, the backbone atoms are rather rigid (Figure S7a, Supporting Information). A limited level of flexibility is also shown by Phe side chains. Indeed, the flexibility of Phe side chain located in the intersheet dry interface is comparable to the mobility of the backbone atoms (Figure S7b, Supporting Information). Phe side chains of the solvent-exposed interface, although displaying larger RMSF values, still retain a restricted mobility. The limited flexibility of Phe side chains is also highlighted by the analysis of their rotameric states. Each strand presents rather recurrent values of the χ_1 dihedral angle (Figure S8, Supporting Information). All residues within the same strand adopt predominantly the same χ_1 value. Furthermore, strands with all gauche+ (g^+) Phe side chains alternate with strands showing all-*trans* (t) rotameric states. This trend does not depend on the location of the Phe residue in terms of dry interface or exposed surface. The inspection of the Phe side chain interactions clearly indicates that this recurrent rotameric motif plays an important role in the stabilizations of the SH2_ST50_F6 assembly. Indeed, the juxtaposition of alternating anti-parallel F6 strands with side chains presenting either g^+ or t states leads to the formation of staggered π -stacking interactions within the same β -sheet (Figure 11 a). In line with litera-

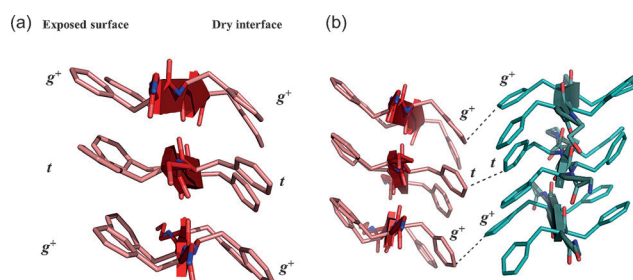


Figure 11. Conformations of the Phe side chains and their interactions at the exposed interface and at the dry interface. The interstrand interaction within the same sheet are reported in panel (a) whereas the intersheet interactions are reported in panel (b). The rotameric states of Phe residues are shown in both panels. The T-shaped interactions established at the dry interface are also indicated in panel (b).

ture classification of these interactions,^[37] the distance between the centers of mass of the stacking aromatic rings is on average close to 5.0 Å. This particular configuration of the Phe side chains within the individual sheets is suitable for the formation of stabilizing interactions at the intersheet level. As shown in Figure 11 b, the dry interface is characterized by the presence of recurrent T-shaped aromatic interactions. These findings provide a clear structural pattern for the stabilization of anti-parallel β -sheets by Phe side chains. They also indicate that individual Phe-rich β -sheets are preorganized to form steric zipper assemblies.

However, Phe side chains, although closely packed through the formation of hydrophobic and steric interactions, do not lead to the interdigitation that frequently characterizes amyloid-like peptides.^[26,35]

Conclusion

Diphenylalanine homodimer has showed stimulating potentiality for the development of novel peptide-based materials. The mechanical, electrical, electrochemical, or optical properties of the supramolecular materials are strongly dependent on the structural organization of the building blocks and on the physicochemical properties of the nanomaterials. A better understanding of how their inner molecular organization governs their self-aggregation process could allow the engineering of novel supramolecular materials with enhanced functionalities. Nevertheless, the literature lacks studies that explain how the supramolecular organization of the material can be affected by chemical modifications, such as the replacement of phenylalanine with naphthylalanine, tyrosine, or tryptophan residues, or the elongation of the aromatic framework. Herein, we showed the effect of elongating the aromatic portion of FF on the aggregation process. The PEG₈-F6 building block is able to self-assemble in water solution after five-fold dilution of a stock solution in HFIP. The structural characterization in solution provides evidence for the high tendency of the aromatic peptide to self-assemble at very low concentration ($\sim 0.01 \text{ mg mL}^{-1}$) in nanostructures with a hydrodynamic diameter of $\sim 60 \text{ nm}$. Moreover, their size does not seem to be affected significantly by the concentration and the time. The spectroscopic characterization of the aggregates, both in solution and in the solid state, clearly indicated an arrangement of the peptide in anti-parallel β -sheets. As expected for β -sheet-rich structures, PEG₈-F6 shows blue photoluminescence both in solution and at the solid state. Structural features of nanostructures were deeply investigated at the atomic- (WAXS), nano- (SAXS), and micro-scale (SEM) to gain a full study of the different hierarchical organization of the aggregates. SEM images indicate that PEG₈-F6 at 2.0 mg mL^{-1} assembles in a sheaf of fibers, each of them formed by small fibers of 65–350 nm width, placed side by side. Beside them, long nanostructures (up to 4000 μm) with high morphological variability (flat or twisted ribbon shape) were observed. The hypothesis that arises from the SEM images is that large and long supramolecular nanostructures are obtained from the aggregation of small fibers. Wide-angle X-ray scattering data, recorded on dried fibers, reveal a typical „cross- β “ diffraction pattern of amyloid-like fibers, with a diffraction peak of 4.8 Å along the meridian, representing the inter-chain distance between the hydrogen-bonded strands, and a diffraction peak of 12.5 Å along the equatorial direction, distinctive of the stacking of β -sheets perpendicularly to the fiber axis. The value of equatorial d -spacing is higher than the value usually expected ($\sim 10 \text{ Å}$). No differences in diffraction pattern were found moving across fiber in the different positions, proving a high lateral homogeneity of the fiber. Present molecular dynamics data suggest that the F6 spine is likely constituted by facing twisted β -sheets separated by a dry interface. This

follows the aggregation scheme experimentally shown for a variety of amyloid-like peptides.^[26] The model is endowed with a remarkable rigidity and stability in the simulation timescale. The intersheet separation observed in these twisted models is in line with the detection in the WAXS data of a strong equatorial reflection at $\sim 12.5 \text{ Å}$. Although the observed twisting of the SH2_ST50_F6 may be biased by a number of factors (limitations of the force field accuracy, omission of the PEG moieties, and reduction of the fiber spine to a pair of sheets), it is suggestive of the presence of long-range regularities in this system that may be experimentally characterized by future SAXS experiments at very small angles. Thanks to their photoluminescence properties, hexaphenylalanine-based nanostructures herein described can be used for the fabrication of novel optoelectronic nanomaterials. However, the high stability and water solubility of these supramolecular aggregates, attributable to the PEG chain, make these materials potentially suitable for applications in nanomedicine for the delivery of bioactive molecules as drugs or contrast agents.

Experimental Section

Materials

Protected N^t-Fmoc-Phe-OH, coupling reagents, and Rink amide MBHA (4-methylbenzhydrylamine) resin, commercially available from Calbiochem-Novabiochem (Laufelfingen, Switzerland), were used. The Fmoc-8-amino-3,6-dioxaoctanoic acid, Fmoc-AdOO-OH, was purchased from Neosystem (Strasbourg, France). All other chemicals commercially available by Sigma-Aldrich (Milan, Italy), Fluka (Bucks, Switzerland), or LabScan (Stillorgan, Dublin, Ireland) were used as received unless otherwise stated. All solutions were prepared by weight with doubly distilled water. The purifications by preparative RP-HPLCs were carried out on a LC8 Shimadzu HPLC system (Shimadzu Corporation, Kyoto, Japan) equipped with a UV lambda-Max Model 481 detector using a Phenomenex (Torrance, CA) C18 column. Elution solvents are H₂O/0.1% TFA (A) and CH₃CN/0.1% TFA (B), from 20 to 80% over 30 min at 20 mL min^{-1} flow rate. Purity and identity of the products were assessed by analytical LCMS analyses by using Finnigan Surveyor MSQ single quadrupole electrospray ionization (Finnigan/Thermo Electron Corporation San Jose, CA), column: C18-Phenomenex eluted with an H₂O/0.1% TFA (A) and CH₃CN/0.1% TFA (B) from 20 to 80% over 15 min at $200 \mu\text{L min}^{-1}$ flow rate.

Synthesis of PEGylated peptide PEG₈-F6

PEGylated peptide PEG₈-F6 was synthesized according to standard solid-phase Fmoc procedures. The Rink amide MBHA resin (substitution 0.65 mmol g^{-1}) was used as the solid-phase support to provide the peptides as C-terminus amides, and synthesis was performed on a scale of 0.2 mmol. The synthesis was carried out in DMF/NMP (1:1, v/v).^[38] Before starting with the elongation of the peptide, the resin was swelled for 30 min. Fmoc deprotection was performed twice (each treatment for 10 min) using 30% (v/v) piperidine in DMF/NMP. The amino acid coupling was achieved by adding 2-fold molar excess of amino acid, mixed with equimolar amounts of 1-hydroxybenzotriazole (HOBt), benzotriazol-1-yl-oxy-tris-pyrrolidino-phosphonium (PyBop), and a 4-fold molar excess of diisopropylethylamine (DIPEA) in DMF/NMP. All couplings were performed twice for 1 h. Four residues of Fmoc-AdOO-OH were se-

quentially coupled as previously described.^[39] Crude peptide was fully cleaved from the resin with TFA (trifluoroacetic acid)/H₂O (95/5 v/v) mixture at room temperature for 2 h. PEGylated peptide was precipitated with ice-cold water and freeze-dried. The purification of the crude products was carried out by RP-HPLC. Mass spectra and ¹H NMR spectrum confirm the products identity.

PEG₈-F6 characterization

$t_R = 14.05$ min, MS (ESI+): m/z : 1480.7 calcd for C₇₈H₁₀₁N₁₁O₁₈: [M+H⁺] = 1480.9; ¹H NMR (CD₃OD) (chemical shifts in δ , CH₃OH as internal standard 3.55) = 7.51–7.42 (m, 30 CH aromatic), 4.86–4.75 (m, 6H, CH Phe α), 3.80 (s, 16H, OCH₂CH₂O), 3.75 (t, 8H, RNH-CH₂CH₂O), 3.65 (s, 8H, OCH₂COR), 3.60 (t, 8H, RNH-CH₂CH₂O), 3.16–2.90 ppm (m, 12H, CH₂ Phe β).

Preparation of PEG₈-F6 solutions

PEG₈-F6 peptide was dissolved in HFIP at 100 mg mL⁻¹.^[40] Subsequently, this solution was ten-fold diluted in water and the organic solvent was removed with N₂ flow. The concentration of the final solution was determined by absorbance on a UV/Vis Thermo Fisher Scientific Inc (Wilmington, Delaware USA) Nanodrop 2000c spectrophotometer equipped with a 1.0 cm quartz cuvette (Hellma) by using a molar absorptivity (ϵ_{257}) of 1170 M⁻¹ cm⁻¹.

Fluorescence studies

Critical aggregate concentration (CAC) of PEG₈-F6 was determined by fluorescence measurements using 8-anilino-1-naphthalene sulfonic acid ammonium salt (ANS) as the fluorescent probe.^[41] Fluorescence spectra were recorded at room temperature by a Jasco Model FP-750 spectrofluorophotometer in a 1.0 cm path length quartz cell. Equal excitation and emission bandwidths (5 nm) were used throughout the experiments with a recording speed of 125 nm min⁻¹ and automatic selection of the time constant. Small aliquots of PEG₈-F6 solutions, at several concentrations, were added to 200 μ L of aqueous solution of ANS (20 μ M). Data analysis was performed on spectra after blank correction. The fluorescence intensity of ANS was followed as a function of the peptide concentration. The CAC values were determined by linear least-squares fitting of the fluorescence emission at 470 nm, upon excitation at 350 nm, versus the hexaphenylalanine concentration.

Circular dichroism

Far-UV CD spectra of the PEG₈-F6 in aqueous solution were collected on a Jasco J-810 spectropolarimeter equipped with a NesLab RTE111 thermal controller unit using a 0.1 mm quartz cell at 25 °C. The spectra were recorded from 280 to 195 nm using samples at several concentrations (10.0, 5.0, 2.5, 1.0, 0.5, and 0.1 mg mL⁻¹). Other experimental settings were: scan speed, 10 nm min⁻¹; sensitivity, 50 mdeg; time constant, 16 s; bandwidth, 1 nm. Each spectrum was obtained by averaging three scans and corrected for the blank contribute. Here θ represents the mean residue ellipticity (MRE), that is, the ellipticity per mole of peptide divided by the number of amino acid residues in the peptide.

FTIR spectroscopy

FTIR spectra of PEG₈-F6 (2.0 mg mL⁻¹) were collected on a Jasco FT/IR 4100 spectrometer (Easton, MD) in an attenuated total reflection (ATR) mode using a Ge single-crystal at a resolution of 4 cm⁻¹. All the spectral data were processed using built-in software. Spec-

tra were collected in transmission mode and then converted in emission. Each sample was recorded with a total of 100 scans with a rate of 2 mm s⁻¹ against a KBr background.

Dynamic light scattering

Mean diameter and diffusion coefficient (D) of supramolecular aggregates were measured by DLS. DLS measurements were carried out using a Zetasizer Nano ZS (Malvern Instruments, Westborough, MA) that employs a 173° backscatter detector. Other instrumental settings were: measurement position (mm) of 4.65; attenuator of 9; temperature of 25 °C; disposable sizing cuvette as the cell. DLS measurements in triplicate were carried out on aqueous samples at 5.0, 2.0, 1.0, 0.5, 0.1, and 0.05 mg mL⁻¹, after room temperature centrifugation at 13,000 rpm for 5 min. Measurements were recorded each week for up to one month.

Congo Red spectroscopic assay

Congo Red (CR) spectroscopy assay was carried out by UV/Vis measurements. A stock solution of CR (3.5 mg in 500 μ L) was freshly prepared in 10 mm phosphate buffer, at pH 7.4 and filtered through 0.2 μ m syringe immediately prior to use. A small aliquot (5 μ L) of this solution was diluted with water at 12.5 μ M final concentration and the UV/Vis spectrum was recorded between 400 and 700 nm at room temperature. 5 or 50 μ L of PEG₈-F6 solution (20 mg mL⁻¹) were added to CR solution to obtain a final peptide concentration of 0.1 or 1.0 mg mL⁻¹. After incubation for 30 min at room temperature, the spectra were recorded and background subtracted using a Congo Red spectrum in phosphate buffer as a reference solution.

CR staining and polarized optical microscopy

A dried film of PEG₈-F6 was prepared by placing 30 μ L of the peptide solution (0.25 wt%) in deionized water onto a glass slide, which was then left to dry at room temperature. The air-dried samples were stained with 25 μ L of CR solution just prepared adding a saturating amount of CR in ethanol containing 20% of NaCl saturated water. After deposition, CR extra solution was detached from the glass slide with a filter paper. Fibers containing CR were prepared, according to the method described below in the wide-angle X-ray scattering section, adding 4 μ L of CR staining solution to 100 μ L of peptide solution (0.25 wt%). Both film and solid fiber were observed under bright-field illumination and between crossed polars by using a Nikon AZ100 microscope.

Scanning electron microscopy

Morphological analysis of the nanostructures was carried out using field emission scanning electron microscope (Nova NanoSem 450-FEI). Samples, at several concentrations (0.05, 0.2, 0.5, 1.0, and 2.0 mg mL⁻¹), were prepared for sequential dilution from a stock solution (20 mg mL⁻¹) obtained as above described. Briefly, the samples were placed on an aluminum stub by using a graphite adhesive tape. A thin coat of gold and palladium was sputtered at a current of 20 mA for 90 s. The sputter-coated samples were then introduced into the specimen chamber and the images were acquired at an accelerating voltage of 2–5 kV, spot 3, through the Everhart Thornley Detector (ETD) and the Through the Lens Detector (TLD).

Wide- and small-angle X-ray scattering

Fiber diffraction WAXS and SAXS patterns were recorded from dried fibers prepared by the stretch-frame method.^[29] Briefly, a droplet (10 μL) of peptide aqueous solution (3 wt%) was suspended between the ends of a wax-coated capillary (spaced 2 mm apart). The droplet was allowed to dry gently at room temperature overnight to obtain oriented fibers. WAXS and SAXS data were collected at the X-ray Microlensing Laboratory (XMI-L@b) equipped with a Fr-E+ SuperBright rotating anode copper anode micro-source ($\text{Cu}_{K\alpha}$, $\lambda = 0.15405$ nm, 2475 W), a multilayer focusing optics (Confocal Max-Flux; CMF 15–105) and a three-pinhole camera (Rigaku SMAX-3000).^[42] For WAXS data collection an image plate (IP) detector with 100 μm pixel size was placed at 10 cm from the sample and calibrated by means of the Si NIST standard reference material (SRM 640b); for SAXS data collection a Triton 20 gas-filled photon counter detector with ~ 200 μm pixel size was placed at 2.2 m from the sample and calibrated by means of silver behenate. A detailed description of the XMI-L@b performances can be found in Altamura et al.^[42] and Sibillano et al.^[43]

Optical spectrofluorometry

Measurements of PL were performed using Jasco Model FP-750 spectrofluorophotometer in a 1.0 cm path length quartz cell. Aqueous PEG₈-F6 nanostructures (10 mg mL⁻¹) were prepared as previously described, diluting HFIP in water. PL was measured on freshly prepared samples excited at 370 or 410 nm.

Fluorescence and confocal microscopy

15 μL of PEG₈-F6 solution at 10 mg mL⁻¹ were deposited on a clean coverslip glass, dried and imaged with fluorescence and confocal microscopies. Immunofluorescence images were taken with a Leica DFC320 video-camera (Leica, Milan, Italy) connected to a Leica DMRB microscope equipped with 10 \times and 40 \times objectives and the Image J Software (National Institutes of Health, Bethesda, MD) was used for analysis. Confocal images were obtained with a Leica TCS-SMD-SP5 confocal microscope ($\lambda_{\text{ex}} = 405$ nm and $\lambda_{\text{em}} = 490$ –510 nm). 0.8 μm -thick optical slices were acquired with a 63 \times or 40 \times /1.4 NA objective.

Molecular modeling and molecular dynamics simulation: Systems and notations

A 3D model for the F6 peptide was generated by using the steric zipper structure of the hexapeptide fragment KLVFFA of the amyloid-beta peptide.^[44] In particular, the coordinates of the polymorph II (Protein Data Bank entry 3OW9) refined at 1.80 \AA resolution were considered (Figure S9a,b, Supporting Information). The asymmetric unit of this structure contains two copies of the peptide arranged as an antiparallel two-stranded β -sheet. Steric zipper pairs of β -sheets were built by using the symmetry operations of KLVFFA structure space groups (C2). The side chains of non-Phe residues of the model were replaced by Phe to generate a 3D structure of F6 (Figure S9c). Models with a different number of β -strands per β -sheet were generated. Following our previous notation^[36,45] these models were denoted as SH_xSTy_F6, in which x and y indicate the number of β -sheets and β -strands per sheet, respectively. Preliminary analyses were conducted on SH2_ST10_F6 and SH2_ST26_F6. More extensive analyses were, however, conducted on SH2_ST50_F6.

Molecular dynamics protocol

MD simulations were performed using the GROMACS software package 4.5.7^[46] with the OPLS-AA force field. The energy of the structures generated by modeling was initially minimized in vacuo. Minimized models were then immersed in triclinic boxes filled with water molecules (TIP4P water model). The number of the water molecules along with other simulation parameters (box dimensions and simulation timescale) for the different systems are reported in Table S1, Supporting Information. Simulations were run by applying periodic boundary conditions. Equilibration of the system was conducted in order to stabilize the temperature (300 K) and the pressure (1 atm.). Energies were initially minimized by fixing the protein atoms and then without restraints. The Particle Mesh Ewald (PME) method (grid spacing of 0.12 nm)^[47] was used to calculate the electrostatic interactions, whereas a cutoff of 10 \AA was applied to treat Lennard–Jones interactions. The LINCS algorithm was used to constrain bond lengths. Trajectory structures were analyzed by using in-house programs, VMD,^[48] and Gromacs routine.^[46] The achievement of an adequate convergence in the MD simulation of SH2_ST50_F6 has been checked by calculating the root-mean-square inner product (RMSIP = 0.82) between the two halves of the equilibrated trajectory (20–60 ns and 60–100 ns).^[49]

Acknowledgements

We are indebted to the Italian Minister for Research (M.I.U.R.) for financial support under FIRB 'RINAME' RBAP114AMK. The authors thank Dr. M. Stornaiuolo for the fluorescence and confocal microscopy analysis. The authors thank L. Zona, G. Sorrentino, and R. Lassandro for technical support.

Keywords: diphenylalanine · molecular dynamics · nanostructures · peptide materials · photoluminescence

- [1] S. I. Stupp, *Nano Lett.* **2010**, *10*, 4783–4786.
- [2] a) S. Fleming, R. V. Uljijn, *Chem. Soc. Rev.* **2014**, *43*, 8150–8177; b) R. de La Rica, H. Matsui, *Chem. Soc. Rev.* **2010**, *39*, 3499–3509.
- [3] M. Reches, E. Gazit, *Science* **2003**, *300*, 625–627.
- [4] L. Adler-Abramovich, E. Gazit, *Chem. Soc. Rev.* **2014**, *43*, 6881–6893.
- [5] X. Yan, P. Zhu, J. Li, *Chem. Soc. Rev.* **2010**, *39*, 1877–1890.
- [6] G. Demirel, N. Malvadkar, M. C. Demirel, *Langmuir* **2010**, *26*, 1460–1463.
- [7] P. Kumaraswamy, R. Lakshmanan, S. Sethuraman, U. M. A. Krishnan, *Soft Matter* **2011**, *7*, 2744–2754.
- [8] J. Ryu, C. B. Park, *Adv. Mater.* **2008**, *20*, 3754–3758.
- [9] L. Adler-Abramovich, N. Kol, I. Yanai, D. Barlam, R. Z. Shneck, E. Gazit, I. Rouso, *Angew. Chem. Int. Ed.* **2010**, *49*, 9939–9942; *Angew. Chem.* **2010**, *122*, 10135–10138.
- [10] M. Wang, L. Du, X. Wu, S. Xiong, P. K. Chu, *ACS Nano* **2011**, *5*, 4448–4454.
- [11] S. Vasilev, P. Zelenovskiy, D. Vasileva, A. Nuraeva, V. Shur Ya, A. L. Kholkin, *J. Phys. Chem. Solids* **2016**, *93*, 68–72.
- [12] a) T. Nikitin, S. Kopyl, V. Shur Ya, Y. V. Kopelevich, A. L. Kholkin, *Phys. Lett. A* **2016**, *380*, 1658–1662; b) A. Handelman, N. Kuritz, A. Natan, G. Rosenman, *Langmuir* **2016**, *32*, 2847–2862.
- [13] A. Handelman, B. Apter, N. Turko, G. Rosenman, *Acta Biomater.* **2016**, *30*, 72–77.
- [14] L. Adler-Abramovich, M. Reches, V. L. Sedman, S. Allen, S. J. B. Tendler, E. Gazit, *Langmuir* **2006**, *22*, 1313–1320.
- [15] J. Ryu, C. B. Park, *Biotechnol. Bioeng.* **2010**, *105*, 221–230.
- [16] C. H. Görbitz, *Chem. Eur. J.* **2001**, *7*, 5153–5159.
- [17] P. Tamamis, L. Adler-Abramovich, M. Reches, K. Marshall, P. Sikorski, L. Serpell, E. Gazit, G. Archontis, *Biophys. J.* **2009**, *96*, 5020–5029.
- [18] T. H. Han, T. Ok, J. Kim, D. O. Shin, H. Ihee, H. S. Lee, S. O. Kim, *Small* **2010**, *6*, 945–951.

- [19] L. Chronopoulou, S. Lorenzoni, G. Masci, M. Dentini, A. R. Togna, G. Togna, F. Bordini, C. Palocci, *Soft Matter* **2010**, *6*, 2525–2532.
- [20] P. Tamamis, L. Adler-Abramovich, E. Gazit, G. Archontis in *From Computational Biophysics to Systems Biology (CBSB08), Vol. 40* (Eds.: U. H. E. Hansmann, J. H. Meinke, S. Mohanty, W. Nadler, O. Zimmermann), John von Neumann Institute for Computing (Jilich), NIC Series, **2008**, pp. 393–396.
- [21] a) E. Mayans, G. Ballano, J. Casanovas, A. Díaz, M. M. Pérez-Madrugal, F. Estrany, J. Puiggali, C. Cativiela, C. Alemán, *Chem. Eur. J.* **2015**, *21*, 16895–16905; b) V. Castelletto, I. W. Hamley, *Biophys. Chem.* **2009**, *141*, 169–174; c) N. Tzokova, C. M. Fernyhough, P. D. Topham, N. Sandon, D. J. Adams, M. F. Butler, S. P. Armes, A. J. Ryan, *Langmuir* **2009**, *25*, 2479–2785; d) N. Tzokova, C. Fernyhough, M. F. Butler, S. P. Armes, A. J. Ryan, P. D. Topham, D. J. Adams, *Langmuir* **2009**, *25*, 11082–11089; e) C. Diaferia, E. Gianolio, P. Palladino, F. Arena, C. Boffa, G. Morelli, A. Accardo, *Adv. Funct. Mater.* **2015**, *25*, 7003–7016; f) C. Diaferia, F. A. Mercurio, C. Giannini, T. Sibillano, G. Morelli, M. Leone, A. Accardo, *Sci. Rep.* **2016**, *6*, 26638.
- [22] L. Adler-Abramovich, D. Aronov, P. Beker, M. Yevnin, S. Stempler, L. Buzhansky, G. Rosenman, E. Gazit, *Nat. Nanotechnol.* **2009**, *4*, 849–854.
- [23] A. Morisco, A. Accardo, E. Gianolio, D. Tesaro, E. Benedetti, G. Morelli, *J. Pept. Sci.* **2009**, *15*, 242–250.
- [24] J. Kong, S. Yu, *Acta Biochim. Biophys. Sin.* **2007**, *39*, 549–559.
- [25] W. E. Klunk, R. F. Jacob, R. P. Mason, *Anal. Biochem.* **1999**, *266*, 66–76.
- [26] D. Eisenberg, M. Jucker, *Cell* **2012**, *148*, 1188–1203.
- [27] a) T. S. Burkoth, T. L. S. Benzinger, D. N. M. Jones, K. Hallenga, S. C. Meredith, D. G. Lynn, *J. Am. Chem. Soc.* **1998**, *120*, 7655–7656; b) T. S. Burkoth, T. L. S. Benzinger, V. Urban, D. G. Lynn, S. C. Meredith, P. Thiyagarajan, *J. Am. Chem. Soc.* **1999**, *121*, 7429–7430.
- [28] a) I. W. Hamley, *Biomacromolecules* **2014**, *15*, 1543–1559; b) V. Castelletto, G. Cheng, S. Fuzeland, D. Atkins, I. W. Hamley, *Soft Matter* **2012**, *8*, 5434–5438.
- [29] M. Sunde, L. C. Serpell, M. Bartlam, P. E. Fraser, M. B. Pepys, C. C. Blake, *J. Mol. Biol.* **1997**, *273*, 729–739.
- [30] A. V. Semenyuk, D. I. Svergun, *J. Appl. Crystallogr.* **1991**, *24*, 537–540.
- [31] A. Handelman, A. Natan, G. Rosenman, *J. Pept. Sci.* **2014**, *20*, 487–493.
- [32] a) L. L. del Mercato, P. P. Pomp, G. Maruccio, A. D. Torre, S. Sabella, A. M. Tamburro, R. Cingolani, R. Rinaldi, *Proc. Natl. Acad. Sci. USA* **2007**, *104*, 18019–18024; b) D. Pinotsi, A. K. Buell, C. M. Dobson, G. S. Kaminski, C. F. Kaminski, *ChemBioChem* **2013**, *14*, 846–850.
- [33] J. R. Lakowicz, *Principles of Fluorescence Spectroscopy*, Springer, New York, **2006**.
- [34] G. Cattani, L. Vogeley, P. B. Crowley, *Nat. Chem.* **2015**, *7*, 823–828.
- [35] M. R. Sawaya, S. Sambashivan, R. Nelson, M. I. Ivanova, S. A. Sievers, M. I. Apostol, M. J. Thompson, M. Balbirnie, J. J. Wiltzius, H. T. McFarlane, A. Ø. Madsen, C. Riekel, D. Eisenberg, *Nature* **2007**, *447*, 453–457.
- [36] L. Esposito, A. Paladino, C. Pedone, L. Vitagliano, *Biophys. J.* **2008**, *94*, 4031–4040.
- [37] G. B. McGaughey, M. Gagné, A. K. Rappé, *J. Biol. Chem.* **1998**, *273*, 15458–15463.
- [38] G. B. Fields, C. G. Fields, *J. Am. Chem. Soc.* **1991**, *113*, 4202–4207.
- [39] A. Accardo, A. Morisco, E. Gianolio, D. Tesaro, G. Mangiapia, A. Radulescu, A. Brandt, G. Morelli, *J. Pept. Sci.* **2011**, *17*, 154–162.
- [40] T. O. Mason, D. Y. Chirgadze, A. Levin, L. Adler-Abramovich, E. Gazit, T. P. J. Knowles, A. K. Buell, *ACS Nano* **2014**, *8*, 1243–1253.
- [41] a) K. S. Birdi, H. N. Singh, S. U. Dalsager, *J. Phys. Chem.* **1979**, *83*, 2733–2737; b) A. Accardo, L. Del Pozzo, G. Mangiapia, L. Paduano, G. Morelli, *J. Pept. Sci.* **2008**, *14*, 903–910.
- [42] D. Altamura, R. Lassandro, F. A. Vittoria, L. De Caro, D. Siliqi, M. Ladisa, C. Giannini, *J. Appl. Crystallogr.* **2012**, *45*, 869–873.
- [43] T. Sibillano, L. De Caro, D. Altamura, D. Siliqi, M. Ramella, F. Boccafroschi, G. Ciasca, G. Campi, L. Tirinato, E. Di Fabrizio, C. Giannini, *Sci. Rep.* **2014**, *4*, 6985.
- [44] J. P. Colletier, A. Laganowsky, M. Landau, M. Zhao, A. B. Soriaga, L. Goldschmidt, D. Flot, D. Cascio, M. R. Sawaya, D. Eisenberg, *Proc. Natl. Acad. Sci. USA* **2011**, *108*, 16938–16943.
- [45] a) L. Esposito, C. Pedone, L. Vitagliano, *Proc. Natl. Acad. Sci. USA* **2006**, *103*, 11533–11538; b) A. De Simone, L. Esposito, C. Pedone, L. Vitagliano, *Biophys. J.* **2008**, *95*, 1965–1973.
- [46] D. Van Der Spoel, E. Lindahl, B. Hess, G. Groenhof, A. E. Mark, H. J. Berendsen, *J. Comput. Chem.* **2005**, *26*, 1701–1718.
- [47] T. A. Darden, D. M. York, L. G. Pedersen, *J. Chem. Phys.* **1993**, *98*, 10089–10092.
- [48] a) W. Humphrey, A. Dalke, K. Schulten, *J. Mol. Graph.* **1996**, *14*, 27–33.
- [49] a) A. Amadei, A. B. Linssen, H. J. Berendsen, *Proteins Struct. Funct. Bioinf.* **1993**, *17*, 412–425; b) A. Merlino, L. Vitagliano, M. A. Ceruso, L. Mazzarella, *Proteins Struct. Funct. Bioinf.* **2003**, *53*, 101–110.

Received: August 30, 2016

Published online on October 5, 2016



Gadolinium containing telechelic PEG-polymers end-capped by diphenylalanine motives as potential supramolecular MRI contrast agents

Carlo Diaferia,^a Eliana Gianolio,^b Antonella Accardo^a and Giancarlo Morelli^{a*}

Telechelic PEG-polymers end-capped by diphenylalanine (FF) motives and containing a DOTA-Gd complex, bound on a lysine side chain at the centre of peptide moiety, are studied for their assembling properties and for the relaxometric behavior. The observed variations in terms of relaxivity are correlated to the assembling properties of the aggregates by using several techniques: fluorescence, Circular Dichroism (CD) and Fourier Transform Infrared (FTIR) for aggregation tendency and secondary structure determination; Dynamic Light Scattering (DLS) and Transmission Electron Microscopy (TEM) for morphological definition. Self-aggregation in water solution of the peptide conjugates, due to interaction of the phenylalanine frameworks, starts at concentration around 1 mg/ml with a first evidence of the coexistence of fibrillary networks and hydrogels at 10 mg/ml. Definitive presence of well-structured fibrillary networks, dominated by an antiparallel β -sheet arrangement, occurs at 50 mg/ml. At the latter concentration relaxivity values measured at 20 MHz and 298 K, are around $11 \text{ mM}^{-1} \text{ s}^{-1}$, in line with a possible use of the these aggregates as MRI contrast agents. Copyright © 2016 European Peptide Society and John Wiley & Sons, Ltd.

Additional supporting information may be found in the online version of this article at the publisher's web site.

Keywords: oligo-phenylalanines; telechelic polymers; MRI contrast agents; nanofibers; self-assembling

Introduction

The self-assembling of hydrophobic, amphiphilic, and aromatic peptides is a promising route for the obtainment of new nanomaterials displaying a wide range of properties and applications [1–3]. Peptide-based self-assembled compounds organized in a high ordered architecture are able to give new functional materials that open application in emerging fields such as optical devices [4], artificial photosynthesis [5], rechargeable batteries [6], biosensors/chips [7], coating for tissue engineering and cell adhesion [8], and healthcare (regenerative medicine and drug delivery) [8,9].

However, the knowledge of the forces that permit to obtain an ordered organization of the nanostructure at micro-scale and nano-scale could help in projecting new peptide based materials for more attractive applications.

Peptide materials based on diphenylalanine (FF) motif [10] and all its analogues (Fmoc-FF, Fmoc-FFF, Boc-FFF, FFFF, Fmoc-FFFF, and polymeric polyethylene oxide, PEO, and polyethylene glycol, PEG conjugates) have been strongly studied for their ability to give a wide range of structures (nanotubes, nanowires, nanofibrils, spherical vesicles, and organogels) with physicochemical properties suitable for several applications in the earlier mentioned emerging fields [11–13]. Many studies reported in literature are principally focused on clarifying the physicochemical aspects responsible for array stability in these nanostructures [14–16] and on the study of relationship between the structural organization of the building blocks, the preparation method of the samples and the physicochemical properties of the nanomaterials [17,18].

However, only few studies have been devoted in the investigation of FF aggregates for biomedical applications, essentially due to their intrinsic low water solubility [19]. To increase their solubility, hydrophilic polymers of appropriate lengths can be bound to the aromatic framework.

We have recently developed new potential Magnetic Resonance Imaging (MRI) contrast agents (CAs) based on oligo-phenylalanine aggregates derivatized with oxoethylene linkers and a chelating agent (DTPA or DOTA) able to complex the paramagnetic gadolinium(III) ion [20]. In particular, tetraphenylalanine peptides modified on the N-terminus with the 21-amino-4,7,10,13,16,19-hexaaxaheneicosanoic acid [Ahoh-OH, (L_6)] spacer and with the DOTA(Gd) or DTPA(Gd) complexes [DOTA(Gd)- L_6 -F4 and DTPA(Gd)- L_6 -F4] self-assemble in water solution, also at low concentration, giving well soluble nanoaggregates. Single peptides in the aggregates are in a beta-sheet conformation with an antiparallel alignment along the fiber axis, and aggregating forces essentially are due to the interactions between phenylalanine aromatic frameworks. Both compounds have been also fully

* Correspondence to: Giancarlo Morelli, Department of Pharmacy, Research Centre on Bioactive Peptides (CIRPeB), University of Naples "Federico II", Via Mezzocannone 16, 80134-Naples, Italy. E-mail: gmorelli@unina.it

^a Department of Pharmacy, Research Centre on Bioactive Peptides (CIRPeB), University of Naples "Federico II", Via Mezzocannone 16, 80134, Naples, Italy

^b Department of Molecular Biotechnologies and Health Science, University of Turin, Via Nizza 52, 10125, Turin, Italy

characterized for their relaxometric properties and cell uptake and internalization in view of a potential use as MRI CAs. Even if the relaxometric parameters are in line with other examples of Gd (III) based supramolecular (micelles or liposomes) CAs [21,22], and more performing respect to classical low molecular weight CAs, the τ_R values extracted from the fitting procedure are quite short if compared with those usually found for nano-sized aggregates (1–30 ns) [20]. The low τ_R values we found can be attributed to the occurrence of a quite fast internal motility of the Gd-complexes along the linker spacer with respect to the overall fibril-like structures.

Here, we report the design and the synthesis of a novel supramolecular CA based on the self-assembling of FF-AdOO-Lys(DOTA-Gd)-AdOO-FF [FF-DOTA(Gd)-FF], a telechelic-polymer end-capped by FF motives (Figure 1), in which the Gd-complex is placed at

the centre of F4-motive. The objective of this study is aimed to evaluate how the relaxivity properties of the self-assembled CA can be affected by the different position having the gadolinium complex in the aromatic framework. The effect of the phenylalanine chirality on assembled structure and therefore on the relaxivity properties, are also evaluated by replacing two L-Phe with two D-Phe residues at the N-terminus [ff-DOTA(Gd)-FF]. On the basis of the literature, the building block based on the D-amino acid analogue of the FF dipeptide should self-assemble into highly persistent discrete nanotubes having the same structural features as the corresponding L-amino acid peptide [23]. The observed variations in terms of relaxometric performances are analyzed and correlated to the structural morphology of the aggregate using several techniques: fluorescence, Circular Dichroism (CD), and Fourier Transform Infrared (FTIR) spectroscopies for aggregation

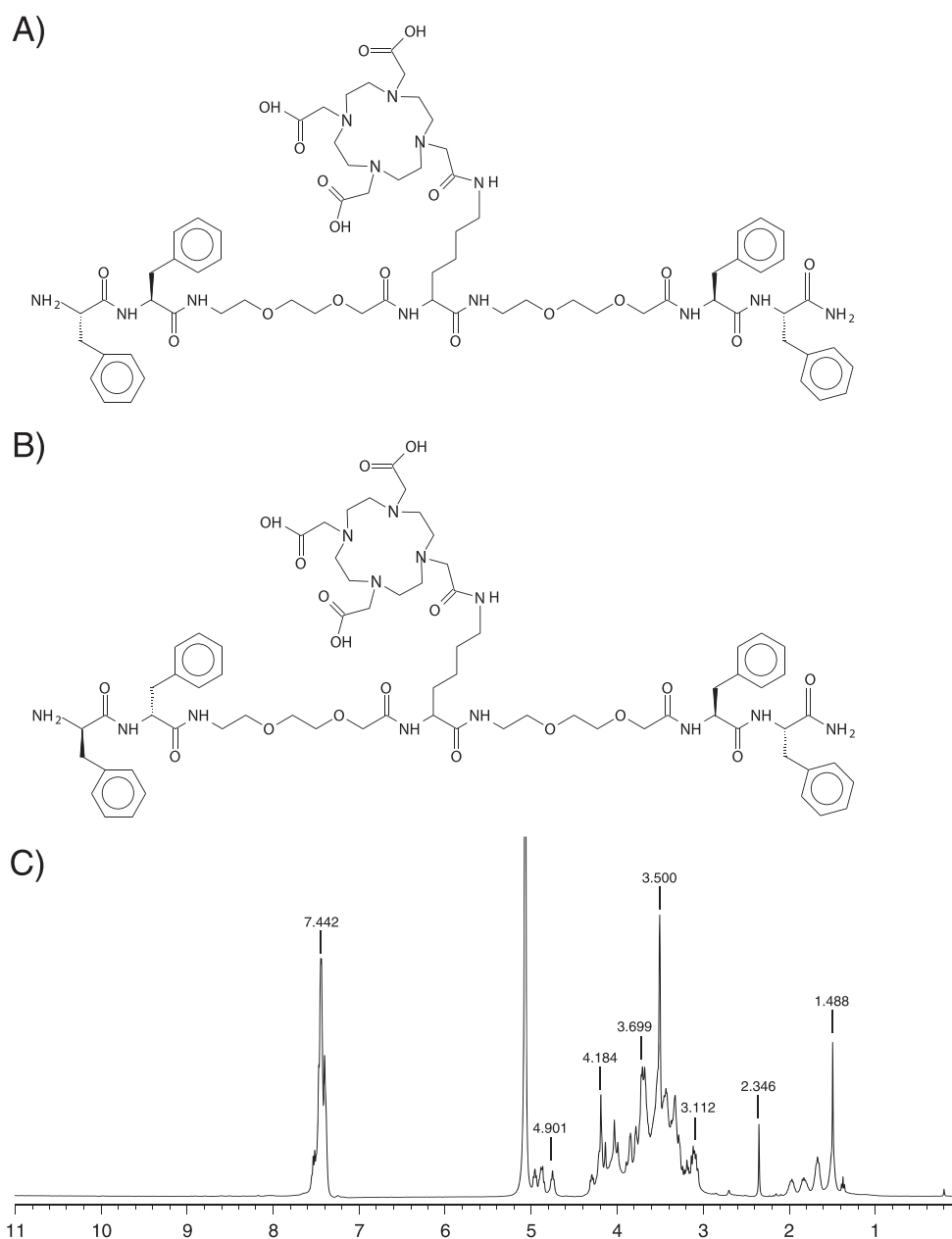


Figure 1. Schematic representation of (A) FF-DOTA-FF and (B) ff-DOTA-FF. (C) ¹H-NMR spectrum of FF-DOTA-FF registered at 600 MHz in CD₃OD.

tendency and secondary structure determination; Dynamic Light Scattering (DLS) and Transmission Electron Microscopy (TEM) for morphological definition.

Materials and Method

Protected N^α-Fmoc-amino acid derivatives, coupling reagents, and Rink amide MBHA (4-methylbenzhydrylamine) resin were purchased from Calbiochem-Novabiochem (Laufelfingen, Switzerland). The Fmoc-8-amino-3,6-dioxaoctanoic acid (Fmoc-AdOO-OH) was purchased from Neosystem (Strasbourg, France). DOTA(OtBu)₃-OH chelating agent was purchased from Chemateck (Dijon, France). All other chemicals were commercially available by Sigma-Aldrich or Fluka (Bucks, Switzerland) or LabScan (Stillorgan, Dublin, Ireland) and were used as received unless otherwise stated. All solutions were prepared by weight with doubly distilled water. Preparative RP-HPLCs were carried out on a LC8 Shimadzu HPLC system (Shimadzu Corporation, Kyoto, Japan) equipped with a UV lambda-Max Model 481 detector using Phenomenex (Torrance, CA) C18 column. Elution solvents are H₂O/0.1% trifluoroacetic acid (TFA) (A) and CH₃CN/0.1% TFA (B), from 5% to 70% over 30 min at 20 ml min⁻¹ flow rate. Purity and identity were assessed by analytical LC-MS analyses by using Finnigan Surveyor MSQ single quadrupole electrospray ionization (Finnigan/Thermo Electron Corporation San Jose, CA), column: C18-Phenomenex eluted with an H₂O/0.1% TFA (A) and CH₃CN/0.1% TFA (B) from 5% to 70% over 15 min at 200 μL min⁻¹ flow rate.

Synthesis of peptide derivative

Peptide conjugates were synthesized by using standard solid-phase 9-fluorenylmethoxycarbonyl (Fmoc) procedures [24]. The Rink amide MBHA resin (substitution 0.65 mmol g⁻¹) was used as the solid phase support to provide the peptides as C-terminus amide, and synthesis was performed on a scale of 0.2 mmol. The resin was swelled in dimethylformamide (DMF) for 30 min and the Fmoc deprotection reaction was performed twice with 30% piperidine in DMF. The amino acid coupling was achieved by adding twofold molar excess of amino acid, mixed with equimolar amounts of 1-hydroxybenzotriazole (HOBt), benzotriazol-1-yl-oxy-tris-pyrrolidino-phosphonium (PyBop), and fourfold molar excess of diisopropylethylamine (DIPEA) in DMF. All couplings were performed twice for 1 h. Fmoc-AdOO-OH ethoxylic spacer was coupled as previously described [21,25]. DOTA(OtBu)₃-OH was coupled to the Lys side chain after selective removal of Mtt protecting group from the lysine epsilon amine function. Peptide-DOTA derivatives were fully deprotected and cleaved from the resin with the TFA/TIS (triisopropylsilane)/H₂O (92.5/5.0/2.5) mixture for 2 h at room temperature. Peptide conjugates were precipitated with ice-cold ethyl ether, dissolved in H₂O/CH₃CN, and lyophilized. Purification of the crude products was carried out by RP-HPLC. Mass spectra confirm the product identities. ¹H-NMR spectra, registered on Varian 600 MHz, present identical patterns for both compounds, with principal signals as reported below.

FF-AdOO-Lys(DOTA)-AdOO-FF [*FF-DOTA-FF*] and *ff-AdOO-Lys(DOTA)-AdOO-FF* [*ff-DOTA-FF*]

¹H-NMR (CD₃OD) (chemical shifts in δ, CH₃OH as internal standard 3.55) = 7.51–7.42 (m, 20 CH aromatic), 4.98–4.76 (m, 4H, CH Phe α), 4.3 (dd, 1H, CH Lys α), 3.72 (s, 12H, OCH₂CH₂O), 3.70 (s, 6H, R₂NCH₂COOH), 3.68 (t, 4H, RNH-CH₂CH₂O), 3.65 (s, 4H, OCH₂COR),

3.45 (s, 16H, R₂N-CH₂CH₂NR₂), 3.40–3.36 (m, 2H, R₂NCH₂CONH), 3.36–3.25 (m, 8H, CH₂ Phe β), 3.27–3.20 (dd, 2H, R₂N-CH₂CH₂NR₂), 3.1 (m 2H, CH₂ Lys ε), 1.90 (m, 2H, CH₂ Lys β), 1.6 (m, 2H, CH₂ Lys δ), 1.45 (m, 2H, CH₂ Lys γ).

Retention time, R_t = 12.65 min; MS (ESI+): m/z 1407.5 calcd. For C₇₀H₉₉N₁₃O₁₈: [M+H⁺] = 1408.5

Preparation of Gadolinium Complex

The complexation of gadolinium(III) ions to the DOTA containing peptide conjugate has been carried out by adding 1 : 1 molar ratio of GdCl₃ to the aqueous solutions of the DOTA derivatives at neutral pH and room temperature. The amount of residual free Gd³⁺ ions was assessed by the orange xylenol UV method [26] and removed by complexing it upon addition of the corresponding amount of each ligand.

Preparation of Peptide Solutions

Peptide solutions were prepared by dissolving the lyophilized powder in double distilled water and the concentration was experimentally determined by absorbance on UV-Vis Thermo Fisher Scientific Inc (Wilmington, Delaware USA) Nanodrop 2000c spectrophotometer equipped with a 1.0 cm quartz cuvette (Hellma) using a molar absorptivity (ε₂₅₇) of 780 M⁻¹ cm⁻¹.

Water Proton Relaxation Measurements

The proton 1/T₁ nuclear magnetic relaxation dispersion (NMRD) profiles (field dependence of the longitudinal water proton relaxation rates) were measured at 25 °C on a fast field-cycling Stelar relaxometer over a continuum of magnetic field strengths from 0.00024 to 0.47 T (corresponding to 0.01–20 MHz proton Larmor frequencies). The relaxometer operates under computer control with an absolute uncertainty in 1/T₁ of ± 1%. Additional data points in the range 21.5–70 MHz were obtained on the Stelar Spinmaster spectrometer. The temperature was controlled with a Stelar VTC-91 air-flow heater equipped with a copper constantan thermocouple (uncertainty 0.1 °C). The concentration of the solutions used for the relaxometric characterization was determined according to a previously reported relaxometric method [27].

Fluorescence Studies

The values of critical aggregate concentration (CAC) were obtained by fluorescence measurements. Fluorescence spectra were recorded at room temperature on a Jasco Model FP-750 spectrofluorophotometer in a 1.0 cm path length quartz cell. Equal excitation and emission bandwidths (5 nm) were used throughout the experiments with a recording speed of 125 nm min⁻¹ and automatic selection of the time constant. The CAC values were measured by using 8-anilino-1-naphthalene sulfonic acid ammonium salt (ANS) as the fluorescent probe [28,29]. Small aliquots of peptide conjugate aqueous solutions, as free bases or as gadolinium complexes, were added to a fixed volume (1.0 ml) of ANS (20 μM) dissolved in water. Final spectra, to be used for calculations, were obtained after blank correction and adjustment for dilution. The intensity was followed as a function of the peptide concentration. The CAC values were determined by linear least-squares fitting of the fluorescence emission at 460 nm, upon excitation at 350 nm versus the oligo-phenylalanine concentration lower and higher than the change of slope, as previously reported [20,30].

Dynamic Light Scattering

Mean diameter and diffusion coefficient (D) of oligo-phenylalanine nanostructures were measured by DLS using a Zetasizer Nano ZS (Malvern Instruments, Westborough, MA) that employs a 173° backscatter detector. Other instrumental settings were: measurement position (mm) of 4.65; attenuator of 8; temperature of 25°C ; disposable sizing cuvette as cell. Each measurement was performed in triplicate on aqueous samples at 10.0 mg/ml, after centrifugation at 13 000 rpm for 5 min.

Transmission Electron Microscopy Images

Transmission electron microscopy observations were performed with a transmission electron microscope FEI TECNAI G12 Spirit-Twin (LaB6 source) equipped with a bottom mounted FEI Eagle-4 k CCD camera (Eindhoven, The Netherlands), operating with an acceleration voltage of 120 kV. (LaMest Pozzuoli, Italy). A droplet of the sample solution (10 mg/ml) was placed onto a 400 mesh holey-carbon coated copper grid, air-dried for 1 h, and then negatively stained with phosphotungstic acid in water solution (1 wt%). Tomography holder with FEI Eagle 4 K CCD camera and Xplore3D software were used to obtain digital images.

Circular Dichroism

Far-UV CD spectra of the peptide conjugates in aqueous solution were collected at room temperature on a Jasco J-810 spectropolarimeter equipped with a NesLab RTE111 thermal controller unit using a 0.1 mm quartz cell at 25°C . The spectra of samples at several concentrations ranged between 0.5 and 20 mg/ml were recorded from 280 to 195 nm. Other experimental settings were: scan speed, 10 nm min^{-1} ; sensitivity, 50 mdeg; time constant, 16 s; bandwidth, 1 nm. Each spectrum, run in duplicate, was obtained by averaging three scans, corrected for the blank and adjusted for dilution. Ellipticities are reported as the mean residue ellipticity (MRE), which is the ellipticity per mole of peptide divided by the number of amino acid residues in the peptide.

Fourier Transform Infrared Spectroscopy

Fourier transform infrared spectra of samples, as free bases and as Gd-complexes at 10 mg/ml, were collected on a Jasco FT/IR 4100 spectrometer (Easton, MD) in an attenuated total reflection (ATR) mode and using a Ge single-crystal at a resolution of 4 cm^{-1} . All the spectral data were processed using built-in software. Spectra were collected in transmission mode and then converted in emission. Each sample was recorded with a total of 100 scans with a rate of $2\text{ mm}\cdot\text{s}^{-1}$ against a KBr background.

Results

Synthesis

Schematic representation of FF-AdOO-Lys(DOTA-Gd)-AdOO-FF [FF-DOTA(Gd)-FF] peptide conjugate and its analogue ff-AdOO-Lys(DOTA-Gd)-AdOO-FF [ff-DOTA(Gd)-FF] is reported in Figure 1A and 1B. Peptide synthesis of the two gadolinium free compounds was performed by using solid phase methods as reported in Scheme 1 in supporting information. In agreement with our previous synthesis of F4-conjugate, Rink amide MBHA resin, which releases peptide adducts as amide on the C-terminus, was used. After the coupling of two phenylalanine residues and of

Fmoc-AdOO-OH ethoxylic spacer on the solid support, a lysine residue orthogonally protected with Mtt on the epsilon amino function was added. The removal of the Mtt protecting group allowed introduction of DOTA(OtBu)₃-OH on the Lys side chain. The synthesis was completed by introducing the second ethoxylic spacer and the other two phenylalanine residues; therefore, the peptide-DOTA derivatives were fully deprotected, cleaved from the resin and purified by RP-HPLC. Purity (>95%) and identity of the products were confirmed by HPLC and mass spectra. $^1\text{H-NMR}$ studies were also performed in CD_3OD solution at 600 MHz and the mono-dimensional spectrum is reported in Figure 1C. The complexation of gadolinium(III) ions to the DOTA containing peptide conjugates to obtain FF-DOTA(Gd)-FF and ff-DOTA(Gd)-FF has been carried

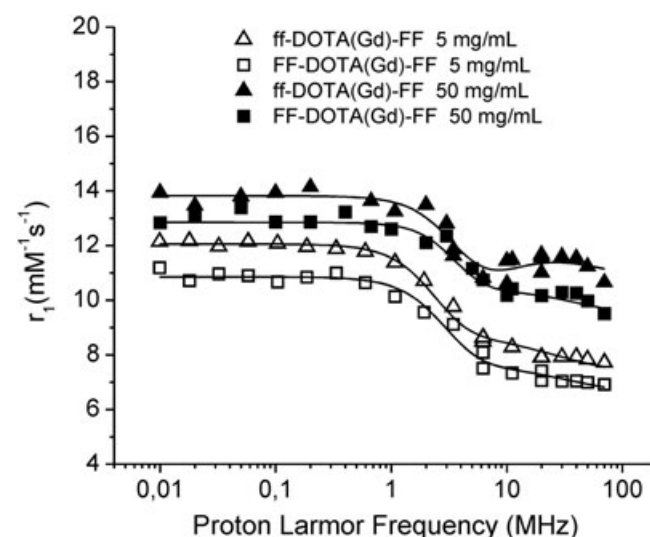


Figure 2. The magnetic-field dependence of the relaxivity (r_1) measured over an extended range of magnetic field strengths (from 0.01 to 70 MHz). The nuclear magnetic relaxation dispersion (NMRD) profiles were obtained for the aqueous suspensions of FF-DOTA(Gd)-FF at 5 mg/ml (\square) and 50 mg/ml (\blacksquare) and ff-DOTA(Gd)-FF at 5 mg/ml (\triangle) and 50 mg/ml (\blacktriangle). The temperature was set to 298 K and data were normalized to 1 mM concentration of Gd^{3+} .

Table 1. Main relaxometric parameters derived from fitting of NMRD profiles reported in Figure 2.^a

System		r_{1p} ($\text{mM}^{-1}\text{s}^{-1}$)	Δ^2 (s^{-2}) ^b	τ_V (ps) ^c	τ_{s0} (ps) ^d	τ_R (ps) ^e
LLLL isomer	monomer	7.1	1.66×10^{19}	32.8	153	190
	aggregate	10.1	1.86×10^{19}	41.0	109	270
LLDD isomer	monomer	7.9	1.06×10^{19}	41.7	188	227
	aggregate	11.5	2.21×10^{19}	35.0	108	341

^aOn carrying out the fitting procedure, some parameters were fixed to reasonable values: $r_{\text{Gd-H}}$ (distance between Gd and protons of the inner sphere water molecule) = 3.1 Å; a (distance of minimum approach of solvent water molecules to Gd^{3+} ion) = 3.8 Å; D (solvent diffusion coefficient) = $2.2 \times 10^{-5}\text{ cm}^2\text{ s}^{-1}$.

^bSquared mean transient zero-field splitting (ZFS) energy.

^cCorrelation time for the collision-related modulation of the ZFS Hamiltonian.

^dElectronic relaxation time at zero field (calculated as $1/\tau_{s0} = 12\Delta^2 \times \tau_V$)

^eReorientational correlation time.

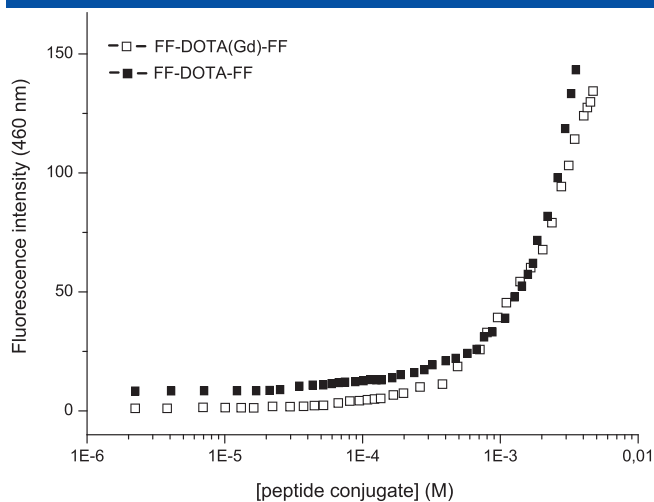


Figure 3. (A) Fluorescence intensity emission of ANS fluorophore at 470 nm versus concentration of FF-DOTA-FF as free basis and as gadolinium complex. CAC values are established from the break point; (B) DLS intensity profiles of FF-DOTA(Gd)-FF at 5 mg/ml.

out by adding equimolar amounts of GdCl_3 to the aqueous solutions of the DOTA derivatives at neutral pH and room temperature, as already reported [25].

Relaxivity Measurements

The relaxivity of a Gd-containing system, which is directly related to its efficacy as potential MRI contrast agent, depends on the complex interplay of structural, dynamic, and electronic parameters [31]. At the frequencies most commonly used in commercial tomographs (20–60 MHz), r_{1p} is generally determined by the reorientational correlation time (τ_R) of the chelate so that high molecular weight systems display higher relaxivity. For this reason, a wide range of high-molecular weight supramolecular systems, including dendrimers [32], micelles and liposomes [33], proteins [34], gold [35], and silica [36] nanoparticles, have been applied as slowly moving carriers for Gd(III)-complexes. The analysis of the magnetic field dependence of the relaxivity, obtained through

the registration of the NMRD profiles, allows the determination of the principal parameters characterizing the relaxivity of a Gd(III) chelate. The NMRD profiles of FF-DOTA(Gd)-FF and ff-DOTA(Gd)-FF, measured at 50 and 5 mg/ml concentrations, are reported in Figure 2. From a qualitative point of view, the shape of the profiles gives information on the aggregation state of the system: low molecular weight Gd-complexes, in fact, show NMRD profiles with a dispersion in the region 1–10 MHz, while a characteristic peak of relaxivity appears, in the region of proton Larmor frequencies 10–70 MHz, in the case of high molecular weight Gd-containing systems. Inspection into Figure 2 reveals that both FF-DOTA(Gd)-FF and ff-DOTA(Gd)-FF are mostly in monomeric form at a concentration of 5 mg/ml, while, at a concentration ten times higher, the aggregation process is definitively completed, particularly in the case of ff-DOTA(Gd)-FF where the high field relaxivity peak is better evidenced. Data were fitted to the conventional Solomon-Bloembergen-Morgan theory [37,38] and the relative fitting parameters are reported in Table 1. The high field relaxivity of the two complexes are quite similar, being, at 20 MHz and 298 K, 10.1 and 11.5 $\text{mM}^{-1} \text{s}^{-1}$ in the aggregated form and 7.1 and 7.9 $\text{mM}^{-1} \text{s}^{-1}$ in the monomeric form, for FF-DOTA(Gd)-FF and ff-DOTA(Gd)-FF, respectively. The τ_R values found for the two complexes reflect the slight increase in relaxivity passing from LLLL isomer to the DLLL one.

Structural Characterization

Critical aggregation concentration values of peptide conjugate FF-DOTA-FF and of its corresponding Gd-complex were determined using the fluorescence spectroscopy. ANS is a well-known fluorescent probe able to emit between 460 and 480 nm only when immersed in a hydrophobic environment, such as in the hydrophobic core of micelles [39]. On the contrary, no fluorescence is observed for ANS in water solution. Upon titration of ANS (20 μM in cuvette) with increasing amounts of our peptide conjugates a distinctive emission peak at 460 nm appears. The CAC values have been determined from the graphical break points of the plot in Figure 3A, in which is reported the variation of the ANS fluorescence intensity as function of peptide concentration. The CAC values of FF-DOTA-FF peptide conjugate and its Gd-complex are $7.7 \cdot 10^{-4}$ M (1.1 mg/ml) and $5.8 \cdot 10^{-4}$ M (0.9 mg/ml), respectively.

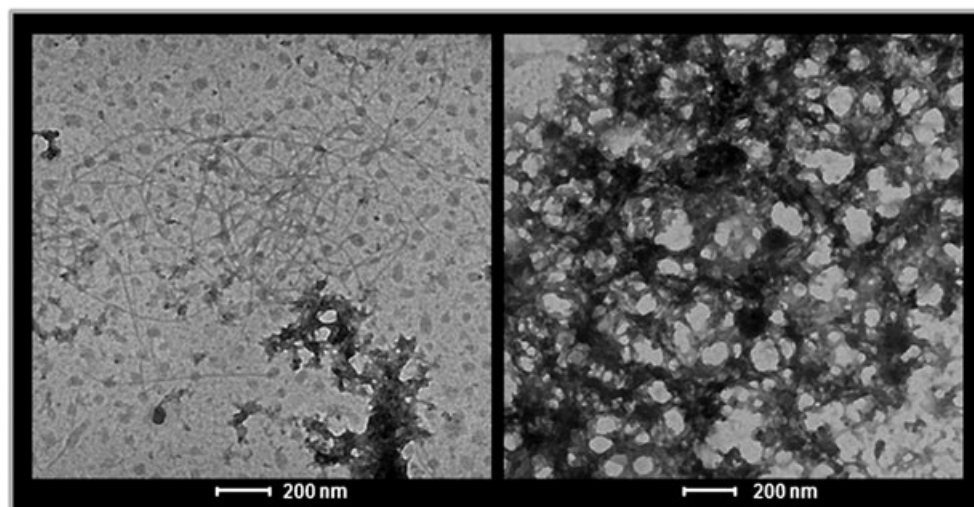


Figure 4. Selected TEM images for FF-DOTA(Gd)-FF at 10.0 mg/ml.

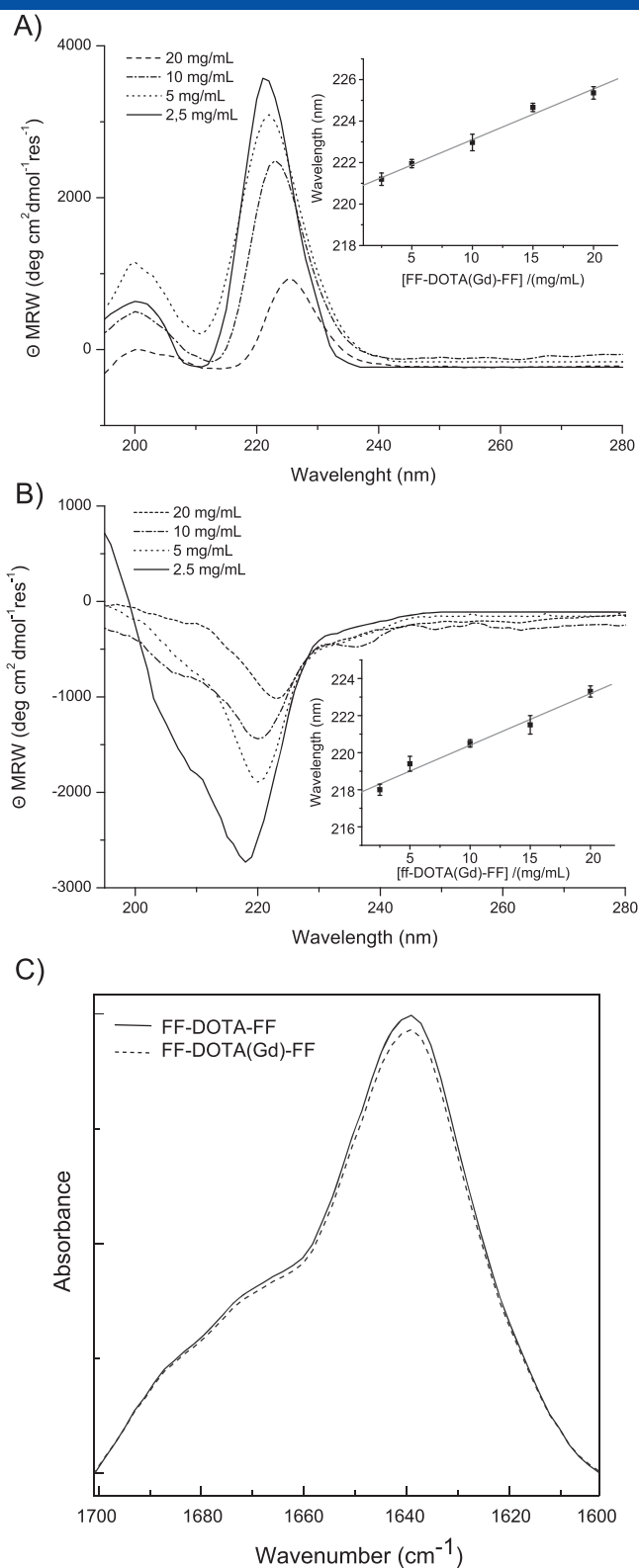


Figure 5. Selected Far-UV CD spectra of (A) FF-DOTA-FF and of (B) ff-DOTA-FF in a concentration range of 2.5–20 mg ml⁻¹. Spectra are recorded between 280 and 195 nm. In the insert it is reported the variation of the wavelength as function of the peptide concentration. (C) FTIR amide I region for FF-DOTA-FF and FF-DOTA(Gd)-FF.

The same values were found for ff-DOTA-FF and ff-DOTA(Gd)-FF analogues (Figure S1). Self-assembled aggregates were further

characterized from the structural and morphological point of view. Mean diameters and diffusion coefficients of the gadolinium self-assembled CAs in water solution were measured by DLS at 10 mg/ml. The intensity profile of FF-DOTA(Gd)-FF, reported in Figure 3B shows a mono-modal distribution due to translational diffusion process of aggregate (Figure S2) with an apparent translational diffusion coefficient $D = 2.2 \times 10^{-12} \text{ m}^2 \text{ s}^{-1}$. Through the Stokes-Einstein equation, we calculate a mean diameter of $\sim 230 \text{ nm}$, which is compatible with supramolecular aggregates. The morphology of the self-assembled nanostructures assessed by TEM is reported in Figure 4 and S3. Images of the Gd-complex in water solution at 10 mg/ml⁻¹ show coexistence of fibrillary networks.

Secondary Structure

The secondary structure of the peptide conjugates in water solution was achieved by CD and FTIR spectroscopies (Figure 5). CD measurements of the peptides were recorded between 280 and 195 nm at several concentrations in 2.5–20 mg/ml range and spectra are reported in Figure 5A. CD spectrum of FF-DOTA(Gd)-FF, recorded at 2.5 mg/ml, show two maxima at 202 and 221 nm. These maxima can be attributed to the stacking of the aromatic side chains. The main maximum at 221 nm undergoes to a red-shift as function of the concentration, indicating an increase of the β -sheet content. In Figure 5B, CD spectrum of ff-DOTA(Gd)-FF at 2.5 mg/ml reveals a minimum at 218 nm, consistent with a substantial β -sheet content. As for FF-DOTA(Gd)-FF analogue, a progressive red-shift of the minimum, due to the increase of concentration, was observed. Further information on the secondary structure adopted by peptide conjugates and their Gd-complexes was obtained investigating the amide I region of FTIR spectra in aqueous solution (10 mg/ml). FTIR spectra of LLLL isomer and DDLL one showed a similar profile, with very slight differences between the free bases and the Gd-complexes. From the inspection of the spectra of FF-DOTA-FF and FF-DOTA(Gd)-FF, reported in Figure 5C, it is possible to detect with three peaks at 1637, 1674, and 1680 cm⁻¹. The peak at 1674 cm⁻¹ is associated with residual trifluoroacetate counterions, deriving from the peptide chromatographic purification. Instead, both 1637 and 1680 cm⁻¹ are indicative of β -sheet formation with an antiparallel orientation [40]. CD and FTIR results, together with TEM images, indicate the ability of the peptide Gd-complex to self-aggregate in fibrillary and intricate network dominated by an antiparallel β -sheet arrangement.

Discussion

Analysis of the results here described allows several interesting observations regarding the synthesized telechelic-polymers end capped by FF-motives. FF-DOTA(Gd)-FF peptide contains a hydrophilic gadolinium complex as central core of a symmetric telechelic polymer decorated with hydrophobic FF end groups that, thanks to their high tendency to associate via non covalent interactions, promote self-assembly phenomena. This peptide conjugate has been designed with the idea to confer higher rigidity to the DOTA(Gd) complex with respect to the already studied tetraphenylalanine DOTA(Gd)-L₆-F₄, in which the chelating agent is anchored to a long and flexible oxoethylene linker. The two phenylalanine residues on the N and C termini of the lysine residue bearing the gadolinium complex should guarantee aggregating properties for the final adducts. In order to investigate the effect of the phenylalanine

containing Phe in D configuration, the aromatic framework composed of four Phe residues is interrupted by the -AdOO-Lys[DOTA(Gd)]-AdOO- motif. At high concentration, it is feasible that a folding of the peptide backbone occurs as reported in Figure 6. This folding should favor the approach of phenyl rings of the C and N termini and permits their T-shape staking. As suggested by CD and FTIR data, the peptide conjugates interact with an antiparallel β -arrangement and the Gd-DOTA complexes point far from the spine of the aggregate.

Conclusions

Self-aggregation of the telechelic-polymer end-capped by FF motives in water solution starts at concentration around 1 mg/ml with a first evidence of the coexistence of fibrillary networks and long hydrogels at 10 mg/ml and definitive presence of well-structured fibrillary and intricate networks dominated by an antiparallel β -sheet arrangement at 50 mg/ml. At the latter concentration relaxivity values measured at 20 MHz and 298 K, are around $11 \text{ mM}^{-1} \text{ s}^{-1}$, in line for a possible use of these aggregates as MRI CAs. However, these peptide conjugates, in which the Gd-complex is placed at the centre of F4-motive show lower relaxivity values with respect to DOTA(Gd)-tetraphenylalanine conjugates previously published [20]. The decrease of the relaxivity can be directly related to the τ_R values, which are affected both by the rigidity and the size of the gadolinium based CA. In principle a higher τ_R value was expected for FF-DOTA(Gd)-FF respect to DOTA(Gd)-tetraphenylalanine, in which the Gd-complex is anchored at the end of a long oxoethylene spacer. However, the experimental data suggest that the low tendency of the telechelic compound to aggregate, more than the flexibility, affects significantly the relaxivity value of the contrast agent. The proposed model well explain as the Gd-DOTA complex, pointing far from the spine of the aggregate, is free to move, while the folding of the peptide backbone allows the approach of phenyl rings of the C and N termini, permits their T-shape staking as well an antiparallel β -arrangement of the peptide chains.

Acknowledgements

The authors thank Leopoldo Zona for excellent technical assistance in NMR characterization.

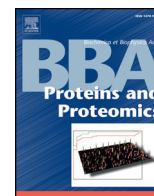
References

- Fleming S, Ulijn RV. Design of nanostructures based on aromatic peptide amphiphiles. *Chem. Soc. Rev.* 2014; **43**: 8150.
- Ma Z, Wang Z, Xu Z, Jia X, Wei Y. Controllable multicolor switching of oligopeptide-based mechanochromic molecules: from gel phase to solid powder. *J. Mater. Chem. C.* 2015; **3**: 3399.
- Cavalli S, Albericio F, Kros A. Amphiphilic peptides and their cross-disciplinary role as building blocks for nanoscience. *Chem. Soc. Rev.* 2010; **39**: 241.
- Chen C, Liu K, Li J, Yan X. Functional architectures based on self-assembly of bio-inspired dipeptides: structure modulation and its photoelectronic applications. *Advances in Colloid and Interface Science* 2015; **225**: 177.
- Kwak J, Kim M-C, Lee S-Y. An enzyme-coupled artificial photosynthesis system prepared from antenna protein-mimetic tyrosyl bolaamphiphile self-assembly. *Nanoscale* 2016; **8**: 15064.
- Ryu J, Kim SW, Kang K, Park CB. Mineralization of self-assembled peptide nanofibers for rechargeable lithium ion batteries. *Adv. Mater.* 2010; **22**: 5537.
- Piccoli JP, Santos A, Santos-Filho NA, Lorenzon EN, Cilli EM, Bueno PR. The self-assembly of redox active peptides: synthesis and electrochemical capacitive behavior. *Biopol. Pept. Sci* 2016; **106**(3): 357.
- Hosseinkhani H, Hong PD, Yu DS. Self-assembled proteins and peptides for regenerative medicine. *Chem. Rev.* 2013; **113**: 4837.
- Yu CY, Huang W, Li ZP, Lei XY, He DX, Sun L. Progress in self-assembling peptide-based nanomaterials for biomedical applications. *Current Topics in Medicinal Chemistry* 2016; **16**(13): 281.
- Reches M, Gazit E. Casting metal nanowires within discrete self-assembled peptide nanotubes. *Science* 2003; **300**(5619): 625.
- Yan X, Zhu P, Li J. Self-assembly and application of diphenylalanine-based nanostructures. *Chem. Soc. Rev.* 2010; **39**(6): 1877.
- Alder-Abramovich L, Gazit E. The physical properties of supramolecular peptide assemblies: from building block association to technological applications. *Chem. Soc. Rev.* 2014; **43**(20): 6873.
- Castillo-Leon J. In *Micro and Nanofabrication Using Self-Assembled Biological Nanostructures*, Castillo-León J, Svendsen W (eds.). Elsevier, 2014 Ch.2.
- Görbitz CH. The structure of nanotubes formed by diphenylalanine, the core recognition motif of Alzheimer's β -amyloid polypeptide. *Chem Commun.* 2006; **2332**.
- Yan X, Cui Y, He Q, Kewei W, Li J, Mu W, Wang B, Ou-yang Z. Reversible transitions between peptide nanotubes and vesicle-like structures including theoretical modeling studies. *Chem. Eur. J.* 2008; **14**: 5974.
- Guo C, Luo Y, Zhou R, Wei G. Probing the self-assembly mechanism of diphenylalanine-based peptide nanovesicles and nanotubes. *ACS Nano* 2012; **6**(5): 3907.
- Kumaraswamy P, Lakshmanan R, Sethuramana S, Krishnan UM. Self-assembly of peptides: influence of substrate, pH and medium on the formation of supramolecular assemblies. *Soft Matter* 2011; **7**: 2744.
- Huang R, Su R, Qi W, Zhao J, He Z. Hierarchical, interface-induced self-assembly of diphenylalanine: formation of peptide nanofibers and microvesicles. *Nanotechnology* 2011; **22**: 245609.
- Mason TO, Chirgadze DY, Levin A, Adler-Abramovich L, Gazit E, Knowles TPJ, Buell AK. Expanding the solvent chemical space for self-assembly of dipeptide nanostructures. *ACS Nano* 2014; **8**(2): 1243.
- Diaferia C, Gianolio E, Palladino P, Arena F, Boffa C, Morelli G, Accardo A. Peptide materials obtained by aggregation of poly-phenylalanine conjugates as gadolinium based MRI contrast agents. *Adv. Funct. Mater.* 2015; **25**(45): 7003.
- Accardo A, Morisco A, Gianolio E, Tesauro D, Mangiapia G, Radulescu A, Brandt A, Morelli G. Nanoparticles containing octreotide peptides and gadolinium complexes for MRI applications. *J. Pept. Sci* 2011; **17**(2): 154.
- Tesauro D, Accardo A, Gianolio E, Paduano L, Teixeira J, Schillén K, Aime S, Morelli G. Peptide derivatized lamellar aggregates as target-specific MRI contrast agents. *ChemBioChem* 2007; **8**(8): 950.
- Adler-Abramovich L, Reches M, Sedman VL, Allen S, Tendler SJB, Gazit E. Thermal and chemical stability of diphenylalanine peptide nanotubes: implications for nanotechnological applications. *Langmuir* 2006; **22**(3): 1313.
- Chang WC, White PD. *Fmoc Solid Phase Peptide Synthesis, a Practical Approach*. Oxford University Press: New York, USA, 2000.
- Accardo A, Ringhieri P, Palumbo R, Morelli G. Influence of PEG length on conformational and binding properties of CCK peptides exposed by supramolecular aggregates. *Biopolymers (Pept. Sci.)* 2014; **102**(4): 304.
- Barge A, Cravotto G, Gianolio E, Fedeli F. How to determine free Gd and free ligand in solution of Gd chelates. A technical note. *Contrast Media Mol. Imaging* 2006; **1**: 184.
- Arena F, Singh JB, Gianolio E, Stefania R, Aime S. β -Gal gene expression MRI reporter in melanoma tumor cells. Design, synthesis, and in vitro and in vivo testing of a Gd(III) containing probe forming a high relaxivity, melanin-like structure upon β -Gal enzymatic activation. *Bioconj. Chem* 2011; **22**: 2625.
- Birdi KS, Singh HN, Dalsager SU. Interaction of ionic micelles with the hydrophobic fluorescent probe 1-anilino-8-naphthalenesulfonate. *J. Phys. Chem* 1979; **83**(2733): 26.
- De Vendittis E, Palumbo G, Parlato G, Bocchini V. A fluorimetric method for the estimation of the critical micelle concentration of surfactants. *Anal. Biochem.* 1981; **115**: 278.
- Diaferia C, Mercurio FA, Giannini C, Sibillano T, Morelli G, Leone M, Accardo A. Self-assembly of PEGylated tetra-phenylalanine derivatives: structural insights from solution and solid state studies. *Sci. Rep.* 2016; **6**: 26638.
- Aime S, Geninatti C, Gianolio E, Giovenzana GB, Tei L, Terreno E. High sensitivity lanthanide(III) based probes for MR-medical imaging. *Coord. Chem. Rev.* 2006; **250**: 1562.

- 32 Huang C-H, Nwe K, Al Zaki A, Brechbiel MW, Tsourkas A. Biodegradable polydisulfide dendrimer nanoclusters as MRI contrast agents. *ACS Nano* 2012; **6**: 9416.
- 33 Accardo A, Tesaro D, Aloj L, Pedone C, Morelli G. Supramolecular aggregates containing lipophilic Gd(III) complexes as contrast agents in MRI. *Coord. Chem. Rev.* 2009; **253**: 2193.
- 34 Bruckman MA, Jiang K, Simpson EJ, Randolph LN, Luyt LG, Yu X, Steinmetz NF. Dual-modal magnetic resonance and fluorescence imaging of atherosclerotic plaques in vivo using VCAM-1 targeted tobacco mosaic virus. *Nano Lett.* 2014; **14**: 1551.
- 35 Song Y, Xu XY, MacRenaris KW, Zhang XQ, Mirkin CA, Meade TJ. Multimodal gadolinium-enriched DNA-gold nanoparticle conjugates for cellular imaging. *Angew. Chem. Int. Ed.* 2009; **48**: 9143.
- 36 Carniato F, Tei L, Arrais A, Marchese L, Botta M. Selective anchoring of Gd(III) chelates on the external surface of organo-modified mesoporous silica nanoparticles: A new chemical strategy to enhance relaxivity. *Chem. Eur. J.* 2013; **19**: 1421.
- 37 Blombergen N. Proton relaxation times in paramagnetic solutions. *J. Chem. Phys.* 1957; **27**: 572.
- 38 Solomon I. Relaxation processes in a system of two spins. *Phys. Rev.* 1955; **99**: 559.
- 39 Accardo A, Tesaro D, del Pozzo L, Mangiapia G, Paduano L, Morelli G. Micelles by self-assembling peptide-conjugate amphiphile: synthesis and structural characterization. *J. Pept. Sci.* 2008; **14**(8): 903.
- 40 Moran SD, Zanni MT. How to get insight into amyloid structure and formation from infrared spectroscopy. *J. Phys. Chem. Lett.* 2014; **5**(11): 1984.
- 41 G rbitz CH. Nanotube formation by hydrophobic dipeptides. *Chem. Eur. J.* 2001; **7**: 5153.
- 42 Tamamis P, Adler-Abramovich L, Reches M, Marshall K, Sikorski P, Serpell L, Gazit E, Archontis G. Self-assembly of phenylalanine oligopeptides: insights from experiments and simulations. *Biophys. J.* 2009; **96**: 5020.
- 43 Guo C, Luo Y, Zhou R, Wei G. Probing the self-assembly mechanism of diphenylalanine-based peptide nanovesicles and nanotubes. *ACS Nano* 2012; **6**(5): 3907.
- 44 Jeon J, Mills CE, Shell MS. Molecular insights into diphenylalanine nanotube assembly: all-atom simulations of oligomerization. *J. Phys. Chem. B* 2013; **117**(15): 3935.
- 45 Diaferia C, Sibillano T, Balasco N, Giannini C, Roviello V, Vitagliano L, Morelli G, Accardo A. Hierarchical analysis of self-assembled PEGylated hexaphenylalanine photoluminescent nanostructures. *Chem. Eur. J.* 2016; **22**: 16586–16597.

Supporting information

Additional supporting information may be found in the online version of this article at the publisher's web site.



Insights into amyloid-like aggregation of H2 region of the C-terminal domain of nucleophosmin



Anna Russo^a, Carlo Diaferia^a, Sara La Manna^a, Cinzia Giannini^b, Teresa Sibillano^b, Antonella Accardo^a, Giancarlo Morelli^a, Ettore Novellino^a, Daniela Marasco^{a,*}

^a Department of Pharmacy, CIRPEB: Centro Interuniversitario di Ricerca sui Peptidi Bioattivi- University of Naples "Federico II", 80134 Naples, Italy

^b Institute of Crystallography (IC), National Research Council, Bari 70125, Italy

ARTICLE INFO

Article history:

Received 2 September 2016

Received in revised form 29 October 2016

Accepted 14 November 2016

Available online 17 November 2016

Keywords:

Misfolding

Aggregation

Acute myeloid leukemia

Wide-angle X-ray scattering

ABSTRACT

Nucleophosmin (NPM1) is a multifunctional protein involved in a variety of biological processes including the pathogenesis of several human malignancies and is the most frequently mutated gene in Acute Myeloid Leukemia (AML). To deepen the role of protein regions in its biological activities, lately we reported on the structural behavior of dissected C-terminal domain (CTD) helical fragments. Unexpectedly the H2 (residues 264–277) and H3 AML-mutated regions showed a remarkable tendency to form amyloid-like assemblies with fibrillar morphology and β -sheet structure that resulted as toxic when exposed to human neuroblastoma cells. More recently NPM1 was found to be highly expressed and toxic in neurons of mouse models of Huntington's disease (HD). Here we investigate the role of each residue in the β -strand aggregation process of H2 region of NPM1 by performing a systematic alanine scan of its sequence and structural and kinetic analyses of aggregation of derived peptides by means of Circular Dichroism (CD) and Thioflavin T (Th-T) assay. These solution state investigations pointed out the crucial role exerted by the basic amyloidogenic stretch of H2 (264–271) and to shed light on the initial and main interactions involved in fibril formation we performed studies on fibrils deriving from the related Ala peptides through the analysis of fibrils with birefringence of polarized optical microscopy and wide-angle X-ray scattering (WAXS). This analysis suggested that the presence of branched Ile²⁶⁹ conferred preferential packing patterns that, instead, appeared geometrically hampered by the aromatic side-chain of Phe²⁶⁸. Present investigations could be useful to deepen the knowledge of AML molecular mechanisms and the role of cytoplasmic aggregates of NPM1c+.

© 2016 Elsevier B.V. All rights reserved.

1. Introduction

In processes of protein misfolding the amyloid fibrillization is a unique ordered state governed by specific patterns of molecular interactions and not an aspecific aggregation [1,2]. The process that leads to the formation of amyloid aggregates is a heterogeneous multistep reaction with many parallel events [3] and, nevertheless the common structural features of final fibrils [4,5], initiation steps of the aggregation by different proteins can be significantly diverse. Even if the primary sequences do not determine uniquely the structures of final fibrils [6–8], the details

of structural variations can be markedly sequence-dependent [9]. The determination of conformational elements that underlay molecular recognition and self-assembly is crucial to understand amyloid formation [10]. Normally folded proteins can access to amyloidogenic states as a result of thermal fluctuations of the native state [11] or disruption of the quaternary structure [12] and the amyloidogenic state is often considered as an ensemble of native-like conformations with locally unfolded elements [13,14]. The characterization of these amyloidogenic species is crucial to elucidate potential aggregation under native conditions and for *in vivo* aggregation events [15]. Many peptides and proteins convert *in vitro* into highly organized amyloid structures and the investigations of the effects of sequence changes on the aggregation can help the development of therapeutic strategies for amyloid-associated diseases [16].

Nucleophosmin (NPM1, B23, No38 and numatrin) is a multifunctional protein, present in the granular region of nucleoli [17,18], belonging to the nucleoplasmin family of nuclear chaperones [19] that shuttles between the nucleus and cytoplasm [20]. In human cells this protein is expressed in three distinct isoforms: B23.1, the longest and the most abundant (294 residues), B23.2 and B23.3 splicing variants lacking the

Abbreviations: TIS, Triisopropylsilane; TFA, Trifluoroacetic acid; DMF, Dimethylformamide; HBTU, 1-H-Benzotriazolium, 1-[bis(dimethylamino)methylene]-Hexafluorophosphate(1-),3 oxide; HOBt, N-hydroxybenzotriazole; DIEA, Diisopropylethylamine; Fmoc, Fluorenylmethoxycarbonyl; HPLC, High Performance Liquid Chromatography; LC-MS, Liquid Chromatography Mass Spectrometry; CD, Circular dichroism; CTD, C-terminal domain; NPM1, Nucleophosmin 1; AML, Acute myeloid leukemia; ThT, Thioflavin T; CR, Congo Red; WAXS, Wide-angle X-ray scattering.

* Corresponding author at: Department of Pharmacy, University "Federico II", Via Mezzocannone, 16, 80134 Naples, Italy.

E-mail address: daniela.marasco@unina.it (D. Marasco).

C-terminal 35 amino-acids and a 29 amino-acid stretch (residues 195–223) in the basic region, respectively [21]. Structural investigations showed that the protein is endowed with a modular structure: i) the N-terminal region is an oligomerization domain crucial for chaperone function [22,23], the central portion presents two IDRs (Intrinsically Disordered Regions) [24] and is crucial for DNA/RNA recognition mechanism [25–27] and the C-terminal domain (CTD) with a three helix bundle tertiary structure [28]. A NMR structural study allowed to delineate the first helix, H1, (243–259), the second, H2, (264–277), and the third H3 (280–294), within the wt CTD that demonstrated to fold through a compact transition state with an extended nucleus and unfolds keeping a malleable residual secondary structure at the interface between H2 and H3 helices [29–31].

NPM1 is overexpressed in solid tumors correlating with mitotic index and metastatization [32] and is the most frequently mutated gene in Acute Myeloid Leukemia (AML) patients: specific mutations in the exon 12 of the NPM1 gene occur, accounting for approximately 30% of cases [19,33–39]. Mutations in the H3 region of the CTD cause its unfolding [28,40], the impairment of several functions such as DNA/RNA recognition [39] and the aberrant accumulation of the protein in the cytoplasm of the leukemic cells (thus the term NPM cytoplasmic positive NPMc + AML) [36]. AML NPM1 mutations revealed involved in leukemia cell viability and invasion and, in this process, Matrix metalloproteinases MMPs (regulated by the K-Ras/ERKMAPK signaling pathway) play a key role [41]. The aberrant cytoplasmic accumulation of AML mutated protein is due both to the loss of the NoLS (nucleolar localization signal) and to the oligomerization level of the protein depending on N-terminal and/or C-terminal domains. Recently a study focused on the role of NPM1 in neurons of mouse models of Huntington's disease (HD) was reported. It demonstrated that NPM1 has complex roles in the regulation of neuronal survival in dependence on its levels of expression, oligomerization and subcellular localization: in particular NPM1 resulted highly expressed and toxic with a cytoplasmic localization [42].

Lately, following a structure-based protein dissection approach, we demonstrated that the H2 [43] and H3 AML mutated regions [44] of the CTD of NPM1 form amyloid-like assemblies endowed with fibrillar morphology and β -sheet structure that resulted toxic in cell viability assays. Actually, our mechanistic hypothesis is that the AML-associated mutations destabilize the α -helical structure of the H3 region in the native NPM1 and disrupts the CTD tertiary structure predisposing it to the formation of toxic aggregates since it induces the exposure of the H2 region, which is the most amyloidogenic region of the whole NPM1-CTD.

Here we investigate the role of each residue in the aggregation process of H2 region of NPM1 through the characterization of a series of peptides deriving from a systematic alanine scan [45] of its sequence. Bioinformatics analyses pointed out the chameleon nature of this region and that Alanine-substitutions deeply affect the “basic amyloidogenic unit” (264–271) as confirmed by structural and kinetic analyses of aggregation processes by means of Circular Dichroism, Infrared spectroscopies and Th-T assay. Further, to shed light on the initial and main interactions in fibril formation, we analyzed amyloid fibrils of H2 wt and several sequences bearing Ala substitutions with birefringence of polarized optical microscopy and wide-angle X-ray scattering (WAXS).

2. Results and discussion

2.1. Chameleon behavior of H2-Ala scan peptides

To investigate the specific role of the residues of the region H2 of NPM1-CTD (264–277), we performed a systematic alanine scan of the sequence and thirteen peptides (Table 1) were synthesized and purified with good yields (>90%).

A bioinformatic analysis of each primary sequence of the H2 Ala-scan peptides was carried out using the PASTA server [46]. Their tendencies to assume β -strand secondary structure and to aggregate in

Table 1

Sequences and names of analyzed peptides derived from Ala scan of H2 wt. Molecular weight (MW) and isoelectric point (pI) for each peptide sequence are also reported.

Name	Sequence	MW (amu)	pI
H2wt	VEAKFINVYKNCFR	1772	10.15
H2A1, Ala/Val ²⁶⁴	AEAKFINVYKNCFR	1744	10.15
H2A2, Ala/Glu ²⁶⁵	VAAKFINVYKNCFR	1714	10.76
H2A4, Ala/Lys ²⁶⁷	VEAAFVINYKNCFR	1715	9.06
H2A5, Ala/Phe ²⁶⁸	VEAKAIVNYKNCFR	1696	10.15
H2A6, Ala/Ile ²⁶⁹	VEAKFANVYKNCFR	1730	10.15
H2A7, Ala/Asn ²⁷⁰	VEAKFIAYVYKNCFR	1729	10.15
H2A8, Ala/Tyr ²⁷¹	VEAKFINAVKNCFR	1680	10.64
H2A9, Ala/Val ²⁷²	VEAKFINVYKNCFR	1744	10.15
H2A10, Ala/Lys ²⁷³	VEAKFINVYKNCFR	1715	9.06
H2A11, Ala/Asn ²⁷⁴	VEAKFINVYKACFR	1729	10.15
H2A12, Ala/Cys ²⁷⁵	VEAKFINVYKNAFR	1740	10.78
H2A13, Ala/Phe ²⁷⁶	VEAKFINVYKNCAR	1696	10.15
H2A14, Ala/Arg ²⁷⁷	VEAKFINVYKNCFA	1687	9.01

an amyloid-like way respect to disorder were analyzed and probability profiles were reported in Figs. S1 and S2, respectively. Notably a similar analysis, carried out on the NPM1-CTD wt outlined the chameleon character of H2 sequence and defined a shorter region as the “basic amyloidogenic unit” (named H2 short^{265–272}) [43]. Here PASTA analysis indicates that Alanine point substitutions do not alter β secondary structure preferences respect to H2 wt. Exceptions were for the Ala/Asn²⁷⁰ (H2A7) and Ala/Lys²⁷³ (H2A10) (to a lesser extend) replacements (Fig. S1G,J) for which the probability to assume a beta conformation seems comparable to aggregation. Similarly the greater probability to aggregate respect to disorder is not affected by substitutions except for Ala/Ile²⁶⁹ (H2A6) (Fig. S2F) that seemed, in turn, to decrease the tendency of the related sequence to aggregate.

The effects of Ala substitutions on conformational features were experimentally evaluated by CD spectra over time. H2 wt sequence revealed able to self-assemble in an amyloid-like way at physiological pH but basic pHs demonstrated to speed this process and in order to compare the β -sheet aggregating propensities of Ala sequences in the absence of net positive charges, we performed studies at pH 10, that is the closest value to theoretical pIs (Table 1) [43]. H2 Ala derived peptides freshly dissolved in 10 mM borate buffer, at pH 10.0, exhibited different far-UV CD spectra (Fig. 1). Each spectrum was followed within 24–48 h. Most spectra presented decreases over time in the overall signal, resulting from the formation of large aggregates that escape experimental detection. The large mean residue ellipticity in the 215–220 nm range indicated a β -structure content [47]. This feature was mainly detected in H2A9, H2A11, H2A12 and H2A14 sequences: notably all of them, except H2A9, present Ala substitutions outside the indicated basic amyloidogenic stretch (Fig. 1H,J,K,M). Visually H2A9 did not formed fibrils in the explored time-course (differently from several other sequences), presumably the substitution Ala/Val²⁷² allowed a major solubility of prefibrillar oligomers suggesting that Val²⁷² is not determinant in the oligomerization mechanism and could only enhance insolubility of wt sequence as confirmed by the solubility profile reported in Fig. S3–I, see below. Conversely, spectra of H2A5, H2A6 and H2A8 did not assume β -strand profiles within 24–48 h: while H2A5 and H2A8 showed only decreased Cotton effects with a substantial random profile H2A6 presented a transition from random to $\alpha + \beta$ mixed conformation, as predicted by PASTA analysis (Fig. 1D,E,G). Aromatic interactions can greatly affect to the self-assembly process: indeed stacking interactions can provide energetic contributions, as well as order and directionality in the aggregation [48]. H2 sequence contains three aromatic residues: two inside the shortest amyloidogenic region, Phe²⁶⁸ and Tyr²⁷¹, and one outside it, Phe²⁷⁶. Their Ala substitutions caused that none of related peptides presented β -like CD spectra (Fig. 1D,G,L) at micromolar concentrations: notably this effect is more evident for Phe²⁶⁸ with respect to Phe²⁷⁶, pointing out the dependence of the local context on conformational behavior. This dependence is also evident in the

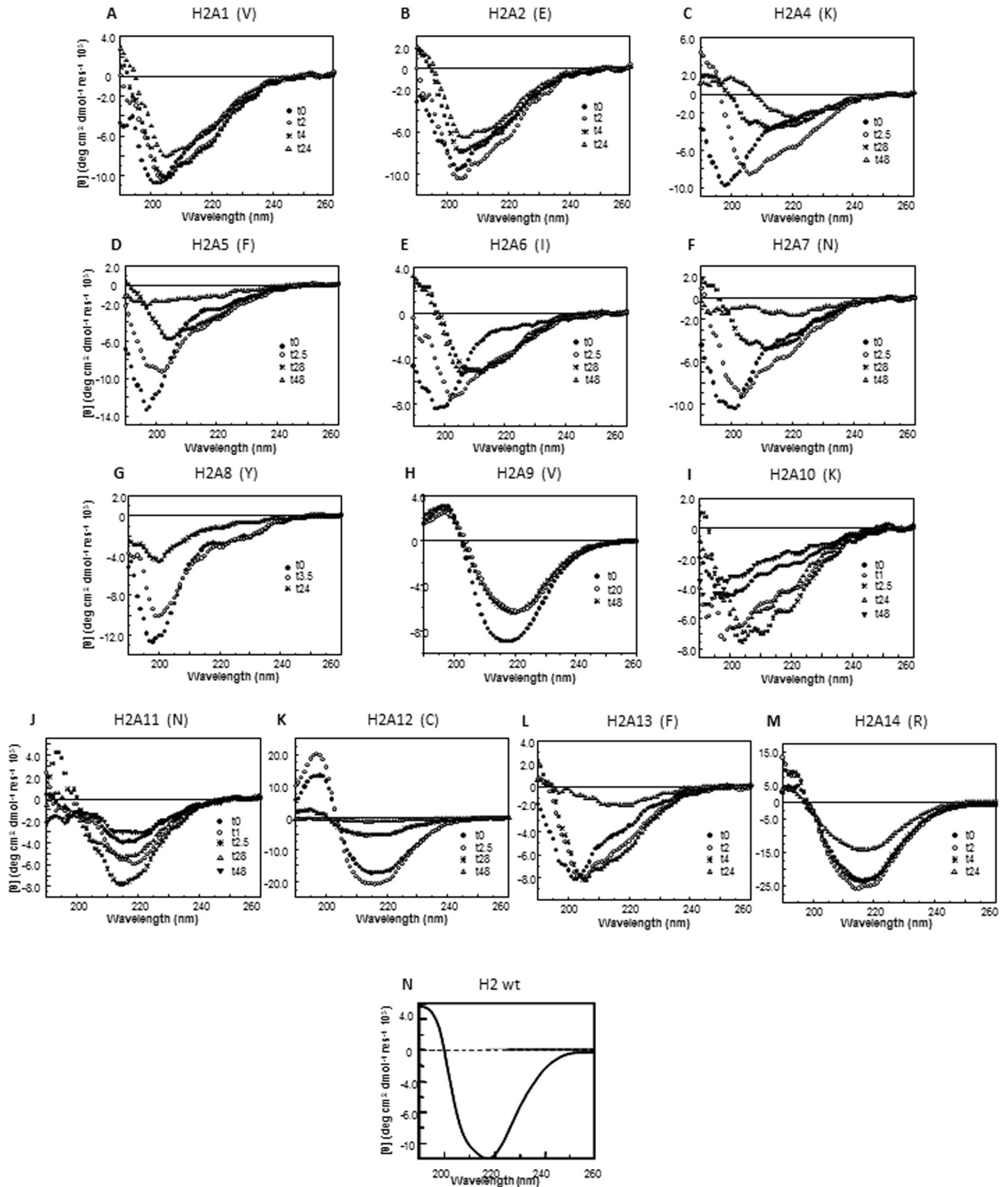


Fig. 1. CD analysis of H2 Ala derived peptides. Overlay of CD spectra recorded at indicated time (h) from freshly prepared samples at 100 μ M in 10 mM borate buffer, pH 10. For a better comprehension substituted residue in parenthesis is reported above each panel CD spectrum of H2 wt (at $t = 0$) is also showed [43].

comparison of CD features of Ala/Asn substituted peptides at different positions: at 270, inside, and 274 positions, outside the amyloidogenic core. CD spectra analyses and of H2A7 and H2A11 suggest that the

Ala/Asn substitution caused a transition to β -like structure after long time (24 h) (Fig. 1F, confirming PASTA prediction). Similarly for charged residues inside and outside the shortest amyloidogenic fragment.

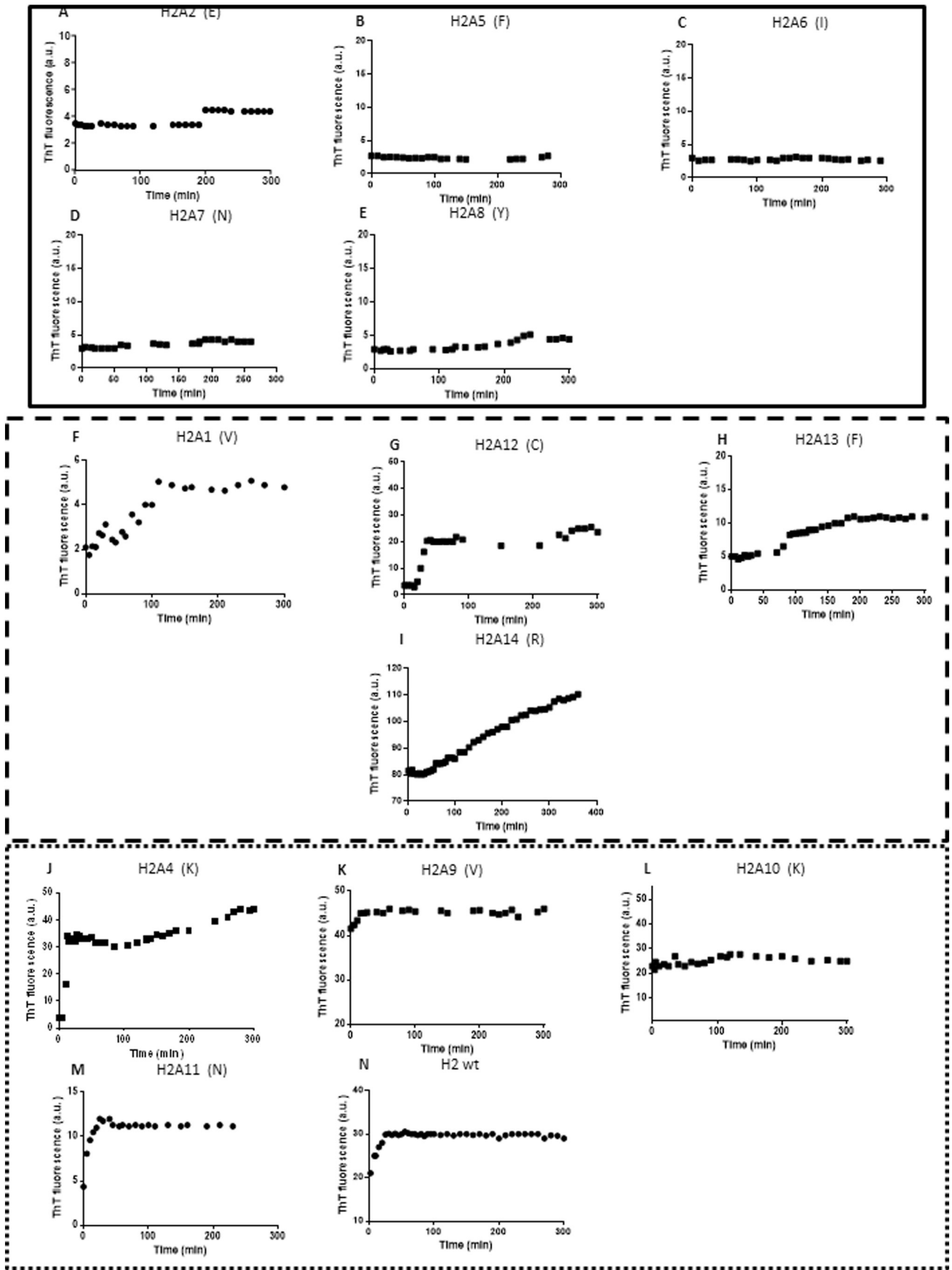


Fig. 2. Kinetic of oligomers formation at indicated H2 Ala peptides, determined by ThT fluorescence assay, at 100 μ M at pH 10. They were grouped in: upper “not aggregating” (full line); central “slow aggregating” (dashed line), lower panel as “aggregated” (dotted line) sequences, respectively. For a better comprehension substituted residue in parenthesis is reported above each panel, H2 wt kinetic profile is also reported [43].

Indeed H2A12 and H2A14 CD spectra (Fig. 1K,M), showed a β -like profile, while H2A2 CD spectra (Fig. 1B), did not show transition toward β -sheet conformation, suggesting a primary role for Glu265 to create ionic interactions stabilizing β -structure.

2.2. Kinetic aggregation studies of H2-Ala scan peptides

The effects of Ala-substitution in the H2 region of NPM1 were also investigated with respect to the kinetic of aggregation. To this purpose, the time course of ThT fluorescence intensity of freshly prepared solutions was monitored, at 100 μ M and pH 10.0, under stirring and reported in Fig. 2 [49]. In general a sigmoidal shape of fluorescence intensity versus time is typical of a nucleation-dependent growth mechanism of amyloid fibril formation, while H2 wt was almost fully aggregated at $t = 0$, as here shown (Fig. 2N) and previously reported [43]. For a matter of clarity we have grouped Ala-scan sequences into: “not aggregating”, “slow aggregating” and “aggregated” peptides in three panels of Fig. 2. The members of first group are peptides with Ala replacement in the 264–271 fragment, that show very low fluorescence intensity that did not increase in 300 min (Fig. 2A–E). An interesting group is represented by the “slow aggregating sequences” in which the replacement of native residue significantly delay aggregation. To this group H2A1 sequence belongs (Fig. 2F) suggesting an important role exerted by the N-terminal Val²⁶⁴ in the aggregation process. Most of the sequences bearing Ala substitution outside amyloidogenic stretch showed a high fluorescence signal even at $t = 0$ and were defined as “aggregated sequences” (Fig. 2J–M). But this behavior was not shown by H2A12, A13, A14 for which native amino acids, Cys, Phe and Arg, gave a contribution to the aggregation process (Fig. 2G–I). The substitutions of Lys²⁶⁸ and Cys²⁷⁵ (H2A4, H2A12) showed a fast kinetic aggregation (time of saturation ~ 10 and 20 min, respectively) suggesting electrostatic contributions to the self-recognition. These considerations were corroborated by the total suppression of aggregation showed from H2A2 (Fig. 2A), indicating that Glu266 can create favourable electrostatic interactions. Sequences H2A9 and H2A14 (Fig. 2K,I) appeared the most intense at $t = 0$ suggesting higher soluble aggregated states with respect to others. This finding was also confirmed by an additional progressive slow aggregation of H2A14 sequence.

The lag times of fibril growth is strictly dependent on the solubility of each sequence as evidenced by different solubility profiles reported in Fig. S3 obtained with CamSol program [50]. Changes in amyloid propensity through mutational analyses require to be evaluated also in the light of reduced/enhanced solubility caused by mutations. Indeed small sequence variations can produce dramatic effects on the solubility and the lag times of amyloid formation of amyloidogenic proteins and peptides [51–52]. Several residues including proline, arginine and lysine increase solubility and their incorporations in the flanking regions of aggregation-prone sequences reduce aggregation propensity and amyloid formation [53]. Solubility profiles of Ala-H2 peptides (Fig. S3) confirmed these indications since the Ala substitution of two of these residues in H2A10 and H2A14, that cause lower solubility respect to the wt sequence, exhibited ThT assays in which sequences resulted already aggregated at $t = 0$ (Fig. 2I,L).

2.3. Fibrils characterization of H2-Ala scan peptides

With the aim to gain deeper insights into the role exerted by residues in the amyloidogenic core of H2 wt we selected three sequences (H2A5, H2A6 and H2A8) bearing the Ala substitution of aromatic (Phe²⁶⁸, Tyr²⁷¹) and branched (Ile 269) residues. Their β -structures were further analyzed at millimolar concentrations by FTIR and VIS CR spectroscopies. Subsequently fibrils deriving from these peptides were analyzed at solid state by polarized optical microscopy (with CR staining) and WAXS techniques.

FTIR spectra of peptide solutions (~ 2.3 mM) were recorded in transmission configuration. In Fig. 3A FTIR spectra in the amide I region are

reported for H2 wt, H2A5, H2A6 and H2A8. They show two bands: a principal maximum at 1637 cm^{-1} and a minor peak at ~ 1675 cm^{-1} . The maximum at 1637 cm^{-1} is typical of peptides in a β -sheet conformation, whereas the lower peak (~ 1675 cm^{-1}) indicated an antiparallel orientation of the β -sheets [54]. From the deconvolution of the FTIR data, it results that all four peptides have high β -sheet content ($\sim 80\%$ for H2 and H2A5 and $\sim 60\%$ for H2A6 and H2A8 analogs) [55]. FTIR spectra of dried films of these peptides resulted quite similar to spectra of samples in solution (data not shown).

While the UV–vis spectrum of CR alone showed its typical maximum at 490 nm, after the incubation with 1.0 mg/mL of H2A5, H2A6 and H2A8 peptides for 30 min a significant shift of the CR band from 490 to 540 nm was observed for all sequences (see Fig. 3B). The shift of the maximum clearly indicates the presence in solution of fibrillar aggregates, a similar behavior was previously showed by H2 wt [43].

To speculate on potential differences in the morphology of fibrils we analyzed those deriving from H2 wt, H2A5 and H2A6 fibrils through solid state techniques. Notably the sequence H2A8 (Ala/Tyr²⁷¹) demonstrated not able to fibril in the same explored conditions confirming the major aromatic contribution to self-recognition in the fibrillar process. Both air-dried films of peptides stained with CR and peptide dried fibrils containing CR exhibited intense green birefringence when analyzed with polarized optical microscopy (Fig. 4). Moreover, the dried fibrils, reported in Fig. S4, show a dendritic spherulite arrangement of category 1 [56] in which they grown radially from the nucleation site, branching intermittently to maintain a space filling character. The interference of growth from the neighboring spherulites resulted in structures with high density and small size. These spherulites did not show the typical “Maltese cross” pattern exhibited for amyloid fibrils of bovine insulin [57] or of pro-islet amyloid polypeptide (ProlAPP_{1–48}) [58] but a pattern similar to those observed for crystallizing polymers such as polyethylene glycol (PEG) or PEG peptides derivatives able to form fibril [59]. Usually spherulites are observed on a long length scale (> 1 μ m) with diameters generally between 6 and 12 nm [57]. Accordingly previous AFM analysis for H2 wt revealed that the fibril reaches a height of 9.5 ± 0.5 nm after 1 h aggregation [43].

The same fibrils were also analyzed through WAXS investigations [60] and in Fig. 5 the results of experiments related to H2 wt, H2A5 and H2A6 are summarized: in the top the investigated fibrils are shown; the collected 2D WAXS patterns, are reported in the middle of Fig. 5. These WAXS profiles display the typical “cross- β ” diffraction pattern of amyloid fibrils, with a Bragg spacing of 4.8–4.9 Å along the meridional direction and a more diffuse periodicity of ~ 10 Å in the equatorial direction, usually ascribed to the staking of these β -sheets perpendicularly to the fibril axis [61,62]. The 2D WAXS data were centered, calibrated and radially folded into unidimensional (1D) profiles. Two 1D WAXS patterns were integrated separately along the equatorial and meridional directions (white arrows of the 2D WAXS data), reported as red (meridional) and black (equatorial) profiles at the bottom of Fig. 5. The most intense peak of the meridional profiles corresponds to the β -strands distance of 4.76 ± 0.3 Å.

Despite similar morphology of fibrils we investigated potential different orders of amyloids caused by Ala substitutions, to this purpose the analysis of azimuthal data was carried out. The alignment of the fibers in the X-ray beam was carried out with a photodiode close to the sample to monitor the transmitted primary beam intensity. The sample position in which we collected WAXS data coincides with the minimum transmitted intensity (center of the fiber).

Each 2D WAXS pattern (Fig. 6A) was transformed into polar coordinates (Fig. 6B) with q and azimuth as new axes. Two computing windows were selected and displayed in Fig. 6A as yellow ($\Delta q = 0.65$ – 0.85 Å⁻¹) and red ($\Delta q = 1.25$ – 1.45 Å⁻¹) rectangular areas, in correspondence of the most intense equatorial and meridional reflections, respectively. The 2D WAXS data were integrated along each Δq , and the resulting 1D WAXS azimuthal profiles were plotted for each sample in Fig. 6C ($\Delta q = 0.65$ – 0.85 Å⁻¹) and in Fig. 6D ($\Delta q = 1.25$ – 1.45 Å⁻¹),

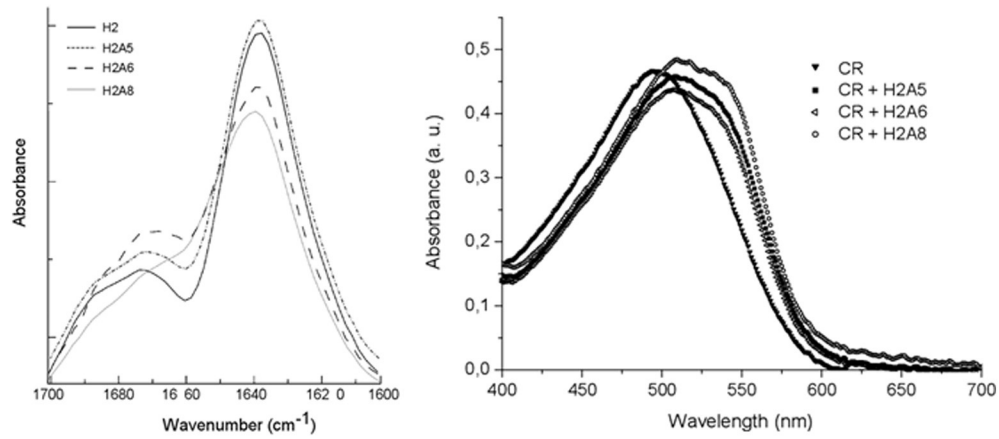


Fig. 3. (A) FTIR spectra in the amide I region (B) UV Vis spectra of H2 wt, H2A5, H2A6 and H2A8 peptides (1.0 mg/mL) with Congo Red. The spectrum of Congo Red is also reported for comparison.

respectively. The full-width-at-half maximum (FWHM) was fitted for all 1D WAXS azimuthal profiles, reported in Fig. 6C–D, and summarized in Table 2. The analysis of FWHM values support an increasing order for fibrils as follows H2A5 > H2 wt > H2A6 [63].

3. Conclusions

Both in natively unfolded and globular proteins, very short amino acid stretches are primarily responsible of fibrillation process and are defined as “hot spots” [64–66]. In the wt NPM1-CTD [67] the core of the three helix bundle is mainly supported by aromatic interactions by residues belonging both to the H2 and H3 regions (Tyr²⁷¹, Phe²⁶⁸, Phe²⁷⁶, Trp²⁸⁸ and Trp²⁹⁰). On the basis of previous studies we hypothesized that an aggregation could occur upon the structural destabilization of the bundle primarily at the interface of H2 and mutated H3 regions and both bioinformatic and experimental investigations suggested a prominent role exerted by H2 as “hot sequence” in the aggregation. Herein we present novel investigations, at solution as well as

fibrillar states, by exploring the entire H2 sequence through a systematic alanine scanning approach. Solution studies revealed that the fragment 264–271 is crucial for the initial steps of self-recognition process. Substitutions within this stretch dramatically affect the β -conformations and the tendency to aggregate of the H2 region: indeed the Ala mutations of related amino acids hampered, almost completely, the aggregation of H2 fragment at micromolar concentrations. In particular the absence of aromatic residues in this fragment (Phe²⁶⁸ and Tyr²⁷¹) enhanced this feature. Circular dichroism and IR spectroscopic analyses confirmed the concentration dependent conformational changes of the peptides. To deepen this aspect we structurally characterized fibrils of H2 wt and other derived peptides bearing Ala in the smallest stretch 268–271. The analysis of amyloid fibrils indicated the formation of spherulites, that are common structures both for synthetic peptides [67,68], including a helix–turn–helix peptide [69] and in tissues of patients with amyloid disorders [57]. They contain a large quantity of well-defined amyloid fibrils, suggesting that they are formed at least in part as a consequence of the self-assembly of pre-formed fibrils.

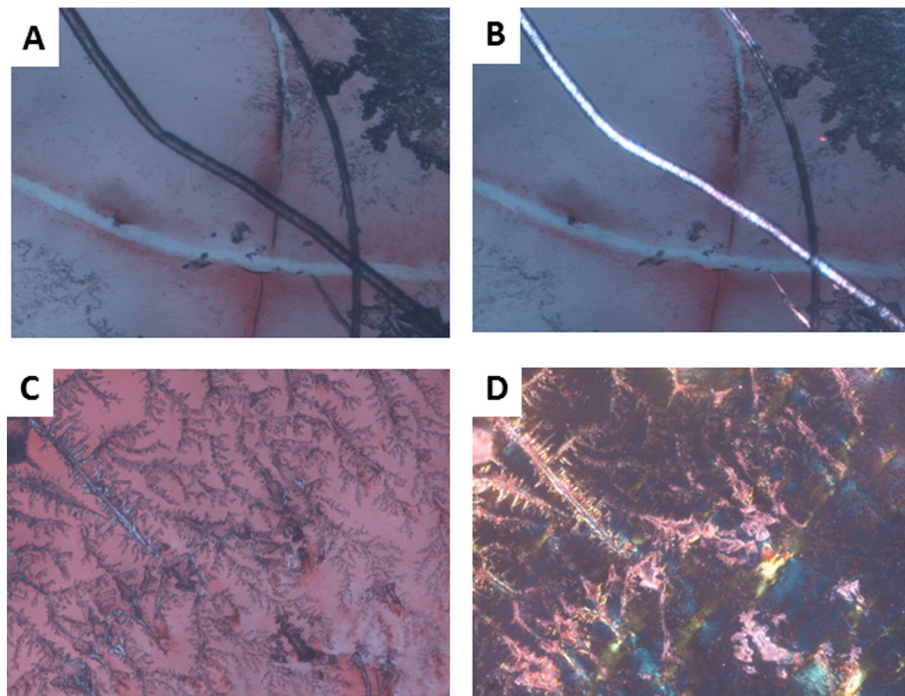


Fig. 4. Polarized optical microscopy H2A5 fibers images containing CR (A, B) and dried H2 wt (C, D) stained with Congo Red solution onto a glass slide and observed with a Nikon microscope under bright field illumination (A, C) and between crossed polars (B, D).

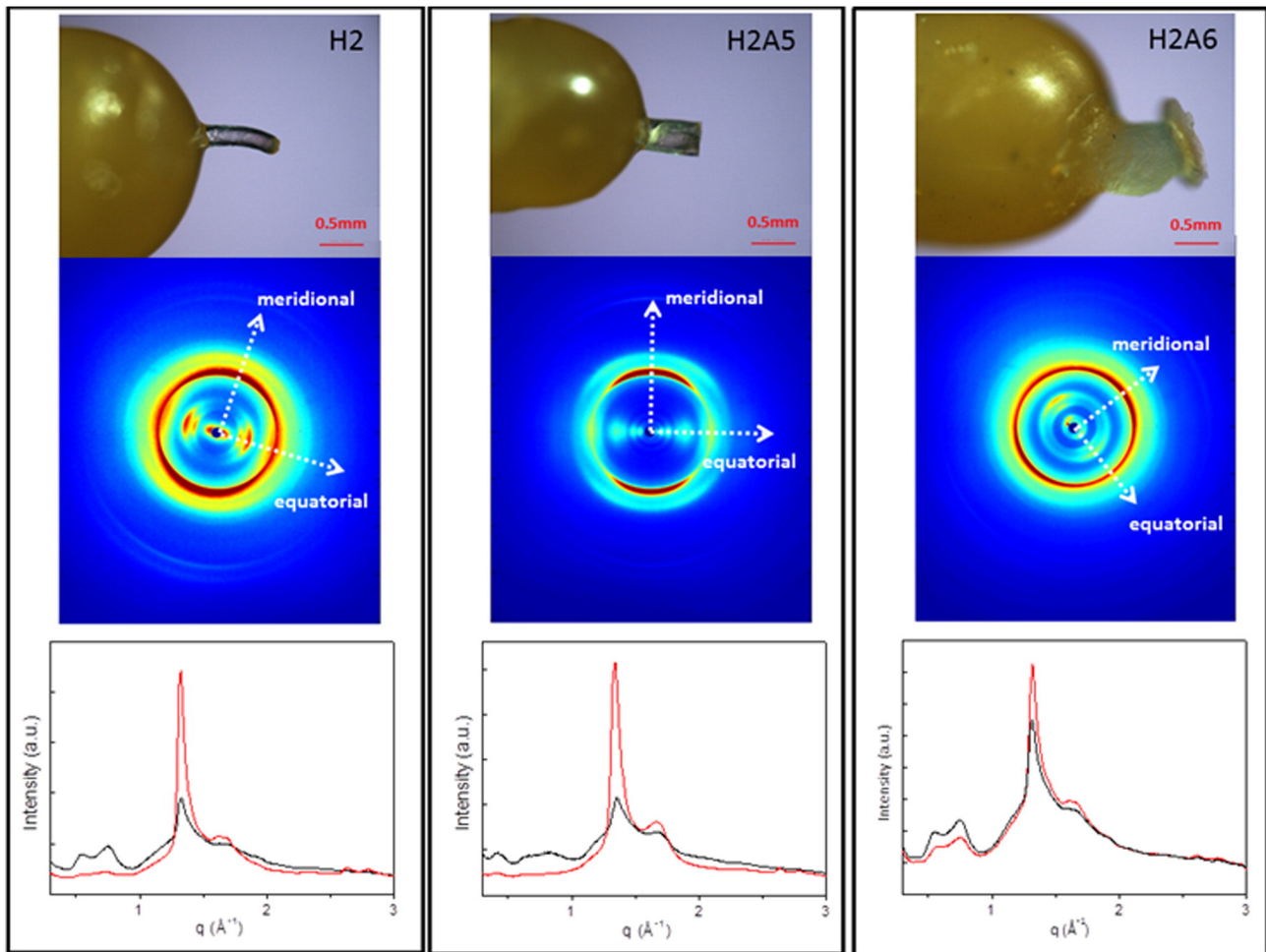


Fig. 5. WAXS analysis of H2wt, H2A5 and H2A6: Top: picture of the analyzed fibers; Middle: 2D WAXS fiber diffraction data; Bottom: 1D WAXS fiber diffraction profiles (red: meridional profile; black equatorial profile).

WAXS analyses of fibrils of H2 wt, H2A5 and H2A6 Ala confirmed the presence of the main amyloid structural feature i.e. the cross- β architecture constituted by intermolecular β -sheets with β -strands oriented perpendicular to the fibril axis [70,71] while azimuthal data of the diffraction patterns [72] were employed allowed to establish a lower order of the fibril associated to the H2A6 sequence with respect to H2 wt suggesting that the presence of branched Ile269 conferred preferential packing patterns that, instead, appeared geometrically hampered by the aromatic side-chain of Phe²⁶⁸. These results confirm that the interdigitation of the side chains between β -sheets is crucial for ordered amyloid fold. It is likely that the antiparallel arrangement of β -strands would allow proper orientation of aromatic residues to permit π -interactions and stacking of the side chains. Most probably aromatic residues, for H2 in antiparallel orientation, are not favorably positioned thereby reducing the order of amyloidogenic state [73]. Recently a direct correlation between amyloid-like aggregation and cancer was demonstrated for p53/p73 mutants [74,75], with relevant therapeutic approaches [76]. With the aim to investigate a potential link between aggregation of NPM1 and AML and the molecular mechanisms of this severe and widespread pathology, work is now in progress in our laboratory on the biophysical characterization of other AML-mutated sequences in the H3 region and are preparing by chemical synthesis the entire mutated-CTDs of NPM1. In conclusion our investigations could be useful to deepen the knowledge of AML molecular mechanisms and the role of cytoplasmic aggregates of NPM1c+. Indeed interfering with the levels or the oligomerization status of NPM1 may influence its capability to properly build up the nucleolus in NPM1- mutated AML

cells. Many therapeutical approaches targeting NPM1 propose the identification of molecules able to interfere with its biological functions: its subcellular localization, its oligomerization properties or ways driving to its degradation [39].

3.1. Experimental procedures

3.1.1. Peptide synthesis

Reagents for peptide synthesis were from Iris Biotech (Germany). Solvents for peptide synthesis and HPLC analyses were from Romil (Dublin, Ireland); reversed phase columns for peptide analysis and the LC-MS system were from ThermoFisher (Waltham, MA). Solid phase peptide syntheses were performed on an automated multichannel synthesizer Syro I (Multisynthech, Germany). Preparative RP-HPLC was carried out on a Shimadzu LC-8A, equipped with a SPD-M10 AV detector and with a Phenomenex C18 Jupiter column (50 × 22 mm ID; 10 μ m). LC-MS analyses were carried out on a LCQ DECA XP Ion Trap mass spectrometer equipped with an OPTON ESI source, operating at 4.2 kV needle voltage and 320 °C with a complete Surveyor HPLC system, comprised of MS pump, an autosampler and a photo diode array (PDA). The peptides reported in Table 1 were synthesized following standard Fmoc strategies on a 50 μ mol scale [77]. To better mime protein regions the peptides investigated in this study were acetylated and amidated at the extremities. Rink-amide resin (substitution 0.5 mmol/g) was used as solid support. Activation of amino acids was achieved using HBTU/HOBt/DIEA (1:1:2), whereas Fmoc deprotection was carried out using a 20% (v/v) piperidine solution in DMF. Peptides

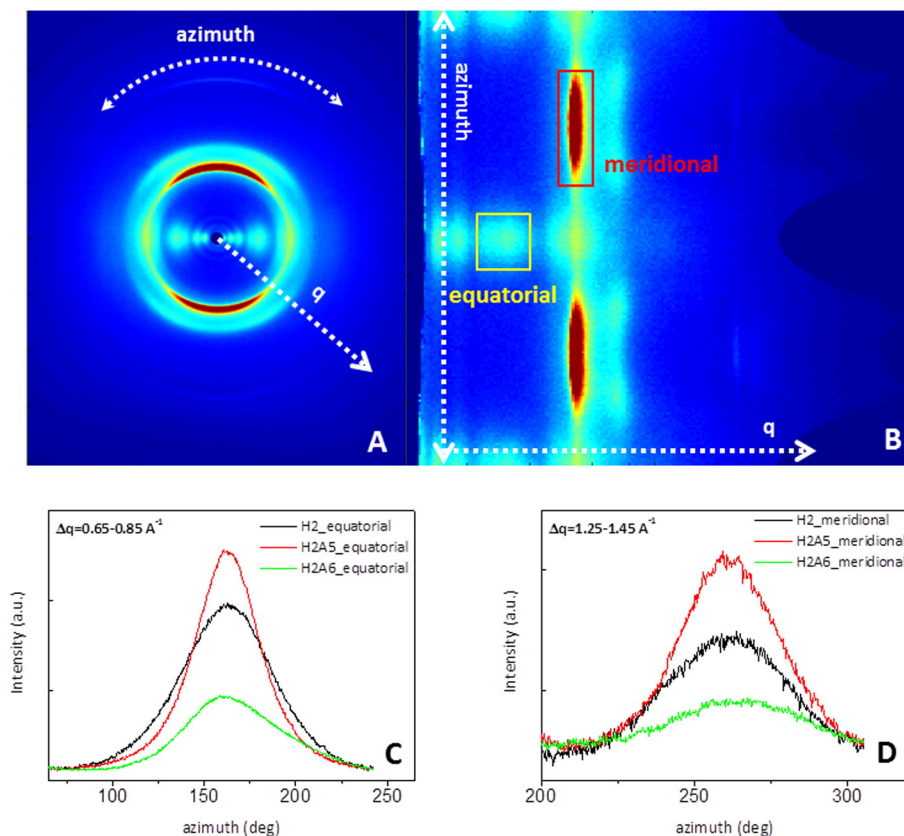


Fig. 6. 2D WAXS analysis: (A) 2D WAXS fiber diffraction of H2A fiber; (B) same 2D WAXS fiber diffraction pattern shown in (A), here reported in polar coordinates (q , azimuth); (C) 1D WAXS azimuthal profiles obtained by integration along $\Delta q = 0.65\text{--}0.85 \text{ \AA}^{-1}$ of the rectangular region of the 2D WAXS pattern in (B), marked in yellow; (D) 1D WAXS azimuthal profiles obtained by integration along $\Delta q = 1.25\text{--}1.45 \text{ \AA}^{-1}$ of the rectangular region of the 2D WAXS pattern in (B), marked in red.

were removed from the resin by treatment with a TFA:TIS:H₂O (90:5:5, v/v/v) mixture for 90 min at room temperature; then crude peptides were precipitated in cold ether, dissolved in a water/acetonitrile (1:1, v/v) mixture and lyophilized.

Products were purified by RP-HPLC applying a linear gradient of 0.1% TFA CH₃CN in 0.1% TFA water from 5% to 65% over 12 min using a semi-preparative 2.2 × 5 cm C18 column at a flow rate of 20 mL/min. Peptides and purity and identity were confirmed by LC-MS. Purified peptides were lyophilized and stored at $-20 \text{ }^{\circ}\text{C}$ until use.

3.1.2. Far-UV CD spectroscopy

Samples were prepared by dilution of freshly prepared stock solutions (2 mM peptide on average), whose peptide concentrations were determined by UV absorbance employing a ϵ_{275} value of $1390 \text{ cm}^{-1} \text{ M}^{-1}$ (except for H2A8). CD spectra were recorded on a Jasco J-815 spectropolarimeter (JASCO, Tokyo, Japan). CD spectra were registered at $25 \text{ }^{\circ}\text{C}$ in the far-UV region from 190 to 260 nm. Other experimental settings were: 20 nm/min scan speed, 2.0 nm band width, 0.2 nm resolution, 50 mdeg sensitivity, and 4 s response. Each spectrum was obtained averaging three scans, subtracting contributions from corresponding blanks and converting the signal to mean residue ellipticity ($[\theta]_{\text{res}}$) in units of $\text{deg cm}^2 \text{ dmol}^{-1}$. Peptide concentration was

100 μM and a 0.1 cm path-length quartz cuvette was used. CD spectra were acquired in 10 mM borate buffers pH 10.0 [78,79].

3.1.3. ThT fluorescence assay

ThT assays were carried out at 100 μM of both ThT and peptides at $25 \text{ }^{\circ}\text{C}$. ThT fluorescence was measured using a Varian Cary Eclipse spectrofluorimeter (Varian, California, USA) and a cell of 10 mm path-length quartz cuvette, under magnetic stirring. Measurements were collected every 1–5 min for 300–400 min, using excitation and emission wavelengths of 440 and 450–600 nm, respectively.

3.1.4. Fourier transform infrared spectroscopy (FTIR)

FT-IR characterization was performed on peptides in solution ($\sim 2 \text{ mM}$) and at the solid state. FT-IR spectra were collected with a Jasco FT/IR 4100 spectrometer (Easton, MD) in an attenuated total reflection (ATR) mode and using a Ge single-crystal at a resolution of 4 cm^{-1} . All the spectral data were processed using built-in software. Spectra were collected in transmission mode and then converted in emission. Each sample was recorded with a total of 100 scans with a rate of $2 \text{ mm} \cdot \text{s}^{-1}$ against a KBr background.

3.1.5. Congo Red spectroscopic assay

UV-vis spectra of Congo Red (CR) alone or incubated with a peptide solution (1.0 mg/mL, $\sim 500 \mu\text{M}$) were carried out on Thermo Fisher Scientific Inc (Wilmington, Delaware USA) Nanodrop 2000c spectrophotometer equipped with a 1.0 cm quartz cuvette (Hellma). A stock solution of CR (3.5 mg in 500 μL) was freshly prepared in 10 mM phosphate buffer pH 7.4 and filtered through 0.2 μm syringe immediately prior to use. A small aliquot (5 μL) of this solution was diluted with the buffer at 12.5 μM final concentration or with H2A5, H2A6 or H2A8 peptide solutions. These solutions were left under stirring for 30 min

Table 2
FWHM of the 1D WAXS profiles, reported in Fig. 6C and D.

Fibril	Equatorial (rad)	Meridional (rad)
H2A5	0.63	0.54
H2	0.88	0.71
H2A6	1.04–1.55	0.73

at room temperature and then the UV–vis spectra were recorded between 400 and 700 nm at room temperature and background was subtracted.

3.1.6. Congo Red staining and polarized optical microscopy

Dried films of H2, H2A5 and H2A6 peptides were obtained placing 30 μL of the peptide (0.25 wt.%), dissolved in deionized water, onto a glass slide and left drying at room temperature.

The air-dried samples were stained with 50 μL of a freshly prepared CR solution. This solution was prepared adding a saturating amount of CR in ethanol containing 20% of NaCl saturated water. After the deposition of CR on the air-dried sample, the extra solution was quickly removed from the glass slide with a filter paper. CR containing fibrils were prepared, according to the stretch frame method [80], described in the Wide-Angle X-ray Scattering section, adding 4 μL of CR staining solution to 100 μL of peptide solution. Both air-dried samples on glass slide and CR containing fibrils were observed under bright field illumination and between crossed polars using a Nikon AZ100 microscope.

3.1.7. Wide-angle X-ray scattering

Fibril diffraction WAXS patterns were recorded from stalks prepared by the stretch frame method [80]. Briefly, a droplet (10 μL) of peptide aqueous solution (3 wt.%) was suspended between the ends of a wax-coated capillary (spaced 2 mm apart). The droplet was allowed to dry gently at room temperature overnight to obtain oriented fibrils.

The WAXS experiments were performed with the laboratory set-up of the XMI-Lab^{1–2} equipped with Fr-E + SuperBright rotating anode copper anode microsource (Cu K α , $\lambda = 0.15405$ nm, 2475 W), multilayer focusing optics (Confocal Max-Flux; CMF 15–105) and three-pinhole camera (Rigaku SMAX-3000). An image plate (IP) detector with 100 μm pixel size was placed at 10 cm from the sample and calibrated by means of the Si NIST standard reference material (SRM 640b) [81,82].

Author contributions

A.R., C.D., S. L. M., T. S., performed experiments, E. N., G. M., C.G. A. A., D. M. conceived studies and analyzed data, D. M. wrote the paper.

Transparency document

The Transparency document associated with this article can be found, in the online version.

Acknowledgments

The authors thank Luca De Luca, Giosue' Sorrentino and Maurizio Amendola for their excellent technical assistance and the European Fund for Regional Development - Cross-Border Cooperation Programme Italy-Slovenia 2007–2013, (Project PROTEO, Code N. CB166), to A.R.

Appendix A. Supplementary data

Supplementary data to this article can be found online at <http://dx.doi.org/10.1016/j.bbapap.2016.11.006>.

References

- [1] F. Bemporad, A. De Simone, F. Chiti, C.M. Dobson, Characterizing intermolecular interactions that initiate native-like protein aggregation, *Biophys. J.* 102 (2012) 2595–2604.
- [2] J. Singh, J.B. Udgaonkar, Molecular mechanism of the misfolding and oligomerization of the prion protein: current understanding and its implications, *Biochemistry* 54 (2015) 4431–4442.
- [3] F. Chiti, C.M. Dobson, Protein misfolding, functional amyloid, and human disease, *Annu. Rev. Biochem.* 75 (2006) 333–366.
- [4] F. Bemporad, G. Calloni, S. Campioni, G. Plakoutsi, N. Taddei, F. Chiti, Sequence and structural determinants of amyloid fibril formation, *Acc. Chem. Res.* 39 (2006) 620–627.
- [5] L.C. Serpell, M. Sunde, M.D. Benson, G.A. Tennent, M.B. Pepys, P.E. Fraser, The protofibril substructure of amyloid fibrils, *J. Mol. Biol.* 300 (2000) 1033–1039.
- [6] J.L. Galea, R. Sarroukh, P. Yunes-Quartino, J.M. Ruyschaert, V. Raussens, M.S. Celej, Structural remodeling during amyloidogenesis of physiological N(alpha)-acetylated alpha-synuclein, *Biochim. Biophys. Acta* 1864 (2016) 501–510.
- [7] J. Zhang, F. Wang, S. Chatterjee, Molecular dynamics studies on the buffalo prion protein, *J. Biomol. Struct. Dyn.* 34 (2016) 762–777.
- [8] C.M. Dobson, Protein folding and misfolding, *Nature* 426 (2003) 884–890.
- [9] T.P. Knowles, M. Vendruscolo, C.M. Dobson, The amyloid state and its association with protein misfolding diseases, *Nat. Rev. Mol. Cell Biol.* 15 (2014) 384–396.
- [10] E. Gazit, Mechanisms of amyloid fibril self-assembly and inhibition. Model short peptides as a key research tool, *FEBS J.* 272 (2005) 5971–5978.
- [11] K. Pagano, F. Bemporad, F. Fogolari, G. Esposito, P. Viglino, F. Chiti, A. Corazza, Structural and dynamics characteristics of acylphosphatase from *Sulfolobus solfataricus* in the monomeric state and in the initial native-like aggregates, *J. Biol. Chem.* 285 (2010) 14689–14700.
- [12] A. Olofsson, J.H. Ippel, S.S. Wijmenga, E. Lundgren, A. Ohman, Probing solvent accessibility of transthyretin amyloid by solution NMR spectroscopy, *J. Biol. Chem.* 279 (2004) 5699–5707.
- [13] J.S. Elam, A.B. Taylor, R. Strange, S. Antonyuk, P.A. Doucette, J.A. Rodriguez, S.S. Hasnain, L.J. Hayward, J.S. Valentine, T.O. Yeates, P.J. Hart, Amyloid-like filaments and water-filled nanotubes formed by SOD1 mutant proteins linked to familial ALS, *Nat. Struct. Biol.* 10 (2003) 461–467.
- [14] G. Plakoutsi, F. Bemporad, M. Monti, D. Pagnozzi, P. Pucci, F. Chiti, Exploring the mechanism of formation of native-like and precursor amyloid oligomers for the native acylphosphatase from *Sulfolobus solfataricus*, *Structure* 14 (2006) 993–1001.
- [15] M. Landreh, A. Rising, J. Presto, H. Jorvall, J. Johansson, Specific chaperones and regulatory domains in control of amyloid formation, *J. Biol. Chem.* 290 (2015) 26430–26436.
- [16] A.P. Pawar, K.F. Dubay, J. Zurdo, F. Chiti, M. Vendruscolo, C.M. Dobson, Prediction of “aggregation-prone” and “aggregation-susceptible” regions in proteins associated with neurodegenerative diseases, *J. Mol. Biol.* 350 (2005) 379–392.
- [17] Y.J. Kang, M.O. Olson, C. Jones, H. Busch, Nuclear phosphoproteins of normal rat liver and Novikoff hepatoma ascites cells, *Cancer Res.* 35 (1975) 1470–1475.
- [18] M. Okuwaki, K. Matsumoto, M. Tsujimoto, K. Nagata, Function of nucleophosmin/B23, a nucleolar acidic protein, as a histone chaperone, *FEBS Lett.* 506 (2001) 272–276.
- [19] B. Falini, I. Nicoletti, N. Bolli, M.P. Martelli, A. Liso, P. Gorello, F. Mandelli, C. Mecucci, M.F. Martelli, Translocations and mutations involving the nucleophosmin (NPM1) gene in lymphomas and leukemias, *Haematologica* 92 (2007) 519–532.
- [20] B. Falini, N. Bolli, A. Liso, M.P. Martelli, R. Mannucci, S. Pileri, I. Nicoletti, Altered nucleophosmin transport in acute myeloid leukaemia with mutated NPM1: molecular basis and clinical implications, *Leukemia* 23 (2009) 1731–1743.
- [21] V.M. Nambodiri, I.V. Akey, M.S. Schmidt-Zachmann, J.F. Head, C.W. Akey, The structure and function of *Xenopus* NO38-core, a histone chaperone in the nucleolus, *Structure* 12 (2004) 2149–2160.
- [22] H.H. Lee, H.S. Kim, J.Y. Kang, B.I. Lee, J.Y. Ha, H.J. Yoon, S.O. Lim, G. Jung, S.W. Suh, Crystal structure of human nucleophosmin-core reveals plasticity of the pentamer-pentamer interface, *Proteins* 69 (2007) 672–678.
- [23] D.M. Mitrea, C.R. Grace, M. Buljan, M.K. Yun, N.J. Pytel, J. Satumba, A. Nourse, C.G. Park, M. Madan Babu, S.W. White, R.W. Kriwacki, Structural polymorphism in the N-terminal oligomerization domain of NPM1, *Proc. Natl. Acad. Sci. U. S. A.* 111 (2014) 4466–4471.
- [24] D. Marasco, P.L. Scognamiglio, Identification of inhibitors of biological interactions involving intrinsically disordered proteins, *Int. J. Mol. Sci.* 16 (2015) 7394–7412.
- [25] A. Arcovito, S. Chiarella, S. Della Longa, A. Di Matteo, C. Lo Sterzo, G.L. Scaglione, L. Federici, Synergic role of nucleophosmin three-helix bundle and a flanking unstructured tail in the interaction with G-quadruplex DNA, *J. Biol. Chem.* 289 (2014) 21230–21241.
- [26] P.L. Scognamiglio, C. Di Natale, M. Leone, M. Poletto, L. Vitagliano, G. Tell, D. Marasco, G-quadruplex DNA recognition by nucleophosmin: new insights from protein dissection, *Biochim. Biophys. Acta* 1840 (2014) 2050–2059.
- [27] J.K. Box, N. Paquet, M.N. Adams, D. Boucher, E. Bolderson, K.J. O'Byrne, D.J. Richard, Nucleophosmin: from structure and function to disease development, *BMC Mol. Biol.* 17 (2016) 19.
- [28] C.G. Grummitt, F.M. Townsley, C.M. Johnson, A.J. Warren, M. Bycroft, Structural consequences of nucleophosmin mutations in acute myeloid leukemia, *J. Biol. Chem.* 283 (2008) 23326–23332.
- [29] F. Scaloni, S. Gianni, L. Federici, B. Falini, M. Brunori, Folding mechanism of the C-terminal domain of nucleophosmin: residual structure in the denatured state and its pathophysiological significance, *FASEB J.* 23 (2009) 2360–2365.
- [30] F. Scaloni, L. Federici, M. Brunori, S. Gianni, Deciphering the folding transition state structure and denatured state properties of nucleophosmin C-terminal domain, *Proc. Natl. Acad. Sci. U. S. A.* 107 (2010) 5447–5452.
- [31] S. Chiarella, L. Federici, A. Di Matteo, M. Brunori, S. Gianni, The folding pathway of a functionally competent C-terminal domain of nucleophosmin: protein stability and denatured state residual structure, *Biochem. Biophys. Res. Commun.* 435 (2013) 64–68.
- [32] E. Colombo, M. Alcalay, P.G. Pelicci, Nucleophosmin and its complex network: a possible therapeutic target in hematological diseases, *Oncogene* 30 (2011) 2595–2609.
- [33] R. Balusu, W. Fiskus, R. Rao, D.G. Chong, S. Nalluri, U. Mudunuru, H. Ma, L. Chen, S. Venkannagari, K. Ha, S. Abhyankar, C. Williams, J. McGuirk, H.J. Khoury, C. Ustun, K.N. Bhalla, Targeting levels or oligomerization of nucleophosmin 1 induces differentiation and loss of survival of human AML cells with mutant NPM1, *Blood* 118 (2011) 3096–3106.

- [34] B. Falini, M.P. Martelli, N. Bolli, R. Bonasso, E. Ghia, M.T. Pallotta, D. Diverio, I. Nicoletti, R. Pacini, A. Tabarrini, B.V. Galletti, R. Mannucci, G. Roti, R. Rosati, G. Specchia, A. Liso, E. Tiacci, M. Alcalay, L. Luzi, S. Volorio, L. Bernard, A. Guarini, S. Amadori, F. Mandelli, F. Pane, F. Lo-Coco, G. Saglio, P.G. Pelicci, M.F. Martelli, C. Mecucci, Immunohistochemistry predicts nucleophosmin (NPM) mutations in acute myeloid leukemia, *Blood* 108 (2006) 1999–2005.
- [35] B. Falini, C. Mecucci, E. Tiacci, M. Alcalay, R. Rosati, L. Pasqualucci, R. La Starza, D. Diverio, E. Colombo, A. Santucci, B. Bigerna, R. Pacini, A. Pucciarini, A. Liso, M. Vignetti, P. Fazi, N. Meani, V. Pettirossi, G. Saglio, F. Mandelli, F. Lo-Coco, P.G. Pelicci, M.F. Martelli, G.A.L.W. Party, Cytoplasmic nucleophosmin in acute myelogenous leukemia with a normal karyotype, *N. Engl. J. Med.* 352 (2005) 254–266.
- [36] B. Falini, I. Nicoletti, M.F. Martelli, C. Mecucci, Acute myeloid leukemia carrying cytoplasmic/mutated nucleophosmin (NPMc+ AML): biologic and clinical features, *Blood* 109 (2007) 874–885.
- [37] M. Okuwaki, A. Sumi, M. Hisaoka, A. Saotome-Nakamura, S. Akashi, Y. Nishimura, K. Nagata, Function of homo- and hetero-oligomers of human nucleoplasm/nucleophosmin family proteins NPM1, NPM2 and NPM3 during sperm chromatin remodeling, *Nucleic Acids Res.* 40 (2012) 4861–4878.
- [38] R.F. Schlenk, K. Dohner, J. Krauter, S. Frohling, A. Corbacioglu, L. Bullinger, M. Habdank, D. Spath, M. Morgan, A. Benner, B. Schlegelberger, G. Heil, A. Ganser, H. Dohner, Mutations and treatment outcome in cytogenetically normal acute myeloid leukemia, *N. Engl. J. Med.* 358 (2008) 1909–1918.
- [39] A. Di Matteo, M. Franceschini, S. Chiarella, S. Rocchio, C. Travaglini-Allocatelli, L. Federici, Molecules that target nucleophosmin for cancer treatment: an update, *Oncotarget* 7 (28) (2016) 44821–44840.
- [40] S. Chiarella, A. De Cola, G.L. Scaglione, E. Carletti, V. Graziano, D. Barcaroli, C. Lo Sterzo, A. Di Matteo, C. Di Ilio, B. Falini, A. Arcovito, V. De Laurenzi, L. Federici, Nucleophosmin mutations alter its nucleolar localization by impairing G-quadruplex binding at ribosomal DNA, *Nucleic Acids Res.* 41 (5) (2013) 3228–3239.
- [41] J. Xian, H. Shao, X. Chen, S. Zhang, J. Quan, Q. Zou, H. Jin, L. Zhang, Nucleophosmin mutants promote adhesion, migration and invasion of human leukemia THP-1 cells through MMPs up-regulation via Ras/ERK MAPK signaling, *Int. J. Biol. Sci.* 12 (2016) 144–155.
- [42] J.A. Pfister, S.R. D'Mello, Regulation of neuronal survival by nucleophosmin 1 (NPM1) is dependent on its expression level, subcellular localization and oligomerization status, *J. Biol. Chem.* (2016).
- [43] C. Di Natale, P.L. Scognamiglio, R. Cascella, C. Cecchi, A. Russo, M. Leone, A. Penco, A. Relini, L. Federici, A. Di Matteo, F. Chiti, L. Vitagliano, D. Marasco, Nucleophosmin contains amyloidogenic regions that are able to form toxic aggregates under physiological conditions, *FASEB J.* (2015).
- [44] P.L. Scognamiglio, C. Di Natale, M. Leone, R. Cascella, C. Cecchi, L. Lirussi, G. Antoniali, D. Riccardi, G. Morelli, G. Tell, F. Chiti, D. Marasco, Destabilisation, aggregation, toxicity and cytosolic mislocalisation of nucleophosmin regions associated with acute myeloid leukemia, *Oncotarget* (2016) Aug 1, <http://dx.doi.org/10.18632/oncotarget.10991>.
- [45] C.A. Hauser, R. Deng, A. Mishra, Y. Loo, U. Khoe, F. Zhuang, D.W. Cheong, A. Accardo, M.B. Sullivan, C. Riekel, J.Y. Ying, U.A. Hauser, Natural tri- to hexapeptides self-assemble in water to amyloid beta-type fiber aggregates by unexpected alpha-helical intermediate structures, *Proc. Natl. Acad. Sci. U. S. A.* 108 (2011) 1361–1366.
- [46] I. Walsh, F. Seno, S.C. Tosatto, A. Trovato, PASTA 2.0: an improved server for protein aggregation prediction, *Nucleic Acids Res.* 42 (2014) W301–W307.
- [47] I.C. Martins, I. Kuperstein, H. Wilkinson, E. Maes, M. Vanbrabant, W. Jonckheere, P. Van Gelder, D. Hartmann, R. D'Hooge, B. De Strooper, J. Schymkowitz, F. Rousseau, Lipids revert inert Abeta amyloid fibrils to neurotoxic protofibrils that affect learning in mice, *EMBO J.* 27 (2008) 224–233.
- [48] E. Gazit, A possible role for pi-stacking in the self-assembly of amyloid fibrils, *FASEB J.* 16 (2002) 77–83.
- [49] S.A. Hudson, H. Ecroyd, T.W. Kee, J.A. Carver, The thioflavin T fluorescence assay for amyloid fibril detection can be biased by the presence of exogenous compounds, *FEBS J.* 276 (2009) 5960–5972.
- [50] P. Sormanni, F.A. Aprile, M. Vendruscolo, The CamSol method of rational design of protein mutants with enhanced solubility, *J. Mol. Biol.* 427 (2015) 478–490.
- [51] C.L. Pashley, E.W. Hewitt, S.E. Radford, Comparison of the aggregation of homologous beta2-microglobulin variants reveals protein solubility as a key determinant of amyloid formation, *J. Mol. Biol.* 428 (2016) 631–643.
- [52] G.G. Tartaglia, M. Vendruscolo, The Zyggregator method for predicting protein aggregation propensities, *Chem. Soc. Rev.* 37 (2008) 1395–1401.
- [53] S.L. Crick, K.M. Ruff, K. Garai, C. Frieden, R.V. Pappu, Unmasking the roles of N- and C-terminal flanking sequences from exon 1 of huntingtin as modulators of polyglutamine aggregation, *Proc. Natl. Acad. Sci. U. S. A.* 110 (2013) 20075–20080.
- [54] S.D. Moran, M.T. Zanni, How to get insight into amyloid structure and formation from infrared spectroscopy, *J. Phys. Chem. Lett.* 5 (2014) 1984–1993.
- [55] R.W. Sarver Jr., W.C. Krueger, Protein secondary structure from Fourier transform infrared spectroscopy: a data base analysis, *Anal. Biochem.* 194 (1991) 89–100.
- [56] D.R. Norton, A. Keller, The spherulitic and lamellar morphology of melt-crystallized isotactic polypropylene, *Polymer* 26 (1985) 704–716.
- [57] M.R. Krebs, C.E. Macphee, A.F. Miller, I.E. Dunlop, C.M. Dobson, A.M. Donald, The formation of spherulites by amyloid fibrils of bovine insulin, *Proc. Natl. Acad. Sci. U. S. A.* 101 (2004) 14420–14424.
- [58] C. Exley, E. House, T. Patel, L. Wu, P.E. Fraser, Human pro-islet amyloid polypeptide (ProIAPP(1–48)) forms amyloid fibrils and amyloid spherulites in vitro, *J. Inorg. Biochem.* 104 (2010) 1125–1129.
- [59] V. Castelletto, I.W. Hamley, Self assembly of a model amphiphilic phenylalanine peptide/polyethylene glycol block copolymer in aqueous solution, *Biophys. Chem.* 141 (2009) 169–174.
- [60] C. Lara, S. Gourdin-Bertin, J. Adamcik, S. Bolisetty, R. Mezzenga, Self-assembly of ovalbumin into amyloid and non-amyloid fibrils, *Biomacromolecules* 13 (2012) 4213–4221.
- [61] L.C. Serpell, Alzheimer's amyloid fibrils: structure and assembly, *Biochim. Biophys. Acta* 1502 (2000) 16–30.
- [62] C. Diaferia, E. Gianolio, P. Palladino, F. Arena, C. Boffa, G. Morelli, A. Accardo, Peptide materials obtained by aggregation of polyphenylalanine conjugates as gadolinium-based magnetic resonance imaging contrast agents, *Adv. Funct. Mater.* 25 (2015) 7003–7016.
- [63] M.F.A., C. Diaferia, C. Giannini, T. Sibillano, G. Morelli, L. M., A. Accardo, Self-assembly of PEGylated tetra-phenylalanine derivatives: structural insights from solution and solid state studies, *Sci. Rep.* 6 (2016), 26638 2016 May 25.
- [64] C.M. Dobson, Protein misfolding, evolution and disease, *Trends Biochem. Sci.* 24 (1999) 329–332.
- [65] R. Linding, J. Schymkowitz, F. Rousseau, F. Diella, L. Serrano, A comparative study of the relationship between protein structure and beta-aggregation in globular and intrinsically disordered proteins, *J. Mol. Biol.* 342 (2004) 345–353.
- [66] A.M. Fernandez-Escamilla, F. Rousseau, J. Schymkowitz, L. Serrano, Prediction of sequence-dependent and mutational effects on the aggregation of peptides and proteins, *Nat. Biotechnol.* 22 (2004) 1302–1306.
- [67] A. Aggeli, M. Bell, L.M. Carrick, C.W. Fishwick, R. Harding, P.J. Mawer, S.E. Radford, A.E. Strong, N. Boden, pH as a trigger of peptide beta-sheet self-assembly and reversible switching between nematic and isotropic phases, *J. Am. Chem. Soc.* 125 (2003) 9619–9628.
- [68] A. Aggeli, G. Fytas, D. Vlassopoulos, T.C. McLeish, P.J. Mawer, N. Boden, Structure and dynamics of self-assembling beta-sheet peptide tapes by dynamic light scattering, *Biomacromolecules* 2 (2001) 378–388.
- [69] Y. Fezoui, D.M. Hartley, D.M. Walsh, D.J. Selkoe, J.J. Osterhout, D.B. Teplow, A de novo designed helix-turn-helix peptide forms nontoxic amyloid fibrils, *Nat. Struct. Biol.* 7 (2000) 1095–1099.
- [70] T.R. Jahn, O.S. Makin, K.L. Morris, K.E. Marshall, P. Tian, P. Sikorski, L.C. Serpell, The common architecture of cross-beta amyloid, *J. Mol. Biol.* 395 (2010) 717–727.
- [71] M. Sunde, C. Blake, The structure of amyloid fibrils by electron microscopy and X-ray diffraction, *Adv. Protein Chem.* 50 (1997) 123–159.
- [72] J.C. Rodriguez-Perez, I.W. Hamley, A.M. Squires, Determination of orientations of aromatic groups in self-assembled peptide fibrils by polarised Raman spectroscopy, *Phys. Chem. Chem. Phys.* 15 (2013) 13940–13950.
- [73] M.R. Sawaya, S. Sambashivan, R. Nelson, M.I. Ivanova, S.A. Sievers, M.I. Apostol, M.J. Thompson, M. Balbirnie, J.J. Wiltzius, H.T. McFarlane, A.O. Madsen, C. Riekel, D. Eisenberg, Atomic structures of amyloid cross-beta spines reveal varied steric zippers, *Nature* 447 (2007) 453–457.
- [74] J.L. Silva, C.V. De Moura Gallo, D.C. Costa, L.P. Rangel, Prion-like aggregation of mutant p53 in cancer, *Trends Biochem. Sci.* 39 (2014) 260–267.
- [75] D.C. Costa, G.A. de Oliveira, E.A. Cino, I.N. Soares, L.P. Rangel, J.L. Silva, Aggregation and prion-like properties of misfolded tumor suppressors: is cancer a prion disease? *Cold Spring Harb. Perspect. Biol.* 8 (2016).
- [76] A. Soragni, D.M. Janzen, L.M. Johnson, A.G. Lindgren, A. Thai-Quynh Nguyen, E. Tiourin, A.B. Soriaga, J. Lu, L. Jiang, K.F. Faull, M. Pellegrini, S. Memarzadeh, D.S. Eisenberg, A designed inhibitor of p53 aggregation rescues p53 tumor suppression in ovarian carcinomas, *Cancer Cell* 29 (2016) 90–103.
- [77] G.B. Fields, R.L. Noble, Solid phase peptide synthesis utilizing 9-fluorenylmethoxycarbonyl amino acids, *Int. J. Pept. Protein Res.* 35 (1990) 161–214.
- [78] G.N. Roviello, G. Roviello, D. Musumeci, E.M. Bucci, C. Pedone, Dakin-West reaction on 1-thymyl acetic acid for the synthesis of 1,3-bis(1-thymyl)-2-propanone, a heteroaromatic compound with nucleopeptide-binding properties, *Amino Acids* 43 (2012) 1615–1623.
- [79] G.N. Roviello, C. Vicidomini, S. Di Gaetano, D. Capasso, D. Musumeci, V. Roviello, Solid phase synthesis and RNA-binding activity of an arginine-containing nucleopeptide, *RSC Adv.* 6 (2016) 14140–14148.
- [80] M. Sunde, L.C. Serpell, M. Bartlam, P.E. Fraser, M.B. Pepys, C.C. Blake, Common core structure of amyloid fibrils by synchrotron X-ray diffraction, *J. Mol. Biol.* 273 (1997) 729–739.
- [81] D. Altamura, R. Lassandro, F.A. Vittoria, L. De Caro, D. Siliqi, M. Ladisa, C. Giannini, X-ray microimaging laboratory (XMI-LAB), *J. Appl. Crystallogr.* 45 (2012) 869–873.
- [82] T. Sibillano, L. De Caro, D. Altamura, D. Siliqi, M. Ramella, F. Boccafoschi, G. Ciasca, G. Campi, L. Tirinato, E. Di Fabrizio, C. Giannini, An optimized table-top small-angle X-ray scattering set-up for the nanoscale structural analysis of soft matter, *Sci. Rep.* 4 (2014).

SCIENTIFIC REPORTS



OPEN

Cross-beta nanostructures based on dinaphthylalanine Gd-conjugates loaded with doxorubicin

Carlo Diaferia¹, Eliana Gianolio², Teresa Sibillano³, Flavia Anna Mercurio⁴, Marilisa Leone⁴, Cinzia Giannini³, Nicole Balasco⁴, Luigi Vitagliano⁴, Giancarlo Morelli¹ & Antonella Accardo¹

Received: 26 October 2016

Accepted: 1 February 2017

Published online: 22 March 2017

Very recently we proposed novel di- and tetra-phenylalanine peptides derivatized with gadolinium complexes as potentials supramolecular diagnostic agents for applications in MRI (Magnetic Resonance Imaging). It was observed that in very short FF dipeptide building blocks, the propensity to aggregate decreases significantly after modification with bulky moiety such as Gd-complexes, thus limiting their potential as CAs. We hypothesized that the replacement of the Phe side chain with more extended aromatic groups could improve the self-assembling. Here we describe the synthesis, structural and relaxometric behavior of a novel water soluble self-assembled peptide CA based on 2-naphthylalanine (2NaI). The peptide conjugate Gd-DOTA-L₆-(2NaI)₂ is able to self-assemble in long fibrillary nanostructures in water solution (up to 1.0 mg/mL). CD and FTIR spectroscopies indicate a β sheet secondary structure with an antiparallel orientation of single strands. All data are in good agreement with WAXS and SAXS characterizations that show the typical “cross- β pattern” for fibrils at the solid state. Molecular modeling indicates the three-dimensional structure of the peptide spine of aggregates is essentially constituted by extended β -sheet motifs stabilized by hydrogen bonds and hydrophobic interactions. The high relaxivity of nanoaggregates (12.3 mM⁻¹ s⁻¹ at 20 MHz) and their capability to encapsulate doxorubicin suggest their potential application as supramolecular theranostic agents.

Since its identification as recognition motif of the Alzheimer's β -amyloid peptide, the aromatic homodimer diphenylalanine (FF) has been largely studied for its capability to self-organize into a large variety of nanostructures (NSs) from nanotubes to nanofibrils, vesicles and organogels^{1,2}. The morphological variability of NSs structurally depends on the experimental procedure adopted for their preparation such as the polarity of the solvent³, the pH value⁴ or temperature⁵. In addition, chemical modifications of the aromatic homodimer, including the introduction of a thiol group or of a fluorenylmethyloxycarbonyl (Fmoc) group, can cause variations in the morphology of the aggregate². The morphology of the FF-NSs seems to be determinant for their physicochemical properties. Mechanical, electrochemical and optoelectronic properties of FF-NSs² leave envisage a their potential application in nanofabrication and industrial fields. However, only a few studies have been devoted, until now on their potential abilities in the biomedical field². Moreover, also their applications in the diagnostic field remains unexplored, overall for the low intrinsic water solubility of these derivatives. Very recently we described the first example of supramolecular aggregates based on PEGylated cationic di-phenylalanine and tetra-phenylalanine conjugates as enhanced contrast agents (CAs) for diagnostic applications in Magnetic Resonance Imaging (MRI)⁶. These conjugates contain two (FF or F2) or four (F4) phenylalanine residues for promoting the self-assembly, a branched or linear bifunctional chelating agent such as DOTA (1,4,7,10-tetraazacyclododecane-N,N,N,N-tetraacetic acid) or DTPA (diethylenetriamine penta-acetate), for achieving the kinetically stable and thermodynamically inert coordination of the gadolinium paramagnetic ion and an ethoxylic linker at six PEG units (L₆) between the chelating agent and the oligopeptide. In zwitterionic FF homodimer the self-assembling pathway is driven by head-to-tail hydrogen-bonding between the charged termini of neighbouring dipeptides and “T-shaped” contacts between the amino acid side-chains^{7,8}. On the contrary, in capped uncharged dipeptide FF the loss of the

¹Department of Pharmacy, Research Centre on Bioactive Peptides (CIRPeB), University of Naples “Federico II”, Via Mezzocannone 16, 80134, Naples, Italy. ²Department of Molecular Biotechnologies and Health Science, University of Turin, Via Nizza 52, 10125, Turin, Italy. ³Institute of Crystallography (IC), CNR, Via Amendola 122, 70126, Bari, Italy. ⁴Institute of Biostructure and Bioimaging (IBB), CNR, via Mezzocannone 16, 80134, Naples, Italy. Correspondence and requests for materials should be addressed to A.A. (email: antonella.accardo@unina.it)

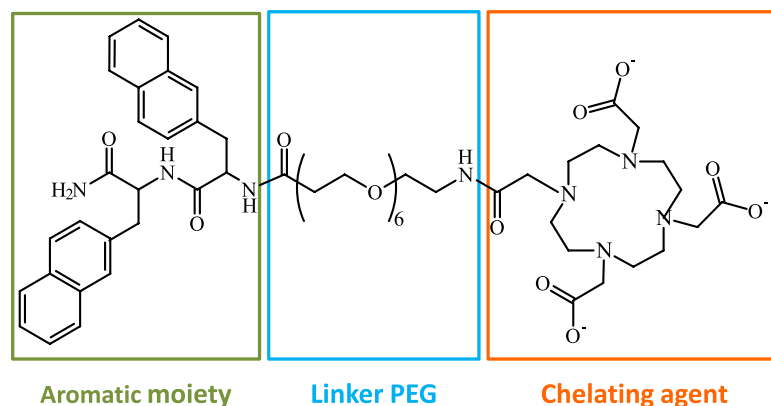
head-to-tail hydrogen-bonding occurs. Nevertheless, the aromatic stacking interactions allow for recovering the self-aggregation behaviour⁹. However, we observed that in very short peptide building blocks the propensity to aggregate decreases significantly after modification with bulky moiety such as Gd-complexes⁶. On the contrary F4 conjugates, with a more extended aromatic framework, keep their capability to self-aggregate giving well-structured nanofibres, also after the complexation of the gadolinium ions. These results point out that the elongation of the aromatic framework from two to four residues can represent a successful strategy to recover the aggregation propensity. As an alternative, the replacement of the Phe side chain with more extended aromatic groups could increase the self-assembling propensity of these compounds. Here, we report the synthesis of a novel peptide conjugate DOTA-L₆-(2Nal)₂ (Fig. 1a) obtained replacing the phenylalanine with the non-coded amino acid 2-naphthylalanine (2Nal). Both the aromatic conjugate DOTA-L₆-(2Nal)₂ (mentioned as 2Nal₂) and its gadolinium complex Gd-DOTA-L₆-(2Nal)₂ (reported as Gd-2Nal₂) are able to self-assemble spontaneously in water solution. The morphology of the supramolecular assemblies was evaluated with transmission electron microscopy (TEM). A deep characterization of nanostructures at the nano and atomic scale was achieved both in solution and at the solid state with SAXS/WAXS, fluorescence, ¹HNMR, Fourier Transform Infrared (FTIR), circular dichroism (CD), and molecular modelling. The relaxivity properties of these nanostructures were studied. Moreover, fluorescence spectroscopy and ¹HNMR studies and optical microscopy images provide the evidence for their capability to encapsulate anticancer drugs such as doxorubicin.

Results and Discussion

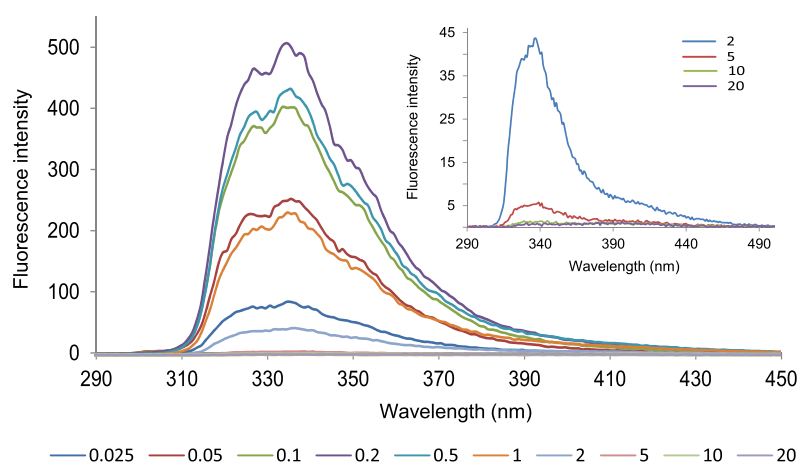
Design synthesis and fluorescence studies. The very short peptide conjugate Gd-DOTA-L₆-F2 was previously synthesized and characterized in our previous work⁶. Physicochemical characterization pointed out that DOTA-L₆-F2 is able to weakly self-aggregate and only before gadolinium coordination. The aggregation is mediated by π -stacking between the aromatic side chains of phenylalanine residues. Due to steric repulsion of the Gd-complex, after metal coordination, the dipeptide seems unable to keep π - π interactions. The replacement of the phenyl group with a more extended aromatic one (such as 2-naphthyl group) could in principle restore the stacking. In this perspective, we synthesized and fully characterized DOTA-L₆-(2Nal)₂ (here indicated as 2Nal₂), an analogue of the parental DOTA-L₆-F2, in which the two phenylalanine residues were replaced with the non-coded amino acid 2-naphthylalanine (2-Nal). Peptide synthesis of 2Nal₂ was achieved according to the standard protocols of the solid phase synthesis with Fmoc/tBu strategy, the peptide was then characterized with LC-MS (see Figure S1A) and ¹H-NMR. After purification, the DOTA chelating agent was complexed with lanthanide metal ions, i.e. gadolinium (Gd) or lanthanum (La) for MRI or NMR studies, respectively. Nevertheless in spite of the higher hydrophobicity of the naphthyl group with respect to the phenyl one, the Gd-2Nal₂ derivative keeps high water solubility, and the solutions remain perfectly clear up to 50 mg/mL; whereas a further increase of the concentration causes its hydrogelation. Lowering the temperature below 5 °C, fast hydrogel formation occurs yet at 20 mg/mL. The peptide conjugate Gd-2Nal₂ shows high stability also in physiological conditions (10 mM phosphate buffer 0.9 wt.% NaCl at pH 7.4) (see Figure S2). Self-organization of the peptide conjugates at the atomic level was further characterized also in solution with fluorescence, UV-Vis, ¹HNMR, CD and FTIR spectroscopies. In Fig. 1b and c are reported fluorescence spectra of 2Nal₂ and Gd-2Nal₂ at several concentrations (from 0.025 to 20.0 mg/mL) obtained by exciting the samples at 280 nm, which corresponds to the wavelength of absorption for the 2-naphthylalanine (Figure S1B). From inspection of Fig. 1b, the typical emission spectrum of the 2-naphthyl group with three maxima at 325, 340 and 355 nm, respectively, can be detected. The fluorescence intensity of 2Nal₂ (see Fig. 1b) increases gradually in the range of concentration between 0.025 and 0.2 mg/mL. After this concentration a progressive intensity decrease, attributable to the stacking of the aromatic rings, occurs. Since 2.0 mg/mL, the fluorescence intensity is very low. From inspection of the inset in Fig. 1b a weak peak, that is centered between 380–430 nm and indicative of excimer formation, is visible. These results suggest that the peptide derivative begins to undergo self-aggregation phenomena at 0.2–0.5 mg/mL (150–375 μ M). However, the appearance of the excimer peak above 2.0 mg/mL leaves us to hypothesize that very stable aggregates can be formed above 2.0 mg/mL. A similar behaviour was observed after the gadolinium coordination (see Fig. 1c). However in Gd-2Nal₂, both the decrease of the fluorescence intensity (0.1 mg/mL) and the appearance of the excimeric peak (1.0 mg/mL) were observed at lower concentration with respect to 2Nal₂, thus confirming that the neutralization of the negative charges on the chelating agent, after the Gd-coordination, induces a better self-assembling in these peptide conjugates. Determination of the critical aggregation concentration (CAC) value of Gd-2Nal₂ was carried out using a fluorescence-based method, in which ANS was used as fluorescent probe. This dye is completely silent at the fluorescence in aqueous solution, but emits in the range 460–480 nm when is surrounded by a hydrophobic environment¹⁰. A solution of ANS in cuvette (20 μ M) was titrated with Gd-2Nal₂ and the fluorescence intensities maximum measured at 470 nm have been plotted in Figure S3. CAC value, determined from the graphical breakpoint, is $\sim 6.70 \cdot 10^{-4}$ M (0.86 mg/mL). This value is 10-fold higher than the CAC value ($5.1 \cdot 10^{-5}$ M, 0.076 mg/mL) previously found for tetraphenylalanine Gd-complex Gd-DOTA-L₆-F4. This consideration suggests that the replacement of the phenyl ring with the naphthyl one allows to increase the aggregation propensity with respect to diphenylalanine conjugates (Gd-DOTA-L₆-F2). However from the comparison of CAC values (Gd-DOTA-L₆-F2 > Gd-DOTA-L₆-Nal₂ > Gd-DOTA-L₆-F4) it emerges that the increase of the number of aromatic residues⁶ causes a better aggregation with respect to the replacement of Phe with more extended aromatic group.

NMR studies. This trend was also confirmed by ¹HNMR measurements (see Figure S4). We have recently analyzed the conformational properties of DOTA-L₆-F4 in aqueous solution by mono- and multi-dimensional, homo- and hetero-nuclear NMR techniques¹¹. In the present work we have used a similar approach and thus implemented 1D [¹H] and 2D [¹H, ¹H] NMR spectroscopy to study two different compounds: DOTA-L₆-F2 and 2Nal₂ analogue in absence and in presence of the DOTA coordinated metal ion lanthanum (III), La. We used lanthanum (III) since it gives rise to a NMR “easy to handle” diamagnetic complex. Both DOTA-L₆-F2 and

(a)



(b)



(c)

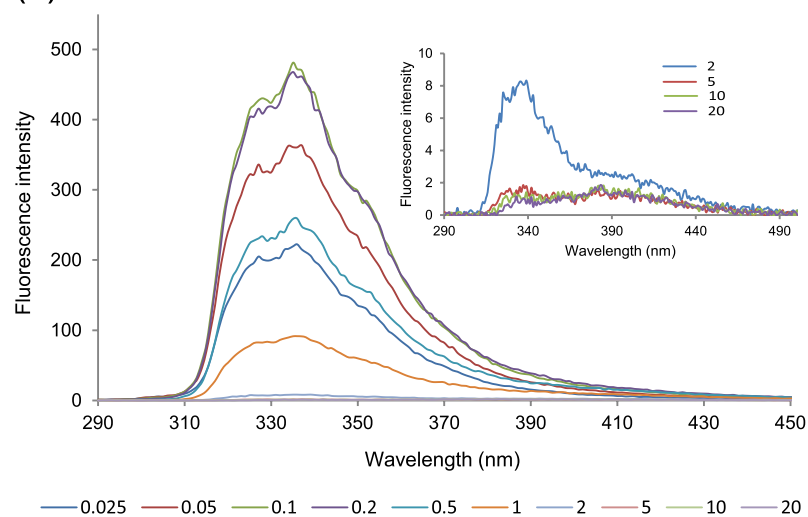


Figure 1. (a) Schematic representation of di-aromatic compounds obtained by SPPS with Fmoc chemistry. Conjugates contain an aromatic framework consisting of two 2-naphthylalanine (2-Nal) residues, an ethoxylic linker (L_6) formed by six PEG units and bifunctional and macrocyclic chelating agent (DOTA) for gadolinium (III) coordination. (b and c) Fluorescence spectra of 2NaI₂ and Gd-2NaI₂ in 0.025–20.0 mg/mL concentration range. Samples were excited at $\lambda = 280$ nm and recorded between 290 and 500 nm.

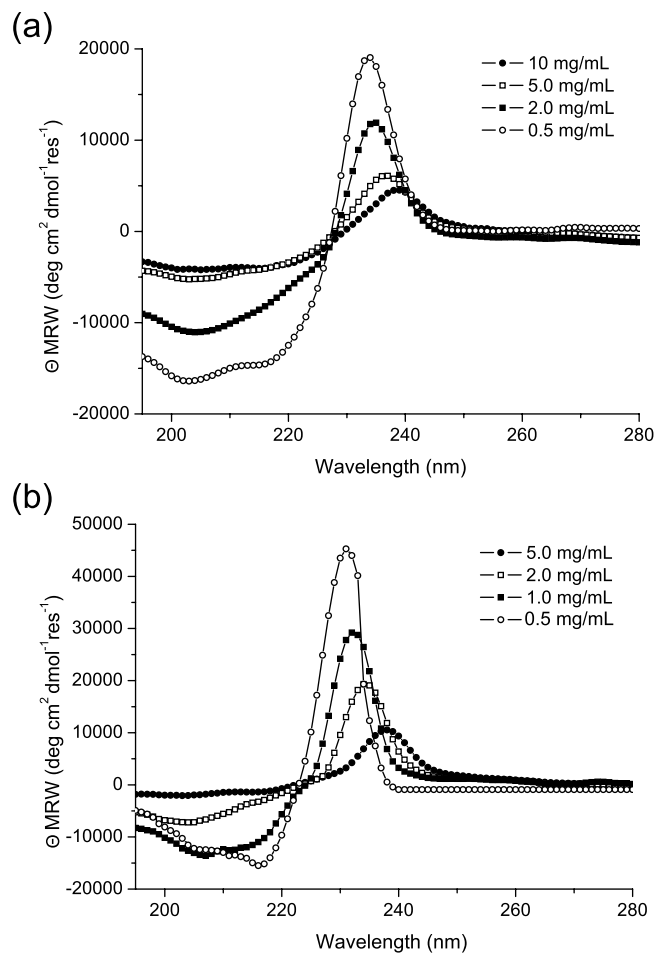


Figure 2. Selected Far-UV CD spectra of 2NaI_2 (a) and $\text{Gd-}2\text{NaI}_2$ (b) in a concentration range of 0.5–20.0 mg mL^{-1} . Spectra are recorded between 280 and 195 nm.

2NaI_2 present low aggregation propensities. The process of resonance assignments of the two molecules could be easily achieved at a concentration equal to 1 mM (see Supplemental Material Tables S1, S2 and Figure S5). For the DOTA- L_6 -F2 relevant changes in the spectra, indicating occurrence of potential aggregation processes, take place at a concentration higher than 1.2 mg/mL (Figure S4a-left panel). In detail by comparing spectra recorded at 0.3 mg/mL and 5.0 mg/mL chemical shift changes appear relevant in the spectral regions between 8.0 and 8.2 ppm, where signals from HN amide protons are present and between 3.0 and 3.5 ppm where several peaks overlap (Table S1). However, even at the highest investigated concentrations, peaks in the NMR spectra remain rather sharp thus pointing towards formation of small size aggregates. Once complexed with La (III) the DOTA- L_6 -F2 presents similar weak aggregation propensity (Figure S4b-left panel). For 2NaI_2 in the absence of coordinated metal ions, from 0.1 mg/mL till 5.0 mg/mL , we cannot reveal significant aggregation as the signals in the NMR spectra do not become broad or change their chemical shifts (Figure S4a-right panel). Once La (III) is inserted in 2NaI_2 the aggregation tendency increases and line broadening starts to affect the spectra thus indicating formation of aggregated species already at 0.8 mg/mL concentration; at 2.5 mg/mL concentration extensive line broadening causes partial signal loss thus indicating the presence of larger aggregates (Figure S4b-right panel). Aggregation as witnessed by line broadening is affecting all signals in the NMR spectrum of 2NaI_2 (See for instance the H_N amide and aromatic protons region in Figure S4b-right panel). This different aggregation property in presence and absence of the metal ion likely indicates that La (III) by neutralizing DOTA negative charges is favoring intermolecular interaction by lowering electrostatic repulsions. Moreover, NMR data show that La- 2NaI_2 has a higher tendency to aggregate with respect to La-DOTA- L_6 -F2; this outcome can be easily explained by the larger aromatic patches present in the former molecule which are likely favoring larger intermolecular π -stacking interactions. These data indicate consequently that the $\text{Gd-}2\text{NaI}_2$ may work better as a potential MRI contrast agent than $\text{Gd-DOTA-}\text{L}_6$ -F2.

Secondary structure characterization. Secondary structure assumed by 2NaI_2 and $\text{Gd-}2\text{NaI}_2$, was investigated by Circular Dichroism (CD) and by Fourier Transform Infrared (FTIR) spectroscopies. CD spectra, reported in Fig. 2a and b, were recorded both below and above the self-aggregation concentration. Independently from the coordination of the metal, 2NaI_2 peptide shows a similar dichroic signature: at 0.5 mg/mL , there are two minima around 205 and 218 nm and a maximum at 232 nm. This dichroic signature is perfectly identical and

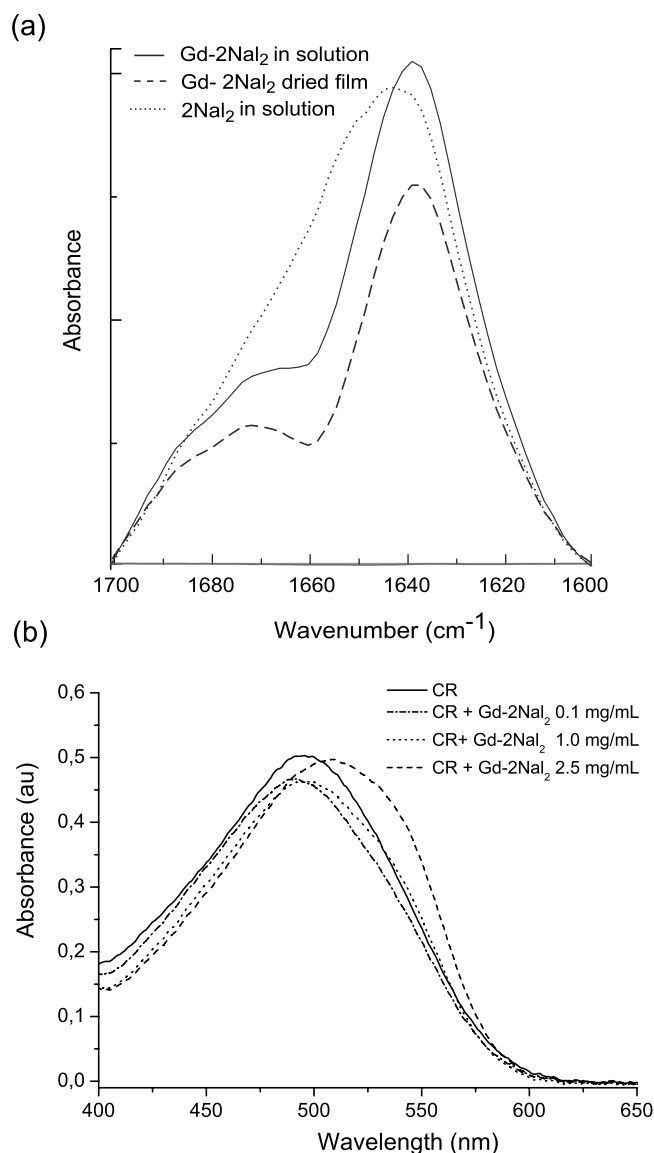


Figure 3. (a) FTIR spectra of 2Nal₂ and Gd-2Nal₂ in the amide I region at 5.0 mg/mL. (b) UV-Vis spectra of 2Nal₂ and Gd-2Nal₂, stained with Congo Red at 0.1 and 1.0 mg/mL. The spectrum of Congo Red is also reported for comparison.

symmetric to that previously observed for tetra-phenylalanine conjugates⁶. The two minima are attributable to the stacking between the 2-naphthyl aromatic rings, whereas the maximum is typically observed in presence of β -structure. Above this concentration value a progressive red-shift of the maximum (up to 340 nm), as function of the peptide concentration, occurs. This spectral shift is accompanied by the decrease of the maximum and by the presence of an isobestic point. Both the shift and the decrease of the maximum indicate the formation in solution of nanostructures with a dominant β -sheet arrangement. Further information on the secondary structural organization of the peptide conjugates was achieved using FTIR spectroscopy in the region of the amide I vibrational band (1600–1700 cm^{-1}). FTIR spectra of 2Nal₂ and Gd-2Nal₂ at 5.0 mg/mL in the amide I region are reported in Fig. 3a. Spectrum of Gd-2Nal₂ as dried film is also reported. Gd-2Nal₂ FTIR spectra, both at the solid state and in solution, show a dominant peak around 1638 cm^{-1} , expected for β -sheet formation. In addition, both spectra have a secondary peak around 1680 cm^{-1} , that is normally observed for antiparallel orientation of the β -sheet. By comparing these spectra with spectrum of 2Nal₂, it appears a very broad peak at 1642 cm^{-1} .

Congo Red spectroscopic assay. The high tendency of Gd-2Nal₂ to self-aggregate in amyloid-like fibrillary nanostructures in solution was confirmed by Congo Red (CR) staining assay. CR is a well-known azoic dye, used as indicator of the occurrence of amyloid like fibrils¹². CR alone exhibits in UV-Vis a typical absorbance maximum at 490 nm (see Fig. 3b). When incubated with fibrillary aggregates, its spectral profile changes and a shift of the CR band from 490 to 540 nm is expected. In our experiment, depicted in Fig. 3b, CR UV-Vis

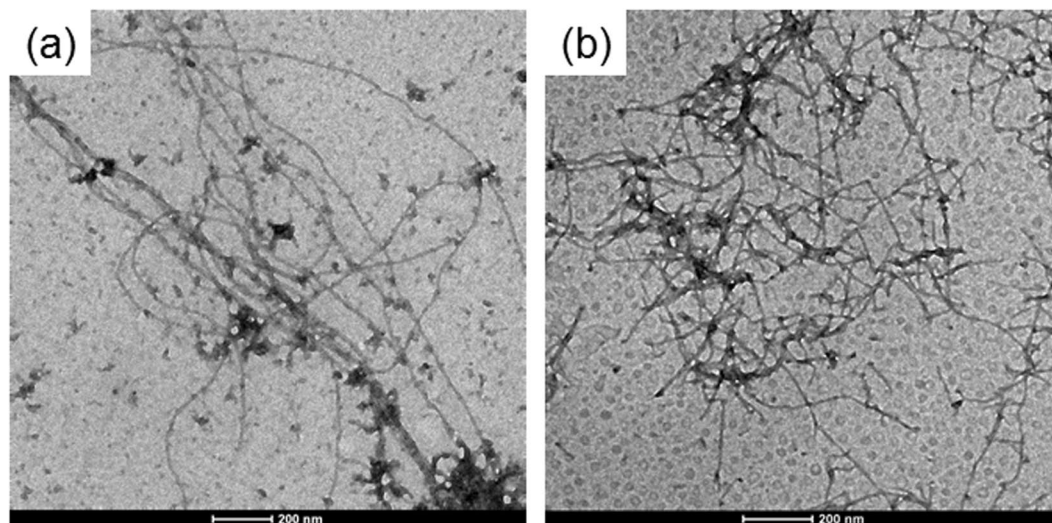


Figure 4. Selected TEM images for 2NaI₂ (a) and Gd-2NaI₂ (b) at 5.0 mg/mL.

maximum undergoes a clear shift after incubation with Gd-2NaI₂ at 2.5 mg/mL. Instead, any variation or a slight shift can be evidenced for CR incubated with 0.1 and 1.0 mg/mL, respectively.

Materials characterization and molecular modelling. Self-assembled peptide conjugate at 5.0 mg/mL, as free base or as metal complex, was initially characterized using TEM. TEM images reported in Fig. 4a and b demonstrate the assembling of both 2NaI₂ and Gd-2NaI₂ in long fibrillary nanostructures. On the other hand, TEM images of Gd-DOTA-L₆-F2 do not show any supramolecular aggregate (data not shown). To further analyze the supramolecular morphology of 2NaI₂ and Gd-2NaI₂ at the micro and nano scale, WAXS and SAXS measurements were performed on dried fibres prepared according to the stretch frame method¹³. Figures 5a,b and 6a,b present the two-dimensional (2D) WAXS and SAXS patterns collected on the 2NaI₂ and Gd-2NaI₂ samples, respectively. The 2D patterns, once centered, calibrated and radially folded into 1D profiles, are shown in Figs 5c,d and 6c,d, respectively. The low-*q* region of each WAXS pattern is displayed separately in Figs 5e and 6e to better visualize the diffraction peaks. The red and black WAXS/SAXS profiles correspond to the meridional and equatorial directions marked by the red arrows in panels (b). The position of most intense meridional and equatorial diffraction peaks are reported in Table 1. Both fibers present the classic cross- β fiber 2D WAXS diffraction pattern with the β -strands distance at $d_{\beta 1} = 4.7 \pm 0.3 \text{ \AA}$ along the meridional direction (fiber axis). The 2D SAXS patterns display a clear diffraction structure. The most intense peaks lay along the equatorial direction, for both samples. The presence of a diffraction pattern both in SAXS and in WAXS is fingerprint of a hierarchical organization of the molecules in fibers from the atomic to the nanoscale. The most intense SAXS peak in the Gd-2NaI₂ sample, labelled as e1 in Fig. 6d, corresponding to $d = 57 \text{ \AA}$, almost disappears in the 2NaI₂, where the most intense SAXS peak occurs at $d = 48 \text{ \AA}$ (e2 equatorial peak in Fig. 5d). We estimated the full-width-at-half-maximum along the azimuth angle for the e1 and e2 peaks in the insets of Figs 5d and 6d, which are FWHM (e1-Gd-2NaI₂) = 27° and FWHM (e2-2NaI₂) = 19°, respectively. Furthermore, for both aggregates intense equatorial peaks were observed in WAXS experiments (d range 21–25 Å). Although peaks in this region occur in both 2NaI₂ and Gd-2NaI₂ samples their location and intensity are not identical. This observation suggests that the metal complexation of 2NaI₂ induces some structural rearrangements. Altogether, SAXS and WAXS experiments provide some interesting clues on the organization of the peptide spine of these assemblies at different structural level. In particular, (a) the meridional peak at 4.7 Å atomic distance clearly indicates a cross- β structure in which the β -strands run perpendicular to the fiber axis, (b) the equatorial reflections at 21–25 Å likely represent regularities within the inter-sheet distances, and (c) the peaks at $d = 48$ and 57 Å provide some preliminary information on the nanofiber organization. In this framework, we performed molecular modeling analyses to gain insights into the atomic structure of the peptide moiety of these assemblies using the programs Coot and Pymol^{14,15}. Accordingly, we generated antiparallel cross- β models, which were stabilized by four inter-strand hydrogen bonds, to check whether NaI side chains could contribute to the stabilization of this motif. In particular, we evaluated the interactions between NaI side chains of consecutive β -strands within the cross β -sheet by considering all its possible rotameric states. We found combinations of rotameric states that maximized hydrophobic interactions between side chains of consecutive strands (Fig. 7a). Then, we evaluated how different β -sheets could laterally interact. We found that optimal interactions between the NaI side chains of facing β -sheets could be established when the inter-sheet distance was about 16–17 Å (Fig. 7b). Notably, although as minor peaks, equatorial reflections with this spacing were observed for both samples (Figs 5e and 6e). However, as mentioned above, the largest equatorial peaks that likely correspond to inter-sheet distances present spacings with $d = 21\text{--}25 \text{ \AA}$. This observation suggests that there are multiple ways in which β -sheets interact in these assemblies and that other species may mediate these inter-sheet interactions. In this scenario, it cannot be excluded that the hydrophobic rings of individual NaI molecules intercalate within the hydrophobic surfaces of facing β -sheets (Figure S6). In conclusion, our observations suggest that the basic structural elements of these assemblies is a cross β -sheet that is stabilized by both the hydrogen bonding

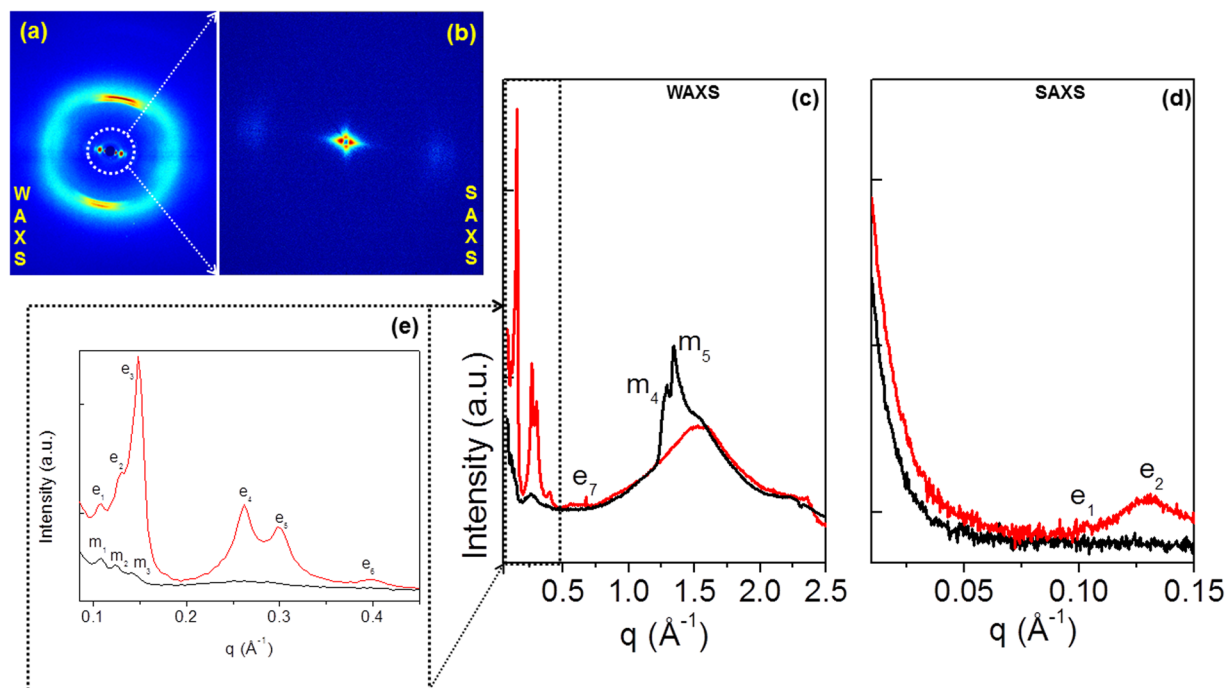


Figure 5. 2Na_2 fiber at solid state: (a,b) 2D WAXS and SAXS data; (c,d) 1D WAXS and SAXS profiles (red and black corresponding to the meridional and equatorial directions) as obtained once the corresponding 2D WAXS (a) and SAXS (b) data are centered, calibrated and radially folded; the inset in panel (d) refers to the equatorial e_2 reflection, with an estimated FWHM ($e_2\text{-}2\text{Na}_2$) = 19° ; (e) expanded WAXS region marked by a dotted rectangle in (c).

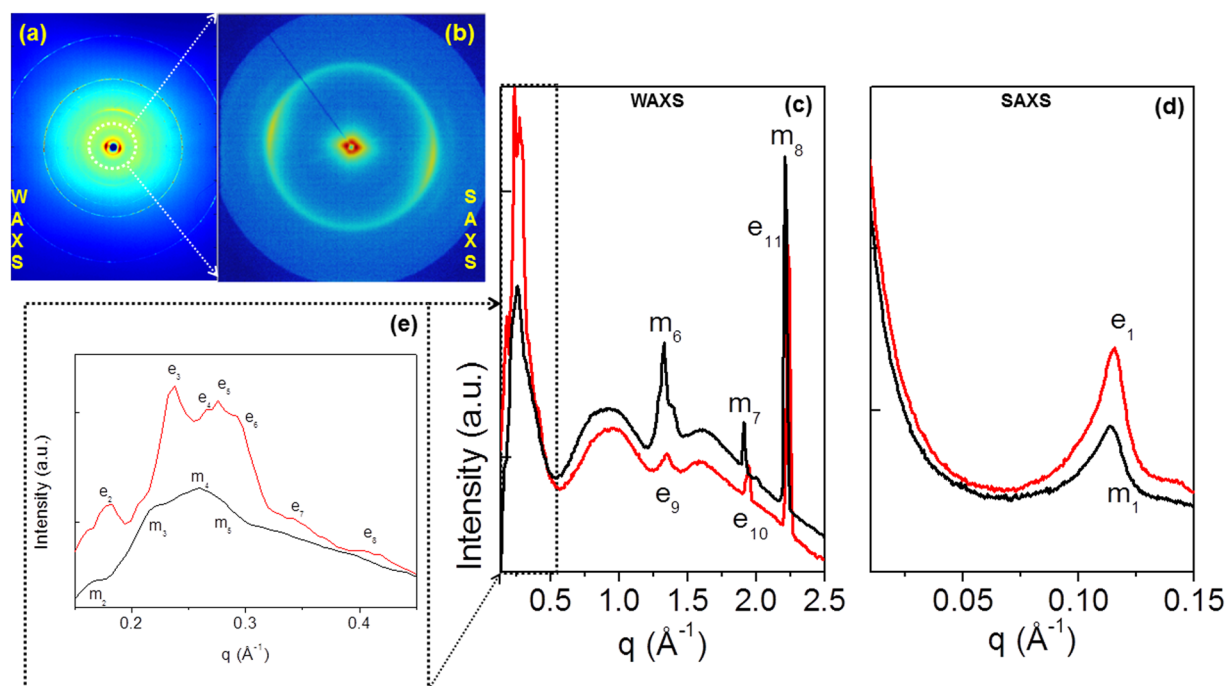


Figure 6. $\text{Gd-}2\text{Na}_2$ fiber at solid state: (a,b) 2D WAXS and SAXS data; (c,d) 1D WAXS and SAXS profiles (red and black corresponding to the meridional and equatorial directions) as obtained once the corresponding 2D WAXS (a) and SAXS (b) data are centered, calibrated and radially folded; the inset in panel (d) refers to the equatorial e_1 reflection, with an estimated FWHM ($e_1\text{-Gd-}2\text{Na}_2$) = 27° ; (e) expanded WAXS region marked by a dotted rectangle in (c).

Label	2-Nal		Gd-2Nal ₂	
	q (Å ⁻¹)	d (Å)	q (Å ⁻¹)	d (Å)
e1	0.11	57	0.11	57
e2	0.13	48	0.18	35
e3	0.15	42	0.24	26
e4	0.26	24	0.26	24
e5	0.3	21	0.28	22.5
e6	0.4	16	0.29	22
e7	—		0.34	18.5
e8	—		0.40	16
e9	—		1.35	4.5
e10			1.94	3
			2.23	2.8
m1	0.11	57	0.11	57
m2	0.125	50	0.17	37
m3	0.14	45	0.22	28.5
m4	1.28	5	0.26	24
m5	1.34	4.7	0.28	22.5
m6	—		1.32	4.75
m7	—		1.9	3.3

Table 1. q positions, and corresponding $d = 2\pi/q$ values, of meridional and equatorial reflections for the 2-Nal and Gd-2Nal₂ fibers. The error on the d values amounts to ± 0.3 Å.

and hydrophobic interactions established by Nal aromatic side chains. The larger size of the Nal hydrophobic side chain compared to Phe makes dipeptide cross β -sheets formed by the former residues stable enough to generate well-defined aggregates at microscale level. Finally, individual β -sheets can then mutually interact in different ways to generate the structural variability of the lateral packing observed in these aggregates.

Water proton relaxation measurements. The paramagnetic relaxivity (r_{1p}) of Gd (III) complexes is given by:

$$r_{1p} \propto \frac{1}{T_{1M}^H} = K f(\tau_R) \quad (1)$$

where K is a constant related to the strength of the dipolar interaction between the protons and the electronic magnetic moment, and τ_R is the correlation time associated with the reorientation of the Gd-H magnetic vector. This means that slowly moving high molecular weight systems are endowed with higher relaxivity than rapidly reorienting low molecular weight ones. In the case of self assembling Gd-containing systems, the extent of aggregation may be evaluated through the measure of the water proton longitudinal relaxation rate of its aqueous solution. In Fig. 8 are reported the NMRD (Nuclear Magnetic Resonance Dispersion) profiles of Gd-2Nal₂ acquired at 21.5 MHz (0.5 T) and 298 K as a function of the complex concentration. The enhancement in relaxivity indicates that Gd-2Nal₂ starts to self-aggregate at very low concentration (ca. 1.0 mg/mL), confirming the values determined by fluorescence spectroscopy and ¹H-NMR. At concentrations higher than 10–15 mg/mL the relaxivity assumes an almost stable value which corresponds to the system in the completely aggregated form. By analyzing the profile of the relaxivity data as a function of the applied field strength (NMRD - Nuclear Magnetic Relaxation Dispersion) it is possible to obtain an accurate determination of the reorientational correlation time (τ_R)¹⁶, that is strictly related to the molecular size of the investigated system. NMRD profiles were acquired below (black circles) and above (white ones) the CAC values determined by ANS titration and ¹HNMR. In Fig. 8b the NMRD profiles of Gd-2Nal₂ at 1.0 and 25.0 mg/mL concentrations are reported and compared to those of the corresponding di-phenylalanine conjugate Gd-DOTA-L₆-F2 at the same concentrations. Data were analyzed using the Solomon-Bloembergen-Morgan model^{17,18}, considering one water molecule in the inner coordination sphere ($q = 1$) and fixing the exchange lifetime (τ_M) to a reliable value (700 ps) on the basis of those previously reported for mono-amido DOTA derivatives^{19–22}. The quantitative analysis of the NMRD profile of the aggregated form was not satisfactory when the simple inner- outer-sphere model was used, so the Lipari-Szabo approach was used for the description of the rotational dynamics. This model allows one to take into account the presence of a certain degree of internal rotation superimposed on the overall tumbling motion^{23,24}. These two types of motion, a relatively fast local rotation of the coordination cage about the linker to the peptide scaffold superimposed on the global reorientation of the system, are characterized by different correlation times: τ_R^1 and τ_R^g , respectively. The degree of correlation between global and local rotations is given by the parameter S^2 , which takes values between 0 (completely independent motions) and 1 (entirely correlated motions). Both the shape of the profiles and the τ_R values determined from the fitting of the experimental results (Table 2) validate the hypothesis of the formation of aggregates for Gd-2Nal₂ at 25.0 mg/mL. On the contrary, the system is in the monomeric state when it is dissolved in solution at 1 mg/mL concentration. In the case of Gd-DOTA-L₆-F2, both qualitative and quantitative analysis confirm the inability of the system to self-aggregate even at high concentration. The quantitative analysis of the

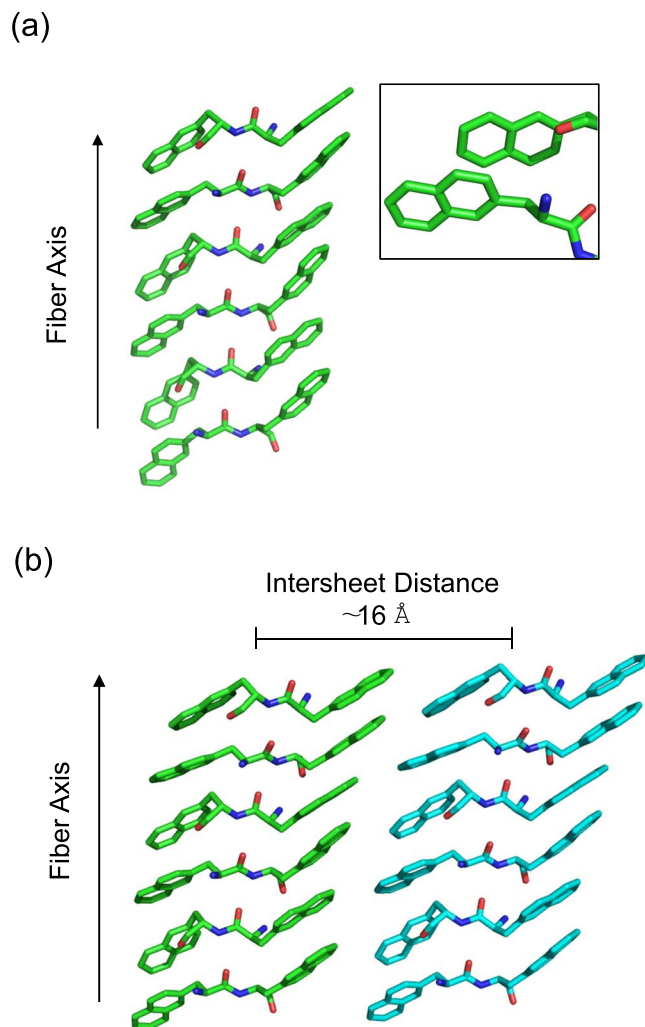


Figure 7. Three-dimensional model of the assembly formed by the peptide moiety of 2Nal₂/Gd-2Nal₂. In panel (a) the cross β-structure of a single β-sheet is reported. In the inset the extensive hydrophobic interactions established by Nal side chains are highlighted. The possible direct interactions between two facing β-sheets is reported in panel (b).

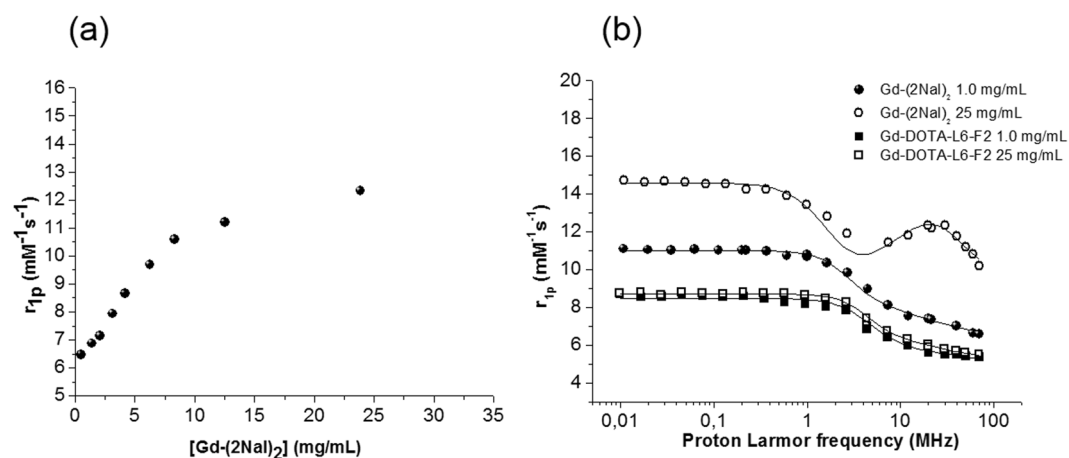


Figure 8. (a) Longitudinal proton relaxivity of Gd-DOTA-L₆-(2Nal)₂ measured at 21.5 MHz (0.5 T) and 298 K as a function of the concentration of the Gd-complex. (b) NMRD profiles of Gd-DOTA-L₆-(2Nal)₂ (1.0 mg/mL (●) and 25.0 mg/mL (○)) compared to those of Gd-DOTA-L₆-F₂ (1.0 mg/mL (■) and 25.0 mg/mL (□)). Experimental data points were measured on aqueous solutions of the Gd-complexes at 298 K. The data refer to 1 mM concentration of the paramagnetic complexes.

System		r_{1p} (mM ⁻¹ s ⁻¹)	Δ^2 (s ⁻²) ^[b]	τ_v (ps) ^[c]	τ_R (ps) ^[e]		
Gd-DOTA-L ₆ -(2Nal) ₂	1 mg/mL	7.3	1.02×10^{19}	50	184		
	25 mg/mL	12.3	8.10×10^{18}	43	τ_R^1	τ_R^2	S ²
					423	4800	0.23
Gd-DOTA-L ₆ -F2	1 mg/mL	5.7	2.97×10^{19}	28	120		
	25 mg/mL	6.0	2.28×10^{19}	35	127		

Table 2. Relaxometric parameters extracted from the fitting of NMRD profiles reported in Fig. 8^[a]. ^[a]On carrying out the fitting procedure, some parameters were fixed to reasonable values: r_{Gd-H} (distance between Gd and protons of the inner sphere water molecule) = 3.1 Å; a (distance of minimum approach of solvent water molecules to Gd³⁺ ion) = 3.8 Å; D (solvent diffusion coefficient) = $2.2 \cdot 10^{-5}$ cm² s⁻¹. ^[b]Squared mean transient zero-field splitting (ZFS) energy. ^[c]Correlation time for the collision-related modulation of the ZFS Hamiltonian. ^[d]Electronic relaxation time at zero field (calculated as $1/\tau_{s0} = 12\Delta^2 \times \tau_v$). ^[e]Reorientational correlation time.

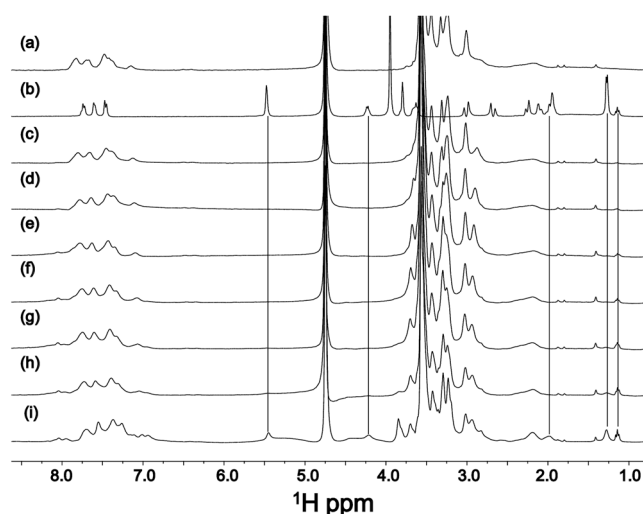


Figure 9. 1D ¹H NMR spectra acquired at 298 K of (a) La-(2-Nal)₂ at 2.5 mg/mL, (b) DOX 0.5 mg/mL, (c) La-(2-Nal)₂ at 2.5 mg/mL + DOX 0.05 mg/mL, (d) La-(2-Nal)₂ at 2.5 mg/mL + DOX 0.1 mg/mL, (e) La-(2-Nal)₂ at 2.5 mg/mL + DOX 0.2 mg/mL, (f) La-(2-Nal)₂ at 2.5 mg/mL + DOX 0.3 mg/mL, (g) La-(2-Nal)₂ at 2.5 mg/mL + DOX 0.4 mg/mL, (h) La-(2-Nal)₂ at 2.5 mg/mL + DOX 0.5 mg/mL, (i) La-(2-Nal)₂ at 2.5 mg/mL + DOX 1 mg/mL. In the lowest spectrum a few peaks arising from doxorubicin appear, as indicated by the black lines.

NMRD profiles indicates that both the local and the global rotational correlation times (Table 2) are significantly increased as compared to the τ_R value of the Gd-complex in the monomeric form, whereas the S² value is relatively low (S² = 0.23), suggesting great flexibility of Gd-coordination cage around the oxoethylene linker.

Doxorubicin loading and release. In order to prepare a potential theranostic agent, we assayed to incorporate cytotoxic doxorubicin (DOX) model drug in the Gd-2Nal₂ paramagnetic nanostructures. DOX is an established anticancer agent clinically effective for the treatment of many cancer types (breast and ovarian cancers). The incorporation and release of DOX into nanostructures was estimated by fluorescence spectroscopy (Figures S7 and S8). The addition of increasing amounts of the peptide conjugate to the DOX solution causes a progressive decrease of the fluorescence intensity of DOX (Figure S7a). This quenching effect is attributable to the electrostatic interaction between the aromatic ring of the anthracycline with the naphthylalanine one. By plotting the fluorescence intensity in the maximum at 590 nm as function of the Gd-2Nal₂ concentration (Figure S7b) we estimated that $g_{Drug}/g_{Peptide}$ is 0.028 (~60 µg of DOX for ~2.0 mg of peptide). The leakage assay, reported in Fig. 8 indicate a very low efflux of DOX across the peptide aggregate (~6% of drug released after 72 h).

The ability of 2Nal₂ aggregates to encapsulate DOX was also checked by running 1D [¹H] spectra of La-2Nal₂ (at 2.5 mg/mL) at increasing DOX concentrations (Fig. 9). At a concentration equal to 2.5 mg/mL, as indicated above, La-2Nal₂ has formed relatively large aggregates (Fig. 9a). In absence of La-2Nal₂, doxorubicin NMR spectrum in water (0.5 mg/mL concentration) contains sharp peaks (Fig. 9b). In presence of La-2Nal₂ aggregates, doxorubicin signals are large and can be barely recognized in the spectrum, thus indicating the encapsulation of the drug inside the aggregates (Fig. 9c–i). The extensive line broadening and loss of signal is caused by the improved relaxation rate reflecting an increase of molecular weight with respect to the free doxorubicin. Once all the pores inside the supramolecular aggregates of La-2Nal₂ are saturated, the drug starts to be released and this occurs at a concentration of doxorubicin close to 1.0 mg/mL (Fig. 9i). At this drug concentration signals are still affected by

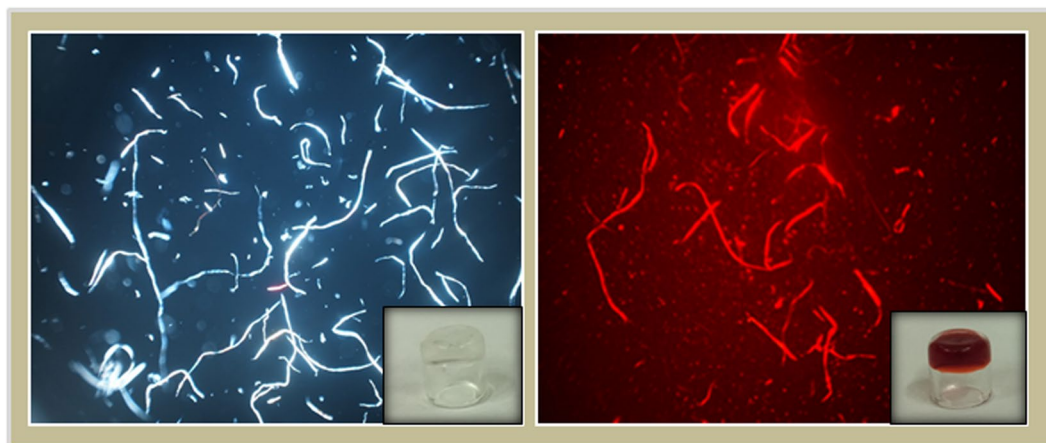


Figure 10. Polarized optical microscopy image of 1-cm vials containing (a) Gd-2Nal₂ and (b) DOX encapsulating Gd-2Nal₂ hydrogels. Images are observed with a Nikon microscope.

line broadening thus indicating that most of the molecules are still entrapped inside the aggregates. Incorporation of DOX in Gd-2Nal₂ nanostructures was further examined by optical microscopy. Figure 10 shows polarizing optical micrographs (POM) of empty Gd-2Nal₂ nanostructures compared to DOX filled Gd-2Nal₂ ones. Polarized light interacts strongly with both the birefringent samples, generating contrast with the background.

Conclusions

Diphenylalanine peptide remains the most largely studied peptide building block until now for self-aggregating peptide materials. Their capability to self-aggregate can considerably decrease hereafter the modification with bulky moiety such as Gd-complexes. This consideration is particularly true for the cationic FF peptide, in which the replacement of the carboxylic group at the C-terminus with the amidic one causes the loss of the head-to-tail hydrogen-bonding. In CAs based FF (Gd-DOTA-L₆-F2 and Gd-DTPA-L₆-F2), the steric repulsion between the Gd-complexes weakens the π - π interactions of the phenyl rings. Here we demonstrated that the replacement of the two phenylalanine residues in Gd-DOTA-L₆-F2 with two 2-naphthylalanine ones allows restoring the stacking interactions. TEM images, at 5.0 mg/mL, show that Gd-2Nal₂ is able to aggregate in long fibrillary nanostructures, whereas Gd-DOTA-L₆-F2 remains in an unaggregated form. At the atomic level, the peptide conjugates in the aggregates assume a β sheet secondary structure with an antiparallel orientation of single strands. WAXS/SAXS characterization of the sample, at the solid state, confirms a fibrillary organization with a typical “cross- β pattern”. At the best of our knowledge, this di-naphthylalanine derivative is the most little linear peptide able to give cross- β interactions. Fluorescence studies suggest that Gd-2Nal₂ peptide derivative begins to self-aggregate at ~ 0.1 mg/mL (75 μ M), forming stable aggregates when concentration is about 10-fold higher (~ 1.0 mg/mL). This CAC value, assessed by fluorescence and proton NMR spectroscopies, is higher than the value (0.076 mg/mL) previously found for tetraphenylalanine Gd-complex Gd-DOTA-L₆-F4. In the Larmor region, the NMRD profile of Gd-2Nal₂ (25.0 mg/mL) presents a peak of relaxivity typical of high molecular weight Gd-containing systems. POM images and ¹H NMR spectra confirmed the incorporation of doxorubicin drug model inside 2Nal based nanostructures. The high values of r1p (12.3 mM⁻¹ s⁻¹ at 20 MHz) and the capability to encapsulate the doxorubicin anticancer drug suggest a potential use of Gd-2Nal₂ nanostructures as theranostic systems.

Experimental section

Materials and chemicals. All chemical reagents for the peptide synthesis (amino acids, coupling reagents, and the Rink amide 4-methylbenzhydrylamine resin) were available from Calbiochem-Novabiochem (Laufelfingen, Switzerland). Fmoc-Ahoh-OH (Fmoc-21-amino-4,7,10,13,16,19-hexaoxaheneicosanoic acid) and DOTA (OtBu)₃-OH were purchased from Neosystem (Strasbourg, France) and Chemateck (Dijon, France), respectively. All other chemical reagents and solvents were purchased by Sigma-Aldrich or Fluka (Bucks, Switzerland) and used as received unless otherwise stated. Purification of peptide conjugates was achieved by employing an HPLC LC8 Shimadzu (Kyoto, Japan) using a UV-detector (lambda-Max Model 481) and a C18-Phenomenex (Torrance, CA) column. Samples were eluted with 0.1% TFA containing H₂O (A) and 0.1% TFA containing CH₃CN (B), with a flow rate of 20 mL min⁻¹ and a gradient method that moves the B% from 5% to 70% over 30 minutes. Analytical analyses, aimed to identify the products and to assess their purity, were performed using a single quadrupole electrospray ionization, Finnigan Surveyor MSQ (San Jose, CA). Samples were eluted on an analytical C18-Phenomenex column with A and B, with a flow rate of 200 μ L min⁻¹ and a gradient method that moves the B% from 5% to 70% over 15 minutes.

Synthesis of peptide derivatives. DOTA-L₆-F2 and DOTA-L₆-(2Nal)₂ were synthesized as previously reported^{6,25,26}. Briefly, peptide conjugates were synthesized on Rink amide MBHA resin (scale 0.2 mmol, substitution grade 0.65 mmol/g). Deprotection of the 9-fluorenylmethoxycarbonyl group (Fmoc) was performed twice for 10 minutes each by treating the peptidyl-resin with a piperidine/N, N-dimethylformamide (70/30, v/v) mixture. The couplings of the amino acids were performed in N, N-dimethylformamide by using 2 equivs. of the amino

acid, 2 equivs. of 1-hydroxybenzotriazole (HOBt) and benzotriazol-1-yl-oxy-tris-pyrrolidino-phosphonium (PyBop) and 4 equivs. of diisopropylethylamine (DIPEA) respect to the synthetic scale. After the cleavage from the resin, the crude products were purified by RP-HPLC chromatography and their purity and the identity confirmed by ESI mass spectrometry and ¹H-NMR spectroscopy.

DOTA-L₆-(2Nal)₂ [2Nal₂]. ¹H-NMR (CD₃OD) (chemical shifts in δ, CH₃OH as internal standard 3.55) = 7.51–7.42 (m, 10 CH aromatic), 4.86–4.75 (m, 2H, CH Phe α), 3.80 (s, 22H, OCH₂CH₂O), 3.75 (t, 2H, RNHCH₂CH₂O), 3.70 (s, 6H, R₂NCH₂COOH), 3.60 (t, 2H, RNHCH₂CH₂O), 3.45 (s, 16H, R₂NCH₂CH₂NR₂), 3.40–3.36 (m, 2H, R₂NCH₂CONH), 3.16–2.90 (m, 4H, CH₂ Phe β), 2.58 (t, 2H, NHCOCH₂CH₂O). Retention time, R_t = 12.17 min; MS (ESI+): m/z 1132.8 calcd. For C₅₇H₈₀N₈O₁₆: [M + H⁺] = 1133.8; [M + Na⁺] = 1155.7; [M + 2H⁺]/2 = 568.1.

Preparation of gadolinium complexes. Gadolinium complexes were prepared through the addition of GdCl₃ to the DOTA-functionalized ligands in a molar ratio 1:1 at room temperature and neutral pH. The absence of any residual free Gd³⁺ ions was checked by the well-known UV-Vis method of the orange xylenol²⁷; the eventual residual was removed from the solution by adding a further amount of ligand corresponding to the Gd³⁺ excess.

Preparation of peptide solutions. 2Nal₂ and Gd-2Nal₂ peptide solutions were prepared by dissolving the lyophilized powder in double distilled water. The concentration of the final solution was determined by absorbance on UV-vis Thermo Fisher Scientific Inc (Wilmington, Delaware USA) Nanodrop 2000c spectrophotometer using a 1.0 cm quartz cuvette (Hellma). The molar absorptivity (ε₂₈₀) for 2Nal₂ and Gd-2Nal₂ peptide employed for the spectroscopic measurements was 6070 M⁻¹ cm⁻¹.

Fluorescence studies. The determination of CAC (critical aggregate concentration) values was determined as previously described⁶ by the titration of the fluorescent probe ANS (8-anilino-1-naphthalene sulfonic acid ammonium salt)^{28,29} with the peptide conjugates³⁰. Fluorescence spectra of 2Nal₂ and Gd-2Nal₂ were recorded at room temperature at several concentrations, exciting samples at 280 nm and recording spectra between 290 and 500 nm.

NMR experiments. NMR experiments were acquired in the temperature range of 298–303 K on either a Varian Unity Inova 600 MHz spectrometer provided with a cold probe or a 400 MHz Varian instrument provided with a 5-mm triple resonance probe and z-axis pulsed-field gradients. All samples were dissolved in a mixture H₂O/D₂O (98% D, Armar Chemicals, Dottingen, Switzerland) 90/10 v/v with a total volume equal to 600 μL. The DOTA-L₆-F2 was analyzed in the concentration range 0.3 mg/mL (i.e., 0.3 mM)–5.0 mg/mL (i.e., 4.8 mM); for the La-DOTA-L₆-F2 the examined concentration range was 0.3 mg/mL (i.e., 0.3 mM)–10.0 mg/mL (i.e., 8.5 mM). The 2Nal₂ compound was analyzed in the concentration range 0.1 mg/mL (i.e., 0.1 mM)–5.0 mg/mL (i.e., 4.4 mM) and La-2Nal₂ in the range 0.2 mg/mL (i.e., 0.2 mM)–2.5 mg/mL (i.e., 2 mM). 1D [¹H] experiments along with a series of 2D experiments [(i.e., 2D [¹H, ¹H] TOCSY (Total Correlation Spectroscopy)³¹ (70 ms mixing time), 2D [¹H, ¹H] NOESY (Nuclear Overhauser Enhancement Spectroscopy)³² (300 ms mixing time), and 2D [¹H, ¹H] ROESY (Rotating frame Overhauser Enhancement Spectroscopy)³³ (200 and 250 ms mixing times)] were recorded. 1D spectra were usually acquired with a relaxation delay d1 of 1.5 s and 32–512 scans; 2D experiments were recorded with 16–64 scans, 128–256 FIDs in t1, 1024 or 2048 data points in t2. Assignments of the DOTA-L₆-F2 and 2Nal₂-lacking the La (III) ion- were obtained at 1 mM concentration with a canonical protocol³⁴ involving comparison of 2D [¹H, ¹H] TOCSY³⁵ (70 ms mixing time), and 2D [¹H, ¹H] ROESY³³ (200 ms mixing time). Water suppression was achieved by Excitation Sculpting³⁵. Spectra were processed with VNMRJ (Varian by Agilent Technologies, Italy) and analyzed with NEASY³⁶ comprised in the CARA software package (<http://www.nmr.ch/>).

Circular Dichroism. Far-UV CD spectra of the 2Nal₂ and Gd-2Nal₂, in 0.5–20 mg/mL concentration range, were recorded on the spectropolarimeter Jasco J-810 equipped with a NesLab RTE111 thermal controller unit. Spectra were recorded between 280 to 195 nm at room temperature, using a standard quartz cell with a path length of 0.1 mm, a scan speed of 10 nm/min a sensitivity of 50 mdeg, a time constant of 16 s and a bandwidth of 1 nm. All the spectra were obtained by averaging three scans, after correction for the solvent and for dilution. Ellipticities were reported as the mean residue ellipticity (MRE).

Fourier Transform Infrared spectroscopy (FTIR). Fourier Transform Infrared spectra of 2Nal₂ and Gd-2Nal₂ in solution at the concentration of 5.0 mg/mL and at the solid state were collected on the spectrometer Jasco FT/IR 4100 (Easton, MD) in ATR mode, using a Ge single-crystal at a resolution of 4 cm⁻¹. All the spectra (100 scans with a rate of 2 mm · s⁻¹ against a KBr background) were collected in transmission mode and then converted in emission.

Congo Red spectroscopic assay. Congo Red (CR) UV-Vis assay was carried out on aforementioned spectrophotometer as previously described⁶. Briefly, 5, 50 and 125 μL of di-naphthylalanine stock solution (20 mg/mL) were added to a CR solution (12, 5 μM) prepared immediately before to use. The solutions containing peptide conjugate incubated with CR were left at room temperature for 30 min and then their UV-Vis spectra were recorded between 400 and 700 nm. The spectrum of CR alone at the same concentration was also recorded in the this spectral region.

Transmission Electron Microscopy (TEM) images. TEM images were acquired by LaMest (Pozzuoli, Italy) with a FEI TECNAI G12 Spirit-Twin microscope (LaB₆ source) endowed of a bottom mounted FEI Eagle-4k CCD camera (Eindhoven, The Netherlands), working at 120 kV. The samples for the observation were prepared by placing 10 μL of a solution (5.0 mg/mL) on a holey-carbon coated copper grid (400 mesh). The sample was left

to dry at room temperature for 1 hour and stained with a solution (1 wt%) of phosphotungstic acid. Digital images were obtained by FEI Eagle 4 K CCD camera and Xplore 3D software.

Wide-Angle and Small-Angle X-ray Scattering. Fiber diffraction WAXS and SAXS patterns were recorded from dried fibers prepared according to the well-known method of the stretch frame¹³, in which a droplet (10 μ L) of 3 wt% peptide solution, hanged between two wax-coated capillary, was left to dry slowly overnight at room temperature. WAXS and SAXS data were collected at the X-ray MicroImaging Laboratory (XMI-L@b) equipped with a Fr-E+ Super Bright rotating anode copper anode microsource (Cu K α , λ = 0.15405 nm, 2475 W), a multilayer focusing optics (Confocal Max-Flux; CMF 15-105) and a three-pinhole camera (Rigaku SMAX-3000)³⁷. For WAXS data collection an image plate (IP) detector with 100 μ m pixel size was placed at 8.5 cm from the sample and calibrated by means of the Si NIST standard reference material (SRM 640b). For SAXS data collection a Triton 20 gas-filled photon counter detector with \sim 200 μ m pixel size was placed at 2.2 m from the sample and calibrated by means of silver behenate. A detailed description of the XMI-L@b performances can be found in Altamura *et al.*³⁷ and Sibillano *et al.*³⁸.

Water proton relaxation measurements. Measure of R_1 (longitudinal water proton relaxation rates) of Gd-2NaI₂ were carried out on a Stellar Spinmaster spectrometer (Pavia, Italy) operating at 0.5 T which corresponds to 21.5 MHz Proton Larmor Frequency. R_1 ($1/T_1$) values were measured at 298 K by mean of the standard inversion-recovery technique. For the measure of the proton $1/T_1$ NMRD (Nuclear Magnetic Resonance Dispersion) profiles, a fast field-cycling Stellar relaxometer, operating over a continuum of magnetic field strengths from 0.00024 to 0.47 T (corresponding to 0.01–20 MHz proton Larmor frequencies) was used. The temperature was set at 298 K. The relaxometer is computer controlled and the absolute uncertainty is $1/T_1 \pm 1\%$. Additional data points were obtained on a Stellar Spinmaster spectrometer coupled to an electromagnet tunable at different Larmor Frequencies between 21.5 and 70 MHz. Experimental temperature control was obtained with an air-flow heater (Stellar VTC-91) endowed of a copper constantan thermocouple (uncertainty 0.1 °C). A previously reported relaxometric method³⁹ was used for the determination of the concentrations of the solutions used for the relaxometric characterization. The conventional Solomon-Bloembergen-Morgan theory was used for fitting of experimental data.

Doxorubicin loading and leakage. A DOX solution ($1 \cdot 10^{-4}$ M) was placed in the cuvette and titrated with small amount of Gd-2NaI₂ peptide conjugate at 50 mg/mL. The fluorescence of each sample was monitored on Jasco Model FP-750 spectrofluorophotometer as above described. Excitation wavelength was settled at 480 and UV-Vis spectra were collected between 490 and 700 nm. At the end of the titration the DOX filled Gd-2NaI₂ aggregates were 10-fold diluted and the DOX fluorescence was monitored up to 72 h. The extent of the DOX leakage was calculated as follows: $Leakage (\%) = 100 (F_1 - F_0)/(F_{100} - F_0)$, where F_1 represents the level of fluorescence measured for each time point, whereas F_{100} and F_0 are the fluorescence levels before and after the peptide addition in cuvette, respectively.

Doxorubicin loading of by ¹H NMR and polarized optical microscopy (POM). To explore encapsulation of doxorubicin in 2NaI₂, a sample at a concentration of 2.5 mg/mL was used and 1D [¹H] NMR spectra were recorded in absence and presence of doxorubicin (concentration going from 0.05 to 1 mg/mL). POM images of Gd-2NaI₂ at 20 mg/mL and of Gd-2NaI₂/DOX (20 and 1 mg/mL, respectively) in water solution were obtained observing samples with AZ100 microscope (Nikon) between crossed polars.

References

- Adler-Abramovich, L. & Gazit, E. The physical properties of supramolecular peptide assemblies: from building block association to technological applications. *Chem Soc Rev* **43**, 6881–6893, doi:10.1039/c4cs00164h (2014).
- Yan, X., Zhu, P. & Li, J. Self-assembly and application of diphenylalanine-based nanostructures. *Chem Soc Rev* **39**, 1877–1890, doi:10.1039/b915765b (2010).
- Demirel, G., Malvadkar, N. & Demirel, M. C. Control of protein adsorption onto core-shell tubular and vesicular structures of diphenylalanine/parylene. *Langmuir: the ACS journal of surfaces and colloids* **26**, 1460–1463, doi:10.1021/la903571y (2010).
- Kumaraswamy, P., Lakshmanan, R., Sethuraman, S. & Krishnan, U. M. Self-assembly of peptides: influence of substrate, pH and medium on the formation of supramolecular assemblies. *Soft Matter* **7**, 2744–2754, doi:10.1039/c0sm00897d (2011).
- Ryu, J. & Park, C. B. High-Temperature Self-Assembly of Peptides into Vertically Well-Aligned Nanowires by Aniline Vapor. *Adv Mater* **20**, 3754–+, doi:10.1002/adma.200800364 (2008).
- Diaferia, C. *et al.* Peptide Materials Obtained by Aggregation of Polyphenylalanine Conjugates as Gadolinium-Based Magnetic Resonance Imaging Contrast Agents. *Adv Funct Mater* **25**, 7003–7016, doi:10.1002/adfm.201502458 (2015).
- Gorbitz, C. H. Nanotube formation by hydrophobic dipeptides. *Chemistry—a European Journal* **7**, 5153–5159, doi:10.1002/1521-3765(20011203)7:23<5153::Aid-Chem5153>3.0.Co;2-N (2001).
- Tamamis, P. *et al.* Self-Assembly of Phenylalanine Oligopeptides: Insights from Experiments and Simulations. *Biophysical Journal* **96**, 5020–5029, doi:10.1016/j.bpj.2009.03.026 (2009).
- Guo, C., Luo, Y., Zhou, R. H. & Wei, G. H. Probing the Self-Assembly Mechanism of Diphenylalanine-Based Peptide Nanovesicles and Nanotubes. *ACS Nano* **6**, 3907–3918, doi:10.1021/nn300015g (2012).
- Accardo, A. *et al.* Amphiphilic CCK peptides assembled in supramolecular aggregates: structural investigations and *in vitro* studies. *Molecular Biosystems* **7**, 862–870, doi:10.1039/c0mb00238k (2011).
- Diaferia, C. *et al.* Self-assembly of PEGylated tetra-phenylalanine derivatives: structural insights from solution and solid state studies. *Sci Rep-Uk* **6**, doi:Artn 26638 10.1038/Srep26638 (2016).
- Klunk, W. E., Jacob, R. F. & Mason, R. P. Quantifying amyloid beta-peptide (A beta) aggregation using the Congo red A beta (CR-A beta) spectrophotometric assay. *Anal Biochem* **266**, 66–76, doi:10.1006/abio.1998.2933 (1999).
- Sunde, M. *et al.* Common core structure of amyloid fibrils by synchrotron X-ray diffraction. *J Mol Biol* **273**, 729–739, doi:10.1006/jmbi.1997.1348 (1997).
- Emsley, P. & Cowtan, K. Coot: model-building tools for molecular graphics. *Acta Crystallogr D* **60**, 2126–2132, doi:10.1107/S0907444904019158 (2004).
- The PyMOL Molecular Graphics System, V. S., LLC.
- Aime, S., B., M., Fasano, M., Terreno, E. Vol. 5 (eds Wiley, E. Toth John & Merbach, A. E.) 193 (2001).

17. Bloembergen, N. Proton Relaxation Times in Paramagnetic Solutions. *J. Chem. Phys.* **27**, 572 (1957).
18. Solomon, I. Relaxation Processes in a System of Two Spins. *Phys. Rev.* **99**, 559 (1955).
19. Battistini, E. *et al.* High-relaxivity magnetic resonance imaging (MRI) contrast agent based on supramolecular assembly between a gadolinium chelate, a modified dextran, and poly-beta-cyclodextrin. *Chemistry-a European Journal* **14**, 4551–4561, doi:[10.1002/chem.200701587](https://doi.org/10.1002/chem.200701587) (2008).
20. Tei, L., Gugliotta, G., Baranyai, Z. & Botta, M. A new bifunctional Gd-III complex of enhanced efficacy for MR-molecular imaging applications. *Dalton T* 9712–9714, doi:[10.1039/b917566k](https://doi.org/10.1039/b917566k) (2009).
21. Tei, L. *et al.* Target Visualization by MRI Using the Avidin/Biotin Amplification Route: Synthesis and Testing of a Biotin-Gd-DOTA Monoamide Trimer. *Chemistry-a European Journal* **16**, 8080–8087, doi:[10.1002/chem.201000508](https://doi.org/10.1002/chem.201000508) (2010).
22. Barge, A. *et al.* Design and Synthesis of a (18)-Cyclodextrin Oligomer: A New Platform with Potential Application as a Dendrimeric Multicarrier. *Chemistry-a European Journal* **19**, 12086–12092, doi:[10.1002/chem.201301215](https://doi.org/10.1002/chem.201301215) (2013).
23. G. Lipari, S. S. Model-free approach to the interpretation of nuclear magnetic resonance relaxation in macromolecules. 1. Theory and range of validity. *J. Am. Chem. Soc.* **104**, 4546–4559 (1982).
24. G. Lipari, S. S. Model-free Approach to the interpretation of nuclear magnetic resonance relaxation in macromolecules. 2. Analysis of experimental results. *J. Am. Chem. Soc.* **104**, 4559–4570 (1982).
25. White, W. C. a. P. In *oxford University Press* (New York, 2000).
26. Accardo, A., Ringhieri, P., Palumbo, R. & Morelli, G. Influence of PEG length on conformational and binding properties of CCK peptides exposed by supramolecular aggregates. *Biopolymers (Pept Sci)* **102**, 304–312, doi:[10.1002/bip.22500](https://doi.org/10.1002/bip.22500) (2014).
27. Barge, A., Cravotto, G., Gianolio, E. & Fedeli, F. How to determine free Gd and free ligand in solution of Gd chelates. A technical note. *Contrast Media Mol Imaging* **1**, 184–188, doi:[10.1002/cmml.110](https://doi.org/10.1002/cmml.110) (2006).
28. Birdi, K. S., Singh, H. N. & Dalsager, S. U. Interaction of ionic micelles with the hydrophobic fluorescent probe 1-anilino-8-naphthalenesulfonate. *J. Phys. Chem.* **83**, 2733–2737 (1979).
29. De Vendittis, E., Palumbo, G., Parlato, G. & Bocchini, V. A fluorimetric method for the estimation of the critical micelle concentration of surfactants. *Anal Biochem* **115**, 278–286 (1981).
30. Diaferia, C. *et al.* Hierarchical Analysis of Self-Assembled PEGylated Hexaphenylalanine Photoluminescent Nanostructures. *Chemistry*, doi:[10.1002/chem.201604107](https://doi.org/10.1002/chem.201604107) (2016).
31. Griesinger, C., Otting, G., Wuethrich, K. & Ernst, R. R. Clean TOCSY for proton spin system identification in macromolecules. *Journal of American Chemical Society* **110**, 7870–7872 (1988).
32. Kumar, A., Ernst, R. R. & Wuethrich, K. A two-dimensional nuclear Overhauser enhancement (2D NOE) experiment for the elucidation of complete proton-proton cross-relaxation networks in biological macromolecules. *Biochem. Biophys. Res. Commun.* **95**, 1–6 (1980).
33. Bax, A. & Davis, D. G. Practical Aspects of Two-Dimensional Transverse Noe Spectroscopy. *J Magn Reson* **63**, 207–213, doi:[10.1016/0022-2364\(85\)90171-4](https://doi.org/10.1016/0022-2364(85)90171-4) (1985).
34. Wuethrich, K. *NMR of proteins and nucleic acids* (1986).
35. Hwang, T. L. & Shaka, A. J. Water Suppression That Works - Excitation Sculpting Using Arbitrary Wave-Forms and Pulsed-Field Gradients. *J Magn Reson Ser A* **112**, 275–279, doi:[10.1006/jmra.1995.1047](https://doi.org/10.1006/jmra.1995.1047) (1995).
36. Bartels, C., Xia, T. H., Billeter, M., Guntert, P. & Wuethrich, K. The Program Xeasy for Computer-Supported Nmr Spectral-Analysis of Biological Macromolecules. *J Biomol Nmr* **6**, 1–10, doi:[10.1007/BF00417486](https://doi.org/10.1007/BF00417486) (1995).
37. Altamura, D. *et al.* X-ray microimaging laboratory (XMI-LAB). *J Appl Crystallogr* **45**, 869–873, doi:[10.1107/S0021889812025733](https://doi.org/10.1107/S0021889812025733) (2012).
38. Sibillano, T. *et al.* An Optimized Table-Top Small-Angle X-ray Scattering Set-up for the Nanoscale Structural Analysis of Soft Matter. *Sci Rep-Uk* **4**, doi:Artn 6985 [10.1038/Srep06985](https://doi.org/10.1038/Srep06985) (2014).
39. Arena, F., Singh, J. B., Gianolio, E., Stefania, R. & Aime, S. beta-Gal Gene Expression MRI Reporter in Melanoma Tumor Cells. Design, Synthesis, and *in Vitro* and *in Vivo* Testing of a Gd (III) Containing Probe Forming a High Relaxivity, Melanin-Like Structure upon beta-Gal Enzymatic Activation. *Bioconjugate Chem* **22**, 2625–2635, doi:[10.1021/bc200486j](https://doi.org/10.1021/bc200486j) (2011).

Acknowledgements

The authors thanks CIRCMSB (Consorzio Interuniversitario di Ricerca in Chimica dei Metalli nei Sistemi Biologici). This study was partially supported by the project “Tecnologie Abilitanti per Produzioni Agroalimentari Sicure e Sostenibili” (T.A.P.A.S.S.) - PELM994” (CUP B38C14002040008) founded by Regione Puglia, Area politiche per lo Sviluppo economico, il lavoro e l’innovazione in the framework of the grant “Aiuti a Sostegno dei Cluster Tecnologici Regionali per l’Innovazione”. We gratefully acknowledge the skillful technical assistance of Rocco Lassandro and Candida Giovanelli from the XMI-L@b, of Leopoldo Zona and Luca De Luca from IBB-CNR.

Author Contributions

C.D. synthesized peptide conjugates, C.D. and A.A. performed CAC, CD and FTIR experiments. A.A. and G.M. analyzed fluorescence, CD and FTIR data. M.L. and F.A.M. recorded and analyzed solution NMR experiments. T.S. and C.G. realized WAXS and SAXS experiments and analyzed SAXS and WAXS data. L.V. and N.B. discussed molecular modelling. E.G. performed and analysed NMRD experiments. A.A., C.G., L.V. discussed the results and wrote the paper in close collaboration with all the authors.

Additional Information

Supplementary information accompanies this paper at doi:[10.1038/s41598-017-00332-3](https://doi.org/10.1038/s41598-017-00332-3)

Competing Interests: The authors declare that they have no competing interests.

Publisher's note: Springer Nature remains neutral with regard to jurisdictional claims in published maps and institutional affiliations.



This work is licensed under a Creative Commons Attribution 4.0 International License. The images or other third party material in this article are included in the article’s Creative Commons license, unless indicated otherwise in the credit line; if the material is not included under the Creative Commons license, users will need to obtain permission from the license holder to reproduce the material. To view a copy of this license, visit <http://creativecommons.org/licenses/by/4.0/>

© The Author(s) 2017

Photoluminescence

Photoluminescent Peptide-Based Nanostructures as FRET Donor for Fluorophore Dye

Carlo Diaferia,^[a] Teresa Sibillano,^[b] Cinzia Giannini,^[b] Valentina Roviello,^[c] Luigi Vitagliano,^[d] Giancarlo Morelli,^[a] and Antonella Accardo^{*[a]}

Abstract: A great interest has been recently generated by the discovery that peptide-based nanostructures (NSs) endowed with cross- β structure may show interesting photoluminescent (PL) properties. It was shown that NSs formed by PEGylated hexaphenylalanine (PEG₈-F6, PEG = polyethylene glycol) are able to emit at 460 nm when excited at 370 or 410 nm. Here, the possibility to transfer the fluorescence of these PEG₈-F6-based NSs by foster resonance electron transfer (FRET) phenomenon to a fluorescent dye was explored. To achieve this aim, the 4-chloro-7-nitrobenzofurazan (NBD) dye was encapsulated in these NSs. Structural data in solution and in solid state, obtained by a variety of techniques (circular dichroism, Fourier-transform infrared spectroscopy, wide-angle X-ray scattering, and small-angle X-ray scatter-

ing), indicated that the organization of the peptide spine of PEG₈-F6 NS, which consists of anti-parallel β -sheets separated by a dry interface made of interacting phenylalanine side chains, was maintained upon NBD encapsulation. The spectroscopic characterization of these NSs clearly showed a red-shift of the emission fluorescence peak both in solution and in solid state. This shift from 460 to 530 nm indicated that a FRET phenomenon from the peptide-based to the fluorophore-encapsulated NS occurred. FRET could also be detected in the PEG₈-F6 conjugate, in which the NBD was covalently bound to the amine of the compound. On the basis of these results, it is suggested that the red-shift of the intrinsic PL of NSs may be exploited in the bio-imaging field.

Introduction

In the last few years an explosion of interest has been focused on peptide-based materials for interdisciplinary nanoscience applications.^[1] There are several advantages for using peptides as building blocks, such as intrinsic biological origin, low cost, high stability, ability for specific molecular recognition, long-term storage, and easy handling. One of the most studied representative building blocks, able to self-assemble in supra-molecular nanostructures (NSs), is the diphenylalanine homodimer (FF).^[2] FF self-assembles in nanotubes that show notewor-

thy mechanical rigidity^[3] along with a multiplicity of other chemical and physical functionalities,^[4] making it promising for potential application in nanomedicine,^[5] nanofabrication,^[6] tissue engineering,^[7] bio-imaging,^[8] drug delivery,^[9] and fabrication of biosensors.^[10] However, the low water solubility of these peptide NSs has partially limited their application in nanomedicine. Very recently, we described the first examples of NSs based on PEGylated (PEG = polyethylene glycol) cationic poly-phenylalanines^[5b,8,11] or their analogues (di-naphthylalanine)^[12] for bio-imaging applications. These peptide derivatives contain an aromatic region to allow the self-assembly of the NS, a gadolinium (Gd) complex for applications as in vivo contrast agent in magnetic resonance imaging (MRI), and a PEG spacer at different length between the Gd-complex and the peptide moiety. These peptides could be potentially proposed for application in MRI owing to their high uptake and moderately low toxicity on selected cell lines.^[8] In more recent years, a great interest has been generated around peptide-based NSs with interesting photoluminescent (PL) properties. Peptide-based NSs can exhibit blue photoluminescence when excited at a wavelength of 370 or 410 nm. This PL phenomenon has also been observed in FF and FFF NSs upon thermally induced reconstructive phase transition (heating sample at 140–180 °C) as shown by Rosenman and co-workers,^[4a,13] or in amyloid-like fibrils rich in β -sheet structures.^[14] Some hypotheses on the origin of this PL, such as electron delocalization through hydrogen bonds in the β -sheet-rich structure^[13] or proton transfer,^[15] have been proposed until now. We recently reported on

[a] Dr. C. Diaferia, Prof. G. Morelli, Dr. A. Accardo
Department of Pharmacy, Research Centre on Bioactive Peptides (CIRPeB)
University of Naples "Federico II" and DFM Scarl
Via Mezzocannone 16, 80134 Naples (Italy)
E-mail: Antonella.accardo@unina.it

[b] Dr. T. Sibillano, Dr. C. Giannini
Institute of Crystallography (IC), CNR
Via Amendola 122, 70126 Bari (Italy)

[c] Dr. V. Roviello
Analytical Chemistry for the Environment and CeSMA
(Centro Servizi Metereologici Avanzati)
University of Naples "Federico II"
Corso Nicolangelo Protopisani, 80146, Naples (Italy)

[d] Dr. L. Vitagliano
Institute of Biostructures and Bioimaging (IBB), CNR
Via Mezzocannone 16, 80134 Naples (Italy)

Supporting Information for this article can be found under:
<https://doi.org/10.1002/chem.201701381>.

the synthesis and structural characterization of a novel PEGylated hexaphenylalanine peptide, PEG₈-F6 (Figure 1a), made of aromatic and hydrophilic moieties, which forms NSs with remarkable PL properties.^[16] The structural characterization of PEG₈-F6 in solution highlighted its strong propensity to self-assemble in stable and well-organized NSs with a hydrodynamic diameter of approximately 60 nm and an antiparallel β -sheet arrangement. Wide-angle X-ray scattering (WAXS) characterization on dried fibers also revealed a typical cross- β diffraction pattern observed for amyloid-like fibers with meridional and equatorial peaks at 4.8 and 12.5 Å, respectively. PEG₈-F6 NSs showed a blue PL between 420 and 460 nm when excited at wavelengths of 370 or 410 nm.^[16] Here, we explored the possibility to transfer by foster resonance electron transfer (FRET) phenomenon the fluorescence of a cross- β material (donor) such as PEG₈-F6-based NSs into an encapsulated fluorescent dye such as 4-chloro-7-nitrobenzofurazan (NBD, Figure 1b). Owing to its spectral window ($\lambda_{\text{ex}} = 465 \text{ nm}$; $\lambda_{\text{em}} = 530 \text{ nm}$), the poorly water-soluble NBD was chosen as a suitable model fluorophore to investigate the capability of these peptide-based NSs to transfer by FRET their intrinsic fluorescence to a fluorophore, strictly associated with the peptide NS. The FRET should cause a red-shift of the PL of the NSs, thus providing an opportunity for their application in the bio-imaging field.^[17] Nowadays, the major obstacle for many applications of light in biomedicine is represented by the limited penetration of light into biological tissue. Optical fibers represent the current gold-standard solution in clinical uses.^[18] However, most light-guiding systems are based on solid materials, which are not compatible with *in vivo* application.^[19] In contrast, optical wave-

guides based on biocompatible materials such as PEG,^[20] silk, and agarose gel^[21] present a scarce efficiency for delivering light over an organ-scale distance. The employment of water-soluble, biocompatible optical fibers based on peptide building blocks with enhanced PL properties could help to overcome these limitations.

Results and Discussion

Synthesis of NBD-filled NSs

PEG₈-F6, composed of six phenylalanine residues and eight ethoxylic groups, is poorly soluble in water but soluble in 1,1,1,3,3,3-hexafluoro-2-propanol (HFIP) up to 100 mg mL⁻¹. Stable and well-organized NSs were obtained by five-fold diluting this stock solution in water and removing the organic solvent by a slow nitrogen flow. NBD dye also shows very limited water solubility and good solubility in HFIP. Consequently, NBD-filled NSs were synthesized by dissolving both PEG₈-F6 and NBD powders (Figure 1a,b) in HFIP in a 10:1 (*w/w*) ratio. In this solution, the starting peptide and fluorophore concentrations were 100 and 10 mg mL⁻¹, which corresponds to 6.8×10^{-5} and 5.0×10^{-5} mol, respectively. Subsequently, this solution was diluted in water, HFIP was removed, and the resulting solution was centrifuged to remove the excess of non-encapsulated NBD (Figure 1c). The light-yellow supernatant was further purified from potential traces of free NBD by gel-filtration on a Sephadex G-50 column. According to the dilution achieved during the purification, the final concentration of hexaphenylalanine estimated by UV/Vis spectroscopy was 10 mg mL⁻¹. Owing to its low water solubility, the detection and the quantification of encapsulated NBD were unfeasible in water. As a consequence, the amount of NBD encapsulated in NSs (200 $\mu\text{g mL}^{-1}$) was determined by UV/Vis spectroscopy on a sample lyophilized and re-dissolved in methanol (Figure S1 in the Supporting Information). From the experimental quantification of the species, the molar ratio between NBD and PEG₈-F6 peptide was determined to be 1:7. The fluorescent dye remained associated with the NS even after repeated washing, suggesting the existence of a strong interaction between the dye and the NS. To exclude the occurrence of a covalent bond between the NBD fluorophore and the N-terminus of the oligo-peptide, we analyzed NBD/PEG₈-F6 NSs by liquid chromatography–mass spectrometry (LC–MS). The mass spectrum, reported in Figure S2 in the Supporting Information, showed only the mass corresponding to the peptide. Altogether, these experiments suggest that in this preparation protocol the NBD encapsulation is favored by the self-aggregation of the peptide-based NS directly around the NBD dye as a consequence of the HFIP evaporation.

Structural characterization of NBD-filled NSs: secondary structure

To evaluate the potential structural modifications induced by the NBD encapsulation in the PEGylated peptide NSs, NBD/PEG₈-F6 was deeply characterized at the atomic level by circu-

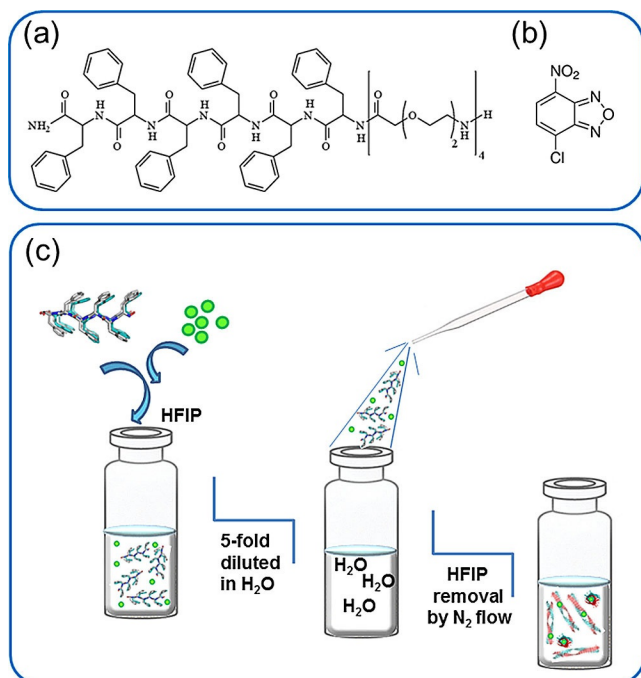


Figure 1. Schematic representation of (a) PEG₈-F6 and (b) NBD chloride, respectively; (c) preparation of NBD/PEG₈-F6 NSs: both PEG₈-F6 and NBD were dissolved in HFIP in 10:1 (*w/w*) ratio. Then, this solution was ten-fold diluted in water, and HFIP was removed with a slow nitrogen flow.

lar dichroism (CD) and Fourier-transform infrared (FTIR) spectroscopy. CD and FTIR spectra of the filled peptide NSs are reported in Figure 2 and Figure 3, respectively. Spectra of the empty NSs are also shown for comparison. The CD spectrum of NBD/PEG₈-F6 at 10 mg mL⁻¹ (Figure 2a) showed the same dichroic tendency previously observed for the empty peptide NSs with a maximum around 205 nm, attributable to aromatic side-chain stacking, and a minimum around 230 nm, associated with a β -structure. A slight red-shift of the minimum from 227 to 230 nm occurred for NSs encapsulating NBD. Moreover, the molar ellipticity (θ) of NBD/PEG₈-F6 at 230 nm did not change significantly as a function of time (see Figure 2b). A slight variation of θ was detectable over time with a more significant variation during the first 10 min. This trend suggests a time-dependent structural rearrangement of the dye-containing NSs. Analogously to the CD data, the FTIR spectra of NBD-filled PEG₈-F6 in the region of the amide I vibrational band (1600–1700 cm⁻¹) were very similar to spectra of empty PEG₈-F6 both in solution and solid state (Figure 3). The FTIR spectra showed a peak at approximately 1637–1640 cm⁻¹ typically attributable to β -sheet formation. In addition to this peak, all spectra showed a secondary broad peak at approximately 1680 cm⁻¹ that indicates an antiparallel orientation of the β -sheet. These results clearly demonstrate that, despite the strong binding be-

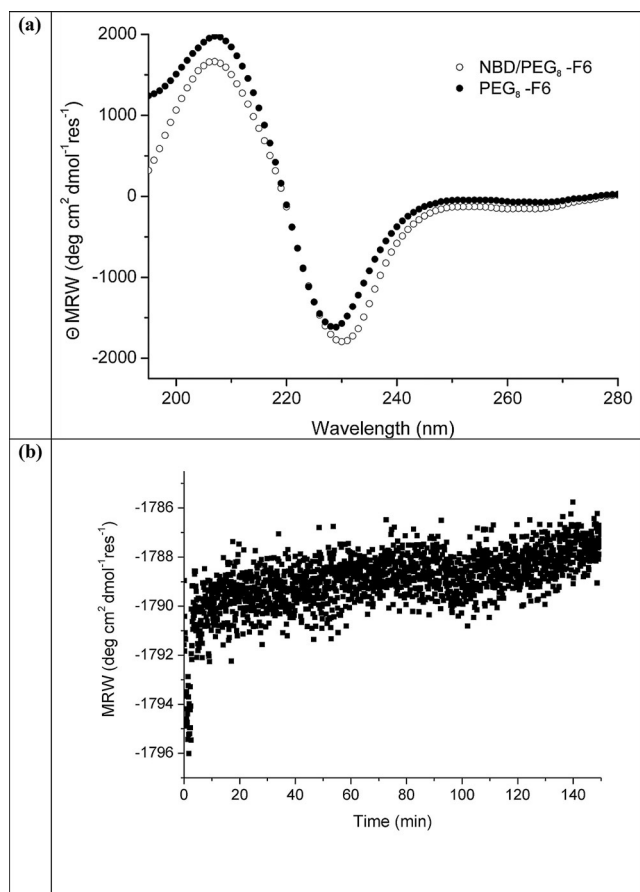


Figure 2. (a) Comparison between the CD spectra of PEG₈-F6 and NBD/PEG₈-F6 in water at 10 mg mL⁻¹. Spectra were recorded in the range between 280 and 195 nm and reported in mean residue ellipticity (θ); (b) molar ellipticity of NBD/PEG₈-F6 in the minimum at 230 nm as function of time.

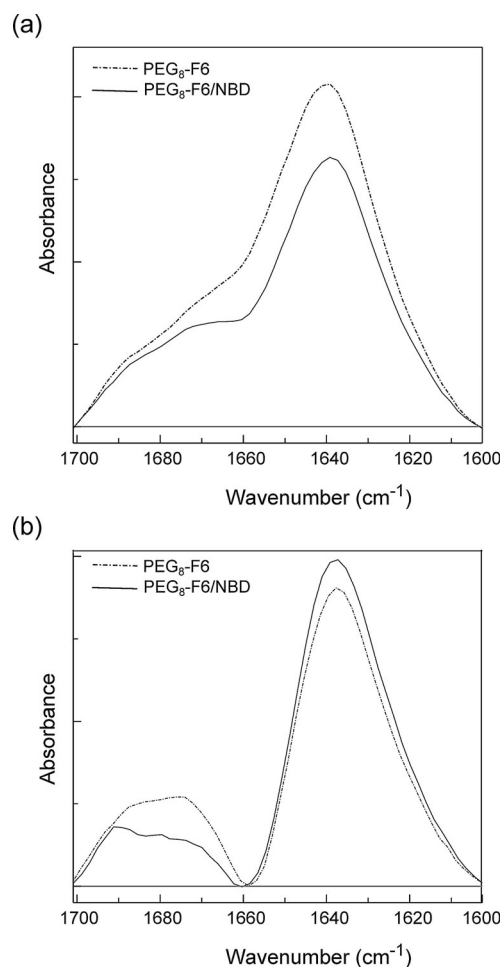


Figure 3. Characterization of the secondary structure: FTIR spectra of PEG₈-F6 and NBD/PEG₈-F6 in (a) solution and (b) solid state in the amide I region.

tween the dye and the peptide NSs, the encapsulation of NBD did not significantly alter the secondary structure of the supramolecular aggregate.

Photoluminescence properties

Recently, several authors reported a surprising PL phenomenon for fibrillary networks such as amyloid fibrils and for peptide-based NSs, both of them characterized by a high content of cross- β structures.^[13–16] These systems show a fluorescence emission peak at 460 nm when excited at 370 or at 410 nm. Owing to the close relationship between the optoelectronic properties and the structural motif in these systems, PL is currently used as a promising probe to detect the formation of amyloid fibrils. We demonstrated that empty PEG₈-F6-based NSs, at a concentration of 10 mg mL⁻¹, are able to emit at 460 nm (Figure S3 in the Supporting Information).^[16] At this very high concentration it was possible to detect a broad peak between 370 and 410 nm in the UV/Vis spectrum (Figure S4 in the Supporting Information), partially affected by the tail of the main absorbance peak centered at 257 nm, which is typical for the phenyl ring. Here, we investigated how NBD encapsulation in PEG₈-F6 NSs can alter their optoelectronic properties

both in solution and solid state (Figure 4 and Figure 5). In contrast to the spectra of empty PEG₈-F6 NSs (Figure S3 in the

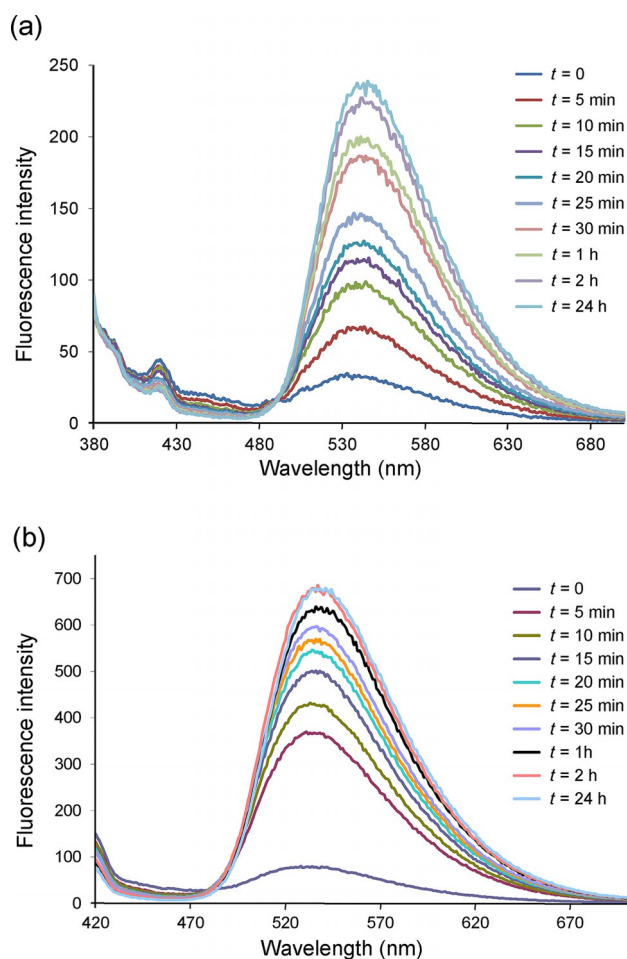


Figure 4. PL of NBD/PEG₈-F6 NSs at 10 mg mL⁻¹ as function of time. PL emission spectra for sample in solution upon excitation at (a) 370 nm and (b) 410 nm.

Supporting Information), showing an emission peak at 460 nm, NBD/PEG₈-F6 spectra (see Figure 4a,b) showed a peak at 535 nm, corresponding to the typical emission wavelength of NBD. The occurrence of this red-shift and the simultaneous disappearance of the expected maximum at 460 nm led us to speculate that the NBD dye was close enough to the NSs to accept the energy emitted by the NS according to a FRET phenomenon. FRET is a distance-dependent physical process by which energy of an excited fluorophore (donor) is transferred non-radiatively to another fluorophore (acceptor). FRET strongly depends on the proximity between the donor and the acceptor species, and the maximum efficiency occurs if the donor and acceptor are positioned within the Förster radius (the distance at which half the excitation energy of the donor is transferred to the acceptor; typically 3–6 nm). From a qualitative point of view, a macroscopic variation in the color of the solution from light to dark yellow was also detected during the time (Figure S5 in the Supporting Information). This change of color pushed us to follow the fluorescence of the sample over time. Surprisingly, we observed a progressive increase of the fluorescence up to 2 h, whereas no further increases was observed after this time. The same behavior was also observed for two other preparations, in which the peptide concentration was kept fixed at 10 mg mL⁻¹, whereas the NBD amount was reduced to 100 or 10 μg mL⁻¹ (see Figure S6 in the Supporting Information). It is plausible to speculate that this increase of the fluorescence intensity was the result of an increase of the fibrillary species in solution over time. To verify this hypothesis, the kinetics of aggregation of empty PEG₈-F6 NSs were studied up to 24 h at the same concentration (Figure S7 in the Supporting Information). However, no significant variation could be detected in the fluorescence spectra of empty NSs. This result indicated that the kinetics of aggregation for empty NSs were very fast and thus not observable. In contrast, the increase of the fluorescence of NBD/PEG₈-F6 (Figure 4) could depend on a molecular rearrangement of the

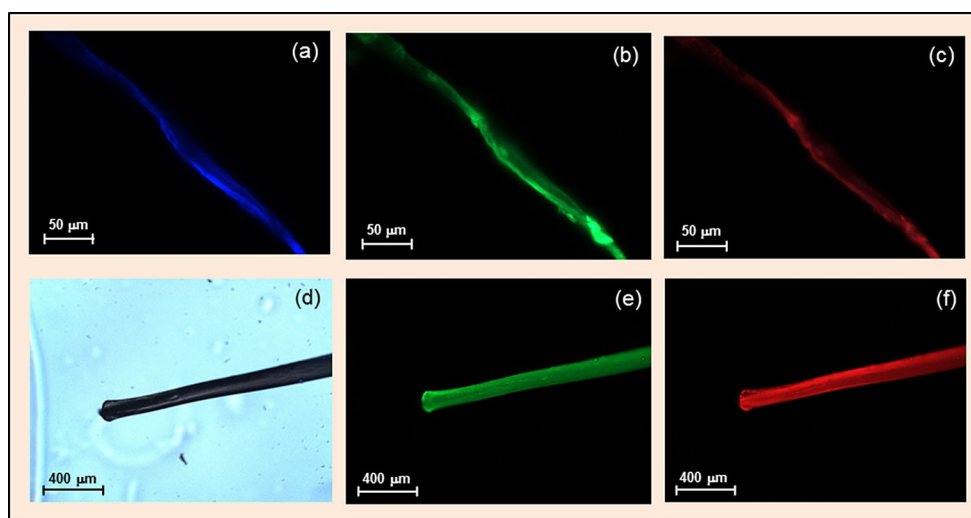


Figure 5. Fluorescence microscopy images of a dried film of NBD/PEG₈-F6 obtained by exciting in the UV spectral region of (a) 4',6-diamidino-2-phenylindole (DAPI), (b) green fluorescent protein (GFP), and (c) rhodamine filters; images of NBD/PEG₈-F6 fibers recorded by exciting in (d) bright light, (e) GFP, and (f) rhodamine filters.

dye in the peptide aggregate or on a slowing of the kinetics of aggregation of the NS owing to the NBD encapsulation. NBD/PEG₈-F6 also emitted PL in the solid state. Figure 5 shows, respectively, the immunofluorescence images of the dried sample deposited on a clean coverslip glass (Figure 5a–c) and of the oriented fibers (Figure 5d–f) obtained with the stretch-frame method.^[22] Both the microscopy images of the dried film (Figure 5a–c) and of the oriented fiber (Figure 5d–f) demonstrate the capability of NBD/PEG₈-F6 to emit in blue, green, and red fields. This result is in agreement with the width of the emission peak observed for the sample in solution (Figure 4). We ascertained that it was also possible to obtain self-assembled NSs (Figure S8a in the Supporting Information) starting from the peptide conjugate NBD-PEG₈-F6, in which NBD was covalently bound to the amine function of the PEGylated hexaphenylalanine. These NSs, which have a univocally defined NBD/PEG₈-F6 ratio (1:1), retained the optoelectronic properties of the NBD-filled NSs (see Figure S8b in the Supporting Information) even if they presented a lower water solubility owing to the N-terminus functionalization. The FRET observed for NBD-PEG₈-F6 was in good agreement with that detected for the covalently conjugates between the α -Synuclein and Yellow Fluorescent Protein (AS-YFP).^[23] The definition of the structural determinants of these intriguing PL properties exhibited by cross- β -rich systems is still a debated topic and the subject of intense current investigations. However, a proven explanation on the origins of this unexpected PL has not been provided until now, and this topic remains under debate. The most accredited hypotheses concerning the origin

of the PL are electron delocalization through hydrogen bonds in the β -sheet-rich structure^[13] or proton transfer.^[15] Moreover, it is important to underline that the fluorescence signal of these fibrillary structures is weak and that PL is obtained only at very high concentrations.

Wide- and small-angle X-ray scattering

To gain deeper insight into the assembly process and molecular organization, we acquired wide-angle and small-angle X-ray scattering (WAXS/SAXS) data on ordered fibers prepared by the stretch-frame method.^[22] Figure 6a,b show the as-prepared fibers, which were placed under the X-ray beam in transmission geometry. The 2D WAXS and SAXS fiber diffraction patterns, collected on PEG₈-F6 and PEG₈-F6/NBD samples, are displayed in Figure 6c,d and e,f, respectively. Two main directions are indicated by the white arrows: the meridional direction, which coincides with the fiber axis, and the equatorial direction, which is perpendicular to it. They show a cross- β diffraction pattern both in WAXS (atomic distances) and in SAXS (nanoscale distances), the fingerprint of hierarchically organized fibers. The 2D patterns were centered, calibrated, and radially folded into 1D profiles. WAXS data were integrated across the meridional and equatorial axes, and the resulting 1D WAXS profiles displayed in Figure 6g (blue for PEG₈-F6 and red for NBD/PEG₈-F6), separately reporting the meridional (upper) and equatorial (lower) profiles. SAXS data were integrated across the whole azimuth, and the 1D SAXS profiles are reported in Figure 6h. The peak positions (in q) of the most in-

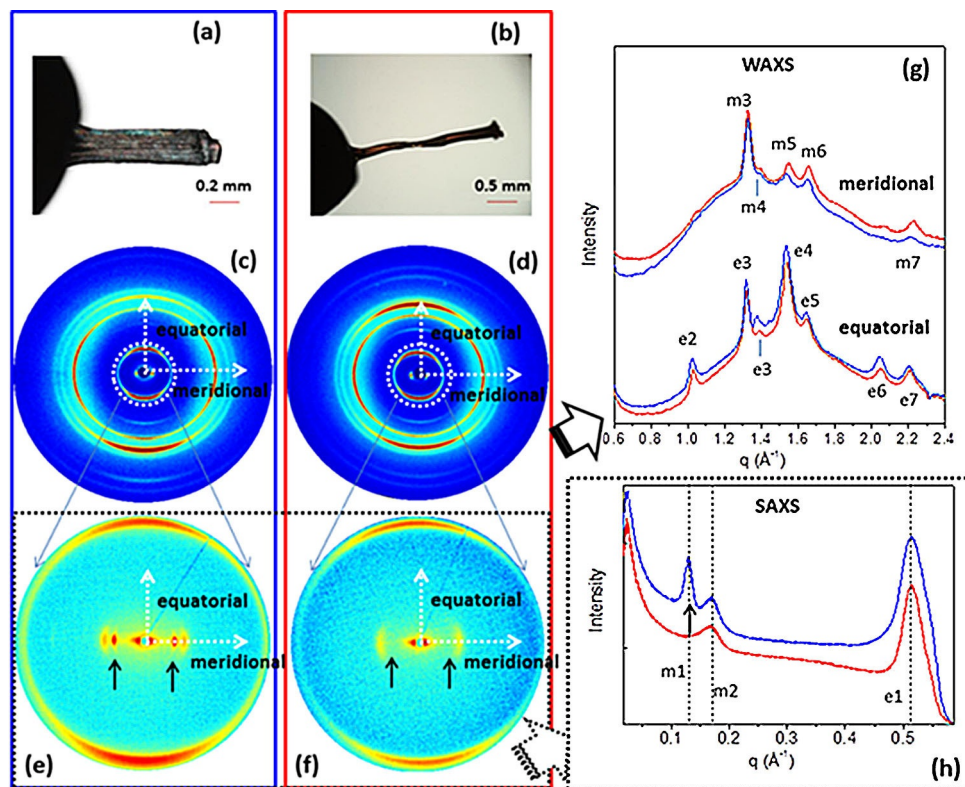


Figure 6. (a, b) As-prepared fibers; (c, d) 2D WAXS data; (e, f) 2D SAXS data; (g) 1D WAXS profiles (upper: meridional, lower: equatorial); (h) 1D SAXS profiles; blue lines refer to empty PEG₈-F6; red lines to NBD/PEG₈-F6.

tense WAXS and SAXS peaks, measured along the equatorial and meridional directions, are summarized in Table 1. Collectively, these experiments indicate that the encapsulation of the dye had a minimal impact on the atomic structure of the peptide spine of these assemblies. PEG₈-F6 and NBD/PEG₈-F6 share

Table 1. Meridional and equatorial reflections of NBD/PEG ₈ -F6 measured from WAXS and SAXS data.		
Label	q [Å]	d [Å] ± 0.3 Å
Equatorial reflections		
e1	0.51	12
e2	1.0	6.1
e3	1.3	4.8
e5	1.4	4.5
e6	1.6	4.1
e7	1.7	3.8
e8	2.1	3.1
e9	2.2	2.8
Meridional reflections		
m1	0.13	48
m2	0.17	37
m3	1.3	4.8
m4	1.4	4.5
m5	1.6	4.1
m6	1.7	3.8
m7	2.2	2.8

several meridional and equatorial reflections. The only significant difference is related to the m1 reflection ($d=48$ Å) of PEG₈-F6, which disappears in NBD/PEG₈-F6 (marked by the arrows in Figure 6e,f,h). These observations suggest that the 3D model proposed for the peptide spine PEG₈-F6, which corresponds to anti-parallel β -sheets separated by a dry interface consisting of interacting Phe side chains,^[16] can be reliably extended to NBD/PEG₈-F6. In particular, the preservation of the equatorial reflection e1 at 12.2 Å, which is indicative of the inter-sheet distance, suggests that the dye was not inserted in the dry interface, in contrast with observations on the complexation of the dye orange G with the cross- β assembly formed by the peptide KLVFFA.^[24] It is likely that, in analogy with the proposed binding of ThT to amyloid-like nanofibers,^[25] the dye may either bind at the groove parallel to the fiber axis formed by the side-chain ladders or at the edges of the flat β -sheet surface.

Scanning electron microscopy

Scanning electron microscopy (SEM) images of NBD-filled NSs at different concentrations (50, 200 $\mu\text{g mL}^{-1}$, and 2.0 mg mL^{-1}) are reported in Figure 7. Our previous SEM studies on the empty PEG₈-F6 self-assembled NSs indicated a high morphological variability of this aromatic peptide. At low concentrations (50 and 200 $\mu\text{g mL}^{-1}$), NBD/PEG₈-F6 formed either amorphous conglomerates or crystalline structures (Figure 7a,b), in line with the empty PEG₈-F6 aggregates. However, at high concentration (2.0 mg mL^{-1}), images of NBD-containing NSs revealed the presence of branched structures instead of the sheaf of fibers and of long NSs (flat or twisted ribbon shape) previously observed for empty NSs. These branched structures are typically observed for aromatic peptides dissolved in solutions with high ionic strength. According to the models proposed for these solutions, branched architectures in NBD/PEG₈-F6 could be explained hypothesizing that the some NBD crystals coat the surface of peptide fibers, and the growth of the branch occurs in correspondence to these nucleation sites.

Conclusion

Recently, PL phenomena have been observed in fibrillary networks such as amyloid fibrils and in others peptide-based NSs with a high content of cross- β structures. However, the intensity of fluorescence emitted by these structures is weak, and the signal remains confined in the near-Vis region. The development of biocompatible peptide NSs as bio-imaging tools requires the improvement of their performance in terms of PL intensity and wavelength range compatible with in vivo applications. A possible strategy could be the close association (encapsulation, binding, or absorption) of a small fluorescent dye such as NBD to the photoluminescent NS. The close proximity at the atomic level between the dye and the NS should promote the energy transfer. With this goal in the mind, we encapsulated NBD in PEG₈-F6 NSs that exhibit blue PL owing to the high content of cross- β structures. The entrapment of NBD in these NSs caused a red-shift from 460 to 530 nm that we attribute to a FRET phenomenon. Structural characterization performed on NBD-filled PEG₈-F6 NSs, both in solution and solid state, did not highlight significant differences of the sample compared to empty PEG₈-F6 NSs. However, SEM images acquired at 2.0 mg mL^{-1} showed the presence of branched structures. The branching of the peptide structures could be attrib-

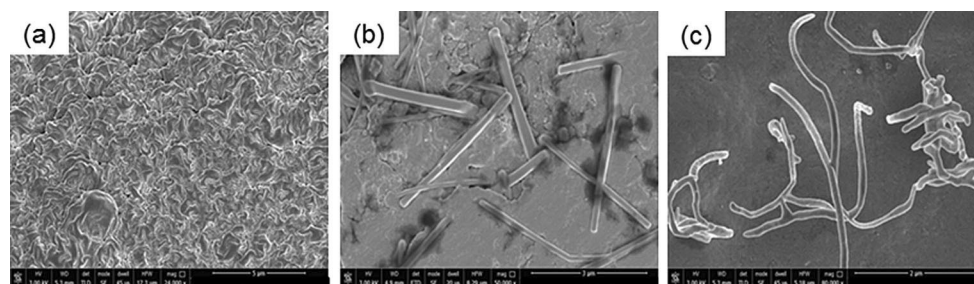


Figure 7. Selected SEM microphotographs for NBD-filled PEG₈-F6: (a) 50 $\mu\text{g mL}^{-1}$ (24000 \times , 5 μm scale bar); (b) 200 $\mu\text{g mL}^{-1}$ (50000 \times , 3 μm scale bar); (c) 2.0 mg mL^{-1} (80000 \times , 2 μm scale bar).

uted to the coating of the fiber surface with NBD crystals. Further structural information on the positioning of the NBD in the 3D model proposed for the peptide-spine PEG₈-F6 was obtained by WAXS/SAXS measurements. From the comparison of the diffraction patterns, it emerged that in NBD/PEG₈-F6 the m1 reflection ($d = 48 \text{ \AA}$) disappeared, whereas the equatorial reflection e1 at 12.2 \AA , indicative of the inter-sheet distance, was preserved. These findings suggest that NBD was arranged outward from the dry interface but remained close enough to the origin of the PL to accept the energy transfer. The capability to transfer fluorescence between the NS and the dye was retained even if the dye was covalently bound to the peptide NS. This evidence led us to envisage new applications for dye-encapsulating peptides as innovative biomaterials. Encapsulation or conjugation of small-molecule dyes in/to NSs represents an alternative and complementary strategy^[23] for the detection of the aggregation process of endogenous proteins, which, in their physio-pathological form, are known to adopt a cross- β structural motif.

Experimental Section

Material and Methods: NBD and HFIP were purchased from Sigma-Aldrich (Milan, Italy). All solutions were prepared by weight with doubly distilled water. UV/Vis measurements were performed on a Thermo Fisher Scientific Inc (Wilmington, Delaware USA) Nanodrop 2000c spectrophotometer equipped with a 1.0 cm quartz cuvette (Hellma). Analytical LC-MS analyses were assessed using a Finnigan Surveyor MSQ single quadrupole electrospray ionization (Finnigan/Thermo Electron Corporation San Jose, CA), with a C18-Phenomenex column eluted with H₂O/0.1% TFA (A) and CH₃CN/0.1% TFA (B) from 20 to 80% over 20 min at $200 \mu\text{L min}^{-1}$ flow rate.

Peptide synthesis: The PEGylated peptide PEG₈-F6, reported in Figure S1 in the Supporting Information, was synthesized by solid-phase synthesis and purified by reverse-phase (RP)-HPLC chromatography, according to the procedure previously described.^[16]

Synthesis of NBD/PEG₈-F6 NSs: PEG₈-F6 peptide NBD-filled NSs were prepared by dissolving fluorescent NBD dye and PEG₈-F6 peptide in HFIP. The peptide and NBD concentrations in HFIP were 100 and 10 mg mL^{-1} , respectively. This solution was ten-fold diluted in water, and the organic solvent was removed by a slow nitrogen flow. The solution was centrifuged 5 min at 13500 rpm, and the supernatant was purified from free NBD by gel-filtration with a Sephadex G-50 column pre-equilibrated with water. For the determination of the amount of NBD encapsulated in NSs, a sample was lyophilized and spectroscopically investigated by UV/Vis measurements at $\lambda = 340 \text{ nm}$ on the powder dissolved in CH₃OH. The molar absorptivity (ϵ) at 340 nm ($9352 \text{ M}^{-1} \text{ cm}^{-1}$) was calculated by a calibration curve. The identity of NBD after loading in PEG₈-F6 was determined by LC-MS.

Synthesis of NBD/PEG₈-F6 peptide conjugate: NBD-PEG₈-F6 peptide conjugate was synthesized according to the standard solid-phase 9-fluorenylmethoxycarbonyl (Fmoc) protocols on Rink amide MBHA resin (substitution 0.65 mmol g^{-1}). The elongation of PEG₈-F6 on the resin was achieved as previously reported.^[16] NBD-labeling was performed on resin-bound peptides as previously reported by Rapaport and Shai.^[26] Briefly, after removal of the Fmoc protecting group of the N-terminal amino acid, the resin-bound peptide was treated with NBD-Cl in *N,N*-diisopropylethylamine (2 M in DMF,

3–4 equiv.). After 24 h, the resin-bound peptides were washed thoroughly with CH₂Cl₂, and the peptides were cleaved and purified as previously described. The identity of the NBD peptides was confirmed by LC-MS. Retention time = 18.1 min; MS (ESI⁺): m/z calcd for C₈₄H₁₀₂N₁₄O₂₁: $1642.2 [M + 2H]^+ / 2 = 822.6$.

Dynamic Light Scattering (DLS): Mean diameter and diffusion coefficient (D) of NBD-PEG₈-F6 NSs were measured by DLS measurements using a Zetasizer Nano ZS (Malvern Instruments, Westborough, MA) that employs a 173° backscatter detector. Other instrumental settings were: measurement position 4.65 mm; attenuator 9; temperature 25 °C; disposable sizing cuvette as cell. DLS measurements in triplicate were performed on the peptide conjugate at 1 mg mL^{-1} after room temperature centrifugation at 13000 rpm for 5 min.

CD: Far-UV CD spectra of the NBD/PEG₈-F6 NSs in aqueous solution were recorded on a Jasco J-810 spectropolarimeter equipped with a NesLab RTE111 thermal controller unit and a 0.1 mm quartz cell at 25 °C. The spectra were acquired from 280 to 195 nm for samples at concentrations ranging between 0.5 and 10.0 mg mL^{-1} . Other experimental settings were: scan speed 10 nm min^{-1} ; sensitivity 50 mdeg; time constant 16 s; bandwidth 1 nm. Each spectrum was obtained by averaging three scans and corrected for the blank contribute. Here, θ represents the mean residue ellipticity (MRE), that is, the ellipticity per mol peptide divided by the number of amino acid residues in the peptide.

FTIR spectroscopy: FTIR spectra of NBD/PEG₈-F6 and NBD (2.0 mg mL^{-1}) were collected on a Jasco FT/IR 4100 spectrometer (Easton, MD) in an attenuated total reflection (ATR) mode with a Ge single-crystal at a resolution of 4 cm^{-1} . All spectral data were processed using built-in software. Spectra were collected in transmission mode and then converted into emission. Each sample was recorded with a total of 100 scans with a rate of 2 mm s^{-1} against a KBr background.

Optical Spectrofluorometry: Measurements of PL were performed on a Jasco Model FP-750 spectrofluorophotometer in a 1.0 cm path length quartz cell. Aqueous NBD/PEG₈-F6 NSs (10 mg mL^{-1}) were prepared as previously described by diluting HFIP in water. Immediately after the purification of the NSs by gel-filtration, the fluorescence measurements on the sample were recorded by exciting it at 370 or 410 nm. This acquisition was indicated as time = 0. Starting from this measure, we followed the fluorescence behaviour up to 24 h, recording a spectrum at different time points. NBD-PEG₈-F6 conjugate (1.0 mg mL^{-1}) was prepared by sonicating the powder in acetonitrile (1.5 mL) for 5 min and then diluting the solution with water (1:1). After this dilution, the sample appeared perfectly clear, and the fluorescence emission was measured according to the experimental details reported above.

Fluorescence microscopy: NBD/PEG₈-F₆ solution ($15 \mu\text{L}$; 10 mg mL^{-1}), prepared 24 h before, was deposited on a clean coverslip glass, dried, and imaged with fluorescence microscopy. Immunofluorescence images were taken with a Leica DFC320 video camera (Leica, Milan, Italy) connected to a Leica DMRB microscope equipped with 10 X and 40 X objectives, and the Image J Software (National Institutes of Health, Bethesda, MD) was used for analysis.^[27]

WAXS and SAXS: Fiber diffraction WAXS and SAXS patterns were recorded from dried fibers prepared by the stretch-frame method.^[22] Briefly, a droplet ($10 \mu\text{L}$) of peptide aqueous solution (3 wt%) was suspended between the ends of a wax-coated capillary (spaced 2 mm apart). The droplet was allowed to dry gently at room temperature overnight to obtain oriented fibers. WAXS and SAXS data were collected at the X-ray MicroImaging Laboratory

(XMI-L@b) equipped with a Fr-E+ SuperBright rotating anode copper anode microsource (CuK_{α} , $\lambda = 0.15405$ nm, 2475 W), a multi-layer focusing optics (Confocal Max-Flux; CMF 15–105), and a three-pinhole camera (Rigaku SMAX-3000).^[3] For WAXS data collection an image plate (IP) detector with 100 μm pixel size was placed at 10 cm from the sample and calibrated by means of the Si NIST standard reference material (SRM 640b); for SAXS data collection a Triton 20 gas-filled photon counter detector with approximately 200 μm pixel size was placed at 2.2 m from the sample and calibrated by means of silver behenate. A detailed description of the XMI-L@b performances can be found in reports by Altamura et al.^[28] and Sibillano et al.^[29]

SEM: Morphological analysis of the NSs was performed by using a field-emission scanning electron microscope (Nova NanoSem 450-FEI). Samples at several concentrations (50, 200 $\mu\text{g mL}^{-1}$, and 2.0 mg mL^{-1}) were prepared by sequential dilution of NBD/PEG₈-F6, prepared as described above. These peptide solutions were placed on an aluminum stub. The air-dried sample was covered with a thin coat of gold and palladium sputtered on the stub at a current of 20 mA for 90 s. The images of the sample were acquired with an Everhart Thornley Detector (ETD) and a Through the Lens Detector (TLD) using an accelerating voltage of 2–5 kV.

Acknowledgements

The authors would like to acknowledge Rocco Lassandro of the XMI-L@b for technical assistance. Part of the work was supported by the Apulia Regional Government through the Project “TAPASS” (cod. PELM994–CUP B38C14002040008).

Conflict of interest

The authors declare no conflict of interest.

Keywords: cross-beta nanostructures · FRET · peptides · photoluminescence · polyphenylalanines

- [1] a) J. Sung, R. N. Zuckermann, *ACS Nano* **2013**, *7*, 4715; b) Y. Yang, U. Khoe, X. Wang, A. Horii, H. Yokoi, S. Zhang, *Nano Today* **2009**, *4*, 269; c) *Self-Assembled Peptide Nanostructures- Advances and Applications in Nanobiotechnology* (Eds.: J. Castillo-Léon, L. Sasso, W. E. Svendsen), CRC Press, Boca Raton, **2012**.
- [2] a) M. Reches, E. Gazit, *Science* **2003**, *300*, 625; b) G. Demirel, F. Buyukserin, *Langmuir* **2011**, *27*, 12533.
- [3] P. Zelenovskiy, I. Kornev, S. Vasilev, A. Kholkin, *Phys. Chem. Chem. Phys.* **2016**, *18*, 29681.
- [4] a) T. Cipriano, G. Knotts, A. Laudari, R. C. Bianchi, W. A. Alves Wendel, S. Guha, *ACS Appl. Mater. Interfaces* **2014**, *6*, 21408; b) A. Handelman, B. Apter, N. Turko, G. Rosenman, *Acta Biomater.* **2016**, *30*, 72; c) A. Handelman, N. Kuritz, A. Natan, G. Rosenman, *Langmuir* **2016**, *32*, 2847; d) S. Vasilev, P. Zelenovskiy, D. Vasileva, A. Nuraeva, V. Y. Shur, A. L. Kholkin, *J. Phys. Chem. Solids* **2016**, *93*, 68.
- [5] a) Y. Kuang, Y. Gao, B. Xu, *Chem. Commun.* **2011**, *47*, 12625; b) C. Diaferia, F. A. Mercurio, C. Giannini, T. Sibillano, G. Morelli, M. Leone, A. Accardo, *Sci. Rep.* **2016**, *6*, 26638.
- [6] J. S. Lee, J. Ryu, C. B. Park, *Soft Matter* **2009**, *5*, 2717.
- [7] M. Zhou, R. V. Ulijn, J. E. Gough, *J. Tissue Engin.* **2014**, *5*, 204173141453159.
- [8] C. Diaferia, E. Gianolio, P. Palladino, F. Arena, C. Boffa, G. Morelli, A. Accardo, *Adv. Funct. Mater.* **2015**, *25*, 7003.
- [9] F. Silva Rendes, D. R. Araujo, E. R. Silva, A. Ando Romulo, A. Alves Wendel, *Langmuir* **2013**, *29*, 10205.
- [10] S. Almohammed, S. O. Oladapo, K. Ryan, A. L. Kholkin, J. H. Rice, B. J. Rodriguez, *RSC Adv.* **2016**, *6*, 41809.
- [11] C. Diaferia, E. Gianolio, A. Accardo, G. Morelli, *J. Pept. Sci.* **2017**, *23*, 122–130.
- [12] C. Diaferia, E. Gianolio, T. Sibillano, F. A. Mercurio, M. Leone, C. Giannini, N. Balasco, L. Vitagliano, G. Morelli, A. Accardo, *Sci. Rep.* **2017**, Mar 22;7(1):307.
- [13] a) A. Handelman, A. Natan, G. Rosenman, *J. Pept. Sci.* **2014**, *20*, 487; b) N. Amdursky, M. Molotskii, D. Aronov, L. Adler-Abramovich, E. Gazit, G. Rosenman, *Nano Lett.* **2009**, *9*, 3111.
- [14] a) L. L. del Mercato, P. P. Pomp, G. Maruccio, A. D. Torre, S. Sabella, A. M. Tamburro, R. Cingolani, R. Rinaldi, *Proc. Natl. Acad. Sci. USA* **2007**, *104*, 18019; b) D. Pinotsi, A. K. Buell, C. M. Dobson, G. S. Kaminski, C. F. Kaminski, *ChemBioChem* **2013**, *14*, 846.
- [15] D. Pinotsi, L. Grisanti, P. Mahou, R. Gebauer, C. F. Kaminski, A. Hassanali, G. S. Kaminski Schierle, *J. Am. Chem. Soc.* **2016**, *138*, 3046.
- [16] C. Diaferia, T. Sibillano, N. Balasco, C. Giannini, V. Roviello, L. Vitagliano, G. Morelli, A. Accardo, *Chem. Eur. J.* **2016**, *22*, 16586.
- [17] M. Choi, M. Humar, S. Kim, S. H. Yun, *Adv. Mater.* **2015**, *27*, 4081.
- [18] a) G. Keiser, F. Xiong, Y. Cui, P. P. Shum, *J. Biomed. Opt.* **2014**, *19*, 080902; b) M. J. Gora, J. S. Sauk, R. W. Carruth, K. A. Gallagher, M. J. Suter, N. S. Nishioka, L. E. Kava, M. Rosenberg, B. E. Bouma, G. J. Tearney, *Nat. Med.* **2013**, *19*, 238.
- [19] S. Nizamoglu, M. C. Gather, S. H. Yun, *Adv. Mater.* **2013**, *25*, 5943.
- [20] M. Choi, J. W. Choi, S. Kim, S. Nizamoglu, S. K. Hahn, S. H. Yun, *Nat. Photonics* **2013**, *7*, 987.
- [21] A. Jain, A. H. Yang, D. Erickson, *Opt. Lett.* **2012**, *37*, 1472.
- [22] M. Sunde, L. C. Serpell, M. Bartlam, P. E. Fraser, M. B. Pepys, C. C. Blake, *J. Mol. Biol.* **1997**, *273*, 729–739.
- [23] a) T. J. van Ham, A. Esposito, J. R. Kumita, S. T. Hsu, G. S. Kaminski Schierle, C. F. Kaminski, C. M. Dobson, E. A. Nollen, C. W. Bertoncini, *J. Mol. Biol.* **2010**, *395*, 627–42; b) G. S. Kaminski Schierle, C. W. Bertoncini, F. T. Chan, A. T. van der Goot, S. Schwedler, J. Skepper, S. Schlachter, T. van Ham, A. Esposito, J. R. Kumita, E. A. Nollen, C. M. Dobson, C. F. Kaminski, *ChemPhysChem* **2011**, *12*, 673–80.
- [24] M. Landau, M. R. Sawaya, K. F. Faull, A. Laganowsky, L. Jiang, S. A. Sievers, J. Liu, J. R. Barrio, D. Eisenberg, *PLoS Biol.* **2011**, *9*, e1001080.
- [25] M. Biancalana, S. Koide, *Biochim. Biophys. Acta Proteins Proteomics* **2010**, *1804*, 1405–1412.
- [26] D. Rapaport, Y. Shai, *J. Biol. Chem.* **1991**, *266*, 23769.
- [27] S. F. Generoso, M. Giustiniano, G. La Regina, S. Bottone, S. Passacantilli, S. Di Maro, H. Cassese, A. Bruno, M. Mallardo, M. Dentice, R. Silvestri, L. Marinelli, D. Sarnataro, S. Bonatti, E. Novellino, M. Stornaiuolo, *Nat. Chem. Biol.* **2015**, *11*, 280–288.
- [28] D. Altamura, R. Lassandro, F. A. Vittoria, L. De Caro, D. Siliqi, M. Ladisa, C. Giannini, *J. Appl. Crystallogr.* **2012**, *45*, 869.
- [29] T. Sibillano, L. De Caro, D. Altamura, D. Siliqi, M. Ramella, F. Boccafoschi, G. Ciasca, G. Campi, L. Tirinato, E. Di Fabrizio, C. Giannini, *Sci. Rep.* **2014**, *4*, 6985.

Manuscript received: March 28, 2017

Accepted manuscript online: May 16, 2017

Version of record online: June 5, 2017

■ Peptide-Polymer Conjugates

Structural Characterization of PEGylated Hexaphenylalanine Nanostructures Exhibiting Green Photoluminescence Emission

Carlo Diaferia,^[a] Teresa Sibillano,^[b] Davide Altamura,^[b] Valentina Roviello,^[c] Luigi Vitagliano,^[d] Cinzia Giannini,^[b] Giancarlo Morelli,^[a] and Antonella Accardo^{*[a]}

Abstract: Peptides containing aromatic residues are known to exhibit spontaneous phenomena of supramolecular organization into ordered nanostructures (NSs). In this work we studied the structural behavior and optoelectronic properties of new biocompatible materials obtained by the self-assembly of a series of hexaphenylalanines (F6) modified at the N terminus by a PEG chain of different lengths. PEG₁₂-F6, PEG₁₈-F6, and PEG₂₄-F6 peptides were synthesized by coupling sequentially two, three, or four units of amino-carboxy-PEG₆ blocks, each one containing six oxyethylene repetitions. Changes in the length and composition of the PEG

chain were found to modulate the structural organization of the phenylalanine-based nanostructures. An increase in the self-aggregation tendency was observed with longer PEG chains, whereas, independently of the PEG length, the peptide NSs display cross- β -like secondary structures with an antiparallel β -strand arrangement. WAXS/GIWAXS diffraction patterns indicate a progressive decrease in fiber order along the series. All the PEG-F6 derivatives present blue photoluminescent (PL) emission at 460 nm, with the adduct with the longest PEG chain (PEG₂₄-F6) showing an additional green emission at 530 nm.

Introduction

Self-assembling peptides are a class of building blocks that undergo spontaneous supramolecular organization into ordered structure on the nanoscale. The ability of peptides to self-assemble, adopting stable secondary conformations, has allowed them to be used in nanotechnology and in materials science as very multifunctional tools.^[1] Superhydrophobic coating,^[2] tissue engineering,^[3] cell culturing,^[4] biosensing,^[5] and drug delivery^[6] are only some of the possible areas of application of peptide-based supramolecular systems. The driving forces that hold up spontaneous aggregations are pinpointed in hydrogen bonds and hydrophobic and aromatic interactions. Peptides

also exhibit versatile features such as resistance to pH^[7] as well as high^[8] or low temperatures,^[9] mutual recognition,^[10] functionality,^[11] high mechanical performance,^[12] and intrinsic biocompatibility.^[13] In addition to these characteristics, the rational design of peptide building blocks and the convenient synthetic procedures of decoration also make it possible to combine self-assembling peptides with a range of other functional moieties (such as lipids,^[14] metallic centers,^[15] and nucleic acid derivatives).^[16] The mix of peptides with synthetic polymers (e.g., poly(ethylene oxide) (PEO),^[17] poly(ethylene glycol) (PEG),^[18] polycaprolactone (PCL),^[19] poly(propylene oxide) (PPO),^[20] or poly(acrylic acid) (PPA)^[21]) allows (generally in amphiphilic blocks) peptide functionality and recognition capability to be synergistically combined with polymer cheapness and responsiveness to obtain new hybrid materials. Since the early 1950s, when Jatzkewitz described the first example of a peptide/polymer conjugate,^[22] several reviews,^[23] communications,^[24] and perspectives^[25] on their synthesis and potential applications have been reported. It has been observed that the conjugation of polymers (with particular reference to PEG chains) to natural or synthetic peptides such as poly(γ -benzyl-L-aspartate),^[26] [(AG)₃EG]₁₀,^[27] DGRFFF,^[28] (LELL)₄,^[29] and oligo(phenylalanines)^[17] can strongly affect their structural properties. Moreover, owing to the crystallization phenomenon, PEG could inhibit the fibrillation of amyloid peptide sequences (i.e., A β ₁₆₋₂₀^[30] and A β ₁₀₋₃₅^[31]), a function not available to the unmodified peptide.

In the last decade, homo-peptides have been identified as the simplest class of self-assembling elements and diphenylalanine (FF) represents the most well-known peptide building block.^[32] Also, tetra- and pentaphenylalanines have been proposed as promising building blocks for future technological

[a] Dr. C. Diaferia, Prof. G. Morelli, Dr. A. Accardo
Department of Pharmacy
Research Centre on Bioactive Peptides (CIRPeB)
University of Naples "Federico II" and DFM Scarl
Via Mezzocannone 16, 80134 Naples (Italy)
E-mail: Antonella.accardo@unina.it

[b] Dr. T. Sibillano, Dr. D. Altamura, Dr. C. Giannini
Institute of Crystallography (IC), CNR
Via Amendola 122, 70126 Bari (Italy)

[c] Dr. V. Roviello
Analytical Chemistry for the Environment
and Centro Servizi Metrologici Avanzati
University of Naples "Federico II"
Corso Nicolangelo Protopisani, 80146, Naples (Italy)

[d] Dr. L. Vitagliano
Institute of Biostructures and Bioimaging (IBB), CNR
Via Mezzocannone 16, 80134 Naples (Italy)

Supporting information and the ORCID identification number(s) for the author(s) of this article can be found under <https://doi.org/10.1002/chem.201703055>.

applications.^[33] We recently proposed and investigated the supramolecular properties of an FF analogue, PEG₈-F6, in which the aromatic framework, formed by triplication of the FF motif (i.e., hexaphenylalanine, F6), was decorated at the N terminus with eight repeating oxyethylene units (PEG₈).^[34] The F6 homo-peptide is poorly soluble in water, and PEGylation leads to a notable increase in its water solubility maintaining unaltered the net charge of the peptide derivative. PEG₈-F6 self-aggregates in well-ordered and stable nanostructures in water solution exhibiting photoluminescence (PL) properties. The PL phenomenon has been ascribed to the dipolar coupling between the excited states of aromatic residues^[35] or associated with the dense network of hydrogen bonds interlocking the β -strands. Indeed, fluorescence has also been observed from fibrils free of any aromatic group.^[36] The most accredited hypothesis is that the proton transfer occurring in the extensive hydrogen-bond network in peptide fibrils may be responsible for the fluorescence of these structures.^[37] However, the fluorescence intensity of these structures is rather weak and the signal remains confined to the near-Vis region. To develop novel bioimaging tools based on peptide nanostructures (NSs), we recently encapsulated a small fluorescent dye, 4-chloro-7-nitrobenzofurazan (NBD), in self-assembled PEG₈-F6 NSs (NBD/PEG₈-F6).^[38] The close proximity, at the atomic level, of the dye and PL nanostructure promotes a redshift of the emission peak from 460 to 530 nm, attributable to a Foster resonance electron transfer (FRET) phenomenon.

Here we report the synthesis, self-assembling properties, and PL behavior of a series of PEGylated hexaphenylalanines (PEG₁₂-F6, PEG₁₈-F6, and PEG₂₄-F6), obtained by coupling, through an amide bond, two, three, or four amino-hexaoxyethylene acid moieties at the N terminus of the hexaphenylalanine. The supramolecular behavior of the F6 copolymers, both in solution and in the solid state, has been investigated by fluorescence, circular dichroism (CD), Fourier-transform IR (FTIR) spectroscopy, polarized optical microscopy (POM), dynamic light scattering (DLS), scanning electron microscopy (SEM), and wide-angle X-ray scattering (WAXS) both in transmission and reflection (GIWAXS) mode. Particular attention was given to the effects of PEG polymer length and the presence of the amide bonds on the supramolecular organization. The optoelectronic properties of the PEG series were also studied and compared with the PL properties of the PEG₈-F6 or NBD/PEG₈-F6 NSs previously reported.^[34,38] Our investigations have revealed the capability of the cross- β nanostructures based on these PEGylated hexaphenylalanines to exhibit green fluorescence emission.

Results and Discussion

Design, synthesis, and fluorescence studies

PEGylated hexaphenylalanine conjugates (PEG₁₂-F6, PEG₁₈-F6, and PEG₂₄-F6), schematically represented in Figure 1a, were manually synthesized by a solid-phase method according to the fluoren-9-ylmethoxycarbonyl (Fmoc) protocols. The polymer/peptide derivatives PEG₁₂-F6, PEG₁₈-F6, and PEG₂₄-F6 were

obtained in good yields and with high purity, by coupling, respectively, two, three, or four units of commercial poly(ethylene glycol) using the Fmoc derivative Fmoc-Ahoh-OH (PEG₆), each containing six oxyethylene repetitions. The coupling reaction of Fmoc-Ahoh-OH was achieved directly in the solid phase by carbodiimide activation. This synthetic method, largely used to prepare short PEG conjugates with molecular weights of 350–800,^[23a,25] allows the preparation of PEGylated conjugates with monodisperse profiles.

Nullifying the predictable effect of PEG polydispersity, it is possible to obtain amphiphilic peptides with a well-defined hydrophile/lipophile balance (HLB). The PEG moiety is expected to enhance the peptide water solubility; nevertheless, owing to the high hydrophobicity of phenylalanine residues, the three peptides show moderate solubility (ca. 20.0 mg mL⁻¹). As is predictable, the progressive increase in oxyethylene fragments also translates into shorter retention times (t_R) in RP-

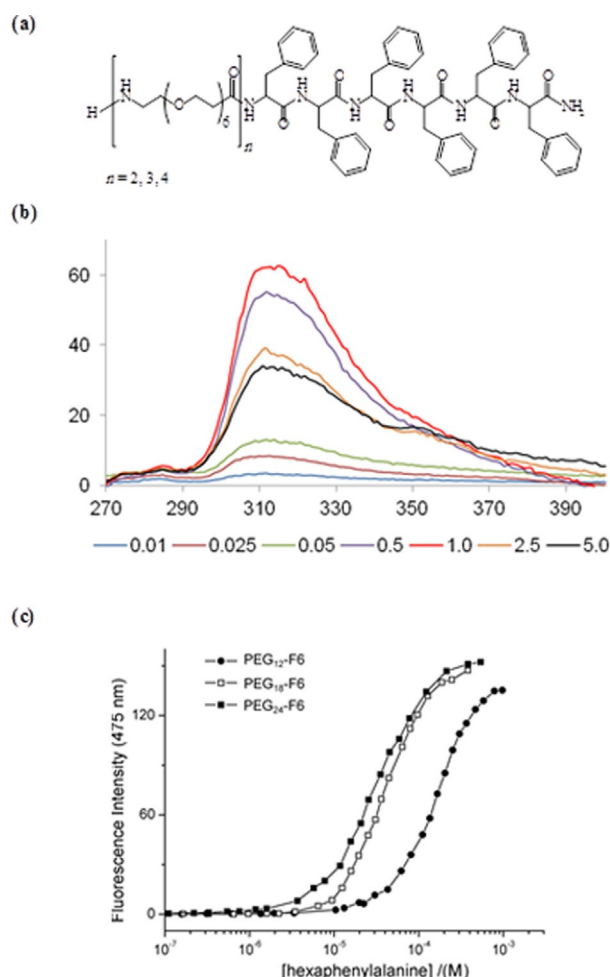


Figure 1. (a) Schematic representation of PEGylated hexaphenylalanine PEG₁₂-F6, PEG₁₈-F6, and PEG₂₄-F6. (b) Fluorescence emission spectra of PEG₂₄-F6 at several concentrations in the range 0.01–5.0 mg mL⁻¹. Samples were excited at 257 nm and the spectra recorded between 270 and 400 nm. Both PEG₁₂-F6 and PEG₁₈-F6 show the same behavior as PEG₂₄-F6 (data not shown). (c) Fluorescence intensity of the ANS fluorophore at 475 nm versus concentration of PEG₁₂-F6, PEG₁₈-F6, and PEG₂₄-F6. CAC values are established from the break points.

HPLC for the three polymer/peptide conjugates (see Table 1). Similarly to the previously studied PEG₈-F6 compound, which contains the same F6 aromatic framework, these peptides also show a high tendency to self-assemble. The first evidence for their aggregation phenomena comes from the inspection of the fluorescence spectra, presented in Figure 1b, for peptides at different concentrations (between 0.025 and 5.0 mg mL⁻¹). Samples were excited at 257 nm, which corresponds to the λ_{max} of the Phe residue, and the emission spectra were recorded between 270 and 400 nm. All the spectra show a weak emission peak at 282 nm, expected for the nude Phe chromo-

Table 1. Formulae, retention times (*R*_t), theoretical molecular weights (*M*_w) of PEGylated hexaphenylalanines, and critical aggregate concentrations (CACs) of the PEGylated derivatives.^[a]

Sample	Formula	<i>R</i> _t [min]	<i>M</i> _w [u.m.a.]	CAC [μM]	CAC [μg mL ⁻¹]
PEG ₁₂ -F6	C ₈₄ H ₁₁₅ N ₉ O ₂₀	12.5	1570	38.8	60.9
PEG ₁₈ -F6	C ₉₉ H ₁₄₄ N ₁₀ O ₂₇	11.9	1905	10.7	20.4
PEG ₂₄ -F6	C ₁₁₄ H ₁₇₃ N ₁₁ O ₃₄	11.2	2240	6.2	13.9

[a] The RP-HPLC method and column details are reported in the Experimental Section. The CAC values were determined by titration against the ANS fluorophore.

phore, and a well-observable peak centered at 312 nm, typically attributed to Phe excimers, induced by π-π interactions between the aromatic side-chain rings. Besides these two peaks, a third band centered around 350–360 nm appears at concentrations above 1.0 mg mL⁻¹. These peaks (312 and 350 nm) are indicative of a complex supramolecular organization of PEGylated hexaphenylalanines.

The aggregation properties of these PEGylated peptides were analytically characterized by a fluorescence-based method, which allows evaluation of the critical aggregate concentration (CAC). The fluorescent probe, 8-anilino-naphthalene-1-sulfonate ammonium salt (ANS), was titrated with increasing amounts of the peptides.^[39] No fluorescence emission is expected for the ANS fluorophore in water. However, ANS shows an emission peak at 460–480 nm when surrounded by a hydrophobic environment, such as in a micelle core.^[39] CAC values for the three peptide polymers were established from the graphical break points of the plots in Figure 1c. The CAC values, summarized in Table 1, are 60.9, 20.4, and 13.9 μg mL⁻¹ for the PEG₁₂, PEG₁₈, and PEG₂₄ oligopeptides, respectively. These values suggest a direct dependence of the PEG length on the aggregation tendency: Self-aggregation seems favored in polymers with the highest hydrophilicity (PEG₁₂ > PEG₁₈ > PEG₂₄). However, in traditional di- or tri-block copolymers, the CAC value depends on the hydrophobic/hydrophilic ratio, and the CAC is expected to be higher for monomers with shorter hydrophilic portions.^[40] The observed discrepancy led us to speculate that the self-assembling phenomena in these compounds could be due to more than one factor. In addition to aromatic stacking, we suggest the formation of additional intramolecular hydrogen bonds between the amide bonds in the PEG chain. These hydrogen bonds could encourage the

self-aggregation of the entire PEG-peptide conjugates. This hypothesis is also supported by comparison of the CAC value found for PEG₂₄-F6 with those of two other hexaphenylalanine PEGylated analogues: PEG₈-F6 and PEG_{MW1300}-F6 (see Figure S1a and the experimental details in the Supporting Information). The first, PEG₈-F6, previously characterized by us,^[34] contains four amide bonds in the PEG fraction, like PEG₂₄-F6, and exhibits a CAC value of about 10 μg mL⁻¹ (7.5 μM), slightly lower than that of PEG₂₄-F6. However, PEG_{MW1300}-F6, with a PEG chain similar to that in PEG₂₄-F6 but lacking the amide bonds, self-assembles above a CAC value of 40 μg mL⁻¹ (15.2 μM), which is roughly three-fold higher than the CAC value of the analogous peptide containing amide bonds in the PEG chain (see Figure S1b).

Dynamic light scattering (DLS)

The capability of the peptides to self-assemble above their CAC values was assessed by DLS. DLS studies, previously reported for PEGylated hexaphenylalanine PEG₈-F6, indicated the high kinetic stability of the self-assembled nanostructures and the low incidence of the concentration on their size. The same size stability over time was also observed for the series of PEG-peptides studied here (data not shown). The intensity profiles of the PEG₁₂, PEG₁₈, and PEG₂₄ oligopeptides in water solution, at 5.0 mg mL⁻¹, are presented in Figure 2. The intensity profile of PEG₁₂-F6 shows a monomodal distribution with a mean diameter of around 172 nm. In contrast, both the PEG₁₈ and PEG₂₄ derivatives show a bimodal distribution, which indicates the presence of two aggregate populations, the first centered at 185 nm and the second at 25 nm.

Secondary structure characterization

The secondary structures of the PEGylated oligopeptides in solution were fully investigated by circular dichroism (CD), FTIR, and UV/Vis spectroscopy. The first two techniques are typically

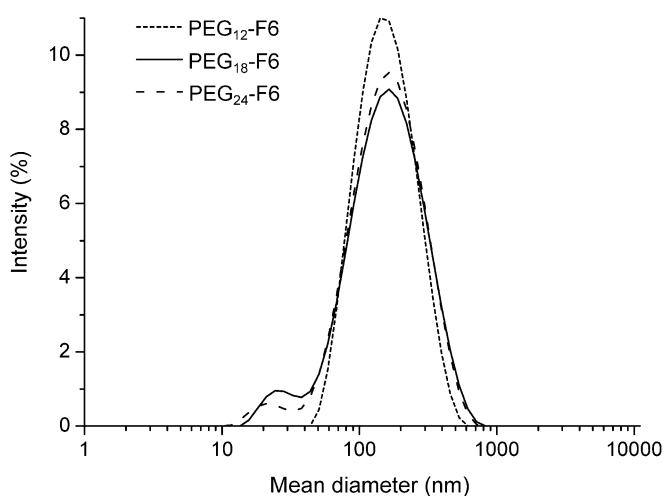


Figure 2. DLS intensity profiles of PEGylated hexaphenylalanine at 5.0 mg mL⁻¹ in water.

employed for revealing secondary structural features of peptide-based nanostructures.^[41] Figure 3a shows the CD spectra of the three PEGylated hexaphenylalanine conjugates at 5.0 mg mL⁻¹, well above their CAC values. All the spectra show a maximum centered between 205 and 207 nm, typical of the stacking of aromatic side-chains, and a minimum at 227 nm, associated with a β -sheet arrangement.^[42] This dichroic tendency is similar to that previously observed for the PEG₈-F6 analogue.^[34] However, a progressive reduction of the intensity of the two peaks can be detected upon increasing the PEG length. The reduction of both peaks confirms the capability of the PEG length to affect the self-aggregation propensity of the hexaphenylalanine and, in agreement with the fluorescence studies, the polymeric peptide containing the PEG₂₄ moiety presents a higher tendency to self-aggregate under the same conditions of concentration.

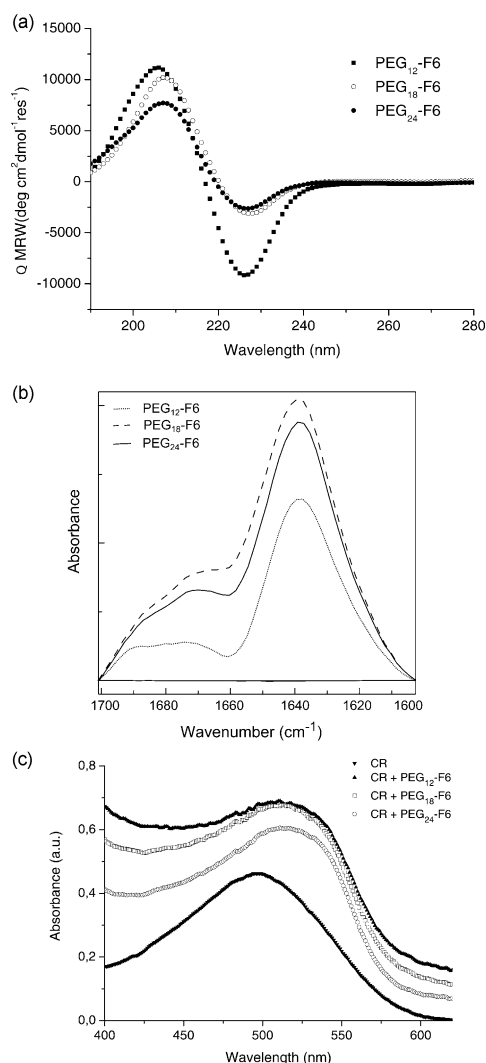


Figure 3. (a) CD spectra of PEG₁₂-F6, PEG₁₈-F6, and PEG₂₄-F6. All the samples are at 5.0 mg mL⁻¹ (concentration above the CAC). (b) FTIR spectra of the F6 polymer conjugates at 2.0 mg mL⁻¹ in the amide I region. (c) UV/Vis spectra of PEG₁₂-F6, PEG₁₈-F6, and PEG₂₄-F6 at 2.5 mg mL⁻¹ after incubation with Congo Red. The spectrum of Congo Red is also presented for comparison.

The occurrence of β -sheet formation was also confirmed by FTIR spectroscopy in the amide I spectral region (1600–1700 cm⁻¹). The deconvolution of the absorbance of the FTIR spectra in this region for secondary structure prediction is presented in Figure 3b (2.0 mg mL⁻¹ in water solution). All the hexaphenylalanine derivatives show a similar FTIR spectrum with two peaks at 1638 and 1680 cm⁻¹. This profile is typically observed for β -sheets with antiparallel orientation of the β -strands.^[43] Moreover, the NH stretching occurring at 3280 cm⁻¹ in the amide A region (see Figure S2 in the Supporting Information) indicates strong intermolecular amide–amide bonds. The absence of a band at around 3400 cm⁻¹ and the presence of a band at 1530 cm⁻¹ in the amide II region indicate that all the NH groups in PEG₂₄-F6 are involved in strong intermolecular hydrogen-bonding interactions in the fibrillary network. As previously observed for PEG₈-F6, the FTIR spectra of these peptides dissolved in 1,1,1,3,3,3-hexafluoroisopropanol (disaggregating conditions) do not show peaks in the amide I region (data not shown).

All these structural data support the hypothesis of a supramolecular organization in an amyloid-like fibrillary nanostructure. Confirmation of this structural organization was obtained through a Congo Red (CR) staining assay. CR, an azoic dye that exhibits a UV/Vis absorbance maximum at around 490 nm, undergoes a redshift of the maximum to 540 nm when interacting with amyloid like-fibrillary structures.^[44] As expected, the UV/Vis spectra show a bathochromic shift of the maximum when the azoic dye is incubated with the PEGylated-F6 peptides at 1.0 and 2.5 mg mL⁻¹ (Figure 3c and Figure S3 in the Supporting Information), which supports the hypothesis of amyloid-like organization.

Wide-angle X-ray scattering (WAXS)

A detailed characterization of the nanostructures in the solid state was performed by WAXS and grazing-incidence WAXS (GIWAXS) techniques in transmission and reflection modes, respectively. Figure 4b–d (left panel) display the two-dimensional (2D) WAXS patterns collected for the fibers with PEGs of different lengths (PEG₁₂, PEG₁₈, and PEG₂₄, respectively). The 2D WAXS pattern of the PEG₈ derivative, previously studied,^[34] is also presented for comparison (Figure 4a). The 2D patterns, once centered, calibrated, and radially folded into 1D profiles, are shown in Figure 4a–d (right panel). Figure 4e shows the same 1D patterns shifted vertically for the sake of comparison. It reveals that the diffraction patterns are almost identical, with two important peaks occurring at $q=0.518$ and 1.32 \AA^{-1} , which we have assigned to the equatorial β -sheet distance $d_e=12.2 \pm 0.3 \text{ \AA}$ and to the meridional β -strand distance of $d_m=4.8 \pm 0.3 \text{ \AA}$, respectively. The reflection corresponding to $d=4.8 \text{ \AA}$ could, in principle, be ascribed to PEG crystallization (4.7 \AA).^[45] However, the simultaneous presence of the equatorial reflection at $d=12.2 \text{ \AA}$ is symptomatic of cross- β amyloid structures. Overlaying the diffraction patterns so that their backgrounds coincide, as shown in Figure 4f, allows one to appreciate the difference in the intensities of the most significant reflection at $q=0.518 \text{ \AA}^{-1}$, which corresponds to the equatorial

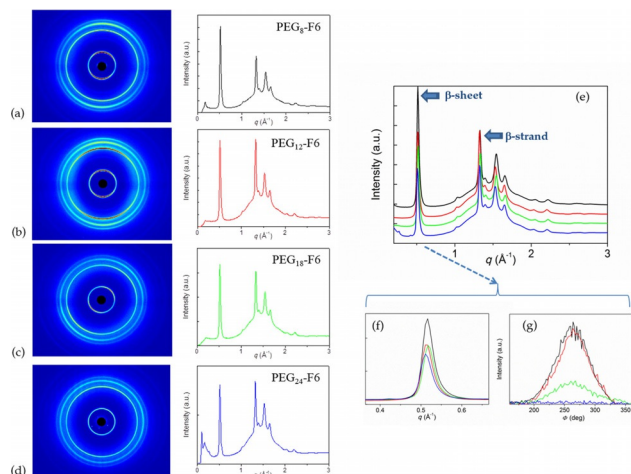


Figure 4. (a–d) 2D (left panel) and 1D (right panel) WAXS data. (e) 1D WAXS patterns vertically shifted for comparison. (f) Detail of the equatorial β -sheet distance at $q = 0.158 \text{ \AA}^{-1}$ ($d_e = 12.2 \pm 0.3 \text{ \AA}$). (g) Equatorial β -sheet reflection integrated along the azimuth Φ angle (i.e., across the diffraction circle).

β -sheet. Thus, it can be seen that the most intense peak is registered for PEG₈, almost equal intensities are found for PEG₁₂ and PEG₁₈, and the lowest intensity for the PEG₂₄ fiber. This difference in intensity can be attributed to the partial effect of PEG crystallization that occurs in proportion to the PEG length/molecular weight. Finally, for the same equatorial β -sheet reflection, we estimated the full-width-at-half-maximum (FWHM) along the azimuth Φ angle (i.e., along the diffraction circle): $\text{FWHM}(\text{PEG}_8) = \text{FWHM}(\text{PEG}_{12}) = 54 \pm 2^\circ$, $\text{FWHM}(\text{PEG}_{18}) = 62 \pm 2^\circ$, and $\text{FWHM}(\text{PEG}_{24}) > 180^\circ$ (see Figure 4g). These values reflect a clear increase in fiber disorder,^[15] which is a maximum for the PEG₂₄ sample, for which it is not possible to identify any preferred orientation direction of the fiber. We exclude that fiber disorder can be attributed to PEG crystallization. Indeed, polarized optical microscopy images of dried samples at high concentration (5 wt%) do not show the typical spherulite structures of PEG crystallization, but the formation of a liquid crystal phase through birefringence (data not shown). To analyze possible differences in the fiber structure due to different sample preparation or influences of the substrate, fibers were deposited on the top surface of silicon substrates and studied by GIWAXS. Figure 5a–d shows the GIWAXS 2D data for the PEG₈, PEG₁₂, PEG₁₈, and PEG₂₄ fibers, respectively (upper panels); the corresponding lower panels display the horizontal cut (green line) extracted from each set of 2D GIWAXS data along the green arrow, which are compared with the relevant meridional WAXS profiles (black line) previously shown in Figure 4. The comparison clearly shows that the same peaks at $q = 0.518 \text{ \AA}^{-1}$ (equatorial β -sheet distance $d_e = 12.2 \pm 0.3 \text{ \AA}$) and $q = 1.32 \text{ \AA}^{-1}$ (meridional β -strands of $d_m = 4.8 \pm 0.3 \text{ \AA}$) are measured for the fibers studied in both the transmission (WAXS, Figure 4) and reflection (GIWAXS, Figure 5) modes, which proves that the sample preparation does not modify the atomic arrangement of the fibers. The WAXS and GIWAXS characterizations of PEG_{MW1300}-F6 are presented in Figure 6. Figure 6a,b show the optical microscopy images of a single fiber of PEG_{MW1300}-F6 and

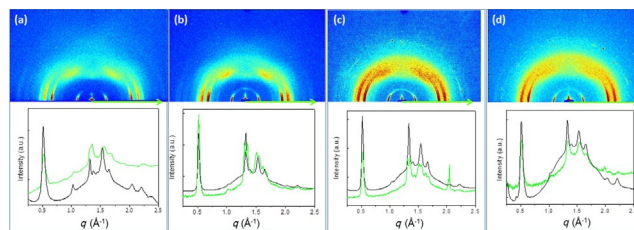


Figure 5. 2D GIWAXS (upper panels) and corresponding 1D GIWAXS data (lower panels, green curves) for (a) PEG₈, (b) PEG₁₂, (c) PEG₁₈, and (d) PEG₂₄ fibers deposited on silicon substrates. The black lines in the lower panels are the corresponding WAXS profiles collected for the same samples.

of the same material deposited on silicon substrate, respectively. The corresponding 2D WAXS and GIWAXS data are displayed in Figure 6c,d with the integrated 1D profiles shown in Figure 6e as green (GIWAXS cut of the 2D data, extracted along the green arrow) and black (WAXS) lines. Also, in this case, the most important reflections, which correspond to the equatorial β -sheet ($d_e = 12.2 \pm 0.3 \text{ \AA}$) and the meridional β -strand ($d_m = 4.8 \pm 0.3 \text{ \AA}$) distances, coincide in the WAXS and GIWAXS data. In analogy to the measurements taken on the PEG₈, PEG₁₂, PEG₁₈, and PEG₂₄ fibers (see Figure 4g), we also estimated for the PEG_{MW1300}-F6 sample the full-width-at-half-maximum (FWHM) along the azimuth Φ angle for the same equatorial β -sheet reflection (see comparison in Figure S4 in the Supporting Information, in which the added magenta profile corresponds to the PEG_{MW1300}-F6 sample). The FWHM(PEG_{MW1300}) value is same to that measured for PEG₁₈-F6, which confirms an effect of the amide bonds in the PEG chain also on fiber order.

Scanning electron microscopy (SEM)

The SEM images of PEGylated F6 peptides at 2.0 mg mL^{-1} , presented in Figure 7, confirm their aptitude to self-assemble in supramolecular NSs. The micrograph of PEG₁₂-F6 (Figure 7a) shows braid-like microstructures growing from thin scratches. PEG₁₈-F6 self-aggregates in a sheaf formed by small fibers of 60–500 nm placed side by side. Each fiber has a thickness of between 60 and 200 nm. In contrast, SEM images of PEG₂₄-F6 show nanostructures with lengths of 600–1000 μm and widths of around 20 μm with a twisted ribbon shape (Figure 7c,d).

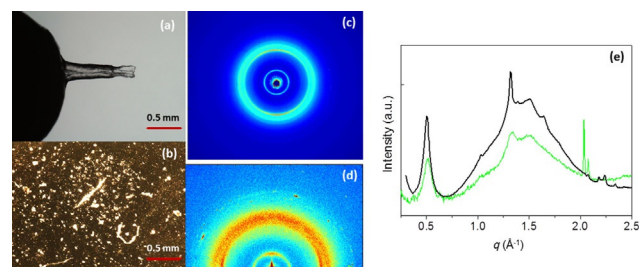


Figure 6. Optical microscopy images of (a) a single PEG_{MW1300}-F6 fiber and (b) fibers deposited on a silicon substrate. (c) 2D WAXS data for a single fiber and (d) 2D GIWAXS data for fibers on a silicon substrate. (e) Integrated 1D GIWAXS (green) and WAXS (black) profiles.

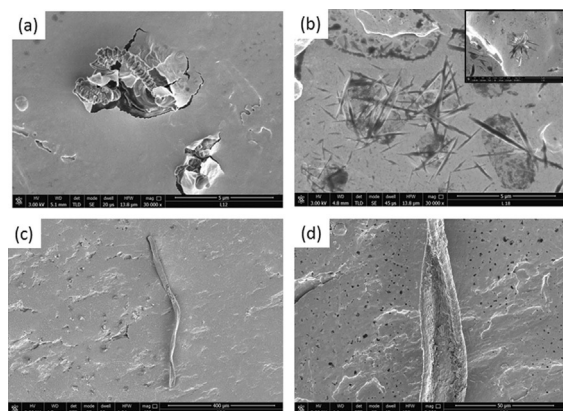


Figure 7. Selected SEM images of PEGylated oligomers: (a) PEG₁₂-F6 (30000 \times , 5 μ m scale bar), (b) PEG₁₈-F6 (30000 \times , 5 μ m scale bar), and (c,d) PEG₂₄-F6 (400 \times , 400 μ m and 3000 \times , 50 μ m scale bar, respectively). In the insert of panel (b) an additional view of PEG₁₈-F6 (30000 \times , 5 μ m scale bar) on an aluminum stub showing an intricate sheaf of fibers.

These kinds of structures are expected for amyloid peptides functionalized with short PEG chains.

In accord with the results of polarized optical microscopy, we do not observe in the SEM images the effect of crystallization typically displayed by PEGylated peptides. The absence of crystallization phenomenon in the SEM images further confirms that the continuous rings measured in the WAXS diffraction patterns are due to the low orientation of dried PEG₂₄-F6 fibers in space. A comparison of the SEM images of the three PEGylated derivatives shows that the PEG length affects the hierarchical organization of the peptide and the elongation of the nanostructure. The trend observed here is opposite to the conventional one shown by Hamley for PEGylated amyloid peptides.^[23a] However, the fibers observed for PEG₂₄-F6 are very similar to those previously observed for PEG₈-F6, in which the oxyethylene chain is shorter than in PEG₂₄-F6, but the number of the amide bonds in the PEG moiety is the same. This result suggests once more a strong relationship between the number of amide bonds and the structural aggregation of these peptides.

Photoluminescence in peptide nanofibers

The fluorescence behavior of the PEGylated peptides (PEG₁₂-F6, PEG₁₈-F6, and PEG₂₄-F6) was investigated both in solution (Figure 8) and in the solid state (Figure 9) and compared with the fluorescence of PEG₈-F6 nanostructures, empty or filled with the NBD dye.^[34,38] Several hypotheses have been proposed to explain the origin of the blue-green photoluminescence (PL) of peptide-based nanostructures containing only chromophore groups typical of peptides and proteins (i.e., amide bonds and aromatic rings).^[36a,46] One of the most accredited hypotheses reported in the literature for this unexpected fluorescence invokes electron delocalization through hydrogen bonds in the β -sheet-rich structure.^[37] Indeed, PEG₈-F6 NSs, rich in cross- β structures, exhibit blue PL both in aqueous solution (at a concentration of 10 mg mL⁻¹) and in the

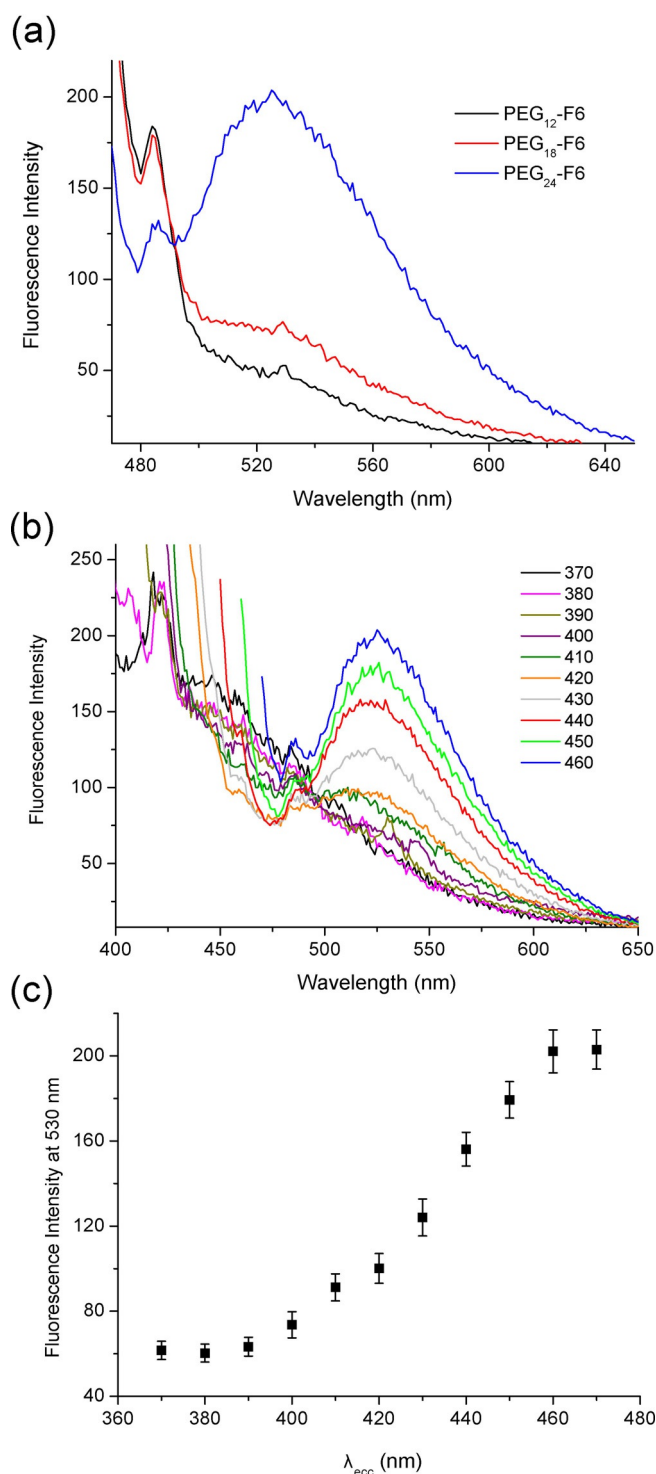


Figure 8. (a) PL emission spectra of the PEGylated-F6 nanostructures at 10 mg mL⁻¹ upon excitation at $\lambda_{exc} = 460$ nm. (b) Selected PL emission spectra of PEG₂₄-F6 excited at several wavelengths in the range 370–480 nm. (c) Plot of the fluorescence intensity of PEG₂₄-F6 at 530 nm as a function of the excitation wavelength.

solid state.^[34] The maximum fluorescence is observed at 460 nm when a sample is excited at 370 or 410 nm. These optoelectronic properties were also observed in NBD-encapsulating PEG₈-F6 NSs.^[38] However, in this latter case, we observed a redshift of the emission peak from 460 to 535 nm, which corre-

sponds to the characteristic emission wavelength of NBD. The redshift was attributed by us to a FRET phenomenon between the PL of the NS (donor) tightly associated with the NBD fluorophore (acceptor). Moreover, a significant increase in terms of relative signal was also observed. Similarly to PEG₈-F6 NSs, the PEG₁₂-F6, PEG₁₈-F6, and PEG₂₄-F6 derivatives, having a high content of β -sheet structures, also show optoelectronic properties in water when excited at 370 or 410 nm (see Figure S5 in the Supporting Information). However, in addition to the emission peak at 460 nm, a PL emission peak at 530 nm can also be observed upon excitation of the solutions at 460 nm (Figure 8a). This peak at 530 nm is most evident for PEG₂₄-F6, whereas it appears to be absent or very weak for PEG₁₂-F6 and PEG₁₈-F6 (Figure 8a). The green PL emission of the PEG₂₄ derivative is also easily distinguishable when the peptide solution is excited at different wavelengths (Figure 8b). The plot of fluorescence intensity at the maximum as a function of the excitation wavelength is presented in Figure 8c. This additional excitation/emission pair for PEG₂₄-F6 can be traced back to the formation of more stable electronic states resulting from the additional contribution of amide noncovalent interactions.

The fluorescence microscopy images of the air-dried samples deposited on clean coverslip glasses are presented in Figure 9 and Figure S6 in the Supporting Information. Owing to the wide spectral region over which the samples in solution can be observed, immunofluorescence images in the solid state were obtained by using as filters 4',6-diamidino-2-phenylindole (DAPI), Green Fluorescent Protein (GFP), and Rhodamine (Rho), which cover the entire range of excitation and emission wavelengths. The images of PEG₂₄-F6 (Figure 9) show the capability of this peptide nanostructure to emit in the blue, green, and red regions. On the other hand, the images of PEG₁₂ and PEG₁₈ show good emission only in the blue region (see Figure S6).

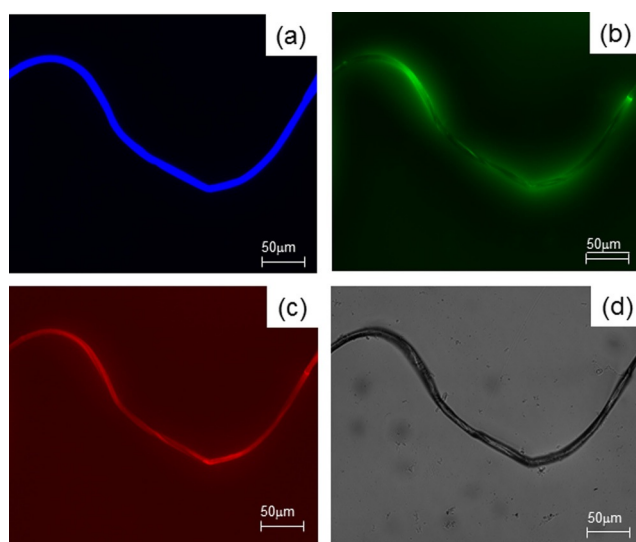


Figure 9. Fluorescence microscopy images of PEG₂₄-F6 at 10 mg mL⁻¹ deposited on clean coverslip glasses and slowly dried at room temperature. The PL images were obtained by exciting the air-dried sample in the spectral regions of (a) DAPI ($\lambda_{\text{exc}} = 359$ nm, $\lambda_{\text{em}} = 461$ nm), (b) GFP ($\lambda_{\text{exc}} = 488$ nm, $\lambda_{\text{em}} = 507$ nm), (c) Rho ($\lambda_{\text{exc}} = 555$ nm, $\lambda_{\text{em}} = 580$ nm), and (d) in brightfield. The scale bar is 50 μm for all images.

These results indicate the capability of these peptides to retain the same optoelectronic properties both in solution and in the solid state. Taking into account the different number of hydrogen-bonding donors/acceptors in PEG₂₄-F6 compared with other PEGylated analogues, we assumed that the distinct PL behavior of these compounds could be, at least in part, due to the different hydrogen-bonding potential of these compounds. This hypothesis has been supported by the investigation of the PL properties of PEG_{MW1300}-F6, which has a PEG moiety comparable in size to that of PEG₂₄-F6, although lacking the amide groups that could be potentially involved in hydrogen bonding. In line with our suggestion, PEG_{MW1300}-F6 does not show an emission peak at 530 nm under the same experimental conditions, although it retains the usual emissions when excited at 370 and 410 nm (see Figure S7 in the Supporting Information).

Conclusion

The PEGylation of natural or synthetic peptides permits hybrid materials to be obtained. The in vivo stability to protease degradation of PEGylated materials, like micelles and liposomes, makes them potentially suitable for biomedical applications. In this work we studied the effect of PEG derivatization, both length and composition of the PEG chain, on the hierarchical organization and optical properties of hexaphenylalanine (F6)-based nanostructures. PEG₁₂-F6, PEG₁₈-F6, and PEG₂₄-F6 peptides were synthesized by coupling sequentially two, three, or four units of amino-carboxy-PEG₆ blocks, each one containing six oxyethylene repetitions. On the other hand, PEG_{MW1300}-F6 was synthesized by coupling a single polydisperse PEG chain having the desired molecular weight to the peptide. The two synthetic approaches yield final peptide derivatives with different degrees of polydispersity and different numbers of amide bonds. Owing to their capability to stabilize new intermolecular hydrogen bonds, the amide bonds in the PEG chains affect the structural and functional properties of the peptides. We observed that independently of the PEG length and the number of amide bonds, all the peptide NSs display cross- β -like secondary structures with an antiparallel β -strand arrangement. However, a certain decrease in fiber order was observed along the series PEG₈ > PEG₁₂ > PEG₁₈ > PEG₂₄. All the peptide nanostructures exhibit blue PL emission at 460 nm upon excitation at 370 or 410 nm. In addition to this blue fluorescence emission, PEG₂₄-F6 also shows an additional green PL emission at 530 nm when excited at 460 nm. This different optoelectronic behavior can plausibly be attributed to the higher number of amide bonds in the PEG chain, which may either produce a more extended electron delocalization through hydrogen bonds or a fine re-adjustment of the cross- β structure of the peptide spine. As a result of the ample debate on the origins of PL phenomena,^[35–37] we do not completely exclude other factors that can affect the PL behavior. The interpretation of the PL properties of PEG₂₄-F6 could represent an interesting challenge for future studies. The possibility to modulate structural organization and to obtain new biocompatible and biodegradable materials, able to emit fluorescence at high wave-

length, opens new perspectives in the field of bioimaging, that is, the detection of the aggregation of endogenous proteins, which, in their physio-pathological form, are known to adopt cross- β structural motifs.

Experimental Section

Materials: Protected *N*^t-Fmoc-amino acid derivatives, coupling reagents, and Rink amide MBHA (4-methylbenzhydrylamine) resin were purchased from Calbiochem-Novabiochem (Laufelfingen, Switzerland). The Fmoc-21-amino-4,7,10,13,16,19-hexaoxaheneicosanoic acid (Fmoc-Ahoh-OH, PEG₆) was purchased from Neosystem (Strasbourg, France). All other chemicals were commercially available from Sigma-Aldrich (Milan, Italy), Fluka (Bucks, Switzerland), or LabScan (Stillorgan, Dublin, Ireland) and were used as received unless stated otherwise. All solutions were prepared by weight with doubly distilled water. Preparative RP-HPLC was carried out on an LC8 Shimadzu HPLC system (Shimadzu Corporation, Kyoto, Japan) equipped with a UV lambda-Max Model 481 detector using a Phenomenex (Torrance, CA) C18 column. Elution solvents were H₂O/0.1% TFA (A) and CH₃CN/0.1% TFA (B) from 5 to 70% over 30 min at a flow rate of 20 mL min⁻¹. The purity and identities of the products were assessed by analytical LC-MS analyses using a Finnigan Surveyor MSQ single quadrupole electrospray ionization spectrometer (Finnigan/Thermo Electron Corporation San Jose, CA) with a C18-Phenomenex column eluting with H₂O/0.1% TFA (A) and CH₃CN/0.1% TFA (B) from 5 to 70% over 15 min at a flow rate of 200 μ L min⁻¹.

Synthesis of peptide derivatives: PEGylated hexaphenylalanines were synthesized by using standard solid-phase fluoren-9-ylmethoxycarbonyl (Fmoc) procedures. The Rink amide MBHA resin (substitution 0.65 mmol g⁻¹, 0.2 mmol) was used as the solid-phase support to provide the peptides as C-terminus amides. The resin was swollen in DMF for 30 min. Fmoc removal was performed twice, treating the resin for 10 min with a mixture of DMF/piperidine (70:30, v/v). The coupling of the Fmoc-Phe-OH and of the Fmoc-Ahoh-OH was achieved by adding a two-fold molar excess of the amino acid, mixed with equimolar amounts of 1-hydroxybenzotriazole (HOBt), benzotriazol-1-yloxytripyrrolidinophosphonium (PyBop), and a four-fold molar excess of *N,N*-diisopropylethylamine (DIPEA) in DMF for 1 h. The peptides were fully deprotected from the resin by using TFA/H₂O (95:5, v/v) at room temperature for 3 h. The peptides were precipitated with ice-cold diethyl ether, dissolved in H₂O/CH₃CN, and freeze-dried. The crude products were purified by RP-HPLC. The mass spectra confirmed the identities of the products. The retention times (*R*_t) and molecular weights (*M*_w) of the peptide derivatives are reported in Table 1.

PEG₁₂-F6: ¹H NMR (CD₃OD; CH₃OH as internal standard, δ = 3.55 ppm): δ = 7.51–7.42 (m, 30H; CH aromatic), 4.86–4.75 (m, 6H; CH Phe α), 3.80 (s, 44H; OCH₂CH₂O), 3.75 (t, 4H; RNHCH₂CH₂O), 3.60 (t, 4H; RNHCH₂CH₂O), 3.16–2.90 (m, 12H; CH₂ Phe β), 2.58 ppm (t, 4H; NHCOCH₂CH₂O).

PEG₁₈-F6: ¹H NMR (CD₃OD; CH₃OH as internal standard, δ = 3.55 ppm): δ = 7.51–7.42 (m, 30H; CH aromatic), 4.86–4.75 (m, 6H; CH Phe α), 3.80 (s, 66H; OCH₂CH₂O), 3.75 (t, 6H; RNHCH₂CH₂O), 3.60 (t, 6H; RNHCH₂CH₂O), 3.16–2.90 (m, 12H; CH₂ Phe β), 2.58 ppm (t, 6H; NHCOCH₂CH₂O).

PEG₂₄-F6: ¹H NMR (CD₃OD; CH₃OH as internal standard, δ = 3.55 ppm): δ = 7.51–7.42 (m, 30H; CH aromatic), 4.86–4.75 (m, 6H; CH Phe α), 3.80 (s, 88H; OCH₂CH₂O), 3.75 (t, 8H; RNHCH₂CH₂O), 3.60 (t, 8H; RNHCH₂CH₂O), 3.16–2.90 (m, 12H; CH₂ Phe β), 2.58 ppm (t, 8H; NHCOCH₂CH₂O).

Preparation of peptide solutions: Peptide solutions were prepared by dissolving the lyophilized powder in double-distilled water sonicating the sample for 15 min. The peptide concentration was determined with a UV/Vis Thermo Fisher Scientific (Wilmington, Delaware USA) Nanodrop 2000c spectrophotometer equipped with a 1.0 cm quartz cuvette (Hellma) based on a molar absorptivity (ϵ_{257}) of 1170 M⁻¹ cm⁻¹.

Fluorescence studies: Critical aggregate concentrations (CACs) were determined by fluorescence measurements. Fluorescence spectra were recorded at room temperature on a Jasco Model FP-750 spectrofluorophotometer in a 1.0 cm path length quartz cell. Equal excitation and emission bandwidths (5 nm) were used throughout the experiments with a recording speed of 125 nm min⁻¹ and automatic selection of the time constant. The CAC values were measured by using 8-anilino-1-naphthalenesulfonic acid ammonium salt (ANS) as the fluorescent probe.^[33] Small aliquots of peptide derivatives in water solutions were added to aqueous solutions of ANS (20 μ M, 1.0 mL). The final spectra, to be used for calculations, were obtained after blank correction and adjustment for dilution. The fluorescence intensity of ANS was monitored as a function of peptide concentration. The CAC values were determined, upon excitation at 350 nm, by linear least-squares fitting of the fluorescence emission at 475 nm versus the poly-phenylalanine concentration, as the crossing point between the changes of slope.

DLS measurements: The hydrodynamic radii (*R*_H) and diffusion coefficients (*D*) of the hexaphenylalanine nanostructures were measured by DLS. The DLS measurements were carried out by using a Zetasizer Nano ZS instrument (Malvern Instruments, Westborough, MA) employing a 173° backscatter detector. Other instrumental settings were as follows: measurement position: 4.65 mm; attenuator: 8; temperature: 25 °C; cell: disposable sizing cuvette. DLS measurements in triplicate were carried out on aqueous samples at 2.0 mg mL⁻¹ after centrifugation at room temperature at 13000 rpm for 5 min.

Circular dichroism: Far-UV CD spectra of the peptides in aqueous solution were collected on a Jasco J-810 spectropolarimeter equipped with a NesLab RTE111 thermal controller unit using a 0.1 mm quartz cell at 25 °C. The spectra of samples at 5.0 mg mL⁻¹ were recorded in the range 280–195 nm. Other experimental settings were as follows: scan speed: 10 nm min⁻¹; sensitivity: 50 mdeg; time constant: 16 s; bandwidth: 1 nm. Each spectrum was obtained by averaging three scans and was corrected with the blank. Here, θ represents the mean residue ellipticity (MRE), that is, the ellipticity per mole of peptide divided by the number of amino acid residues in the peptide.

Fourier-transform infrared spectroscopy: The FTIR spectra of dried films (2.0 mg mL⁻¹) were recorded on a Jasco FT/IR 4100 spectrometer (Easton, MD) in attenuated total reflection (ATR) mode using a single crystal of germanium at a resolution of 4 cm⁻¹. To estimate the secondary structures, all the spectral data were processed by using built-in software. The spectra were collected in transmission mode and then converted into emission. Each sample was recorded with a total of 100 scans at a rate of 2 mm s⁻¹ against a KBr background.

Congo Red spectroscopic assay: The UV/Vis spectra of the Congo Red (CR) dye alone or incubated with oligo-phenylalanine derivatives were recorded on a Nanodrop 2000c spectrophotometer equipped with a 1.0 cm quartz cuvette (Hellma). A stock solution of CR (3.5 mg in 500 μ L) was freshly prepared in 10 mM phosphate buffer at pH 7.4 and filtered through a 0.2 μ m syringe. A small aliquot (5 μ L) of this solution was diluted with water to give a final concentration of 12.5 μ M and the UV/Vis spectrum was recorded

between 400 and 700 nm at room temperature. Aliquots of 5, 50, and 125 μL of PEG₁₂-F6, PEG₁₈-F6, or PEG₂₄-F6 (20 mg mL⁻¹) were added to the CR solution and the samples were incubated for 30 min at room temperature. The spectra were recorded and background-subtracted by using the Congo Red spectrum in phosphate buffer as the reference solution.

Wide-angle X-ray scattering: Fiber diffraction WAXS patterns were recorded from stalks by the stretch frame method.^[47] Briefly, a droplet (10 μL) of aqueous peptide solution (3 wt%) was suspended between the ends of a wax-coated capillary (spaced 2 mm apart) to collect wide-angle X-ray scattering data (WAXS) in transmission mode. The droplet was allowed to dry slowly at room temperature overnight to obtain oriented fibers. For WAXS in reflection mode (GIWAXS) some droplets of solutions were deposited on the top surface of silicon substrates and allowed to dry at room temperature. WAXS and GIWAXS data were collected at the X-ray Microimaging Laboratory (XMI-L@b) with a Fr-E+ SuperBright rotating anode copper anode microsource (Cu_{K α} , $\lambda = 0.15405$ nm, 2475 W), a multilayer focusing optics (Confocal Max-Flux; CMF 15-105), and a three-pinhole camera (Rigaku SMAX-3000).^[48] For data collection an image plate (IP) detector with 100 μm pixel size was placed at 10 cm (WAXS) and 8.7 cm (GIWAXS) from the sample and calibrated by using the silicon NIST standard reference material (SRM 640b). A 200 μm (diameter) X-ray beam was employed. GIWAXS patterns were collected at an incidence angle of 0.2°. A detailed description of the XMI-L@b performances can be found in reports of Altamura et al.^[48a] and Sibillano et al.^[48b]

Polarized optical microscopy: Dried films of PEGylated hexapeptidylalanines were obtained by placing the aqueous peptide solution (10 μL , 5 wt%) on a glass slide and leaving it to dry at room temperature. Then, the air-dried samples were observed between crossed polars by using a Nikon AZ100 microscope.

Scanning electron microscopy: Morphological analysis of the nanostructures was carried out by field-emission scanning electron microscopy (Nova NanoSem 450-FEI). Samples at 2.0 mg mL⁻¹, prepared as above described, were placed on an aluminium stub by using a graphite adhesive tape. A thin layer of gold and palladium was sputtered at a current of 20 mA for 90 s. The coated samples were then introduced into the specimen chamber and the images were acquired at an accelerating voltage of 2–5 kV, spot 3, by using an Everhart Thornley detector (ETD) and a through-lens detector (TLD).

Optical spectrofluorimetry: Photoluminescence (PL) measurements were performed by using a Jasco Model FP-750 spectrofluorophotometer in a 1.0 cm path length quartz cell. Aqueous PEGylated nanostructures (10 mg mL⁻¹) were prepared as described above, and the PL was measured on samples excited at various wavelengths in the range 370–480 nm.

Fluorescence microscopy: PEGylated oligopeptide solutions at 10 mg mL⁻¹ were deposited on clean coverslip glasses, dried, and imaged by fluorescence microscopy. Immunofluorescence images were collected with a Leica DFC320 video camera (Leica, Milan, Italy) connected to a Leica DMRB microscope equipped with 10 \times and 40 \times objectives and the Image J Software (National Institutes of Health, Bethesda, MD) was used for analysis.^[49]

Acknowledgements

This work was partially supported the Apulia Regional Government through the Project "TAPASS" (cod. PELM994—CUP B38C14002040008). We gratefully acknowledge the skillful

technical assistance of Roberto Lassandro from XMI-L@b and Leopoldo Zona and Giosuè Sorrentino from IBB-CNR.

Conflict of interest

The authors declare no conflict of interest.

Keywords: aggregation • luminescence • nanostructures • peptides • polymers • wide-angle X-ray scattering

- [1] E. De Santis, M. G. Ryadnov, *Chem. Soc. Rev.* **2015**, *44*, 8288.
- [2] S. Maity, S. Nir, T. Zada, M. Reches, *Chem. Commun.* **2014**, *50*, 11154.
- [3] R. Gharaei, G. Tronci, R. Davies, P. Goswami, S. J. Russell, *MRS Advances* **2016**, *1*, 711–716.
- [4] A. Raspa, G. A. A. Saracino, R. Pugliese, D. Silva, D. Cigognini, A. Vescovi, F. Gelain, *Adv. Funct. Mater.* **2014**, *24*, 6317–6328.
- [5] R. J. Williams, R. J. Mart, R. V. Ulijn, *Biopolymers* **2010**, *94*, 107–117.
- [6] E. M. Wolin, A. Manon, C. Chassaing, A. Lewis, L. Bertocchi, J. Richard, A. T. Phan, *J. Gastrointest. Cancer* **2016**, *47*, 366–374.
- [7] P. Kumaraswamy, R. Lakshmanan, S. Sethuraman, U. M. Krishnan, *Soft Matter* **2011**, *7*, 2744–2754.
- [8] J. Ryu, C. B. Park, *Adv. Mater.* **2008**, *20*, 3754–3758.
- [9] S. Nikitin, S. Kopyl, V. Shur Ya, Y. V. Kopelevich, A. L. Kholkin, *Phys. Lett. A* **2016**, *380*, 1658–1662.
- [10] U. Adhikari, S. Scheiner, *J. Phys. Chem. A* **2013**, *117*, 489–496.
- [11] J. B. Matson, R. H. Zha, S. I. Stupp, *Curr. Opin. Solid State Mater. Sci.* **2011**, *15*, 225–235.
- [12] C. P. Brown, C. Harnagea, H. S. Gill, A. J. Price, E. Traversa, S. Licoccia, F. Rosei, *ACS Nano* **2012**, *6*, 1961–1969.
- [13] K. Rapsch, F. F. Bier, M. von Nickisch-Rosenegk, *Mol. Pharm.* **2014**, *11*, 3492–3502.
- [14] E. Pazos, E. Sleep, C. M. Rubert Perez, S. S. Lee, F. Tantakitti, S. I. Stupp, *J. Am. Chem. Soc.* **2016**, *138*, 5507–5510.
- [15] C. Diaferia, F. A. Mercurio, C. Giannini, T. Sibillano, G. Morelli, M. Leone, A. Accardo, *Sci. Rep.* **2016**, *6*, 26638.
- [16] N. Gour, D. Kedracki, I. Safir, K. X. Ngo, C. Vebert-Nardin, *Chem. Commun.* **2012**, *48*, 5440–5442.
- [17] N. Tzokova, C. M. Fernyhough, M. F. Butler, S. P. Armes, A. J. Ryan, P. D. Topham, D. J. Adams, *Langmuir* **2009**, *25*, 11082–11089.
- [18] C. Diaferia, E. Gianolio, A. Accardo, G. Morelli, *J. Pept. Sci.* **2016**, *22*, 122–130.
- [19] M. S. K. Liberato, E. R. da Silva, D. R. de Araujo, S. Guha, W. A. Alves, *J. Mater. Chem. B* **2016**, *4*, 1405–1413.
- [20] L. Jia, C. Guo, J. Xiang, N. Wang, L. Yang, Y. Tang, H. Liu, *Langmuir* **2012**, *28*, 1725–1732.
- [21] B. A. Paik, M. A. Blanco, X. Jia, C. J. Roberts, K. L. Kiick, *Soft Matter* **2015**, *11*, 1839–1850.
- [22] H. Jatzkewitz, *Hoppe Seylers Z Physiol. Chem.* **1954**, *297*, 149–156.
- [23] a) I. W. Hamley, *Biomacromolecules* **2014**, *15*, 1543–1559; b) M. Mireia, J. Puiggali, *Polymer* **2013**, *5*, 188–224; c) T. J. Deming, *Adv. Polym. Sci.* **2006**, *202*, 1–18.
- [24] a) J. Nicolas, G. Mantovani, D. M. Haddleton, *Macromol. Rapid Commun.* **2007**, *28*, 1083–1111; b) H. M. König, A. F. Kilbinger, *Angew. Chem. Int. Ed.* **2007**, *46*, 8334–8340; *Angew. Chem.* **2007**, *119*, 8484–8490.
- [25] C. Diaferia, T. Sibillano, F. A. Mercurio, M. Leone, C. Giannini, N. Balasco, L. Vitagliano, G. Morelli, A. Accardo, *Sci. Rep.* **2017**, *7*, 307.
- [26] S. Tanaka, A. Ogura, T. Kaneko, Y. Murata, M. Akashi, *Macromolecules* **2004**, *37*, 1370–1377.
- [27] J. M. Smeenk, P. Schön, M. B. J. Otten, S. Speller, H. G. Stunnenberg, J. C. M. van Hest, *Macromolecules* **2006**, *39*, 2989–2997.
- [28] V. Castelletto, R. J. Gouveia, C. J. Connon, I. W. Hamley, *Eur. Polym. J.* **2013**, *49*, 2961–2967.
- [29] M. Tanaka, S. Abiko, T. Koga, N. Koshikawa, T. Kinoshita, *Polym. J.* **2009**, *41*, 153–156.
- [30] V. Castelletto, G. Cheng, S. Fuzeland, D. Atkins, I. W. Hamley, *Soft Matter* **2012**, *8*, 5434–5438.

- [31] T. S. Burkoth, T. L. S. Benzinger, V. Urban, D. G. Lynn, S. C. M. Meredith, P. Thiyagarajan, *J. Am. Chem. Soc.* **1999**, *121*, 7429–7430.
- [32] M. Reches, E. Gazit, *Science* **2003**, *300*, 625–627.
- [33] Z. Arnon, L. Adler-Abramovich, A. Levin, E. Gazit, *Isr. J. Chem.* **2015**, *55*, 756–762.
- [34] C. Diaferia, T. Sibillano, N. Balasco, C. Giannini, V. Roviello, L. Vitagliano, G. Morelli, A. Accardo, *Chem. Eur. J.* **2016**, *22*, 16586–16597.
- [35] a) N. Amdursky, M. Molotskii, D. Aronov, L. Adler-Abramovich, E. Gazit, G. Rosenman, *Nano Lett.* **2009**, *9*, 3111–3115; b) P. Hanczyc, M. Samoc, B. Norden, *Nat. Photonics* **2013**, *7*, 969–972.
- [36] a) D. Pinotsi, A. K. Buell, C. M. Dobson, G. S. Kaminski Schierle, C. F. Kaminski, *ChemBioChem* **2013**, *14*, 846–850; b) F. T. S. Chan, G. S. Kaminski Schierle, J. R. Kumita, C. W. Bertoncini, C. M. Dobson, C. F. Kaminski, *Analyt* **2013**, *138*, 2156–2162.
- [37] D. Pinotsi, L. Grisanti, P. Mahou, R. Gebauer, C. F. Kaminski, A. Hassanali, G. S. Kaminski Schierle, *J. Am. Chem. Soc.* **2016**, *138*, 3046–3057.
- [38] C. Diaferia, T. Sibillano, C. Giannini, V. Roviello, L. Vitagliano, G. Morelli, A. Accardo, *Chem. Eur. J.* **2017**, *23*, 8741.
- [39] A. Morisco, A. Accardo, E. Gianolio, D. Tesauro, E. Benedetti, G. Morelli, *J. Pept. Sci.* **2009**, *15*, 242–250.
- [40] a) L. Ren-Shen, H. Yi-Ting, *Polym. J.* **2010**, *42*, 304; b) C. Allen, D. May-singer, A. Eisenberg, *Colloids Surf. B* **1999**, *16*, 3.
- [41] V. Castelletto, I. W. Hamley, *Biophys. Chem.* **2009**, *141*, 169–174.
- [42] S. D. Moran, M. T. Zanni, *J. Phys. Chem. Lett.* **2014**, *5*, 1984–1993.
- [43] A. Handelman, N. Kuritz, A. Natan, G. Rosenman, *Langmuir* **2016**, *32*, 2847–2862.
- [44] W. E. Klunk, R. F. Jacob, R. P. Mason, *Anal. Biochem.* **1999**, *266*, 66–76.
- [45] Y. Takahashi, H. Tadokoro, *Macromolecules* **1973**, *6*, 672–665.
- [46] a) A. Handelman, A. Natan, G. Rosenman, *J. Pept. Sci.* **2014**, *20*, 487–493; b) L. L. del Mercato, P. P. Pompa, G. Maruccio, A. Della Torre, S. Sabella, A. M. Tamburro, R. Cingolani, R. Rinaldi, *Proc. Natl. Acad. Sci. USA* **2007**, *104*, 18019–18024.
- [47] M. Sunde, L. C. Serpell, M. Bartlam, P. E. Fraser, M. B. Pepys, C. C. Blake, *J. Mol. Biol.* **1997**, *273*, 729–739.
- [48] a) D. Altamura, R. Lassandro, F. A. Vittoria, L. De Caro, D. Siliqi, M. Ladisa, C. Giannini, *J. Appl. Crystallogr.* **2012**, *45*, 869–873; b) T. Sibillano, L. De Caro, D. Altamura, D. Siliqi, M. Ramella, F. Boccafoschi, G. Ciasca, G. Campi, L. Tirinato, E. Di Fabrizio, C. Giannini, *Sci. Rep.* **2014**, *4*, 6985.
- [49] V. Lemma, M. D'Agostino, M. G. Caporaso, M. Mallardo, G. Oliviero, M. Stornaiuolo, S. Bonatti, *Sci. Rep.* **2013**, *3*, 2659.

Manuscript received: July 3, 2017

Accepted manuscript online: August 7, 2017

Version of record online: September 12, 2017

Amyloid-like fibrillary morphology originated by tyrosine containing aromatic hexapeptides.

Carlo Diaferia,^[a] Nicole Balasco,^[b] Teresa Sibillano,^[c] Moumita Ghosh,^[d] Lihi Adler-Abramovich,^[d] Cinzia Giannini,^[c] Luigi Vitagliano,^[b] Giancarlo Morelli,^[a] and Antonella Accardo*^[a]

Abstract: Diphenylalanine based nanostructures have attracted great attention in the material science for their functional properties. These properties strongly depend from that hierarchic organization of the nanostructure that in turn can be fine tuned by punctual chemical modifications of the building blocks. Here we investigate how the partial or the complete replacement of the Phe residue with Tyr one (PEG₈-Y6 and PEG₈-(FY)3) in ancestor PEG₈-F6 can alter the structure of the nanomaterial. The effect of the PEG derivatization was also evaluated in peptides lacking of the PEG moiety (Y6 and (FY)3). Both PEG₈-Y6 and PEG₈-(FY)3 self-assemble in water at micromolar concentration in β -sheet rich nanostructures. Instead, WAXS diffraction patterns show significant structural differences between the samples. (FY)3 and Y6 show a 2D WAXS profile typically observed in cross- β amyloid like structures with a meridional and the equatorial reflections at 4.7 and 12.5 Å, respectively. The addition of the PEG moiety affects the diffraction pattern of PEG₈-Y6, there are circle typically observed in presence of PEG crystallization. MD simulations are in good agreement with experimental WAXS data. Gelation phenomenon was detected only for PEG₈-(FY)3 above a concentration of 1.0 wt% as confirmed by storage ($G' \sim 100$ Pa) and loss ($G'' \sim 28$ Pa) moduli in rheological studies. The cell viability on CHO cells of this soft hydrogel was certified to be 90% after 24 hours of incubation.

Introduction

In the last years, nanotechnology has imposed itself as revolutionary scientific area at the interface between different disciplines, which include chemistry, medicine, material science and biology. A large variety of nanoplatforms (NPs) with different morphology, shape, compatibility and functionality have been obtained by opportunely manipulating matter.^[1] The need to

obtain nanostructures (NSs) with well-defined characteristics of uniformity, purity, size, and chemical compositions brought to the development of many technologies and approaches for their manufacturing.^[2] One of the most common strategy takes advantage of self-assembling phenomena that rely on associations through non-covalent interactions between monomers.^[3] Intensive investigations, carried out over the last two decades, have highlighted an extraordinary propensity of proteins, peptides and even single amino acids to form assemblies with well-defined structural, chemical and physical properties.^[3-4] Protein and peptide self-association has a huge impact in different, apparently unrelated, scientific areas. Indeed, it is commonly believed that protein/peptide self-association generates the molecular species that are causative agents of neurodegenerative diseases.^[5] On the other hand, the ability of proteins, peptides and amino acids to form non-covalent, through highly stable, assemblies have been envisaged as an extremely powerful tool to generate innovative entities with widespread applications. Interestingly, being the process of protein/peptide aggregation common to all these studies, there has been a fruitful flow of information from one field to the other. The tendency of these compounds to undergo self-aggregation is obviously linked to the ability of main chain atoms to form hydrogen bonding interactions. A contribution to the formation of these assemblies can also be occasionally provided by electrostatic interactions established by terminal charged groups. In addition to that, it has been well established that also interactions involving side chains may be crucial for these associations. For example, it has been shown that glutamine (Gln) and asparagine (Asn) residues can stabilize amyloid-like aggregates as their side chains can form ladders of hydrogen bonds.^[6] Moreover, the suggestion that aromatic side chains could stabilize amyloid fibrils through the formation of π -interactions^[7] has led to the development of assemblies with mechanical, thermal and chemical properties that are not typically well-spotted in biological matter.^[8] Particularly impressive in this context is the case of the diphenylalanine homopeptide (FF) which is the most studied peptide able to self-assemble in well-organized amyloid-like materials.^[9] Indeed, depending on the experimental conditions,^[10] FF is able to self-organize in different kind of nano and micro morphologies (hollow nanotubes,^[9] fibers,^[11] vesicles,^[10c] metastable hydrogels^[12] or organogels^[13]) through the combination of π - π stacking and hydrogen-bonding interactions.^[14] Based on this evidence, FF became one of the prototypes of the amyloid-based materials and many structural analogues were synthesized and studied (for example FW^[15], FFF^[16], PEGylated FFFF,^[17] di-3,4-dihydroxyphenylalanine/DOPA-DOPA,^[18] Fmoc-FG,^[19] and Fmoc-FF^[20]). In this scenario, we recently reported on the synthesis and on the structural characterization of a novel PEGylated Phe-based compound, which is composed by six phenylalanine (F6) residues and eight PEG repetitive units (PEG₈) (PEG₈-F6).^[21]

- [a] Dr. C. Diaferia, Prof. G. Morelli, Dr. A. Accardo
Department of Pharmacy, Research Centre on Bioactive Peptides (CIRPeB), University of Naples "Federico II" and DFM Scarl, Via Mezzocannone 16, 80134 Naples (Italy)
E-mail: Antonella.accardo@unina.it
- [b] Dr. N. Balasco, Dr. L. Vitagliano
Institute of Biostructures and Bioimaging (IBB), CNR, Via Mezzocannone 16, 80134 Naples (Italy)
E-mail: luigi.vitagliano@cnr.it
- [c] Dr. T. Sibillano, Dr. C. Giannini
Institute of Crystallography (IC), CNR, Via Amendola 122, 70126 Bari (Italy)
E-mail: cinzia.giannini@ic.cnr.it
- [d] Dr. M. Ghosh, Dr. Lihi Adler-Abramovich
Department of Oral Biology, The Goldschleger School of Dental Medicine, Sackler Faculty of Medicine, Tel Aviv University, Tel Aviv 69978, Israel
Supporting information for this article is given via a link at the end of the document.

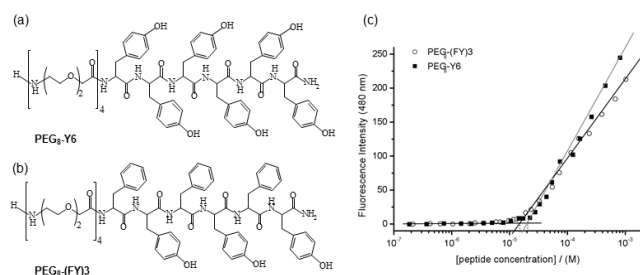


Figure 1: Schematic representation of PEGylated hexapeptides: PEG₈-Y6 (a) and PEG₈-(FY)3 (b). Fluorescence intensity emission of ANS fluorophore at 475 nm vs. concentration of PEG₈-Y6 and PEG₈-(FY)3 (c). CAC values are established from the break points.

This peptide-polymer conjugate is able to self-assemble in stable and well-organized nanostructures endowed with a cross- β structure. The supramolecular organization of PEG₈-F6 in β -rich materials confers them interesting optoelectronic properties.^[21] Based on these results and, considering that aromaticity is a key factor for ordered aggregation, we here investigated the properties of PEG₈-F6 analogues in which some or all of Phe residues were replaced with Tyr (Y). This residue was selected as, at its side chain, the aromaticity is coupled to a phenolic group that can be involved in H-bond formation as acceptor and donor. Here we report on the characterization of two analogues of the ancestor PEG₈-F6, named as PEG₈-Y6 and PEG₈-(FY)3, depicted in Figure 1.

In the former the peptide moiety is composed exclusively by Tyr whereas in the latter there is a Phe-Tyr alternation. In order to evaluate the effect of PEG on the structural properties of these hexapeptides, we also synthesized the corresponding peptides without the PEG moiety (named Y6 and (FY)3). All these hexapeptides were structurally characterized both in solution and at the solid state by fluorescence, Circular Dichroism (CD), Fourier Transform Infrared spectroscopy (FTIR), Transmission Electron Microscopy (TEM) and Wide Angle X-ray Scattering (WAXS). The physicochemical behavior of these peptides was also compared with the previously studied PEG₈-F6 homologous. Moreover, an atomic-level definition of the three-dimensional structure of the peptide spine of both PEG₈-(FY)3 and PEG₈-Y6 was achieved through extensive molecular dynamics (MD) simulations. Although, on the basis of the sequence, the properties of PEG₈-(FY)3 were expected to be intermediate between those exhibited by PEG₈-F6 and PEG₈-Y6, this analog showed a distinct behavior with a remarkable propensity to form a hydrogel. Rheological properties and *in vitro* cell toxicity of this hydrogel are here preliminary investigated.

Results

Design, synthesis and fluorescence studies

PEG₈-F6 peptide is a synthetic polymer-peptide able to self-assemble in fibrillar amyloid like networks.^[21] This structural

behavior was expected for phenylalanine (Phe) containing polypeptides.^[9] The impact of this key aromatic amino acid on the supramolecular structural organization was here evaluated by replacing it in PEG₈-F6 with tyrosine, another aromatic residue. Similar to its ancestor peptide PEG₈-F6, PEG₈-Y6 (Figure 1a) keeps the same molecular architecture composed of an aromatic framework of six amino acid residues and a polymer functionality. In order to evaluate the effect of a partial replacement of Phe with Tyr, we also synthesized PEG₈-(FY)3 (Figure 1b) in which the two aromatic residues are alternated in the sequence. PEG moiety in these peptides is expected to increase their water solubility. According to this finding, we observed a clear drop of the water solubility and self-assembling capability for PEG₈-F6 as a consequence of the PEG removal (data not shown). However, an additional role of PEG in alteration of the structural/functional properties of these systems cannot be excluded. Indeed, it is well-known from the literature that PEG moiety bound at N or C-terminus of short peptides can induce crystallization effects,^[22] particularly evident in dried samples.^[23] In order to assess the influence of PEG on the self-assembling process, we also synthesized Y6 and (FY)3, that are two analogues peptides without PEG functionalization. All the peptides were synthesized in good yields and high purity according to the standard protocols of the solid phase peptide synthesis (Fmoc/tBu). For PEGylated peptides, PEG moiety was inserted at the N-terminus of the peptide sequences through the sequential coupling of four monodisperse commercial oxyethylene linkers (Fmoc-AdOO-OH, PEG₂). Differently from PEG₈-F6, which requires a pre-dissolution in 1,1,1,3,3,3-hexafluoro-2-propanol (HFIP),^[21] PEG-tyrosinate analogues, having additional sites for hydrogen bonding and an increased side chain polarity, present good solubility in water and were directly dissolved in water at the final desired concentration. Fluorescence spectra of PEG₈-(FY)3 and of PEG₈-Y6 peptides (Figure S1 and S2) were recorded in water at several concentrations (0.05, 0.1, 0.25, 0.5, 1.0, 2.0, 4.0 and 10 mg/mL). Spectra of PEG₈-(FY)3 were recorded by exciting the peptide at both 257 and 276 nm, that correspond to the absorbance wavelengths for Phe and Tyr chromophores, respectively. On the other hand, PEG₈-Y6 samples were excited only at 276 nm. Independently from the λ_{ex} and from the concentration studied, all the spectra of PEG₈-(FY)3 show only the emission peak at 305 nm, typically observed for Tyr residue, whereas the peak at 282 nm, associated to the Phe emission, is absent. The absence of this peak can easily be explained as a consequence of a RET (resonance energy transfer) phenomenon occurring between Phe and Tyr residues. Beside the peak at 305 nm, two additional peaks at 360 and 376 nm appear for the sample at the highest studied concentration (10 mg/mL). The same peaks were also found in the fluorescence spectrum of PEG₈-Y6 at 10 mg/mL. The critical aggregate concentration (CAC) of PEGylated peptides was achieved by the well-known fluorescence-based method, in which the fluorescent probe, 8-anilinonaphthalene-1-sulfonate ammonium salt (ANS), is titrated with increasing amount of the peptide. ANS fluorophore shows a typical emission peak between 460-480 nm when surrounded by a hydrophobic environment,

such as in the micelle core or in the dry interface of peptide nanostructures. On the contrary, ANS fluorescence is completely silent when the fluorophore is immersed in water solution. CAC values were established from the graphical break point of the plots in Figure 1c. ANS dye shows a very similar behavior upon titration with PEG₈-(FY)3 and PEG₈-Y6 solutions and the CAC values are $1.5 \cdot 10^{-5}$ M (22.8 μ g/mL) and $2.0 \cdot 10^{-5}$ M (31.4 μ g/mL), respectively. These values are of the same order of magnitude and slightly higher than the CAC value previously found for the more hydrophobic hexaphenylalanine analog (7.5 μ M, 10 μ g/mL). This result was expected due to the higher hydrophobicity of the phenylalanine with respect to the tyrosine. Moreover, the partial or complete replacement of the phenylalanine residues with the tyrosine ones does not affect significantly the aggregation propensity of the peptide derivative.

Structural characterization in solution

The structural organization of PEGylated aromatic hexapeptides was investigated by Circular Dichroism (CD) and by Fourier Transform Infrared (FTIR), two spectroscopic techniques largely utilized for determining secondary structure in peptide-based nanostructures.^[21, 24] CD spectra of PEG₈-(FY)3 and PEG₈-Y6 in water at several concentrations (0.1, 1.0, 2.0 and 5.0 mg/mL) are reported in Figures 2a and 2b. All the spectra of PEG₈-(FY)3, in Figure 2a, show a very similar dichroic tendency with respect to PEG₈-F6 with two maxima at 226 and 202 nm, and a minimum around 235 nm. The two maxima (226 and 202 nm) can be associated with the $n \rightarrow \pi^*$ transition of the peptide bond and to the $\pi \rightarrow \pi^*$ transition of the peptide bond and/or phenyl moieties, respectively. In details, the peak at 202 nm is characteristic of peptides in which an aromatic side-chain stacking occurs, whereas the minimum at 235 nm is associated with a β -sheet secondary structure arrangement. The decreasing intensity of the peak at 202 nm, as function of concentration, is due to a gradual subtraction and consequent silencing of chromophores in the final spectrum. This evidence confirms a progressive self-aggregation of the peptide derivative driven by aromatic interactions. The other PEGylated peptide, PEG₈-Y6, shows a slightly different CD behavior compared to PEG₈-(FY)3. In the spectra of PEG₈-Y6 in Figure 2b, two maxima red shifted at 207 and 230 nm are well detectable. Beyond these two maxima, there is a pronounced minimum at 193 nm, whereas the minimum around 235-240 nm is absent. These spectral differences reflect fine dissimilarities in the secondary structure of the two compounds. The obtained aggregates were also structurally examined by FTIR spectroscopy in the spectral region of the stretching of amide I (1600-1700 cm^{-1}). FTIR spectra of PEG₈-(FY)3 and PEG₈-Y6 peptides in water solution at 5.0 mg/mL, reported in Figure 2c, show a similar profile with two peaks at 1638 and 1680 cm^{-1} . This profile, typically observed for β -sheets with an antiparallel orientation of the β -strands, was previously observed also for PEG₈-F6.^[21]

Structural characterization at the solid state

Self-assembled aromatic peptides and their PEGylated analogues were further characterized at the solid state by Transmission Electron Microscopy (TEM) and WAXS techniques.

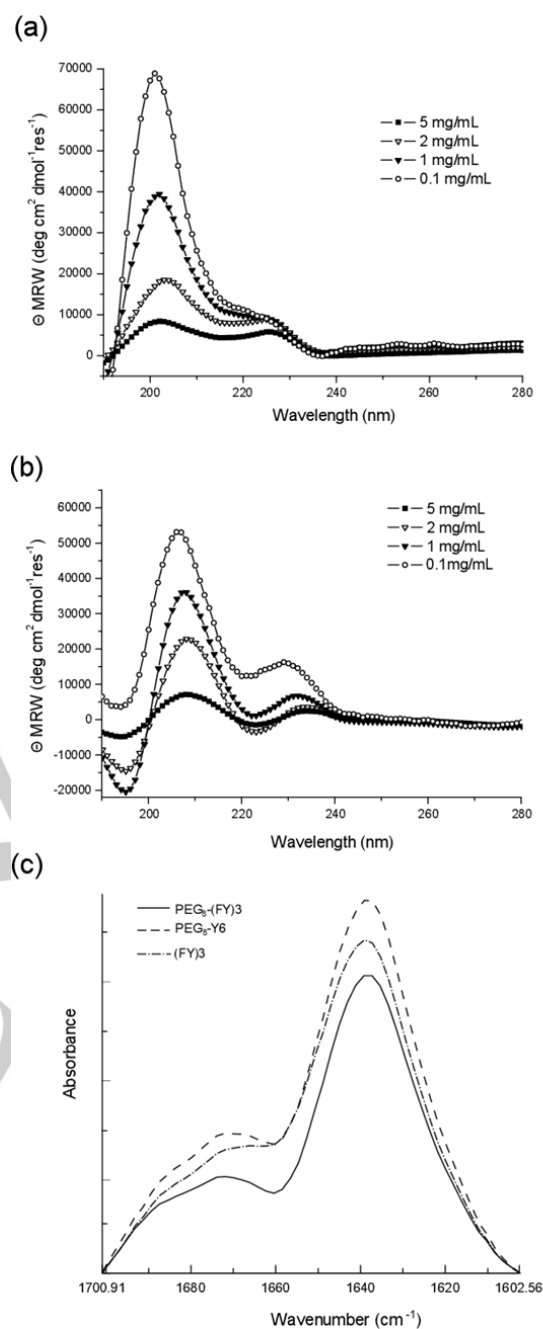


Figure 2: CD spectra of: (a) PEG₈-(FY)3 and (b) PEG₈-Y6 in water at several concentrations (0.1, 1.0, 2.0 and 5.0 mg/mL). (c) FTIR spectra of PEG₈-Y6 and PEG₈-(FY)3 in water at 5.0 mg/mL in the amide I region.

In Figure 3 TEM images of at 5.0 mg/mL are reported. Images of PEG₈-(FY)3 in Figure 3e and 3f show a continuous network of fibers interconnected by physical cross-link points. The analogue (FY)3, lacking of PEG decoration, showed a smaller amount of fibrils at the same concentration. This result can be related to a less fiber entangling that has as consequence the absence of gelation ability for (FY)3.

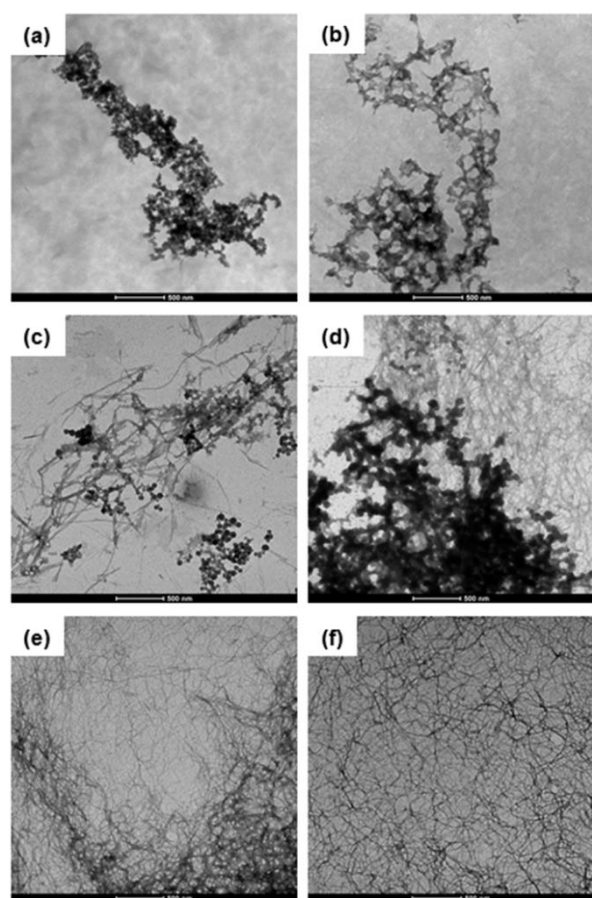


Figure 3: Selected TEM images for oligomers: (a) Y6, (b) PEG₈-Y6, (c,d) (FY)3, and (e,f) PEG₈-(FY)3.

WAXS measurements were collected on dried fibers obtained by the stretch frame method.^[25] Figure 4 shows the microscopic image of the fibers (upper row), the 2D WAXS data (middle row), and the 1D WAXS profiles (lower row). A comparative analysis of these experiments highlights analogies and differences.

Table 1: Meridional and equatorial peaks position in q (\AA^{-1}) and corresponding distance $d=2\pi/q$ (\AA).

	(FY)3		PEG ₈ -(FY)3		Y6		PEG ₈ -Y6	
	$q(\text{\AA}^{-1})$ ± 0.02	$d(\text{\AA})$ ± 0.5	$q(\text{\AA}^{-1})$ ± 0.02	$d(\text{\AA})$ ± 0.5	$q(\text{\AA}^{-1})$ ± 0.02	$d(\text{\AA})$ ± 0.5	$q(\text{\AA}^{-1})$ ± 0.02	$d(\text{\AA})$ ± 0.5
0	0.32	19.6	0.29	21.5				
1	0.49	12.8	0.52	12.0	0.51	12.3	0.53	11.9
2	1.12	5.6	1.12	5.6	1.05	6.0	1.05	6.0
3	1.33	4.7	1.33	4.7	1.29	4.9	1.29	4.9

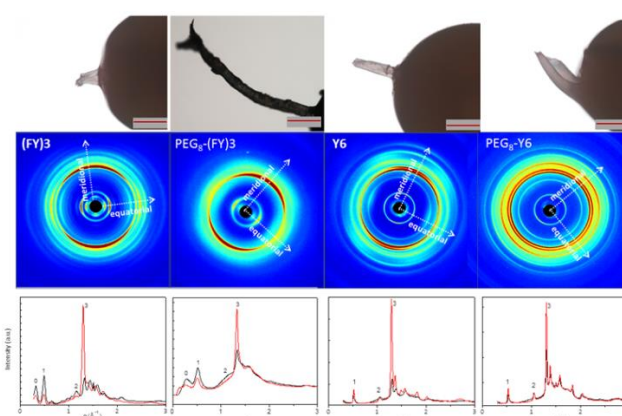


Figure 4: Microscopic image of the fibers (upper row), 2D WAXS data (middle row), 1D WAXS meridional/equatorial (red/black) profiles (lower row). The scale bar of the images is 0.5 mm.

In all cases, the WAXS data present the typical fiber diffraction pattern with two crossed main axes: the meridional along the fiber direction and the equatorial perpendicular to it (see white dotted arrows). The 2D data were integrated along these orthogonal axes and the corresponding 1D profiles, displayed in Figure 4 (lower row) as red (meridional) and black (equatorial) profiles, present almost the same reflections. The 0-3 labelled meridional and equatorial peaks were summarized in the Table 1, where the diffraction peak at $q=1.29-1.33 \text{ \AA}^{-1}$ ($d=4.7-4.9 \text{ \AA}$) corresponds to the distance between adjacent peptide backbones organized into β -strands along the fiber axis^[26] and the diffraction peak at $q=0.49-0.52 \text{ \AA}^{-1}$ ($d=11.9-12.8 \text{ \AA}$) corresponds to the distance between two distinct β -sheets.^[21]

It is, however, important to note that the addition of the PEG moiety has different consequences on (FY)3 and Y6 assembly. Indeed, while the (FY)3 fiber are marginally affected by the addition of the PEG, the 2D WAXS diffraction patterns of Y6 and PEG₈-Y6 show significant differences. In particular, the pattern exhibited by PEG₈-Y6 is characterized by the presence of additional circles which are likely produced by the crystallization of PEG.

Molecular modelling and dynamics

In order to gain atomic-level structural data on the peptide moiety of the assemblies formed by Y6 and (FY)3 we performed molecular modelling and molecular dynamics (MD) analyses. As detailed in the methods section, different models made of one, two, or three β -sheets, each composed of fifty β -strands, were generated taking the crystalline assembly of the hexapeptide KLVFFA fragment as reference.^[27] For the Y6 hexapeptide, models composed by either one or two sheets were considered (Y_ST50_SH1 and Y_ST50_SH2). For the (FY)3 system, which is endowed with a larger sequence complexity, we generated models made of either two or three β -sheets (FY_ST50_SH2 and

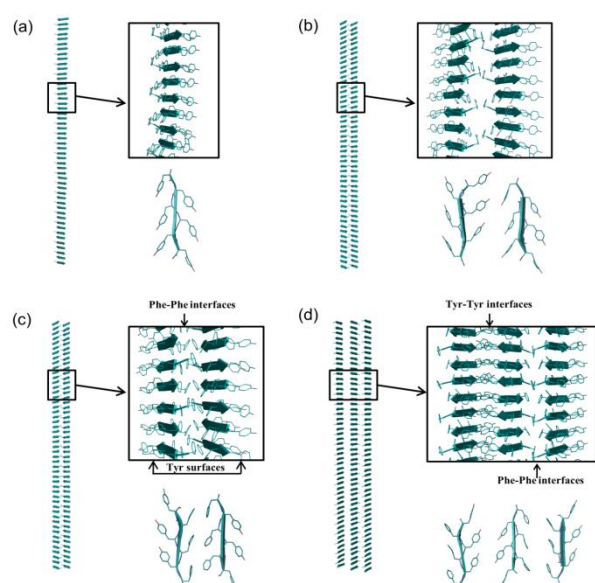


Figure 5: Three-dimensional representations of the starting flat models used in the Molecular Dynamics studies: Y_ST50_SH1 (a), Y_ST50_SH2 (b), FY_ST50_SH2 (c), and FY_ST50_SH3 (d).

FY_ST50_SH3). Representations of the starting models are shown in Figure 5. Timescales and parameters of the simulations are reported in Table S1. The RMSIP values reported in this table indicate that all simulations reached a satisfactory level of convergence.

Y6 system

To gain insights into the ability of a Tyr-rich peptide to adopt β -structures, initial MD investigations were performed considering a single sheet made of fifty β -strands (Y_ST50_SH1, Figure 5a). The evaluation of the geometrical parameters commonly used to assess the structural stability of trajectory structures (RMSD deviations from the starting structure and gyration radius) indicates that the system undergoes a major structural transition in the initial 50 ns of the simulation associated with the overall twisting (Figure S3). Although the secondary structure of the system is rather conserved (Figure S3c), significant fluctuations are evident also in the later stages of the trajectory (Figure S3a,b). These findings indicate that Y6 has a propensity to adopt β -structures, although the overall structure of the single sheet model is somewhat unstable. We, then, evaluated the possibility that Y6 could form assemblies through the tight lateral association of Tyr side chains. To this aim, we generated a double strand model denoted as Y_ST50_SH2 and shown in Figure 5b. The inspection of the trajectory frames of the resulting simulation clearly indicates that, after an initial structural transition (0-100 ns), the model reaches a rather stable structural state (Figure S4). The analysis of the individual trajectory structures demonstrates that the initial structural transition corresponds to the twisting of the originally flat model (Figure S4c and Figure 5b).

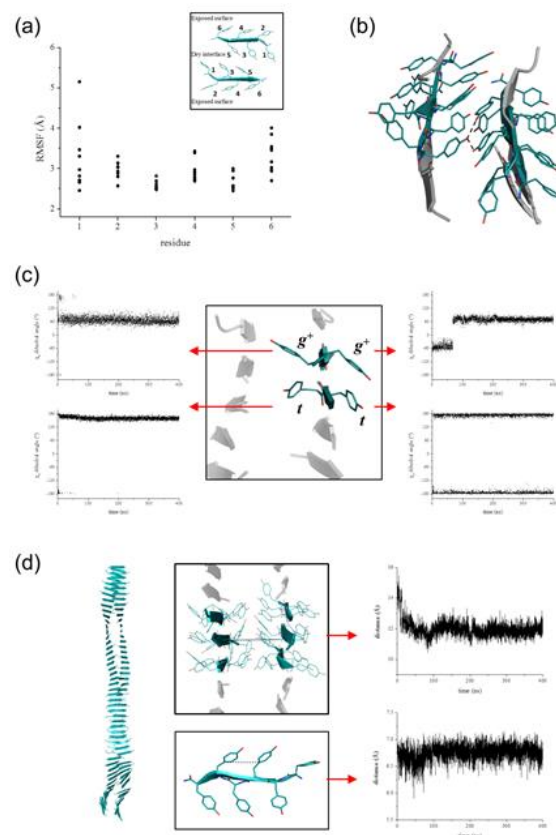


Figure 6: RMSF values of the Y_ST50_SH2 model computed in the equilibrated region of the trajectory (100-400 ns) are shown in panel (a). For clarity only the values of the central ten β -strands are reported. Representative examples of inter-sheet H-bonding interactions are reported in panel (b). Conformations of the Tyr side chains at the exposed and dry interfaces are shown in panel (c). Representative examples of the time evolution of the χ_1 dihedral angle are reported. The time evolution of the distance between two representative Ca atoms of the facing sheets along the trajectory and of the distance along the same polypeptide chain between Tyr residues which present the same orientation of the side chain is reported in panel (d).

The evaluation of the main chain and side chain flexibility of Y6 residues indicates that Tyr side chains located at the inter-sheet interface are endowed with a limited mobility (Figure 6a). It is also worth mentioning that also the flexibility of the solvent exposed residues is rather limited. To unravel the structural determinants that confer stability to this assembly, we evaluated the occurrence of preferred Tyr rotameric states and H-bonding interactions. Interestingly, the structure of the assembly is characterized by an alternation of Y6 peptides in which all Tyr side chains adopt trans states ($\approx 180^\circ$) for the χ_1 dihedral angle with peptides whose residues are in gauge (either $\approx -60^\circ$ or $\approx 60^\circ$) rotameric states (Figure 6c). This juxtaposition of the side chains combined with the antiparallel arrangement of the main chain leads to the formation of stacking interactions between Tyr residues of

consecutive strands (Figure 6b). These stacking intra-sheet interactions also occur for exposed Tyr residues, thus limiting their mobility and somewhat favoring their propensity to form larger Y6 aggregates. Networks of inter-sheet H-bonds contribute to the overall stability of the Tyr interface (Figure 6b). The analysis of other structural periodicities of Y_ST50_SH2 assembly indicates that the distance along the same polypeptide chain between Tyr residues which present the same orientation of the side chain is $\approx 6.5 - 7.0 \text{ \AA}$ (Figure 6d). The inter-sheet distance between facing Tyr residues is approximately 12.5 \AA (Figure 6d). Notably, these values are in close agreement with the equatorial reflections detected in the WAXS analyses (Table 1).

(FY)₃ system

A three-dimensional model for (FY)₃ was generated by using a step-wise procedure. As detailed in the methods section, taking into account the elevated hydrophobicity of Phe residues, we preliminarily generated a model composed of two sheets with facing Phe side chains at the dry interface and exposed Tyr side chains (FY_ST50_SH2) (Figure 5c). MD simulations carried out on this system clearly indicate that it reaches a stable state after an initial structural transition (0-250 ns) (Figure S5). As for Y6, this transition corresponds to the twisting of the model (Figure S5). The inspection of the trajectory structures indicates that, for the Phe moieties, this system recapitulates the structural features of the previously characterized F6 assembly^[21]. On the other hand, the exposed Tyr residues behave like the exposed residues of Y6 (data not shown).

The ability of the Phe residues of (FY)₃ to form a stable apolar interface and the capability of Tyr residues of Y6 to tightly associate led us to generate a three-sheet model characterized by two distinct interfaces: one apolar made of Phe residues and the other more polar made of Tyr residues (Figure 5d). MD simulations clearly indicate that this assembly is rather stable as demonstrated by the monitoring of several structural parameters (Figure S6). The analysis of both the apolar and polar interface clearly unravels the basis of their stability. In both of them the alternation of peptides with *trans* and *gauche+* rotameric states of the side chains leads to the formation of stabilizing stacking interactions (Figure 7b-c). At the Phe-interface additional interactions are established by the aromatic rings of facing residues. On the other hand, the Tyr-interface is stabilized by both intra-sheet and inter-sheet H-bonds (Figure 7b). As expected, the inter-sheet distances of both Phe- and Tyr-interface are approximately 12.5 \AA (Figure 7d). The combination of these two interfaces leads to a model characterized by a periodicity of 21 \AA (Figure 7d). These values are in close agreement with those experimentally derived by WAXS (Figure 4 and Table 1).

PEG₈-(FY)₃ gel: rheological characterization

From the qualitative point of view, PEG₈-(FY)₃ showed a certain tendency to gelificate in water above a concentration of 0.5wt %. Indeed in the inverted vial images, a progressive gain of viscosity can be observed by increasing the concentration and a stable self-supporting hydrogel is obtained when the peptide concentration is brought to 1.0wt % (Figure S7).^[28] The monitoring of the stability of the 1.0wt % gel over time indicated that at this

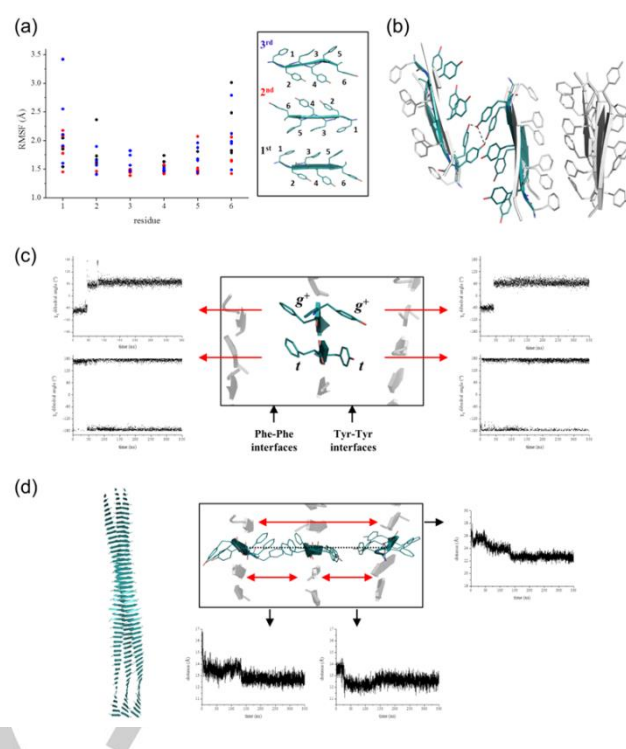


Figure 7: RMSF values of the FY_ST50_SH3 model computed in the equilibrated region of the trajectory (100-350 ns) are shown in panel (a). For clarity only the values of the central fifteen β -strands are reported. Representative examples of inter-sheet H-bonding interactions at the Tyr-Tyr interfaces are reported in panel (b). Conformations of the residue side chains are shown in panel (c). Representative examples of the time evolution of the χ_1 dihedral angle are reported. The time evolution of the distance between two representative Ca atoms of the external sheets along the trajectory is reported in panel (d).

concentration the gel maintains its ultrastructure up to 60 days (Figure 8a). Although, based on sequence considerations, PEG₈-(FY)₃ is expected to have intermediate properties between PEG₈-F6 and PEG₈-Y6, none of these two latter compounds form hydrogels under the same concentration and temperature used to prepare the PEG₈-(FY)₃ hydrogel. For the PEG₈-(FY)₃ system the PEG moiety is essential for gelification as the peptide (FY)₃ peptides, lacking the PEG portion, present a very limited water solubility, also after pre-dissolution in organic solvent, leading to the formation of solid precipitates.

In order to further examine the mechanical properties of the PEG₈-(FY)₃ hydrogel, rheological analysis was performed at 1.0wt % concentration. The results of the experiments are reported in terms of storage modulus (G') and of loss modulus (G''). The optimal measurement parameters were defined according to dynamic strain sweep (at a frequency of 1 Hz) and frequency sweep (at 0.1 % strain) oscillatory tests, both of them reported in Figure S8.^[29] A linear viscoelastic region (LVR) is present in the range 0.1-15 Hz in the frequency sweep diagram. The effect of the oscillatory strain was studied performing a 0.01-100% strain sweep and a breakage strain was detected at 16.6 %.

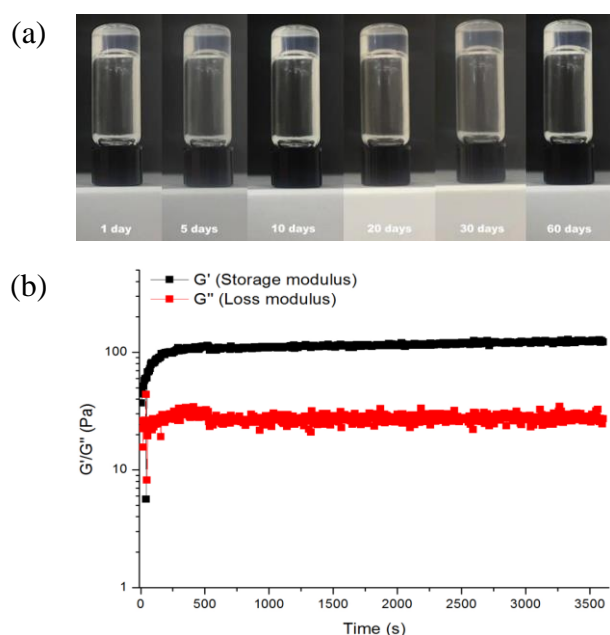


Figure 8: (a) Inverted tube test for PEG8-(FY)3 at 1.0wt % until two months. (b) Time sweep (1 hour experiment) for PEG8-(FY)3 gel at 1.0wt % concentration. Rheological results expressed in terms of storage (G') and loss modulus (G'').

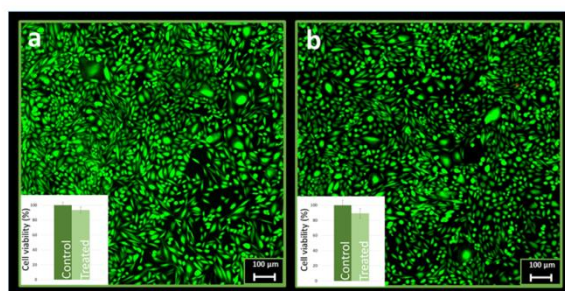


Figure 9: Representative merged image for live/dead assay after six (a) and twenty-four (b) hours incubation of CHO cells with extract media of PEG8-(FY)3 at 1.0wt %. The MTT viability test result are reported in the insert of the two panels.

According to these results, the time sweep measurement was performed with 1 Hz frequency and 0.1 % strain for a time period of 1 h. G' and G'' time sweep curves are presented in Figure 8b. The evidence that the value of storage modulus ($G' \sim 100$ Pa) is higher than that of the loss one ($G'' \sim 28$ Pa) confirms analytically the gel state of the system, excluding the possibility that the supramolecular material has a high viscose liquid behaviour.^[29] Furthermore, if compared with other organogelator system,^[30] this modulus values point out the weak nature of the self-supporting hydrogel.

***In vitro* biocompatibility profiles of PEG₈-(FY)3 gel**

Biocompatibility of the PEG₈-(FY)3 hydrogel at a concentration of 1.0 wt% was evaluated on Chinese Hamster Ovarian (CHO) cells

cultured in Dulbecco's Modified Eagle's medium (DMEM). The elution test, coupled with MTT viability assay, is an *in vitro* cytotoxicity study designed to detect the possible presence of toxic material eluted in the media from the gel sample. The DMEM media was incubated with the gel overnight. The extracted media was used to culture CHO cells and the viability was determined after six and twenty-four hours of incubation. The cell viability, estimated by MTT assay, was certified to be 93 % and 90% for six and twenty-four hours incubation times, respectively (Figure 9a and 9b, inserts).

Viability test on cells, treated with DMEM alone were also reported in graph for comparison. Simultaneously, after the treatment with the extracted media, cells were analysed for viability using live-dead staining with fluorescein diacetate (FDA), a cell membrane dye indicating live cells (green), and with propidium iodide (PI), a DNA stain indicating dead cells (red)^[31]. The degree of death was determined by fluorescence microscopy imaging. Fluorescence micrograph (merged in red and green field) for live/dead assay after six hours shows high confluent live cells with no red spots (Figure 9a). A very similar result was detected for the sample with longer incubation (Figure 9b). The high cytocompatibility detected *in vitro* can be probably attributed to the hydrogel preparation method that, contrarily to others peptide hydrogels, does not require the employment of any organic solvents (like DMSO, HFIP or MeOH).^[32]

Discussion

The high propensity of Phe-based oligopeptides to self-assemble has been investigated in many literature studies.^[9-13] Indeed, the discovery that the FF homodimer, a core motif in A β ₄₀ and A β ₄₂ peptides, is able to self-assemble in well-ordered nanostructures at high morphological variability^[9] has stimulated the use of FF and its variants as biocompatible building blocks for the development of novel nanostructures. In this scenario, it has been shown that the elongation of this aromatic framework from two to four or to six residues favors the progressive increase of β -structures in solutions.^[21] This structural behavior, at the atomic level, was obviously ascribed to the increase of π -stacking interactions between the aromatic rings of Phe side chains. Here we investigated the effect of the partial or the complete replacement of Phe residues in the previously characterized PEG₈-F6 self-assembling compound with the more hydrophilic Tyr one. The effect of the PEG chain on the aggregation properties was also investigated. The hydroxyl group in the tyrosine side chain should favor a major number of hydrogen bonding interactions with water molecules or main chain carbonyls with respect to the Phe residue. Indeed, Tyr is often positioned on the solvent-exposed surface of proteins. The structural characterization performed in solution highlights a similar behavior of the three PEGylated peptides (PEG₈-(FY)3, PEG₈-Y6, and PEG₈-F6) thus showing that, at micromolar concentration, these systems share a common mechanism of self-assembling characterized by the formation of nanostructures which are rich in antiparallel β -sheets. However, significant structural differences were observed for the samples at the solid

state. Both PEGylated peptides (PEG₈-(FY)3 and PEG₈-Y6) and their analogues lacking of the PEG chain ((FY)3 and Y6) show fibrillary nanostructures in TEM images. WAXS diffraction pattern recorded on the dried fibers of (FY)3 and Y6 show the typical meridional and equatorial reflections (4.7 and 12.5 Å, respectively) of cross-β amyloid like structures. MD simulations, which represent a powerful tool to obtain atomic level representation on self-assembling systems (see for example ref. [33]), confirmed the capability of Tyr-rich peptides to form cross-β structures characterized by stable anhydrous interfaces, in which the inter-sheet distances of both Phe- and Tyr-interface at ~12.5 Å are in good agreement with experimental WAXS data. These interfaces are stabilized by both stacking interactions and H-bonding pattern. (FY)3 is characterized by the combination of an apolar Phe-rich and a more polar Tyr-rich interface. 2D WAXS diffraction patterns highlight the effect of the PEG moiety on (FY)3 and Y6 assembly. It was extensively reported that the addition of long PEG moiety (3000-5000 Da) on short aromatic peptides causes crystallization effect in samples at the solid state. In our case very short PEG moiety (~600 Da) seems not affect the structural organization of (FY)3 nanostructure. On the contrary a clear difference can be evidenced between the diffraction patterns of Y6 and PEG₈-Y6 fibers. In the diffraction pattern of PEG₈-Y6 there are circles typically observed in presence of PEG crystallization effect. These most evident effect of the PEG on Y6 with respect to (FY)3 is likely due to the more limited hydrophobic interactions occurring in Y6. It is likely that the presence of a more polar interface that can be efficiently solvated somewhat limits the formation of large ordered fibers.

At macroscopic level, we observed that up to 1.0 wt% PEG₈-(FY)3 forms stable hydrogels in water, whereas solutions of PEG₈-Y6 and PEG₈-F6 appear not gelificated in the same experimental conditions. This finding is somewhat surprising since the sequence and the hydrophobicity of PEG₈-(FY)3 are intermediate between those exhibited by PEG₈-Y6 and PEG₈-F6. The inability of PEG₈-F6 to form gels is due to the elevated hydrophobicity of this system. On the other hand, the inability of PEG₈-Y6 to gelificate seems to be a direct consequence of the relative ratio between the two hydrophilic/hydrophobic blocks ($MW_{Tyr}/MW_{PEG} \sim 1.70$). It is worth mentioning that the different balance between the two blocks is an essential requirement for hydrogel formation. Indeed, Heise *et al.* [34] reported several PEGylated poly-tyrosines (for example PEG_{MW2000}-Y6) that undergoes thermosensitive hydrogelation in the concentration range 0.25-3.0 wt %. PEG_{MW2000}-Y6, in which the relative ratio between the hydrophilic/hydrophobic blocks (MW_{Tyr}/MW_{PEG}) is ~ 0.50 is able to gelificate, whereas an increase of MW_{Tyr}/MW_{PEG} ratio above 0.80 brought to the loss of gelification. In our case, PEG₈-Y6 has a relative ratio between the two blocks of ~ 1.70. Collectively, these findings indicates that the PEG adduct of (FY)3 presents an efficient compromise between hydrophobicity/hydrophilicity to achieve gelification. Rheological studies performed on PEG₈-(FY)3 gel at 1.0 wt% confirms analytically the gel state of the system. Furthermore, if compared with other hydrogelator systems, the modulus values point out the weak nature of the self-supporting hydrogel formed by PEG₈-(FY)3. The *in vitro* cell

viability assays shown that this soft hydrogels present a very low toxicity on CHO cells up to 24 hours.

Conclusions

Structural and functional properties of oligophenylalanine based nanostructures are strongly affected by punctual chemical modifications. The partial or complete replacement of the six Phe residues in PEG₈-F6 peptide-polymer with the more hydrophilic aromatic Tyr alters the supramolecular hierarchic organization of the nanostructure. PEG₈-(FY)3 forms stable soft hydrogels above 1.0 wt%. The hydrogel formation is attributable to the higher tendency of Tyr to establish extended hydrogen bonding networks. The good water solubility and the low toxicity of PEG₈-(FY)3 suggest that this polymer-peptide could be fruitfully exploited for generating self-supporting biocompatible hydrogels in future studies.

Experimental Section

Materials: Protected N^ε-Fmoc-amino acid derivatives, coupling reagents and Rink amide MBHA (4-methylbenzhydrylamine) resin were purchased from Calbiochem-Novabiochem (Laufelfingen, Switzerland). The Fmoc-8-amino-3,6-dioxaoctanoic acid, [Fmoc-AdOO-OH,PEG₂] was purchased from Neosystem (Strasbourg, France). All other chemicals were commercially available by Sigma-Aldrich (Milan, Italy) or Fluka (Bucks, Switzerland) or LabScan (Stillorgan, Dublin, Ireland) and were used as received unless otherwise stated. All solutions were prepared by weight with doubly distilled water. Preparative RP-HPLCs were carried out on a LC8 Shimadzu HPLC system (Shimadzu Corporation, Kyoto, Japan) equipped with a UV lambda-Max Model 481 detector using Phenomenex (Torrance, CA) C18 column. Elution solvents are H₂O/0.1% TFA (A) and CH₃CN/0.1% TFA (B), from 5% to 70% over 30 minutes at 20 mL/min flow rate. Purity and identity of the products were assessed by analytical LC-MS analyses by using Finnigan Surveyor MSQ single quadrupole electrospray ionization (Finnigan/Thermo Electron Corporation San Jose, CA), column: C18-Phenomenex eluted with an H₂O/0.1% TFA (A) and CH₃CN/0.1% TFA (B) from 5% to 70% over 15 minutes at 1 mL/min flow rate.

Peptide synthesis: Peptides Y6 and (FY)3 and their PEGylated analogues PEG₈-Y6, PEG₈-(FY)3 were synthesized according to the experimental protocol previously reported.^[21] Briefly, peptides were elongated on Rink amide MBHA resin (substitution 0.65 mmol/g, 0.2 mmol) by adding amino acids and PEG spacers twice in N, N-dimethylformamide for 30 min in presence of activating agents. Peptides were cleaved from the polymeric support treating the peptidyl resin with a solution of TFA (trifluoroacetic acid)/ TIS (triisopropylsilane)/ H₂O (92.5/5.0/2.5 v/v/v) at room temperature for 2 hours. Crude product were precipitated with ice-cold ethyl ether, dissolved in H₂O/CH₃CN and freeze-dried. Products were then purified by RP-HPLC chromatography and characterized by ESI mass spectra, analytical RP-HPLC and ¹H NMR.:

Y6 characterization: $t_R = 13.30$ min, MS (ESI+): m/z 966.1 calcd. for C₅₄H₅₇N₇O₁₂: [M+H⁺] = 967.1; ¹H-NMR (CD₃OD) (chemical shifts in δ, CH₃OH as internal standard 3.55) = 7.26-7.14 (m, 6 CH_δ aromatic Tyr), 6.88-6.85 (m, 6 CH_ε aromatic Tyr), 4.77-4.58 (m, 6H, CH_αTyr), 3.28-2.92 (m, 12H, CH₂βTyr).

PEG₈-Y6 characterization: $t_R = 11.56$ min, MS (ESI+): m/z 1576.7 calcd. for C₇₈H₁₀₁N₁₁O₂₄: [M+H⁺] = 1577.7; ¹H-NMR (CD₃OD) (chemical shifts in

δ , CH₃OH as internal standard 3.55) = 7.18-7.10 (m, 6 CH δ aromatic Tyr), 6.91-6.82 (m, 6 CH ϵ aromatic Tyr), 4.73-4.51 (m, 6H, CH α Tyr), 3.87 (s, 16H, OCH₂CH₂O), 3.82 (t, 8H, RNH-CH₂CH₂O), 3.74-3.71 (m, 8H, OCH₂COR), 3.63 (t, 8H, RNH-CH₂CH₂O), 3.31-2.92 (m, 12H, CH₂ β Tyr).

(FY)3 characterization: t_R = 14.52 min, MS (ESI+): m/z 948.1 calcd. for C₅₄H₅₇N₇O₉: [M+H]⁺ = 949.1; ¹H-NMR (CD₃OD) (chemical shifts in δ , CH₃OH as internal standard 3.55) = 7.48-7.35 (m, 15 CH aromatic Phe), 7.18-7.10 (m, 6 CH δ aromatic Tyr), 6.88-6.85 (m, 6 CH ϵ aromatic Tyr), 4.81-4.54 (m, 6H, CH α of Phe and Tyr), 3.35-2.94 (m, 12H, CH₂ β of Phe and Tyr).

PEG₈-(FY)3 characterization: t_R = 12.21 min, MS (ESI+): m/z 1528.7 calcd. for C₇₈H₁₀₁N₁₁O₂₁: [M+H]⁺ = 1526.7; ¹H-NMR (CD₃OD) (chemical shifts in δ , CH₃OH as internal standard 3.55) = 7.48-7.35 (m, 15 CH aromatic Phe), 7.18-7.10 (m, 6 CH δ aromatic Tyr), 6.88-6.85 (m, 6 CH ϵ aromatic Tyr), 4.81-4.54 (m, 6H, CH α of Phe and Tyr), 3.83 (s, 16H, OCH₂CH₂O), 3.80 (t, 8H, RNH-CH₂CH₂O), 3.75-3.72 (m, 8H, OCH₂COR), 3.63 (t, 8H, RNH-CH₂CH₂O), 3.35-2.94 (m, 12H, CH₂ β of Phe and Tyr).

Preparation of peptide solutions: PEG₈-Y6 and PEG₈-(FY)3 solutions were prepared dissolving the powders in water at the desired concentration. The concentration of the solutions was spectroscopically determined by absorbance on UV-vis Thermo Fisher Scientific Inc (Wilmington, Delaware USA) Nanodrop 2000c spectrophotometer equipped with a 1.0 cm quartz cuvette (Hellma) using a molar absorptivity (ϵ) of 1170, 7290 and 4230 M⁻¹ cm⁻¹ for F6, Y6 and (FY)3, respectively.

Fluorescence studies: Critical aggregate concentration (CAC) values for peptides were measured by fluorescence spectroscopy, using 8-anilino-1-naphthalene sulfonic acid ammonium salt (ANS) as fluorescent probe. All the spectra were recorded at room temperature with a spectrofluorophotometer Jasco (Model FP-750) and the sample was allocated in a quartz cell with 1.0 cm path length. The others setting are: excitation and emission bandwidths = 5 nm; recording speed = 125 nm/min and automatic selection of the time constant. The experiment was carried out by adding small aliquots of peptide derivatives in 1 mL of 20 μ M ANS water solution. Spectra were corrected for the blank and adjusted for dilution. Fluorescence emission of PEG₈-Y6 and PEG₈-(FY)3 was studied for peptide water solutions at several concentrations (0.05, 0.1, 0.25, 0.5, 1.0, 2.0, 4.0 and 10 mg/mL). Spectra of PEG₈-Y6 were obtained by exciting sample at λ_{ex} = 276 nm, whereas spectra of PEG₈-(FY)3 were obtained by exciting sample both at λ_{ex} = 257 and 276 nm.

Circular Dichroism: Far-UV CD spectra of the peptides in water were collected with a Jasco J-810 spectropolarimeter equipped with a NesLab RTE111 thermal controller unit using a 0.1 mm quartz cell at 25 °C. The spectra of samples at several concentrations are recorded from 280 to 195 nm. Other experimental settings were: scan speed = 10 nm/min, sensitivity = 50 mdeg, time constant = 16 s, bandwidth = 1 nm. Each spectrum was obtained by averaging three scans and corrected for the blank. Here □□ represents the mean residue ellipticity (MRE), i.e. the ellipticity per mole of peptide divided by the number of amino acid residues in the peptide.

Fourier Transform Infrared spectroscopy (FTIR): Fourier Transform Infrared spectra of PEGylated peptides in solution at the concentration of 5.0 mg/mL and at the solid state were collected on a Jasco FT/IR 4100 spectrometer (Easton, MD) in an attenuated total reflection (ATR) mode and using a Ge single-crystal at a resolution of 4 cm⁻¹. Each sample was recorded with a total of 100 scans with a rate of 2 mm·s⁻¹ against a KBr background. After collection in transmission mode, spectra were converted in emission.

Transmission Electron Microscopy (TEM) images: TEM images were acquired with FEI TECNAI G12 Spirit-Twin microscope (LaB6 source) equipped with a bottom mounted FEI Eagle-4k CCD camera (Eindhoven, The Netherlands), operating with an acceleration voltage of 120 kV. (LaMest Pozzuoli, Italy). The samples for the observation were prepared by placing a droplet of the solution (5.0 mg/mL) onto a 400 mesh holey-carbon coated copper grid. The sample was air-dried for 1 hour and then negatively stained with phosphotungstic acid in water solution (1.0 wt %). Digital images were obtained by Tomography holder with FEI Eagle 4K CCD camera and Xplore3D software.

Wide-Angle X-ray Scattering (WAXS): Fiber diffraction WAXS patterns were recorded from stalks by the stretch frame method.^[25] Briefly, a droplet (10 μ L) of peptide (2.0 wt %) was suspended between the ends of a wax-coated capillary (spaced 2 mm apart), and was left to air dry. Fibers of PEGylated and not PEGylated peptides were prepared by starting from peptide solution in water and in MeOH, respectively. WAXS data were collected at the X-ray Microimaging Laboratory (XMI-L@b) equipped with a Fr-E+ SuperBright rotating anode table-top microsource (Cu K α , λ = 0.15405 nm, 2475W), a multilayer focusing optics (Confocal Max-Flux; CMF 15-105) and a three-pinhole camera (Rigaku SMAX-3000). An image plate (IP) detector with 100 μ m pixel size was placed at 10 cm from the sample to acquire WAXS data. Once acquired, 2D data were calibrated^[35] by means of the Si NIST standard reference material (SRM 640b) and folded into 1D profiles. A detailed description of the XMI-L@b performances can be found in Altamura *et al.*^[36] and Sibillano *et al.*^[37]

Rheological characterization: Gels of PEG₈-(FY)3 1.0 wt % were prepared by suspending the peptide powder in water at above described. A bath sonication was required for obtain homogeneous self-supporting gels. Inverted and sloping tube tests were performed with a sample volume of 500 μ L. Rheological measurements for 1.0 wt % PEG₈-(FY)3 self-supporting gels were performed on an AR-G2 controlled-stress rheometer (TA Instruments, USA). A parallel plate geometry was used. Oscillatory frequency (0.01-100 Hz) and strain sweep (0.01-100%) at 4 °C were conducted with the aim to determine the linear viscoelastic region. Time-sweep oscillatory test was performed for one hour on 300 μ L of fresh gelat temperature of 4 °C with 0.1 % strain and 1 Hz frequency. All the rheological data were reported in Pascal (Pa) as G' and G'', the storage and loss moduli, respectively.

Biocompatibility profile of PEG₈-(FY)3 gels: *In vitro* biocompatibility profile of PEG₈-(FY)3 gels was studied performing elution test and live/dead assay. The cell line was Chinese Hamster Ovarian (CHO) cells, purchased from ATCC. CHO cell line was cultured in Dulbecco's Modified Eagle's medium (DMEM) supplemented with 100 U mL⁻¹ penicillin, 100 U mL⁻¹ streptomycin, 10% fetal calf serum, and 2 mmol L⁻¹ of L-glutamine (all these materials are available at Biological Industries, Israel). The cells were stored in a wall-plate in a 5% CO₂ humidified atmosphere at the temperature of 37 °C. For elution test, 200 μ L of PEG₈-(FY)3 gel at 1.0 wt % were prepared in sterile condition (with UV-sterilization) and incubated overnight with 1 mL of DMEM (ratio gel-extracting media 1/5 v/v). No color change was detected for the media after the incubation and the tested pH value (7.5-7.8) was suitable for culturing. The efficient gel extraction and permeability was confirmed by its pink coloration. The extracted media was used to grow the cells for 6 hours and, after this time incubation, the viability was determined by MTT test. 20 μ L of a MTT solution (5 mg/mL) in phosphate buffer saline (PBS) was added to each well. After 4 hour incubation, 100 μ L of DMSO was added to extract the MTT reduced adduct (Formazan). All the samples were shaken for 20 minute to allow a complete dissolution of the precipitated Formazan in DMSO. Absorbance was measured using Tecan Spark plate reader at 570 nm. Background was measure at 680 nm. The viability was expressed as percentage. The live/dead assay was performed using a kit (Sigma Aldrich) containing FDA

(6.6 µg/mL) and PI (5 µg/mL). After the addition of the two fluorescent dyes, cells were incubated for ~10 minutes in the same previously reported condition. Labeled cells were immediately viewed using a Nikon Eclipse Tifluorescent microscope and images (reported as merged figure) were captured by a ZylascMOS camera using Nikon Intensilight C-HGFI fluorescent lamp.

Molecular modelling and dynamics

Systems and notations: Three-dimensional model for Y6 and (FY)₃ aggregates were generated following the procedure reported in Diaferia *et al.*^[21] In particular, monomers for the two peptides were generated using the structure of the hexapeptide fragment KLVFFA of the amyloid-beta peptide II (Protein Data Bank entry 3OW9)^[27] by replacing the non-Phe/non-Tyr residues of the model with Phe or Tyr. A single sheet model of Y6 was generated starting from the hexapeptide fragment KLVFFA by replacing all side chains with Tyr residues. Starting from these structures, models composed of a single β-sheet made of fifty strands were generated (Y_ST50_SH1 and FY_ST50_SH1). For both systems steric zipper models were generated through the association of a pair of these sheets using the organization of the KLVFFA in the crystalline state^[27] (Y_ST50_SH2 and FY_ST50_SH2) (Figures 5b-c). Taking into account the hydrophobicity/hydrophilicity of Tyr and Phe, the two-sheet model of (FY)₃ was built by locating the Phe side chain at the dry interface. Consequently Tyr residues were solvent exposed. For (FY)₃ a more complex system was generated through the association of a further β-sheet to FY_ST50_SH2. This assembly (FY_ST50_SH3) contains two distinct steric zipper interfaces: a hydrophobic one composed by Phe side chains and a more hydrophilic one made of Tyr residues (Figure 5d).

Molecular dynamics protocol: Molecular Dynamics (MD) simulations were performed on the generated models (Y_ST50_SH1, Y_ST50_SH2, FY_ST50_SH2, and FY_ST50_SH3) using the GROMACS software package 5.1.2^[38] with Amber03 as force field. The models were immersed in triclinic boxes filled with water molecules (TIP4PEW water model). Timescales and several parameters of the simulations (box dimensions, number of water molecules) are reported in Table S1. The simulations were run applying periodic boundary conditions. The systems were equilibrated at the temperature of 300 K and the pressure of 1 atm. We first minimized energies by fixing the protein atoms and subsequently without any restraint. The Particle Mesh Ewald (PME) method^[39] using a grid spacing of 0.12 nm was used to calculate the electrostatic interactions. For Lennard-Jones interactions a cutoff of 10 Å was applied. Bond lengths were constrained using the LINCS algorithm.^[40] The analysis of trajectory structures was performed by using the VMD program^[41] and Gromacs routines.^[38] The achievement of an adequate convergence in the MD simulation was checked by calculating the root mean square inner product (RMSIP)^[42] between the two halves of the equilibrated trajectories (Table S1).

Acknowledgements

CINECA Supercomputing (framework ISCRA@CINECA - project code HP10CUX1WZ) is acknowledged for computational support.

Author information

Corresponding Author

*E-mail: antonella.accardo@unina.it.

Tel: +0039-0812532045

C. Diaferia and N. Balasco contributed equally

Keywords: self-assembling peptides • soft hydrogels • nanostructures • WAXS • MD simulation • Amyloid-like fibers.

- [1] a) M. A. Farrukh, *InTech-Open Access Publisher* **2016**; b) J. Ramsdem, *2nd ed. Andrew W., Eds.; Elsevier: San Diego, CA* **2016**; c) T. H. LaBean, *Nature* **2009**, *459*, 331-332.
- [2] C. Daradio and S. Jin, *Fundamental biomedical technologies, 16th ed.; Silva, G. A., Parpura, V., Eds.; Springer* **2012**, *2012*, 27-44.
- [3] G. M. Whitesides and B. Grzybowski, *Science* **2002**, *295*, 2418-2421.
- [4] a) S. Perween, B. Chandanshive, H. C. Kotamarthi and D. Khushalani, *Soft Matter* **2013**, *9*, 10141-10145; b) M. Reches and E. Gazit, *Current Nanoscience* **2006**, *2*, 105-111.
- [5] a) F. Chiti and C. M. Dobson, *Annual review of biochemistry* **2017**, *86*, 27-68; b) M. Jucker and L. C. Walker, *Nature* **2013**, *501*, 45-51.
- [6] R. Riek and D. S. Eisenberg, *Nature* **2016**, *539*, 227-235.
- [7] E. Gazit, *FASEB journal : official publication of the Federation of American Societies for Experimental Biology* **2002**, *16*, 77-83.
- [8] a) L. Niu, X. Chen, S. Allen and S. J. Tendler, *Langmuir : the ACS journal of surfaces and colloids* **2007**, *23*, 7443-7446; b) L. Adler-Abramovich, M. Reches, V. L. Sedman, S. Allen, S. J. Tendler and E. Gazit, *Langmuir : the ACS journal of surfaces and colloids* **2006**, *22*, 1313-1320.
- [9] M. Reches and E. Gazit, *Science* **2003**, *300*, 625-627.
- [10] a) Q. Li, H. Ma, Y. Jia, J. Li and B. Zhu, *Chemical communications* **2015**, *51*, 7219-7221; b) J. Castillo-Leon, R. Rodriguez-Trujillo, S. Gauthier, A. C. O. Jensen and W. E. Svendsen, *Microelectronic Engineering* **2011**, *88*, 1685-1688; c) G. Demirel, N. Malvadkar and M. C. Demirel, *Langmuir : the ACS journal of surfaces and colloids* **2010**, *26*, 1460-1463.
- [11] K. Biswas and C. N. R. Rao, *ACS applied materials & interfaces* **2009**, *1*, 811-815.
- [12] M. P. Conte, N. Singh, I. R. Sasselli, B. Escuder and R. V. Ulijn, *Chemical communications* **2016**, *52*, 13889-13892.
- [13] X. H. Yan, Y. Cui, Q. He, K. W. Wang and J. B. Li, *Chemistry of Materials* **2008**, *20*, 1522-1526.
- [14] C. Guo, Y. Luo, R. Zhou and G. Wei, *ACS nano* **2012**, *6*, 3907-3918.
- [15] C. H. Gorbitz, *Chemical communications* **2006**, 2332-2334.
- [16] E. Mayans, J. Casanovas, A. M. Gil, A. I. Jimenez, C. Cativiela, J. Puiggali and C. Aleman, *Langmuir : the ACS journal of surfaces and colloids* **2017**, *33*, 4036-4048.
- [17] a) C. Diaferia, E. Gianolio, P. Palladino, F. Arena, C. Boffa, G. Morelli and A. Accardo, *Advanced Functional Materials* **2015**, *25*, 7003-7016; b) V. Castelletto and I. W. Hamley, *Biophysical chemistry* **2009**, *141*, 169-174; c) N. Tzokova, C. M. Fernyhough, P. D. Topham, N. Sandon, D. J. Adams, M. F. Butler, S. P. Armes and A. J. Ryan, *Langmuir : the ACS journal of surfaces and colloids* **2009**, *25*, 2479-2485; d) N. Tzokova, C. M. Fernyhough, M. F. Butler, S. P. Armes, A. J. Ryan, P. D. Topham and D. J. Adams, *Langmuir : the ACS journal of surfaces and colloids* **2009**, *25*, 11082-11089.
- [18] G. Fichman, L. Adler-Abramovich, S. Manohar, I. Mironi-Harpaz, T. Guterman, D. Seliktar, P. B. Messersmith and E. Gazit, *ACS nano* **2014**, *8*, 7220-7228.
- [19] R. Orbach, I. Mironi-Harpaz, L. Adler-Abramovich, E. Mossou, E. P. Mitchell, V. T. Forsyth, E. Gazit and D. Seliktar, *Langmuir : the ACS journal of surfaces and colloids* **2012**, *28*, 2015-2022.
- [20] N. A. Dudukovic and C. F. Zukoski, *Soft Matter* **2015**, *11*, 7663-7673.
- [21] C. Diaferia, T. Sibillano, N. Balasco, C. Giannini, V. Roviello, L. Vitagliano, G. Morelli and A. Accardo, *Chemistry* **2016**, *22*, 16586-16597.
- [22] a) V. Castelletto, G. Cheng, S. Furzeland, D. Atkins and I. W. Hamley, *Soft Matter* **2012**, *8*, 5434-5438; b) I. W. Hamley, *Biomacromolecules* **2014**, *15*, 1543-1559.
- [23] M. J. Krysmann, S. S. Funari, E. Canetta and I. W. Hamley, *Macromolecular Chemistry and Physics* **2008**, *209*, 883-889.
- [24] V. Castelletto and I. W. Hamley, *Biophysical chemistry* **2009**, *141*, 169-174.
- [25] M. Sunde, L. C. Serpell, M. Bartlam, P. E. Fraser, M. B. Pepys and C. C. Blake, *Journal of molecular biology* **1997**, *273*, 729-739.
- [26] C. Diaferia, F. A. Mercurio, C. Giannini, T. Sibillano, G. Morelli, M. Leone and A. Accardo, *Scientific reports* **2016**, *6*, 26638.
- [27] J. P. Colletier, A. Laganowsky, M. Landau, M. Zhao, A. B. Soriaga, L. Goldschmidt, D. Flot, D. Cascio, M. R. Sawaya and D. Eisenberg, *Proceedings of the National Academy of Sciences of the United States of America* **2011**, *108*, 16938-16943.
- [28] S. R. Raghavan and B. H. Cipriano, *Weiss R.G. and Terech P. (eds.), Springer* **2005**, *Chapter 8*, 233-244.
- [29] *Moldenaers P. and Keunings R. (eds.), Elsevier* **1992**.
- [30] a) L. Adler-Abramovich and E. Gazit, *Chemical Society reviews* **2014**, *43*, 6881-6893; b) R. Orbach, I. Mironi-Harpaz, L. Adler-Abramovich, E. Mossou, E. P. Mitchell, V. T. Forsyth, E. Gazit and D. Seliktar, *Langmuir : the ACS journal of surfaces and colloids* **2012**, *28*, 2015-2022.
- [31] Z. Huang, C. Cheng, J. Wang, H. Wei, X. Liu, X. Yan, Y. Zhou, Y. Liu and S. Yang, *Cellular physiology and biochemistry : international journal of*

- experimental cellular physiology, biochemistry, and pharmacology* **2017**, *41*, 1572-1583.
- [32] N. A. Dudukovic and C. F. Zukoski, *Langmuir : the ACS journal of surfaces and colloids* **2014**, *30*, 4493-4500.
- [33] D. Zanuy, J. Poater, M. Sola, I. W. Hamley and C. Aleman, *Physical chemistry chemical physics : PCCP* **2016**, *18*, 1265-1278.
- [34] J. Huang, C. L. Hastings, G. P. Duffy, H. M. Kelly, J. Raeburn, D. J. Adams and A. Heise, *Biomacromolecules* **2013**, *14*, 200-206.
- [35] D. Siliqi, L. De Caro, M. Ladisa, F. Scattarella, A. Mazzone, D. Altamura, T. Sibillano and C. Giannini, *Journal of Applied Crystallography* **2016**, *49*, 1107-1114.
- [36] D. Altamura, R. Lassandro, F. A. Vittoria, L. De Caro, D. Siliqi, M. Ladisa and C. Giannini, *Journal of Applied Crystallography* **2012**, *45*, 869-873.
- [37] T. Sibillano, L. De Caro, F. Scattarella, G. Scarcelli, D. Siliqi, D. Altamura, M. Liebi, M. Ladisa, O. Bunk and C. Giannini, *Journal of Applied Crystallography* **2016**, *49*, 1231-1239.
- [38] D. Van Der Spoel, E. Lindahl, B. Hess, G. Groenhof, A. E. Mark and H. J. Berendsen, *Journal of computational chemistry* **2005**, *26*, 1701-1718.
- [39] T. Darden, D. York and L. Pedersen, *Journal of Chemical Physics* **1993**, *98*, 10089-10092.
- [40] B. Hess, H. Bekker, H. J. C. Berendsen and J. G. E. M. Fraaije, *Journal of computational chemistry* **1997**, *18*, 1463-1472.
- [41] W. Humphrey, A. Dalke and K. Schulten, *Journal of molecular graphics* **1996**, *14*, 33-38, 27-38.
- [42] a) A. Amadei, M. A. Ceruso and A. Di Nola, *Proteins* **1999**, *36*, 419-424; b) A. Merlino, L. Vitagliano, M. A. Ceruso and L. Mazzarella, *Proteins* **2003**, *53*, 101-110.